

ACS SYMPOSIUM SERIES 415

Spectroscopic Characterization of Minerals and Their Surfaces

Lelia M. Coyne, EDITOR
San Jose State University

Stephen W. S. McKeever, EDITOR
Oklahoma State University

David F. Blake, EDITOR
NASA—Ames Research Center

Developed from a symposium sponsored
by the Division of Geochemistry
at the 196th National Meeting
of the American Chemical Society,
Los Angeles, California,
September 25–30, 1988



American Chemical Society, Washington, DC 1990



Library of Congress Cataloging-in-Publication Data

Spectroscopic Characterization of Minerals and Their Surfaces

Lelia M. Coyne, editor, Stephen W. S. McKeever, editor,
David F. Blake, editor

p. cm.—(ACS Symposium Series; 415).

Developed from a symposium sponsored by the Division of Geochemistry at the 196th National Meeting of the American Chemical Society, Los Angeles, California, September 25–30, 1988.

Includes bibliographical references.

ISBN 0-8412-1716-5

1. Mineralogy, Determinative—Congresses. 2. Spectrum analysis—Congresses.

I. Coyne, Lelia M. II. McKeever, Stephen W. S.
III. Blake, David F. IV. American Chemical Society.
Division of Geochemistry. V. American Chemical Society.
Meeting (196th: 1988: Los Angeles, Calif.) VI. Series

QE369.S65S64 1989
549'.1—dc20

89-27755

CIP

The paper used in this publication meets the minimum requirements of American National Standard for Information Sciences—Permanence of Paper for Printed Library Materials, ANSI Z39.48–1984.



Copyright © 1989

American Chemical Society

All Rights Reserved. The appearance of the code at the bottom of the first page of each chapter in this volume indicates the copyright owner's consent that reprographic copies of the chapter may be made for personal or internal use or for the personal or internal use of specific clients. This consent is given on the condition, however, that the copier pay the stated per-copy fee through the Copyright Clearance Center, Inc., 27 Congress Street, Salem, MA 01970, for copying beyond that permitted by Sections 107 or 108 of the U.S. Copyright Law. This consent does not extend to copying or transmission by any means—graphic or electronic—for any other purpose, such as for general distribution, for advertising or promotional purposes, for creating a new collective work, for resale, or for information storage and retrieval systems. The copying fee for each chapter is indicated in the code at the bottom of the first page of the chapter.

The citation of trade names and/or names of manufacturers in this publication is not to be construed as an endorsement or as approval by ACS of the commercial products or services referenced herein; nor should the mere reference herein to any drawing, specification, chemical process, or other data be regarded as a license or as a conveyance of any right or permission to the holder, reader, or any other person or corporation, to manufacture, reproduce, use, or sell any patented invention or copyrighted work that may in any way be related thereto. Registered names, trademarks, etc., used in this publication, even without specific indication thereof, are not to be considered unprotected by law.

PRINTED IN THE UNITED STATES OF AMERICA

American Chemical Society
Library
1155 16th St., N.W.
Washington, D.C. 20036

In Spectroscopic Characterization of Minerals and Their Surfaces; Coyne, L., et al.; ACS Symposium Series; American Chemical Society: Washington, DC, 1990.

ACS Symposium Series

M. Joan Comstock, *Series Editor*

1989 ACS Books Advisory Board

Paul S. Anderson
Merck Sharp & Dohme Research
Laboratories

Alexis T. Bell
University of California—Berkeley

Harvey W. Blanch
University of California—Berkeley

Malcolm H. Chisholm
Indiana University

Alan Elzerman
Clemson University

John W. Finley
Nabisco Brands, Inc.

Natalie Foster
Lehigh University

Marye Anne Fox
The University of Texas—Austin

G. Wayne Ivie
U.S. Department of Agriculture,
Agricultural Research Service

Mary A. Kaiser
E. I. du Pont de Nemours and
Company

Michael R. Ladisch
Purdue University

John L. Massingill
Dow Chemical Company

Daniel M. Quinn
University of Iowa

James C. Randall
Exxon Chemical Company

Elsa Reichmanis
AT&T Bell Laboratories

C. M. Roland
U.S. Naval Research Laboratory

Stephen A. Szabo
Conoco Inc.

Wendy A. Warr
Imperial Chemical Industries

Robert A. Weiss
University of Connecticut

Foreword

The ACS SYMPOSIUM SERIES was founded in 1974 to provide a medium for publishing symposia quickly in book form. The format of the Series parallels that of the continuing ADVANCES IN CHEMISTRY SERIES except that, in order to save time, the papers are not typeset but are reproduced as they are submitted by the authors in camera-ready form. Papers are reviewed under the supervision of the Editors with the assistance of the Series Advisory Board and are selected to maintain the integrity of the symposia; however, verbatim reproductions of previously published papers are not accepted. Both reviews and reports of research are acceptable, because symposia may embrace both types of presentation.

Preface

THE EARTH CAN BE SEEN as a 2.5-billion-square-mile heterogeneous catalytic surface. Two thirds of this surface interfaces aqueous solutions, one third a gaseous one, and a small, but disproportionately important part of it cycles irregularly between liquid and gaseous interfaces.

The earth's crust is a mineral assemblage. Mineral-based assemblages, that is, soil systems, support our natural and cultivated vegetation, both physically and nutritionally. Fossil fuels, the mainstay of our physical and economic survival, were generated via mineral-catalyzed chemical reactions. The water we drink flows over and percolates through mineral assemblages. In bathing these assemblages, the sorptive and reactive powers of minerals purify this water of and contaminate it by the chemical products of geology, biology, agriculture, and industry.

Unlike laboratory chemistry, geological chemistry occurs in thermodynamically open systems. That is to say, there is flagrant exchange of materials and energy between the system and the environment. Not only is the system as a whole not isolated from the environment, but the materials of interest are rarely isolated from each other. To further the complexity, interaction of mineral catalysts with those forms of energy most likely to affect surface-mediated reactions has barely been characterized in model systems.

The chapters in this volume have been collected in order to chart a course toward a more holistic, thus more realistic, view of mineral reactivity than can be garnered from equilibrium modeling. Spectroscopies are the tools by which structure, dynamics, and reactivity can be most directly examined. Examples include numerous means of mineral spectroscopy applied to numerous ends, such as determination of composition, purity, interaction with energy, characterization of chemically and spectroscopically special (active) centers, and adsorbate interactions. Coverage of both spectroscopy and minerals is intended to be illustrative, not exhaustive.

The initial chapters on nonoptical methods are supplied as instruction in how to describe a mineral and its surface before studying it. A distinction is made between bio- and geominerals because they are not equivalent, despite identities of their chemical formulae and crystal

structural parameters. The focus on energy storage in part two is meant as a word to the wise for those serious about consideration of the surface loci suspected of directing interfacial chemistry, lest they forget bulk influences.

In the face of all wisdom concerning choice of models, the section on active centers takes clay as a model, the mineral class that is most, rather than least, complex. Clays happen to be the mineral class most studied with respect to natural reactivity. They are among the more important classes of minerals reactive in natural systems, and they are known to include most of the generic site types thought to be influential in mineral interfacial chemistry. A special emphasis is placed on acidic and oxidizing entities because of their importance and because evidence is accumulating to indicate that they are interrelated.

It is hoped that this book will stimulate new thinking and new methodologies, and new integrations of these by physicists, chemists, geologists, and fuel, soil, agricultural, and environmental scientists who are interested in interfacial chemistry of geological surfaces. It is also hoped that it will prove useful to catalysis chemists humble enough to acknowledge that Nature may have used a few reactive tricks they've missed.

We can use our knowledge of the earth to achieve the crucial goal of stabilizing our environment, thus allowing us to develop a sensible policy for the management of energy. Realistic energy management would permit the development of a more sensibly based economy, of which one reward could be resources for further exploration. Many of us would like to see that exploration move from the terrestrial to the extraterrestrial realm, and spectroscopy can serve as a central tool in this search. We believe the approach outlined here will permit us to begin that search.

LELIA M. COYNE¹
Department of Chemistry
San Jose State University
San Jose, CA 95192

STEPHEN W. S. MCKEEVER
Department of Physics
Oklahoma State University
Stillwater, OK 74078-0444

DAVID F. BLAKE
Planetary Biology Branch
NASA-Ames Research Center
Moffett Field, CA 94035

April 18, 1989

¹Current address: Mail Stop 239-4, NASA-Ames Research Center, Moffett Field, CA 94035

Chapter 1

Spectroscopic Characterization of Minerals and Their Surfaces

An Overview

Lelia M. Coyne^{1,3} and Stephen W. S. McKeever²

¹Department of Chemistry, San Jose State University, San Jose, CA 95192

²Department of Physics, Oklahoma State University,
Stillwater, OK 74078-0444

The lithosphere is both literally and figuratively the bedrock, the solid foundation, on which understanding of geology rests. To characterize the lithosphere is to characterize not only what is, but, because of the chemical reactivity of rocks and their surface activity, it is also to characterize what was and what may become.

The first step in such a characterization process is to identify the mineral type(s), in terms of crystal structure and elemental composition. Although this information may be adequate to define what is, and to a significant degree what was, it is far from adequate to project what might become. To move toward a more predictive, rather than simply a naturalistic geology, it is essential to understand the details of chemical structure at the electronic level as well. To understand the reactions mediated by mineral surfaces it is not adequate to know the details only of the overall atomic arrangement. It is essential also to grasp the subtle, sometimes not so subtle, variations in structure and properties that can be produced by chemical alteration of a few special structural moieties, by introduction of defects (extended and point), and by interactions not only of the bulk structure, but also of these occasional centers, with energy sources. In addition, it must be constantly born in mind that the electronic structure of the surface and the bulk, while related, are far from identical, because of the termination of long-range structure at the surface. The surface of a mineral is activated relative to its bulk both chemically and electronically. To sketch the process of characterization of bulk and surface chemical and electronic structure of minerals and interrelationships between their bulk and surface properties is the purpose of this volume. The utility of such detailed characterization will become

³Current address: Mail Stop 239-4, NASA-Ames Research Center, Moffett Field, CA 94035

0097-6156/90/0415-0001\$08.25/0
© 1990 American Chemical Society

increasingly appreciated as the role of soils in environmental stability or degeneration becomes more widely recognized and better understood.

The introductory chapter and the book itself is organized around three ideas: What is the chemical structure? What is the electronic structure? What governs the surface chemical reactivity? of minerals.

The first major section of this overview will be devoted to general spectroscopic characterization with particular application to minerals. Source material on spectroscopic theory, methods and applications used in the subsequent papers will be provided in the initial paragraphs as an introduction or review. A focus will then be placed on those aspects of spectroscopy allowing investigation of the alteration of minerals by excitation, energy storage and energy transfer. These alterations occur primarily via the production of metastable excited electronic states. Such alterations may be familiar to mineralogists within the confined context of mineral spectroscopy and dating, but possibly have not been adequately appreciated with respect to their possible significance to reactivity on mineral surfaces. In connection to the degree to which excitation of minerals may alter their surface reactivity, there will be a mention of infrequently considered energy sources and the means, consequences of, and efficiency of excitation by these sources. Reference will be made to the extent to which the quantitative theory of the detailed process and degree of electronic excitation of minerals and their defect centers has not been sufficiently developed to enable useful estimations of the chemical utility of electronic excitation, particularly by non-optical energy sources.

The second major section will focus on those special centers of minerals thought to be of importance to their catalytic activity, with an emphasis on the known and possible effects of electronic excitation on the population and mode of action of these centers. Metastable states constitute a hidden variable in defective solids, a non-negligible one for non-stoichiometric ones. With regard to concepts of mineral catalysis, the only systems for which extensive spectroscopic information on mineral catalytic centers has been definitively coupled to the mechanism of a well understood surface chemical reaction is H_2/D_2 exchange on binary oxides. Existing data for the radiatively-produced catalytic center of SiO_2 will be reinterpreted and that for the thermally-produced center on MgO will be further assessed in terms of mineral structure in the second section of this overview. The MgO -promoted exchange proceeds via classical catalysis. The silica-promoted exchange proceeds only via electronic excitation of the catalyst and probably involves a one:one stoichiometric relationship between catalytic centers and exchanged product. Interestingly, in the light of this contrast is the fact that the catalytic centers of the two materials are closely chemically and electronically related.

Both these catalytic centers and the reaction mechanism on them have been better than average well-characterized by the spectroscopic methods discussed and applied in this volume. The comparison between anticipated locations of the catalytic centers for these materials also points up the importance of methodology for determining not only the number, but the accessibility of catalytic sites. Therefore, it is thought that comparisons and contrasts between thermal and "photo" chemistry, as well as many aspects of the state of present comprehension of mineral spectroscopy and mineral-mediated catalysis will be well-illustrated by a reexamination of published studies of H_2/D_2 exchange, even though this reaction is not directly relevant to applications of spectroscopy discussed in the succeeding papers.

Use of Molecular Spectroscopy to Study Bulk and Surface Electronic Structure, Energy Transfer and Storage Processes of Defined Mineral Phases

Spectroscopy is the experimental tool for the determination of chemical and electronic structure. General discussions of electronic structure can be found in (1-2), of inorganic molecular structure in (3-7) and discussions more particularly directed to that of minerals in (8-10). Discussions of spectroscopic theory and measurement techniques must, of course, be governed by the region of the electromagnetic spectrum or the particle energy distribution required to excite and/or detect the transitions of interest, given a specific material. Numerous spectroscopies were employed in the specific applications detailed in the following chapters of this book. General introductions to various spectroscopies are found in (11-12), of NMR in (13-14), of ESR in (15-16), IR in (17-18), vis/uv absorption in (19-20), luminescence and thermoluminescence in (21-23), vacuum uv in (24), electron, X and gamma-ray spectroscopies in (25-27), Mossbauer in (28). Applications of these methods specifically to minerals may be found in (29-32) and to clay minerals, in particular, in (33).

Spectroscopy is also extensively applied to determination of reaction mechanisms and transient intermediates in homogeneous systems (34-37) and at interfaces (38). Spectroscopic theory and methods are integral to the very definition of photochemical reactions, i.e. chemical reactions occurring via molecular excited states (39-42). Photochemical reactions are different in rate, product yield and distribution from thermally induced reactions, even in solution. Surface mediated photochemistry (43) represents a potential resource for the direction of reactions which is multifaceted and barely tapped. One such facet, that of solar-excited electrochemical reactions, has been extensively, but by no means, exhaustively studied under the rubric photoelectrochemistry (PEC) (44-48).

Special Considerations in Spectroscopic Studies of Mineral Structure and Energetics of Importance to Surface Chemistry

Form, Impurities and Imperfections. Minerals, being natural materials, may be selected, but not delimited by the investigator. Also, a large specific surface area is important to efficient heterogeneous catalysis. Therefore, the most notable minerals driving chemistry in geological settings frequently do not present themselves in forms readily amenable to spectroscopic examination. I.e., the minerals of surface chemical interest in geology and biology typically are not large, optically transparent, single crystals that are brilliantly colored by transition metal substituents, or artistically tinted by an occasional single type of point defect, or ionic substitution. They tend to be defective, even poorly crystallized, finely divided, high-bandgap photoconductors. They typically are not pure compounds, intrinsically, due to non-stoichiometry from inherent structural substitutions and inclusions, and extrinsically, due to mineral admixing and adsorbed organics. They are the sedimentary and soil binary oxides, hydroxides, oxy-hydroxides, silicates, aluminosilicates (the clay minerals prime among them), carbonates, sulfates, sulfides, phosphates. They support (49), may have spawned (50-51), planetary life. Characterization of their elemental composition, crystal structure and dynamics offers a difficult, but not insuperable aesthetic and intellectual challenge.

Environmental History. The complexity of their makeup might seem adequate deterrent to their systematic analysis of minerals, but, in addition to their makeup, crustal minerals bear an experience. In anthropomorphic terms, their "behavior" (properties) derives from both a "heredity" (composition and structure) and an

“environment” (geological milieu). I.e., they have been, and are continually being subjected to thermal, mixing, mechanical, chemical and radiative alterations. Spectroscopy can be applied not only to mineral structure determination, monitoring of surface-adsorbed reactants and products and reaction kinetics, but also to the production and monitoring of excited states of the mineral which may produce a different type of reactivity than the ground state substance.

The most likely of the environmental variables to be significant both to spectroscopic features of the mineral and to reactivity under geological conditions, but the one least often considered, is electronic excitation, both past and ongoing. Because of the high energies required for excitation, e.g. 8.5 e.v. for silica (52), of many of the important crustal materials, and the very high absorptivity for allowed transitions in the solid state, solar illumination is an efficient energy source for electronic excitation only for near-surface phenomena. More transmissible energy sources are required if the entire regolith is to be used as an active surface but more transmissible energy sources are available in natural systems. Their contributions to natural chemistry must also be assessed.

Whereas gamma irradiation is a low level energy source at present, gamma and particle fluxes were higher in earlier times (53). Furthermore, since the capacity of many minerals for long term electronic energy storage (23, 31) is significant in “molar” terms (54), a low level source operating over a long time period can produce significant residual excitation.

A possibly more abundant, on-going, energy source for mineral excitation is mechanical stress, producing friction or fracture. Such operations have been shown to excite very high energy transitions in organic materials and adsorbed atmospheric gases (55-56). Minerals, too, produce light when rubbed or fractured (57-58), but with them it is less apparent whether the mechanical stress is the immediate source of excitation, or whether it has triggered the release of previously-stored energy (54), or has mobilized trapped molecular fragments (59), which combine and emit light.

Another environmental factor of prime importance is weathering, i.e. cyclic exposure to water, atmospheric gases, temperature variations, abrasion. These natural processes produce alteration of the surface composition and introduce point defects which have special adsorptive and energetic properties.

Catalytically active defects of both radiation-induced and formation or “weathering-like” origins will be exemplified in the sections on H_2/D_2 exchange on simple binary oxides. This reaction will be considered in detail because it is the simplest possible chemical reaction and the mineral sites producing it have been the best characterized by spectroscopic techniques.

Mineral Sensitized Chemistry - Natural Routes to Organic Synthesis

Because minerals can be electronically excited under common geological conditions and can, to varying degrees, store energy, it is necessary at the outset to consider any mineral-mediated reaction occurring under natural conditions as possibly “photo”-catalyzed or “photo”-assisted over and beyond its activity as a classical catalytic surface or source of reactants. For minerals storing appreciable amounts of electronic excitation, a similar statement may apply to reactions studied in the laboratory. Conversely, exposure to radiation can also serve a surface deactivating or protecting role, depending on the nature of the chemical entities involved.

Contrasts Between Organic and Mineral Sensitized Photochemistry. Organic photochemistry in homogeneous solution (direct and sensitized via energy transfer from another molecule) is a highly developed field (e.g. 39-42). However, sensitization of the same organic reactions via mineral surfaces might be expected to proceed by very different routes than via other dissolved organic molecules. This is because the reactions are interfacial and because mineral sensitizers undergo different modes of excitation and energy transfer than do organic molecules, which in their solid phase tend to form molecular, rather than the more ionic mineral crystals. Most notably, in minerals, excitation can be transported via mobile charges, as well as photons. Because of their capacity for charge separation, minerals can store electronic energy.

A more detailed description of the electronic basis for, and some possible consequences of, these differences between mineral and organic photosensitizers is summarized in the following four paragraphs.

Excitation and Energy Transfer. In organic (molecular) crystals, excitation traverses the crystal via excitons (60) i.e. coupled movement of electrons and holes. In minerals, also, excitons can be created, either directly, by the absorption of an amount of energy less than the band gap (because of the mutual coulombic attraction that exists between the electron and the hole), or indirectly, by the formation of free electrons and holes which subsequently associate to form the exciton. The binding energy is typically of the order of 0.1 eV and dissociation lifetimes as small as 10^{-11} - 10^{-12} s (due to thermal promotion to the conduction band) can be expected in most insulating systems at room temperature. Nevertheless, the exciton mobility in minerals is extremely high and energy migration via exciton diffusion can take place over distances of several hundred angstroms (61). In some systems longer exciton lifetimes and higher mobilities can result in exciton diffusion over millimeters at certain temperatures (62).

By contrast to that of molecular crystals, the excited state structure of most minerals is sufficiently ionic that the electron/hole pair produced by excitation not only can migrate via excitons, as described above, but is, in addition, capable of being separated into independently mobile charge pairs. Separated electron/hole pairs have considerably longer intrinsic lifetimes than do coupled ones and thus can move through the bulk and to the surface over much greater distances than can excitons. Thus the effects of electronic excitation of a mineral can be expressed over longer ranges and in terms either of independent, or coupled charges. For instance, a reactive adsorbate may intercept an excitation in the form of a charge, rather than as a photon. The interconvertibility of photons and charge pairs in these materials is certain to be of importance in the nature of their interfacial properties. Whether any given sensitized reaction would proceed via electronic excited states or via radical or charged intermediates is not predictable in general terms.

Relaxation and Energy Storage. The other crucial distinction between minerals and organic molecular crystals is in the capacity for long-term electronic energy storage. Because of separation of the charge pairs mobilized by excitation, these pairs may be more efficiently trapped than recombined, if the trap density and energetics are favorable. Relaxation of an excited mineral crystal may take place radiatively and vibrationally, as in molecular crystals, but also by charge recombination. Recombination may, in itself, be a radiative process, and, if preceded by trapping, may be delayed by as much as centuries from the original excitation.

One key structural factor in the capacity for energy storage, particularly in such non-stoichiometric minerals as clays, is the prevalence of point defects. Neutral, charge deficient, or charge excess ionic substitutions, insertions, or displacements within the crystal structure are rife. Isomorphic (same shape, equal, or smaller size) substitution, or molecular displacement, in a molecular crystal is significantly more difficult to achieve. In silica, for instance (both crystalline and amorphous) Al is frequently found in Si sites (23). Other common types of traps result from either cation or anion vacancies. Extended defects, like steps and kinks (6) are also observed. Since charges produced by excitation can be separated, minerals can independently trap the electrons and holes in defect centers at appreciable distance from each other. The effect of this trapping is storage of some fraction (depending on the energy excess between the energy of an exciting photon and the bandgap of the crystal and the means by which this excess is dissipated) of the energy of an exciting photon as one (or more) separated charge pairs. Light, heat, mechanical stress, or electric fields can trigger the release of these trapped charges, producing long-delayed recombinations, some of which may be radiative (5-7, 23, 31).

Mineral Energetic Factors in Surface Chemistry. Minerals promote surface reactions of importance to geology, agriculture and environment by a number of means. They serve as adsorptive surfaces, classical catalysts and reservoirs of reactants. Some more complex aspects of the roles of mineral surfaces in natural chemistry are poorly understood and frequently not even generally appreciated. A defective solid typically is energetically "activated" relative to a perfect crystal in a manner analogous to the previously-mentioned activation of the surface relative to the bulk. In addition, electronic excitation can be stored in defect centers activating them still further, relative to a perfect infinite crystal. Trapped charges may, in themselves, serve as adsorptive or catalytic centers in addition to sites characteristic of the basic structure. They may affect the overall facility of charge transfer between adsorbate and catalyst and may constitute an energy reservoir, or a blocker of excitation transfer. Defect centers, represented by localized interspersed states in the overall electronic energy-level diagram, may also intercept or contribute charges, even independent of band gap excitation of the material. The utility of defects or their detriment to surface chemistry, whether in the presence or absence of energy sources, has not been adequately assessed. All aspects of these relationships are amenable to spectroscopic characterization.

Mineral Energetic Factors Expected to Influence Organic Surface Reactivity Using Clay Minerals as Examples

Despite their overawing complexity, clay minerals are to receive particular emphasis in this book as model systems. They are of high abundance and of key importance in sedimentary and soil systems (63-64), as ceramic materials (65) and as industrial fillers (66); they exhibit essentially all of the generic spectroscopic and surface chemical properties of reactive minerals in general; and there are good reasons to believe that many of the spectroscopic and chemical attributes of minerals as a whole may be exaggerated in clays.

For instance, clays are of particular interest with respect to energy storage, because of the frequency and variety of isomorphic, positive charge deficient, cation substitutions. These result in significant numbers of stable hole trapping sites (67-68). The fate of the associated electrons in clays is more speculative (69-70). They

may remain trapped in various adventitious electron trapping sites or emitted as exoelectrons. In the latter case, some effect might be expected on the cation exchange capacity. The energy storage capacity of these and other non-stoichiometric minerals, judged simply on the basis of their molecular equivalent formulas (71-72), is of the order of milli-molar (mM) in 1:1, and nearly molar (M) in 2:1 clays.

In addition to the high density of isomorphic substitutions, clays have several other important features which would tend to maximize the possibility of contributions from energy storage to their surface chemistry.

- a. The energy of band-to-band excitation in clays is expected to be very high (of the order of 8 eV or more by analogy to substituted silica and alumina), so the energy of the stored photon, even degraded by the trapping process, can be large compared to the energy of chemical reaction on a photon/bond energy basis.
- b. Also due to the lattice charge deficiency (71-72) and the space-charge potential (5-7, 44-48), a high emf is expected to exist between surface and interior ions. This electrical potential would aid in separating charge pairs during excitation of the material, thus promoting migration and trapping, rather than instantaneous recombination. Despite the photoconducting electronic energy structure of these materials, excitation typically does not efficiently produce spatially separated electron/hole pairs without such an electric field (73).
- c. Due to the intrinsically small particle size of clays, this emf would also be expected to connect surface and structural electronic states more or less throughout the material. Surface reactivity can thus be influenced by the bulk-stored energy.
- d. Due to the afore-mentioned interconvertibility of light and charge, there exists a natural means of energy conversion by clays which may involve acceptable, perhaps even desirable, energy degradation in the transformation process.

Experimental data from various sources would give reason to believe that the capacity to store energy is realized to a significant degree in nature. Three examples are cited. First, ESR studies of natural and synthetic x-irradiated kaolinites by Angel, et al. (67) have demonstrated the presence, as O^- -centers, of up to 10^{19} spins per gram ($\sim 2 \times 10^{21}$ per gram equiv. formula weight) after modest irradiation. This concentration is comparable to the number of isomorphic substitutions judged on the basis of a typical kaolinitic cation-exchange capacity (54) of 2-10 meq/100 gm, i.e. $\sim 2-10 \times 10^{21}$ isomorphic substitutions/gram equiv. formula weight. Secondly, studies of the magnetic susceptibility of natural montmorillonites have demonstrated a susceptibility which is in excess of that accounted for by the content of paramagnetic ions. The excess susceptibility shows a relationship to the expected relative stability of trapped holes (69). Probably also related to energy storage, is the observation that measurements of the relationship between the change in layer charge and the degree of reduction of structural ferric iron in montmorillonites (reviewed by Stucki and Lear in Part III of this volume) have shown considerable discrepancies between measured and predicted values. These may well be explainable in terms of charge exchange between O^- -centers, structural iron and possibly other species, as yet unidentified.

Some Important, Unsolved Problems In Mineral Energetics

Consideration of the importance of electronic excitation to mineral surface chemistry is impeded by deficiencies in our understanding of the interactions between the electronic structure of minerals and those energy sources having adequate energy and transmissibility to excite them appreciably. There exist only the rudiments of theories to express how mechanical stress excites electronic transitions (74). Excitation by penetrating radiation, such as gammas, is, on first thought, better understood, but on deeper inspection presents its own uncertainties. For example, Cuttler (75) has given a thorough estimation in terms of the atomic density, the energy of excitation of the inner shell electrons and the x-ray flux, of the expected x-ray dose required to saturate the isomorphically substituted centers in a typical kaolinite.

However, alternatively, the interaction with energy can be considered to be with the electronic energy structure of the crystal as a whole, rather than with individual atoms. An estimate by Coyne (54) based on experimental data for silica (73), assuming similar charge pair production by an equivalent gamma dose in clays and silica, gives a saturating dose nearly two orders of magnitude lower. The Coyne model is based on two assumptions: excitation into the molecular band structure of the material, rather than into its atomic energy level manifold; and efficient funnelling of excitation of the bulk crystal into the trapping centers. This model bears strong resemblance to that of photosynthetic systems where light is harvested by an antenna pigment system and is directed into reaction centers (76). The mineral model differs from the photosynthetic one mainly in that charge separation in photosynthetic systems takes place after trapping (via an electron transport chain), whereas, in minerals, it is intrinsic to the mineral defect structure itself.

Both atomic and molecular excitation/relaxation phenomena must be operative, but the true relative efficiencies of excitation in these modes, and transfer of energy between them, are not well-delineated. Understanding such distinctions will be crucial, ultimately, in estimating energy fluxes in geological settings and in assessing their effectiveness in mediating chemistry.

Summary

In theory, the electronic energy structure of minerals is well-understood, at least in general terms. The practice of spectroscopy is kaleidoscopic in its variability of investigational patterns. Energy storage is likely to be an important factor in crustal mineral surface chemistry, as are solid state effects resulting from small particle size and defect structure. Interactions between minerals, adsorbed reactants and energy sources are inadequately understood in terms of the well-articulated principles of solid state physics. The reactivity of mineral surfaces is empirically well-documented, but inadequately systematized. It is hoped, by bringing together insights from surface chemical studies, spectroscopy and solid state theory, that investigational strategies for studies of geological surface chemistry can be moved into an area more dynamic (and more realistic) than equilibrium interfacial modelling.

The Role of Special Structural Entities - Active Sites - in Mineral-Mediated Chemistry

A primary goal of this volume is to outline strategies by which mineral spectroscopy can be used to elucidate mineral-mediated reactions. The chosen articles do directly

address this issue in terms of modern methods and theory. However, nowhere, more than in the study of heterogeneous catalysis, particularly in natural systems, does the parable of the blind man and the elephant seem more apt for describing the status quo.

An extensive literature search has revealed the existence of much excellent, well-described, theoretical and experimental work. In spite of this, the needed systematic studies have yet to be performed and pulled together in order to fully explain even an academic reaction (H_2/D_2 exchange) on a simple catalytic mineral surface (SiO_2) in terms of long known general physical principals (e.g., collision theory, transition state theory, electronic structure of ground and excited states) or familiar chemical concepts (e.g., adsorption, diffusion, acidity, redox potential). It is strongly suggested that missing links, essential to concept synthesis are due consideration of electronic energy storage and bulk to surface charge gradients resulting from solid state effects at interfaces.

The content of this section of the overview chapter will be more problem, than solution, more approach, than summary, oriented. The goals will be to:

1. Outline the problems of studying mineral chemistry in general terms and in terms of those structurally-based properties and entities which mediate surface reactions;
2. Reference some well-established methods of investigation and examples of their application;
3. Point out some areas of ambiguity in present-day concepts and nomenclature;
4. Use published data concerned with H_2/D_2 exchange on binary oxides to update current insights regarding reaction-promoting active sites on mineral surfaces and their modes of production;
5. Encourage investigators to work more as a community to standardize approaches and descriptions to a sufficiently high degree that the results from one application can be melded with and/or applied to others;
6. Assure the community that the needed theory and experimental approaches are available, but need to be brought together from those scattered disciplines requiring similar materials information and expressed in mutually useful terms.

Mineral Catalysis: Applications and Mechanisms

Industrial (77) and natural reactions, such as petroleum and coal formation (78-79), needing catalysts are multitudinous. The literature postulating mechanisms by which catalysts are alleged to promote these processes is voluminous. In some cases, these allegations even provide semblance of predictability, particularly for metal catalysts where the reactive surface can be modelled using large single crystals. For metals, structural features, including generic imperfections, can be detailed using surface spectroscopies (80-82). There is also a massive body of data and theoretical calculations concerned with detailed design of zeolite catalysts (83), also heavily used in industry.

Clay minerals and their substituent oxides will be emphasized here. Clays are among the most important natural catalysts (63-64, 84-86). Zeolites, clays and a few substituent binary oxides of clays, namely SiO_2 , Al_2O_3 , MgO , CaO , TiO_2 , and Fe-oxides and hydroxides are among the best characterized mineral catalysts, in spite of

the fact that, in industrial practice, clays and metal oxides, except for iron oxides, typically are considered to be "inert" supports, or fillers for more active catalysts (66, 87). In spite of this bias, non-transition metal oxides such as alkali-activated CaO or MgO are powerful catalysts for controlled partial oxidation of methane to methyl alcohol and Ca-doped MgO is being used as a catalyst in automotive exhaust converters. Zeolites, which are framework, rather than layered aluminosilicates, and the binary oxides are better analogs of naturally occurring reaction-promoting minerals than are metals. For these analogs, performance is less likely to be complicated by the action of impurities and electronic energy storage than for natural materials. However, they must be contrasted, as well as compared with clays and other natural minerals, because, as mentioned earlier, soil minerals have a number of unique features which may well set them apart from other materials.

Heterogeneous promotion of chemical reactions can be achieved by various devices. These can be divided into such general classes as:

1. **Selection** of the desired reactant from an ensemble of undesired reactants (81, p. 382, 49);
2. **Concentration** of a selected reactant (relative to the product) so as to favor the forward reaction by the law of mass action (49);
3. Increasing the rate of the reaction by **increasing the frequency** of reaction-promoting contacts, or **favorable orientation** of reactants (88);
4. Increasing the rate of the reaction by **lowering the energy barrier** to reaction (82, p. 309);
5. **Sensitization** (reaction mediated via energy transfer) of "photochemical" reactions. ("Photochemistry" is used here in the broadest sense to include reactions produced via excited states and leading to non-thermodynamic product distributions, regardless of whether the excitation is produced via optical photons or alternative excitation sources.);
6. **Stabilization** of desired products in the given environmental milieu (66, chapter 5.4.3).

The theory underlying influences 1) and 2) is that of adsorption. General discussions of this theory can be found in (89). The theory of 3) and 4) was articulated by Arrhenius, and has been developed to include the concept of a transition state, intermediate between products and reactants. The theory of reaction kinetics is summarized at an elementary level in (88, 90-91) Theories of energized surface chemical reactions, 5) of which PEC is the best developed (44-48) are relatively recent, and can not be considered to be complete. Stabilization by surfaces, 6) is an empirical concept, for which no general theory has been developed, nor may even be possible.

Typically, the formal study of catalysis has focussed on 3) and 4), but these processes are of no greater intrinsic importance than are the others in achieving a resultant product distribution in a given natural setting. For instance, the credibility of scenarios presuming to rationalize such significant events as the emergence of life from the chemical assemblage of the primitive earth rests largely on the effectiveness of 1), 2), and 6). For some decades, the atmospheric discharge models of Oparin (92), experimentally developed by Miller and Urey (93) and the more geochemically pertinent one of Haldane (94), experimentally developed by Calvin et al. (95), have

dominated alternative models of the prebiotic formation of biologically significant molecules, such as amino acids and nucleotide bases. These molecules are proposed to have rained into the prebiotic oceans in which they were oligomerized and self-organized. More recent speculations have implicated the participation of mineral surfaces and cyclic reaction conditions in selection, concentration and oligomerization (49, 96-98), self-organization of systems of oligomers (99), and possibly monomer syntheses as well (100-101), thereby spawning a variety of models, e.g. (96, 98, 102-106) which are, geochemically, at least equally compelling.

Structural Determinants of Catalytic Activity

Experimental development of the theory of reaction mechanisms has been substantially focussed on lowering of the activation barrier. It was first proposed by H. S. Taylor (107-108) that this might be achieved by special adsorptive sites. The concept of active sites has been a highly productive one in understanding biological catalysis by coenzymes and enzymes (109-110). Work with coenzyme models of Vitamin B₁₂ (111) have demonstrated conclusively that it is the variable oxidation states of the central cobalt ion that control the catalysis. A variety of ligands stabilizing Co in each of its I, II and III oxidation states can be substituted for the natural corrin ring. In a protein, very simple compositional changes can seriously disturb or destroy its biological activity. E.g., the genetic disease sickle cell anemia, is caused by a deficiency of the oxygen-transporting protein, hemoglobin. It occurs when only one amino acid residue of the heme protein (which contains the oxygen-binding iron porphyrin) is altered (109, p. 335). Tests of the catalytic activity of isolated active sites of proteins appear not yet to have been undertaken, even though many active sites have been characterized and peptide synthesis methods are available.

Association of isolated structural moieties with reaction promotion by minerals was predicted, (102), but would not be expected to be so generally successful, because minerals, being considerably more ionic than are proteins, thus capable of conducting both charges and energy from the bulk to the surface, would thus be expected to interact more holistically. This is to say that a) the properties of the surface are intimately associated with the properties and condition of the bulk; and that b) the surface, as a whole, will have activity, to some degree, over and above that of specific surface structural entities; and that c) the action even of special surface structural entities will be influenced by the properties and condition of both surface and bulk. In particular, surface charge transfer properties of mineral catalysts are expected to be strongly affected by electronic and energetic factors in the bulk mineral.

Even so, it is clear that certain structural features and special entities do influence catalysis by mineral surfaces, as well. The most common means by which they operate fall into four general classes, three of which have been extensively investigated. Covalent linkages in clays are less common than the others, being dependent on grafting to SiOH, which entities are not numerous in clays (10).

- a. Geometric by means of which reactants are selected and/or oriented by complexation, or size exclusion.
- b. Acid/base
 - i. Protonic (Bronsted), H⁺, OH⁻ donation.
 - ii. Aprotic (Lewis), electron pair acceptance, donation.

- c. Redox, electron/hole donation, acceptance.
- d. Covalent, electron pair sharing.

Geometric. Clearly the means by which geometric influences are produced may involve b-d, but it is important to distinguish classes of sites in which size exclusion or substrate orientation effects dominate substrate/catalyst bonding interactions.

Clay minerals and zeolites are interesting with respect to possibilities for **geometric influences**. Activation can be produced, as in enzyme catalysis, by constraining the reactive molecule, via surface complexation, in a configuration in which it is destabilized relative to that of the free molecule, yet still accessible to other reactants. A possible example is hydrazine complexed with kaolinite. The conformation of hydrazine is flattened relative to that of the free molecule (See Cliff Johnston's paper in Part III of this volume). It has been shown that hydrazine is readily air-oxidized by kaolinite (Coyne, submitted for publication).

Reactions can also be controlled geometrically by altering the space available for them. Zeolites, with their 3-dimensional framework structure and consequent structural cavities, have been tailored for size exclusion to a remarkable degree, e.g. (83). Clays, on the other hand, being layered, rather than framework, present a two-dimensional adsorptive sheet, convenient for polymerization reactions, among others. The spacing between sheets constrains the degree to which large molecules may adsorb end-on, or must lie flat on the surface, as measured by exchange with alkyl ammonium groups and XRD (113-114). A number of factors determine the "swelling", i.e. interlayer spacing, first of all, the layer structure itself (71-72). 2:1 clays, having two adjacent silica layers "swell" much more freely than do 1:1 clays for which the adjacent silica and aluminum hydroxide layers produce sufficiently strong layer/layer interaction that only a relatively few intercalating agents can separate them at all (86, 115). Therefore only the 2:1 clays are considered to be swelling. For these, the primary factors in the swelling, which can alter adsorbate configuration by adjusting interlayer spacing, derive from the type and condition of exchangeable cations, summarized below.

Due to charge deficient isomorphous structural cation substitutions, clays, like zeolites, have charge-compensating exchangeable cations. The type, number, distribution and environment of these cations powerfully affects clay swelling properties. Effects of cation charge and ionic strength of surrounding aqueous solution are discussed in (116) and references herein, of cation coordination in (117), of density and tetrahedral vs. octahedral location of substitution in (118-119), of hydration in (120-122), of solvent in (123) and of replacement of soluble ions by robust, immobile pillars in (85, pp. 311-314). The topic of clay swelling has been recently reviewed in (86).

In 1979, Low, et al. (124) introduced the concept that the swelling distance was controlled primarily by interactions of the layers between themselves or with interlayer water rather than by the ion gradient between the interlayer and external bulk water. This concept has been vigorously developed and defended in subsequent work, e.g. (125). It has not found general acceptance because spectroscopic studies show no long range perturbation by the surface on the water frequencies (120-121). It is the opinion of this author, who has observed ultraviolet luminescence from 1:1 clays (which have low levels of exchangeable cations) at a critical moisture content representing many 10's of molecular layers of water (126-127) that this controversy

has yet to reach final resolution. Admittedly, the interactions producing luminescence are inter-particle rather than interlayer and attraction between kaolinite particles would be expected to be influenced by the presence of both oxygen and hydroxyl surfaces, but some structural and energetic features of these different clays are in common.

The exchangeable cations can exert geometric effects over and above their influence on swelling. Surface complexation, generally thought to be stronger than that occurring directly with the silicate surface (86, p. 395), is possible with the exchangeable cations of clays and zeolites. Particularly when the exchangeable cations are made up of transition metals agents, selective adsorption by complexation can be achieved to a high degree. The biologically significant 3'-5' nucleotide bases have been complexed with order of magnitude selectivity over the 2'-5' isomers on Zn-catalyzed montmorillonites (128). Unpublished work of Lawless and Levy has indicated that possibly a similar situation exists for selection of the biologically significant alpha amino acids on Cu-exchanged clays. Copper-catalyzed deamination (129) may be in part responsible for uncertainties in these results. Mortland (129) has developed the concept of enzyme mimetic catalysis on clays using a copper exchanged montmorillonite as a protein substitute in conjunction with a coenzyme, pyridoxyl phosphate.

Protonic Acid Sites. Numerous reactions, e.g. (66, 84) are pH sensitive, i.e. many classes of reactions are catalyzed by protonic acids and bases. There are various sources of **protonic, or Bronsted acidity** of binary oxides. Oxides have been classified to be intrinsically acidic or basic by virtue of properties related to the position of their cation in the periodic table (82, p. 396) However, relating a simple bulk compositional classification such as this to activity in catalyzing acid-promoted surface reactions is less than straightforward. For instance, SiO_2 , an acidic oxide, so classified because of its solubility in base, shows no acidic sites (130) whereas Al_2O_3 , which is amphoteric, by virtue of its solubility in acids and bases, has Lewis acid sites (130, p. 229) and silica-alumina has both protonic and aprotic sites (131), as do H-zeolites. The Bronsted acidity of zeolites, silica-alumina, and, to some extent, tetrahedrally substituted clays, has been attributed to dissociation of the proton on hydroxyl groups bridging silicon and aluminum cations (132). In clay minerals, however, the most significant source of their surface acidity has been shown to be Bronsted acidity resulting from dissociation of the waters of hydration surrounding the exchangeable cations (133-134).

Lewis Acid Sites. Many other mechanisms (66, 85) are best described in terms of the more general concept of **aprotic, or Lewis acidity** which is defined in terms of the capacity to donate or share pairs of electrons. Aprotic acid sites are commonly derived from the coordinatively unsaturated cations at crystal edges or adsorbed on crystal faces, from dehydration of hydroxylated surfaces, and from deamination or deamination and dehydration of silica-aluminum catalysts or similarly treated clays having extensive tetrahedral substitution (130, 132). Formation of Lewis acid sites by deamination or deamination-dehydration is dependent on inversion of the basal oxygens of the aluminum-substituted tetrahedron away from the surface, in order to expose the aluminum (131).

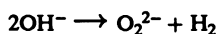
The degree of acidity measured is a function of the measurement method. There are several ways of measuring acidity, both wet chemical and spectroscopic (85, 135). It is not necessarily reliable to compare acidities determined by different methods, as

they are based on different models of acidity and are measured under different conditions known to affect the property under consideration. Models of acidity have been proposed (130-132) but these concepts are under active development.

Covalently Bonding Centers. In some cases, the intermediates may be covalently bonded to the catalyst (86), oftentimes at surface hydroxyl groups. Such reactions are less well characterized in natural systems and would likely lead to mineral/organic systems rather than separated products.

Oxidizing/Reducing Entities. Other reactions depend on oxidation/reduction processes. Among them is polymerization of various aromatic molecules. Such polymerizations are preceded by formation of radical cations of the aromatic hydrocarbon. Cu-montmorillonites are capable of catalyzing such reactions (136).

Valence deficient oxygen species (O^- , O_2^{2-} , O_3^{3-}) produced by: a) ionizing radiation and associated with lattice defects; b) N_2O or O_2 adsorption, possibly followed by incorporation of O^- into the lattice; c) thermal dehydroxylation of hydroxides in part via:



repeatedly have been implicated in mineral catalysis of redox, and other reactions, as well. The subject has been extensively reviewed in (137). Freund, et al. (138, p. 1822) have suggested a fourth mechanism for O_2^{2-} production in oxides, by surface dissolution of water into the MgO lattice during the crystal growth. The dissolution is equivalent to formation of two OH^- plus one cation vacancy for each dissolved H_2O , i.e. missing Mg^{++} . Another expression of the equivalence is that one molecule of water is isomorphically substituted for Mg^{++} . The resultant H_2O + lattice O^{2-} + cation vacancy is equivalent to a hydroperoxy entity which is doubly positively charged with respect to the crystal lattice and thus can isomorphically substitute for the cation. The hydroperoxy entity can dissociate to an O^- dimer (peroxy entity) and hydrogen at ambient temperatures according to the reaction above. The peroxy, O_2^{2-} , can be dissociated thermally (137) to 2 O^- . Freund, (private communication) has suggested that the dissociation may also be induced by uv light. Fracture has been shown to be able to induce reaction of peroxy entities and other dissolved simple gases to produce hydrocarbons and a variety of other neutral and charged species (59). The dissolution mechanism to produce the other reactive precursors is described in (139-140).

Interrelationships Between Site Types As A Factor In Mineral Surface Chemistry

The foregoing discussion has been couched in terms of the electronic structure of minerals and its consequent effects on adsorbate reactions. Redox, aprotic acid, and covalent site types can all be considered to operate by electron/hole transfers, whether this be singly or in pairs, uni- or equi-lateral, partial or complete. Expressed in these terms, it is clear that these canonical site types, and reactions produced by them, represent limiting cases. The boundary lines between them must grow very fuzzy if additional electron delocalization is provided by excitation of either reactant or catalyst. Because of the electronic energy structure of minerals and their

interfaces, the effects of such additional delocalization can be expressed over very great distances and times as well. Thus the effects of charge delocalization, whether mobile or trapped, must be included along with consideration of ground state interactions between mineral and adsorbate.

Charge transfer comprises also particle transfer, especially when a proton is present. Therefore, even protonic acidity itself can not be completely distinguished from the capacity to transport electrons and holes, i.e. oxidation/reduction, if for instance, hole migration to the surface can provoke proton dissociation. Protonic and aprotic acidities have long been known to be interlinked. In some, but not all, cases, Lewis acids can be converted to Bronsted ones by addition of water (132).

It should additionally be emphasized that the behavior in chemical reactions of a solid oxidic or silicic catalyst may depend almost as much on the nature of the adsorbate as on the catalyst itself. Also, the nature of the surrounding fluid will also have a strong impact on the properties of highly dispersed mineral systems, via alteration of the space charge potential, as previously mentioned.

Yet further, it should be emphasized that the listed site types may not act either solely, as reactions typically proceed through multiple steps, nor independently, as sites may interact. Site interaction is strongly indicated in the case of kaolinites, where spectroscopic properties and/or populations of certain catalytic entities, i.e. structural iron, and O⁻-centers have been shown to be simultaneously modified in the presence of synthetically introduced interlayer water (141).

Perhaps there is need for careful reconsideration of the terminology of reaction mechanisms on photoconducting solids. The terms should more accurately represent the differences in their electronic structure from those of other catalyst types and should simply express the types of changes in critical properties on electronic excitation.

Catalysis of H₂/D₂ Exchange on Silica - A Radiation-Induced Catalytic Entity

Some of the extensive literature surrounding a relatively simple reaction, H₂/D₂ exchange on silica will be summarized in this section and contrasted with that for magnesium oxide in the next section. This reaction proceeds via O⁻-centers on both catalysts, but the sites, modes of production and the reaction mechanisms themselves are very different. This reaction is very useful for illustrating the possible effects, on mineral catalysts, of processes common in natural systems, i.e., artifacts of mineral formation and weathering and electronic excitation.

H₂/D₂ exchange on silica is unique, or at least highly unusual in that silica is inactive as a catalyst for this reaction if it has not been previously activated by ionizing radiation. It is unique on both SiO₂ and MgO in that the reaction proceeds at 77° K, indicating an activation energy of ≤2 kcal/mole. Radiation activates alumina and magnesium oxides similarly to silica, but with these substances, equal or superior activation can be produced by heating under vacuum (142), as is not the case for silica.

Apparently, the first suggestion that ionizing radiation might influence catalytic activity was made by Guenther in 1934 (143). In 1959, Kohn and Taylor reported the first discovery of ionizing radiation-induced catalytic activity that could not be equivalently produced by heating under vacuum (144). H₂/D₂ exchange was the reaction studied. The lack of adsorptive and catalytic capacities of the unirradiated substance, coupled with their decay over time after irradiation, led them to assign the

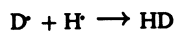
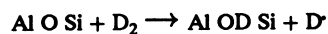
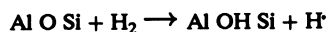
catalytic activity to radiation-induced production of a catalytic site. The increase in catalytic activity was accompanied by coloration of the silica and irreversible H_2 adsorption (145). Optical analogies were noted (146) between the color center and the trapped hole (O^- -center) in smoky quartz, previously associated (147-148) with isomorphically substituted Al for Si. The production of the catalysis, color center and adsorption capacity by soft x-rays, the destruction of the latter two by ultraviolet light, and the association of all three phenomena with charge deficient cation substitutions of Al for Si in the crystal lattice, led Kohn and Taylor to assign the phenomena to excitation-produced trapped charges (146). The simultaneity of production or decay of coloration with the capacity of the material for hydrogen chemisorption, led them to equate the color centers with the adsorption sites (145). They were discouraged, however, from also associating catalysis with the hole center by uv induced bleaching of the color center and H_2 adsorption capacity, yet concurrent enhancement of catalytic activity, (149).

What Is the Catalytic Site? Over subsequent years, many detailed studies, reviewed in (149), were performed to retest the hypothesis that the hole center was also the catalytic site. However, this relationship remained elusive because of the aforementioned uv activation of catalysis, yet bleaching and destruction of the chemisorption capacity for H_2 . On the basis of studies showing that all three phenomena were annealed at the same temperature, (150) Boreskov, et al. concluded that the catalytic site, too, was the hole center. This conclusion has been generally accepted by subsequent workers (151) although no explanation of the ultraviolet bleaching, yet activation paradox was made.

Since the hole center had been rejected by Kohn and Taylor as being the catalytic site, they considered the next most probable site, the surface hydroxyl groups as catalytic centers. They performed several detailed studies to determine both the degree of surface hydroxyl participation and to count the number of exchangeable hydroxyl sites. These experiments were performed in such a manner as to carefully exclude direct participation of the hole centers. The participation of OH, *Experiment 1*, was measured by exchanging all surface hydroxyl with deuterioxyl by repeated soaking in D_2 , followed by irradiation of the deuterated catalyst, prior to admission of pure H_2 . It was found that only a few deuterioxyls exchanged at room temperature, perhaps not surprising, given the expected high ($\sim 7Kcal/M$) activation energy (152) for such a process and the fact that only a few of these surface deuterioxyls would be in proximity to the hole centers. Sites were counted, *Experiment 2*, by admitting D_2 to an irradiated H-catalyst, then pumping off excess D_2 before admitting pure H_2 and measuring exchange. No definite conclusion was reached as to the number of the sites, because the measured rate of the conversion by hydroxyl was so small compared to the observed conversion rate under the normal conditions of the experiments and the number of available hydroxyls, so large compared to the reacted species, that the true site population could not be identified. Estimates were made only of the rate/site required to explain the overall rate assuming a catalyzed reaction on the basis of various assumed site populations.

Is the Reaction Catalyzed? The authors state explicitly (146, p. 1465) that the number of adsorption sites in no case exceeded the number of tri-valent impurity atoms and this assertion was rechecked using their published dose rates and sample preparation parameters, as well as those of the Russian group (150). Experiments of

both groups were conducted under static, not flow conditions. Typically, also, the applied radiation ($\sim 1\text{--}10$ Mrads.) was adequate to saturate Al-substituted sites with hole centers. Either the number of these centers exceeded the amount of reactants, or the reaction was carried only part way to completion (e.g. (153), p. 1018). Thus no turnover numbers were measured and there is no proof of the catalytic nature of the reaction. It would seem reasonable, on the basis of the published facts, to postulate that the reaction is not catalytic, but stoichiometric, that it does proceed through the hole center as active site, possibly via the following reaction sequence:



etc. for other isotopic combinations.

Experiments (149, p. 157) mentioned above were performed to: 1) determine the participation of hydroxyl in the reaction mechanism; and 2) to estimate the number of sites. They were done under conditions such that exchange by radical/radical recombination subsequent to chemisorption, would not have been detected. Fortunately, the experimental design not only confined the investigation to contributions by hydroxyl exchange, but also maximally isolated the contributions of hydroxyl exchange by each of the two kinds of hydroxyls that must be considered, terminal SiOH groups and SiOHAl bridging hydroxyls. The surface deuteration procedure described would exchange both terminal hydroxyls and those bridging ones extant before the irradiation/hydrogenation. The deuterated catalyst, used to measure "exchangeable" hydroxyls would produce a small amount of deuteroyl exchange at room temperature, proceeding through the reactions:



Experiment 1. During gamma irradiation, hole centers would be produced at Al-substituted sites in the catalyst in which all surface sites are deuterated. After admission of pure hydrogen to the deuterated, irradiated catalyst, new SiOHAl centers would be produced from these holes along with reactive H^\cdot . Neither radical/radical recombination nor interaction of these newly produced hydroxyls with the reactant H_2 will lead to radiation-induced exchange as only H^\cdot radicals are produced as the result of chemisorption and only H_2 is available to exchange with the radiation-produced SiOHAl centers. The observed exchange will be dominantly of type a), with a small contribution from type b) from exchange of those few bridging OD groups present before the irradiation and exchanged along with the terminal hydroxyls.

Experiment 2. In the site-counting experiment, a surface hydroxylated catalyst was irradiated and exposed to D_2 , the D_2 was then pumped off and H_2 admitted. Some

small exchange analogous to reaction a) would be expected when the D_2 is allowed to react with the terminal hydroxyls of the irradiated catalyst. This exchange would be radiation-independent. Radical/radical recombination would not lead to exchange because only D' was produced by the radiation-induced chemisorption of the pure D_2 reaction mixture. The reactive D' produced by the chemisorption of D_2 (accompanied by the production of $AlODSi$ centers) would almost certainly have recombined and been removed in the evacuation step prior to the introduction of H_2 . Even if any D' survived evacuation, its reaction with H_2 would require activation (152). After admission of H_2 , an additional small exchange would be produced by reaction with the irradiation-produced $SiODAl$ centers, according to reaction b). However, this exchange is incidental to the radiation, which serves in this case only to create a population of bridging deuteroyls during interaction of deuterium with the previously irradiated clay. The reaction of H_2 with the irradiated, D_2 -treated material occurring via reaction a) would not lead to exchange. The observed exchange in experiment two will be dominated by reaction b).

The deuterated product counted by these two experiments was 0.7×10^{16} molecules/gm.hr in an hour in the first experiment and 40×10^{16} molecules/gm.hr, in the second. These relative rates would imply that the reaction b) is nearly two orders of magnitude faster than a), which is to be expected on the expected difference in the strengths of the two OH bond types. Both rates are negligible relative to the yield of 2×10^{18} molecules/gm/min observed when an equimolar H_2/D_2 mixture is introduced to the irradiated catalyst. This latter figure also corresponds to the amount of H_2 that can be chemisorbed. It would appear, from the experiments performed, that hydroxyl participation was the only predicated mechanism under test. The carefully designed experiments provide a strong suggestion, if not proof, that neither terminal, nor bridging hydroxyls significantly participate. A test of participation of radicals produced in a stoichiometric reaction could be achieved by measuring the increase of hydroxyl/deuteroyl groups on the catalyst produced by the radiation-induced reaction, but apparently was not performed.

It is reported (149) that hydrogen adsorption is irreversible. The above mechanism would predict irreversible H_2 loss, but of only half of the chemisorbed hydrogen. Experimental details, thoroughly documented in the later papers, are scanty in the discussion of chemisorption in (145), where the work was originally reported. However, it seems likely that the gas restored to the reaction mixture by the atom/atom recombination mechanism would either have been pumped off before the heating to $300^\circ C$, or would have been discounted as a background in the measurement of the gas desorbed on heating. Thus the partial desorption predicted by the above mechanism is probably consistent with the measured results (145, 149).

Kohn and Taylor also report that the deuterated product yield was greater when the H_2/D_2 reaction mixture was on the catalyst during irradiation than it was when the mixture is added post irradiation of the catalyst to the same overall dose. It would be expected that the chemisorption might be somewhat reversible in the radiation field. Thus some turnover might be expected when the catalyst is irradiated in the presence of the reactant mixture.

Participation of surface OH (hydroxyl) groups is not required in the above-postulated exchange sequence, though a type of OH (OD) is produced precedent to it. The atom/atom recombination would not be expected to have a high activation energy, and could thus proceed rapidly at $77^\circ K$. That analogous centers can

dissociate H_2 has been reported (137, p. 93). The above mechanism is consistent with the observed bleaching and H_2 poisoning of the sites, and also the oxygen poisoning, as the chemisorbed O_2 , i.e. O_2^- , should be an excellent trap for migrating H^\cdot (producing hydroperoxy radical), without affecting the color center itself. It is also consistent with the observed hydrogenation capacity of irradiated silica (154) and the presence of measurable contents of SiOH and SiH in hydrogen-impregnated gamma-irradiated silicas studied by several subsequent workers (155). These latter studies were not quantitatively correlated with hole production or irradiation produced chemisorption by the workers reporting them.

The above mechanism would predict deactivation by uv (not observed). However, subsequent work by Freund has indicated that trapped peroxy entities in MgO, to be expected also in this system, might be dissociated by uv into pairs of O^- -centers. Thus the uv activation dilemma may be resolved by postulating uv activation of a more active set of centers to compensate for the holes it recombines.

Is the Reaction Confined to the Surface? There is one possible difficulty with this postulated mechanism. H^\cdot/H^\cdot recombinations would not be expected to have a high activation energy, and thus could proceed readily at liquid N_2 temperature. However, the O^- -centers produced by the irradiation would be distributed throughout the bulk, not only on the surface, at least for those catalysts in which the Al impurity was intrinsic, rather than surface-doped. That all the hole centers were bleached by chemisorption implies that the H_2 had to diffuse to the interior to react. H_2 diffusion would be expected to be, and has, in fact, been found to be (156) an activated process. The activation energy is ~ 7 Kcal/mol at room temperature, similar to that of the activation energy for the hydroxyl-mediated exchange of a hydrogen atom, thus slow at $78^\circ K$. Shelby (151, p. 16 ff.) reports that the activation energy increases as a function of increasing temperature over a temperature range from less than $0^\circ C$ - $1000^\circ C$ (presumably due to competition from OH and hydride formation), but there are no reported data for $77^\circ K$. Migration would be significantly slowed at $77^\circ K$, but by how much is not clear.

Although there does not seem to be sufficient data to resolve the question of low temperature H_2 diffusion, a brief synthesis of available information is in order. Studies by Shelby (158) have shown that, at room temperature, bleaching of irradiation-produced centers in a quartz plate has proceeded through $\sim 400\mu$ in ~ 50 hours. The $>300 m^2/gram$ particles of silica used as exchange catalysts by Taylor and Kohn can be estimated, using a crude approximation of close-packed cubes, to have a diameter of 10 nm. Whereas the distance to be traveled is only $10^{-4} x$ as far as in Shelby's room temperature system, diffusion at $77^\circ K$ is $\sim 6 x 10^{-16}$ as fast as at RT, hardly compensatory, unless the frequency factor in the Arrhenius equation is large enough to provide the necessary encounters. It is possible that bulk to surface charge inhomogeneities, which become significant for small particles, may facilitate diffusion in finely divided materials. Similarly the number of gas encounters with the surface is increased in a high surface area system. No experimental data could be found to compare the diffusion rates into powdered material with a plate.

Summary and Prediction. Exchange of H_2/D_2 on irradiated silica is postulated here to be a stoichiometric reaction producing one SiOAl bridging hydroxyl for each chemisorbed hydrogen. A stoichiometric reaction, such as proposed here, would be of little utility in industrial catalysis, as presently practiced. However, in natural

systems, with appropriate ongoing radioactive or mechanical energy sources, such reactions could be responsible for the production of substantial chemistry. For instance, in clays, "bulk" sites are close to the surface and the possible concentration of such centers is much higher. Therefore, O⁻-center-mediated reactions are likely to be a significant factor in reactivity, judging by the efficiencies observed in the silica system.

It can be predicted from the foregoing discussion that gamma-irradiation, followed by hydrogenation, of an Al-doped silica or a highly tetrahedrally substituted, metal-exchanged clay, should produce an effective Bronsted acid. For silica itself because of the low number of sites, the route is circuitous and unlikely to yield a material vastly different from the original, unless the electrons trapped as a result of the irradiation have their own interesting chemistry. However, for a highly tetrahedrally substituted, metal-cation-exchanged clay, a material with novel reactive properties might well result. It is known (152) that Bronsted acidity is more effective than is Lewis acidity in promoting skeletal transformations in hydrocarbons. These are the transformations of petroleum cracking.

Catalysis of H₂/D₂ Exchange on Al₂O₃ and MgO - A Formation, or "Weathering"-Induced Catalytic Entity

It appears that the catalytic activity of the irradiation-produced O⁻-center in silica is somewhat special. Whereas catalytic O⁻-centers are also produced by gamma-irradiation of other oxides, such as silica-alumina, alumina, MgO and CaO, equivalent, or even superior catalytic activation can be produced simply by heating these materials under vacuum. This fact was reported originally by Kohn (144) and has been subsequently confirmed by other workers (159-161). Taylor and Kohn proposed that the annealing process removes water from catalytic sites (149). Boudart, et al. (151) offers a more complex hypothesis. This group attributes exchange on MgO to a surface-only, tetrameric, grouping of single negative charge deficient lattice positions called a V_I center which is comprised of three O⁻-centers and an OH⁻ grouped around a cation vacancy. Freund has postulated that the center is more likely to have two nearby, or adjacent, cation vacancies, rather than only one, and thus be fully balanced, chargewise (private communication). A number of centers related to V_I, also analyzed by ESR (162), can be generated by combining heating with various chemical treatments.

The V_I centers are comparable, but not truly analogous with the radiation-induced hole center in silica. The V_I has a structural cavity rather than a charge deficient isomorphically substituted cation, and consists of an O⁻ aggregate, rather than the more familiar O⁻-monomer, or O⁻-dimer (peroxy entity). V_I centers occur only on the surface, unlike the O⁻-centers of silica, which are distributed throughout the bulk. The V_I center is poisoned by oxygen (a fact likely related to its polymeric nature and the possibility of peroxy-oxygen disproportionation reactions of types discussed in the literature (147)), unlike the silica O⁻ center. It is not poisoned by H₂, also unlike the silica center (149). It is postulated to be formed by high temperature dissociation of hydroperoxy (164) as discussed earlier (138). How this precursor becomes converted to a V_I center upon vacuum heating is unclear, but the spectroscopic assignment of Boudart, et al. will be accepted for the purposes of this discussion.

An imposing array of correlative evidence for the association of the V_I center in

MgO with the low temperature catalysis of H_2/D_2 exchange (151) was published and the mechanism was proposed to be of the Rideal-Eley type (adsorbed molecule/gaseous molecule interaction). The reaction, performed in a flow system, is clearly catalytic, exhibiting a high turnover number. Even so, both the spectroscopic assignments for the centers (137) and the catalytic mechanism itself (163) have been challenged by other authors. The basis for the challenge to the catalytic mechanism stems from the apparent incongruity between the observed efficiency of the catalysis at 77°K in the face of the high measured (152) and calculated (164) activation energy for dissociation of OH. Also the proposed high temperature formation mechanism for the center (138, 164) as an equilibrium dissociation of two hydroxyls to produce a peroxy entity and molecular hydrogen might seem to predict poisoning of the center by H_2 , at least for the low temperature reaction. H_2 poisoning is not observed, even under "drastic conditions" (137). An alternative center, based on low coordination oxygen on extended steps (analogous to metallic-type catalytic sites) has been proposed (163), but has not been supported by experimental measurements.

In defense of the V_1 center it should be pointed out that Freund (138) determined that the dissociation of hydroperoxy to H_2 + peroxy is 90% complete at ambient temperatures in MgO. True, this implies too high an activation energy for efficient reaction at 77°K, but this measured dissociation efficiency was predicated on O-dimers rather than the postulated trimer + OH^- center. The calculations of Derouane, et al (164) also considered only a linear pseudomolecule and an hydroperoxy centered at a single vacancy. Therefore it is not clear that prior existing data concerning the activation energy for release of the product is as damaging to the postulated mechanism as was suggested it might be in (163).

However, a somewhat modified explanation for the observed phenomena is offered here, based on a hybrid mechanism between the Rideal-Eley interaction proposed by Boudart, et al. and the free radical mechanism proposed here earlier for exchange on silica. It is suggested here that the site comprises the dual vacancy proposed by Freund, rather than the single one offered by Boudart, et al., because the resulting lattice is charge-balanced and because hydrogen going into a strongly positive crystal environment might tend to form H^+ rather than H^\cdot . Given a dual vacancy site, it also seems that effective sharing and orientation of the O^- centers might be better done if the two vacancies are stacked on each other, rather than linearly adjacent on the same surface. Each single cavity is of the nominal dimensions of 2.9 Å V - V or $O^- - O^-$ across the diagonal (164). One, perhaps more than one, molecular hydrogen(s) can be incorporated within either single cavity with freedom of orientation, and without disturbing any of the inter-atomic dimensions of the lattice. One atom of the H_2 will combine with one of the O^- centers in a manner analogous to that on the silica. However the other does not have to be released as a mobile hydrogen atom, as in the case postulated for silica, but, as a weakly chemisorbed hydrogen molecule, can approach the O of the adjacent OH^- (postulated by Boudart, et al. to be essential to catalysis) within a distance not too much in excess of either the normal O-H or H-H bond lengths (particularly if the structure collapses somewhat around the vacancy). Of the three resulting H's (D's) within the cavity two are now attached to an oxygen and thus either the original H_2 (D_2), or a newly formed one containing the H of the catalytic center can desorb, producing exchange. There would be a very low activation for the exchange as OH and HH bonds are of similar strength. The catalyst is altered only by a shift of the catalytic OH moiety

from one position to another within the cavity, a structurally immaterial change. No hydrogen poisoning would be anticipated, because, even if several O^- positions of the site fill up initially with hydrogen, there is room for new hydrogen to enter and the exchange mechanism can proceed undisturbed using any available OH-H, OD-D groups in interaction with OH of the original catalyst, or even those produced by the chemisorption. Also on this center, dissociated, O^- -bound H^+ atoms may be less strongly bound than on silica, should some of the H_2 's be dissociated as on the silica. No experiments were reported to assess how many of the O^- -sites are occupied with H^+ or H_2 during the reaction. It is suggested here that a pseudomolecule, containing the three O^- -centers and the OH group proposed by Boudart, et al., perhaps, however, with a double vacancy, is the minimal entity that could be expected to approximate the behavior of the active site. This reaction is catalytic, rather than stoichiometric, as for silica, because the catalytic center is regenerated on dissociation of the exchanged product, rather than removed by permanent binding to one of the hydrogen atoms of the reactant.

It would appear that assignment of the V_I as the catalytic center for these other oxides is in accord with observations, but perhaps still open to some question. If V_I however, is not the center, the numerous reported correlations between catalysis and changes in V_I population on annealing and chemical treatment will still require rationalization in terms of the new alternative.

Conclusions and Projections

Unfortunately, the complexity of the relationship between mineral properties and their surface reactivity is multiplicatively, rather than additively, proportional to the interactions between the various structural elements involved. These elements can be composed of structural entities of the catalyst, reactants, intermediates and products. In most practical cases, the distribution of products is the resultant of numerous individual steps. Each step is likely dependent on structural elements of both adsorbed (reacting) and adsorbing (catalytic) species, even assuming the promoting mineral is not consumed by the process and the reaction proceeds to an equilibrium, or a steady state. The same structural element can have an enhancing or inhibiting effect, depending on the individual reaction step under consideration. Its effect on the overall process is the resultant of its effect on the various individual steps in which it plays a role. That interaction of each structural element of the composite system with energy must also be considered does not simplify matters. No simple answers or trivial generalities should be anticipated. However, a different perspective on the nature of catalytic processes which truly considers all of the pertinent variables might well serve to provide more effective means of systematization of reaction types.

The challenge to the investigator to systematize is not diminished by the fact that associations between catalytic structure and reaction mechanism are made by the process of correlation, which is unavoidably subject to the risk of post hoc, ergo propter hoc, fallacy. Even so, only real time spectroscopic monitoring of reactive intermediates is a more direct avenue of systematic investigation and assignment. Oftentimes the direct approach is impractical. Fortunately, the dangers inherent in correlation can be significantly diminished by the use of multiple techniques and redundant measurements, a possibility recently made possible by the profusion of new experimental methods. Those of the new methods than are those using high energy non-optical techniques (such as that described by Coyne, et al. in this volume) which are less perturbing of the experimental system may now be adequately sensitive so as to permit real time spectroscopic examination of the reacting system.

It is certain that application of basic principles obtained from laboratory studies, and practical insights obtained from industrial practice, are helping to provide insight into surface chemistry in natural systems. On the other hand, a wealth of chemistry is achievable at moderate temperatures in natural systems. In addition to gentler temperature regimes, natural systems differ from laboratory and industrial ones primarily in the availability of electronic, rather than thermal excitation sources, and in the normality of pulsed or cycling, rather than steady state, reaction conditions. The most promising available energy sources in natural systems, radioactive decay, mechanical stress, and perhaps, to a lesser extent, solar irradiation, presently are considered to be sources of residual toxic waste, unproductive friction, or skin cancer. It appears, however, that Nature found them adequate to generate prodigious, even staggering, quantities of fossil fuel and perhaps even life itself. It would seem equally plausible that reactions performed under protocols modelling geological processes will give equivalent insights into the development of improved, less thermal energy intensive, and less polluting and perhaps more environmentally aesthetic industrial processes.

Acknowledgments

Lelia Coyne wishes to acknowledge Grant NCC2-153 from the Exobiology Program and Grant NCC2-345 from the Planetary Biology Program of NASA Headquarters. She also thanks Drs. Friedemann Freund, Andrew Pohorille and Helga Stan-Lotter, associated with the NASA-Ames Research Center, for stimulating and informative conversations.

Literature Cited

1. Szabo, A.; Ostlund, N. S. *Modern Quantum Chemistry: Introduction to Advanced Electronic Structure*; MacMillan: New York, 1982; 446 pp.
2. Pauling, L.; Wilson, E. B. *Introduction to Quantum Mechanics with Applications to Chemistry*; McGraw Hill: New York and London, 1935; 468 pp.
3. Ballhausen, C. J. *Introduction to Ligand Field Theory*; McGraw Hill: New York, 1962; 298 pp.
4. Burns, G. *Solid State Physics*; Acad. Press: Orlando, 1985; 775 pp.
5. Stoneham, A. M. *Theory of Defects in Solids*; Oxford Univ. Press: Oxford, 1979; 955 pp.
6. Harrison, W. H. *Electronic Structure and the Properties of Solids*; W. H. Freeman: San Francisco, 1980; 582 pp.
7. Bube, R. *Photoconductivity of Solids*; Wiley and Sons: New York, 461 pp.
8. Smith, F. G. *Physical Geochemistry*; Addison-Wesley: Reading, MA., Palo Alto, CA, London, 1963; 624 pp.
9. Burns, R. G. *Mineralogical Applications of Crystal Field Theory*; Cambridge University Press: Cambridge, 1970; 224 pp.
10. Marfunin, A. S. *Physics of Minerals and Inorganic Materials*; Springer-Verlag: Berlin, 1979; 340 pp.
11. Williams, D., Ed. *Methods of Experimental Physics*, Vol. III of *Molecular Physics*; Marton, L., Gen. Ed.; Academic Press: New York and London, 1962; 769 pp.
12. Weissberger, H. and Rossiter, B. W. Gen. Eds.; *Physical Methods of Chemistry*, Parts III A-D of Vol. I of *Techniques of Chemistry*; Wiley-Interscience: New York, 1972; 791 pp.
13. Muller, N., *ibid.* In *Interferometry, Light Scattering, Microscopy, Microwave and Magnetic Resonance Spectroscopy; Optical, Spectroscopic and Radioactivity Methods*, Chapter VII.

14. Rieger, P. *ibid.*, Chapter VI.
15. Gordy, W. T. *Theory and Applications of Electron Spin Resonance*, Vol. XV of *Techniques of Chemistry*, Weissberger, H, Gen. Ed. Wiley Interscience: New York, 1980, 625 pp.
16. Wertz, J. E.; Bolton, J. R. *Electron Spin Resonance Elementary Theory and Practical Applications*; McGraw-Hill: New York, 1972; 497 pp.
17. Davies, M., Ed. *Infrared Spectroscopy and Molecular Structure*; Elsevier: Amsterdam, 1963; 468 pp.
18. Kortum, G. *Reflectance Spectroscopy: Principles, Methods, Applications*; Springer-Verlag: New York, 1969; 366 pp.
19. Grum, F. in *Spectroscopy and Spectrometry in the Infrared, Visible and Ultraviolet; Optical, Spectroscopic and Radioactivity Methods*, Part IIIB of *Physical Methods of Chemistry*, which is Vol. I of *Techniques of Chemistry*; Weissberger, H.; Rossiter, B. W. Gen. Eds; Wiley-Interscience: New York, 1972; 715 pp.; Chapter III.
20. Nassau, K. *The Physics and Chemistry of Color: The Fifteen Causes of Color*; Wiley-Interscience: New York, 1983; 454 pp.
21. Leverenz, H. G. *Luminescence of Solids*; Dover: New York, 1968; 569 pp.
22. Lumb, M. D., Ed., *Luminescence Spectroscopy*, Academic Press: New York, 1978; 375 pp.
23. McKeever, S. *Thermoluminescence of Solids*; Cambridge Univ. Press, Cambridge, 1985; 376 pp.
24. Samson, J. A. R. *Vacuum Ultraviolet Spectroscopy*, Wiley: New York; 1967, reprinted Pied Pub: Lincoln Neb., 1980; reprinted Wiley: New York, 1982; 348 pp.
25. Berkowitz, J. *Photoabsorption, Photoionization and Photoelectron Spectroscopy*, Academic Press: New York, 1979; 469 pp.
26. Spinks, J. W. T.; Woods, R. J. *Introduction to Radiation Chemistry*, 2nd Ed.; John Wiley & Sons: New York, 1976; 504 pp.
27. Attix, F. H.; Roesch, W. C., Eds. *Radiation Dosimetry*, 2nd Edition, Vol I: *Fundamentals*; Academic Press: New York, 1968; 405 pp.
28. Bancroft, G. M. *Mossbauer Spectroscopy, An Introduction for Inorganic Chemists and Geochemists*; Wiley: New York, 1973; 251 pp.
29. Marfunin, A. S. *Spectroscopy, Luminescence and Radiation Centers in Minerals*; Springer-Verlag: Berlin, 1979; 352 pp.
30. Karr, C. Jr. *Infrared and Raman Spectroscopy of Lunar and Terrestrial Minerals*; Academic Press: New York, 1975; 375 pp.
31. Mc Dougall, D. J., Ed.; *Thermoluminescence of Geological Materials, Proceedings of NATO Advanced Research Institute on Applications of Thermoluminescence to Geological Problems*; Academic Press: London, 1968; 678 p. See in particular Townsend, P. D. Chapter 2. 4; Roach C. H. Chapter 1.
32. Stone, E. E.; Torres-Sanchez, R. -M. *J. Chem. Soc.*, Faraday Trans, 1 1988, 84, 117-132.
33. J. W. Stucki; Banhart, L. Eds. *Advanced Chemical Methods for Soil and Clay Minerals Research*; Reidel: Holland, 1980; 488 pp.
34. W. G. Herckstroeter In *Optical, Spectroscopic and Radioactivity Methods, Part IIIB* of Vol. I of *Techniques of Chemistry*, Weissberger, H.; Rossiter, B. W., Gen. Eds.; John Wiley: New York, 1972; Chapter VI.
35. Bernasconi, C. F. Ed. *Investigation of Elementary Reaction Steps in Solution and Fast Reaction Techniques*, Part II of *Investigations of Rates and Mechanisms of*

- Reactions*, which is Vol. VI of *Techniques of Chemistry*; Weissberger, H.; Rossiter, B. W., Gen. Eds; Wiley-Interscience: New York, 1972; 673 pp.
36. Pimentel, G. C. In *Vib. Spectrosc. - Mod. Trends* Barnes, A. J.; Orville-Thomas, W. J. Eds.; Elsevier: Amsterdam, Neth., 1977; 79-88.
 37. Pimentel, G. C. *Ber. Bunsenges. Phys. Chem.* **1978**, *82*, 2-6.
 38. Little, L. H. *Infrared Spectra of Adsorbed Species*; Academic Press: London, 1966; 428 pp.
 39. Lamola, A. A.; Turro, N. J., Eds. In *Energy Transfer and Organic Photochemistry* Vol. XIV In *Techniques of Organic Chemistry*, Leermakers, P. A.; Weissberger, S., Gen. Eds.; Interscience: New York, 1965; 374 pp.
 40. *Series: Advances in Photochemistry*, Vols, 1-15, Wiley: New York.
 41. Calvert, J. C.; Pitts, J. N. Jr. *Photochemistry*; Wiley: New York, 1988; 899 pp.
 42. Turro, N. J. *Modern Molecular Photochemistry*; Benjamin-Cummings: Menlo Park, CA, 1981; 628 pp.
 43. Thomas, J. K. *The Chemistry of Excitations at Interfaces*, ACS Monograph #181; ACS, Washington, 1984; 320 pp.
 44. Morrison, S. R. *Electrochemistry at Semiconductor and Oxidized Metal Electrodes*; Plenum Press: New York, 1980; 401 pp.
 45. Bard, Allen J. *J. Photochem.* **1979**, *10*, 59-75.
 46. Wrighton, M. S., Ed. *Advances in Chemistry Series # 184: Interfacial Photoprocesses: Energy Conversion and Synthesis*; American Chemical Society: Washington, D. C., 1980; 315 pp.
 47. Bard, A. J. In *Electrochemistry in Research and Development*; Kalvoda, R.; Parsons, R. Eds. Plenum: New York, 1986, 35-48.
 48. Fox, M. A. *Acc. Chem. Res.* **1983**, *16*, 314-321.
 49. Bernal, J. D. *The Physical Basis of Life*; Routledge and Kegan Paul: London, 1952; 80 pp.
 50. Cairns-Smith, A. G. *The Genetic Takeover and the Mineral Origins of Life*; Cambridge University Press: Cambridge, New York, 1982; 477 pp.
 51. Cairns-Smith, A. G.; Hartman, H. *Clay Minerals and the Origin of Life*; Cambridge University Press: Cambridge, 1986; 193 pp.
 52. Powell, R. J. *IEEE Trans. Nucl. Sci.* **1975**, *NS-22*, 2240.
 53. Swallow, A. J. *Radiation Chemistry of Organic Compounds International Series of Monographs on Radiation Effects in Materials* Vol 2; Pergamon Press, The MacMillan Co; New York, 1960; p. 38, p. 244.
 54. Coyne, L. *Origins of Life* **1985**, *15*, 161-206.
 55. Zink, J. T. *Accounts of Chemical Research* **1978**, *11*, 289-297.
 56. Chandra, B. P.; Zink, J. I. *J. Phys. Chem. Solids* **1981**, *42*, 529-532.
 57. Wolff, G.; Gross, G.; Stranski, I. N. Z. *Elektrochemie* **1952**, *56*, 420-428.
 58. Lahav, N.; Coyne, L.; Lawless, J.; *Clays and Clay Minerals* **1982**, *30*, 73-35.
 59. Dickinson, J. T.; Jensen, L. C; McKay, M. R.; Freund, F. J. *Vac. Sci. Technol. A* **1986**, *4*, 1648-52.
 60. Davydov, A. S. *Theory of Molecular Excitons*; McGraw-Hill: New York, 1962; 174 pp.
 61. Knox, R. S. *Theory of Excitons*; Academic Press; New York, 1963; 207 pp.
 62. Wolfe, J. P. *Physics Today*, March 1982.
 63. Greenland, D. J.; Hayes, M. H. B. *The Chemistry of Soil Constituents*; John Wiley & Sons: New York, 1978; 508 pp.

64. Sposito, G. *The Surface Chemistry of Soils*; Oxford University Press: New York, 1984; 234 pp.
65. Grimshaw, R. W. *The Physics and Chemistry of Clays and Allied Ceramic Materials*, 4th Edition; Ernest Benn, Ltd.: London, 1971; 1024 p.
66. Solomon, D. H.; Hawthorne, D. G. *Chemistry of Pigments and Fillers*; John Wiley & Sons: New York, 1983; 309 pp.
67. Angel, B. R.; Jones, J. P. E.; Hall P. L. *Clay Minerals* 1974, 10, 247-255.
68. Hall, P. L. *Clay Minerals* 1980, 15, 321-335.
69. Callaway, W. S. 3rd; McAtee, J. L. Jr. *American Mineralogist* 1985, 70, 996-1003.
70. Cuttler, A. H. *Clay Minerals* 1980, 15, 429-444.
71. Grim, R. *Clay Mineralogy*; McGraw Hill: New York, 1978; 384 pp.
72. Van Olphen, H. *An Introduction to Clay Colloid Chemistry*; Wiley Interscience: New York, 1977; 318 pp.
73. Hughes, R. C. *Phys. Rev. B Condensed Matter* 1979, 19, 5318-5328.
74. Lin, S. H.; Wutz, D.; Ho, Z. Z.; Eyring, H. *Proc. Natl. Acad. Sci. USA* 1980, 77, 1245-1247.
75. Cuttler, A. H. *Clay Minerals* 1981, 16, 69-80.
76. Clayton, R. K. *Molecular Physics in Photosynthesis*; Blaisdell: New York, 1965; 205 pp.
77. Greek, B. F. *Chemical and Engineering News* May 29, 1989, 29-56.
78. Johns, W. D. *Dev. Sedimentol.* 1982, 35 Int. Clay Conf. Bologna, Pavia, Italy, 1981, 655-64.
79. Bostick, N. H.; Nicksic, C. P. *Bibliography and Index of Coal and Dispersed Organic Matter in Sedimentary Rocks; Petrography, Catagenesis, Relation to Petroleum and Natural Gas and Geochemistry*; Illinois State Geological Survey: Urbana, Ill. 1975; 92 pp.
80. Somorjai, G. A. *Chimia* 1981, 35, 1-9.
81. Somorjai, G. A. *Chemistry in Two Dimensions, Surfaces*; Cornell Univ. Press: Ithaca, N. Y. 1981; 552 pp.
82. Somorjai, G. A. In *New Horizons of Quantum Chemistry*; Lowdin, P. -O.; Pullman, B., Eds. Proceedings of the 4th Inter. Cong. of Quantum Chemistry, Uppsala, Sweden, Reidel: Dordrecht, Holland, 1982; 450 pp.
83. Rabo, J., Ed; *Zeolite Chemistry and Catalysis*; American Chemical Society Monograph 171, A. C. S.: Washington, D. C., 1976; 796 pp.
84. Newman, A. C. D. *Phil. Trans. Roy. Soc. Lond. A* 1984, 311, Fowden, L.; Barrer, R. M.; and Tinker, P. B., Eds. 419-432.
85. Rupert, J. T.; Granquist, W. T. and Pinnavaia, T. J. *Chemistry of Clays and Clay Minerals Mineralogical Society Monograph No. 6*; A. C. D. Newman, Ed.; John Wiley and Sons: New York, 1987; Chapter 6, 480 pp.
86. Rausell-Colom and Serratos, J. M. *Ibid.* Chapter 8.
87. *Ibid.*, Taylor, R. M., Chapter 2.
88. Johnson, F. H. Eyring, H. Stover, B. J. *The Theory of Rate Processes in Biology and Medicine*; John Wiley and Sons: New York, 1974; Chapter 1, pp 1-25.
89. Burchill, S.; Hayes, M. H. B.; Greenland, D. J. *op cit.* 63, Chapter 6, 221-398.
90. Moore, W. J. *Physical Chemistry*, 2nd Ed.; Prentice-Hall: Englewood Cliffs, N. J., 1955; 633 pp.
91. Boudart, M. In *Physical Chemistry, an Advanced Treatise*; Eyring, H., Ed; Academic Press: New York, 1975; Chapter 7, 349-411.

92. Oparin, A. I. *Proiskhozhdenie Zhizny*; Izd. Moskovskii Rabochii: Moscow 1924. (Reprinted in translation in Bernal, J. D. *The Origin of Life*; Weidenfeld and Nicolson: London, 1967, 199-234. Reference obtained from Cairns-Smith, G. *The Genetic Takeover*; Cambridge University Press: Cambridge 1982, p. 445.
93. Miller, S. L. *Science* 1953, 117, 528-529.
94. Haldane, J. D. S. *Rationalist Annual*. 1967, 3 (Reprinted in Bernal, Ibid. 242-249.) Reference from Cairns-Smith, Ibid.
95. Garrison, W. M.; Morrison, D. C.; Hamilton, J. G; Benson, A. A.; Calvin, M. *Science* 1951, 114, 416-418.
96. Lahav, N.; Chang, S. *J. Mol. Evol.* 1976, 8, 357-380.
97. Lahav, N.; White, D. H; Chang, S. *Science* 1978, 201,67-69.
98. Lahav, N.; White, D. H. *J. Mol. Evol.* 1980, 16, 11-21.
99. Deamer, D. W. Barchfield, G. L. *J. Mol. Evol.* 1982, 18, 203-206.
100. Theng, B. K. G. *The Chemistry of Clay Organic Reactions*; John Wiley and Sons: New York, 1974; references given on p. 275.
101. Ferris, J. P.; Huang, C. -H.; Hagan, W. J. *Origins of Life* 1988, 18,121-123.
102. Ingmanson, D. E.; Dowler, M. J. *Origins of Life* 1977,8, 221-224. and subsequent publications.
103. Corliss, J. B.; Baross, J. A.; Hoffman, S. E. *Oceanologica Acta* 1981, Proc. 26 th Int. Geol. Conf., 59-69.
104. Nisbet, E. G. *The Young Earth*; Allen and Unwin: Winchester, Mass, 1987; 400 pp.
105. Nisbet, E. G. *Nature*, 1989, 337, 23.
106. Overbeck, V. R.; McKay, C. P.; Scattergood, T. W.; Carle, G. C. and Valentin, J. R. *Origins of Life and Evolution of the Biosphere* 1988, 18, Kluwer: Dordrecht, Holland In Press.
107. Taylor, H. S. *Proc. Roy. Soc. A (London)* 1925, 108, 105.
108. Taylor, H. S. *J. Phys. Chem.* 1926, 30, 145-171.
109. Zubay, G., Gen. Ed. *Biochemistry*, 2nd ed., MacMillan: New York, 1988; Chapter 9, p. 286.
110. Wood, W. B., Wilson, J. H., Benhow, R. M., Hood, L. E. *Biochemistry, A Problems Approach*, 2nd Ed.; Benjamin-Cummings: Menlo Park, CA, 1981; 498 pp.
111. Halpern, J. In *Horizons in Organo-Metallic Chemistry*; Bernal, I. Ed.; *Annals of the New York Acad. of Sciences* 239 1974, 2-21.
112. Boudart, M. *Proc. Robert A. Welch Found, Conf. Chem. Res.*, 1970, 299-327.
113. Lagaly, G.; Fernandez Gonzalez, M.; Weiss, A. *Clay Miner.* 1976, 11, 173-187.
114. Lagaly, G.; Weiss, A. *Proc. Int. Clay Conf.* Tokyo; Heller, L., Ed; Israel Univ. Press: Jerusalem, 1969, 61-80.
115. Giese, R. F. Jr.; Costanzo, P. M. In *Geochemical Processes at Mineral Surfaces* Davis, J. A.; Hayes, K. F. ACS Symposium Series 323, 1986; Chapter 3, 37-54.
116. Pashley, R. M.; Quirk, J. P. *Colloids and Surfaces* 1984, 9, 1-17.
117. Heller-Kallai, L.; Yariv, S. *Colloid and Interface Sci.* 1981, 79, 479-485.
118. Malla, P. B. and Douglas, L. A. *Proc. Int. Clay Conf.*, Denver; Van Olphen, H.; Schultz, L. G; Mumpton, F. A. Eds.; Clay Minerals Society: Bloomington, Ind., 1985; 277-283.
119. Malla, P. B., Douglas, L. A. *Clays and Clay Minerals* 1987, 35, 232-236.
120. Prost, R. *Proc. of the Int. Clay Conference*; Applied Publishing Ltd.: Wilmette, Ill. 60091, 1975; 351-359.
121. Spósito, G.; Prost, R. *Chemical Reviews* 1982, 82, 553-573.

122. Newman, A. C. D. op cit. 9, Chapter 5.
123. Murray, R. S.; Quirk, J. P. *Soil Sci. Soc. Am. J.* **1982**, *46*, 865-868.
124. Low, P. F.; Margheim, J. F. *Soil Sci. Soc. Am. J.* **1979**, *43*, 473-481.
125. Low, P. F. *Langmuir* **1987**, *3*, 18-25. .
126. Coyne, L. M.; Lahav, N.; Lawless, J. G. *Nature* **1981**, *292*, 819-921.
127. Lahav, N.; Coyne, L. M.; Lawless, J. G. *Clays and Clay Minerals* **1985**, *33*, 207-213.
128. Lawless, J. G.; Edelson, E. H. *Life Sci. Space Res.* **1979**, *18*, 83-88.
129. Mortland, M. M. *Journal of Molecular Catalysis* **1984**, *27*, 143-145.
130. Connell, G. I.; Dumesic, J. A. *Journal of Catalysis* **1986**, *102*, p 228.
131. Uytterhoeven, J. B. Christner, L. G. and Hall, W. K. *Journal of Physical Chemistry* **1965**, *69*, 2117-2126.
132. Connell, G.; Dumesic, J. A. *Journal of Catalysis* **1987**, *105*, 285-298.
133. Mortland, M. M.; Raman, K. V. *Clays and Clay Minerals* **1968**, *16*, 393-399.
134. Mortland, M. M.; Fripiat, J. J.; Chaussidon, J.; Uytterhoeven, J. J. *Phys. Chem.* **1963**, *67*, 248-258.
135. Forni, L. *Catal. Rev.* **1973**, *8*, 65-115.
136. Boyd, S. A.; Mortland, M. M. *Nature* **1985**, *316*, 532-535.
137. Che, M.; Tench, A. J. In *Advances in Catalysis* 31; Eley, D. D.; Pines, H.; Weisz, P. B., Eds.; Academic: New York, 1982; Chapter 2, 78-128.
138. Freund, F.; Wengeler, H.; Martens, R.; *Geochem. Cosmochem. Acta* **1982**, *46*, 1821-1829.
139. Freund, F. *Contrib. Mineral. Petrol.* **1981**, *76*, 474-482.
140. Freund, F. *High Temperatures - High Pressures*, **1983**, *15*, 335-346.
141. Coyne, L. M.; Costanzo, P.; Theng, B. K. G. *Clay Minerals*, in press.
142. Kohn, H. W.; Taylor, E. H. *J. Phys. Chem.* **1959**, *63*, 500-505.
143. Guenther, P. *Ergebnisse tech., Roentgenkunde* **1934**, *4*, 100-112.
144. Kohn, H. W.; Taylor, E. H. *J. Phys. Chem.* **1959**, *63*, 966-970.
145. Kohn, H. W. *Nature* **1959**, *184*, 630.
146. Kohn, H. W.; Taylor, E. H. *Actes 2nd Cong. Intern. Catalyse*, Paris **1960**, Vol. II; Editions Technip: Paris, 1961; 1461-1481.
147. Ditchburn, R. W.; Mitchell, E. W. J.; Paige, E. G. S.; Custers, J. F.; Dyer, H. B.; Clark, C. D.; *Report of the Conference on Defects in Crystalline Solids at Bristol*; The Physical Society: London, **1955**, p. 92.
148. O'Brien M. C. M. Pryce, M. H. L. *ibid*, p 88.
149. Taylor, E. H. *Advances in Catalysis* Vol. 18, Eley, D. D; Pines, H.; Weisz, P. B. Eds; Academic Press: New York, **1968**; 111-255.
150. Borekov, G. K.; Kazanskii, V. B.; Mishchenko, Y. A.; Pariiskii, B. B. *International Chemical Engineering* **1964**, *5*, 79-82.
151. Boudart, M.; Delbouille, A.; Derouane, E. G.; Indovina, V.; Walters, A. B. *J. Am. Chem. Soc.* **1972**, *94*, 6622-6630.
152. Kondratiev, V. N.; Holtschlag, L. J., *Translator Rate Constants of Gas Phase Reactions, Reference Book*; Fristrom, R. M. Ed.; Office of Standard Reference Data, National Bureau of Standards, U. S. Department of Commerce: Washington, D. C. **20234**, 1972; 428 pp.
153. Kohn, H. W. *J. Phys Chem.* **1962**, *66*, 1017-1021.
154. Nagai, S.; Arai, H.; Hatada, M. *Radiat. Phys. Chem.* **1981**, *18*, 807-815.
155. Shelby, J. E. *J. Appl. Phys.* **1979**, *50*, 3702-3706.
156. Shelby, J. E. *J. Appl. Phys.* **1977**, *48*, 3387-3394.

157. Shelby, J. E. *Treatise of Materials Science and Technology*, Vol. 17, Academic Press: New York, 1977, Chapter I.
158. Shelby, J. E. *J. Appl. Phys.* **1986**, *60*, 4325-4327.
159. Lunsford, J. H.; Leland, T. W. *J. Phys. Chem.* **1962**, *66*, 2591-2597.
160. Harkins, C. G.; Shang, W. W.; Leland, T. W. *J. Phys. Chem.* **1969**, *73*, 130-141.
161. Benson, J. E.; Walters, A. B.; Boudart, M. *J. Chem. Phys.* **1968**, *72*, 4587-4589.
162. Derouane, E. G.; Indovina, V.; Walters, A. B.; Boudart, M. *Reac. Solids, Proc. 7th Int. Symp.*; Anderson, J. S. Ed.; Chapman and Hall: London, 1972; 703-716.
163. Fujioka, H.; Yamabe, S.; Yanagisawa, Y.; Matsumura, K.; Huzimura, R. *Surface Science* **1985**, *149*, L53-L58.
164. Derouane, E. G.; Fripiat, J. G.; Andre, J. M. *Chemical Physics Letters* **1974**, *28*, 445-448.

RECEIVED September 19, 1989

Chapter 2

Thin-Film Elemental Analyses for Precise Characterization of Minerals

Ian D. R. Mackinnon

Electron Microscope Centre, University of Queensland,
St. Lucia QLD 4067, Australia

The Analytical Electron Microscope (AEM), with which secondary X-ray emission from a thin (<150nm), electron-transparent material is measured, has rapidly become a versatile instrument for qualitative and quantitative elemental analyses of many materials, including minerals. With due regard to sources of error in experimental procedures, it is possible to obtain high spatial resolution (~ 20 nm diameter) and precise elemental analyses ($\sim 3\%$ to 5% relative) from many silicate minerals. In addition, by utilising the orientational dependence of X-ray emission for certain multi-substituted crystal structures, site occupancies for individual elements within a unit cell can be determined though with lower spatial resolution. The relative ease with which many of these compositional data may be obtained depends in part on the nature of the sample, but, in general, is comparable to other solid state analytical techniques such as X-ray diffraction and electron microprobe analysis. However, the improvement in spatial resolution obtained with the AEM (up to two orders of magnitude in analysis diameter) significantly enhances interpretation of fine-grained assemblages in many terrestrial or extraterrestrial rocks.

The modern-day Analytical Electron Microscope (AEM) is a very powerful tool for detailed structural and chemical analysis of (a) fine-grained minerals or (b) fine-structures within coarse-grained minerals. As will be apparent in the chapter by Guthrie and Veblen, structural detail of ~ 0.3 nm can be obtained routinely via imaging studies of minerals using an AEM. Spatially precise microdiffraction data and elemental analyses can also be obtained from AEMs, but these data are limited by the size of the electron probe at the sample and by scattering within the specimen. Depending upon the

0097-6156/90/0415-0032\$06.50/0
© 1990 American Chemical Society

particular configuration of AEM used, this can be as small as 0.5nm diameter for a dedicated Scanning Transmission Electron Microscope (STEM), or ~2.0nm diameter with a static or scanned probe in a more conventional AEM. In either case, the combination of imaging, diffraction and elemental analysis from a ~2.0nm diameter region has provided important and rapid advances in our understanding of complex mineralogical problems. For example, the modern-day AEM has allowed tremendous advances in the understanding of interplanetary dust particles through characterisation of nanometer-sized minerals which are often "unknowns" [1,2]. In another discipline, the characterisation of the new generation superconducting ceramics owes much to the analytical power of the modern-day AEM [3].

A spectrometer for the measurement of characteristic secondary X-rays was perhaps the first peripheral analytical device to be attached to a conventional Transmission Electron Microscope (TEM) [4] and this configuration forms the basis of many modern-day AEMs. Other attachments which complement X-ray spectrometers include an electron energy loss spectrometer (EELS), a backscattered electron detector, a secondary electron detector, a CCD- or YAG-based video monitor for TEM images, and a STEM detector. Some of these peripherals will be discussed by authors in other chapters, whilst this chapter will deal only with the use of X-ray detectors on AEMs. In most cases, the X-ray signal is generated from a thin, electron-transparent film of sample, although there is no specific obstacle to performing conventional "bulk" analyses on solids (similar to an electron microprobe or Scanning Electron Microscope with EDS) using an AEM configuration [e.g. 5]. However, the small size of sample holders in most AEMs places some limitations on work of this nature.

Thin-film analysis of samples has a unique advantage over conventional X-ray analysis of bulk samples in that the spatial resolution is significantly improved. This improvement in resolution is due primarily to the considerably smaller volume of sample from which secondary X-rays are generated by incident electrons. Figure 1 shows the X-ray generation volume for both thin-film and infinitely thick (bulk) cases. At any given incident energy, electrons in a bulk sample scatter in various directions and result in the generation of characteristic secondary X-rays from a region much larger in diameter than the actual incident probe. Not all generated X-rays will transmit through a bulk sample to a detector as lower energy signals will be absorbed by the sample. However, a characteristic "tear-drop" shaped region for the production of measurable secondary X-rays results. The extent of this tear-drop in a given sample depends primarily on the incident electron energy and the mean atomic number of the sample. Even at low energy, for example 10kV, the spatial resolution for bulk elemental analysis of infinitely thick samples using incident electrons and an X-ray detector is ~1 μ m diameter.

Figure 1b shows the X-ray generation volume for a typical thin-film in an AEM. Some beam broadening (again, incident energy dependent) occurs, and this essentially defines the region from which secondary X-rays are generated. Thus, for thin samples (generally, <150nm in the direction of incident electrons) the

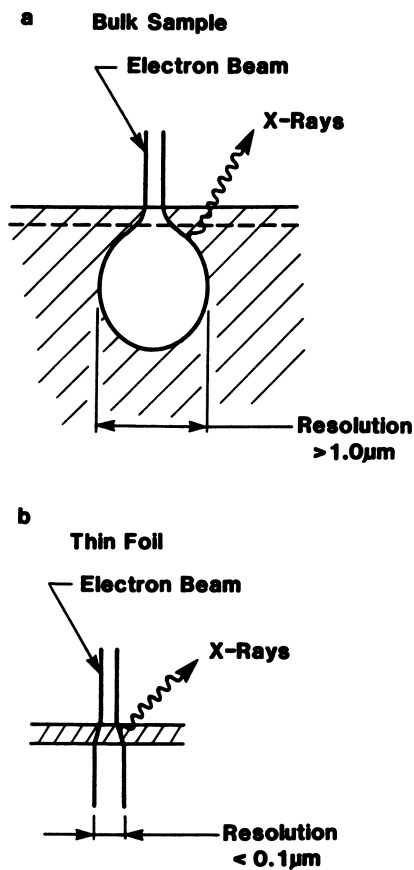


Figure 1. Schematic representation of secondary X-ray production for (a) bulk sample and (b) thin-film sample.

spatial resolution of an elemental analysis is not much larger than the diameter of the incident probe at the specimen surface. For probe sizes <2.0nm most elemental analyses are qualitative due to constraints on collection time caused by low X-ray counts and, for minerals, the potential for element loss during analysis. In general, quantitative analyses can be obtained from regions of larger dimensions (e.g. >20nm) wherein higher count rates provide better statistics for data reduction. A consistent theme throughout this chapter is the application of this thin-film technique for spatially precise, quantitative analyses of minerals.

The successful application of thin-film techniques to the solution of mineralogical problems depends, in part, upon the nature of instrumentation used and also upon the level of precision required for (a) chemical data and (b) the spatial resolution of the analysis. Each of these matters will be described in some detail below whilst utilising examples from the mineral and the materials sciences.

INSTRUMENTATION

A wide range of X-ray detectors are currently manufactured for use on a variety of electron-beam instruments. In general, for AEMs and dedicated STEMs, similar basic principles of installation and operation apply. A good review of these principles can be found in the article by Williams et al. [6], while Lorimer [7] presents a recent overview of thin-film analyses for silicate minerals.

There are two basic types of X-ray detectors in use on electron-beam instruments: a wavelength dispersive spectrometer (WDS) which utilises Bragg diffraction of X-rays at specific wavelengths from a crystal within the spectrometer and an energy dispersive spectrometer (EDS) which monitors electron-hole pairs generated in a semiconducting crystal by incident X-rays. The first type of detectors attached to a TEM were the WDS variety [4] which provided better spectral resolution than EDS detectors [8]. However, WDS detectors are not in common use on AEMs, primarily due to low counting rates and limitations of space in the sample stage area. The basic characteristics of EDS detectors, their limitations and methods for improvement of performance have been documented by a number of workers [9,10]. Lithium-drifted Si and high-purity Ge are the two types of solid-state devices currently used in EDS detectors on AEMs. A compilation of EDS detection principles and characteristics, including less commonly used devices, such as HgI detectors, is given by Heinrich et al. [10].

Si(Li) Detectors. The most common secondary X-ray detector in use on AEMs is the liquid nitrogen cooled Si(Li) type. This detector is small in size, has a relatively large collection angle (commonly ~0.13 steradians) and can be readily mounted in the limited space available between the specimen, stage and pole-piece of a modern AEM. The detector rapidly collects data over a wide energy range and is well-suited to elemental analysis of fine-grained, "unknown" materials because X-ray data from the complete energy spectrum are

collected and displayed simultaneously. Thus, all elements present in a sample above some threshold atomic number, as well as those not present, can be readily determined.

Si(Li) detectors usually contain a thin (between $7\mu\text{m}$ and $12\mu\text{m}$) Be sheet (or "window") for protection from the atmosphere and from the sample environment [11]. This Be window absorbs most low energy X-rays from elements with atomic number (Z) less than 11 (i.e. Na; 1kV) and thus, this detector configuration is used only for analyses of elements with $Z \geq 11$. Most Si(Li) EDS detectors provide an energy resolution ranging from $\sim 140\text{eV}$ to $\sim 160\text{eV}$ depending upon the particular model detector, the manufacturer and degree of damage experienced by the detector over its lifetime. Energy resolution for EDS detectors is usually measured as the full-width at half-maximum (FWHM) for the MnK α peak, and values less than 146eV FWHM at MnK α allow complete resolution of the K-lines for Si (1.74kV) and Al (1.49kV) [11]. Considerable overlap of these two peaks will occur if an energy resolution $>165\text{eV}$ is obtained. In the sections to follow, quantitative thin-film analyses of minerals have been obtained with these Be-window Si(Li) EDS detectors with resolution generally better than 154eV.

Si(Li) detectors without Be windows ("windowless") or with thin metal-coated polymer films (Ultra-Thin Window; UTW) have become an important peripheral to modern-day AEMs for the qualitative detection of elements with $5 < Z < 11$. These detectors have more stringent vacuum requirements because the removal of the Be window increases the probability of detector contamination (from the specimen or column environment) and consequent degradation of performance [12]. Windowless and UTW Si(Li) detectors are commonly installed with additional airlock mechanisms and only on instruments with acceptable levels of vacuum cleanliness. Thus, design constraints on modern AEMs preclude placement of the UTW detector close to the sample. In addition, loss of detection efficiency at low energies ($< 1\text{kV}$), an increase in absorption of low energy X-rays, and overlap of light-element K-lines with the L-lines of transition metals all conspire to limit windowless or UTW EDS analysis of minerals to a qualitative basis only.

A recent innovation in thin-film detectors has appeared on the commercial market in which a standard Si(Li) detector is protected by an apparently strong, X-ray transparent and radiation insensitive thin-film. The exact nature and composition of this thin-film is yet to be disclosed in the open literature. However, according to manufacturer's reports [13] this detector window allows transmission of boron X-rays (0.185kV for K α) and can be operated at atmospheric pressure. In a typical spectrum from this type of detector provided by the manufacturer, a strong oxygen K α line as well as well-defined Si, Al and Na peaks can be observed for albite ($\text{NaAlSi}_3\text{O}_8$). Since these detectors have only recently been installed in the field, details of performance have yet to be reported by users.

Si(Li) crystals provide high detection efficiency between 1.5keV and $\sim 30\text{kV}$, but at higher energies the low photon absorption efficiency of Si results in background levels comparable to peak

intensities. In electron microprobes or SEMs, which usually restrict incident voltages to <40kV, this higher energy limitation is of little concern. However, most AEMs are operated at a minimum voltage of 100kV and many higher voltage instruments (up to 400kV) are commercially available. The inherent advantages apparent in thin-film analyses in the intermediate voltage range (i.e. 200kV-400kV), such as better signal/noise ratio and generation of higher energy X-rays, have been somewhat mitigated by the collection efficiencies of Si(Li) detectors in the X-ray energy range 30kV to ~100kV. Furthermore, Si(Li) detectors are particularly sensitive to damage from backscattered electron radiation when higher incident electron voltages (200kV to 400kV) are used [6]. Documentation on this problem is primarily anecdotal, but accumulated experience [6,14] in this area indicates that users should be wary of extended exposure of Si(Li) detectors to high radiation fluxes in intermediate voltage AEMs.

High Purity Ge (HPGe) Detectors. These detectors have only recently become commercially available in configurations suitable for modern AEMs, although the potential for HPGe detectors in the high energy X-ray region (30kV to ~140kV) has been known for some time [15]. The number of charge carriers in Ge is higher than that in Si by ~26%, and the stopping power of Ge is greater than that for Si. The intrinsic resolution is improved and the efficiency range for Ge detectors is increased over Si(Li) detectors. HPGe detectors are able to detect higher energy X-rays more efficiently and this feature is particularly useful for measuring K-shell transitions from high Z elements (e.g. In, Gd). This capability obviates difficulties associated with peak overlaps for L- and M-lines in the transition metal elements using lower resolution Si(Li) detectors. In the past, a fundamental difficulty with Ge detectors has been peak asymmetry when analysing X-rays in the energy range <30kV [12]. Such problems have been resolved [16] and an energy resolution of 123eV for MnK_{α} (FWHM) has been measured for an HPGe detector. The development of HPGe detectors for AEMs has paralleled the development of intermediate voltage microscopes and there is little doubt that the higher resolution and better detection of K-lines for high-z elements are a driving force.

Geometry and Design. In modern-day AEMs, the EDS detector is usually placed orthogonal to the specimen holder axis and at an angle to the specimen. The angle between the specimen and the detector axis is termed the X-ray take-off angle. The choice of detector angle with reference to the sample holder axis is usually fixed by microscope manufacturers according to predetermined design constraints. Methods for the calculation of effective take-off angle for a variety of configurations are given in reference [17]. Note that errors in transcribing the formalism given in this paper are corrected in [18].

For elemental analysis problems which have geometric or crystallographic considerations, the take-off angle is an important parameter. For example, grain boundaries or precipitates included in a matrix may have a peculiar orientational relationship which requires that the sample be tilted through a considerable angle in

order to identify the object via diffraction contrast images. Detectors at low take-off angle (i.e. parallel with the specimen in the specimen holder plane) have a limited angular range from which X-rays may be collected. Thus, it may not be possible to obtain an appropriate orientation for a sample. Nevertheless, detectors oriented at a relatively low take-off angle can be situated more closely to a sample with a concomitant increase in X-ray count rate. The advantages and disadvantages of common take-off angle configurations for modern-day AEMs have been analysed by Zaluzeć et al. [18]. The most useful detector angles are either at $\sim 20^\circ$ or at $\sim 68^\circ$. At 20° take-off angle, the relative count-rate is high, but a lower sample tilt range and mass sensitivity results. Conversely, the higher detector angle provides better mass sensitivity and sample tilt range, but lower count rates than the 20° angle.

Microscopes. There are two basic modes of operation for X-ray analysis in a modern-day AEM: with a static (or flood) beam and with a rastered beam. This instrument is essentially a conventional TEM with either (a) scanning coils to raster and focus the beam or (b) an extra "mini" (or objective pre-field) condenser lens to provide a small (nm-sized) cross-over of a static beam at the objective plane. Some AEM configurations contain both scanning coils and a third condenser lens whilst others may have only one of these. In either condition, a small-sized electron probe can be obtained as a static or a rastered beam. The basic electron-optical principles which provide nanometer-sized beams for microanalysis are similar to those for electron microdiffraction which are well described by Spence and Carpenter [19].

A distinction should be drawn between two types of commercially available AEM in routine use. The most common, and generally, least expensive type of AEM is a modified TEM column which has a redesigned pole-piece (objective lens) and sample area to accommodate scanning coils and an EDS detector (besides other peripherals) and usually contains a tungsten (W) or LaB_6 electron source since the operating vacuum is of the order 10^{-5} Pa. The smallest probe diameters commonly achieved in this conventional AEM are of the order 2.0nm. The other type of instrument which comes under the AEM descriptor, is a dedicated STEM, sometimes termed D-STEM [19]. This microscope utilises a field emission gun (FEG) as the electron source, and thus, provides coherent illumination at the sample with probe diameters much smaller than a conventional AEM (down to $\sim 0.5\text{nm}$). The FEG requires stringent vacuum conditions ($\sim 10^{-7}$ Pa) and provides a much higher beam current density in a focussed probe than LaB_6 filaments. Because the D-STEM uses a coherent point source of nm-dimensions, less sophisticated condenser optics are required to focus the beam at the sample. For the purposes of this article, examples of thin-film EDS data will be drawn from AEMs of the conventional (or modified TEM) variety.

In both types of microscopes, a common analytical procedure involves the use of a "spot" mode wherein the smallest diameter beam is focussed on a region of interest. With the aid of digital beam control, this focussed spot can be stepped at predetermined intervals to form an automated analysis matrix. An example of

analysis intervals in conventional AEMs is a 20nm step with a 4nm diameter beam for crystallographically-controlled precipitates in a binary oxide [20]. This technique also offers a rapid means for automated, fine-scale analyses of complex materials in order to select candidate particles for subsequent detailed electron-optical analysis [2].

The rastered beam mode provides considerable practical utility in analytical situations for which it is not necessary to obtain the smallest diameter probe, or, for which a sample shows high susceptibility to electron beam damage. Microanalysis at low magnification with a rastered probe tends to decrease effects of electron beam damage in radiation-sensitive materials. Many significant minerals (such as clays, zeolites, chain silicates) suffer electron beam damage to some degree or another in the voltage range 100kV to 400kV [21,22]. The use of a rastered probe during X-ray analysis can provide reliable estimates of sample composition whilst minimising the effects of beam damage or element loss (see below), provided there is chemical homogeneity over the area scanned. In the simplest case, use of a rastered beam is similar to adjusting the second condenser lens in static beam mode so that a probe size larger than the minimum (focussed) size is used.

EXPERIMENTAL PROTOCOLS

For both qualitative and quantitative elemental analyses using EDS detectors in an AEM it is essential that the analyst understands the limitations of a particular experimental configuration and that a consistent protocol which optimises all analyses in a given experiment is employed. There is such a variety of instrument and detector configurations currently in use that only a brief summary of important considerations for modern-day AEMs will be addressed here. In older TEMs which have been modified for quantitative thin-film analysis [23], instrument dependent parameters should be critically assessed before attempts are made to quantify X-ray spectra.

A consistent protocol for the collection and analysis of thin-film EDS data requires an assessment of both instrument and specimen dependent parameters. Major parameters which should be considered for thin-film analyses include spurious X-rays, spectral artifacts, detector geometry, probe diameter, beam broadening, contamination, sample preparation artifacts, sample orientation and temperature and X-ray absorption. Many of these parameters are interdependent during an analysis and the prudent operator will evaluate as many as possible before routine use of an AEM. Further explanations of these parameters can be found in a number of publications [4,6,9,7]. Only selected parameters are discussed below.

Qualitative Analysis. A simple determination of the elements present in a small region of sample and an indication of their relative proportions (e.g. major or minor element) can be rapidly obtained using EDS detectors monitoring X-ray production from a thin-film of sample. If there is some prior knowledge of the likely

composition of a region/phase before analysis and only confirmation of the elemental make-up is required, few precautions are necessary apart from ensuring that the probe is actually sited in the desired area for analysis. However, if the sample is an "unknown" for which there is no reliable information about composition, then additional steps are necessary in order to eliminate the possibility of spurious X-ray signals.

Spurious X-ray signals can arise from regions of the electron column above and below the sample and are common in earlier generation, modified TEMs. The majority of these spurious signals arise from apertures in the upper part of the electron column as well as from the sample holder and surrounding anticontamination device. By employing thick, fixed apertures and C or Be liners in areas around the sample stage [23,25], the amount of spurious X-ray signal is greatly reduced. Similar tests for spurious signals were performed at 200kV on a JEOL 2000FX AEM and significant improvements in performance were obtained in the "as-bought" version [14]. Manufacturers have responded to the need for spectrally-clean column and stage environments in modern-day AEMs. However, it is important to undertake such detailed tests [23] for every installation in order to ensure fidelity of data interpretation. Similar "spectral clean-up" procedures have been presented for other AEMs such as the Philips 300 and 400 series of instruments [26].

Quantitative Analysis. When the relative accuracy of thin-film EDS analyses in an AEM is compared with other analytical techniques, it is instructive to consider the precision in terms of both spatial resolution and elemental abundance. Few techniques offer the same combination of high spatial resolution and elemental analysis for solids - analyses with ~5% relative accuracy from areas <20nm in diameter.

For many analyses, the choice of accelerating voltage and of electron source plays a influential role in the quality of data. In general, an increase in accelerating voltage increases characteristic X-ray signals and decreases continuous Bremsstrahlung radiation for a given sample and electron source [20]. The choice of a W or LaB₆ filament for conventional AEMs depends, in part, upon the usage and level of training available in a laboratory. The more expensive LaB₆ filaments are quite susceptible to operator error in adjusting filament current (and therefore, lifetime), but provide superior probe definition, higher brightness and greater beam current density than W filaments [27].

Spatial Resolution. As indicated in Figure 1b, the initial probe diameter combined with beam broadening within a thin-film sample tend to define the actual spatial resolution of an analysis. Beam broadening for specific operating conditions can be estimated using an analytical model [28], multiple scattering simulations [29] or experimentally, using crystallographically-oriented sample interfaces [30]. Reed [31] defined the spatial resolution, R, for a thin-film analysis as

$$R = (d^2 + b^2)^{1/2} \quad (1)$$

where d is the initial probe diameter at the top surface of the sample and b is the amount of beam broadening. Criteria for estimating both probe diameter and beam broadening in a consistent fashion for conventional AEMs are provided by Williams [32].

The amount of beam broadening is primarily dependant upon sample thickness, mean atomic number and instrument accelerating voltage, whilst for a given lens setting, probe diameter is strongly influenced by emission current [32]. For a given incident voltage and probe size, beam broadening increases with increase in sample thickness and atomic number [27]. For a constant thickness sample, beam broadening decreases with increasing accelerating voltage [19]. Thus, spatial resolution can be optimised for a particular sample by increasing accelerating voltage (to minimise broadening), by optimising the Wehnelt bias (to reduce probe diameter) and by analysing the thinnest regions (to the limit of desired X-ray count rate and sample drift).

Sample orientation is another parameter to consider if a reliable estimate of spatial resolution is required. If a sample is oriented in a Bragg diffracting condition, not only may there be enhanced production of X-rays due to electron channeling effects (see below), but strongly diffracted beams may also generate a significant X-ray signal [33] and thus, increase the degree of beam broadening. For consistent data it is advisable to collect X-ray spectra well away from Bragg diffracting conditions. An additional geometry consideration for ion-milled polymineralic samples is to ensure that the region of interest is correctly oriented relative to the detector. This concern arises because ion-milled polymineralic samples often contain significant relief (due to differential sputtering rates). Thus, the path-length of X-rays through a sample may be increased to a point at which thin-film criteria may not apply.

Elemental Precision. For the determination of element concentrations in a multi-component phase, it is assumed that, for suitably thin samples absorption and fluorescence of X-rays are negligible. Thus, the relative intensities of characteristic X-ray peaks can be related to the concentration ratio of elements by a factor, k [4]. This k -factor accounts for the relative efficiencies of X-ray production and detection during the analysis. This relationship can be expressed by the equation

$$C_a/C_b = k_{ab} I_a/I_b \quad (2)$$

where C_a and C_b are the weight fractions of elements a and b in the binary phase, I_a and I_b are the characteristic X-ray peak intensities and k_{ab} is an instrument dependent factor which can be determined theoretically or experimentally [34]. The absolute X-ray intensities for elements in a multi-component phase are a function of composition and thickness. However, in a very thin sample (e.g. $<<100\text{nm}$) X-ray absorption and fluorescence have little effect on relative peak intensities for elements with $Z>11$. Provided appropriate values for k -factors relative to a common reference

element can be determined, this "thin-film" criterion provides a precise method for the determination of element concentration. Thus, in general, for a sufficiently thin sample, absorption and fluorescence corrections need not be applied to secondary X-ray intensities [6]. Recent developments on this technique consider the effects of absorption and fluorescence, particularly for lower energy X-rays (i.e. $7 < Z < 14$) [24].

In mineralogy, multi-element phases are common, so the application of this Cliff-Lorimer technique [4] to samples with more than two analyzed elements is constrained by the following conditions,

$$C_a + C_b + C_c + \dots + C_n = 1.0 \quad (3)$$

$$\begin{aligned} C_a/C_b &= k_{ab} I_a/I_b \\ &\vdots \\ C_n/C_b &= k_{nb} I_n/I_b \end{aligned} \quad (4)$$

$$k_{ab}/k_{cb} = k_{ac} \quad (5)$$

The condition in Equation 3 is a potential source of error for thin-film analyses in mineralogy because the abundance of low-Z elements (e.g. F, O, N, H) is usually calculated from stoichiometry or inferred from bulk elemental analyses. However, comparisons within a suite of minerals will remain internally consistent, provided assumptions about low-Z elements are appropriately included in data reduction.

The determination of k-factors for minerals requires suitable homogeneous standards on the scale of individual analyses and well-determined data points for the construction of k-factor curves over a wide concentration range of elements. The most common reference element is Si [4,35] because it is present in significant quantities in many rock-forming minerals. Other reference elements have been used, for example, Ca in carbonate systems [36] and Fe for alloys and metals [27].

Figure 2 shows a typical set of k_{xSi} curves determined from a suite of silicate standards including olivine, pyroxene, and amphibole which have been characterized by bulk techniques such as electron microprobe and X-ray fluorescence analysis. These minerals were chosen so as to provide a wide concentration range of many elements within the one set of standards and because beam degradation effects were negligible. In a plot of C_x/C_{Si} versus I_x/I_{Si} , k_{xSi} is determined from the slope of the best fit line and the intercept should be close to zero, since the (0,0) point itself can be considered a data point.

In Figure 2, correlation coefficients for each k_{xSi} plot are all better than 0.98, and, with few exceptions, the standard deviation for each data point (determined as an average of at least 15 individual analyses) is equivalent to the size of the symbol. For each element, the k_{xSi} value is close to a theoretically determined value using reasonable estimates of ionisation cross-sections [37].

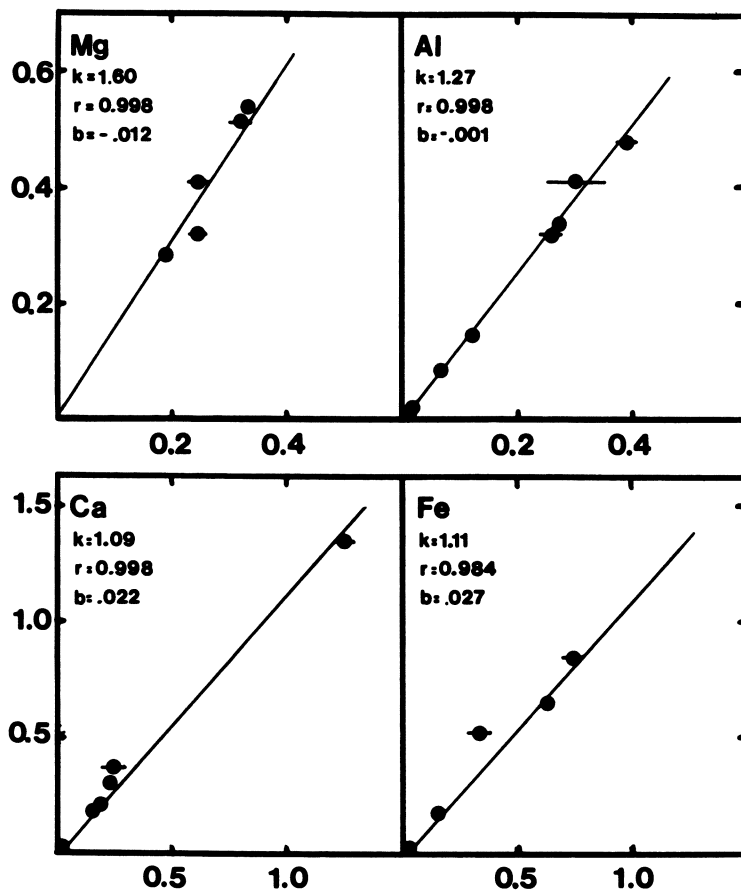


Figure 2. Experimental k_{xSi} plots for Mg, Al, Ca and Fe constructed using standards with a wide range of element concentrations. C_x/C_{Si} is plotted on the abscissa, with I_x/I_{Si} on the ordinate axes.

In the plot for Ca/Si, it is worth noting that the point at the high concentration end (using a titanite, CaTiSiO_5 , standard) provides strong control over the best-fit line. Without this data point, the k_{CaSi} value is 1.21, although the correlation coefficient is 0.99. Thus, a relative error of ~11% would have been introduced into this k_{CaSi} determination if only the low Ca standards were used [14]. The precise determination of k-factors for the chosen experimental protocol is critical for precise elemental analyses of multi-component materials with a modern-day AEM. The sources of error in an elemental analysis include not only errors in characteristic peak definition and intensity determination [6] during the actual data collection, but also include errors in the determination of k_{XSi} . These errors are cumulative, and thus, limit the accuracy of this thin-film technique to ~3% relative under ideal conditions [27].

For multi-component phases commonly encountered in mineralogy, it may not be possible to construct precise experimental k-factor curves for all elements due to uncommon element abundances in silicates or to a lack of suitable standards. For example, Ni or Cr can occur in silicates in low concentrations, but sufficient to be detected using an AEM. In such instances, calculated k-factors can be determined based upon theoretical cross-sections for X-ray production [34] and are generally suitable for higher-Z elements ($Z > \text{Ti}$) to within 10% relative error [37]. Alternatively, the relationship shown in equation 5 can be used to advantage in the calculation of uncommon k-factors, though with a concomitant reduction in accuracy due to accumulation of errors in determination of the individual k values.

With a known mineral, as determined by electron diffraction or other technique (such as X-ray diffraction), determination of the stoichiometry and structural formula can be a suitable test for analytical precision of thin-film elemental analyses. This simple test follows the practice commonly employed for electron microprobe data in which the accuracy (and completeness) of an analysis is judged by the departure from stoichiometry calculated for a given mineral. Thus, thin-film analyses of olivines, pyroxenes, garnets, feldspars and many other common rock-forming minerals can be examined for internal consistency via a calculation of structural formulae.

An additional test of considerable value for standards used to construct k-factor curves is a test for element loss under the conditions of analysis. In modern-day AEMs, the use of LaB_6 filaments and small probe diameters significantly increases beam current density during an analysis. For example, on a 100kV instrument with a nominal beam size (FWHM) of 24nm the measured current is 0.2nA [32], while for a different instrument at 200kV and a nominal beam size (FWHM) of 20nm, the measured current is 1.05nA [38]. The resultant beam current densities are considerably higher for modern-day AEMs than earlier generation modified TEMs. For example, McGill and Hubbard [39] obtained k-factor data for a range of silicates at 100kV using a beam current of 200nA and a probe diameter of only 3 μm . Even at this relatively low beam current density, a significant change in k_{NaSi} with irradiation time was

observed for Amelia albite. This change in k-factor with collection time was interpreted as due to element loss associated with electron beam induced radiation damage [39]. Similar element loss phenomena have been noted for silicate minerals examined with an electron microprobe [40].

Element loss during analysis can be simply determined by plotting an appropriate k-factor (e.g. k_{xSi}) from replicate analyses of a sample over a range of collection times. This type of analysis was also performed for Amelia albite using a 200kV AEM for a range of beam current densities and sample temperatures [14,38]. Figure 3 shows the results of these experiments at -25°C and at -150°C [38]. At ambient temperature, both k_{NaSi} and k_{AlSi} were observed to increase markedly with irradiation time up to about 300sec. Since these experiments were performed under relatively clean vacuum conditions, these changes in k-factors were interpreted as a loss of both Na and Al (though at different rates) with irradiation time. By monitoring microdiffraction patterns of Amelia albite using the same size probe, loss of sample crystallinity could be qualitatively correlated with the abrupt rise in k_{NaSi} at about 100secs irradiation shown in Figure 3.

By reducing the temperature of the sample, element loss was minimised and the precision of these replicate analyses improved significantly. In fact, the estimated standard deviations for all low temperature analyses are less than the size of the symbols plotted in Figure 3. The two data sets at -150°C are for different beam current densities using a W and LaB_6 filament, respectively. A small loss of Na can be observed for the higher current density at collection times of 300secs. Comparison of low temperature and ambient temperature data for Amelia albite also suggests that extrapolation of ambient temperature plots to time, $t=0$, may provide a reasonable estimate of the actual k_{xSi} value for minerals which show significant element loss [38].

Not all minerals show significant differences in k-factors between ambient and low temperature experiments. That is, element loss during AEM analysis need not be assumed for all minerals or in compositionally distinct minerals within a particular family. For example, Mackinnon et al. [14] compare intensity ratios (I_z/I_{Si}) for two sets of analyses (15 observations per set) of a hornblende from Verona, Ontario, at ambient temperature and at -150°C . Within an estimated standard deviation (esd), there is no significant difference in the intensity ratios (i.e. k-factors) for any element at these two temperatures. As noted in the earlier work on Amelia albite, there is a significant improvement in the value of esd's for each element in the lower temperature data. These data on the Verona hornblende indicate that element loss is negligible, or it occurs at the same rate at both temperatures [14]. Further details of low temperature thin-film analyses of minerals using an AEM are given by Mackinnon (Mackinnon, I.D.R., in Electron Microscopy and Microprobe Techniques in Clay Analysis, IDR Mackinnon and FA Mumpton, eds., Allen Press, in press).

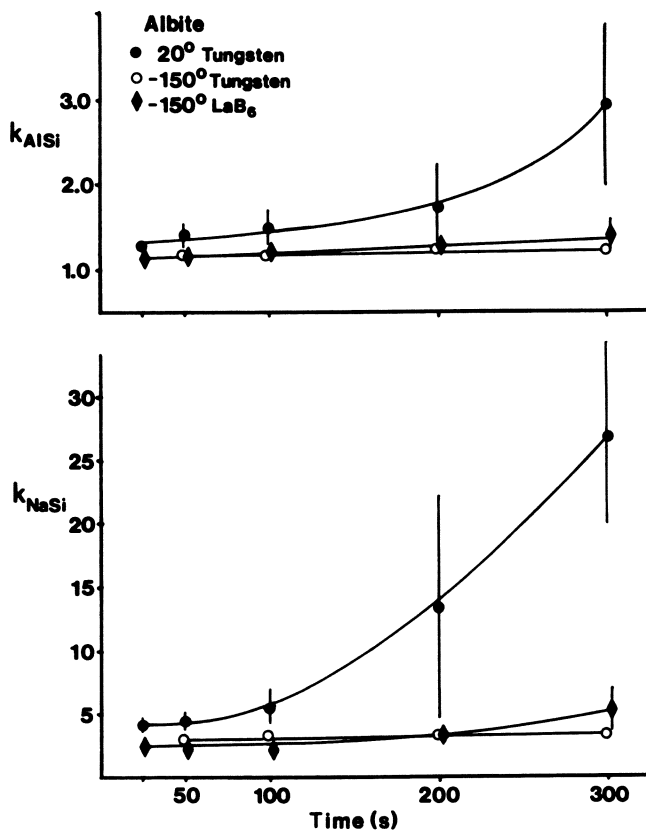


Figure 3. Plots of k_{NaSi} and k_{AlSi} with collection time for Amelia albite at two different temperatures using a LaB₆ or a W filament. (Reproduced with permission from Ref. 38. Copyright 1987 San Francisco Press.)

Analysis Optimisation. An assessment of both instrument and specimen dependent parameters during thin-film analysis provides a good basis for the optimisation of all analyses and for confidence in the precision of measured element concentrations. The primary limits to the detection of elements using this technique are accelerating voltage, beam current density, probe size at the sample, sample thickness and signal collection time. Thus, an analyst may try to work with the highest possible accelerating voltage, an optimized probe size for the object of interest and detector dead-time [24], the thickest part of a sample at which absorption of X-rays is negligible, the highest beam current density and the longest possible collection time within the limits of sample radiation damage and element loss.

Implicit in the above optimisation scheme is the desire to improve the statistics for any given analysis. Thus, optimisation of analyses effectively means improving counting statistics and devising methods to assess the quality of analytical data. This particular aspect of thin-film analyses has received some attention over the years, although primarily directed towards counting statistics and cumulative errors in k-factor determination [27,41]. Less attention has been given to the actual reporting of analytical precision, or, of the reliability of k-factors determined for a specific AEM configuration. Nevertheless, Blake et al. [36] have presented methods for the evaluation of k-factor plots using accepted statistical theory and provided examples using compiled experimental data. A result worth noting is that at least 25 observations are needed in order to provide an accurate estimate of a k-factor [36] (i.e. at the 99% confidence level).

Whilst the above optimisation factors should be considered on a case by case basis for any particular AEM, there are few criteria by which one can measure instrument performance for a given analysis problem. These criteria are of increasing importance with the development of intermediate voltage (300kV to 400kV) AEMs, the continued improvement of AEMs operating at lower voltages (generally, between 100kV and 200kV) and the introduction of new X-ray detectors. These developments offer the analyst a wide array of instrument, detector and operating configurations for the solution of micro- and nano-analysis problems. Many of these technical advances are slanted at improved spatial resolution and, presumably, analytical sensitivity. However, in general, sensitivity degrades as spatial resolution improves [42]. Lyman [42] has demonstrated one approach to measure instrument performance using spatial resolution and detectable minimum mass fraction estimates for various AEMs. In this approach, instruments which detect smaller amounts of solute from smaller excited volumes are considered to have better analytical performance. Some differences in instrument performance can be attributed to improvements in AEM design such as an increased probe current for a given probe size. The predicted performance of both thermionic and FEG AEMs at 300kV are significantly improved over the instrumental equivalents at 100kV or 120kV [42].

American Chemical Society
Library

1155 16th St., N.W.
Washington, D.C. 20036

In Spectroscopic Characterization of Minerals and Their Surfaces; Coyne, L., et al.; ACS Symposium Series 200; American Chemical Society: Washington, DC, 1990.

Cation Site Distribution. Thin-film EDS analysis can also be used to quantitatively determine the site occupancy of atoms in a known crystal structure. Atom Location by Channeling Enhanced Microanalysis (ALCHEMI) is a technique which utilises electron-channeling enhanced X-ray emission for specific atoms in a crystal when appropriately oriented relative to the incident beam [43]. The method involves no adjustable parameters, can be used on relatively small areas of sample and provides fractional occupancies of atom positions [44]. Unlike X-ray diffraction which has had limited success with adjacent elements in the periodic table [e.g. 45], ALCHEMI can provide site occupancies for adjacent elements and is relatively insensitive to sample thickness or the precise electron beam orientation [44].

The orientation dependence of electron-induced X-ray emission in crystalline materials was experimentally demonstrated by Duncumb [46], and a theoretical treatment in terms of solute concentrations within a unit cell was put forward by Gjønnes and Hoier [47]. Tafto [48] provided one of the first practical applications of this technique on the diatomic crystals ZnS, ZnSe and FeS₂. Since that time, over forty separate publications have presented applications of this technique on a wide range of samples, many of which are minerals of considerable significance to the earth sciences. Smyth and McCormick [49] summarise the significance of ALCHEMI to the earth sciences and have proposed likely candidate minerals for further study. ALCHEMI has been used to determine cation distributions in olivine [50,51], spinel [52], garnet [53], feldspar [54], ilmenite and dolomite [55].

ALCHEMI relies on the X-ray emission from a host atom on a known site providing a reference signal for use as an effective internal standard [56]. By comparing the orientation dependence of X-ray signals from substitutional atoms with this reference atom on known planes (or atomic columns) quantitative estimates of the amounts of each substitutional atom can be made using the relative intensities of X-ray counts. In addition, in order for ALCHEMI to provide interpretable results, the intensity of the channeling effect should be large. This large effect can be achieved if there is a large difference in projected electron density between alternating planes of atoms. Thus, crystal-chemical constraints, as well as practical considerations such as statistically significant X-ray intensities, limits the application of ALCHEMI to a few selected minerals such as pseudobrookite, perovskite, andalusite, sillimanite, apatite, epidote and melilite as well as those already studied by this technique [50].

Specific examples in which results from ALCHEMI are compared with X-ray or neutron diffraction studies on the same sample have been presented for olivine [51], clinopyroxene [57] and feldspar [54]. To date, all published planar ALCHEMI studies on mineral samples other than oxides containing high-Z elements (e.g. ceramic nuclear wasteforms, [58]) have been internally consistent and tractable. For example, a combined X-ray diffraction and ALCHEMI study on a complex, nonstoichiometric clinopyroxene [57] has been used to determine the location of vacancies in the structure. In

this instance, single crystal X-ray diffraction established that vacancies in the structure were required in order for site occupancies to be consistent with the mineral composition. The ALCHEMI study was then used to show that more than 90% of the vacancies are in the M2 site of the clinopyroxene [57].

Table 1 gives a comparison of site occupancy determinations using ALCHEMI and X-ray diffraction for an olivine from San Carlos [51] and a high sanidine feldspar [54]. For the olivine, least-squares refinement of 1454 independent X-ray reflections gave a residual, R, of 0.031 and indicated an Fe occupancy for the M1 site of 0.51(1); [51]. Electron channeling on this same olivine gives a value for C_{FeM1} of 0.49(4), where C_{FeM1} is the proportion of iron in the M1 site. Values in parentheses are one estimated standard deviation (esd) and indicate that the two techniques for site occupancy determination provide similar results within the calculated error. However, there is a significant difference in the calculated esds for each technique.

TABLE 1

COMPARISON OF ALCHEMI AND X-RAY DIFFRACTION
SITE OCCUPANCIES

A. San Carlos Olivine [51]

X-RAY	$C_{FeM1} = 0.51 (1)$
ALCHEMI	$C_{FeM1} = 0.49 (4)$

B. High Sanidine [54]

X-RAY	$2t_1 = 0.543$
ALCHEMI	$2t_1 = 0.52 (3)$

The sanidine sample is free of any microstructure (such as exsolution or "tweed structure") and estimates for Al-ordering using the $2t_1$ parameter (obtained from single crystal X-ray diffraction and ALCHEMI) again agree within the estimated error of experiment [54]. Unlike most other ALCHEMI experiments, these data on feldspars were obtained using an accelerating voltage of 300kV. McLaren and Fitzgerald [54] also show that the small probe size using ALCHEMI can be of advantage in determining site occupancies for the exsolved components in a well-developed tweed microstructure in an orthoclase. The significant differences in the two site determination techniques are (a) the rapidity with which electron channeling experiments can be performed in comparison to single crystal X-ray diffraction, (b) the relative simplicity of sample preparation requirements for many ALCHEMI experiments and (c) apparently lower precision for ALCHEMI experiments.

The problems of element loss or low intensity channeling effects have been addressed by Spence et al. [59], by performing ALCHEMI experiments at low temperature (e.g. 90K). In the latter case the atom site occupancy is not temperature dependent, but the ratio of elemental X-ray counts from a crystal in two different

orientations is temperature dependent [59]. A reduction of specimen temperature greatly reduces inelastic phonon scattering [27], and so electron channeling effects, which are masked by inelastic scattering events [56], are enhanced at low temperature. The reduction in diffuse inelastic scattering is dependent on the type of material and on the thickness relative to the mean free path of phonon excitation. Thus, for samples which show a reduction in diffuse inelastic scattering at low temperature (e.g. by the appearance of a sharper diffraction pattern), more accurate site occupancies of impurity atoms can be obtained using ALCHEMI at low temperature.

Site determination using ALCHEMI can also be monitored by EELS [60], and a description of this approach is given by Krishnan in an accompanying chapter. By studying the effects of electron channeling on CaSO_4 in the low energy loss range using EELS, Self and Buseck [61] predict that it may be possible to use oxygen K X-rays as an internal reference for ALCHEMI. This approach then suggests an additional, and significant application for windowless or UTW EDS detectors. Subject to thermal vibration amplitudes of oxygen atoms in the structure, this possibility would greatly extend the range of minerals for which site occupancies can be determined using ALCHEMI. More recent developments in ALCHEMI techniques include the determination of (a) cation valence state, (b) polarity of noncentrosymmetric crystals, and (c) trace amounts of impurity atoms [62]. These latter developments involve refinements of the general ALCHEMI technique which utilise the thickness-dependence of the channeling effect for EELS analysis. A detailed review and theoretical study of the crystallographic implications of this electron channeling effect for both X-ray emission and energy-loss electrons is given by Krishnan [62].

SUMMARY

Applications of the thin-film technique to mineralogy and petrology are many, varied and have increased tremendously over the past ten years. There would be few issues of any mineralogical journal without a paper which utilises the basic attributes of an AEM and the thin-film technique. This rise in popularity of the technique is not only because of the great advances in technical capability and reliability of instrumentation, but also because microstructure and microchemistry play a critical role in determining bulk properties of all materials. A few examples of thin-film analyses have been presented here in order to highlight the breadth of mineralogical problems that can be addressed with these techniques. The reader is referred to other articles in the list of citations for further information on thin-film analyses using an AEM. This list of citations is not exhaustive and should only be used as a guide to the general field.

Developments in AEM techniques over the past ten years have been rapid, effectively commercialised and of tremendous importance to all solid-state research activities. For mineralogists, the modern-day AEM provides unequalled spatial resolution for elemental analyses at quite acceptable levels of mass sensitivity and

elemental precision. An ~5% relative precision for thin-film elemental analysis of the major elements in a multi-component silicate mineral from a region ~20nm diameter is a routine task for the current generation AEM, provided appropriate analytical precautions mentioned above are observed.

For certain minerals with multiple element substitutions on lattice sites, electron channeling experiments can provide estimates of site occupancy using a similar thin-film analysis technique. This latter approach, termed ALCHEMI, utilises an orientational dependence of X-ray emission from specific elements on crystallographic sites. Conventional thin-film analyses, which measure the concentration of elements in a sample, do not require specific, known orientations of a sample, and are best obtained from randomly-oriented or non-Bragg diffracting crystals and with a convergent beam which minimises channeling effects.

These thin-film techniques, which usually entail a small, focussed electron beam (~20-50nm diameter) and an EDS detector for the measurement of secondary X-rays, have been applied to many mineralogical problems with considerable success. Many areas of geology and mineralogy, both terrestrial and extraterrestrial, can benefit from the analytical power of the modern-day AEM because the fundamental relationships between microchemistry and bulk physical properties can be effectively explored.

Acknowledgments: Constructive reviews by David Veblen and Adrian Brearley are appreciated.

LITERATURE CITED

1. IDR Mackinnon and FJM Rietmeijer, Rev. Geophys. 1987, 25 1527-53.
2. JP Bradley, Geochim Cosmochim Acta 1988, 52 889-900.
3. JG Thompson, BG Hyde, RL Withers, LR Wallenburg, JD FitzGerald and JS Anderson, Chem. Aust. 1988, 55 285-8.
4. G Cliff and GW Lorimer, J. Microscopy 1975, 103 203-7.
5. AM Isaacs, in Microbeam Analysis - 1983, 1983, (R. Gooley, ed.) 202-5, San Francisco Press, CA.
6. DB Williams, JI Goldstein and CE Fiori, in Principles of Analytical Electron Microscopy 1986, (DC Joy, AD Romig Jr and JI Goldstein, eds.) 123-153, Plenum Press, NY.
7. GW Lorimer, Min. Mag. 1987, 51 49-60.
8. SJB Reed and NG Ware, J. Petrol. 1975, 16 499-519.
9. PJ Statham, J. Microscopy 1982, 130 165-76.
10. KFJ Heinrich, DE Newbury, RL Myklebust and CE Fiori, Energy Dispersive X-ray Spectrometry 1981, NBS Spec. Pub. 604, US Govt. Print. Off. 441pp.
11. RW Fink, in Energy Dispersive X-ray Spectrometry 1981, NBS Spec. Pub. 604 (KFJ Heinrich, DE Newbury, RL Myklebust and CE Fiori, eds.) US Govt. Print. Off., 5-34.
12. RG Musket, in Energy Dispersive X-ray Spectrometry 1981 NBS Spec. Pub. 604 (KFJ Heinrich, DE Newbury, RL Myklebust and CE Fiori, eds.) US Govt. Print. Off., 97-126; LE Thomas, LA Charlot, GW Franti, AJ Garret-Reed, PJ Goodhew, DC Joy, RJ

- Lee, AC Ng, MR Plichta and NJ Zaluzec, in Analytical Electron Microscopy - 1984 1984 (DB Williams and DC Joy, eds.) San Francisco Press CA 333-36.
13. Kevex Corp. New Product Bulletin 1987, Foster City CA.
14. IDR Mackinnon, GR Lumpkin and SB van Deusen, in Microbeam Analysis - 1986 1986 (AD Romig Jr and WF Chambers, eds.) San Francisco Press CA.
15. NC Barbi and DB Lister, in Energy Dispersive X-ray Spectrometry 1981 NBS Spec. Pub. 604 (KFJ Heinrich, DE Newbury, RL Myklebust and CE Fiori, eds.) US Govt. Print. Off., 35-44.
16. EB Steel, in Microbeam Analysis - 1986 1986 (AD Romig Jr. and WF Chambers, eds.) San Francisco Press CA 439-42.
17. NJ Zaluzec, in Microbeam Analysis - 1981, 1981 (RH Geiss, ed.) San Francisco Press, CA 325-8.
18. NJ Zaluzec, DM Maher and PE Mochel, in Analytical Electron Microscopy - 1981, 1981 (RH Geiss, ed.) San Francisco Press CA 25-28.
19. JCH Spence and RW Carpenter, in Principles of Analytical Electron Microscopy 1986 (DC Joy, AD Romig Jr and JI Goldstein, eds.) Plenum Press, NY 301-52.
20. S Suzuki, T Honda and Y Bando, in Materials Problem Solving with the Transmission Electron Microscope 1986, (LW Hobbs, KH Westmacott and DB Williams, eds.) MRS Symp. Vol. 62, Materials Research Society, Pittsburgh PA 123-8.
21. DR Veblen and PR Buseck, in Proc. 41st Ann. Meet. Elect. Micros. Soc. Amer. 1983, (GW Bailey, ed.) San Francisco Press CA 350-3.
22. RE Klimentidis and IDR Mackinnon, Clays and Clay Mins. 1986, 34 155-64.
23. LF Allard and DF Blake, in Microbeam Analysis - 1982 1982 (KFJ Heinrich, ed.), San Francisco Press, CA 8-20.
24. DB Williams, JI Goldstein and CE Fiori, in Principles of Analytical Electron Microscopy 1986 (DC Joy, AD Romig Jr and JI Goldstein, eds.) Plenum Press, NY 123-53; DB Williams and JI Goldstein, in Analytical Electron Microscopy - 1981 1981 (RH Geiss, ed.) San Francisco Press CA 39-46.
25. IDR Mackinnon, FJM Rietmeijer, DS McKay and ME Zolensky, in Microbeam Analysis - 1985 1985 (JT Armstrong, ed.) 291-297, San Francisco Press CA.
26. NJ Zaluzec, in Introduction to Analytical Electron Microscopy 1979 (JH Hren et al., eds.), Plenum Press NY, 121-67; DB Williams and JI Goldstein, in Energy Dispersive X-ray Spectrometry 1981 NBS Spec. Pub. 604 (KFJ Heinrich, DE Newbury, RL Myklebust and CE Fiori, eds.) US Govt. Pub. Off. 341-349.
27. DB Williams, Practical Analytical Electron Microscopy for Materials Science 1984, Philips Electron Optics Publishing Group, Mahwah NJ 153pp.
28. JI Goldstein, JL Costley, GW Lorimer and SJB Reed, Scanning Electron Micros. 1977 1, 315.
29. IP Jones and AW Nicholls, J. Microscopy 1983, 130 155-64.
30. JI Goldstein, in Introduction to Analytical Electron Microscopy 1979, (JJ Hren, JI Goldstein and DC Joy, eds.) Plenum Press NY 83-96.

31. SJB Reed, Ultramicroscopy 1982, 7 405-10.
32. DB Williams, in Microbeam Analysis -1986 1986 (AD Romig Jr. and WF Chambers, eds.) San Francisco Press CA 443-48.
33. NJ Zaluzec, EMSA Bull. 1984, (R Anderson, ed.) 14(2) 61-72.
34. JI Goldstein, DB Williams and G Cliff, in Principles of Analytical Electron Microscopy 1986, (DC Joy, AD Romig Jr. and JI Goldstein, eds.) Plenum Press NY 155-217.
35. GW Lorimer, in Quantitative Electron Microscopy 1983, (JN Chapman and AJ Craven, eds.) Univ. of Edinburgh, Glasgow 305-39.
36. DF Blake, AM Isaacs and RH Kushler, J. Microscopy 1982 131 249-55.
37. NJ Zaluzec, EMSA Bull. 1984, (R Anderson, ed.) 14(1) 67-75.
38. IDR Mackinnon and SA Kaser, in Microbeam Analysis - 1987 1987 (RH Geiss, ed.), San Francisco Press CA,332-4.
39. RJ McGill and FH Hubbard, in Quantitative Microanalysis with High Spatial Resolution, 1981 (GW Lorimer, MN Jacobs and P. Doig, eds.) The Metals Soc., London 277-82.
40. JV Smith and P. Ribbe, J. Geol., 1966 74 192-210.
41. PJ Statham, in Microbeam Analysis -1982 1982 (KFJ Heinrich, ed.) San Francisco Press CA 1-7; NJ Zaluzec, in Microbeam Analysis - 1981 1981 (RH Geiss, ed.) San Francisco Press CA 329-32.
42. CA Lyman, in Microbeam Analysis - 1986 1986 (AD Romig Jr and WF Chambers, eds.) San Francisco Press CA 434-38.
43. J Tafto and JCH Spence, Science 1982, 218 49-51.
44. JCH Spence and J Tafto, J. Microscopy 1983, 130 147-54.
45. JV Smith, Feldspar Minerals 1974, Vol 1, Springer-Verlag NY.
46. P Duncumb, Phil Mag. 1962, 7 2101.
47. J Gjonnes and R Hoier, Acta Cryst A 1971, 27 166-74.
48. J Tafto, Z. Naturforsch Teil A 1979, 34 452-58.
49. JR Smyth and TC McCormick, Ultramicroscopy 1988, 26 77-86.
50. JR Smyth and J Tafto, Geophys. Res. Lett. 1982, 9 1113-6.
51. TC McCormick, JR Smyth and GE Lofgren, Phys. Chem. Minerals 1987, 14 368-72.
52. J Tafto, J. App. Cryst. 1982, 15 378-81.
53. MT Otten and PR Buseck, Ultramicroscopy 1987, 23 151-58.
54. AC McLaren and JD FitzGerald, Phys. Chem. Minerals 1987, 14 281-92.
55. TC McCormick and JR Smyth, Am. Mineral. 1987, 72 778-81.
56. JCH Spence, M Kuwabara and Y Kim, Ultramicroscopy 1988, 26 103-22.
57. TC McCormick, Am. Mineral. 1986, 71 1434-40.
58. CJ Rossouw, PS Turner and TJ White, Phil Mag. 1988, B57 227-41.
59. JCH Spence, RJ Graham and D Shindo, in Materials Problem Solving with the Transmission Electron Microscope 1986, (LW Hobbs, KH Westmacott and DB Williams, eds.) MRS Vol 62, Materials Research Society Pittsburgh PA, 153-62.
60. OL Krivanek, MM Disko, J Tafto and JCH Spence, Ultramicroscopy 1982, 9 249-57.
61. PG Self and PR Buseck, Phil. Mag. A 1983, 48 L21-L26.
62. KM Krishnan, Ultramicroscopy 1988, 24 125-42; J Tafto and J Gjonnes, Ultramicroscopy 1988, 26 97-102.

RECEIVED May 25, 1989

Chapter 3

Electron Energy-Loss Spectroscopy

Fundamentals and Applications in the Characterization of Minerals

Kannan M. Krishnan

National Center for Electron Microscopy, Materials and Chemicals Sciences
Division, Lawrence Berkeley Laboratory, Berkeley, CA 94720

The combined use of an energy-loss spectrometer and an analytical electron microscope with fine probe forming capabilities provides a wealth of information about the sample at high spatial resolution. Fundamental principles governing the physics of the interaction between the fast electron and a thin foil sample, to account for the fine structure in the inelastically scattered fast electron distribution (Electron-Energy Loss Spectroscopy, EELS), will be reviewed. General application of EELS is in the area of low atomic number elements ($Z < 11$) microanalysis, where it significantly complements the more widely used Energy Dispersive X-ray Spectroscopy (EDXS). However, a careful analysis of the low loss plasmon oscillations and the fine structure in the core-loss edges, can provide additional information related to the bonding and electronic structure of the sample. An illustration of this is presented from our study of C δ diamond residue from the Allende carbonaceous chondrite. Combination of EELS with channeling effects can provide specific site occupation/valence information in crystalline materials. Details of this novel crystallographic method will be outlined and illustrated with an example of the study of chromite spinels. Finally, some pertinent experimental details will be discussed.

The interaction of a fast electron, accelerated through kilovolt potentials in an electron microscope, with a thin foil will produce a variety of signals that can be monitored with appropriate detectors to provide a wealth of information about the crystallography, chemistry and electronic structure of the sample [1-3]. With the advent of improved electron-optics designs and high vacuum/voltage technologies it is increasingly possible to perform these microanalytical characterizations at high spatial resolutions. The

0097-6156/90/0415-0054\$06.25/0

© 1990 American Chemical Society

crystallographic and structural information is contained in the elastically scattered beams and can be effectively interpreted either by the measurement of the electron diffraction patterns or by the recording of the diffraction contrast (conventional) and phase contrast (high resolution) images. On the other hand, the inelastically scattered fast electron intensity distribution and the multitude of emissions produced by the response of the sample to its excitation by the incident beam, incorporate the chemical and electronic structure information. In particular, the de-excitation processes are well understood and form the basis of an assortment of established analytical characterization methods in a transmission electron microscope environment. These include x-ray emission spectroscopy [4], Auger electron spectroscopy [5] and cathodoluminescence [6]. However, it can be argued that, by the conservation of energy principles, all the above signals should have their counterparts in the inelastically scattered primary electron, provided its distribution as a function of energy or momentum (electron energy-loss spectroscopy) [7-9] can be monitored and interpreted. In this article the fundamentals and the current status of this technique, with some examples of its application to the characterization of minerals, are discussed.

FUNDAMENTALS OF ELECTRON ENERGY-LOSS SPECTROSCOPY

A representative EEL spectrum is shown in Figure 1 and can be broadly divided into three regions. The zero-loss peak (ZLP) consists of elastically scattered electrons that emerge on the exit surface of the sample with the same energy as the primary beam. The full width at half maximum (FWHM) of the ZLP is a measure of the energy resolution of the experimental arrangement and is a function of both the energy spread of the primary beam (source) and the resolution of the spectrometer. It is fair to say that for currently available commercial spectrometers, under optimal operating conditions, the resolution is only limited by the thermal spread of the electron source and the abilities of the operator. The low-loss region [9] extending up to energy losses of $\sim 100\text{eV}$, consists of broad resonance peaks called plasmons representing the collective excitation of the delocalized outer-shell electrons by the primary beam. In a simple jellium or free-electron gas model [10] the plasmon energy is proportional to the square root of the number density of free electrons in the thin film [11]. The plasmon line-width is a function of the relaxation time required for the decay of the oscillation and is determined by the average grain size of the material; significant broadening due to grain boundary damping for small crystallite sizes ($\sim 6\text{-}7\mu\text{m}$ diameter) has been reported [12]. In thicker samples secondary plasmons at multiples of the primary plasmon energy, due to plural scattering, can be observed. In fact, a ratio of the ZLP to the total spectrum (ZLP + plasmons) is a simple well tested method of obtaining an estimate of the sample thickness [13]. In a TEM, EELS experiments are best performed at thicknesses where the plasmon is less than one tenth the height of the ZLP.

At higher energy losses, one observes edges corresponding to the interaction of the fast electron with the deeply bound core electrons of the sample. The onset of the edge generally corresponds to the ionization energy of the core electrons. As the binding energies of the core electrons

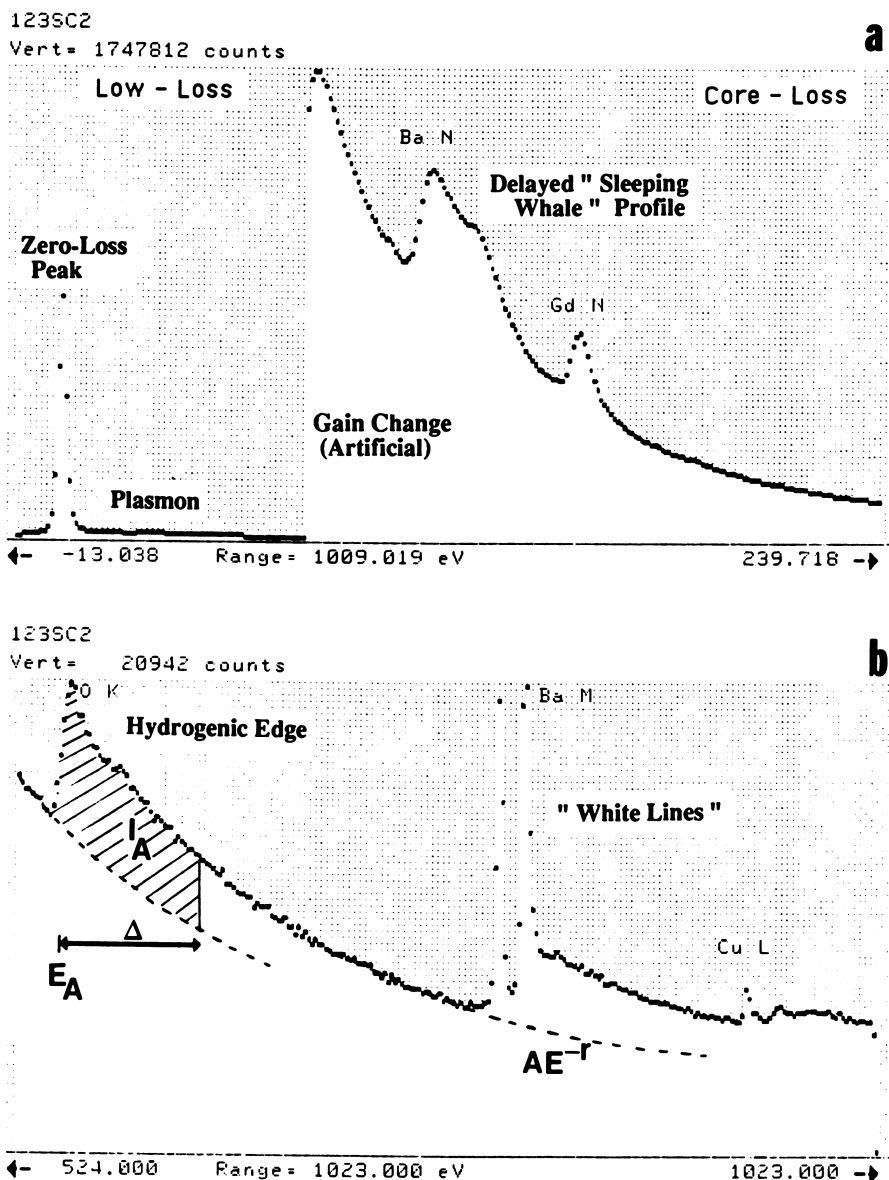


Figure 1. Electron energy-loss spectrum of $GdBa_2Cu_3O_{7-\delta}$ illustrating the various observable types of fine structures; a) the low-loss segment including the outer shell ionization edges; b) the innershell core-loss edges; the background model AE^{-r} and the parameters used in microanalysis (I_A , E_A , Δ) are also shown.

are a function of the atomic number, the position of the edges can be used to unequivocally identify the elements that constitute the sample. In addition, in the process of ejecting the core electron to the continuum, the fast electron can impart varying amounts of energy (up to a maximum of the primary energy minus the binding energy) to it. However, the probability of it doing so decreases with increasing energy-loss. Hence, the overall shape of an EELS core edge is a sharp onset followed by a smooth decay, (Figure 1b), which often results in significant edge overlap. Moreover, preceding edges can impart considerable backgrounds to edges at higher energy losses. The problem is sometimes compounded in thicker samples due to plural scattering. However, signal processing methods for the modelling of the background [14, 15, 7] and the deconvolution of multiply scattered spectra [16,17] are well established. Alternatively, the core electron can be promoted from its initially well defined atomic orbital to a vacant state above the Fermi level (an unoccupied bound state in the conduction band or an empty antibonding molecular orbital level). Extended fine structures resulting from such transitions, and observed above the ionization edge are hence a function of both the initial and final state wave functions of the excited electron and can provide information about the valence of the excited atom as well as its local chemical environment [7].

The inelastic electrons are scattered through relatively small angles when compared with the elastically scattered electrons, i.e., they are strongly forward peaked. In general, primary electrons that lose more energy tend to be scattered through larger angles. In practice this results in not all the energy-lost electrons being detected, as finite collection or entrance apertures to minimize electron-optical aberrations are used. Both the shape of the spectrum as well as the overall intensities (detection efficiency) are affected by these apertures.

When a small (<100 mrad) collection aperture is used, the predominant transitions observed in an energy-loss spectrum are the ones governed by the dipole selection rules. In that sense, EEL spectra are similar to x-ray absorption spectra and the optical selection rules $\Delta l = \pm 1$ apply. Standard spectroscopic nomenclature is used to identify the core edges, i.e., K (1s), L₁ (2s), L₂ (2P_{1/2}), L₃ (2P_{3/2}), M₁ (3s), M₂ (3P_{1/2}), M₃ (3P_{3/2}), M₄ (3d_{3/2}), M₅ (3d_{5/2}),..., etc. In practice, only a few of these transitions can be recorded with ease and the relevant edges are those corresponding to an initial state of maximum l for a given n [8]. Hence, transitions arising from 2p, 3d... initial states are an order of magnitude more intense than the 2s, 3s, 3p... contributions.

Three basic edge shapes (Figures 1a and b) are broadly observed. As the wave functions of the core electrons undergo very little change upon aggregation into a solid, a simple atomic model can predict their general shapes [19, 20]. They are: a) "saw tooth" profile, such as those calculated using hydrogen-like or Hartree-Slater wave functions for K-shell edges. Experimentally observed edges (O-K edge in Figure 1b) conform to this general shape but with some additional fine structure at the onset; b) "sleeping-whale" profile, a delayed maximum observed approximately 20 eV above the ionization edge, usually resulting from a large centrifugal barrier due to the $l'(l' + 1)$ term in the radial Schrodinger equation. These are commonly observed for the L_{2,3} edge of the third period elements Na-

Ar (another typical example is the Ba $N_{4,5}$ edge in Figure 1a); c) "white lines" arising from distinct spin-orbit split levels, and typically observed in the $L_{2,3}$ edges of the fourth period elements (Cu $L_{2,3}$ edge in Figure 1b). $L_{2,3}$ edges probe the s- and d- symmetric portions of the final state wave functions. The latter can become large and narrow and can lead to sharp threshold peaks, particularly in a solid with a high density of unoccupied d states. The L_3/L_2 intensity ratio is often different from the statistical value of 2.0 based on initial state occupancy and can be used to determine the oxidation state [21].

Superimposed on the broad edge shapes are the fine structures due to solid state effects. At the edge threshold one can measure a displacement of the onset or "chemical shift". In EELS, the ionization edge threshold is a function of both the initial state as well as the position and nature of the vacant states at the Fermi level. Band structure effects such as band gaps can be easily resolved (example: diamond C $1s \rightarrow \sigma^* = 288$ eV, graphite C $1s \rightarrow \pi^* = 284$ eV). In addition, positive chemical shifts are also observed with increasing oxidation states [22] because oxidation removes valence electrons, leads to reduced screening of the nuclear field and a deepening of the potential well (of the initial state). The energy loss near edge structures (ELNES) observed ~5-50 eV above the ionization edge can be interpreted, in the first approximation, using a simple one electron transition model between the initial state and a vacant final state in the conduction band:

$$I(E) \propto T(E) N(E) \quad (1)$$

where $T(E)$, the transition probability, is a slowly varying function of energy loss and $N(E)$ is the density of final states. This simple model is a reasonable basis for the interpretation of ELNES, provided $N(E)$ is defined, as and when required, to include the following ideas (a) dipole selection rules apply, i.e., $N(E)$ is interpreted as a symmetry projected density of states clearly distinguishing the K and L edges; (b) core-level states are highly localized - $N(E)$ is a local density of states determined for that particular lattice site and reflecting the local symmetry [23]; (c) $N(E)$ is in reality a joint density of initial and final states and broadening based on the lifetimes of both the core hole and the final states is incorporated.

Finally, extended energy loss fine structure (EXELFS) is also observed as weak oscillations superimposed on the high-energy tail of a core loss spectrum [49]. This is interpreted as a density of states phenomenon, involving scattering of the ejected core electron by the nearest neighbour atoms. Hence, this is a measure of the short range order and gives information regarding nearest neighbour distances and coordination number, provided sufficient counts can be accumulated to make a statistically significant analysis.

FINE STRUCTURE ANALYSIS: TWO EXAMPLES IN THE CHARACTERIZATION OF MINERALS

C8 RESIDUE FROM ALLENDE. C8 diamond residues, obtained by an acid and oxidant treatment of fragments of the Allende CV3 meteorite were

extensively characterized by a variety of electron-optical methods [24, 25, 26] Microdiffraction patterns obtained from nanometer scale residue particles using 10 nm probes confirmed that these particles were indeed diamond with a lattice parameter of 0.365 nm - an expansion of ~2% from the ideal structure. These diamond residues, along with diamond films recently produced by a low pressure chemical vapor deposition (LPCVD) method [27] were characterized by EELS. Both the low-loss plasmon excitations as well as the fine structure in the core-loss edges were measured and interpreted. The low-loss spectra (Figure 2) show that both materials exhibit characteristic bulk diamond plasmon resonances at ~30-34 eV. However, the LPCVD diamond film exhibits a distinct shoulder at 24 eV, a feature that was found to be thickness dependent. Since the EELS were measured for a 20-25 nm thick sample, it was concluded that this feature was a result of surface hydrocarbon contamination. No such shoulder was observed for the C δ residue - the sample surface was very clean. The only significant difference was a broadening of the plasmon half-width. However, the degree of broadening was consistent with the grain boundary damping for 5-10nm crystallites [12]. It could also be argued that the broadening of the plasmon is due to the presence of π bonding on the surface of each particle since the plasmon peak is shifted to lower energy loss and the features are thickness independent.

The C-K edges for the LPCVD and C δ diamonds are shown in Figure 3. The onset of the edge, and the fine structure of the core edge for the LPCVD diamond, including the good agreement with a calculated density of unoccupied states, corresponds to the 1s \rightarrow σ^* transition in the sp³ hybridized carbon in diamond. In the case of the C δ residue an additional π^* feature normally associated with the 1s \rightarrow π^* transition in graphite is observed at 286.8 eV. The analysis of the plasmon resonance data, mentioned earlier, indicated no surface contamination. Hence, the C 1s \rightarrow π^* transition observed has been attributed to the presence of sp² carbon on the surface/interface of nanometer scale diamond residue. In fact, a good match was obtained between the experimentally observed spectrum and an artificial spectrum of 25% sp² and 75% sp³ carbon. In practice, this could easily be achieved if each 10 nm diameter particle were to have 6-8 monolayers of sp² carbon surrounding it. The accompanying relaxation to accommodate the elastic strains resulting from the topological reconstruction caused by the π bonding on the surface of each particle, as has been reported [28] for the (100) diamond surface, would be in agreement with the 2% increase in lattice parameter measured by the microdiffraction experiment.

DETERMINATION OF THE OXIDATION STATES OF THE 4th PERIOD TRANSITION METALS IN MINERALS.

The study of the oxidation states of polyvalent cations is an important component of the characterization of minerals as they not only have vital crystal-chemical implications, but are also useful monitors of the ambient oxygen fugacities [21, 22]. The techniques conventionally employed for the determination of the oxidation states, such as Mössbauer, optical and x-ray absorption, etc., have limited applicability because of the difficulty in obtaining a sufficiently pure amount of the fine grained or inhomogenous mineral sample. EELS avoids

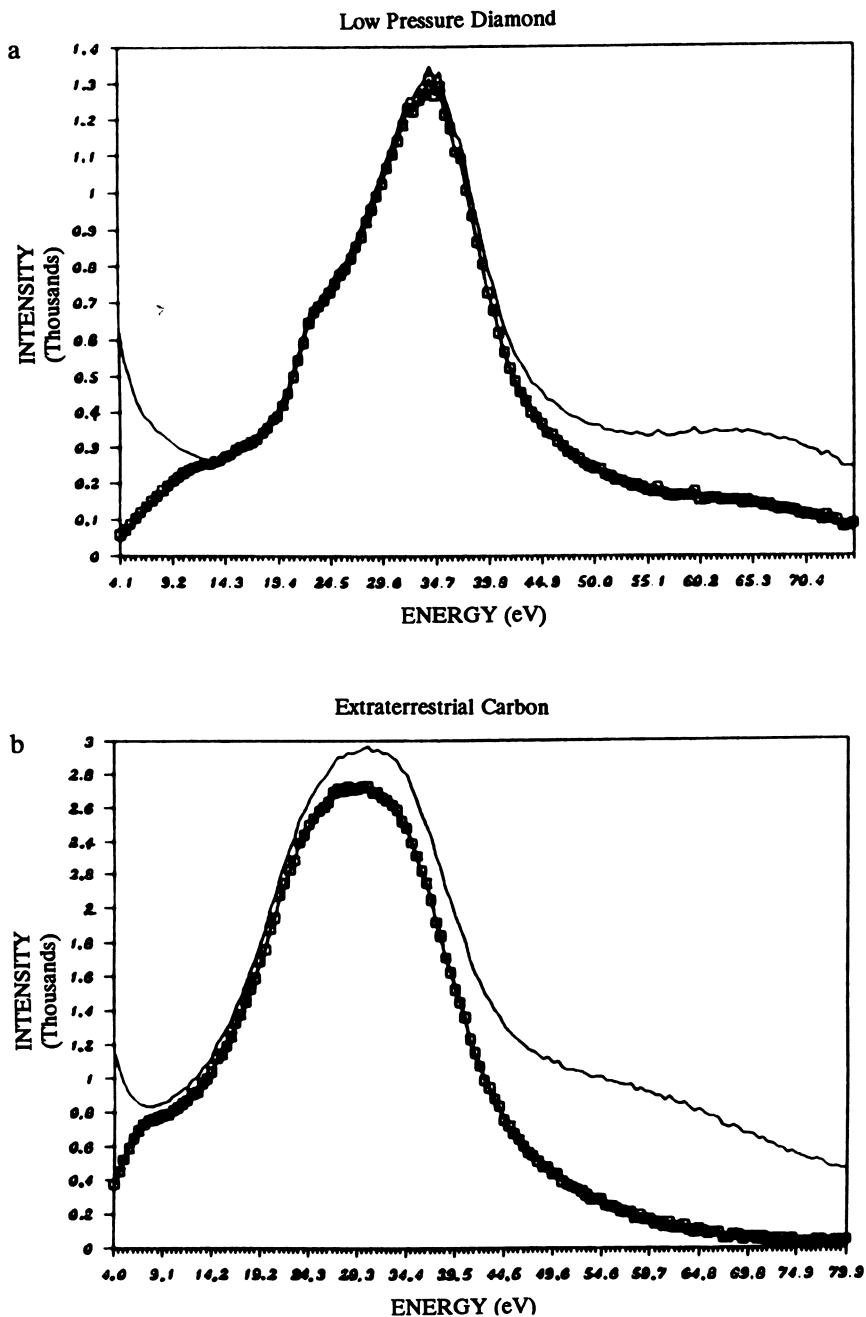


Figure 2. The low-loss plasmon spectrum of a) low pressure chemical vapour deposition diamond films; b) diamond residue from the Allende carbonaceous chondrite.

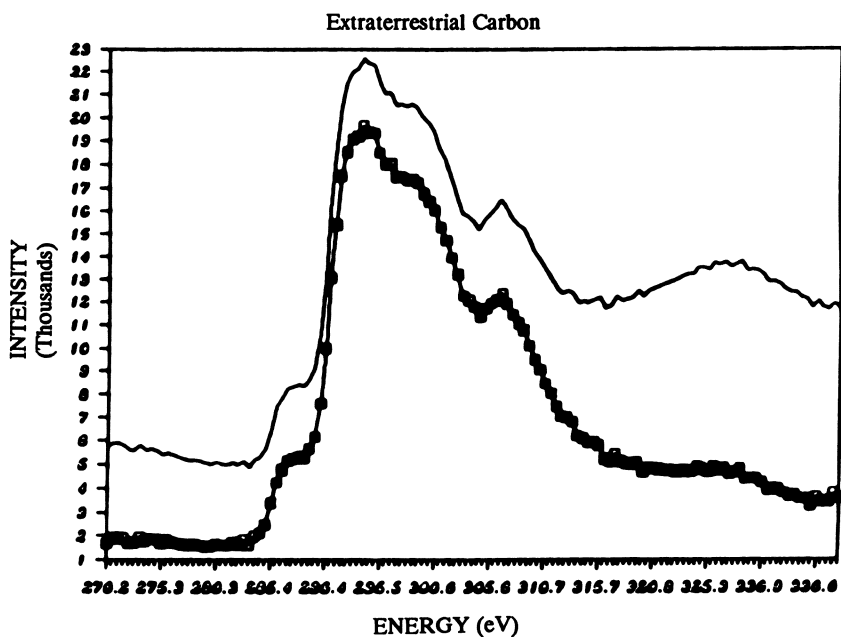
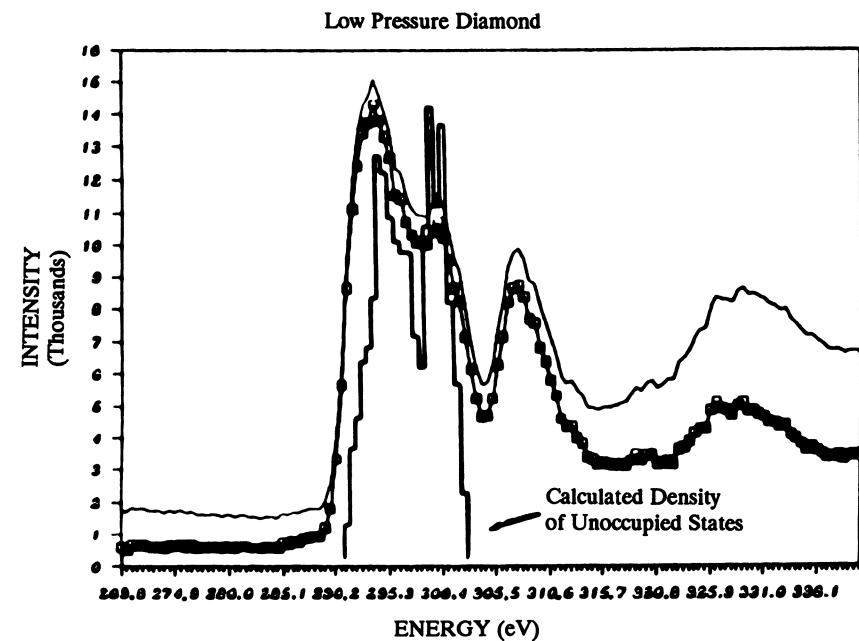


Figure 3. The fine structure of the C-K edges for the two types of diamonds studied. The fine trace is the unprocessed data and the points represent the deconvoluted single scattered distribution.

many of these difficulties, particularly when combined with the fine probe forming capabilities of an analytical electron microscope.

The $L_{2,3}$ edges of the 4th period transition metals are marked by prominent "white line" features due to excitations of the $2p_{3/2}$ (L_3) and $2p_{1/2}$ (L_2) levels, following the allowed dipole transitions, to unoccupied d states. On the basis of the $(2j + 1)$ degeneracy in a one electron model, the L_3/L_2 intensity ratio should be 2:1, but wide departures from this ratio have been observed in transition metals and their oxides [21, 22, 29, 30]. Even though no single factor has been found to account for these observations, these extensive studies form the basis of an empirical catalogue of L_3/L_2 ratios to be used in future determinations of the oxidation states. Further, positive chemical shifts are also observed as a function of oxidation states for Ti^{3+} - Ti^{4+} (2 eV), Mn^{2+} - Mn^{4+} (2 eV), Fe^{2+} - Fe^{3+} (2 eV), etc. [21, 22], for the reasons mentioned earlier. A typical example for manganese is shown in Figure 4. A 2 eV chemical shift in the L_3 peak is observed between Mn^{2+} and Mn^{4+} . The L_2/L_3 ratio changes from 0.25 (MnO) to 0.65 (MnO_2). However, there are some difficulties in performing these experiments, especially in minerals containing mixed valence states, due to the strong overlaps between edges of different oxidation states.

MICROANALYSIS

In addition to the study of fine structures in EELS to obtain bonding and chemical information, this spectroscopic method is being increasingly used for quantitative microanalysis. In particular, the emphasis has been on light element ($Z < 11$) quantification, a domain in which this method complements (and often has significant advantages over) the more commonly used EDXS. For a sample that is sufficiently thin (~30-60nm thick), the procedure is simple and straightforward and involves the measurement of the area under the appropriate ionization edge after background subtraction. However, the detection of hydrogen in a solid is complicated because the H^{1s} electron is involved in the solid state orbitals and the K-edge at 13.6 eV is obscured. It is not certain whether its electron (in a metallic lattice, say) is retained by the hydrogen nucleus or it is transferred to the conduction band, resulting in a shift of the host Fermi level. In fact, shifts in the plasmon energy in hydrides have been observed, and these shifts have been interpreted in terms of the composition in a variety of systems [31, 32]. This approach is difficult, involves an understanding of the modification of the band structure due to the addition of hydrogen, and often leads to detection limits orders of magnitude worse [8] than the simple EELS microanalysis formulation for $Z > 3$.

In a typical EEL spectrum, the count rate I_A (area under the excitation edge after background subtraction, for element A) is a product of the incident electron current density, J_0 , the number of atoms N_A of element A per unit area, and σ_A , the total ionization cross-section per atom for the excitation of the appropriate inner-shell by the incident electrons. However, to preserve good energy resolution, an aperture is placed after the specimen which limits scattering to angles less than β and hence only a fraction of the core loss signal $I_A(\beta)$ is measured. Moreover, in most

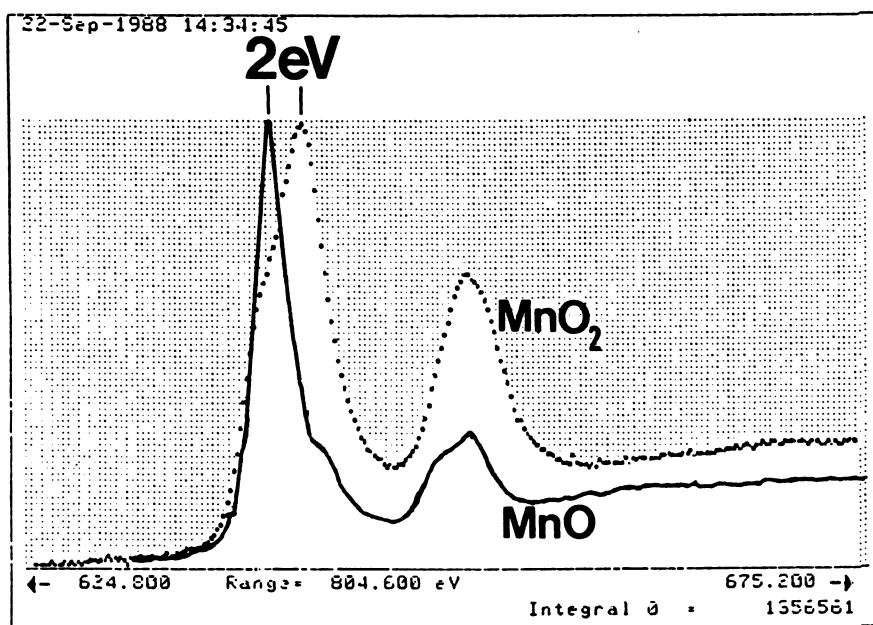


Figure 4. The $L_{2,3}$ edges for the Mn^{2+} and the Mn^{4+} illustrating both the chemical shift (2 eV) and the changes in L_3/L_2 intensity ratios.

microanalytical situations $I_A(\beta)$ is superimposed on a strong background and this problem combined with that of edge overlap is best avoided by measuring $I_A(\beta, \Delta)$ over a limited energy-loss range, Δ following the ionization edge E_A . Hence, the absolute concentration of atoms, N_A is given by [34].

$$N_A = [J_O(\beta, \Delta) \sigma_A(\beta, \Delta)]^{-1} I_A(\beta, \Delta) \quad (2)$$

where $J_O(\beta, \Delta)$ is the total intensity measured with the aperture β for energy losses less than Δ , $\sigma_A(\beta, \Delta)$ is the partial ionization cross-section corresponding to a scattering angle of β and inner-shell losses between E_A and $E_A + \Delta$, and all relevant experimental quantities are shown in Figure 1b. $J_O(\beta, \Delta)$ can be substituted with I_O , the area under the zero-loss peak, if plural inelastic scattering can be corrected for by using appropriate deconvolution procedures [8, 34]. If only relative abundances of two elements A and B are required, then equation 2 becomes

$$\frac{N_A}{N_B} = \frac{I_A(\beta, \Delta)}{I_B(\beta, \Delta)} \frac{\sigma_B(\beta, \Delta)}{\sigma_A(\beta, \Delta)} \quad (3)$$

provided the data for the two edges are measured under identical experimental conditions of illumination, specimen thickness and scattering angles. The accuracy of quantitative analysis using this formulation is largely determined by the errors arising from the removal of the background below the ionization edge and the accuracy of the calculated (or experimental) ionization cross-sections.

Based on empirical observations, an inverse power law function of the form $I = AE^{-r}$, where the exponent r takes values 2-6 is now commonly used for the background [7]; even though it has been argued that there is no physical basis for it [35]. A background fitting region immediately preceding the ionization region is chosen, the constants A and r determined by least squares refinement and the background extrapolated beyond the ionization edge for the required energy window Δ (Figure 1b). Errors can be introduced in the extrapolation procedure due to the statistics of the data in the fitting region and, more significantly, due to a systematic variation of the exponent 'r' with energy loss. In fact, in a recent study [15, 36] using a wide assortment of standards it has been shown that $r \propto \ln(E)$ and hence a polynomial fit [37] to the log-log spectrum gives a more satisfactory (minimizes extrapolation error) fit to the background. Alternatively, the use of library edges scaled to experimental data seems to show some promise, particularly for overlapping edges [38].

Two methods of calculating partial ionization cross-sections are currently in use. An approximate but easily programmable model, SIGMAK, for K shell edges based on hydrogen-like wave functions and scaled to account for the nuclear charge along with a screening constant independent of Z , has shown good agreement with experimental measurements [39]. For

L-shells, (SIGMAL [40]), an additional empirical factor is introduced to match experimental data as the simple treatment for screening is inadequate [34]. Alternatively, the cross-sections can be calculated more accurately, using Hartree-Slater (HS) wave functions [20, 41], assuming that the element is in atomic form, neglecting solid state or excitonic effects and not including dynamic processes. Good agreement between the two theoretical methods is obtained for K edges, the only difference being the presence of sharp threshold peaks in the HS spectra. In the predictions of partial ionization cross-sections, both methods agree to within 5% for K edges and ~10% for L-edges. For the transition metal L_{2,3} edges, both methods do not incorporate the "white lines" arising from the transition to the continuum d states. However, it is clear that their effect on microanalysis can be averaged out by using large (>100 eV) integration windows. In the SIGMAL program, an additional empirical parameter to deal with the white lines can be introduced [34]. Further, it is necessary to incorporate relativistic kinematics in the calculations, particularly at the increasingly common medium (≥ 200 kV) operating voltages [42].

Alternatively, one can measure these ionization cross-sections and use them in much the same way as k-factors [43] are used in EDX microanalysis. Two systematic measurements, one for K, L edges [44] and the other for M_{4,5} edges [45] are reported in the literature. However, experimentally measured cross-sections show large variations [34]. To overcome these difficulties, it is necessary to prepare standards of well known stoichiometry and to measure their thickness accurately. Finally, some of the measurements reported in the literature [33] have been made with large collection angles (~100 mrad) and should be used with caution as they could be erroneous due to lens aberration effects.

In summary, the overall error in microanalysis using EELS is a combination of the statistical error in the measurement of I_A (β, Δ) which for Poisson statistics (applicable in the case of EELS) is given by $\sqrt{I_A}$, the errors in background fitting and extrapolation (~5%) above $\sqrt{I_A}$, and the accuracy of the ionization cross-sections (theory: ~5-15%, experiments: ~2-5%).

Concepts of minimum detectable mass (MDM) and minimum detectable mass function (MMF) prevalent in EDXS quantification have also been defined for EELS microanalysis [46]. It suffices to say that utilizing current technology, $MDM \leq 10^{-20}$ gms. In fact, in a study of uranium clusters using O_{4,5} edges, a practical MDM of ~10 atoms, i.e., 10^{-20} gms, was measured [47]. However, in most practical situations these limits are generally determined by the migration of the atoms and their propensity to suffer radiation damage under the intense electron beam [48]. These effects need more thorough investigation, particularly in materials science and mineralogy applications.

ATOMIC SITE AND SPECIES DETERMINATION USING CHANNELING AND RELATED EFFECTS

For crystalline or microcrystalline materials both the characteristic energy-loss edges and the x-ray emission peak intensities show strong dependence on the orientation of the incident beam as they are governed by phenomena that are highly localized at the atomic sites. In general, an incident plane

wave of electrons under strong dynamical diffraction conditions (Kikuchi lines visible in the diffraction pattern) sets up a standing wave within the crystal. For certain incident beam orientation, the standing wave modulation across the unit cell is such that its maximum coincides with a particular crystallographic site containing a specific atomic species and producing an enhancement of the corresponding characteristic energy-loss edge or x-ray emission peak intensities. Whilst these orientation dependencies could have detrimental consequences on EDXS/EELS microanalysis (and should be avoided either by selecting a non-channeling orientation where no lower order Bragg diffraction vectors are excited or by using a large convergence angle to average out the orientation dependence), they have been developed into a powerful crystallographic technique for specific site occupancy/ valence determinations [50, 51]. Either axial [52] or planar [53, 54] channeling orientations are used. For brevity, only the latter will be discussed here and the principles of the technique illustrated with our measurements for the dolomite structure.

The dolomite structure in the [1210] orientation, with the c-axis exaggerated for clarity, is shown in Figure 5. For a (0001) systematic row (a single row of spots in the diffraction pattern), the wave field of the dynamically diffracted electrons in the crystal is two-dimensional, i.e., constant in a direction normal to the c-axis. In the dolomite structure, the candidate sites of interest (Mg and Ca) occupy alternating planes at one third the unit cell parameter along the c-axis. For the (0001) systematic row, at orientations corresponding to small positive excitation errors ($s > 0$) (Figure 6) of the third order Bragg diffraction condition ($3g$) an enhancement of the Mg $K\alpha$ is observed. For negative excitation errors ($s < 0$) an enhancement of the Ca $K\alpha$ is observed. It can also be seen that the impurity Fe $K\alpha$ intensity, follows that of Mg $K\alpha$, suggesting similar site occupancy. The exact degree of substitution of the impurity atoms (Fe) can be obtained by an elegant method of ratios [53] with respect to the intensities of the reference elements (Mg & Ca) in the host lattice. Site occupancies in a variety of minerals have been measured using this technique [55-57].

In the case of EELS, within the single scattering regime, applying the principle of reciprocity it can be shown that the intensities for different sites can be effectively squared by choosing the position of the detection aperture and placing it at an appropriate part of the diffraction pattern [58]. Further, from a simple application of the uncertainty principle ($\Delta x \cdot \Delta p \geq h$), considerable enhancement of the localization of the inelastic scattering event can be achieved by analyzing electrons scattered over large angles (or large momentum transfer). In practice, this is achieved by shifting the detection apertures parallel to the Kikuchi band (i.e., the (400) band in Figure 7a for the spinel structure) but without any change in the diffraction geometry with respect to the (400) planes. Significant enhancement, even for losses as low as 532 eV (O-K edge), can be achieved by promoting localization in this manner.

An example [59] for chromite spinels, where the EEL spectra are measured at different incident beam orientations and under strong localisation conditions, is shown in Figure 7a. For orientation (a) the octahedral sites were selectively enhanced. For orientation (b) the tetrahedral sites are selected. However, because of the superior energy resolution of EELS (~ 1 eV), it is possible also to detect changes in oxidation states by the small chemical shifts observed in the onset of the core-loss

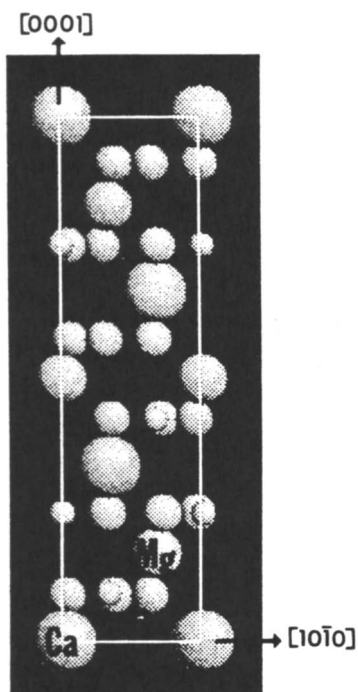


Figure 5. Crystal structure of dolomite in the [1210] orientation.

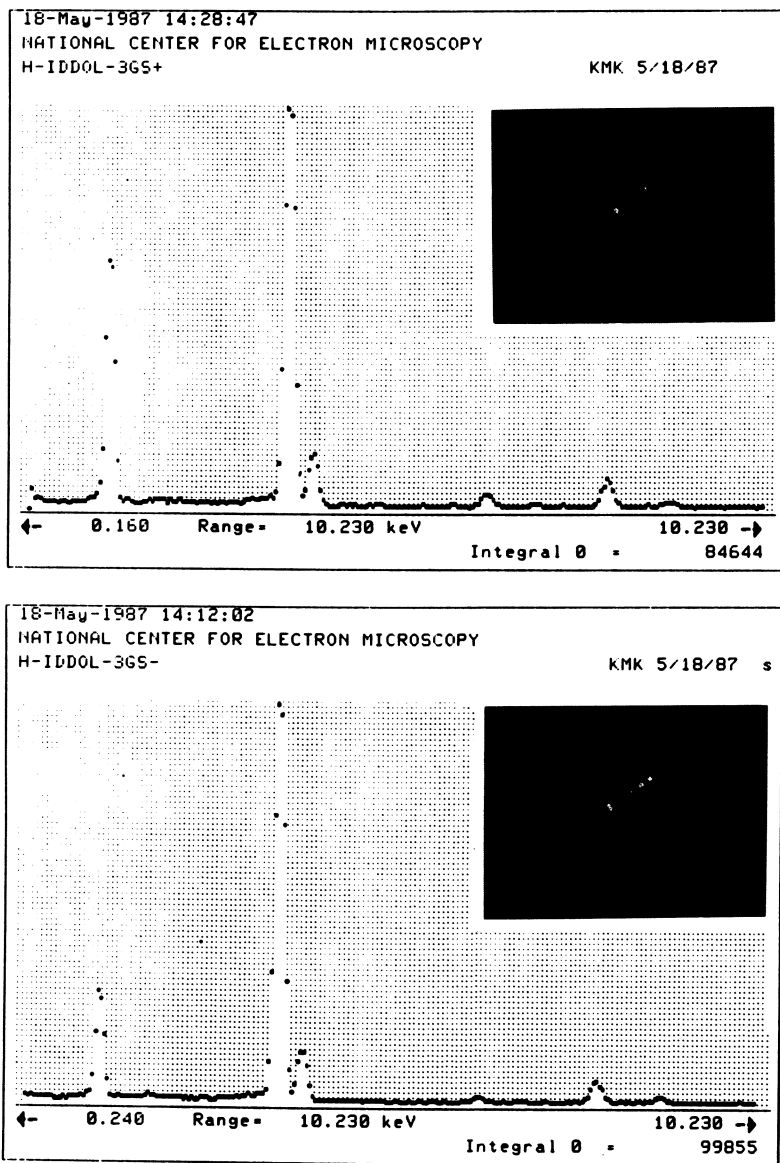


Figure 6. An example of the dependence of characteristic x-ray emissions on incident beam orientation for the dolomite structure.

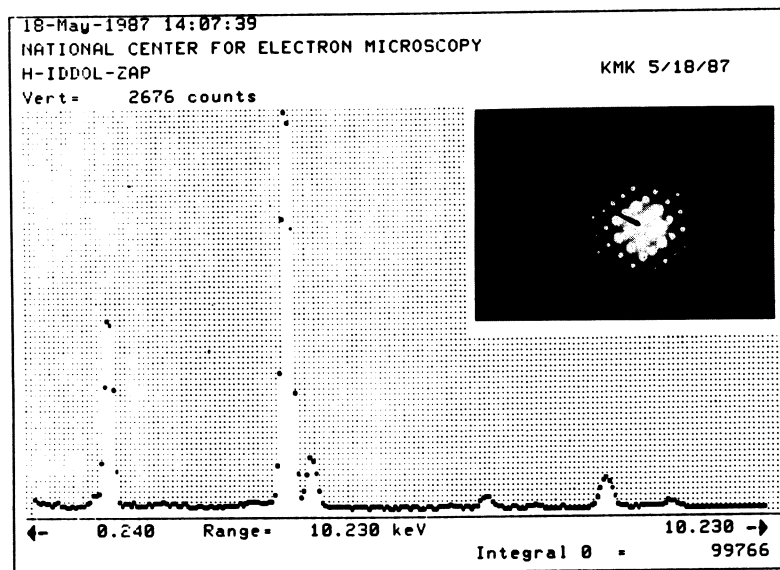
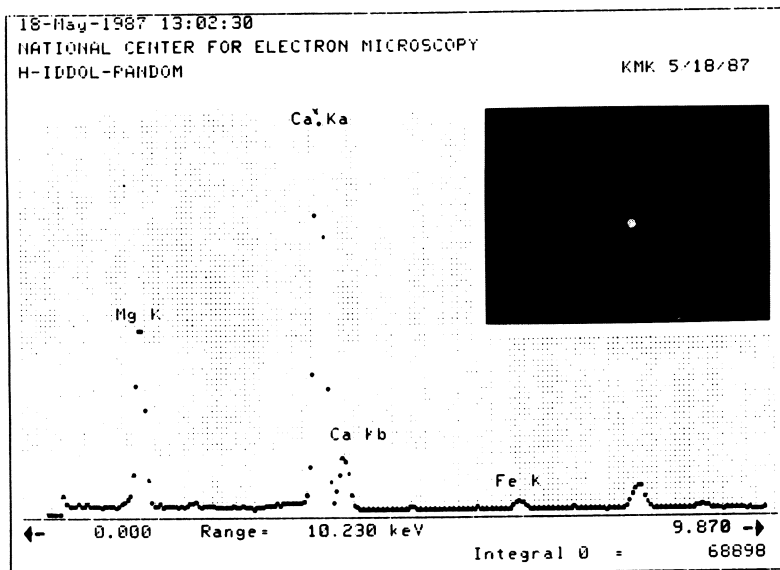


Figure 6. Continued.

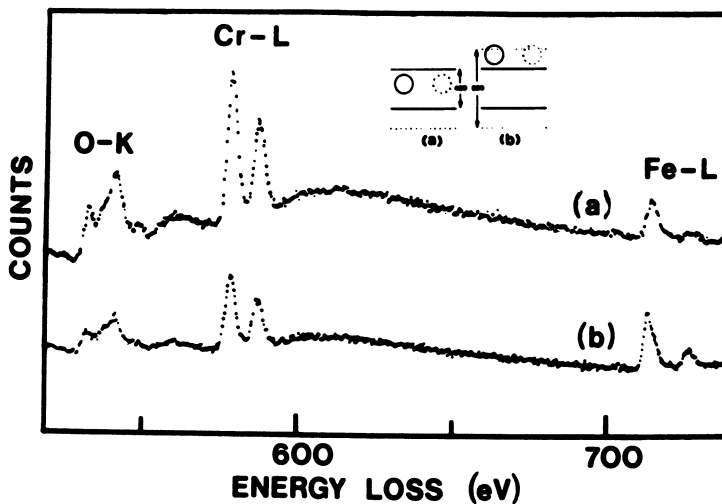


Figure 7a. EEL spectrum of a chromite spinel under different incident beam orientations showing enhancement for the octahedral (a) and tetrahedral (b) sites. The position of the detection aperture to achieve enhanced localization for the low energy O-K edges is shown in the insert.

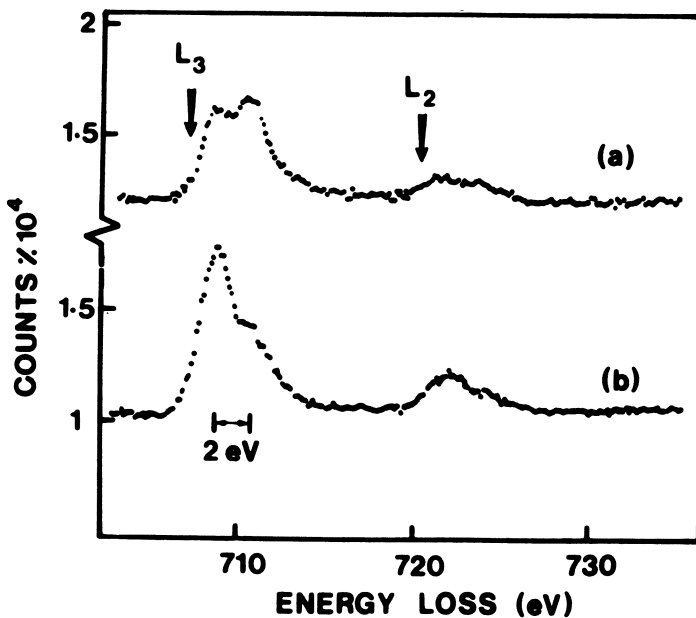


Figure 7b. Details of the Fe $L_{2,3}$ edge for the same orientations.

edges. Combining this chemical shift with the selective enhancement of the different candidate sites by the appropriate choice of incident beam orientations, it is possible to obtain specific site valence information (Figure 7b). For example, a 2 eV chemical shift is observed between Fe^{2+} and Fe^{3+} . The higher energy Fe^{3+} peak intensity is enhanced when the incident electron beam is localized on the octahedral sites, while the Fe^{2+} intensity variation with orientation suggests it occupies only tetrahedral sites in the naturally occurring chromite spinel.

EXPERIMENTAL DETAILS

The discussion is restricted to energy-analyzing devices compatible with analytical electron microscopes. Generally, they are either electrostatic or magnetic prisms placed after the specimen and the most popular commercial spectrometers are based on a magnetic sector design [60]. The principle of operation is quite simple. In a uniform magnetic field, fast electrons have circular paths, the radius of which is a function of both the incident electron energy and the strength of the magnetic field. Therefore, electrons of varying energy entering normal to the field can be brought to a focus at a specific exit point by suitably varying the strength of the magnetic field. However, if the incidence is not normal but over a finite angular range (in practice, defined by β) electrons of the same energy entering a constant magnetic field are spatially separated at the exit plane. Even though the aberration is normally compensated for in the design of the spectrometer, it is impossible to avoid the relationship between the energy resolution and the entrance aperture of the spectrometer; i.e., the smaller the entrance aperture, the better the energy resolution. On the other hand, the collection efficiency (fraction of electrons losing energy E and scattered through β when compared to electrons scattered through all possible angles) depends directly on β . Hence, one gains energy resolution invariably at the expense of collection efficiency.

The spectrum (dispersion of electrons losing varying amounts of energy) is formed along a straight line in the back focal plane of the spectrometer and is recorded in one of two ways. Until recently, a serial mode in which a narrow energy range is recorded at any particular moment using a set of post-spectrometer selection slits or apertures, was the norm. The spectrum was swept past the narrow slits generally by ramping the current in the magnet and thus the magnetic field. This has an inherently low collection efficiency (~ 0.01), because only a small fraction of the spectrum is acquired at any particular time. A typical EEL spectrum has intensities that vary over eight decades of counts and the major advantage of such a system is its dynamic range which can accommodate this variation in signal magnitude. However, a parallel recording system (PEELS) which uses a set of quadrupole lenses to magnify the spectrum in such a manner that it can be simultaneously recorded by a single crystal YAG scintillator coupled to a 1024-channel photodiode array is now commercially available. [61] This system has been shown to achieve much higher efficiencies (>0.25) over the range of intensities relevant to EELS in a TEM. Routine use of such a PEELS requires that the "dark characteristics" (i.e., no incident electrons) of the array under identical conditions of acquisition as the spectrum of interest be recorded and subtracted from it. Moreover, the

response of the individual elements of the photodiode array to the same signal could vary from one to the other and this has to be measured by ramping a constant signal (such as the zero loss peak) across the array in much the same way as in serial detection. The spectrum should then be divided by the "channel to channel gain variation" measured in this fashion to avoid any artefacts. Finally, as the individual elements of the detector saturate at 2^{14} (16384) counts, recording of the ZLP and the low-loss region can be accomplished only in a separate acquisition using very low incident electron illumination and very small acquisition times. This often leads to problems if thin specimens cannot be prepared. In such cases, it is essential to deconvolute the spectrum to eliminate plural scattering and obtain a single scattered distribution. All well established deconvolution procedures [16, 17] require that the low-loss region, including the ZLP, be acquired under the same energy resolution as the core-loss feature of interest. For practical reasons, the Fourier ratio method is easier to apply to PEELS data.

Generally any sample that is suitable for high resolution electron microscopy would also be appropriate for EELS. Increasing the sample thickness would, in principle, increase the signal of interest (linear), increase the probability of multiple scattering and increase the probability of mixed (elastic and inelastic, etc.) events. While the first consequence is desired, the latter two are clearly detrimental. Ultimately, there is no substitute to having a uniformly thin specimen whose thickness optimally [62] would be less than one mean free path length for total inelastic scattering (λ_p). λ_p is proportional to the mean atomic number of the sample and has been recently parameterized [13]. If one is constrained by a lower limit of specimen thickness, an option would be to go to higher acceleration voltages as λ_p would increase linearly with kV. Alternatively, if one is performing an EELS experiment with an optimally thin sample but is interested in the characteristic signal from an element occurring in very small quantities, it is possible to enhance the signal by selecting a larger area and operating in diffraction mode. But if higher spatial resolution is also required there is no option but to use a high current density source, such as a field emission gun. However, such sources should be used with caution [48] as they can cause significant radiation damage, including loss in long range order, breaking of bonds and in some cases, outright vapourization of the sample. On the positive side, it is currently accepted that retaining the sample at cryogenic temperatures can alleviate some of these problems, but to what extent is yet to be determined.

ACKNOWLEDGMENTS

This work was supported by the Director, Office of Energy Research, Office of Basic Energy Sciences, Materials Sciences Division, of the United States Department of Energy under contract No. DE-AC03-76SF00098. The author would like to thank Dr. R. Kilaas for a critical reading of the manuscript.

LITERATURE CITED

1. P.B. Hirsch, A. Howie, R. Nicholson, D. Pashley, and M.J. Whelan, Electron Microscopy of Thin Crystals, (Butterworths, London), 1965.
2. J.J. Hren, J.I. Goldstein and D.C. Joy, Introduction to Analytical Electron Microscopy, (Plenum, New York), 1979.

3. J.M. Cowley, Diffraction Physics, (North Holland, Amsterdam), 1981.
4. S.J.B. Reid, Electron Microprobe Analysis, (Cambridge Univ. Press), U.K.), 1975.
5. M.P. Seah, SEM/IL, 521 (1983).
6. B.G. Yacobi and D.B. Holt, J. Appl. Phys., 59 R1 (1986).
7. R.F. Egerton, EELS in the Electron Microscope, (Plenum, New York), 1986.
8. C. Colliex, in Advances in Optical and Electron Microscopy, ed. V.E. Cosslett and R. Bauer, (Academic, London), 9, 65 (1984).
9. H. Raether, Excitations of Plasmons and Interband Transitions by Electrons, (Springer-Verlag, Berlin), 1980.
10. D. Pines, Elementary Excitation in Solids, Benjamin, New York, (1963).
11. K.M. Krishnan, in Analytical Electron Microscopy, ed. D.C. Joy, San Francisco, 261 (1987)
12. C. von Festerberg, Z. Phys., 207, 47 (1967).
13. R.F. Egerton, S.C. Cheng and T. Malis, Proc. EMSA, 45, 122 (1987).
14. P. Trebbia, Ultramicroscopy, 24 399 (1988).
15. K.M. Krishnan and M.T. Stampfer, Proc. EMSA, 46, 538 (1988).
16. R.F. Egerton, B.G. Williams, D.T.G. Sparrow, Proc. Roy. Soc. Lond., A398, 395 (1985).
17. C.R. Swyt and R.D. Leapman, in Microbeam Analysis, ed. A.D. Romig and J.I. Goldstein, S.F. Press, 45 (1984).
18. R.D. Leapman, et al. in EXAFS Spectroscopy, ed. B.K. Teo and D.C. Joy, Plenum Press, New York, 217 (1981).
19. S.T. Manson, Phys. Rev., A6, 1013 (1972).
20. R.D. Leapman, P. Rez and D.F. Mayers, J. Chem. Phys., 72, 1232 (1980).
21. M.T. Otten, B. Miner, J.H. Rask and P.R. Buseck, Ultramicroscopy, 18, 285 (1985).
22. J.H. Rask, B.A. Miner and P.R. Buseck, Ultramicroscopy, 21, 321 (1987).
23. J. Taftø and J. Zhu, Ultramicroscopy, 9, 349 (1982).
24. R.S. Lewis, M. Tang, J.F. Wacker, E. Anders, and E. Steel, Nature, 326, 160 (1987).
25. D.F. Blake, F. Freund, K.M. Krishnan, C.J. Echer, R. Shipp, T.E. Bunch, A.G. Tielens, R. Lipari, C.J.D. Hetherington, and S. Chang, Nature, 332, 611 (1988).
26. D.F. Blake, F. Freund and K.M. Krishnan, Earth & Planetary Science Letters, in press.
27. J.C. Angus and C.C. Hayman, Science, 241, 913 (1988).
28. D. Vanderbilt and S.G. Louis, Phys. Rev., B30, 6118 (1984).
29. T.G. Sparrow, et al., Chem. Phys. Lett., 108, 547 (1984).
30. R.D. Leapman, L.A. Grunes and P.L. Fejes, Phys. Rev., B26, 614 (1982).
31. A.P. Stephens and L.M. Brown, Inst. Phys. Conf. Ser., 52, 341 (1980).
32. N.J. Zaluzec, T. Schober and D.G. Westlake, Proc. EMSA, 39, 194 (1981).
33. C.C. Ahn and O.L. Krivanek, EELS Atlas, ASU Tempe, AZ. (1983).
34. R.F. Egerton, SEM/II, 505 (1984).
35. M. Isaacson, Proc. XI Int. Cong. Elec. Mic., Kyoto, Japan, 37 (1986).
36. K.M. Krishnan, unpublished data.
37. J. Bentley, G.L. Lehman and P.S. Sklad, Electron Microscopy, 1, 585 (1982).

38. N.J. Zaluzec, Conf. Proc. Analytical Electron Microscopy, ed. R.H. Geiss, S.F. Press, San Francisco, 193 (1981).
39. R.F. Egerton, Ultramicroscopy, **4**, 169 (1979).
40. R.F. Egerton, Proc. EMSA, **39**, 198 (1981).
41. C.C. Ahn and P. Rez, Ultramicroscopy, **17**, 105 (1985).
42. M.M. Disko and R. Ayer, in Inter. Voltage Electron Microscopy, K. Rajan ed., Elec. Opt. Publ. Group, N.J., 72 (1988).
43. K.M. Krishnan, and C.J. Echer, Analytical Electron Microscopy, D.C. Joy ed., S.F. Press, 99 (1987).
44. T. Malis, K. Rajan, J.M. Titchmarsh, and C. Weatherly, Voltage Electron Microscopy, K. Rajan ed., 78 (1987).
45. P. Hofer, P. Golob, and A. Brunegger, AEM-Workshop, UMIST, Manchester (1987).
46. M. Isaacson and D. Johnson, Ultramicroscopy, **1**, 33 (1975).
47. C. Colliex, O.L. Krivanek and P. Trebbia, Inst. Phys. Conf. Ser., **61**, 183 (1981).
48. L.E. Thomas, Ultramicroscopy, **9**, 311 (1982).
49. S. Csillag, D.E. Johnson and E.A. Stern, Analytical Electron Microscopy, ed. R.H. Geiss, 221 (1981).
50. K.M. Krishnan, Ultramicroscopy, **24**, 125 (1988).
51. J. Tafto, J. Appl. Cryst., **15**, 378 (1982).
52. S.J. Pennycook and J. Narayan, Phys. Rev. Lett., **54**, 1543 (1985).
53. J.C.H. Spence and J. Tafto, J. Microscopy, **130**, 147 (1983).
54. K.M. Krishnan, P. Rez and G. Thomas, Acta Cryst., **B41**, 396 (1985).
55. P.G. Self and P.R. Buseck, Phil. Mag., **A48**, L21 (1983).
56. J. Taft and P.R. Buseck, Amer. Mineral., **68**, 944 (1983).
57. M.T. Otten and P.R. Buseck, Ultramicroscopy, **23**, 151 (1987).
58. J. Tafto and O.L. Krivanek, Nucl. Inst. Methods, **194**, 153 (1982).
59. J. Tafto and O.L. Krivanek, Phys. Rev. Lett., **48**, 560 (1982).
60. H.T. Pearce-Percy, SEM/I, 41 (1978).
61. O.L. Krivanek, C.C. Ahn and R.B. Keeney, Ultramicroscopy, **22**, 103 (1987).
62. M. Isaacson, SEM/I, 763 (1981).

RECEIVED September 21, 1989

Chapter 4

High-Resolution Transmission Electron Microscopy Applied to Clay Minerals

George D. Guthrie, Jr., and David R. Veblen

Department of Earth and Planetary Sciences, Johns Hopkins University,
Baltimore, MD 21218

The computer image simulation technique was used to elucidate problems concerning the interpretation of high-resolution transmission electron microscopy images of clay minerals (serpentine, kaolinite, muscovite, biotite, chlorite, illite/smectite, and disordered intergrowths). One-dimensional HRTEM images of clay minerals can be interpreted successfully and can provide useful information, including layer spacing, layer sequence, and compositional periodicity. However, the images vary with specimen orientation and microscope focus, so ambiguities may be present in the interpretation.

The transmission electron microscope (TEM) is a unique instrument for studying chemical and structural relationships among solid phases. Its analytical capabilities allow chemical analysis of volumes as small as 1000 nm^3 (e.g., see Chapter by Mackinnon), and its imaging capabilities allow resolution of structural detail less than 1 nm. Yet, with point-to-point resolutions greater than the size of most atoms or chemical bonds, the TEM is generally incapable of resolving individual atoms directly; hence, detailed structural interpretation of high-resolution TEM (HRTEM) images is not always straightforward but commonly requires computer simulation of the image. Some microscopes with relatively high electron accelerating potentials (e.g., $\geq 400 \text{ keV}$) theoretically are capable of resolving most atoms (e.g., 1); however, other factors, such as beam damage, can degrade resolution significantly, so that detailed interpretation of an image taken with an atomic resolution microscope often requires computer simulation to infer atomic-scale information. Furthermore, HRTEM images vary greatly as a function of crystal orientation and optical parameters, and simulations are necessary for assessing these effects. This chapter will discuss HRTEM techniques and interpretation of HRTEM images of clay minerals using computer image simulations. The process of computer image simulation will also be discussed. Though the images in this chapter were taken with or calculated for a specific microscope, the results are also applicable quantitatively to microscopes with similar optical characteristics and qualitatively to most microscopes. We have calculated images for microscopes with much

0097-6156/90/0415-0075\$06.00/0
© 1990 American Chemical Society

poorer resolutions (i.e., a point-to-point resolution of 0.53 nm) and obtained similar results.

Introduction to TEM

An electron microscope uses a focussed beam of electrons to illuminate a specimen. Electrons are accelerated along the microscope column from a source toward the specimen, and magnetic lenses focus the electrons onto the specimen. In a transmission electron microscope, electrons that pass through the specimen are focussed by additional magnetic lenses to enlarge the electron diffraction pattern that forms on the back focal plane of the objective lens or to project an enlarged image of the specimen that forms on the image plane. Thus, either the image plane or the back focal plane may be projected on to a viewing screen, a sheet of film, or some other recording device. Veblen (2), Spence (3), Cowley (4), and McLaren (5) discuss TEM imaging principles in greater detail.

Low-Resolution Methods. By placing an aperture in one of the image planes below the specimen, a diffraction pattern may be obtained from a specific region of the specimen. Conversely, by placing an aperture in the back focal plane of the objective lens, an image may be formed from specific diffracted beams. With an appropriate placement of the aperture, images in the TEM can be formed by using only the "undiffracted" central beam, one or more diffracted beams, or a combination of the two. In conventional bright-field TEM, images are formed from the central beam to produce high-contrast, low-resolution images: Strongly diffracting crystals will appear dark, while crystals that are not strongly diffracting will appear brighter. In contrast, dark-field TEM images are formed from a diffracted beam, causing crystals that are strongly diffracting electrons into that beam to appear bright compared to other parts of the specimen. Both conventional bright-field and dark-field TEM are simple techniques capable of producing images that show large-scale features, such as the relationships between crystals. These imaging techniques also have been used extensively to study crystal defects (e.g., 3, 5-6).

High-Resolution Methods. Conventional bright- and dark-field TEM produce image contrast based on variations in the amplitude across the specimen of the image-forming beam. In HRTEM, images generally are formed using the central beam and a number of surrounding diffracted beams, and contrast is produced by differences in both the amplitudes and the phases of the image-forming beams. Hence, this technique is sometimes referred to as phase-contrast imaging. Veblen (2) gives a relatively non-technical review of HRTEM imaging and Spence (3) and Cowley (4) provide more rigorous accounts of the method.

Many factors affect the details of images produced by HRTEM, two of which are focus conditions and crystal orientation. The critical lens used to image the specimen is the objective lens, and its focus has a profound influence on the image produced. When the microscope is focussed exactly on the Gaussian image plane (the focal plane on which electrons passing exactly along the microscope's central axis are in focus), a relatively low-contrast image is formed. To improve contrast and to partially compensate for lens deficiencies (such as spherical aberration), the objective

lens is generally weakened to focus on a plane slightly above the specimen (3,7); this focus condition is termed underfocus. Conversely, overfocus refers to conditions when the objective lens is focussed above the Gaussian image plane. The optimum degree of underfocus is a function of the accelerating voltage of the electrons and the spherical aberration coefficient of the objective lens; however, objective lenses normally are underfocussed between 50 and 250 nm. Various criteria may be used to choose the optimum focus condition. The focus condition for the most common set of criteria is termed the Scherzer focus (7).

Under ideal conditions, extreme care can be taken to orient a specimen perfectly in the electron microscope. In this case, HRTEM images may contain detailed information in two dimensions. Such images, when formed at the optimum value of underfocus, commonly reflect variations in the electrical potential of the structure and may be interpreted directly: Dark areas in the image correspond to regions of high potential, and light areas correspond to regions of low potential. These types of images are sometimes referred to as structure images, and they are easily obtainable when problems such as structural damage by incident electrons and large variations in crystal orientation are not significant.

Under non-ideal conditions, it is not always possible to orient a specimen exactly or to focus the objective lens optimally. In these cases, it may be possible to orient the specimen partially in only one direction, thereby forming a one-dimensional image. Images under non-ideal conditions may not be interpreted directly, and computer image simulation of the specific structure and imaging conditions is required to understand such images fully. Even slight misorientations of the specimen and changes in focus can affect the nature of the image, for instance, by changing the character of the dark and light areas or by shifting their positions relative to the real crystal structure. It is the interpretation of these types of images that will be addressed below.

Computer Image Simulation

The point-to-point resolution of most TEMs is larger than most chemical bond lengths; hence, atomic resolution is normally not directly possible. However, atomic-level detail can be obtained in some cases from HRTEM images when computer image simulation techniques are used. Furthermore, computer image simulation may allow the interpretation of images obtained under non-ideal imaging conditions. In computer image simulation, images of a given structural model are calculated for a set of imaging conditions; computed and experimental images are then compared to determine the correspondence between the structural model and the sample. Several detailed discussions address the theory and practice of computer image simulation (e.g., 8-10), so only a brief discussion will be presented here.

Computer image simulation may be achieved by several different techniques (10), but the most common method is the multislice calculation. In this method, input consists of a structural model, the projection direction through the structure, and parameters describing the electron microscope. Slight misorientations of the structure from the ideal projection direction may also be simulated.

In the computation, the crystal is sectioned into slices perpendicular to the electron beam, and the electrical potential of the structure within each slice is projected onto a plane, forming a

"phase-grating" at the bottom of the slice (10). The electron beam is allowed to propagate through one slice-thickness of vacuum prior to each phase-grating, and the effects of Fresnel diffraction are calculated. The electron beam then interacts with the phase-grating, and phase shifts and amplitude changes due to this interaction are calculated. This process is iterated and continues until the desired sample thickness is reached, whereupon the effects of the electron microscope optics are considered. In this step, parameters describing spherical and chromatic aberration, voltage and current fluctuations in the electron beam and magnetic lenses, defect of focus, and aperture sizes may all be varied. The spherical and chromatic aberration coefficients, voltage and current fluctuations, and apertures are calculated or obtained for a given microscope (3); the defect of focus can be varied to simulate different experimental focus conditions.

The simulations presented in this chapter were calculated using the SHRLI computer programs (11), version 80F. Optical parameters characteristic of a Philips 420T electron microscope were used; details of the calculations are given in Guthrie and Veblen (12).

Introduction to TEM of Clay Minerals

Clay minerals are fine-grained sheet silicates that exhibit a large range of structures and compositions. They typically occur as breakdown products from the hydrothermal alteration or weathering of many common rock-forming minerals, and hence they constitute a major portion of soils. The large surface-to-volume ratios resulting from their small sizes provide large surface areas to which water and other substances commonly adsorb. As such, clay mineral surfaces are effective sites for catalysis (13).

Because of their chemical and structural complexities at a small scale, clay minerals and their large-grained equivalents, the macroscopically-crystallized sheet silicates, are commonly studied by electron microscopy. Yet, these minerals typically suffer rapid radiation damage in the electron beam. Furthermore, clay mineral specimens have a small particle size and typically exhibit large variations in crystal orientation. These two problems cause the HRTEM imaging of clay minerals to be plagued by the problem of non-ideal imaging conditions as discussed above; it is generally not possible to orient the specimen or focus the microscope as accurately as is possible with other materials. Thus, clay minerals provide an excellent opportunity to consider the interpretation of HRTEM images, since both ideal and non-ideal imaging conditions may be addressed. Images of large-grained sheet silicates will be used to exemplify ideal imaging conditions, whereas images of fine-grained clay minerals will be used to discuss the non-ideal case.

Structures of Clay Minerals. The term "clay minerals" generally refers to fine-grained ($< 1\mu\text{m}$) sheet silicates. Many detailed discussions of the structures and compositions of clay minerals exist (e.g., 14-16), and their interesting chemical properties have been reviewed previously (13). However, a short introduction to their structures is necessary to understand their HRTEM images.

Clay minerals belong to a structural family of minerals known variously as sheet silicates, layer silicates, or phyllosilicates. Sheet silicates contain SiO_4 tetrahedra that are polymerized in two

dimensions to form sheets. The sheet silicates (and hydroxides) also contain octahedrally-coordinated cations such as Al, Mg, and Fe. Table I lists the structures presented in this discussion.

An octahedral sheet (O) is defined as a two-dimensional array of cations (usually, Al, Mg, Fe) octahedrally coordinated by oxygen and/or OH. The individual octahedra share edges, and the composition of the sheet can vary from $M_2(O,OH)_6$ (all trivalent cations and termed dioctahedral) to $M_3(O,OH)_6$ (all divalent cations and termed trioctahedral), where M signifies the cation. The octahedral sheet forms the basis of the layer-hydroxide minerals, gibbsite (M = Al) and brucite (M = Mg).

A T-O layer (also termed a 1:1 layer) is composed of an octahedral sheet joined to a tetrahedral sheet consisting of corner-sharing $(SiO_4)^{4-}$ tetrahedra. The unshared apical oxygens of the tetrahedral sheet replace 2/3 of the hydroxyl groups from one side of the octahedral sheet, thereby giving a structural formula of $M_2T_2O_5(OH)_4$ to $M_3T_2O_5(OH)_4$. This structural unit forms the basis of the 0.7-nm sheet silicates, the kaolinite (M = Al) and serpentine (M = Mg) groups.

In a T-O-T layer (also termed a 2:1 layer), tetrahedral sheets attach to both sides of an octahedral sheet, thereby giving a structural formula of $M_2T_4O_{10}(OH)_4$ to $M_3T_4O_{10}(OH)_4$. The T-O-T layer forms the basis of the sheet silicates pyrophyllite (M = Al) and talc (M = Mg).

Table I. Fundamental Structural Subunits of Sheet Silicates

Structure	Composition [†]	Thickness (nm) [‡]
Octahedral Layer	$M_2(OH)_6$ to $M_3(OH)_6$	0.48-0.49
T-O Layer	$M_2T_2O_5(OH)_4$ to $M_3T_2O_5(OH)_4$	0.71-0.73
T-O-T-O Layer	$2[M_2T_2O_5(OH)_4]$ to $2[M_3T_2O_5(OH)_4]$	1.40-1.41
T-O-T Layer (A = □) [¥]	$AM_2T_4O_{10}(OH)_2$ to $AM_3T_4O_{10}(OH)_2$	0.91-0.94
T-O-T Layer (A=K,Na)	$AM_2T_4O_{10}(OH)_2$ to $AM_3T_4O_{10}(OH)_2$	0.96-1.01

[†] M: Al, Mg, Fe; T: Si, Al; A: K, Na

[‡] Approximate thickness. Ranges correspond to the thinner aluminum end-members and thicker iron/magnesium end-members. Thicknesses were obtained from values given in Ref. 14.

[¥] The symbol □ signifies a vacancy: A=□ indicates an unoccupied A-site. The thicknesses given for the case of the occupied A-site are for the true micas.

The region between adjacent T-O-T layers is termed the interlayer and can contain large cavities formed by opposing rings in the tetrahedral sheets. When the tetrahedral sheet is entirely

occupied by silicon, the T-O-T layer is charge balanced, and the interlayer is unoccupied. However, aluminum may replace up to 1/2 of the silicon atoms in the tetrahedral sheet, thereby creating a charge on the T-O-T layer. This charge can be compensated by cations (A), such as potassium, sodium, and calcium, occupying the interlayer sites, thus giving a structural formula of $AM_2T_4O_{10}(OH)_4$ to $AM_3T_4O_{10}(OH)_4$. The resulting minerals are called the micas (A = Na or K; $T_4 = 3Si + Al$) and brittle micas (A = Ca; $T_4 = 2Si + 2Al$).

The above structural subunits may be combined to form various structures. The micas, muscovite and biotite, consist of alternating T-O-T layers and filled interlayer sites. The chlorites consist of alternating T-O-T layers and octahedral layers. Disordered intergrowths of chlorites, micas, 0.7-nm sheet silicates, and layer-hydroxides have also been observed (e.g., 18-21).

HRTEM Simulation and Imaging of Clay Minerals

A large variety of sheet silicates may be formed by appropriate combinations of the above structural subunits (e.g., 14 for micas and 22 for other sheet silicates). In this paper we present both experimentally-derived images and computer-simulated images for a range of these structures: serpentine/kaolinite (T-O), chlorite (T-O-T-O), biotite/muscovite (T-O-T-I), and intergrowths of these minerals. Images from well-crystallized specimens of these materials will be used to illustrate the types of images that can be expected under ideal imaging conditions. Experimentally-derived and computer-simulated images for intergrowths of the clay minerals illite and smectite are also presented. These minerals are structurally similar to muscovite (T-O-T-I), but whereas the interlayer for muscovite is almost completely filled with K, illite and smectite have incompletely filled interlayers. The interlayer in illite is commonly approximately 75-percent occupied and the interlayer in smectite is approximately 20- to 60-percent occupied (16). Computer-simulated images of intergrown illite and smectite will be used to illustrate the types of images that can be obtained under non-ideal conditions.

Interpretation of two-dimensional images of sheet silicates has previously been addressed. Computer-simulated images of chlorite (23) and biotite and muscovite (24) show that two-dimensional images of these sheet silicates allow determination of the basal spacing (spacing perpendicular to the sheets) and stacking order (relative rotations and shifts between sheets). Furthermore, these calculations show that at the Scherzer (optimum) focus, many, but not all, aspects of the structures may be interpreted directly.

Oftentimes, images of sheet silicates are one-dimensional, containing information pertaining to the basal spacing only. Since these types of images are commonly obtained in studies of clay minerals, only one-dimensional image interpretation will be addressed here. Interpretation of these types of images for mixed-layer illite/smectite has previously been discussed (12). This discussion extends the interpretation to a wider range of sheet silicates and then reviews the results for illite/smectite.

Microscope Parameters. The computer-simulated images presented here were calculated for the Philips 420T electron microscope (120 kV; $C_s = 2.0$ mm; $C_c = 2.0$ mm), and the conclusions are generally applicable to electron microscopes with similar optics. In fact,

some of the experimental images were obtained on a Philips 400T, yet the differences between these images and images obtained from similar structures on the Philips 420T are practically indistinguishable. Calculations for JEOL 100C optics (12) show that interpretation of sheet silicate images for electron microscopes with extremely different optical parameters is generally similar, but details of the interpretation may vary.

Model Input Structures. Input structures for the computer-simulated images were obtained by slight alteration of published structures. The input structures for serpentine and kaolinite were derived from the lizardite 1T X-ray structure refinement given by Mellini (25). Since the calculations were for one-dimensional images of the basal spacings, only the z-coordinates for the atoms were input with the x- and y-coordinates set to zero. This procedure was used for all of the calculations presented here. A layer spacing of exactly 0.7 nm was used to allow comparison between 0.7-nm and 1.4-nm structures. For the serpentine simulations, magnesium and silicon were assumed to be the only cations occupying octahedral and tetrahedral sites, respectively. For the kaolinite calculations, aluminum and silicon were assumed to be the only cations occupying the octahedral and tetrahedral sites, respectively. Hydrogen atoms were not included in the calculations.

The input structure for chlorite was derived from the atomic coordinates given in Brown and Bailey (26). Aluminum was assumed to substitute for silicon in one-quarter of the tetrahedral sites; this tetrahedral sheet charge was compensated by ferric iron substituting for one-third of the magnesium in the octahedral layer, giving the formula $Mg_5FeSi_3AlO_{10}(OH)_8$. Hydrogen atoms were not included in the calculations. A layer spacing of exactly 1.4 nm was used to allow direct comparison between 0.7-nm and 1.4-nm structures.

The input structure for biotite was derived from the refinement reported by Hazen and Burnham (27). Potassium and magnesium were assumed to be the only cations occupying the interlayer and octahedral sites, respectively. Aluminum was assumed to occupy 1/4 of the tetrahedral sites. A layer spacing of exactly 1.0 nm was used to allow comparison to other 1.0-nm structures.

The input structures for muscovite, smectite, and illite were derived from the refinement of a muscovite reported by Richardson and Richardson (28). One layer from this two-layer structure was used to obtain the atomic coordinates. The details of the procedure are presented by Guthrie and Veblen (12). In the muscovite structure, aluminum was assumed to occupy 1/4 of the tetrahedral sites, and potassium was assumed to entirely fill the interlayer sites. In the smectite structure, aluminum was assumed to occupy 1/20 of the tetrahedral sites, and potassium was assumed to fill 1/5 of the interlayer sites, with vacancies filling the remaining 4/5; the structural formula for this smectite is $K_{0.2}Al_2Si_{3.8}Al_{0.2}O_{10}(OH)_2$. In the illite structure, aluminum was assumed to occupy 3/16 of the tetrahedral sites, and potassium was assumed to fill 3/4 of the interlayer sites, with vacancies filling the remaining 1/4; the structural formula for this illite is $K_{0.75}Al_2Si_{3.25}Al_{0.75}O_{10}(OH)_2$. The mixed-layer structure of illite and smectite was obtained by alternating layers of illite and smectite. To allow comparison to other 1.0-nm structures, a layer spacing of exactly 1.0 nm was used for muscovite and biotite, and a layer spacing of exactly 2.0 nm was used for the 2-layer illite/smectite structure.

HRTEM Images

Serpentine and Kaolinite. Serpentine and kaolinite are T-O sheet silicates with a basal spacing of about 0.7 nm. Serpentine group minerals have magnesium or iron in the octahedral sites, giving a formula of $(\text{Mg,Fe})_3\text{Si}_2\text{O}_5(\text{OH})_4$. Kaolinite has aluminum in the octahedral sites, giving a formula of $\text{Al}_2\text{Si}_2\text{O}_5(\text{OH})_4$. Both mineral groups exhibit a wide range of sheet morphologies: planar structures (lizardite and kaolinite), tubular structures (chrysotile and tubular halloysite), bulbous structures (some halloysite, a kaolinite mineral), and corrugated structures (antigorite). Both groups are common products of the hydrous alteration or weathering of common rock-forming minerals and, as such, have been studied extensively with HRTEM imaging (e.g., 29-32).

Published images of serpentine and kaolinite group minerals characteristically consist of one dark-and-light-stripe pair per 0.7 nm, with dark and light bands of approximately equal thickness. Since no computer-simulated images of these structures have been published, interpretation of these images has been purely intuitive, based on the 0.7-nm periodicity. Furthermore, the correspondence between the dark and light bands and the underlying structure is not known, although it has been assumed that, at optimum defocus, the dark fringes correspond to the T-O layers.

Figure 1 shows an experimental image of a T-O layer silicate (lizardite). The 0.7-nm periodicity is clearly apparent, and no subperiodicities (<0.7 nm) or superperiodicities (>0.7 nm) can be detected. This image was obtained at or near Scherzer focus, and the crystal was oriented such that the basal planes were perfectly parallel to the electron beam, as determined by electron diffraction patterns of the areas from which the images were obtained. Thus, this image was taken under nearly ideal conditions in that both the focus conditions and orientation were carefully controlled.

Interpretation of this image can be made by comparing Figures 1 and 2. Figure 2a shows a computer-simulated image and the corresponding structure for lizardite at Scherzer focus. The experimental and computer images match closely, and the computer images show that light fringes in the images are centered over the space between the T-O layers and dark fringes are centered over the T-O layers. This correspondence, however, is only true for these specific imaging conditions: perfect orientation with the c^* -axis normal to the electron beam (i.e., the electron beam must be perfectly parallel to the sheets) and Scherzer focus. Figure 2b shows a computer-simulated image for an overfocus condition, in which the correspondence between image and structure is reversed: light fringes in the images are centered over T-O layers and dark fringes are centered near the spacing between the T-O layers. Figure 3 shows that the same interpretations are valid for kaolinite.

Chlorite. Figure 4 shows an experimental image for chlorite obtained near the Scherzer focus and with the c^* -axis perfectly perpendicular to the electron beam. The image is characteristic of published images of chlorite (e.g., 33-36), which commonly show a repeating sequence of approximately 1.4 nm consisting of a thick dark fringe/a thin light fringe/a thin dark fringe/a thin light fringe. Figure 5 shows a computer-simulated image and the associated structure under the same conditions. Comparison of the

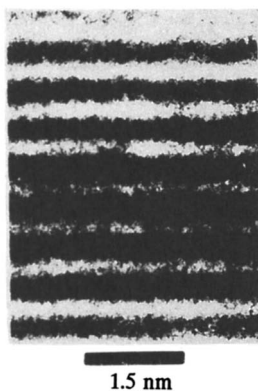


Figure 1. Experimental HRTEM image of a T-O layer silicate (lizardite). Microscope was focussed near the Scherzer focus.

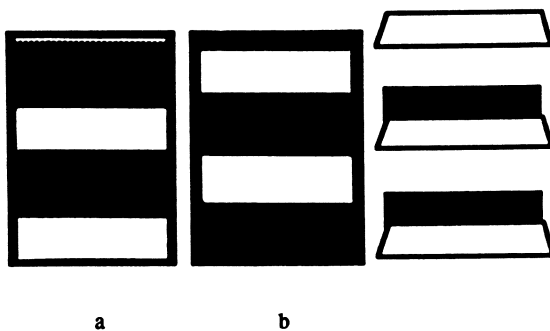


Figure 2. Computer-simulated image of lizardite. a) Scherzer focus. b) +50 nm overfocus.

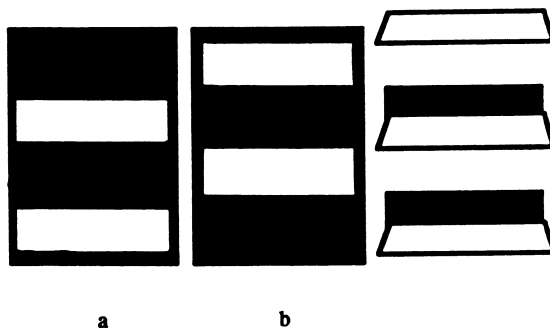


Figure 3. Computer-simulated image of kaolinite. a) Scherzer focus. b) +50 nm overfocus.

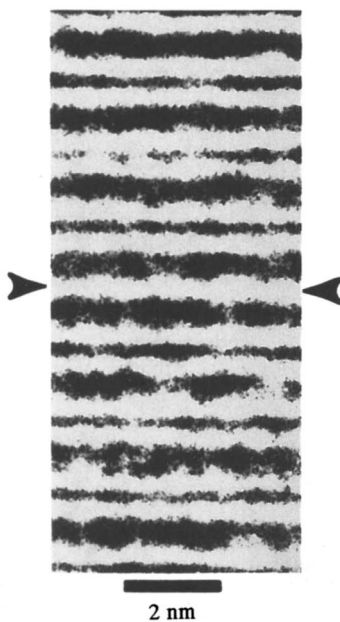


Figure 4. Experimental HRTEM image of chlorite. Microscope was focussed near the Scherzer focus. A biotite layer (arrowed) is intergrown.

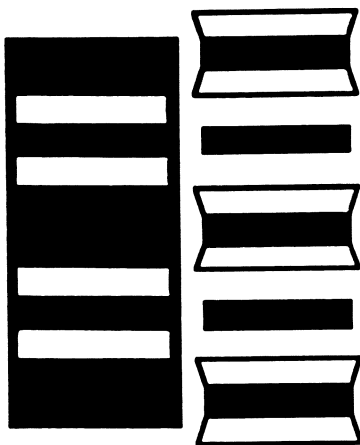


Figure 5. Computer-simulated image at Scherzer focus of chlorite.

two images shows a good match between experimental and simulated images and allows a determination of the correspondence between image and structure. Under these conditions, the thick dark band overlies the T-O-T layer, and the thin dark band overlies the isolated octahedral layer. These results confirm numerous intuitive interpretations from the literature (e.g., 20, 21, 24, 33), as well as those based on the two-dimensional simulations of Spinnler *et al.* (23).

Micas. Figure 6 shows an experimental image of biotite; the image was obtained near Scherzer focus and with the c^* -axis perfectly perpendicular to the electron beam. The image is typical of published images of micas (e.g., 33-34), consisting of light fringe/dark fringe pairs about 1.0-nm thick. Figure 7a shows the respective computer-simulated image for similar focus conditions. Comparison of the experimental and computer images shows that at Scherzer focus the dark fringe is centered over the T-O-T layer, and the light fringe is centered over the interlayer. Figure 7b shows a computer-simulated image for a focus of +50 nm. At moderate overfocus, the correspondence is identical; however, contrast does reverse at a focus between -100 nm and +50 nm (i.e., near -50 nm), such that the light fringe is centered over the T-O-T layer and the dark fringe centered over the interlayer. Figure 8 shows computer-simulated images for muscovite where the correspondence between image and structure reverses in overfocussed images. For Scherzer focus, an extra faint light fringe appears centered over the interlayer. Contrast does not reverse for underfocuses between -100 nm and +50 nm.

Biotite/Chlorite Intergrowths. Both ordered and disordered intergrowths of the various sheet silicates are very common, and one example is the intergrowth of chlorite and biotite (e.g., 30, 33-34, 36). These images have been interpreted intuitively, assuming that the images would resemble a composite of images from pure biotite and pure chlorite. Simulations of their intergrowth have not been published.

Figure 4 shows a biotite layer (arrowed) intergrown with chlorite, and Figure 9 shows the computer-simulated image and model structure of the intergrowth. Comparison of the images shows that biotite/chlorite intergrowths may indeed be interpreted in terms of a composite of a biotite image and chlorite image: the intergrowth of these two structures does not significantly affect the local details of an HRTEM image.

Illite/Smectite. Another common intergrowth of sheet silicates is the mixed-layering of illite and smectite. As discussed above, illite and smectite are clay minerals whose basic structures resemble the mica muscovite. Their compositions may differ significantly from muscovite, but they generally have a lower occupancy of the interlayer sites than mica. Numerous other compositional differences are possible for smectite; however, this discussion will be restricted to a dioctahedral illite and a dioctahedral smectite containing potassium and vacancies in the interlayer sites as given above.

Figures 10a and 10b show experimental images of a mixed-layer illite/smectite obtained with the c^* -axis perpendicular to the electron beam; Figure 10a was obtained with the objective lens near Scherzer focus, and Figure 10b was obtained from the same area with

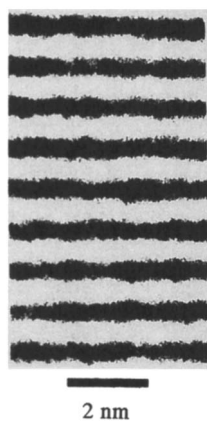


Figure 6. Experimental HRTEM image of biotite. Microscope was focussed near the Scherzer focus.

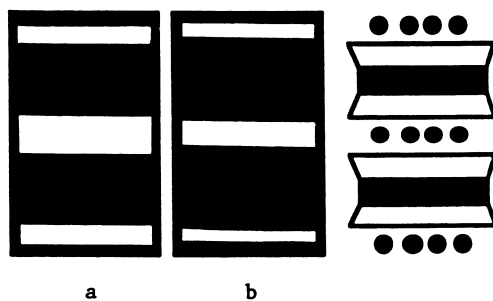


Figure 7. Computer-simulated image of biotite. a) Scherzer focus. b) +50 nm overfocus.

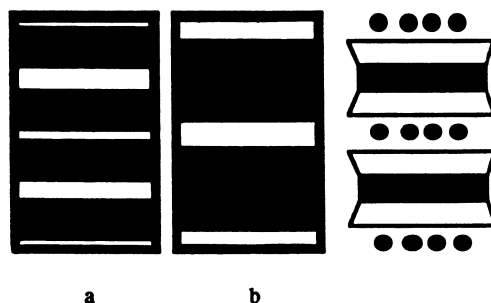


Figure 8. Computer-simulated image of muscovite. a) Scherzer focus. b) +50 nm overfocus.

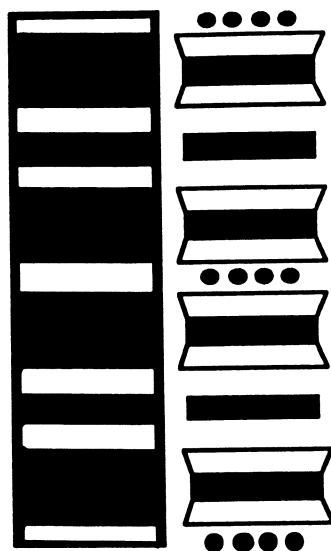


Figure 9. Computer-simulated image at Scherzer focus of biotite intergrown with chlorite.

the objective lens overfocussed by about 100 nm. This sample has been studied extensively by X-ray diffraction (37) and is known to contain 83-percent illite and 17-percent smectite layers (R3-ordered, from Zemplini, Hungary). The exact sequences of illite layers and smectite layers can not be determined by X-ray techniques; however, the smectite layers are believed to be rather evenly distributed throughout the sample, implying an average sequence of approximately illite-illite-illite-illite-smectite.

In principle, actual sequences of illite and smectite layers can be observed directly with HRTEM imaging. However, since the illite and smectite layers differ only slightly in their compositions (subtle differences in K, Al, and Si), they may be difficult to differentiate in HRTEM images. Indeed, the two different layer types are barely distinguishable near the Scherzer focus (Figure 10a), but the two layers are clearly visible for overfocus conditions (Figure 10b). This image allows direct observation of the sequence S-I-S-I-I-I-S-I-I-I-I-I-S-I from top to bottom.

Figures 11a and 11b show calculated images for the structure I-S-I-S-I, at Scherzer focus and overfocus. These calculated images compare well with the experimental images in Figure 10. At Scherzer focus, light bands overlie both the interlayer sites and the octahedral sites within the T-O-T layer; thus, two light bands and two dark bands occur every 1.0 nm. The compositional periodicity (i.e., the smectite layers) can not be distinguished. However, at overfocus, dark bands overlie the interlayer sites, and only one light band and one dark band occur per 1.0 nm. The same effect is seen in the experimental images. Though the computer-simulated images were calculated for a two-layer repeat (I-S), calculations for a four-layer-repeat (I-I-I-S) demonstrate that the conclusions may be extended to the larger repeats (12) seen in Figure 10. Thus, the image simulations show the conditions under which illite/smectite mixed-layer clays can be imaged, and they allow much more rigorous interpretation of ordering patterns than purely intuitive image interpretation.

Discussion

As stated and shown above, HRTEM images are complex functions of many factors. Only under very restricted circumstances do light and dark fringes in an HRTEM image exactly overlie or even resemble regions of low and high electron potential in the specimen. Two requirements for this correspondence are having the crystal in perfect orientation and having the microscope underfocussed to the Scherzer focus. Any deviation from these conditions reduces the degree of correlation between image and structure. Even for the simple one-dimensional images presented here, certain aspects of an image can not be interpreted literally unless orientation and focus are rigorously controlled. Notwithstanding, information can be obtained from these one-dimensional images, provided ambiguities in interpretation are considered.

Apparent Layer Thickness. Many images of sheet silicates and clay minerals exhibit layers of different thicknesses. These thickness variations commonly are measured from micrographs and interpreted as representing true differences in thickness. However, simulations have shown that imperfect orientation and focus can cause the

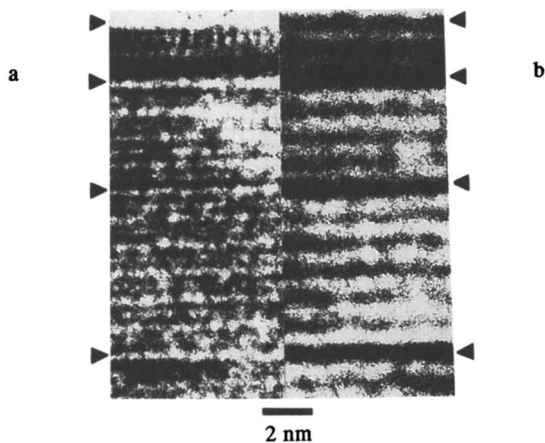


Figure 10. Experimental HRTEM image of illite/smectite. Smectite interlayers are arrowed. a) Scherzer focus. b) ~+50 nm overfocus.

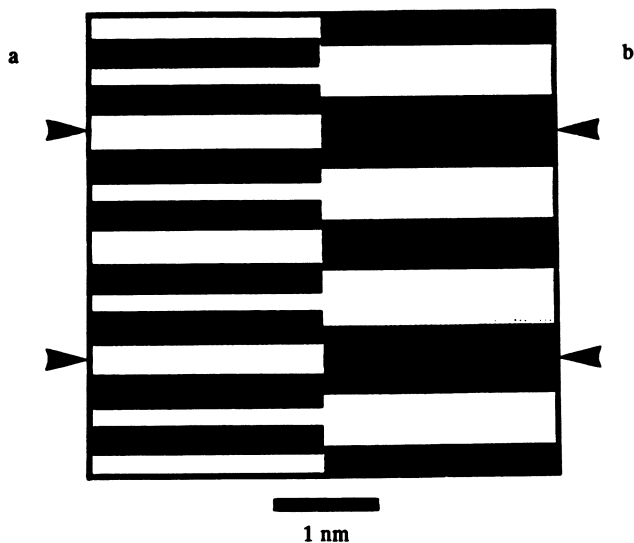


Figure 11. Computer-simulated image of R1-ordered illite/smectite. Smectite interlayers are arrowed. a) Scherzer focus. b) +50 nm overfocus.

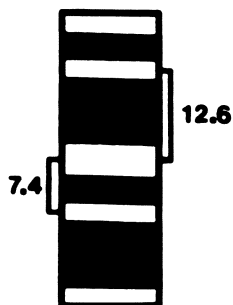


Figure 12. Computer-simulated image of R1-ordered illite/smectite for a JEOL 100C operated at a defocus of -135 nm (see 12 for details). Smectite layers appear thicker than illite layers; however, the model structure assumed a 1.0 -nm basal spacing for both.

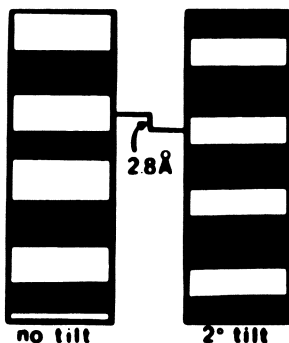


Figure 13. Computer-simulated image of R1-ordered illite/smectite. The fringes were shifted relative to the structure when the crystal was tilted out of perfect orientation about 2° (see 12 for details).

apparent layer thicknesses indicated by fringe spacing to deviate from the layer thicknesses in the imaged structure.

Intergrowths of illite and smectite represent a good example of this phenomenon. Typically, images of these intergrowths show layers of two apparently different thicknesses (i.e., Figure 10b). The apparently thicker layers (arrowed) frequently are thicker by up to a few tenths of a nanometer; thus, they commonly are interpreted as layers of expanded smectite. The computer-simulated images for illite/smectite clearly demonstrate that apparent increases in layer thickness can result from only chemical differences between adjacent layers. Figure 12 illustrates this apparent difference in layer thickness for a mixed-layer illite/smectite. The structural model had a uniform 1.0-nm spacing between layers, yet the image shows layers of 0.7 nm and 1.3 nm. However, the overall periodicity in the image is 2.0 nm.

Correspondence Between Image and Structure. As indicated above, intuitive interpretation of one-dimensional images generally has assumed that, when the microscope is underfocussed to the Scherzer focus, dark fringes in an image correspond to layers of high electrical potential in the structure. For instance, the dark fringes in images of T-O-T (2:1) layer silicates are assumed to overlie the T-O-T layer, whereas the light fringes are assumed to overlie the interlayers. While the computer image simulations have shown this interpretation to be accurate, they have also shown that the position of the fringes is a strong function of the orientation and focus. In other words, deviations from perfect orientation or focus cause the fringes to shift relative to the underlying structure. Figure 13 shows that even slight misorientation can shift the fringes by tenths of nanometers (12).

The computer-simulated images presented above and in Guthrie and Veblen (12) have shown that one-dimensional images of clay minerals and sheet silicates can be interpreted and can provide important information. The simulations have also shown, however, that even these simple images must be interpreted carefully. Problems such as fine grain size and rapid electron beam damage can preclude the extreme care in orienting and focussing that is required for images to be interpreted directly (without computer image simulation). Since apparent compositional periodicity, apparent layer thickness, and correspondence between image and structure are each functions of orientation and focus, some ambiguities may be present in any interpretations based on one-dimensional HRTEM images of clay minerals.

Literature Cited

1. Meike, A.; Wenk, H.-R.; O'Keefe, M. A.; Gronsky, R. Phys. Chem. Minerals, 1988, 15, 427-437.
2. Veblen, D. R. In Applications of Electron Microscopy in the Earth Sciences; White, J. C., Ed.; Mineralogical Association of Canada: Toronto, Canada, 1985; Chapter 3.
3. Spence, J. C. H. Experimental High-Resolution Electron Microscopy; second edition; Oxford University Press: New York, 1988.
4. Cowley, J. M. In Principles of Analytical Electron Microscopy; Joy, D. C., Romig, A. D., Jr., and Goldstein, J. I., Eds.; Plenum Press: New York, 1986; Chapter 3.

5. McLaren, A. C. In Applications of Electron Microscopy in the Earth Sciences; White, J. C., Ed.; Mineralogical Association of Canada: Toronto, Canada, 1985; Chapter 1.
6. Hirsch, P.; Howie, A.; Nicholson, R. B.; Pashley, D. W.; Whelan, M. J. Electron Microscopy of Thin Crystals; second edition; Robert E. Krieger Publishing Co.: Malabar, Florida, 1977.
7. Scherzer, O. J. Appl. Phys., 1949, **20**, 20-29.
8. Cowley, J.; Moodie, A. F. Acta Cryst., 1957, **10**, 609-619.
9. O'Keefe, M. A. In Electron Optical Systems; Hren, J. J.; Lenz, F. A.; Munro, E.; Sewell, P. B., Eds.; AMF O'Hare: Chicago, 1984; p 209-220.
10. Self, P. G. and O'Keefe, M. A. In High-Resolution Transmission Electron Microscopy; Buseck, P. R.; Cowley, J. M.; Eyring, L., Eds.; Oxford University Press: New York, 1988 (in press).
11. O'Keefe, M. A.; Buseck, P. R.; Iijima, S. Nature, 1978, **274**, 322-324.
12. Guthrie, G. D., Jr.; Veblen, D. R. Clays and Clay Minerals, 1989, **37**, 1-11.
13. Barrer, R. M. Zeolites and Clay Minerals as Sorbents and Molecular Sieves; Academic Press: London, 1978; Chapter 8.
14. Bailey, S. W. In Micas; Bailey, S. W., Eds; Mineralogical Society of America: Washington, D. C., 1984; Chapter 1.
15. Bailey, S. W., In Crystal Structures of Clay Minerals and their X-ray Identification; Brindley, G. W. and Brown, G., Eds; Mineralogical Society: London, England, 1980; Chapter 1.
16. Brindley, G. W., In Clays and the Resource Geologist; Longstaffe, F. J., Ed.; Mineralogical Association of Canada: Toronto, Canada, 1981; Chapter 1.
17. Deer, W. A.; Howie, R. A.; Zussman, J. An Introduction to the Rock-Forming Minerals; Longman: London, 1980.
18. Amouric, M.; Gianetto, I.; Proust, D. Bull. Minéral., 1988, **111**, 29-37.
19. Livi, K. J. T. and Veblen, D. R. Am. Mineral., 1987, **72**, 113-125.
20. Maresch, W. V.; Massonne, H. J.; Czank, M. Neues Jahrbuch für Mineralogie, 1985, **152**, 79-100.
21. Veblen, D. R. Am. Mineral., 1983, **68**, 566-580.
22. Hydrous Phyllosilicates; Bailey, S. W., Ed.; Mineralogical Society of America: Washington, D. C. 1988.
23. Spinnler, G. E.; Self, P. G.; Iijima, S.; Buseck, P. R. Am. Mineral., 1984, **69**, 252-263.
24. Amouric, M.; Mercuriot, G.; Baronnet, A. Bull. Minéral., 1981, **104**, 298-313.
25. Mellini, M. Am. Mineral., 1982, **67**, 587-598.
26. Brown, B. E.; Bailey, S. W. Am. Mineral., 1962, **47**, 819-850.
27. Hazen, R. M.; Burnham, C. W. Am. Mineral., 1973, **58**, 889-900.
28. Richardson, S. M.; Richardson, J. W., Jr. Am. Mineral., 1982, **67**, 69-75.
29. Veblen, D. R.; Buseck, P. R. Science, 1979, **206**, 1398-1400.
30. Veblen, D. R. Am. Mineral., 1980, **65**, 1075-1086.
31. Ahn, J. H.; Peacor, D. R. Am. Mineral., 1987, **72**, 353-356.
32. Ahn, J. H.; Peacor, D. R. Proc. Int. Clay Conf., 1987, p. 353-356.

33. Veblen, D. R.; Ferry, J. M. Am. Mineral., 1983, 68, 1160-1168.
34. Banfield, J.; Eggleton, R. A. Am. Mineral., 1985, 70, 902-910.
35. Lee, J. H.; Ahn, J. H.; Peacor, D. R. J. Sed. Pet., 1985, 55, 532-540.
36. Buseck, P. R.; Veblen, D. R. Bull. Minéral., 1981, 104, 249-260.
37. Veblen, D. R.; Guthrie, G. D.; Livi, K. J. T. ; Reynolds, R. C. Clays and Clay Minerals, submitted.
38. This work was supported by NSF grant EAR86-09277. Figures 12 and 13 are with the permission of the Clay Minerals Society.

RECEIVED May 25, 1989

Chapter 5

Skeletal Versus Nonbiogenic Carbonates

UV-Visible-Near IR (0.3-2.7- μm) Reflectance Properties

Susan J. Gaffey

Department of Geology, Rensselaer Polytechnic Institute, Troy, NY 12181

Skeletal carbonates, unlike non-biogenic carbonates, contain organics and comparatively large amounts (up to 3 weight %) of water. Water and organic compounds, which play central roles in carbonate diagenesis, are an intrinsic part of carbonate skeletons incorporated during growth. Organics and water are intimately associated and are disseminated throughout skeletons in minute inter- and intracrystalline voids. VNIR spectroscopy can be used to monitor changes in forms and abundances of water and organics during diagenetic alteration. Skeletal samples prepared for mineralogical and chemical analyses by routine procedures are not representative of these materials as they occur in nature, nor are they 100% aragonite and/or calcite.

The chemical and mineralogical composition of carbonate skeletons is more varied and complex than the usual terms "aragonite" and "high" or "low Mg calcite" imply. Water and organics are an intrinsic part of all carbonate skeletons and can play a major role in the diagenesis of carbonate sediments. Liquid water provides the medium for all diagenetic reactions (1). Presence of H_2O - and OH^- -containing mineral phases can affect the stability and solubility of carbonate skeletons (e.g. 2, 3). Organic compounds can facilitate the precipitation of carbonates, and can affect the mineralogy, chemical composition, and crystal form of the precipitate (e.g. 4-6). Organic compounds form complexes with metal cations, affecting their mobility (5, 7). Breakdown of organic compounds can alter pore water chemistry, affecting Eh and pH, as well as concentrations of dissolved species such as NH_3^+ , SO_4^{-2} , PO_4^{-3} , and CO_2 (7, 8) which can, in turn, affect the solubility and stability of carbonate phases (9). Both water and organics may remain in reduced amounts in ancient carbonate sediments, even after considerable diagenetic alteration (e.g. 10-15).

Despite the importance of water and organic compounds in diagenetic reactions, and although organic compounds and water in various forms (liquid and bound H_2O and OH^-) are known to be

0097-6156/90/0415-0094\$06.75/0
© 1990 American Chemical Society

important constituents not only of skeletal but also of non-skeletal grains such as ooids and peloids (e.g. 2, 5, 10-13, 16-24) there are at present no analytical techniques routinely in use by carbonate petrologists which enable identification and determination of abundances of these components.

Visible and near infrared (VNIR) (0.3 - 2.7 μm) spectroscopy provides a rapid, inexpensive, non-destructive technique for characterizing significant aspects of the mineralogical and chemical composition of geologic samples. Like X-ray diffraction it is non-selective, giving information on all optically active phases present in a sample. Unlike X-ray diffraction (as routinely employed by geologists for mineral identification) it can be used to study many liquid and amorphous phases and to identify many of the atoms or molecular ions which occur in solid solution rather than as discrete mineral phases, providing a useful compliment to X-ray diffraction analyses. VNIR spectroscopy can also be used to study the lighter elements such as C, O, H, and N, which are not amenable to study by techniques more commonly employed by geologists such as microprobe or XRF.

This paper deals only with skeletal carbonates, those which are clearly produced by carbonate-secreting organisms such as corals, mollusks, or calcareous algae (biologically-controlled mineralization, as defined by Mann, [25]), and with non-biogenic carbonates. It does not deal with the products of biologically-induced precipitation, as defined by Mann (25) and Lowenstam (26), although the limited data available suggests that the spectral properties of such biologically-induced products as stromatolites are very similar to those of skeletal carbonates.

Materials and Methods

Most modern and fossil material used in this study was collected on Oahu, Hawaii, between 1980 and 1984, and from San Salvador Island, Bahamas, in March, 1986, and January and June, 1988. Mercenaria shells are from the Pleistocene of Virginia. After collection, skeletal samples are usually either dried, frozen, or cleaned in 5 % sodium hypochlorite solution so they can be shipped and/or stored. For this study calcareous green algae such as Halimeda and Penicillus, and gorgonians were dried in an oven at temperatures of about 40°C. Whole skeletons of coralline red algae, scleractinian corals, hydrozoans, octacorals, and echinoids which were collected live were cleaned in 5 % sodium hypochlorite solution before returning them to the laboratory for analysis. Sands were collected both from beaches and the marine environment so that tests of foraminifera, plates of Halimeda, and segments of coralline red algae could be separated from them. Tests of Homotrema rubrum were removed from coral heads or rock slabs they encrusted. Tests of some foraminifera were also removed from Penicillus and Halimeda. Skeletons of dead echinoids, algae, and corals were collected from bottom sediments and from beaches.

Mineralogy of samples was determined using X-ray diffraction. Modern and fossil samples were examined in thin section and/or with SEM. Treatment of samples from which VNIR (0.3 - 2.7 μm) reflectance spectra were obtained varied. Spectra of skeletons of all groups of organisms studied were obtained from bleached and/or unbleached

powders. Spectra were also obtained from bleached and unbleached coral slabs, bleached slices of mollusc shells, whole mollusc shells, bleached whole echinoid plates, foraminifera, serpulids, bryozoans, and ostracods, and unbleached fossils. Either H_2O_2 buffered to a neutral pH with NaOH or 5% sodium hypochlorite solution was used to bleach samples. Spectra were obtained using the spectrophotometers at RELAB at Brown University, described by Pieters (27) and at the U.S.G.S in Denver, described by Clark, R. N.; King, T. W.; Klewja, M.; Swayze, G. A., (J. Geophys. Res., in press).

Background

When light interacts with a compound certain wavelengths are preferentially absorbed. The number, positions, widths, and intensities of these absorptions are diagnostic of the mineralogical and chemical composition of the sample. Several different processes in compounds and crystals can cause absorption of light: (1) electronic transitions in molecular orbitals; (2) electronic transitions between unfilled d-shells in transition metal ions such as Fe^{2+} and Fe^{3+} ; (3) internal vibrational transitions in molecules and molecular ions such as H_2O or NH_3^+ in which bond lengths and bond angles change; and (4) external vibrational transitions in which the molecule or molecular ion moves as a unit.

Advantages of the VNIR Region. The VNIR region of the spectrum employed in the present study has a number of advantages over the more commonly used mid-infrared (MIR) (3 to 20 μm) and far infrared (FIR) (>20 μm) regions. (1) Because the types of particle size effects which hamper work in the MIR and FIR (28-31) are virtually absent in the VNIR, spectra can be obtained from samples in any form including powders, sands, and broken, sawed, or polished surfaces (32). Unstable or soluble phases such as organics and hydrated mineral phases can be studied in situ, without subjecting materials to grinding, heating, or extraction techniques which may alter, remove, or destroy the phases of interest. (2) The VNIR region contains absorptions due to all four types of transitions listed above, unlike the MIR and FIR which only contain features due to vibrational transitions. (3) A great deal of overlap between absorption bands occurs in the 3 μm region which contains absorptions due to the fundamental O-H, C-H, and N-H stretching modes and the first overtones of the H-O-H and H-N-H bending modes. However, in the VNIR energy differences between different vibrational modes are amplified, and a useful separation exists between absorptions due to overtones and combination tones of these modes (33, 34).

Spectral Properties of Anhydrous Carbonate Minerals. Spectra of all anhydrous carbonate minerals show a series of sharp, narrow absorptions at wavelengths >1.6 μm (Figure 1), whose precise positions and widths vary with mineralogy and chemical composition. These absorption bands are due to combinations of translational lattice modes with internal modes, and in general, bands shift to longer wavelengths with increasing mass of the major cation (35). Solid substitution for the major cation, common in calcite-group minerals, can also produce shifts in band position. For example, in spectra of ferroan dolomites, carbonate bands shift to longer

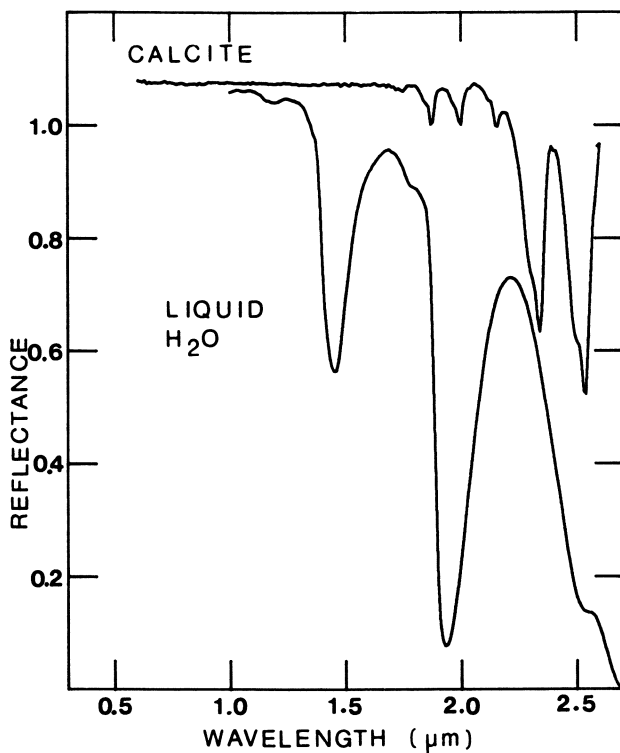


Figure 1. Spectra of non-biogenic calcite (Iceland spar) and liquid H₂O. Calcite spectrum offset vertically by 0.2.

wavelengths at high Fe^{2+} concentrations, again reflecting the influence of cation mass on band position (11).

Spectral Properties of H_2O and OH^- . H_2O has three internal fundamental vibrational modes: a symmetric stretch (ν_1), a bending mode (ν_2), and an antisymmetric stretch (ν_3), as well as an intermolecular mode, ν_L (36). Approximate wavelengths of these fundamental modes are given in Table I, and wavelengths and band assignments for absorptions produced in the NIR are given in Table II. A spectrum of liquid H_2O , obtained from the RELAB general collection, is shown in Figure 1. When H_2O is incorporated in a crystal, hydrogen bonding causes the absorption bands to broaden, intensify, and shift to longer wavelengths (37-39).

OH^- produces a single stretching fundamental near $2.78 \mu\text{m}$ (39). In addition to the absorptions listed in Table II, spectra of OH^- -containing minerals display a number of sharp, narrow absorptions around the O-H stretching fundamental due to combinations of the O-H stretching vibration with lattice modes (39, 40). Spectra of H_2O -containing phases show absorption features near 1.2 and $1.9 \mu\text{m}$ which, because they involve the H-O-H bending mode, do not appear in spectra of OH^- -containing phases. Spectra of minerals containing OH^- , however, will show an absorption feature between 2.0 and $2.3 \mu\text{m}$ due to a combination of the O-H stretch and the M-O-H bending mode, M being the atom to which the OH group is bound (34, 41-44).

The spectra of some H_2O - and OH^- -containing minerals are shown in Figure 2. The spectrum of hydrocerussite ($\text{Pb}_3[\text{CO}_3]_2[\text{OH}]_2$) (45) actually a reagent grade " PbCO_3 " sample, as well as those of brucite ($\text{Mg}[\text{OH}]_2$) and portlandite ($\text{Ca}[\text{OH}]_2$) illustrate absorption features due to OH^- . The hydromagnesite ($\text{Mg}_5[\text{CO}_3]_4[\text{OH}]_2 \cdot 4\text{H}_2\text{O}$) (45) spectrum provides an example of a mineral containing both H_2O and OH^- .

The spectra in Figure 2 illustrate the usefulness of reflectance spectroscopy in studies of water in minerals. While the composition, crystal structure, and spectral properties of $\text{Ca}(\text{OH})_2$ and $\text{Mg}(\text{OH})_2$ are well known, those of many hydrated carbonate minerals are not. The hydrozincite spectrum in Figure 2 is that of a reagent grade " ZnCO_3 ", shown by X-ray diffraction to be the mineral hydrozincite, composition $\text{Zn}_5(\text{CO}_3)_2(\text{OH})_6$ (45). However, the spectrum displays a strong $1.9\text{-}\mu\text{m}$ band, indicating the presence of hydrogen-bonded H_2O . The shapes and positions of the water bands in the magnesite spectrum in Figure 2 show that bound H_2O is present in addition to liquid H_2O in fluid inclusions, despite the fact that only magnesite is detected by X-ray diffraction analysis of this sample. As these spectra show, and as other workers have stated (e.g. 46, 47), the chemical composition of many hydrated carbonate mineral phases are incompletely known, making it difficult to relate hydrated phases encountered in skeletons to specific mineral phases.

Spectral Properties of Organics - General. The following discussion is not intended to give a complete description of the spectral properties of all organics, but to briefly outline the spectral characteristics of broad classes of organic compounds found in carbonate skeletons as well as in the soft, uncalcified tissues of carbonate-secreting organisms. Large organic molecules can be thought of as consisting of rings and/or long chains of atoms joined by covalent bonds to form the backbone of the molecule, and of side

branches or chains. Functional groups such as amino (NH_2), hydroxyl (OH), and methyl (CH_3) groups are the reactive portions of the molecule and may occur either within the main chain or as side branches. Despite the large size and structural complexity of organic molecules, small groups of atoms such as NH_3^+ , OH, or CH_2 within those molecules will behave semi-autonomously, always producing absorptions in the same general region of the spectrum with similar intensities. These are called the characteristic group frequencies. Precise positions of these absorption features will vary depending on the chemical environment of the atomic group (42, 48-50). In many cases these oscillator groups which give the molecule its characteristic spectral properties are the same as the functional groups which determine many of its chemical properties.

Vibrations of these large molecules can be grouped into three basic types: (1) vibrations of portions of the main chain; (2) vibrations of side branches or groups; and (3) wagging, twisting, or rocking vibrations in which the side branches move as a unit relative to the main chain. Wavelengths of absorptions due to fundamental vibrational modes of important oscillator groups are given Table I. Only fundamentals whose overtones and combination tones produce absorptions in the NIR region are included. The reader is referred to (42) for excellent illustrations of these vibrational motions. Following the conventions of Herzberg (51) ν_1 indicates a symmetric stretch, ν_2 a symmetric bending mode, ν_3 an antisymmetric stretch, and ν_4 an antisymmetric bend. The antisymmetric stretching and

Table I. Fundamental Modes of Oscillator Groups (33, 42, 52-54)

Assignment	Wavelength (μm)	Assignment	Wavelength (μm)
H_2O		CH_2	
ν_1	3.05	ν_1	3.57
ν_2	6.08	ν_2	6.90
ν_3	2.94	ν_3	3.45
ν_L	20.00	wag (w)	7.49
		twist (t)	7.82
NH_2			
ν_1	2.99		
ν_2	6.25		
ν_3	2.90		
NH_3		CH_3	
ν_1	3.23	ν_1	3.45
ν_2	6.67	ν_2	7.20
ν_3	3.03	ν_3	3.39
ν_4	6.25	ν_4	6.84
		rock	8.70
Amide I			
(C=O stretch)	5.92		
Amide II			
(C-N-H bend)	6.45		
Amide III			
(C-N-H bend)	8.00		

bending modes are doubly degenerate in molecular groups of four atoms such as NH_3^+ and CH_3 .

The near infrared portion of spectra of organic compounds is dominated by overtones and combination tones of the N-H, C-H, and O-H stretching fundamentals (42). VNIR absorptions of oscillator groups in organic compounds are listed in Table II.

Absorption bands due to NH, NH_2 , and NH_3^+ tend to be broad and diffuse with multiple peaks, and the symmetric stretching mode is stronger than the asymmetric stretch (42, 55). Absorption bands produced by CH, CH_2 , and CH_3 groups tend to be narrow and sharp (42, 54). In addition to the strong absorptions listed for CH_2 and CH_3 in the 2.25 - 2.45 μm region, CH, CH_2 and CH_3 groups may produce a series of weaker absorptions at slightly longer wavelengths due to combinations of the C-H stretching modes with wagging and twisting vibrations (33). OH groups in organic compounds generally produce intense, broad absorptions. However, where hydrogen bonding is weak, these absorptions are narrow, sharp, and occur at shorter wavelengths than those produced by more strongly bound OH groups (56). As with OH-groups, hydrogen bonding causes absorptions due to all these oscillator groups to broaden and shift to longer wavelengths. C-H and N-H absorptions are several orders of magnitude weaker than those produced by an equal concentration of H_2O or OH^- in the NIR spectral region (36, 57, 58).

Table II. Band assignments and approximate positions of VNIR absorption features produced by water and organics (33, 42, 44, 49, 51, 53, 54, 59)

Assignment	Wavelength (μm)	Assignment	Wavelength (μm)
H_2O		OH	
$3\nu_3, 3\nu_1$	0.9	$3\nu_1$	0.9
$\nu_1 + \nu_2 + \nu_3$	1.2	$2\nu_1$	1.4
$2\nu_1, 2\nu_3$	1.4	$\nu_1 + \text{M-O-H bend}$	1.9 - 2.3
$\nu_2 + \nu_3 + \nu_L$	1.8		
$\nu_2 + \nu_3$	1.9		
$3 + L$	2.5		
NH_3^+		CH_3	
$3\nu_1, 3\nu_3$	1.1	$3\nu_1, 3\nu_3$	1.2
$\nu_1 + \nu_2 + \nu_3$	1.25	$2\nu_1, 2\nu_3$	1.7
$2\nu_1, 2\nu_3$	1.5	$\nu_1 + \nu_2, \nu_1 + \nu_4$	2.3 - 2.4
$\nu_2 + \nu_3$	2.0 - 2.2		
NH_2		CH_2	
$3\nu_1$	1.02	$3\nu_1, 3\nu_3$	1.2
$2\nu_3$	1.45	$2\nu_1, 2\nu_3$	1.7
$2\nu_1$	1.49	$\nu_3 + \nu_2$	2.3 - 2.4
$\nu_2 + \nu_1, \nu_2 + \nu_3$	1.95 - 2.05		
Peptide linkage			
$2\nu_{\text{NH}}$	1.45		
NH + Amide I	2.01		
NH + Amide II	2.06		
NH + Amide III	2.17		

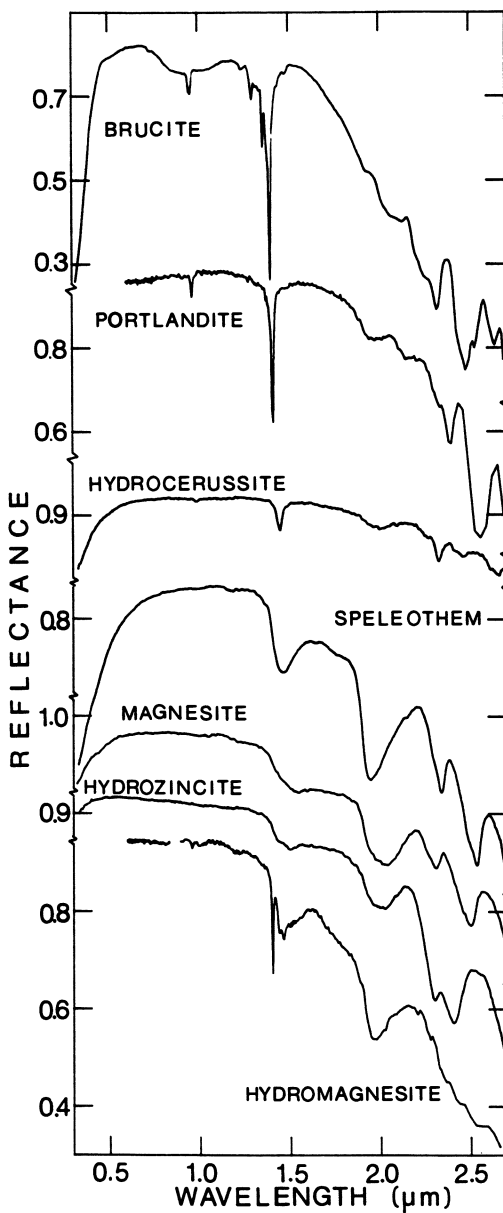


Figure 2. Spectra of non-biogenic mineral samples containing OH^- (brucite, portlandite, hydrocerussite), liquid H_2O (aragonite speleothem) and bound H_2O (magnesite, hydrozincite). Hydromagnesite contains both bound H_2O and OH^- .

Spectra of some organic materials are shown in Figure 3. The Halimeda spectrum was obtained from young, lightly calcified plates. Although the plates were bleached in sodium hypochlorite solution, large amounts of organics remain in the sample. The sapropel sample is from a saline lake in the Bahamas. The coral polyp spectrum was obtained from coral tissue exposed by slabbing a Diploria strigosa head. The coral organics, also from Diploria strigosa, were removed from the skeleton by dissolving it in 1 M HCl. The dead leaf spectrum comes from the RELAB general collection at Brown University. The gorgonian spectrum is that of a lavender sea pen.

Proteins. Spectra of proteins are dominated by absorptions due to vibrations of the peptide or protein chain, although absorptions due to side groups may also occur in spectra (49, 52). Amino acids generally exist in the zwitterion form in which an acidic carboxyl group (-COOH) donates a proton to the amino group (NH₂) forming an ammonium ion (NH₃⁺) (42, 60). Thus protein spectra can contain features due to NH₃⁺ as well as to NH₂, NH, and CH₂ (42, 49, 59, 61). Absorption features due to proteins occur in the coral polyp, coral organics, and gorgonian spectra in Figure 3.

Polysaccharides. NIR spectra of polysaccharides contain features due to OH, CH₂, and CH₃. OH groups produce broad bands near 1.4 and 1.0 μm, the first and second overtones of the O-H stretching fundamental. Sharp narrow O-H features may occur if OH groups are weakly hydrogen bonded, as, for example, in the sapropel spectrum in Figure 3. In addition, two or more broad bands occur between 1.9 and 2.3 μm due to combinations of O-H stretch and C-O-H bending modes (42, 44, 56, 62). The Halimeda, sapropel, and leaf spectra in Figure 3 contain features due to polysaccharides.

Lipids. NIR spectra of lipids are dominated by CH, CH₂, and CH₃ features (33, 53). However, as these features also occur in spectra of proteins and polysaccharides, no features in the spectra in Figure 3 can be unequivocally assigned to lipids at this time.

Organic Pigments. Organic pigments such as chlorophyll and carotene produce very intense absorption features in the visible region due to electronic transitions in molecular orbitals (e.g. 63). These pigments and/or the products resulting from their breakdown can persist in sediments for geologically long periods of time. They serve as biological markers or chemical fossils in organic geochemical studies, and absorptions due to these pigments are found in oils and kerogen extracted from ancient sediments (64). These biomarkers may be studied in situ using VNIR reflectance spectroscopy (65). Spectra containing absorptions due to organic pigments are shown in Figure 3.

Organics in Carbonate Skeletons

Organic compounds occur not only in the soft tissues of carbonate-secreting organisms, but also within their skeletons. All organic compounds can potentially play important roles in carbonate diagenesis. The large number of overlapping features due to carbonate, water, and organics in the VNIR makes identification of

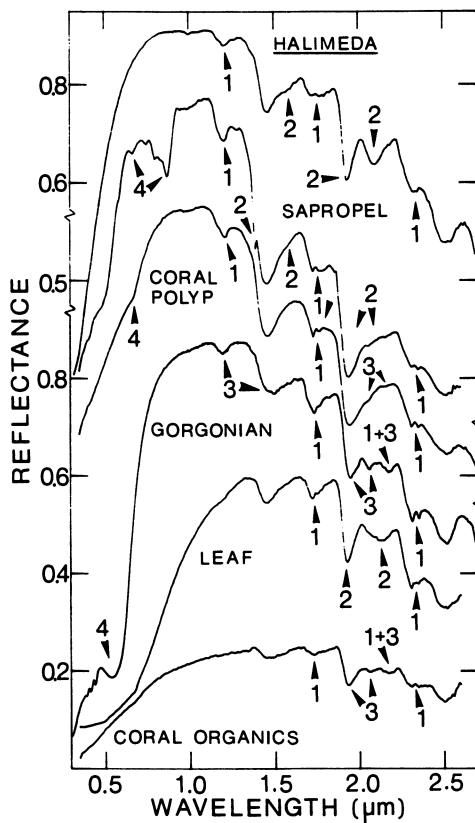


Figure 3. Spectra of organic samples illustrating absorption features due to C-H (1), O-H (2), N-H (3), and organic pigments (4). (*Halimeda* spectrum offset vertically by 0.3, sapropel spectrum by 0.04, coral polyp by 0.04, gorgonian by -0.04, dead leaf by 0.04, and coral organics by -0.065.)

specific phases difficult. However, each compound or functional group produces a distinct set of absorption features. Although a single band cannot be assigned to a given compound with certainty, suites of features considered together reduce ambiguities in identification of compounds (66, 67). H_2O , OH^- , and CO_3^{2-} produce the most intense absorptions in the VNIR, H_2O and OH^- because they are strong absorbers (36), CO_3^{2-} because it is the most abundant phase in these samples. Because C-H and N-H absorptions are comparatively weak in this spectral region, features due to NH- and CH-containing functional groups are most evident in the more transparent regions of the spectrum where features due to OH^- , H_2O and CO_3^{2-} are weak or absent.

There are four principle sources for the organic compounds detected in VNIR spectra of carbonate skeletons: (1) organic matrices; (2) organic pigments produced by the carbonate-secreting organism; (3) endoliths; and (4) soft tissues and body fluids of the organism (68, 69).

Many organisms use an organic matrix to facilitate precipitation of their skeletons (e.g. 24, 26, 70). In others, such as the mollusks, organic compounds also play a structural role by adding strength and toughness to the skeleton (17, 24). Features attributable to organic matrices are most evident in spectra of whole, unpowdered skeletal samples. For example, the Homotrema rubrum spectrum (Figure 4a) contains features near 1.2 and 1.7 μm , and a weak inflection on the 2.3- μm CO_3^{2-} band, due to C-H. While not, strictly speaking, a part of the organic matrix, portions of the organism's soft tissues and/or body fluids may be trapped during growth within and/or between carbonate crystals making up the skeleton (68, 71-73).

Some organic compounds in skeletons are introduced by endoliths. Endolithic algae, bacteria, and/or fungi can infest skeletons during the life or following the death of an organism. The spectrum of the coral Dichocoenia shows very strong absorptions near 0.4 and 0.67 μm due to chlorophyll in the endolithic alga Ostreobium (74, 75). Endoliths can add, alter, or remove organics in carbonate skeletons (68). However, the exact nature of the changes in organic content caused by endoliths isn't well documented.

Although this study is concerned primarily with carbonate skeletons, rapid breakdown of soft tissues after death of the organism can have a major effect on porewater chemistry and thus, on diagenetic processes (7, 8, 76). The spectrum of the slab of the coral Dichocoenia stokesii shows features near 1.2 and 1.7 μm due to C-H, and weak N-H features near 1.25, 1.55, 2.1 and 2.2 μm , due in large part to incomplete breakdown of coral tissues in the unoccupied portions of the skeleton (Zabielski and Gaffey, Proc 4th Symp. Geol. Bahamas, in press).

Even after grinding and bleaching, samples still contain organic compounds. Organic pigments provide the most striking examples. The spectrum of the powdered, bleached Homotrema rubrum sample (Figure 4b) still shows an intense absorption feature near 0.5 μm due to the pigments which give this foraminifera its distinctive red color, although the C-H features seen in the spectrum of the whole tests (Figure 4a) are less evident.

Portions of organic matrices also remain in treated samples, and some absorption features originally attributed to inorganic hydrated

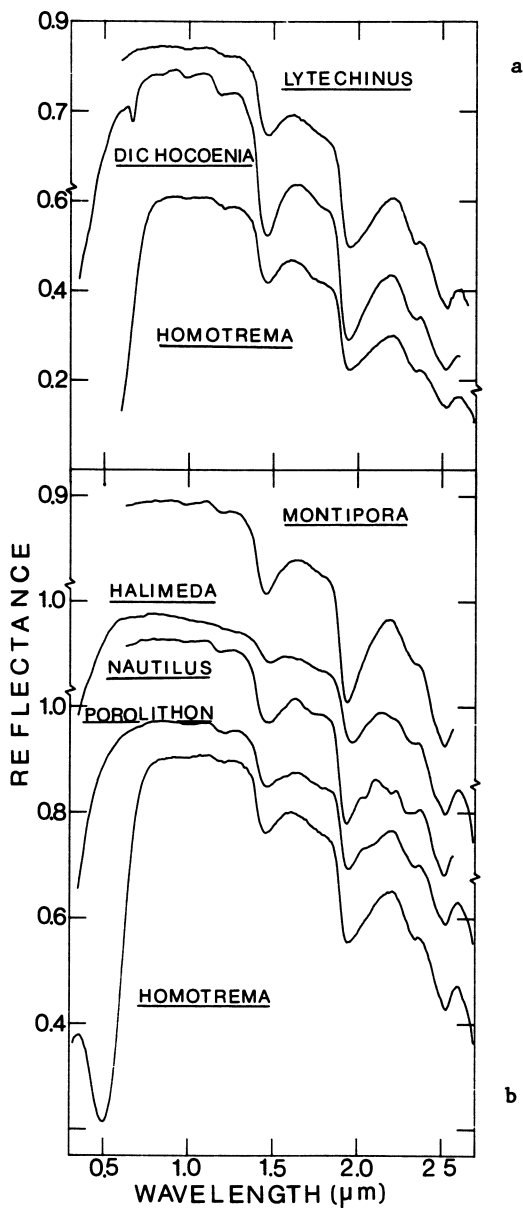


Figure 4. Spectra of bleached whole (a) and powdered (b) samples of skeletal carbonates.

mineral phases (13), appear to be better explained as absorptions due to organic compounds. The *Nautilus* spectrum provides an example. *Nautilus* shells contain >5 % organic matrix by weight, composed of proteins rich in aspartic acid, and polysaccharides (24, 77). The strong absorption feature near 2.05 μm can be attributed to O-H absorptions of polysaccharides, and the sharp narrow features between 2.1 and 2.3 μm to C-H absorptions of polysaccharides and/or proteins. The C-H absorptions near 1.7 and 1.2 μm and the broadening of the 1.4- μm O-H band support this interpretation.

Additional work is needed to establish detection limits for various organic compounds in carbonates. Because H_2O is such a strong absorber in this spectral region, organic compounds present in low concentrations may not be detected in reflectance spectra. *Lytechinus*, like other echinoids, contains very little organic material, the organic matrix comprising < 0.1 weight % of the test (78), and its spectrum (Figure 4a) lacks any absorption features attributable to organics. Although small amounts of organic material remain in coral skeletons after grinding and bleaching (as low as 0.1 % of the skeleton by weight) (68, 71, 72, 79), absorptions due to organics are masked, and all the absorption features in the *Montipora* spectrum (Figure 4b) can be attributed to liquid H_2O and CaCO_3 .

Water in Skeletal Carbonates

Liquid H_2O in Fluid Inclusions. Spectral data show that liquid water in fluid inclusions is nearly ubiquitous in carbonate mineral samples and is particularly abundant in carbonate skeletons (10-13, 18). Electron microscopy studies of a variety of skeletal materials reveal minute inter- and intracrystalline voids, apparently containing water and ranging in size from 0.5 μm to <50 Angstroms in diameter (e.g. 22, 80-82). Total water contents of carbonate skeletons can be as high as 3 weight % (2, 13, 83, 84). Although some non-biogenic carbonate samples, such as the speleothem whose spectrum is shown in Figure 2, contain abundant fluid inclusions, such examples are rare, and in general water contents of skeletal carbonates are an order of magnitude greater than those of non-biogenic carbonate samples (12, 13).

The presence of fluid inclusions in skeletal carbonates is not surprising. Liquid H_2O serves as the medium of transport for Ca^{2+} and CO_3^{2-} to the site of precipitation (17). Rapid growth of crystals in carbonate skeletons results in many twinning and growth dislocations, producing a polycrystalline material containing numerous voids (71, 72, 80, 85).

Bound H_2O and OH^- . Spectral data (2, 11-13, 18, 21) thermodynamic data (e.g. 86, 87), alkalinity determinations (16), DTA (23), NMR (21), and X-ray diffraction data (21, 23) have all indicated the presence of bound H_2O and OH^- in many carbonate skeletons, particularly high Mg calcites. Lowenstam (88) has reported monohydrocalcite and amorphous hydrated CaCO_3 in some mollusk and arthropod samples.

Lippmann (89) notes that Mg has a marked tendency to form hydrous carbonate mineral phases, and attributes this to strong bonds which exist between Mg^{2+} ions and water molecules in aqueous solutions. Rapid precipitation of mineral phases from concentrated

solutions, both in nature and in chemical laboratories, tends to produce metastable, hydrated phases. During formation of biominerals, an amorphous or hydrated phase is often precipitated first and later reverts to a more stable anhydrous phase (25). It may be that some of these unstable, intermediate phases remain in skeletons.

As mentioned above *Lytechinus variegatus* skeletons contain <0.1 weight % organic matter (78), and the broad 1.4- and 1.9- μm bands in its spectrum (Figure 4a) indicate that bound as well as liquid H_2O is present.

The *Halimeda* spectrum also contains absorption features in addition to those due to liquid H_2O and CaCO_3 alone. The spectrum shows a shoulder on the 2.3- μm carbonate band, attributable to $\text{Ca}(\text{OH})_2$. The broadening and shift to longer wavelengths of the 1.4- and 1.9- μm bands can be attributed to the presence of bound H_2O .

Comparison of the *Porolithon* spectrum with the spectra of mineral phases in Figure 2, and the spectra of organic materials in Figure 3 shows that features in this spectrum could be attributed to organic or to inorganic phases. It is known that skeletons of coralline red algae contain OH^- (16, 21, 23). Spectral data (2, 11, 13) suggest that these high Mg calcites contain bound H_2O as well. However, calcification in the coralline red algae results from impregnation of the cell wall with high Mg calcite, a process believed to be controlled by a polysaccharide matrix (90), and the features in these spectra can also be explained as C-H and O-H features caused by polysaccharides. The complexity of this spectrum, and comparison with spectra of other samples of red algae indicate that both organic and hydrated inorganic phases are probably present. However, additional data are needed before all features in the spectrum can be interpreted with confidence.

Grinding and bleaching of samples can aid in distinguishing absorption features due to organics from those due to mineral phases. Absorption features due to liquid water in fluid inclusions and to organics are weakened or removed in spectra of ground and bleached samples, while those due to mineral phases become more prominent. Figure 5 shows spectra of bleached and unbleached samples of one size fraction of a powdered hen's egg. In the spectrum of the bleached sample, bands near 2.17 and 2.05 μm are more prominent than in the spectrum of the unbleached sample, and an additional feature near 2.00 μm is evident. The 2.00- and 2.17- μm features, like the strong 2.3- and 2.5- μm bands are due to calcite. The band near 2.05 μm can be attributed to bound H_2O . Note also that bleaching has removed the absorptions in the 0.5 - 0.6 μm region caused by electronic transitions in molecular orbitals in organic compounds.

Efficacy of Grinding and Bleaching in Removal of Water and Organics

Liquid H_2O and organic compounds remain in carbonate skeletons even after routine grinding and bleaching (Figure 4b). The work of Young et al. (79) is often cited as evidence that organics are disseminated throughout coral skeletons and can only be removed by dissolution of the carbonate. However, samples used in their study were only reduced to coarse sand sizes before the organics were extracted. Better evidence comes from TEM studies which reveal inclusions 1000's to 100's of Angstroms in diameter or less containing water and

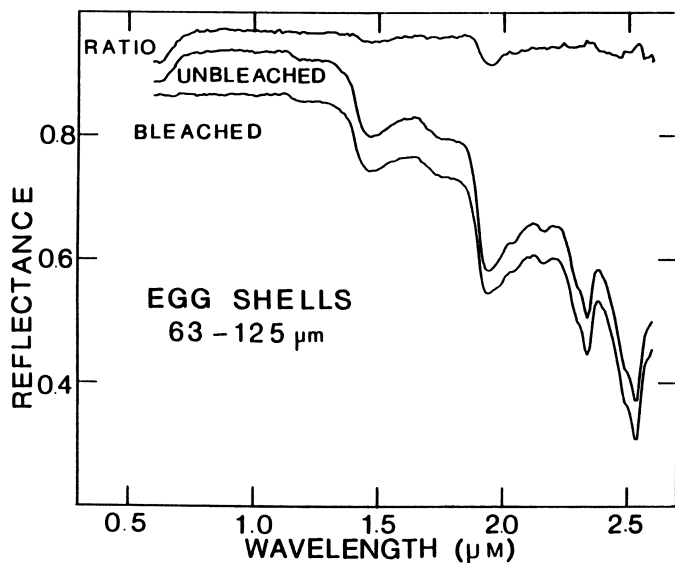


Figure 5. Spectra of bleached and unbleached powdered egg shells, and the ratio of the two spectra showing the differences between them. Removal of organics by bleaching is evidenced primarily as a change in the intensity of the liquid H_2O bands, showing close association of liquid H_2O and organics. Bleached egg spectrum offset vertically by -0.1 .

organics (e.g. [19](#), [22](#), [80](#), [91](#)). The small size of these inclusions makes it impossible to remove all non-carbonate phases by routine sample preparation. Presence of pigments in powdered and bleached samples indicate that some organics remain. Common observations that treated samples heated to high ($>100^\circ C$) temperatures turn brown or gray due to breakdown of organic compounds, and that biogenic aragonites alter to calcite at temperatures much lower than $400^\circ C$, at which this transition is supposed to occur ([92](#)), attest to the presence of water and organics in these samples. DTA-TG analyses of powdered biogenic aragonites yielded up to 3 weight % water due to

release of water and the combustion of organics (84). Fluorescence observed in Raman spectra of some biogenic high Mg calcites is probably due to organics rather than to fluorescing ions, as suggested (93). The short wavelength radiation (488 nm) used in the study causes fluorescence of many organic materials (94). Complete removal of water and organics can only be accomplished by complete dissolution or physical destruction of the skeleton (11-13).

Relationship between water and organics in skeletons.

Organics and liquid H₂O are intimately associated in skeletal carbonates, so much so that often the most obvious effect of bleaching or decay of organics on the spectral properties of biogenic carbonate samples is a decrease in the intensities of the liquid water bands. This is illustrated in ratio spectra in Figures 5 and 6. A ratio of two spectra provides a spectrum of phases present in one sample but absent in the other. As can be seen, all the ratio spectra contain features due to liquid water.

Diagenetic Alteration.

Water and organics in carbonate skeletons both affect and are affected by diagenetic processes in carbonate sediments. Spectral data can also be used to monitor loss of water from carbonate skeletons. Spectra indicate that loss of bound H₂O and OH⁻ take place by incongruent dissolution. Fluid inclusions, on the other hand, are only lost by complete dissolution or physical destruction of the skeleton (11-13). Diagenetic alteration of aragonites and high Mg calcites to low Mg calcites results in an order of magnitude drop in water content (12, 13). However, even after alteration of aragonite to low Mg calcite, fossil skeletons may still be rich in inclusions of water and organics (11-14).

Spectral data can also be used to monitor the loss of organics during diagenesis. Ratio spectra shown in Figure 6 indicate that organic compounds are lost following the death of the organism, even when there is no change in the mineralogy of the skeleton, and that different organic components are lost at different stages of the skeleton's diagenetic history. Spectra were obtained from slices of a number of Pleistocene *Mercenaria* shells with differing states of preservation, as determined by their appearance in the field (i.e. chalky appearance, retention or loss of original coloration, dissolution of growth lines, hinge lines, or outer prismatic layer) (June Mirecki, personal communication, 1987). Although the state of preservation of both shells represented in the first ratio spectrum in Figure 6a was excellent the spectrum indicates a difference in polysaccharide content. The second spectrum in Figure 6a is the ratio between the spectra of two shells, one whose preservation was excellent, the other poor. This spectrum indicates the loss of proteins or amino groups from the poorly preserved shell.

Ratio spectra of corals of differing ages are shown in Figure 6b. The ratio between spectra of living and Pleistocene samples clearly indicates loss of proteins. The ratio of spectra of living

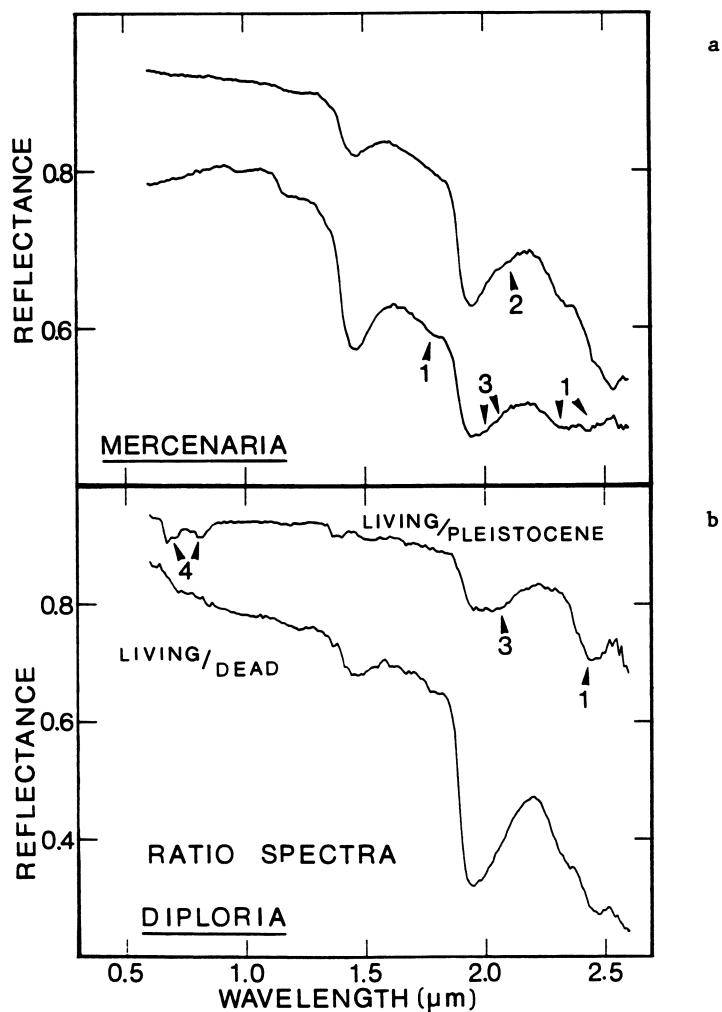


Figure 6. (a) Ratio spectra of slices of Pleistocene *Mercenaria*, and (b) Ratio spectra for three slabbed specimens of the coral *Diploria strigosa*. All three samples are composed of aragonite, variations in organic content being the major compositional difference between them. Numbers indicate absorption features due to C-H (1), O-H (2), N-H (3), and organic pigments (4).

and dead samples documents the rapid loss of organics after death of the coral. As in many ratio spectra of corals, molluscs, and echinoids, although positions of features in this spectrum are similar to those for liquid H₂O, the 1.4- μ m feature is much less intense than the the 1.9- μ m band. While it is not yet clear what organic phase(s) are being lost, preliminary work indicates that relative areas of the 1.4- and 1.9- μ m bands in spectra of skeletal samples may aid in monitoring bulk changes organic content (Zabielski and Gaffey, *Proc. 4th Symp. Geol. Bahamas*, in press).

As long as fluid inclusions and organics remain, they can affect the diagenetic alteration of carbonate skeletons. Stable isotope analyses indicate the C for some carbonate cements is derived from oxidation of CH₄ produced by methanogenic bacteria (95). In sands and muds, breakdown of organics by bacteria can have a profound effect on pore water chemistry and on the stability of carbonate phases (e.g. 7-9). Even in reefs, where large volumes of water are circulated through the framework by waves and tides, decay of organics can create reducing environments throughout the reef framework (96-98).

The presence of organic compounds and water can explain the apparently anomalous observations that dissolution of Pleistocene coral skeletons, and alteration of aragonite to calcite in Triassic corals and calcareous sponges begins from the centers of the radiating bundles of aragonite crystals which make up the skeletons rather than proceeding from the outside as would be expected (72, 80, 81). Breakdown of organic compounds may lower the pH of the water with which they are associated, causing dissolution and/or alteration to take place. High organic content of some shells, such as those of cephalopods, may create reducing microenvironments necessary for replacement with iron sulfides, as has been observed in some ooids (99).

Unanswered Issues.

The complexity and variability in composition of skeletal carbonates and the sensitivity of VNIR reflectance spectroscopy to these variations make it a potentially useful complement to other tools already routinely in use by geologists studying carbonate diagenesis. However, much additional work is needed before this potential can be fully realized. Studies are underway on the effects of grinding, bleaching, and heating on the composition of carbonate samples. The water and organic contents of skeletons are strongly affected by such routine sample preparation, but samples may still contain significant quantities of water and organics even after treatment. Routinely processed samples, while no longer representative of the original materials as they occur in nature, are not pure samples of the aragonite and calcite produced by various organisms. This is true even of fossil specimens from which much organic material is presumably lost.

Because spectral data available in the literature of physics and chemistry are generally inadequate for studies of geologic materials, additional spectra of organic compounds and hydrated mineral species must be obtained. Additional data must also be

acquired employing other analytical techniques (e.g. NMR, ESR, FTIR, coulometry) to completely characterize the water and organic content of skeletons, to provide a quantitative measure of the water and organics in skeletons, and to develop calibration curves allowing abundances of these phases to be determined from reflectance spectra.

Because organic compounds may affect diagenesis of carbonates regardless of their source, all phases present in skeletons must be characterized. Much of the previous work on organics in carbonate skeletons has focused on those compounds believed to make up the organic matrix used by organisms to construct their skeletons, ignoring organics derived from uncalcified tissues or body fluids of plants and animals which build the them, as well as from endoliths which infest skeletons after death.

Conclusions

Unlike non-biogenic carbonates, skeletons produced by carbonate-secreting organisms are intimate mixtures of carbonate minerals, water, and organic compounds. Liquid water and organics are closely associated, and are disseminated throughout skeletons in minute inter- and intracrystalline voids. Some skeletons also contain hydrated mineral phases, and total water contents of skeletal carbonates are generally an order of magnitude greater than those of non-biogenic samples. All of these phases are an intrinsic part of skeletons incorporated during growth. While grinding, bleaching, and heating of skeletal samples removes some of the water and organics, complete removal is only accomplished by dissolution of the skeleton. Samples subjected to routine sample preparation for mineralogical and chemical analyses are no longer representative of naturally occurring materials, nor are they pure samples of carbonate minerals.

Organic compounds and water in its various forms (liquid and bound H_2O and OH^- , both affect, and are affected by, diagenetic processes. VNIR (0.3 - 2.7 μm) reflectance spectroscopy provides a potentially powerful tool for monitoring such diagenetic changes.

Acknowledgments

I would like to thank Don and Kathy Gerace and the staff at the Bahamian Field Station for their logistical support. I thank Carle Pieters at Brown University and Roger Clark at the USGS in Denver for the use of their spectrometers, Steven Pratt at RELAB at Brown University for his assistance in obtaining spectral data and Victor Zabielski for his assistance in the field. Mercenaria shells and data on their source, mineralogy, and state of preservation were provided by June Mirecki. Edward Cloutis, Kenneth Towe, and David Blake provided helpful reviews of the original manuscript. Funding for this work was provided by NSF Grant Number EAR-8721094 and by Gaylord, Leonard and Edna Cobeen and Edith Jenks.

Literature Cited

1. Bathurst, R. G. C. Carbonate Sediments and Their Diagenesis; Elsevier: New York, 1971; p 620.

2. Mackenzie, F. T.; Bischoff, W. D.; Bishop, F. C.; Loijens, M.; Schoonmaker, J.; Wollast, R. In Carbonates: Mineralogy and Chemistry; Reeder, R. J., Ed.; Mineralogical Society of America: Reviews in Mineralogy Vol. 11; Mineralogical Society of America: Washington, DC, 1983; pp 97-144.
3. Morse, J. W. In Carbonates: Mineralogy and Chemistry; Reeder, R. J., Ed.; Reviews in Mineralogy Vol. 11; Mineralogical Society of America: Washington, DC, 1983; pp 227-264.
4. Loreau, J.-P. Sediments Aragonitiques et Leur Genese; Memoires du Museum Nationale d'Histoire Naturelle, Serie C., Geologie, Vol. 47; Museum National d'Histoire Naturelle: Paris, 1982; p 312
5. Mitterer, R. M.; Cunningham, R. In Carbonate Cements; Schneidermann, N.; Harris, P. M., Eds.; SEPM Special Publication 36; Society of Economic Paleontologists and Mineralogists: Tulsa, OK, 1985; pp 17-32.
6. Suess, E. Geochim. Cosmochim. Acta 1973, 37, 2435-2447.
7. Kharaka, Y. K.; LeRoy, M. L.; Carothers, W. W.; Goerlitz, D. F. In Roles of Organic Matter in Sediment Diagenesis; Gautier, D. K., Ed.; SEPM Special Publication 38; Society of Economic Paleontologists and Mineralogists: Tulsa, OK, 1986, pp 111-122.
8. Gautier, D. K. In Relationship of Organic Matter and Mineral Diagenesis; Gautier, D. L.; Kharaka, Y. K.; Surdam, R. C., Eds.; SEPM Short Course Notes No. 17; Society of Economic Paleontologists and Mineralogists: Tulsa, OK, 1985; pp 6-78.
9. Walter, L. M. In Roles of Organic Matter in Sediment Diagenesis; Gautier, D. L., Ed.; SEPM Special Publication 38; Society of Economic Paleontologists and Mineralogists: Tulsa, OK, 1986, pp 1-12.
10. Gaffey, S. J. SEPM Annual Midyear Meeting Abstracts; Society of Economic Paleontologists and Mineralogists: Tulsa, OK, 1984, p 33.
11. Gaffey, S. J. PhD Thesis, University of Hawaii at Manoa, Honolulu, 1984.
12. Gaffey, S. J. Geology 1985, 13, 270-273.
13. Gaffey, S. J. J. Sed. Pet. 1988, 58, 397-414.
14. Sandberg, P. A. Paleontographica Americana 1984, 54, 272-281.
15. Wyckoff, R. W. G. The Biochemistry of Animal Fossils; Sciencetechnica: Bristol, 1972; p 152.
16. Busenberg, E.; Plummer, L. N. Geochim. Cosmochim. Acta 1985, 49, 713-725.
17. Crenshaw, M. A. In Biological Mineralization and Demineralization; Nancollas, G. H., Ed.; Springer-Verlag: New York, 1982, pp 243-258.
18. Gaffey, S. J. Am. Assoc. Petroleum Geologists Bull. 1983, 67, 465.
19. Green, H. W.; Lipps, J. H.; Showers, W. J. Nature 1980, 283, 853-855.
20. Milliman, J. D. Marine Carbonates; Springer-Verlag: New York, 1974; p 375.
21. Schmalz, R. F. Science 1965, 149, 993-996.
22. Towe, K. M.; Thompson, G. R. Calc. Tiss. Res. 1972, 10, 38-48.
23. Weber, J. N.; Kaufman, J. W. Science 1965; 149, 996-997.

24. Weiner, S.; Traub, W.; Lowenstam, H. A. In Biom mineralization and Biological Metal Accumulation; Westbrook, P.; de Jong, E. W, Eds.; D. Reidel: Boston, 1983; pp 205-224.
25. Mann, S. Struct. Bond. 1983, 54, 125-174.
26. Lowenstam, H. A. In Biom mineralization in Lower Plants and Animals; Leadbeater, B. S. C.; Riding, R., Eds.; The Systematics Association Special Volume No. 30; Clarendon: Oxford, 1986; pp 1-17.
27. Pieters, C. M. J. Geophys. Res. 1983, 88, 9534-9544.
28. Estep-Barnes, P. A. In Physical Methods in Determinative Mineralogy, 2nd Ed.; Zussman, J., Ed.; Academic: New York, 1977; pp 529-603.
29. Farmer, V. C.; Russell, J. D. Spectrochim. Acta 1966, 22, 389-398.
30. Russell, J. D. In The Infrared Spectra of Minerals; Farmer, V. C., Ed.; Mineralogical Society Monograph 4; The Mineralogical Society: London, 1974; pp 11-25.
31. Tuddenham, W. M.; Lyon, R. J. P. Analyt. Chem. 1960, 32 1630-1634.
32. Gaffey, S. J. Am. Min. 1986, 71, 151-162.
33. Chapman, D. The Structure of Lipids; Wiley: New York, 1965, p 323.
34. Miller, R. G. J.; Willis, H. A. J. Applied Chem. 1956 6, 385-391.
35. Gaffey, S. J. J. Geophys. Res. 1987, 92, no. B2, 1429-1440.
36. Bayly, J. G.; Kartha, V. B.; Stevens, W. H. Infrared Phys. 1963, 3, 211-223.
37. Falk, M.; Knop, O. In Water, A Comprehensive Treatise; Franks, F., Ed.; Plenum Press: New York, 1973; Vol. 2, pp 55-113.
38. Hamilton, W. C.; Ibers, J. A. Hydrogen Bonding in Solids; W. A. Benjamin: New York, 1968; p 284.
39. Ryskin, Ya. I. In The Infrared Spectra of Minerals; Farmer, V. C., Ed.; Mineralogical Society Monograph 4; The Mineralogical Society: London, 1974; pp 137-182.
40. Mara, R. T.; Sutherland, G. B. B. M. J. Optical Soc. Am. 1953, 43, 1100-1102.
41. Aines, R. D.; Rossman, G. R. J. Geophys. Res. 1984, 89, #B6, 4055-4071.
42. Colthup, N. B.; Daly, L. H.; Wiberly, S. E. Introduction to Infrared and Raman Spectroscopy; Academic: New York, 1964; p 511.
43. Hunt, G. R.; Ashley, R. P. Econ. Geol. 1979, 74, 1613-1629.
44. Whetsel, K. Applied Spec. Rev. 1968, 2, 1-67.
45. Fleischer, M. Glossary of Mineral Species; Mineralogical Record: Tucson, Arizona, 1980; p 192.
46. Pobeguïn, T. C. r. hebd. Seanc. Acad. Sci. Paris 1959, 248, 3585-3587.
47. White, W. B. Am. Min. 1971, 56, 46-53.
48. Kaye, W. Spectrochim. Acta 1954, 6, 257-287.
49. Weber, G.; Teale, F. W. J. In The Proteins, 2nd Ed.; Neurath, H., Ed.; Academic: New York, 1965; Vol. 3, pp 445-516.
50. Wheatley, P. J. The Determination of Molecular Structure; Dover: New York, 1968; p 264.
51. Herzberg, G. Molecular Spectra and Molecular Structure; Van Nostrand Reinhold: New York, 1945; Vol. II, p 632.

52. Cantor, C. R.; Timasheff, S. N. In The Proteins, 3rd Ed., Neurath, H.; Hill, R. L., Eds.; Academic: New York, 1982; Vol. V, pp 145-306.
53. Davenport, J. B. In Biochemistry and Methodology of Lipids; Johnson, A. R.; Davenport, J. B., Eds.; Wiley: New York, 1971; pp 231-242.
54. Perlin, A. S.; Casu, B. In The Polysaccharides; Aspinall, G. O., Ed.; Academic: New York, 1982, pp 133-193.
55. Pearson, J. F.; Slifkin, M. A. Spectrochim. Acta 1972, **28A**, 2403-2417.
56. Zhbankov, R. G. Infrared Spectra of Cellulose and its Derivatives; Consultants Bureau: New York, 1966; p 333.
57. Russell, R. A.; Thompson, H. W. J. Chem. Soc. 1955, 479-482.
58. Russell, R. A.; Thompson, H. W. J. Chem. Soc. 1955, 483-486.
59. Whetsel, K. B.; Robertson, W. E.; Krell, M. W. Analyt. Chem. 1958, **30**, 1598-1604.
60. Wade, L. G., Jr. Organic Chemistry; Prentice-Hall: Englewood Cliffs, NJ, 1987; p 1377.
61. Davies, J.; Littlewood, B. S. Elementary Biochemistry; Prentice-Hall: Englewood Cliffs, New Jersey, 1979; p 346.
62. Basch, A.; Wasserman, T.; Lewin, M. J. Polymer Sci. 1974, **12**, 1143-1150.
63. Clayton, R. K. Photosynthesis; Cambridge University Press: Cambridge, 1980 p 281.
64. Baker, E. W.; Louda, J. W. In Biological Markers in the Sedimentary Record; Johns, R. B., Ed.; Elsevier: New York, 1986; pp 125-225.
65. Holden, P. N. MA Thesis, Rensselaer Polytechnic Institute, Troy, New York, 1988.
66. Adams, J. B. In Infrared and Raman Spectroscopy of Lunar and Terrestrial Minerals; Karr, C., Jr., Ed.; Academic: New York, 1975; pp 91-116.
67. Huguenin, R. L. Icarus 1987, **70**, 162-188.
68. Johnston, I. S. Internat. Rev. Cytology 1980, **67**, 171-214.
69. Pearse, V.; Pearse, J.; Buchsbaum, M.; Buchsbaum, R. Living Invertebrates; Blackwell Scientific: Palo Alto, CA, 1987; p 848.
70. Wilbur, K. M.; Simkiss, K. In Biogeochemical Cycling of Mineral-Forming Elements; Trudinger, P. A.; Swaine, D. J., Eds.; Elsevier: New York, 1979; pp 69-106.
71. Constantz, B. R. Palaios 1986a, **1**, 152-157.
72. Constantz, B. R. In Reef Diagenesis; Schroeder, J. H.; Purser, B. H., Eds.; Springer-Verlag: New York, 1986b; pp 53-76.
73. Johnston, I. S. Scanning Electron Microscopy 1979, **2**, 421-431.
74. Louda, J. W.; Baker, E. W. Organic Marine Geochemistry; Sohn, M. L., Ed.; ACS Symposium Series No. 305; American Chemical Society: Washington, DC, 1986; pp 107-126.
75. Lukas, K. J. J. Phycology 1974, **10**, 331-335.
76. Berner, R. A. Early Diagenesis; Princeton University Press: Princeton, NJ, 1980; p 241.
77. Worms, D.; Weiner, S. J. Experimental Zoology 1986, **237**, 11-20.
78. Swift, D. M.; Sikes, C. S.; Wheeler, A. P. J. Experimental Zool. 1986, **240**, 65-73.
79. Young, S. D.; O'Connor, J. D.; Muscatine, L. Comp. Biochem. Physiol. 1971, **40B**, 945-958.
80. Bruni, S. F.; Wenk, H.-R. J. Sed. Pet. 1985, **55**, 159-170.

81. Gvirtzman, G.; Friedman, G. M. In Reefs and Related Carbonates - Ecology and Sedimentology; Frost, S. H.; Weiss, M. P.; Saunders, J. B., Eds.; AAPG Studies in Geology No. 4; American Association of Petroleum Geologists: Tulsa, OK, 1977; 357-380.
82. James, N. P. J. Paleontology 1974, 48, 785-799.
83. Hudson, J. D. Geochim. Cosmochim. Acta 1967, 31, 2361-2378.
84. Yoshioka, S.; Kitano, Y. Geochemical J. 1985, 19, 245-249.
85. Towe, K. M. Biomineralization Res. Rpts 1972, 4, 1-14.
86. Mucci, A.; Morse, J. W. Geochim. Cosmochim. Acta 1984, 48, 815-822.
87. Turner, J. V.; Anderson, T. F.; Sandberg, P. A.; Goldstein, S. J. Geochim. Cosmochim. Acta 1986, 50, 495-506.
88. Lowenstam, H. A. Science 1981, 211, 1126-1131.
89. Lippmann, F. Sedimentary Carbonate Minerals; Springer-Verlag: New York, 1973, p 228.
90. Cabioch, J.; Giraud, G. In Biomineralization in Lower Plants and Animals; Leadbeater, B. S. C.; Riding, R., Eds; The Systematics Association Special Volume No. 30; Clarendon Press: Oxford, 1986; pp 141-156
91. Conger, S. D.; Green, H. W.; Lipps, J. H. J. Foram. Res. 1977, 7, 278-296.
92. Deer, W. A.; Howie, R. A.; Zussman, J. Rock-Forming Minerals: Vol. 5, Non-Silicates; Longman: London, 1962, p 371.
93. Bischoff, W. D.; Sharma, S. K.; Mackenzie, F. T. Am. Min. 1985, 70, 581-589.
94. Willard, H.; Merritt, L. L.; Dean, J. A.; Settle, F. A. Instrumental Methods of Analysis; D. Van Nostrand Co.: New York, 1981; p 1030.
95. Hudson, J. D. Geol. Soc. London Jour. 1977, 133, 637-660.
96. Sansone, F. J. Proc. 5th Int. Coral Reef Cong., 1985, Vol. 3, pp 415-419.
97. Sansone, F. J.; Tribble, G. W.; Andrews, C. C.; Buddemeier, R. W. In Abstracts 6th Int. Coral Reef Cong.; Choat, J. H., and Bellwood, O., Eds.: 1988, p 90.
98. Trichet, J.; Chambers, L. A.; Wilkinson, C. R. Proc. 5th Int. Coral Reef Congress: 1985, Vol. 3, pp 471-475.
99. Gaffey, S. J. Geol. Soc. Am. Annual Meeting Abstracts with Programs 1982, 10, #7, 493.

RECEIVED July 13, 1989

Chapter 6

Photoluminescence, Candoluminescence, and Radical Recombination Luminescence of Minerals

William B. White

Materials Research Laboratory and Department of Geosciences,
Pennsylvania State University, University Park, PA 16802

The UV and electron beam excited luminescence of many insulator minerals can be ascribed to transition metal and lone-pair-electron ions. Emission and excitation spectra can be related to mineral crystal structure by relatively simple crystal field models. Luminescence due to molecular species such as the uranyl ion, the disulfide ion, and organic molecules occurs occasionally. Some of these centers can be excited by recombination of high energy species in flames (candoluminescence), ion beams, and plasmas. These spectra are similar to, but not identical with, photoemission spectra. Candoluminescent and radical recombination luminescence spectra are strongly temperature dependent with the greatest efficiency often being obtained well above room temperature. Energetic species in the solar wind could excite mineral grains on planetary surfaces.

Many minerals can be made to luminesce under various excitation sources, usually UV light, but in relatively few cases is the mechanism understood in detail. Best understood is luminescence due to transitions between localized states in the unfilled d-orbitals of transition metal ions and localized states in the unfilled f-orbitals of rare earth ions. Rare earth ions, important in the development of synthetic phosphor and laser materials, are uncommon among naturally occurring minerals.

This paper reviews briefly the mechanisms responsible for mineral luminescence, then turns to less common modes of excitation, particularly ion and radical recombination luminescence, and finally discusses luminescence on the scale of remote sensing of planetary surfaces.

The literature on mineral luminescence is somewhat bimodal in character. On one hand those mineral structures that have proved useful as phosphors or as crystal lasers have been studied in great detail and the physics of the energy transfer processes are often well known. The luminescence characteristics of many other minerals

0097-6156/90/0415-0118\$06.00/0
© 1990 American Chemical Society

remain at the level of qualitative descriptions compiled by mineral collectors (e.g. 1). A special case is thermoluminescence which has been investigated in considerable detail (2). The invention of a cathodoluminescence attachment for the polarized light microscope (3) allowed wide use of cathodoluminescence for the examination of growth features in minerals (4). Marshall (5) has recently compiled the literature on cathodoluminescence and its application to petrology and the reader is also referred to the articles by Sears and Steele in this publication.

Background

Molecular, Insulator, and Semiconductor Phosphors. Luminescent materials can be divided into three broad categories: molecular phosphors, insulator phosphors, and semiconductor phosphors (6).

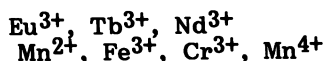
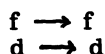
The absorption of energy, its internal redistribution, and emission as luminescent radiation all take place within a single molecule in molecular phosphors. Mostly these are organic compounds which are of relatively little importance in mineral luminescence. Exceptions are the fulvic and humic acids which are carried into sedimentary rocks by circulating groundwater and which give a characteristic phosphorescence to certain freshwater calcite deposits (Brennan and White, unpublished data). Important inorganic molecular activators include the uranyl ion which imparts the well-known green luminescence to many uranium minerals and the disulfide ion which is responsible for a yellow luminescence in scapolite and some other minerals (7).

Most minerals fall into the class of insulator phosphors. The characteristics of the luminescence are usually defined by the electronic structure of an activator ion as modified by the crystal field of the host crystal structure. Although some energy transfer takes place between nearby ions, appearing as the phenomena of co-activation, luminescence poisons, and activator pair interactions, the overall luminescence process is localized in a "luminescent center" which is typically 2 to 3 nm in radius. From a perspective of band theory, luminescent centers behave as localized states within the forbidden energy gap.

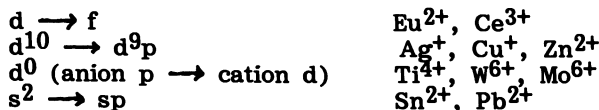
In semiconductor phosphors the energy band structure of the host crystal plays a central role. Some semiconductor luminescence arises from decay of exciton states, other emission arises from decay of donor states generated by impurity or defect centers. It is not the magnitude of the band gap itself that separates insulator from semiconductor phosphors; it is a question of whether the spectrum is characteristic of impurity energy levels as perturbed by the local crystal structure or whether the spectrum is characteristic of the band structure as modified by impurities. Thus the fluorescent nitrogen-doped diamond, with a 5.5 eV band gap, would be considered a semiconductor phosphor.

Activators. It is convenient to classify activator ions for insulator phosphors in terms of their electronic configuration.

Intra-Configurational Transitions



Inter-Configurational Transitions



By far the most important activators in mineral luminescence are the iron group ions which exhibit transitions between partly filled d-orbitals. These will dominate the discussion that follows. Luminescence arising from the trivalent rare earth ions occurs in some phosphate minerals but is dealt with elsewhere in this volume (Wright). The filled d-shell ions are activators for cathodoluminescence phosphors such as ZnS, however, most sulfide mineral phases contain too many luminescence poisons for the transitions from these ions to be observed.

The empty d-shell ions are unusual in that they act as emitting centers even when present in high concentrations. This is in contrast with the transition metal ions which usually concentration-quench in the range of 1 - 5 mole percent of the activator. Minerals containing d^0 ions such as benitoite, fresnoite, scheelite, and powellite are often fluorescent (Figure 1). These ions likewise do not fit neatly into the insulator category. Although the Ti^{4+} ion behaves as an isolated center, a molecular orbital or band model is needed to account for the energy transfer. Likewise the WO_4 and MoO_4 tetrahedra can be treated as molecules but further considerations of the crystal structure are needed to describe the energy transfer (8).

The non-bonding lone pair s-electrons of such ions as divalent lead and divalent tin generate a series of strongly localized states which can be pumped and which emit a broad band luminescence typically in the range of 360 to 500 nm.

Energy Transfer Processes. Luminescence is a complex sequence of energy transfer processes. Figure 2 is a schematic of the most important of these for photoluminescence, cathodoluminescence, and candoluminescence. The ultimate source of energy is the excitation: UV light, electron beam, ion beam, or radical recombination excitation. We are not concerned here about the triggered release of previously trapped energy such as occurs in thermoluminescence and triboluminescence.

The schematic phosphor grain for photoluminescence and cathodoluminescence is shown containing three kinds of centers: activators (A), sensitizers or co-activators (S), and poisons (P). The UV photon may be assumed to have an energy less than the band gap of the phosphor host so the absorption by A, S, and P takes place at the centers. Many activators, particularly Mn^{2+} , have a low absorption cross-section so that direct pumping of the activator is inefficient. Sensitizers, such as Pb^{2+} , are selected to have large absorption cross-sections at UV wavelengths. They then transfer the excitation to the activator which re-emits it as luminescent radiation. Most co-activators have a luminescent emission of their own so that the efficiency of the system depends on the kinetics of energy transfer compared with direct emission of the co-activator. In many mineral systems, one observes both and thus the activator radiation R_A and the sensitizer radiation R_S are

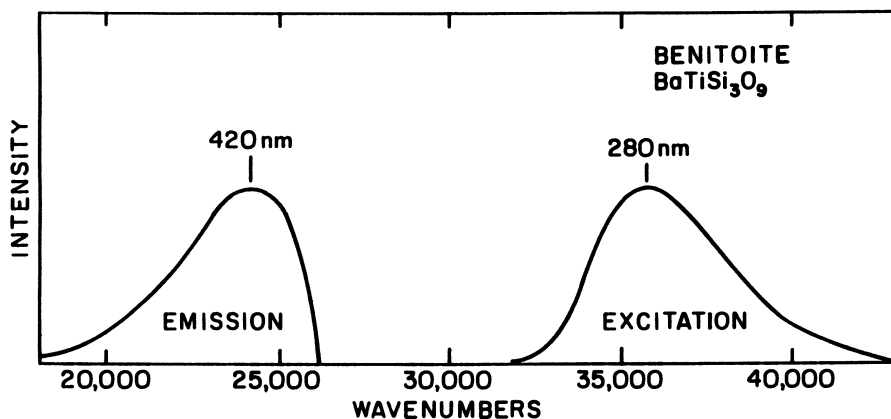


Figure 1. Photoluminescence emission and excitation spectrum for benitoite showing Ti^{4+} luminescence.

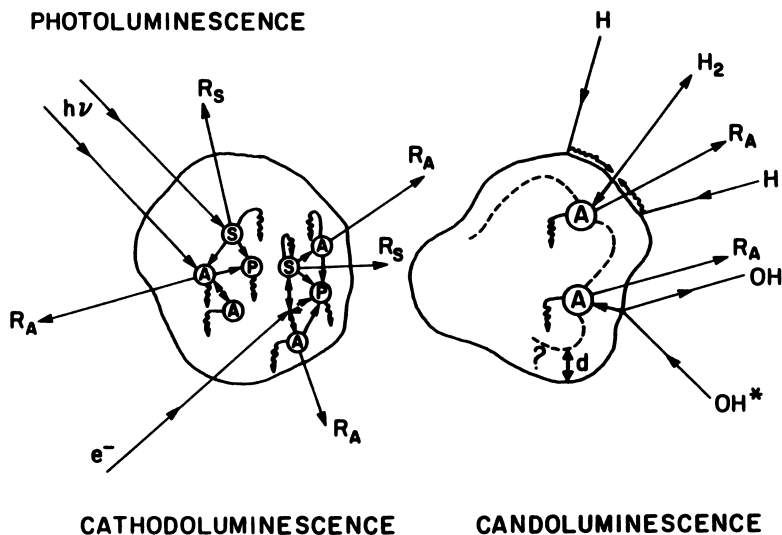


Figure 2. Drawing illustrating energy transfer processes within a phosphor grain. S = co-activator or sensitizer; A = activator; P = poison center. Short wiggly arrows represent non-radiative transitions. Dashed line outlines the unknown depth to which energy from radical recombination excitation can be transferred.

shown in Figure 2. Luminescence poisons are defects and impurities which promote the non-radiative decay of the excitation. In mineral systems, ferrous iron is the most important luminescence poison.

Excitation by impinging electrons (or ions) takes place by a somewhat different mechanism. Energetic electrons penetrate the phosphor grains and lose energy by multiple collision processes. The energy is sufficient to pump the conduction band of the phosphor host and the excitation can move anywhere in the crystal to pump the localized luminescence centers. Cathodoluminescence thus appears at lower concentration thresholds than photoluminescence but is more susceptible to the influence of defects and other luminescence poisons.

Direct pumping of poison centers as well as energy transfer from co-activators, and energy transfer from activators all represent an energy loss in the system. In addition, activators and co-activators also have non-radiative decay routes. Because non-radiative decay is usually phonon-assisted, non-radiative decay is exacerbated by increasing temperature and manifests itself by a characteristic temperature at which luminescence is quenched. The crystallographic relations that provide optimum sensitizer - activator energy transfer are outlined by Blasse (9)

Crystal Structure and Luminescence of Insulator Mineral Phosphors

The energy level structure of partly filled d-orbitals can best be described by crystal field theory as expressed in Tanabe-Sugano diagrams. These account for absorption and luminescence spectra and allow the spectra to be correlated with crystal structure.

Transition metal ion activators that emit in the visible region of the spectrum belong mainly to the d-3 and d-5 electron configurations. d^3 ions have a characteristic narrow band emission that is largely independent of the crystalline host. d^5 ions are broad band emitters with emission wavelengths that are very sensitive to details of the crystal structure.

Narrow Band Emitters. The Tanabe-Sugano diagram for the d^3 configuration is shown in Figure 3 for the specific case of the Cr^{3+} ion. The emitting level is the doublet state that is nearly independent of the crystal field parameter, Dq . If the crystal field is sufficiently strong to make the doublet state the lowest energy excited state, there will be a red luminescence that will not vary much between different crystal hosts. Because the doublet state belongs to the same orbital configuration as the ground state, the Stokes shift and Condon offset will be small. As a result, the line width of the emission is narrow and a considerable amount of phonon fine structure is observed even at room temperature (Figure 4). A similar red luminescence is observed in other minerals activated by chromium such as ruby, emerald, and alexandrite.

Mostly Cr^{3+} appears in minerals as a trace constituent substituting for Al^{3+} in six-fold coordination. As such, the larger Cr^{3+} ion is placed in a site with small metal-ligand distances, the crystal field is large - typically 1650 - 1750 wavenumbers, and only the doublet to quartet transition is seen. At weaker crystal fields, less than 1500 wavenumbers in the diagram in Figure 3, a short lifetime, broad band quartet-quartet transition appears (10).

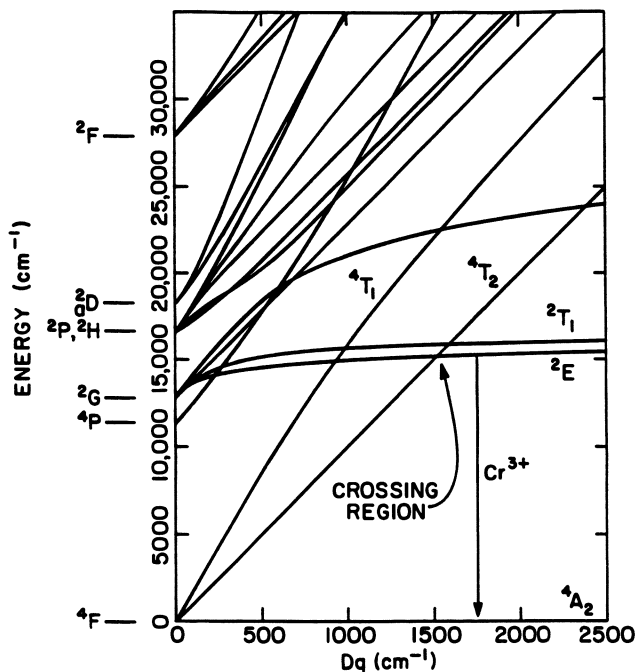


Figure 3. Tanabe-Sugano diagram for d^3 configuration calculated for $B = 755$ and $C = 3257$ wavenumbers.

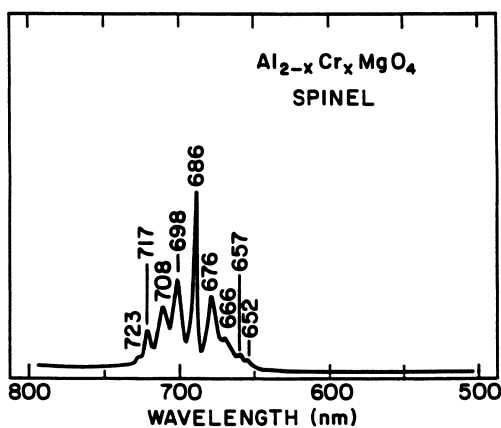


Figure 4. Photoluminescence emission spectrum for natural spinel activated by Cr^{3+} . Mohler and White, unpublished data.

Within the cross-over region there is more complicated mixing between doublet and quartet states and the luminescence band is broad with additional sub-bands (11). Because of the importance of ruby lasers and related Cr^{3+} activated systems, the physics of the doublet-quartet transition has been worked out in considerable detail as has the mechanism of non-radiative transfer and the temperature dependence of the luminescence(12). Although the Cr^{3+} narrow band emission is essentially independent of crystal field and thus of site size and symmetry, the energy of the doublet levels does depend on Racah parameters B and C. The B and C parameters are dependent on the covalency of the metal-ligand bond and thus there is some variability in the Cr^{3+} emission from host to host.

The other common ion with the d^3 configuration is Mn^{4+} which is important as an activator in some phosphors but it does not commonly occur in fluorescent minerals.

Broad Band Emitters. Mn^{2+} and Fe^{3+} are the two most widely occurring activators in fluorescent minerals. Figure 5 shows the Tanabe-Sugano diagram for the d^5 configuration with a typical choice of the Racah parameters B and C. Luminescent emission takes place from the quartet T_1 level to the sextet A_1 ground state. Because these two levels belong to different strong field configurations there is a large Condon offset and a correspondingly large Stokes shift. Typical values for the Stokes shift of Mn^{2+} and Fe^{3+} are sketched in Figure 5 by off-setting the emission levels. Because of the steep slope of the quartet T_1 level, the emission band is highly sensitive to interatomic distances and to distortions in the activator site symmetry. To a first approximation, the emission wavenumber decreases linearly with Dq over the range of observed luminescence bands.

Figure 6 shows a composite spectrum for Mn^{2+} emission from spinel, willemite, olivine (13) and a CaO-SrO solid solution. The red to green color change when Mn^{2+} is moved from six to four-fold coordination is a classic phenomenon and has been known at least since 1942. It is seen in Figure 6 as the comparison between the willemite spectrum and the other spectra. Less well recognized are the variations in emission band with crystal field strength as reflected in bond lengths. This small selection of minerals exhibits a range of 6-coordinated Mn^{2+} emission from yellow to deep red depending on interatomic distance. Figure 7 shows more detail by comparing the emission bands of two solid solution series. The CaO-SrO solid solution data are instructive since the site is strictly cubic and the interatomic distance varies linearly with composition. The absorption spectrum was measured by diffuse reflectance to provide the wavenumber of the T_1 level. The Stokes shift was found to be about 1000 wavenumbers as sketched on Figure 5. Corresponding data for the calcite - magnesite solid solution series (14) show a similar linear trend.

Interpretation of Mn^{2+} emission on the basis of a Tanabe-Sugano diagram has led to some confusion. If the site is non-cubic the triply degenerate T_1 level will split into two or three components and only the lowest energy component will be an emitting state. The emission, however, will appear at lower wavenumbers than predicted by the average interatomic distance and coordination number. Likewise, the Racah parameters depend on the metal-ligand bonding and scale the entire diagram including the emitting level.

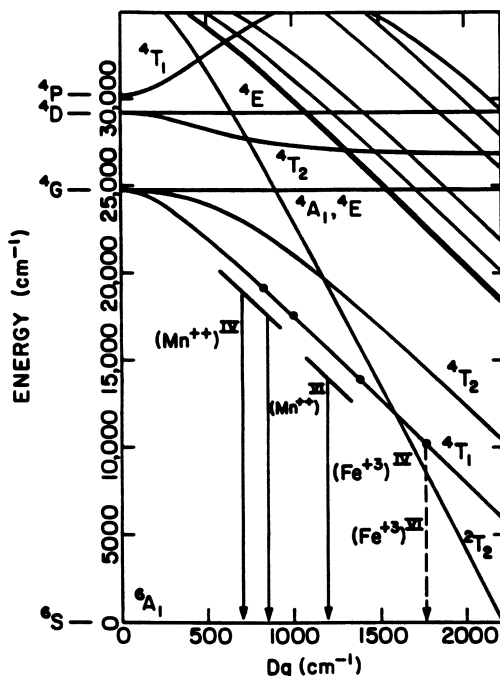


Figure 5. Tanabe-Sugano diagram of d^5 configuration calculated for $B = 636$ and $C = 3678$ wavenumbers. Typical emission levels for four and six coordinated Mn^{2+} and Fe^{3+} are sketched on the diagram.

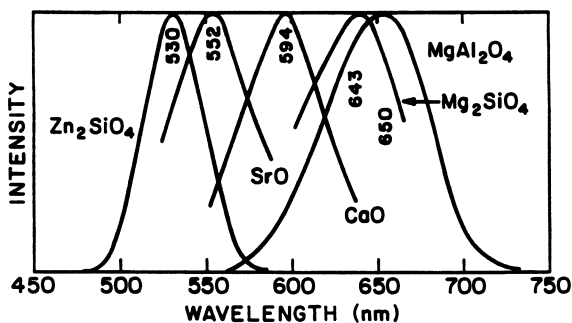


Figure 6. Emission spectra for Mn^{2+} in various hosts. Data for olivine were extracted from (13).

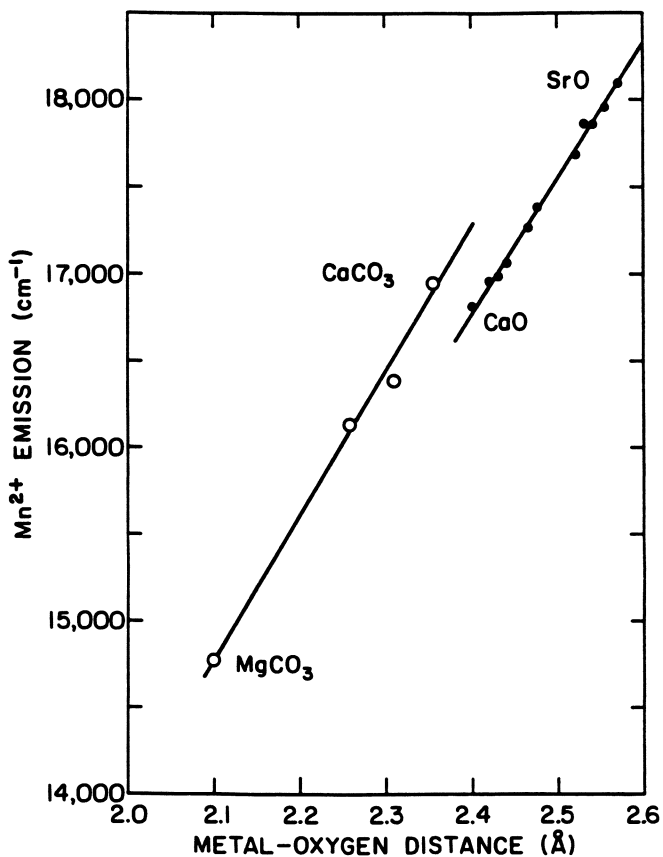


Figure 7. Variation of Mn^{2+} emission wavenumber with interatomic distance for the CaO - SrO solid solution and for the calcite - magnesite solid solution. Data for the latter plot were extracted from (14).

Trivalent iron is an effective activator when it is free of the effects of ferrous iron. Because of the larger value of Dq , the emission is shifted to 700 - 750 nm in the deep red when Fe^{3+} is present on tetrahedral sites. Fe^{3+} in octahedral coordination is predicted to emit in the near infrared at about 900 to 1000 nm but is rarely observed and is thus indicated by a dashed line in Figure 5. Fe^{3+} luminescence in minerals is mainly observed when Fe^{3+} substitutes for Al^{3+} in tetrahedral sites in aluminosilicates. Observations on feldspars (15) provide the transition sketched on Figure 5. In the orthoclase structure the Stokes shift is 1500 wavenumbers. Trivalent iron is the most likely activator for luminescence seen in many terrestrial feldspars and feldspar-containing rocks. The characteristic 700-750 nm band is weak or absent in lunar feldspars (16,17).

Candoluminescence and Radical Recombination Luminescence

Qualitative Observations. Candoluminescence is excited by flames. The emission spectra are similar but often not identical to those excited by UV (18). The energy source is the recombination of free radicals that occurs in the flame and thus flame-excited luminescence is the same as the radical recombination luminescence observed when free neutral radicals from plasmas are used as an excitation source. A simple hydrogen diffusion flame is the simplest source for demonstrating the phenomenon.

Figure 8 shows the recombination energy of various neutral species that can be extracted from nitrogen, hydrogen, and water vapor plasmas and the hydrogen flame. These energies are substantial and are comparable to the pumping energy available from the 365 and 253.7 nm lines of Hg-vapor lamps commonly used as UV excitation sources. Note that some of the interactions, notably OH^* , require only that the excited species collide with the phosphor surface while others require two-body collisions (see sketch in Figure 2). An important question concerning neutral radical excited luminescence is the energy transfer mechanism. As sketched in Figure 2, the extraction of energy from the radicals takes place only on the surface. There must be some mechanism to transfer this energy to the A and S centers in the bulk. It has been argued (19) that OH^* is the most important excitation source in the hydrogen flame.

The most remarkable characteristic of candoluminescence is its temperature dependence. When a hydrogen flame is brushed over the phosphor surface, some time is required to warm up the surface before the luminescence appears. Each phosphor has a characteristic maximum in the temperature-intensity curve and at higher temperatures the intensity falls off again. Maxima for most transition metal ion- and rare earth ion-activated systems are in the range of 100 to 300 C. Candoluminescence thus occurs at much lower temperatures than the onset of purely thermal emission.

Candoluminescence of Minerals. Figure 9 shows a simple experimental set-up for the measurement of candoluminescent spectra. The mineral sample is ground to a fine powder, slurried with water or organic solvent and painted over the surface of a Kanthal metal heating rod. The heating rod with an attached thermocouple allows the phosphor temperature to be controlled independently of the flame. The surface

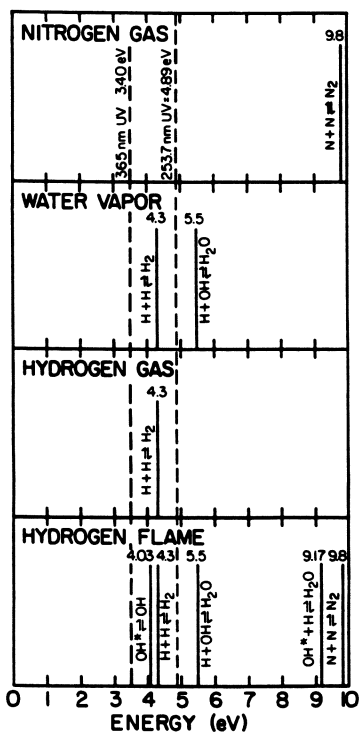


Figure 8. Recombination energies for various active species formed in flames and in microwave discharge induced plasmas. Data taken from Corredor (22).

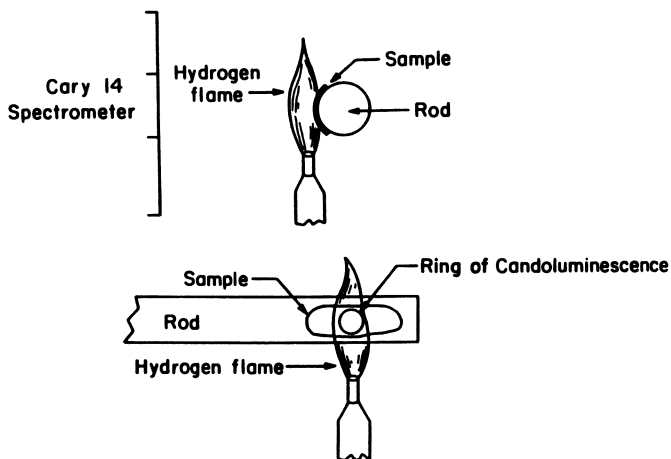


Figure 9. Sketch showing experimental set-up for observation and measurement of candoluminescence and candoluminescence spectra.

of the phosphor patch is brushed with a hydrogen flame and the luminescence spectrum observed by the spectrophotometer through the flame. Flame lines are superimposed on the luminescence spectrum but the narrow flame lines are easy to recognize against the broad band phosphor emission. Some effort must be taken to avoid flame flicker and indeed much of our early work used a spectrograph with photographic plates to avoid the flicker problem. With care, flicker noise can be reduced and useful spectra can be taken with a conventional spectrophotometer.

The candoluminescent and radical recombination spectra of willemite are shown in comparison with the UV-excited spectrum in Figure 10. The envelope of the main emission band at 530 nm is the same in all spectra but the radical recombination excitation brings out another feature at 613 to 642 nm not seen in the photoluminescence spectrum. Similar behavior is seen in other Mn^{2+} activated candoluminescent spectra (20)

The temperature dependence of the 530 nm band is strikingly different for the different sources of excitation. (Figure 11). The intensity of the UV-excited band simply falls off with increasing temperature. The hydrogen radical recombination luminescence spectrum peaks at 40 C and then falls off rapidly. Nitrogen and water vapor radical recombination luminescence peaks near 320 C while the candoluminescent spectrum peaks at 178 C. The temperature response curves are the combined results of adsorption-desorption of the active radical on the phosphor grain, the de-excitation of the active radical, and the transfer of the energy of de-excitation to the activator centers within the grain.

Candoluminescence appears bright when observed in the laboratory. However, efforts to estimate the quantum efficiency of willemite using hydrogen ion bombardment (21) gave 4×10^{-6} photons per incident hydrogen ion when extrapolated to zero accelerating voltage. This number was obtained at room temperature and not at the temperature of maximum candoluminescence. Judging by the dependence of luminescence intensity on temperature shown in Figure 11, the quantum efficiency could be 100 times higher at the temperature of peak brightness. This low quantum efficiency is not consistent with visual observations in flames although it is difficult to know the number of impinging active species in flame excitation.

Planetary Surfaces

Many luminescent features are known in the natural environment on the earth's surface. Many are of biological origin, ranging from fireflies to the phosphorescent sea, and most of these have been known since ancient times (23). Luminescence from inorganic sources is much more limited due to lack of an effective excitation mechanism beneath the earth's atmosphere. Mineral collectors use portable ultraviolet lights to prospect quarries and tailing piles in the dark of night but the natural background of UV is too weak and of too low energy to effectively excite luminescence. Luminescence, however, may be observed on the surfaces of airless bodies such as

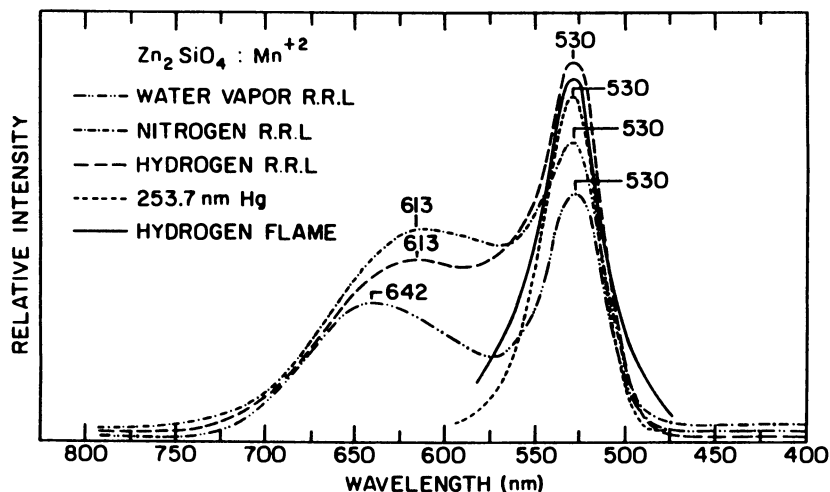


Figure 10. Flame-excited and radical recombination excited emission spectra of willemite. Corredor and White, unpublished data.

mercury, the moon, the asteroids, and possibly the rocky satellites of the outer planets. The band of interplanetary dust responsible for the zodiacal light seems to brighten during magnetic storms possibly due to luminescence (24). Most of the observations concern lunar luminescence (25).

Lunar luminescent phenomena are a fascinating contradiction. On one hand, there is some evidence for a general brightening of the lunar surface both under sunlight and during lunar eclipses as well as substantial observational evidence for transient and localized

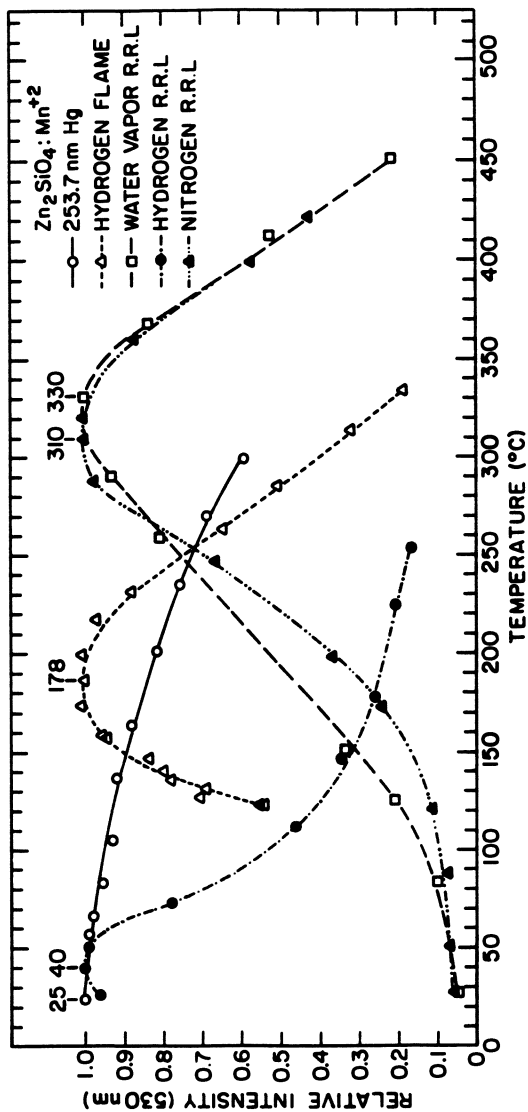


Figure 11. Temperature dependence of the intensity of the 530 nm band of willemite. Corredor and White, unpublished data.

patches of brightening, usually in the red region of the spectrum. On the other hand experimental work shows that the more obvious mechanisms are insufficient by some orders of magnitude to account for the observations.

The general brightening of the lunar disc at times of total eclipse and excess brightness under sunlight has taxed experimental measurements. McCord (26) concluded that large portions of the lunar surface may continuously emit radiation at the level of 0.5 to 1 percent of the solar continuum. Solid state luminescence is one possible explanation. The general brightening of the lunar disc was once thought to be due to thermoluminescence. Trap centers were charged by solar radiation during the lunar day and the energy released by slow decay during eclipses or by heating at the lunar dawn. Analysis of the thermoluminescence explanation (27) shows it to be marginal.

The other and much better established phenomena are transient events seen in specific limited areas of the moon and usually lasting for times on the order of hours or days. Any activity on the supposed "dead" surface of the moon is of interest and catalogs have been made which, as of 1978, had logged 1468 observations (28-30). Many of the lunar transient phenomena take the form of patches of red luminescence, some blue luminescence, and various flashes and related features. A substantial percentage of the events are related to the crater Aristarchus.

The red patches of luminescence have been associated with the arrival of energetic particles emitted during solar flares (31, 32). The lunar transient events could be excited by protons in the solar wind but experiments with silicate minerals in proton beams show that the process is inefficient, quantum efficiencies from 1×10^{-4} to 1×10^{-6} , and given the concentration of protons in the solar wind the mechanism cannot account for the intensity of the observed luminescence (33). Another possibility is that neutral particles in the background solar wind or associated with disturbances on the sun's surface provide the excitation source (34). This would be a process very similar if not identical to the cathodoluminescence and radical recombination luminescence observed in the laboratory.

If the red emission events of the lunar transient phenomena are really due to luminescence, the activator and host must be identified. Ferric iron in feldspars is the dominant red emitter in terrestrial igneous rocks. However, there is little if any ferric iron in the highly reducing environment of the lunar rocks. The samples returned by the Apollo missions were eagerly examined for luminescence (35-40) The results from all of the Apollo landing sites were much the same. The main luminescent phase was plagioclase which often exhibited three emission bands: a blue band at 450 nm thought to be due to defects in the silicate structure, a green band at 560 nm assigned to Mn^{2+} substituting for Ca^{2+} in the plagioclase structure, and a weak deep red band at 780 nm which might be due to ferric iron. The Fe^{3+} luminescence from the lunar plagioclases was much weaker than from terrestrial feldspars as expected both from the lower Fe^{3+} concentration and also the quenching effect of the dominant Fe^{2+} . Experiments by several teams

of investigators included excitation by electron and proton bombardment over a range of energies. It was concluded that the efficiencies of any of these processes was too low to account for the astronomical observations.

This review ends with a question mark. In spite of the intense research activity before and during the Apollo lunar missions, the origin of the supposed luminescence lunar transient phenomena remains in doubt. It is suggested that the recombination of neutral radicals, as a process for the excitation of luminescence, may play a more important role than has previously been ascribed to it.

Acknowledgments

This review draws on the work of former graduate students Rick L. Mohler and Andres Corredor and on the work of the late Arnost Bergstein who was at the time a visiting scientist from Czechoslovakia. The luminescence program was supported by the National Science Foundation.

Literature Cited

1. Gleason, S. Ultraviolet Guide to Minerals; Van Nostrand: New York, 1960; p 244.
2. McKeever, S.W.S. Thermoluminescence of Solids; Cambridge University Press: Cambridge, 1985; p 376.
3. Sippel, R.F.; Glover, E.D. Science 1965, **150**, 1283-87.
4. Remond, G. J. Luminescence 1977, **15**, 121-55.
5. Marshall, D.J. Cathodoluminescence of Geological Materials; Unwin Hyman: Winchester, MA 1988; p 172.
6. White, W.B. Trans. Amer. Cryst. Assoc. 1975, **18**, 31-49.
7. Burgner, R.P.; Scheetz, B.E.; White, W.B. Phys. Chem. Minerals 1978, **2**, 317-24.
8. Treadway, M.J.; Powell, R.C. J. Chem. Phys. 1974, **61**, 4003-11.
9. Blasse, G. Philips Tech. Rev. 1970, **31**, 304-32.
10. Schlafer, H.L.; Gausmann, H.; Witzke, H. J. Chem. Phys. 1967, **46**, 1423-25.
11. Brawer, S.A.; White, W.B. J. Chem. Phys. 1977, **67**, 2043-55.
12. Fonger, W.H.; Struck, C.W. Phys. Rev. B 1975, **11**, 3251-60.
13. Green, G.R.; Walker, G. Phys. Chem. Mineral. 1985, **12**, 271-78.
14. Sommer, S. Chem. Geol. 1972, **9**, 257-73.
15. White, W.B.; Matsumura, M.; Linnehan, D.G.; Furukawa, T.; Chandrasekhar, B.K. Amer. Mineral. 1986, **71**, 1415-19.
16. Telfer, D.J.; Walker, G. Nature 1975, **258**, 694-95.
17. Geake, J.E.; Walker, G. In Infrared and Raman Spectroscopy of Lunar and Terrestrial Minerals; Karr, C., Ed.; Academic: New York, 1975; p. 73-89.
18. Ivey, H.F. J. Luminescence 1974, **8**, 271-306.
19. Sweet, J.R.; White, W.B.; Roy, R.; Henisch, H.K. Phys. Letters 1970, **35A**, 195-7.

20. Hess, J.W.; Sweet, J.R.; White, W.B. J. Electrochem. Soc. 1974, 121, 142-5.
21. Tsong, I.S.T.; Corredor, A.; White, W.B.; Tolk, N.H.; Kraus, J.F. J. Electrochem. Soc. 1978, 125, 2015-19.
22. Corredor, A., Ph.D. Thesis, The Pennsylvania State University, 1977.
23. Harvey, E.N. A History of Luminescence; The American Philosophical Society: Philadelphia, PA, 1957; p. 629.
24. Blackwell, D.E.; Ingham, M.F. Month. Not. Royal Astron. Soc. 1961, 122, 143-55.
25. Sidran, M. In Advances in Astronomy and Astrophysics; Kopal, Z., Ed; Academic: New York, 1968; Vol. 6, pp. 279-307.
26. McCord, T.B. J. Geophys. Res. 1967, 72, 2087-97.
27. Sidran, M. J. Geophys. Res. 1968, 73, 5195-206.
28. Cameron, W.S.; Gilheany, J.J. Icarus 1967, 8, 29-41.
29. Cameron, W.S. Moon 1975, 14, 187-99.
30. Cameron, W.S. Astron. J. 1980, 85, 314-28.
31. Kopal, Z.; Rackham, T.W. Nature 1964, 201, 239-41.
32. Kopal, Z.; Rackham, T.W., Icarus 1963, 2, 481-500.
33. Nash, D.B. J. Geophys. Res. 1966, 71, 2517-34.
34. Snouse, T.W.; Anderson, D.L. J. Geophys. Res. 1970, 75, 1573-78.
35. Greenman, N.N.; Gross, H.G. Geochim. Cosmochim. Acta Suppl. 2, 1971, 3, 2223-33.
36. Nash, D.B.; Conel, J.E. Geochim. Cosmochim. Acta Suppl. 2, 1971, 3, 2235-44.
37. Geake, J.E.; Walker, G.; Mills, A.A.; Garlick, G.F.J. Geochim. Cosmochim. Acta Suppl. 2, 1971, 3, 2265-75.
38. Geake, J.E.; Walker, G.; Mills, A.A.; Garlick, G.F.J. Geochim. Cosmochim. Acta Suppl. 3, 1972, 3, 2971-79.
39. Greenman, N.N.; Gross, H.G. Geochim. Cosmochim. Acta Suppl. 3, 1972, 3, 2981-95.
40. Geake, J.E.; Walker, G.; Telfer, D.J.; Mills, A.A.; Garlick, G.F.J. Geochim. Cosmochim. Acta Suppl. 4, 1973, 3, 3181-89.

RECEIVED September 5, 1989

Chapter 7

Laser-Excited Rare Earth Luminescence as a Probe of Mineral Characteristics

J. C. Wright

Department of Chemistry, University of Wisconsin—Madison,
Madison, WI 53706

The rare earth elements are different from other elements because the optical transitions between levels of the f^n configuration are inherently very sharp-lined and have well-resolved structure characteristic of the local crystal fields around the ion. In minerals, this characteristic provides an excellent probe of the local structure at the atomic level. Examples will be shown from our work of how site selective laser spectroscopy can be used to determine the thermal history of a sample, the point defect equilibria that are important, the presence of coupled ion substitution, the determination of multiple phases, and stoichiometry of the phase. The paper will also emphasize the fact that the usefulness and the interpretation of the rare earth luminescence is complicated by the presence of quenching and disorder in mineral samples. One in fact needs to know a great deal about a sample before the wealth of information contained in the site selective luminescence spectrum can be understood.

Our research group at the University of Wisconsin has developed a new approach to the study of minerals that can provide great detail at the atomic level. Our program is founded on the idea that site selective laser spectroscopy can be used to simplify the spectra of complex materials. Recent reviews of our work are published in reference 1. The methods can be used to:

- 1) Identify different phases in a complex mixture even when the phases differ in concentration by many orders of magnitude.
- 2) Measure the solid state equilibria between point defects to determine the relative number of different defects and the previous temperature history of the mineral that characterized the defect distribution.
- 3) Identify intergrowths of phases and the development of superstructure within the mineral lattice.
- 4) Observe the aggregation kinetics as point defects coalesce to form clusters or other phases.

0097-6156/90/0415-0135\$06.00/0
© 1990 American Chemical Society

- 5) Determine the stoichiometry of phases.
- 6) Identify new sites that are the result of coupled ion substitution where incorporation of one ion encourages incorporation of other ions that can compensate each other in the lattice.

Space limitations prevent the discussion of all the points so this synopsis will be directed toward outlining and giving examples of the fundamental mechanisms that underlie the methodology and its limitations.

Probe Ion Spectra

Crystal Field Splittings. The key idea is to use fluorescent probe ions that have spectra that are sensitive to the crystal fields they experience within a material (2). Such ions are generally ones with unfilled inner orbitals such as lanthanides (e.g. Pr^{3+} , Eu^{3+} , Er^{3+}), actinides (e.g. U), or transition metals (e.g. Cr^{3+} , Re^{4+} , Os^{4+}). The spectra that are seen depend upon the relative strengths of the crystal field and the atomic interactions within the ion such as the Coulombic interactions between electrons and between electrons and the nucleus and the spin orbit interactions between the electrons and the nucleus.

The f electrons within the $4f^n$ configuration of the lanthanides have only weak interactions with the crystal field because they are shielded by outer 5s and 5p electrons. Consequently the spectra are dominated by transitions between the atomic states of the lanthanide ion. The left side of Figure 1 shows the ionic energy levels of Eu^{3+} in the gas phase. When the ion enters a crystal lattice, there will be additional crystal field interactions. The interactions cause small crystal field splittings on the order of 200 cm^{-1} that are superimposed on the atomic transitions and are easily observable. The transitions are inherently extremely sharp so a monochromator with a reasonable resolution or a dye laser (ca. 0.1 cm^{-1}) will be able to observe spectra that are completely resolved and are highly characteristic of the particular crystal fields encountered by the lanthanide ion. In that way, the ion acts as an excellent probe of the local lattice in a mineral. The right side of Figure 1 shows an expanded view of the crystal field splittings for one state of a Eu^{3+} ion in two different crystallographic states. The other states will have a corresponding splitting. When one records an absorption spectrum of this material, the spectrum will contain absorption lines corresponding to transitions from the ground state to each of the five levels in each of the two sites. The spectrum on the far right illustrates a typical spectrum.

The d electrons within the d^n electron configuration of the transition metals have much stronger interactions with the crystal field so crystal field interactions are comparable to the interactions within the atom. The spectral transitions can change more drastically to reflect the changes in the crystal field. The line-widths of the transitions are also much broader. Not all transition metals are useful as probe ions because the lines are too broad to allow one to resolve features in samples where there are multiple local environments about the ion. In fact, only some atomic states of the probe ions are useful because most states interact too strongly with the crystal field to give narrow enough lines.

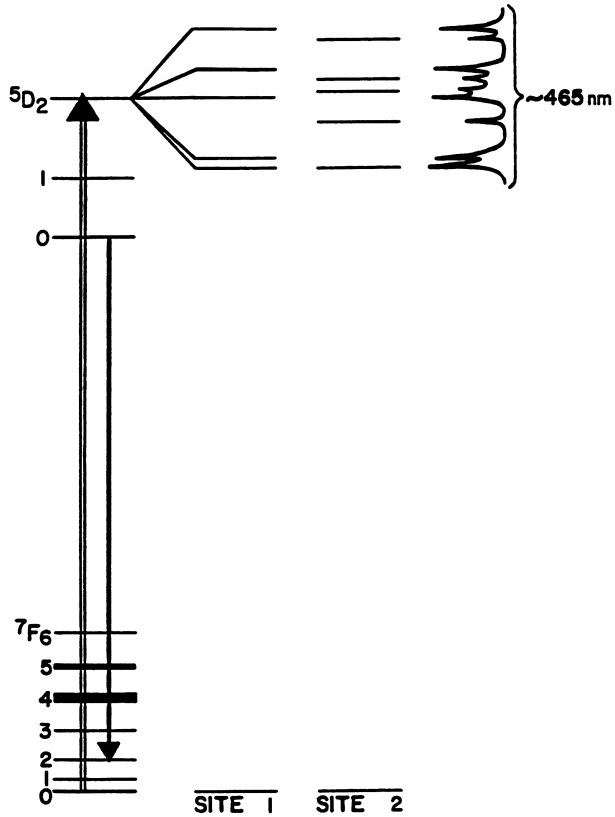


Figure 1. Eu^{3+} energy levels for two different sites.

The $5f^n$ electrons of the actinides represent an intermediate case where there is still shielding of the crystal fields but it is not as effective as in the lanthanides. The crystal field interactions are larger than the lanthanides but not as large as in the transition metals. The lines of most transitions are sharp and all the actinide ions could be used potentially as probes of the local environments of minerals.

Energy Relaxation. The crystal field split energy levels of probe ions can be excited by tuning a laser to their absorption wavelength. The energy relaxation mechanisms are reviewed in more detail in reference 3. The energy that is deposited in the ion can either be re-emitted as fluorescence, lost to the lattice, or transferred to another ion. The latter two processes will determine whether fluorescence will be seen from a mineral sample. Each crystal field level will have a total radiative transition rate that characterizes the probability/second that energy in that level can be emitted as light in a radiative relaxation to a lower energy level. There will also be rates for loss of energy to the lattice and energy transfer. The fluorescence quantum efficiency will be the ratio of the radiative transition rate to the total rate for all three processes. It is therefore important to know the factors that control the two nonradiative relaxation processes.

The rate at which energy is lost to the lattice depends upon how many lattice phonons are required to soak up the energy. A given electronic state will be able to lose energy by relaxing to some lower state. The energy difference between the two states is the energy that must be given to the lattice in the form of phonons or quantized lattice vibrations. The number of phonons required depends on the energy of an individual phonon. If there are energetic phonons in the lattice, fewer phonons are required and the multiphonon relaxation can be efficient. Conversely, if the lattice is soft and the phonons are not energetic, many phonons are required and the multiphonon relaxation is not efficient. Thus, hard lattices with energetic phonons and energy levels with small energy gaps to the next lower level are unfavorable for fluorescence transitions. Levels that are separated by energy gaps that are small enough for a single phonon to accept the energy are so efficiently relaxed that one cannot observe fluorescence. In fact, the relaxation can occur so quickly that the uncertainty principle demands that the level is broadened by the short lifetime.

The energy transfer rate is dependent upon the energy gap as well. The two ions that are exchanging energy will have an initial total energy before transfer occurs and a final total energy after transfer occurs. The difference must be accommodated by lattice phonons and again the efficiency of the transfer is enhanced when the fewest lattice phonons are required. The efficiency also depends on the distance between the two ions exchanging the energy.

Energy transfer is usually subdivided into different classes that depend on the nature of the two ions. If the ions are identical and the energy transfer does not involve any net loss of excitation energy (i.e. the lattice does not receive any energy), the transfer is called migration or exciton propagation. It can be very rapid when the ions are close. If the ions are identical and the transfer

involves loss of energy to the lattice, this process is called ion pair decay. The excited ion decays to a lower level while the neighboring ion is excited to a higher level. Energy differences in the initial and final total energies are released as phonons. If the ion accepting the energy will subsequently lose the energy to the lattice through multiphonon relaxation, one calls the accepting ion a quenching center. Iron often provides a quenching center in minerals and will prevent the site selective methods described in this paper from being applied to many mineral systems. If migration can occur in the lattice because the mineral has a high concentration of the excited ion, it is common that an excitation will rapidly migrate to a quenching center or sink where the fluorescence is quenched.

With this overview of why different probe ions have their characteristic spectra and what happens to an electronic excitation, we are ready to see how the probe ions can be used to study minerals.

Probe Ions in Minerals

Point defects are an important part of the work in this paper. There are many reasons for the formation of point defects in minerals and their presence can exert important perturbations on the properties of the material (4). Point defects are formed because of the thermally driven intrinsic disorder in a lattice, the addition of aliovalent impurities or dopants, the presence of metal-nonmetal nonstoichiometry, and the creation of nonideal cation ratios. The first three source of defects are well-known from binary compounds but the last is unique to ternary compounds. Ternary compounds are much more complex than the binary compounds but they also have gained a great deal of attention because of the variety of important behavior they exhibit including now the presence of superconductivity at high temperatures. The point defects can be measured by introducing probe ions into the lattice.

There are two ways to use probe ions. One can introduce probe ions intentionally in synthetic samples during the process of sample preparation. One can also take advantage of the natural abundance of probe ions in natural minerals because laser techniques provide excellent signal levels that allow one to work at very low concentration levels. In general, a probe ion will replace a lattice ion that has a different valence. In order to maintain charge neutrality, the lattice must have a charge compensation that can be either an interstitial ion, a vacancy, or an electron or hole. Each of these point defects change the local environment or the probe ion and the absorption and fluorescence spectra reflect the resulting changes in crystal field splittings. Any interesting mineral will in general have many types of charge compensation available and the charge compensations can exist in different positions relative to the probe ion. Thus, one commonly has a number of different centers or sites involving the probe ions and site selective spectroscopy is essential for isolating the contribution from the individual defect structures. The relative numbers of the different environments depends on the concentrations of all the possible ions that could be in a mineral, the temperature at which the distribution equilibrated and the atmosphere that was in equilibrium with the mineral. More detailed descriptions require reference to specific crystal systems.

These ideas are illustrated in Figure 2 for CaO. The intrinsic defects are Ca and O vacancies. When a Eu^{3+} ion enters the lattice, it substitutes for a Ca^{2+} and a charge compensation is required. The charge compensation is provided by a Ca^{2+} vacancy which serves to compensate two Eu^{3+} ions. There are different arrangements for the Eu^{3+} and the Ca^{2+} vacancy as illustrated in the figure. The cubic site has the Ca^{2+} vacancy compensation so distant that the local symmetry of the Eu^{3+} is not perturbed. The tetragonal site has the vacancy in the nearest neighbor position. The dimer sites have the vacancy in the nearest neighbor positions for two symmetrically located Eu^{3+} ions. Each of these different Eu^{3+} sites has different crystal field splittings and spectra.

Experimental

The key development for using probe ions to study mineral systems is site selective laser spectroscopy. A tunable dye laser is tuned to match the absorption line of a particular ion with a particular environment or site within the sample. Only that ion will be excited and only that ion will fluoresce so the resulting fluorescence spectrum is much simpler than the conventionally obtained spectrum. Single site excitation spectra can likewise be obtained by monitoring the fluorescence at a specific wavelength of a specific site and scanning the laser over the possible absorption lines. One can systematically dissect an absorption spectrum into the component sites that make it up.

Figure 3 shows the excitation spectrum of CaO doped with Eu^{3+} when fluorescence from all sites in the sample was monitored. The dye laser was scanned over the possible absorption lines and each time the wavelength matched a transition on any site, the fluorescence intensity increased and gave a line. Figure 4 shows the same procedure on the same crystal except now a high resolution monochromator was used to monitor the fluorescence that occurred at a wavelength characteristic of a specific site. Now, one sees increases in the fluorescence only when the dye laser matches an absorption line of the same site that has the fluorescence line being monitored. The result is a single site excitation spectrum. By systematically choosing different fluorescence lines for monitoring, one can correlate all of the lines in Figure 3 with the single site spectra of Figure 4.

These basic techniques can be used in a number of ways to get detailed information about point defect equilibria and dynamics. A succinct summary of the capabilities of the site selective laser methods is given below.

- 1) One can follow changes in site concentration over more than four orders of magnitude.
- 2) One can measure the site concentrations in absolute units to $\pm 25\%$ by measuring the absorption coefficient and radiative transition probability (which in turn comes from the level lifetime, radiative quantum efficiency and radiative branching ratios) or to $\pm 15\%$ by nonlinear regression fitting of relative intensities to total dopant concentration over a range of site distributions.
- 3) One can assign the site symmetry by determining the number of crystal field levels of different electronic states, the polariza-

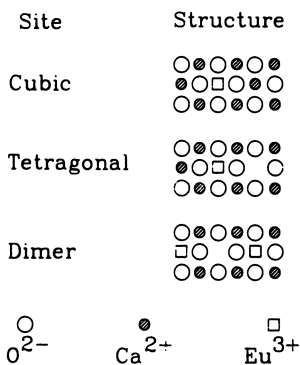


Figure 2. Different Eu^{3+} sites in CaO .

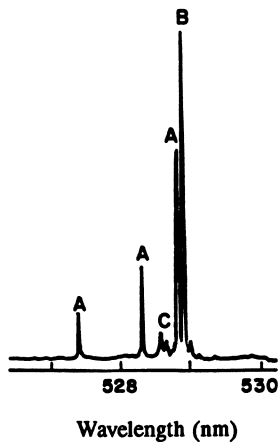


Figure 3. Excitation spectrum of $\text{Eu}:\text{CaO}$ obtained by monitoring all fluorescence wavelengths.

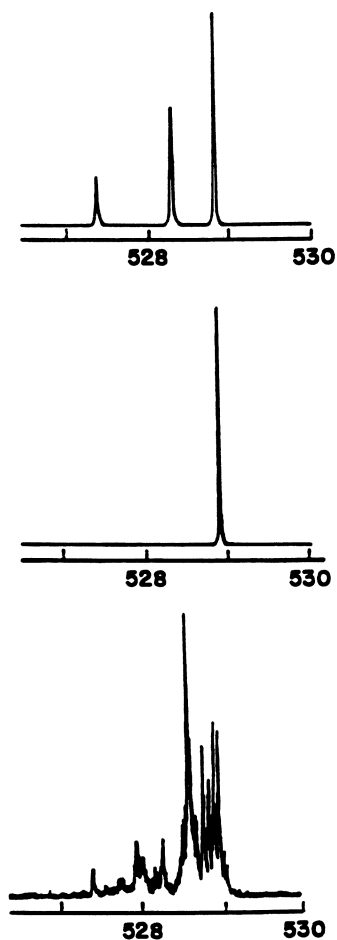


Figure 4. Excitation spectra of Eu:CaO obtained by monitoring all different fluorescence wavelengths.

tion of the transitions, and the anisotropy of the Zeeman splitting as the crystals are rotated about local symmetry axes.

4) One can determine the number of cation dopants associated with a given defect structure by measuring the two body energy transfer rates between probe ions, the efficiency of three body up-conversion, and the effect of adding a second dopant ion in higher concentration on the splittings of the first dopant ion.

5) One can measure the equilibrium constant for defect association between a dopant ion and its charge compensation by measuring the relative concentrations of the paired and dissociated probe ion concentrations over a range of dopant concentrations.

6) One can measure the concentration of the intrinsic lattice defects by measuring the ratio of the paired and dissociated pairs and having a previous value for the equilibrium constant.

7) One can measure the activity coefficients for the nonideality corrections in defect equilibria by comparing the ratios of the relative site concentrations in the high dopant concentration range with the low concentration range.

8) One can determine the association rate constants and thermodynamic activation energies for migration by measuring the changes in site distribution as a sample is annealed over a range of times and temperatures.

These abilities provide the site selective laser techniques with unique capabilities to determine the changes in defect equilibria at a microscopic level. They are complementary to conductivity, diffusion, dielectric and other bulk measurements which measure nonlocal properties that must be modeled to extract microscopic details. They have two advantages over magnetic resonance methods: they are sensitive over a much wider dynamic range of defect concentrations and their selectivity enables one to study even complex materials where there may be large differences in the relative concentrations of different sites.

Our work has applied these techniques to the study of the binary insulating materials including the fluorites, alkali halides, alkaline earth oxides, and perovskites. Many of these are simple materials that are commonly used as models for all solid state defect equilibria. Our work has had the goal of determining at the microscopic level the defect equilibria and dynamics that are important in understanding solid state chemistry as well as developing new tools for the studies of solid materials.

Example Studies of Mineral Systems

Alkaline Earth Oxides. If a trivalent lanthanide is substituted for Ca^{2+} in CaO (5) or a Cr^{3+} is substituted for a Mg^{2+} in MgO (6), the extra positive charge is compensated by a cation vacancy as described earlier. The vacancy can be in a near neighbor position or it can be very distant from the probe ion (7-10). If another ion like Na^+ is in the cation site, it can serve as a charge compensation for the probe ion either as a nearby ion or distantly. This case is coupled ion substitution that commonly affects the partitioning of ions into different mineral phases (11). One can envision many other ions that could also affect the local environment or the probe ion. All of the possibilities lead to different sites with different crystal field splittings.

There is an equilibrium between the different sites that determines the observed distribution. For example, the ratio of the sites with the cation vacancy nearby to those with the vacancy distant will depend upon the concentration of vacancies by the law of mass action. One can write the conventional equilibrium relationships given by mass action considerations for equilibria between vacancies and probe ion sites with local and distant vacancy compensation. The equilibrium constant will depend on the temperature under which the equilibrium was established. Since all of the sites can be observed by site selective laser spectroscopy, one can measure the equilibrium distributions directly. We find that the sites and their distributions are described excellently by the mass action relationships of conventional equilibria. This work is described in more detail elsewhere (5,6).

Fluorites. As the second example, we choose CaF_2 doped also with trivalent rare earth ions. The replacement of divalent Ca by a trivalent lanthanide is accompanied either by an extra fluoride interstitial ion or an external ion such as oxygen or hydrogen. If one excludes other ions, the compensating fluoride interstitial ion can be located in either a nearest neighbor position, a next nearest neighbor position or it can be very distant. The lanthanide's crystal field will reflect either the tetragonal, trigonal or cubic symmetries of the three respective situations. Site selective spectroscopy also reveals many additional lanthanide sites that are caused by clusters of several lanthanides and their fluoride interstitial charge compensations (12). Again, there will be an equilibrium between the different defect sites that will depend on the number of fluoride interstitials.

Using the same arguments as we used in CaO , one would expect that an increased concentration of lanthanide dopant should introduce a like number of fluoride interstitials into the lattice. If the pairing of the interstitials with the lanthanide is not complete, the number of free interstitials would increase. The larger number of interstitials should lead to an increase in the number of lanthanides that have the fluoride interstitial charge compensation in a nearby position relative to the ones that have the interstitial distant according to the law of mass action. Laser spectroscopy shows the opposite effect though.

There has been a long standing question about the nature of the defect equilibria in the fluorites (13-22). Measurements of the conductivity and diffusion in fluorites is commonly interpreted with simple mass action relationships but the site selective laser spectroscopy (as well as other techniques) has shown that the situation is more complex and that simple mass action relationships don't even describe the observed equilibria qualitatively (23-28). The principal reasons for the failure of standard relationships is either other equilibria (in particular, the F_i^- scavenging equilibria) compete for F_i^- , that F^- is an unusual ion that is known for forming associates with itself that could change the defect equilibria, or there are abnormally large nonideality effects. These effects were studied in all of the alkaline earth fluorides and we found the same anomalies were always observed.

We then studied SrCl_2 as a model system (29-31). This material had the fluorite structure but it did not have the F^- . Furthermore, the crystal could be quenched from high temperatures and all possible competing equilibria could be eliminated. The only remaining cause for departures from mass action relationships is nonideality effects. We studied the different sites in SrCl_2 and measured the site distributions as a function of annealing temperature and dopant concentration (29). At low dopant concentrations, the site distributions do follow the expected mass action relationships. At high concentrations there are the same strong deviations that are observed in alkaline earth fluorides with the fluorite structure. We then measured the absolute site concentrations and from comparisons between the low and high concentration regions, we obtained the first measurements of activity coefficients in a solid. These coefficients are required to describe the nonidealities. The values are much larger than one would expect from Coulombic contributions to the activity coefficient and the only remaining forces that would be large enough to explain the nonrandom distribution of defects are strain fields. We also obtained values for the association constant and found them significantly smaller than theoretical estimates would indicate. These values suggest that the theoretical description does not treat the interior interactions correctly. Additionally, we did not observe that clustering had the strong dependence on ionic radius that was predicted from theoretical estimates. These factors point to inadequacies in the potential models that are assumed in the theoretical calculations.

The strong nonideality effects have important consequences for the presence of superionic conductivity in the fluorites. A superionic conductor is a material where one of the ion sublattices undergoes partial melting or disordering at relatively low temperatures so the material acquires a large ionic conductivity. PbF_2 is the best of the fluorites for superionic conductivity and we studied this material to determine how strong the nonideality effects were (32-33). We found that the effects were much stronger in PbF_2 and that they also correlated with the transition to superionic conductivity. The correlation was interpreted as a thermodynamic instability that was caused by the large nonideality effects. Increases in temperature caused more dissociation of defects which led to an increase in the ionic strength of the material. The higher ionic strength caused more shielding and that encouraged more dissociation. There is therefore positive feedback between the ionic strength and the degree of dissociation that can lead to the instability.

The other factor that could cause deviations from the conventional defect models was competing equilibria from F_i^- scavenging equilibria. This behavior was observed in CdF_2 , a material that can undergo a transition from insulating to semiconducting behavior (34-35). We found that clustering was far more extensive in CdF_2 than in any of the other materials we have studied and that some of the clusters could scavenge F_i^- to form charged defect centers. The semiconducting behavior is the result of crystal reduction where F^- are replaced by e^- . This process occurs more readily for the more loosely bound F_i^- that have been scavenged and makes the replacement possible. The importance of the scavenging is a strong function of the dopant radius and those ions that are too large to have strong scavenging equilibria cannot in fact be converted to semiconductors.

The relative site importance in all of the fluorites is a strong function of the temperature that established the equilibrium distribution. At high temperatures, the association between the fluoride interstitial and the lanthanide would be expected to decrease as the sites dissociated. Similarly, the association of several lanthanides and their interstitial compensators into clusters would also be expected to decrease. Experimentally, we observe that higher temperatures cause dissociation of the clusters and the larger numbers of free interstitials that result from the dissociation can associate with individual lanthanide ions. This observation has been used as the key to measuring the kinetics of the defect aggregation. If high temperatures are used to dissociate the clusters and create a non-equilibrium distribution, the crystal can be held at a low temperature to allow the reaggregation of the ions to form the clusters. The rate at which the cluster formation occurs can be measured as a function of dopant concentration and temperature to obtain kinetic information about the defect aggregation mechanism.

KCl. There has been a long standing controversy about the nature of the defect aggregation in alkali halides. Initial experiments showed that aggregation occurred by direct formation of trimers from three monomers (36-42). Others quickly objected stating that trimers require improbable three body collisions and that it is more likely that dimers form initially (43-49). There was also a bitter controversy about the nature of the defects in KCl:Sm^{2+} . One group of researchers found that the compensation could be located in a number of different lattice positions relative to the Sm^{2+} (50-58) while another group found that it was only located in a nearest neighbor position (59-61). Both of these questions were studied by site selective laser spectroscopy and we found that the dominant defect was a simple pair of Sm^{2+} with a nearest neighbor charge compensation (62,63). Other positions of the charge compensation were not observed but there were a number of additional sites formed by clustering of the simple pairs. We also found that these clusters could be dissociated by quenching from high temperatures and that we could then watch the reformation of the clusters by watching the site distribution evolve in time as the crystal was annealed at low temperatures. The kinetics could be followed for each site individually and the rate constant that we obtained could be determined as a function of the dopant concentration. These studies showed definitively that the aggregation dynamics was controlled by the formation of dimers and that only at long times did the dimers aggregate to form larger clusters and other phases (64).

Perovskite Materials. Our studies of these materials are still in their infancy. An important feature of the perovskites is the ability to form many phases through shear planes where layers of a metal oxide can be inserted between multiple perovskite structure layers. Our work has shown that probe ions can be used to watch this process and we have been able to show that site selective laser spectroscopy is sensitive to all of the phases with a high sensitivity to even small concentrations.

Conclusions

Site selective laser spectroscopy is a very powerful tool for studying the local environments that are present in samples. We have shown that defect structures in solids are determined by its previous history and that these structures can be measured with site selective spectroscopy. There has been no application of such techniques to geologically important questions since our work has concentrated on understanding fundamental questions about solid state defect chemistry. Our work suggests though that site selective laser spectroscopy could have important application in geological studies if it were used in the hands of people with that background.

Acknowledgments

The work reported in this paper was supported by the Solid State Chemistry Program of the Materials Science Division of the National Science Foundation under grant DMR-8645405.

Literature Cited

1. Wright, J. C. Latt. Def. and Amorph. Mat. 1985, 12, 505.
2. Hufner, S. Optical Spectra of Transparent Rare Earth Compounds; Academic Press: 1978.
3. Wright, J.C. In Modern Fluorescence; Wehry, E. L., Ed.; Plenum Press: New York, 1981.
4. Kroger, F. A. The Chemistry of Imperfect Crystals; North-Holland: Amsterdam, 1964.
5. Porter, L. C.; Wright, J. C. J. Chem. Phys., 1982, 77, 2322.
6. Poliak, J. R.; Noon, K. R.; Wright, J. C. J. Sol. State Chem. 1989 (accepted for publication).
7. Schawlow, A. L. J. Appl. Phys. 1962, 33, 395.
8. Imbusch, G. F.; Schawlow, A. L.; May, A. D.; Sugano, S. Phys. Rev. B, 1976, 13, 1893.
9. Henry, M. O.; Larkin, J. P.; Imbusch, G. F. Phys. Rev. B, 1976, 13, 1893.
10. Boyrivent, A.; Duval, E.; Mantagna, M.; Villani, A. G.; Pilla, O. J. J. Phys. C: Sol. State Phys. 1979, 12, L803.
11. Nassau, K. J. Phys. Chem. Solids, 1963, 24, 1511.
12. Tallant, D. R.; Wright, J. C. J. Chem. Phys. 1975, 63, 2075.
13. Franklin, A. D.; Marzullo, S. Proc. Brit. Ceram. Soc. 1971, 19, 135.
14. Vlasov, M. V. Sov. Phys. Crystallogr. 1975, 20, 100.
15. Voron'ko, Yu. K.; Osiko, V. V.; Schcherbakov, I. A. Sov. Phys. JETP, 1969, 29, 86.
16. Gil'fanov, F. Z.; Livanova, L. D., Orlov, M. S.; Stolov, A. L. Sov. Phys. Solid State 1970, 11, 1779.
17. Brown, M. R.; Roots, K. G., Williams, J. M.; Shand, W. A.; Groter, C.; Kay, H. F. J. Chem. Phys. 1969, 50, 891.
18. Stott, J. P.; Crawford, J. H., Jr. Phys. Rev. B 1971, 4, 668.
19. O'Hare, J. M. J. Chem. Phys. 1972, 57, 3838.
20. Crawford, J. H., Jr.; Matthews, G. E., Jr. Semicond. Insul. 1977, 2, 213.

American Chemical Society
Library

1155 16th St. N.W.
Washington, D.C. 20036

In Spectroscopic Characterization of Minerals and Their Surfaces; Coyne, L., et al.; ACS Symposium Series 216; American Chemical Society: Washington, DC, 1990.

21. Franklin, A. D. J. Chem. Phys. 1976, 63, 1509.
22. Franklin, A. D. Mater. Sci. Res. 1973, 6, 19.
23. Tallant, D. R.; Miller, M. P.; Wright, J. C. J. Chem. Phys. 1976, 65, 51.
24. Tallant, D. R.; Moore, D. S.; Wright, J. C. J. Chem. Phys. 1977, 67, 289.
25. Moore, D. S.; Wright, J. C. J. Chem. Phys. 1971, 74, 1626.
26. Seelbinder, M. B.; Wright, J. C. J. Chem. Phys. 1981, 75, 5070.
27. Hamers, R. J.; Wietfeldt, J. R.; Wright, J. C. J. Chem. Phys. 1982, 77, 683.
28. Moore, D. S.; Wright, J. C. Chem. Phys. Lett. 1979, 66, 173.
29. Wietfeldt, J. R.; Wright, J. C. J. Chem. Phys. 1987, 86, 400.
30. Wietfeldt, J. R.; Wright, J. C. J. Luminesc. 1984, 31/32, 263.
31. Wietfeldt, J. R.; Wright, J. C. J. Chem. Phys. 1985, 83, 4210.
32. Mho, S. I.; Wright, J. C. J. Chem. Phys. 1985, 83, 4210.
33. Weesner, F. J.; Wright, J. C. Phys. Rev. B 1986, 33, 1372.
34. Mho, S. I.; Wright, J. C. J. Chem. Phys. 1982, 77, 1183.
35. Mho, S. I.; Wright, J. C. J. Chem. Phys. 1984, 81, 1421.
36. Cook, J. S.; Dryden, J. S. Austr. J. Phys. 1960, 13, 260.
37. Cook, J. S.; Dryden, J. S. Proc. Phys. Soc. 1962, 80, 479.
38. Dryden, J. S.; Heydon, R. G. J. Phys. C: Sol. State Phys. 1977, 10, 2333.
39. Dryden, J. S.; Heydon, R. G. J. Phys. C: Sol. State Phys. 1978, 11, 393.
40. Cook, J. S.; Dryden, J. S. J. Phys. C: Sol. State Phys. 1979, 12, 4207.
41. Cook, J. S.; Dryden, J. S. J. Phys. C: Sol. State Phys. 1981, 14, 1133.
42. Cook, J. S.; Dryden, J. S. J. de Phys. 1980, 41, C6-425.
43. Unger, S.; Perlman, M. M. Phys. Rev. B 1972, 6, 3973.
44. Unger, S.; Perlman, M. M. Phys. Rev. B 1973, 10, 3692.
45. Unger, S.; Perlman, M. M. Phys. Rev. B 1975, 12, 809.
46. Crawford, J. H. J. Phys. Chem. Solids 1970, 31, 399.
47. McKeever, S. W. W.; Lilley, E. J. Phys. Chem. Solids 1982, 43, 885.
48. Lilley, E. J. de Phys. 1980, 41, C6-429.
49. Rubio, J.; Murrieta, H.; Powell, R. C.; Sibley, W. A. Phys. Rev. B 1985, 31, 59.
50. Fong, F. K.; Wong, E. Y. In Optical Properties of Ions in Crystals; Crosswhite, H. M.; Moos, H. W., Eds.; John Wiley: New York, 1967.
51. Fong, F. K.; Wong, E. Y. Phys. Rev. 1967, 162, 348
52. Fong, F. K.; Sundberg, M. N.; Heist, R. H.; Chilver, C. R. Phys. Rev. B 1971, 3, 50.
53. Fong, F. K.; Heist, R. H.; Chilver, C. R., Bellows, J. C.; Ford, R. L. J. Luminesc. 1970, 2, 823.
54. Naberhuis, S. L.; Fong, F. K. J. Chem. Phys. 1972, 56, 1174.
55. Fong, F. K. Phys. Rev. 1969, 187, 1099.
56. Fong, F. K. Phys. Rev. 1970, 94, 4157.
57. Fong, F. K.; Bellows, J. C. Phys. Rev. B 1970, 1, 4240.
58. Fong, F. K.; Bellows, J. C. Phys. Rev. B, 1970, 2, 2636.
59. Bradbury, R. E.; Wong, E. Y. Phys. Rev. B 1971, 4, 690.

60. Bradbury, R. E.; Wong, E. Y. Phys. Rev. B 1971, 4, 694.
61. Bradbury, R. E.; Wong, E. Y. Phys. Rev. B 1971, 4, 702.
62. Ramponi, A. J.; Wright, J. C. J. Luminesc. 1984, 31/32, 151.
63. Ramponi, A. J.; Wright, J. C. Phys. Rev. B 1985, 31, 3965.
64. Ramponi, A. J.; Wright, J. C. Phys. Rev. B 1987, 35, 2413.

RECEIVED February 22, 1989

Chapter 8

Mineralogy of Meteorites Revealed by Cathodoluminescence

Ian M. Steele

Department of the Geophysical Sciences, University of Chicago,
Chicago, IL 60637

Within meteorites enstatite, forsterite, plagioclase and glass are the major phases which show cathodoluminescence (CL). For enstatite and forsterite, Cr and Mn both produce CL with Cr emission in the infrared (about 740nm) but extending into the visible and Mn emission in the red (about 660nm). Both phases show a blue emission near 450nm of unknown origin. The visual color is a function of these two elements, the blue intensity and the Fe content which effectively quenches the blue emission in forsterite at the 0.75 wt.% level and the Cr emission at the 2.0 wt.% level. Iron quenching affects enstatite but levels are not known. The wavelength of the Cr emission is not constant and may reflect the distribution of Cr between the two non-equivalent sites of these minerals. Spectral intensity measurements can provide a means of rapidly determining Cr and Mn concentrations if Fe levels are constant. Feldspar is the most common phase showing CL but the activator is not known. The intensity of blue emission in anorthite correlates inversely with the Mg and Na content and allows recognition of zoning in these minor elements. Visual observations of plagioclase luminescence in the carbonaceous chondrites provides evidence of extensive alteration of anorthite to garnet-melilite assemblages. All three silicates show a blue emission to which no activator element has been recognized and strengthens arguments that it is associated with the tetrahedral portion of the structures. Brief observations are made for CL features of melilite, spinel, garnet, fassaite, hibonite, corundum, oldhamite and diopside but systematic studies of these phases have not been made.

Cathodoluminescence (CL), or the emission of light upon electron irradiation, has long been recognized. Initially observations were

0097-6156/90/0415-0150\$06.00/0
© 1990 American Chemical Society

made visually with poor optics but with the advent of electron beam analytical instruments its usefulness was recognized for revealing textures and compositional changes on a micro scale in minerals (1,2). It was recognized that for terrestrial minerals CL was limited to those minerals that are Fe-poor which ruled out CL from many of the rock-forming minerals. Most studies were made on quartz, common carbonates, feldspars and apatite which are common in many terrestrial sedimentary rocks and provide valuable information regarding deposition and subsequent modification of these rocks. Other studies pertain to relatively rare minerals including cassiterite (3). Of these only the feldspars are relatively common in meteorites.

While there are many types of meteorites, from the point of view of CL the most interesting types are the primitive meteorites which formed early, about 4.5 billion years ago, and have remained essentially unaffected by thermal or chemical processes. These meteorites contain some minerals which are very low in Fe and potentially will show CL; in contrast, meteorites which may have formed early but since have been altered now contain mostly Fe-bearing phases and only rarely show CL. The specific groups of meteorites which show CL are: 1) type 1, 2, 3 carbonaceous chondrites (C1, C2 and C3); 2) enstatite chondrites; 3) enstatite achondrites (aubrites); 4) type 3 ordinary chondrites (unequilibrated ordinary chondrites or UOC). While not strictly meteorites, other extraterrestrial samples which may show CL are: 1) deep sea particles which are samples of extraterrestrial material generally less than about 1mm in maximum dimension which can be recovered from deep sea sediments; 2) stratospheric particles which are minute, usually fluffy aggregates which enter the upper atmosphere and remain in the stratosphere to be collected by high flying planes; 3) particles from Greenland lake sediment which are similar to deep sea particles but are concentrated in lakes formed on the Greenland ice sheet.

Cathodoluminescence observations by themselves reveal details of texture among minerals and suggest chemical or structural variation within individual grains. Seldom can the CL observations be interpreted without additional information such as chemical or structural analysis. With this in mind, data obtained from the electron microprobe (EMP), ion microprobe (IMP), scanning electron microscope (SEM), or by thermoluminescence studies complement CL observations and many of the CL examples for meteorites can be best interpreted or related to mineralogy through these data.

Instrumental techniques for CL studies

The most common method of observing CL is by visual observation in a luminoscope which floods an area of several mm² with 10-30 kV electrons producing CL which can be observed through a microscope. A simple modification to the optics allows photographic recording in color. The main drawbacks are the qualitative descriptions which may vary among observers and the wavelength range which is limited to that detected by the eye; with photographic recording, color is often a function of film, exposure, and developing and the color may not match that observed by the eye. However, the color photographs

clearly show textures, contrasting minerals and often subtle features within individual minerals. They form a permanent record but show details of color variation only as a sum of individual emissions. The dynamic range of the film may require graded exposures to represent the entire range of CL from the minerals present; likewise, because exposure time often is a trial and error determination especially for weak CL, graded exposures may be required to represent the entire intensity range. The exposures usually require seconds to tens of seconds but weak CL may require exposures of tens of minutes and some CL features can be affected by the long irradiation times. The main advantage of the luminoscope is the ability to rapidly recognize textures on a coarse scale.

In contrast to a broad electron beam usually used in the luminoscope, a narrow beam of a scanning electron microscope or an electron microprobe can be rastered over an area of selected size. The CL intensity produced at each point can be measured by a photomultiplier tube and used to modulate an image intensity on a CRT; these images are analogous to conventional secondary electron (SE) or backscattered electron (BSE) images. The displayed image intensity is a sum of all colors but because the photomultiplier tube may be most sensitive to a particular wavelength range, the image may not accurately reflect the intensities seen by the eye or recorded on color film. An advantage is that the detection can extend beyond the visible or be restricted to a color range determined by the active photomultiplier material. The resulting image can be photographed. Selective filters can be inserted in the light path but at the expense of intensity. Dispersing elements such as gratings or prisms can be used to select a certain wavelength in conjunction with a scanning beam or to scan a wavelength range for a fixed electron beam. Mechanical spectrometers require a finite time to scan the spectrum, and for minerals sensitive to the electron beam, damage and consequent modification of the CL intensity may occur during the scan. Optical multichannel analyzers (OMA) with light intensifiers are now available which allow an entire spectrum to be recorded at one time and stored in a memory. Electronics are also available to read a selected portion of the spectrum, synchronized with a scanning beam to display the intensity of a selected wavelength range as a function of beam position. The image can be digitized, stored, and computer manipulated by standard image processing techniques.

An important consideration in comparing images from these different types of observations, or the same type of observations from different instruments, is that the transmission of the spectral information may be modified by the overall optical path of the instrument. For accurate and precise work, a calibrated light source should be recorded and any spectra adjusted for the transmission of the instrument. For spectral measurements the wavelength of the emissions must be related to an emission standard such as a Hg-Ne source because small changes may reflect useful mineralogical parameters. Observations can also depend on the accelerating voltage, current density, and dwell time of the beam at a point. Because some of these variables may not be reported, observations may be difficult to reproduce.

Meteoritic Minerals showing Cathodoluminescence

The occurrence of minerals which show CL is highly dependent on the type of meteorite. Possibly the most common phase which occurs is feldspar. Because this mineral accepts very little Fe into the structure, quenching is not a problem; however, because the feldspar structure is quite open, the Na- and K-rich feldspars are easily damaged by electron beams. In contrast anorthite, the Ca rich variety, is quite stable. Pyroxene and olivine are common phases in meteorites but because they both usually contain iron, most do not luminesce. Only in the primitive meteorites do nearly pure enstatite and forsterite occur and both show brilliant CL. Other minerals are rare but include:

CL observed

corundum (Al_2O_3)	diamond (C)
diopside ($\text{CaMgSi}_2\text{O}_6$)	fassaite ($\text{Ca}(\text{Ti}, \text{Al})(\text{Al}, \text{Si})_2\text{O}_8$)
hibonite ($\text{CaAl}_{12}\text{O}_{19}$)	grossular ($\text{Ca}_3\text{Al}_2\text{Si}_3\text{O}_{12}$)
lonsdaleite (C)	melilite ($\text{Ca}_2\text{Al}_2\text{SiO}_7$)
nepheline ($\text{Na}_3\text{K}(\text{AlSiO}_4)_4$)	oldhamite (CaS)
perovskite (CaTiO_3)	quartz (SiO_2)
sinoite ($\text{Si}_2\text{N}_2\text{O}$)	sodalite ($\text{Na}_4\text{Al}_3\text{Si}_3\text{O}_{12}\text{Cl}$)
spinel (MgAl_2O_4)	wollastonite (CaSiO_3)

CL not described but likely

baddeleyite (ZrO_2)	carbonates (e.g. CaCO_3)
moissanite (SiC)	phosphates (e.g. $\text{Ca}_5(\text{PO}_4)_3\text{Cl}$)
zircon (ZrSiO_4)	

The listed chemical formulae are ideal and most of these minerals contain trace and minor elements which undoubtedly affect the CL. Several of these minerals have polymorphic or compositional varieties which also may, or do, show CL (e.g. the silica polymorphs: quartz, cristobalite, tridymite; phosphate compositional varieties: apatite, whitlockite, farringtonite, buchwaldite; carbonate compositional varieties: calcite, dolomite, magnesite). Glass and maskelynite (shock modified feldspar), although not strictly minerals, are relatively common. Below are described the CL observations for the most common phases including enstatite, feldspar and forsterite and they are related to their use for interpreting the mineralogy of meteorites. The observations for the other minerals are sporadic and many details have yet to be studied.

Enstatite The first extensive observations of CL in meteorites were for enstatite (MgSiO_3) probably because it shows particularly brilliant CL colors and it is the major mineral in the enstatite achondrites. The visual CL is commonly described as blue, red or less commonly purple and the early spectra, mainly from powdered samples and using proton irradiation, clearly showed the presence of a blue and red emission (4-6). These emissions were confirmed using electron irradiation and spectra showed a blue peak near 400-420nm

and a red peak near 660-680nm. Neutron activation and electron probe analyses showed that the intensity of the red emission or the visual redness showed some correlation with the Mn concentration; in addition, the wavelength of the red peak for the natural enstatite matched closely that of synthetic Mn-bearing enstatite (7). The cause of the blue emission was not explained although it was observed that blue emission is common to many silicates and was suggested that it is intrinsic to the silicon tetrahedron (8). The blue peak, however, was not observed for synthetic Mn-enstatite (Mn=4.5 wt%) (9,9,10). No correlation of visible blue intensity with the ordering of orthoenstatite (10) suggested that the CL color is not a function of deformation which has affected most enstatite achondrites.

While passing mention of enstatite CL in meteorites can be found in the literature, not until 1980 was interest revived (11-13). In these three papers the visual colors of enstatite in chondrules of the enstatite chondrites were described and the apparent bimodal occurrence of either red or blue CL within individual chondrules was attributed to mechanical mixing of two types of enstatite. In (11) the minor element chemistry of the red and blue enstatites was compared and the following average concentrations (oxide wt. %) were reported for each: oxide - red, blue; CaO - 0.24, 0.7; MnO - 0.16, 0.04; Cr₂O₃ - 0.34, 0.04; TiO₂ - 0.05, 0.005; Al₂O₃ - 0.24, 0.08; Na₂O - 0.05, 0.12; FeO - 0.93, 0.93. While no estimate was made of the variation in red or blue CL intensity, the simple two-fold classification showed a good correlation with the minor element levels. For both enstatites, the FeO levels were essentially identical, while for all other elements except Na red enstatite showed consistently higher levels than blue enstatite. No conclusion can be drawn as to what element (if any of those analyzed) causes the difference in CL color because of strong geochemical correlations, but the higher Mn of the red grains is consistent with the observations noted above that red CL is associated with Mn. In contrast to these observations, Cr and Mn data for enstatite of another enstatite chondrite (14) were shown to bear no unique relation to the visually estimated CL color. These different observations might be explained in several ways including: the limitation of visually determined color, enstatite in different meteorites being different, or a selection of different types of enstatite in the two studies.

To obtain a quantitative measure of the CL intensity of individual CL emissions, an optical multichannel analyzer was coupled to the optical system of an electron microprobe allowing simultaneous collection of CL spectra and minor element data from a single point (Steele, I.M. *Meteoritics*, submitted). For CL spectra obtained with a 15 kV focused beam, enstatite from both enstatite chondrites and achondrites showed three distinct peaks (Fig.1) centered at about 742, 664, and 483nm. To allow assignment of these peaks, spectra from synthetic Mn and Cr doped enstatite are shown in Fig. 2 and the emissions from these two samples closely match the two red peaks of meteoritic enstatite; neither synthetic sample shows a blue peak. The peak positions of Cr and Mn are not constant for different meteoritic enstatites and are not the same as for the Cr and Mn doped standards. The variation is about 20nm

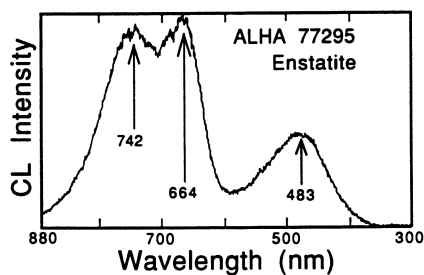


Figure 1. Typical CL spectrum from enstatite in the enstatite chondrite ALHA 77295. Peak positions for this and other spectra are estimated by eye and the spectra are not corrected for instrumental transmission.

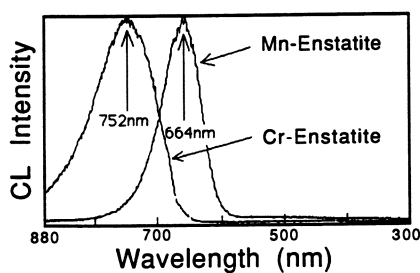


Figure 2. Cathodoluminescence spectra from synthetic Cr- and Mn-doped enstatite.

and might be explained by site occupancy of the Cr, the higher Cr level in the synthetic samples or other structural differences. This variation in peak position among meteoritic enstatites may carry additional information regarding details of the structure. The Cr peak of the synthetic Cr enstatite is well into the infrared but the sample shows visual red CL, and because the intensity-concentration relation is not known, the red CL of enstatite is a function of both Cr and Mn (Steele, I.M. *Meteoritics*, submitted). For enstatite of the Cumberland Falls enstatite achondrite, there is a very good positive correlation between Mn and the intensity of the peak near 664nm (Steele, I.M. *Meteoritics*, submitted), but because Cr correlates positively with Mn, both elements actually show this correlation with CL. The correlation of Cr concentration with the peak near 742nm is not yet proved and would require a study using peak deconvolution techniques to extract the Cr intensity from spectra such as shown in Fig. 1. In the natural samples the blue peak is conspicuous but no correlation with any element determined with the electron probe (Na, Al, Ca, Ti, Cr, Mn, Fe) has been found. Its intensity is highest for the points with the lowest total minor element content but because of the strong correlations between elements due to geochemistry this may have little significance.

The apparent discrepancies (11,14) in the correlation of visible CL color with minor element concentration points to difficulties in interpreting and comparing CL data. In this case the FeO content ranges from 0.1 to 1.5 wt% (14) and, although the quenching effect is not known, data for forsterite (see later) show that the blue peak will be quenched at lower values of Fe than the red. Moreover, the two red peaks may be affected differently. Thus color is a function of several variables and a good correlation between any two can not necessarily be expected. Other effects might be significant including the optical transmission and detection of the near infrared light from Cr. The CL, however, can provide spatial chemical data either qualitatively through observation or quantitatively. Spectra such as that illustrated in Fig. 1 can be collected in several seconds and using a calibration of CL intensity vs Mn (or Cr), a compositional map at these low levels can be obtained much faster than with a microprobe.

Feldspar Unlike enstatite and forsterite, feldspar is present in most meteorites. The meteoritic feldspars are dominated by plagioclase which are those feldspar compositions in the continuous solid solution series ranging from albite ($\text{NaAlSi}_3\text{O}_8$) to anorthite ($\text{CaAl}_2\text{Si}_2\text{O}_8$); compositions near the ends of this series are most common. The earliest CL studies of feldspar were prompted by the lunar program about 1970 and a series of papers compared the CL of lunar, meteoritic and doped synthetic plagioclase. Later observations were made for anorthite in the carbonaceous chondrites.

Because most work has been done on lunar samples and because some meteorites originate from the Moon and some processes affecting both types of sample are similar, a brief description is given of these observations. The CL spectra are dominated by two bands centered near 450 (deviation of +16 to -20nm) and 559nm (deviation of +16 to -6.5nm), while a peak near 730nm (deviation of +20 to

-20nm) found in terrestrial plagioclase is only rarely present, and only weakly (17). Like lunar plagioclase, plagioclase from the basaltic achondrite meteorites (eucrites) has no CL emission at 730nm (16,17). For meteoritic plagioclase which shows shock damage, CL shows broader, less intense peaks with the 559nm peak shifted to longer wavelengths (15,17). For lunar (15) and meteoritic maskelynite only a broad featureless band of CL is present. Using proton bombardment of lunar plagioclase, two bands at 450 and 560nm and a very weak peak at about 770nm can be observed (16). The 560nm peak was attributed to Mn at the several hundred ppm level, and based on circumstantial and weak compositional data it was suggested that the Mn is probably substituting in the Ca site (16). Meteoritic plagioclase does not show a 770nm peak (16), and the 450nm peak is attributed to a lattice defect common to most silicates (8,16). The peak often seen near 780nm is reported to be due to Fe³⁺ in the Ca site (18) and is usually absent or very weak due to the lack of Fe³⁺ in meteorites and on the Moon. For synthetic plagioclase doped with Mn and Fe³⁺, the assignments of the 560nm and 770nm peaks were confirmed (19).

Within carbonaceous chondrites some spherical (chondrules) and other irregular (aggregates) features are present and are characterized by a refractory mineralogy dominated by calcium, aluminum, magnesium, titanium and silicon. The main minerals are melilite, anorthite, spinel, and fassaite. It was recognized that this type of mineralogy is consistent with condensation from a gas of solar composition (20) and intensive study on these objects has been made to derive possible processes operating in the nebula. It was recognized that samples of these high temperature inclusions contained excess ²⁶Mg (21) and it was postulated that this magnesium was derived from the decay of ²⁶Al very early and that the ²⁶Al entered the mineral structure and decayed *in situ* (22). The recognition of the site of excess ²⁶Mg and its correlation with total Al would show that these inclusions had not been appreciably altered since formation and would provide evidence for a time scale for the formation of these inclusions relative to the production of ²⁶Al.

The anorthite within these inclusions was an excellent candidate for searching for a relation between Mg and Al as the Al/Mg ratio is very high and excess ²⁶Mg could be easily detected since non-radiogenic Mg is at the 500ppm level. Examination of polished sections of these inclusions using a CL microscope showed that most phases had brilliant CL and in particular the anorthite had extraordinary textures within single crystals as revealed by CL (23). All plagioclase shows blue CL but within single crystals the intensity ranges by a factor of about 5 with generally sharp, straight boundaries suggesting crystallographic control (see 23 for color photographs illustrating these features). These variations are superposed on the normal twinning of plagioclase. Using color CL photographs as a guide, electron microprobe analyses for points showing different blue intensities within one crystal showed a qualitative negative correlation between Mg and CL intensity, as well as between Na and CL intensity, i.e. the brightest CL areas had the lowest Mg and Na (23). The range in Mg concentration was about a factor of 5 (200-1000ppm) for the extreme CL intensities. No

correlation of CL intensity with Ti concentration (<50-340ppm) was observed although Ti was easily detected. This suggests that Ti does not cause CL for these anorthites in contrast to experimental studies on Ti^{+4} (24). Perhaps the Ti is present as Ti^{+3} which may not show CL in anorthite. Magnesium was not considered the cause of the CL but rather had an effect on the intensity possibly through its effect on lattice defects giving rise to the omnipresent 450nm peak described above. The simple observation that the Mg level could be predicted by CL intensity allowed a rather straightforward means to select points with a predictable range of Mg/Al ratios to perform ion microprobe measurements of the Mg isotopic composition. Data obtained from single crystals of anorthite in the Allende meteorite have shown an excellent correlation of excess ^{26}Mg with the Al/Mg ratio and provides the best evidence of the original $^{26}Al/^{27}Al$ ratio and the incorporation of the ^{26}Al into anorthite before substantial decay.

An important observation using visual and photographic CL on these same refractory inclusions was that many of the anorthite grains have undergone alteration since formation of the chondrule (23). This alteration has, in many cases, affected whole grains to the extent that they may no longer have normal extinction under polarized light and appear nearly isotropic. Furthermore, they have numerous embayments filled with very fine-grained minerals, and in some cases show subround cavities filled with coarse grossular garnet and Mg-rich melilite both surrounded by a fine-grained mineral assemblage. With a normal optical microscope, the fine-grained component of these areas does not transmit light but with CL all phases are quite brilliant and details even from the rough surface of the cavity show the mineralogy of the alteration. In addition, the alteration of the anorthite near the cavity or embayed boundaries shows a distinctly lighter blue hue than the rest of the anorthite crystal and clearly shows the limits of the zonal structure typical of progressive alteration. Examples can be found in (23). The significance of this alteration has not been exploited, but the occurrence of the low Mg garnet provides a constraint on the time of alteration because the high Al/Mg ratio of the grossular should allow measurement of the excess ^{26}Mg by ion microprobe techniques and comparison with the same parameter in the parental anorthite. The presence of alteration revealed by CL also serves as a warning that the chemistry of these important materials may have been modified by poorly-known processes; however the alteration mechanism provides a chemical marker at a time early in nebular history. While CL does not directly answer questions concerning the mechanism and timing of alteration, it is an example where in combination with other techniques CL provides a capability to recognize important features and to indicate spatial aspects of features possibly not recognizable by other techniques.

Forsterite Possibly the most common coarse-grained phase present in all carbonaceous and unequilibrated ordinary chondrites, as well as a minor phase in enstatite chondrites and achondrites, is olivine ($(Mg,Fe)_2SiO_4$). Most olivine contains significant Fe and does not show CL; however a small fraction of the olivine is Mg-rich (forsterite) and shows brilliant CL. This same phase is present in

other extraterrestrial samples including deep sea particles, stratospheric dust and Greenland lake sediment all of which may represent degradation products of meteorites, comets or other bodies (25). Indeed a common mineralogical denominator of these materials is luminescing forsterite.

The visual CL color ranges from red to bright blue; individual grains show a color zoning from blue at the center through red to no CL at the edge. The variation is often not gradational but rather shows sharp concentric changes presumably representing changes in growth conditions and consequently minor element concentration in the structure (26,27). Within single crystals the variation in CL color can reveal complex growth textures which can be related to minor element variation. Such textures would be very difficult or impossible to recognize by any other technique but can be seen immediately during observation in a CL microscope and recorded in seconds using scanning CL imaging. In conjunction with backscattered electron images and minor element profiles obtained with the electron probe, the color variation can be correlated with compositional changes.

Cathodoluminescence spectra obtained with an OMA show two distinct emission bands (Fig. 3) centered near 460nm and 760nm (range: 720-780nm). For spectra obtained at lower beam currents (1nA) or with a scanning beam, a third peak appears near 625nm. Using doped synthetic olivines grown both by flux techniques and by Czochralski growth, these peaks closely match those of Cr (740nm), and Mn (625nm) forsterites (Fig. 4). The 460nm peak cannot be assigned with confidence to any doped element and again is most easily explained by invoking a lattice defect (8). The elements causing these peaks parallel observations for enstatite (see above). For synthetic, Mn-doped forsterite the CL emission is persistent and visible for about a second after removal of the electron beam. The wavelengths of the infrared emission are not constant and show a systematic variation depending on the type of meteorite examined (Fig. 5) and (28). The apparent separation of C3-UOC forsterites from forsterites of other extraterrestrial samples provides a means of classifying individual grains. The close match of the cosmic grains (stratospheric samples), Greenland, and deep sea particles with C2 forsterites suggests a genetic relation. The cause of the infrared shift may be related to the site occupancy of Cr in forsterite where two distinct octahedral sites are present; heating experiments which would tend to disorder a distribution may clarify this suggestion.

The variation of CL intensity and its relation to the growth of forsterites in meteorites requires a detailed study of the chemical variation and the observed CL. Numerous line scans were described (Steele, I.M. *Geochim. Cosmochim. Acta*, accepted for publication) where spectra and composition were obtained at the same point for forsterites in the Ornans (C3) carbonaceous chondrite. Interpretation is complicated by the fact that some elements are strongly correlated and the effect on CL can not be attributed to any one element. The most important influence is found to be Fe which had different quenching effects on the blue and infrared CL emissions. The blue emission is effectively quenched for Fe concentrations above 0.75 wt.% FeO while the infrared emission is

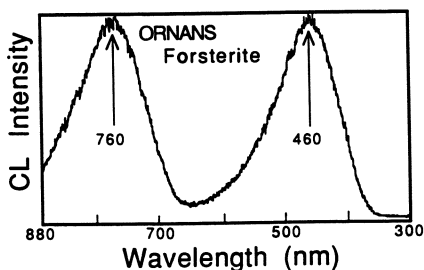


Figure 3. Representative CL spectrum of forsterite from Ormans (C3) carbonaceous chondrite.

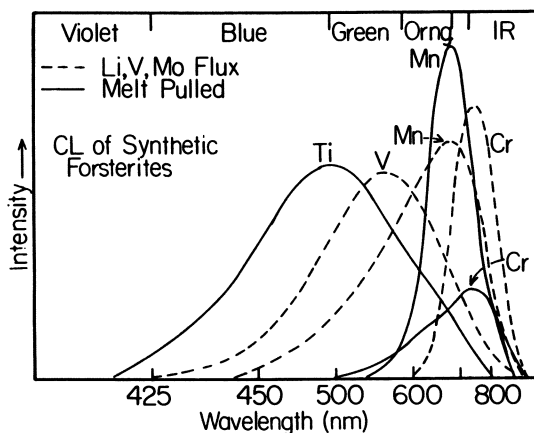


Figure 4. Spectra for a variety of synthetic flux grown and melt pulled forsterites. For both, the positions of the Cr and Mn emissions match closely those of meteoritic forsterites.

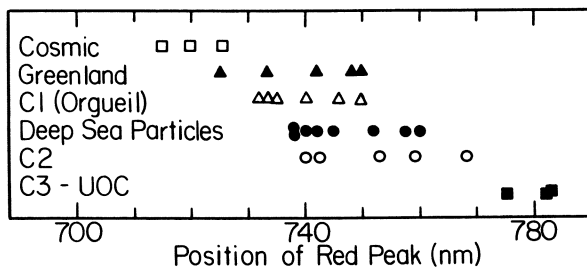


Figure 5. Range of the Cr CL peak position for extraterrestrial forsterites. The separation of forsterites of C3 carbonaceous chondrites and unequilibrated ordinary chondrites from the other types suggests that single grains can be assigned to one of the two groups.

not quenched until FeO reaches 2.0 wt.%. The central portion of the forsterites appear blue because the visible blue dominates over the infrared. Because the forsterites show Fe zoning from 0.25-0.5 wt.% FeO in the core to over 20 wt.% at the rim and a near-constant Cr concentration of 0.1 wt%, the blue emission disappears when FeO reaches 0.75 wt.%. At this point the infrared has sufficient intensity in the visible to give the red color. When the FeO reaches 2.0 wt.% the infrared emission is quenched and there is no CL from that point to the rim.

These CL observations permit rapid recognition of important compositional and growth features within the forsterite grains and have led to conclusions (not all universally accepted) regarding their origin. The visual CL allows rapid estimation of the Fe levels especially at the two concentration boundaries where color changes rapidly. Thus internal morphology can easily be recognized and from visual observation of many grains it was concluded that most olivines have grown unimpeded (26,27, Steele, I.M. Geochim. Cosmochim. Acta, accepted for publication; all show monochrome renditions of CL intensity in forsterites) which led to the suggestion that they result from vapor growth in the gaseous nebula. Most of the mm-sized features, or chondrules, in the chondritic meteorites are Fe-rich and when observed with CL it is apparent that many have a small proportion of grains that are nearly pure forsterite which are not in chemical equilibrium with the Fe-rich grains. This suggests that the forsterite grains acted as nuclei around which the chondrules rapidly grew preventing the forsterite from reacting. However examples can be found where the forsterite has partially reacted as shown by diffuse and irregular CL boundaries. Within single crystals the uniform, blue-luminescing cores represent growth from a homogeneous reservoir but at some time conditions changed rapidly resulting in rapid Fe enrichment present in all forsterite grains irrespective of meteorite type or meteorite. This point marks a nebular-wide event. A significant observation (Clayton, R.N., pers. comm, 1988) is that chondrules with blue luminescing grains are enriched in ^{16}O and one possibility is that the blue luminescing grains are the carriers of an ^{16}O enriched isotopic composition recognized in bulk meteorite samples (29). If this proves to be true, CL observations provide a simple means of recognizing material which may have its origin outside of our nebula.

Other Minerals Up to this point, reference has been made to other luminescing phases within meteorites but in all cases no systematic studies have been reported to: 1) determine the cause of the CL; or 2) to relate the CL to the genesis of the mineral or meteorite. The following comments are made to draw attention to the possible significance of CL observations in other meteoritic minerals; most observations are from the author's personal experience and have not been documented. Oldhamite is a rare mineral in the enstatite chondrites but is known to carry appreciable quantities of rare earth elements (REE). The CL spectra have not been studied in detail but visual CL is yellow and a CL emission at 580nm was reported (5) but with rapid intensity change under the electron beam. A REE activator of the CL is possible. Hibonite is a relatively common

phase occurring in the high temperature inclusions described above. It shows two luminescence colors which can be correlated with the TiO_2 level: blue when TiO_2 is about 0.7 wt.%; orange when TiO_2 is about 7 wt.% (30). Details of the spectra are not known. Melilite also occurs within the high temperature inclusions and shows deep blue CL for the Ca-rich compositions with progressively weaker intensity as aluminum is replaced by Mg and Si. Because crystals are zoned from a Al-rich core to a Mg-, Si-rich rim, the visual CL provides a excellent indicator of zoning; no spectral details have been reported. Spinel is a common phase in the high temperature inclusions and shows red to orange CL (23) but rare, yellow luminescing grains are present. Preliminary examination of CL spectra shows at least six, evenly-spaced sharp peaks but their intensity has not been correlated with composition although several weight percent Fe is sufficient to quench the CL. Particularly interesting is the occurrence of two luminescing varieties (red and very dull) included within single crystals of silicates. This poses a problem as to their origin in that it suggests two sources. Corundum is a very rare phase within the carbonaceous chondrites but it shows brilliant, blue CL. It is usually intergrown with hibonite and, in one case a third phase, with a distinctly different blue CL peak and a composition near CaAl_2O_3 , i.e. intermediate between hibonite and corundum. Grossular garnet occurs associated with anorthite as an apparent alteration product. It shows yellow CL but no details have been reported. Fassaite within the high temperature inclusions does not show CL but rare grains at the boundaries of chondrules do luminesce (23); again no details are known. Diopside in the enstatite achondrites shows yellow to pale green CL and provides easy recognition; no details of spectra are known.

One of the most common phases in meteorites is glass which is interstitial to grains, fills cracks penetrating into discrete features, or forms a matrix from which crystals have grown. These glasses all show blue CL of which the intensity increases as the meteorite is affected by thermal processes. A good correlation has been demonstrated with thermoluminescence as a recorder of thermal effects as discussed elsewhere in this volume (Sears, DeHart and Hasan).

Of the minerals for which brilliant CL is known for terrestrial occurrences, diamond is possibly the most interesting. Some meteorites (ureilites) carry fine-grained diamonds and lonsdaleite both of which show brilliant CL (32); however, recent observations have recognized minute diamonds which carry extraordinary isotopic compositions (31) within carbonaceous chondrites. These diamonds are concentrated by dissolving associated phases producing a small volume of residue. The recognition of diamonds within this residue has been made using electron diffraction but might be as easy with CL if the spectrum is definitive. Likewise a search for *in situ* diamond occurrences in meteorites might be possible especially if the diamonds occur concentrated in clusters. Moissanite from carbonaceous chondrites has been concentrated by techniques similar to those used for diamond, and has also been shown to carry extraordinary isotopic compositions. These grains are up to 10 microns in the largest dimension, and because terrestrial SiC shows CL, *in situ* grains might be found using CL observation.

Acknowledgments

Financial support was derived from NASA NAG 9-47 (J.V. Smith) and instrumental support through NSF EAR-8415791 and NSF EAR-8608299

Literature Cited

1. Smith, J.V.; Stenstrom, R.C. J. Geol. 1965, **73**, 627-35.
2. Long, J.V.P.; Agrell, S.O. Mineralog. Mag. 1965, **34**, 318-26.
3. Nickel, E. Minerals Sci. Engng. 1978, **10**, 73-100.
4. Derham, C.J.; Geake, J.E. Nature 1964, **201**, 62-3.
5. Derham, C.J.; Geake, J.E.; Walker, G. Nature 1964, **103**, 134-6.
6. Geake, J.E.; Walker, G. Geochim. Cosmochim. Acta 1966, **30**, 927-37.
7. Reid, A.M.; Bunch, T.E.; Cohen, A.J.; Pollack, S.S. Nature 1964, **204**, 1292-3.
8. Hanusiak, W.M.; White, E.W. Scanning Electron Microscopy 1975, 125-31.
9. Geake, J.E.; Walker, G. Proc. Roy. Soc. London 1967, **296**, 337-46.
10. Reid, A.M.; Cohen, A.J. Geochim. Cosmochim. Acta 1967, **31**, 661-72.
11. Leitch, C.A.; Smith, J.V. Geochim. Cosmochim. Acta 1982, **46**, 2083-97.
12. Leitch, C.A.; Smith, J.V. Nature 1981, **290**, 228-30.
13. Leitch, C.A.; Smith, J.V. Nature 1980, **283**, 60-1.
14. McKinley, S.G.; Scott, E.R.D.; Keil, K. J. Geophys. Res. 1984, **89** suppl., B567-72.
15. Sippel, R.F.; Spencer, A.B. Proc. Apollo 11 Lunar Sci. Conf., 2413-26.
16. Geake, J.E.; Walker, G.; Mills, A.A.; Garlick, G.F.J. Proc. Second Lunar Sci. Conf. 1971, 2265-75.
17. Sippel, R.F. Proc. Second Lunar Sci. Conf. 1971, 247-63.
18. Geake, J. E.; Walker, G.; Mills, A. A.; Garlick, G.F.J. Proc. 3ed Lunar Science Conf. 1972, 2971-79.
19. Geake, J.E.; Walker, G.; Telfer, D.J.; Mills, A.A.; Garlick, G.F.J. Proc. Fourth Lunar Sci. Conf. 1973, 3181-89.
20. Grossman, L. Geochim. Cosmochim. Acta 1972, **36**, 597-617.
21. Gray, C.M.; Compston, W. Nature 1974, **251**, 495-7.
22. Lee, T.; Papanastassiou, D.A.; Wasserburg, G.J. Astrophys. J. 1977, **211**, L107-10.
23. Hutcheon, I.D.; Steele, I.M.; Smith, J.V.; Clayton, R.N. Proc. Lunar Planet. Sci. Conf. 9th 1978, 1345-68.
24. Mariano, A.N.; Ito, J.; Ring, P.J. Geol. Soc. Amer. Abstracts with Program 1973, **5**, 726.
25. Steele, I.M.; Skirius, C.M.; Smith, J.V. Nature 1985, **313**, 294-7.
26. Steele, I.M. American Mineral. 1986 **71**, 966-70.
27. Steele, I.M. Geochim. Cosmochim. Acta 1986, **50**, 1379-95.
28. Steele, I.M. 49th Annual Meteoritical Society Meeting (abstract) 1986, J-11.

29. Clayton, R.N.; Grossman, L.; Mayeda, T.K. Science 1973, 182, 485-8.
30. Keil, K.; Fuchs, L.H. Earth Planet. Sci Lett. 1971, 12, 184-90.
31. Lewis, R.S.; Ming, T.; Wacker, J.F.; Anders, E.; Steel, E. Nature 1987, 326, 160-2.
32. Berkley, J.L.; Brown, H.G.; Keil, K.; Carter, N.L.; Mercier, J-C.C.; Huss, G. Geochim. Cosmochim. Acta 1976, 40, 1429-37.

RECEIVED March 21, 1989

Chapter 9

Energy-Storage Mechanisms and Thermoluminescence Processes in Minerals

Stephen W. S. McKeever

Department of Physics, Oklahoma State University,
Stillwater, OK 74078-0444

The paper discusses mechanisms by which energy is stored in minerals following the absorption of ionizing radiation, and is subsequently released during heating to produce thermoluminescence (TL). It is discussed how the primary processes of defect formation during irradiation occur via electronic excitation. This can take the form of either the creation of electron-hole pairs, followed by trapping into localized energy states, or of exciton creation leading to the formation of stable vacancy and interstitial defects. Heating the sample after the irradiation causes the release of this stored energy in the form of phonons or photons. Photon emission, i.e. luminescence, results from either electron-hole recombination or from vacancy-interstitial recombination. Several examples of both types are discussed for crystalline CaF_2 and SiO_2 .

In this paper we shall be concerned with those luminescence processes which occur following the absorption of ionizing radiation in some common minerals. In particular, we shall be looking at those processes by which energy from the radiation field is absorbed and stored by the material, and at those processes which result in the emission of visible light from the material as it is then heated (thermoluminescence, TL). For illustration of some of the primary processes involved in these mechanisms we shall use CaF_2 , as an example of a fluorite-structure material, and crystalline SiO_2 (quartz). Both of these materials have significant mineralogical importance. Additionally, we shall occasionally refer to alkali-halide-structured materials, e.g. halite (NaCl) to illustrate some of the important principles.

0097-6156/90/0415-0166\$06.00/0
© 1990 American Chemical Society

Energy Storage Following Irradiation

Electronic Excitation. The storage of energy in an insulating material by the absorption of ionizing radiation occurs via two major processes, namely, electronic excitation and displacement damage. Radiation damage by these processes in insulators has been a topic of intense research for decades and several excellent review articles already exist concerning a variety of material types (eg. oxides (1-5), alkali halides (6-8) and fluorites (9)). It is relevant to ask what is the relative importance of the above two processes at producing radiation damage and thereby storing energy? To answer this we use SiO_2 as an example material and use the arguments of Devine (10) who notes that ^{60}Co gamma photons when absorbed in SiO_2 produce primary Compton electrons of energies of about 1MeV. The threshold for displacement damage in SiO_2 is approximately 150eV and therefore one expects about 4×10^{10} displaced oxygens, per Gy of absorbed dose, per cm^3 . Assuming that only 1/40 of these produce stable defects, this gives an expectation of about 10^9 displaced oxygens per Gy per cm^3 . However, one actually gets approximately 10^{11} per Gy per cm^3 , or two orders of magnitude more defects than expected. The additional defects have come from electronic excitation and most defect formation occurs via this process following absorption of energetic photons.

Further evidence for the importance of electronic excitation as a primary means of defect creation comes from studies of "sub-threshold" damage in which the energy of the incoming particle is less than that required for a "knock-on" collision. Defect formation, sputtering and desorption of surface adsorbates all occur and these are all processes which require coupling of the electronic energy into the lattice (11).

As a result of these considerations, we shall concentrate in this paper on defect formation by electronic excitation only. Energy storage via electronic excitation can be further sub-divided into two categories - electron-hole pair production and exciton creation. With both of these electronic entities, it is important to realize that their wavefunctions are not localized on any particular defect and they are therefore free to wander throughout the lattice immediately after irradiation. As a result of this significant energy migration may take place before these entities are localized, or 'trapped', at particular lattice sites. For example, exciton lifetimes of microseconds to milliseconds can be found and in some materials migration distances of the order of millimeters can occur before exciton annihilation (via recombination). In order to store energy of these defects, therefore, it is necessary to first of all localize the wavefunctions at lattice sites. We now deal with each of these electronic species in turn in order to see how this is done.

Electron-Hole Pairs. Localization of electrons and holes occurs via the processes of non-radiative charge trapping. These processes are represented phenomenologically in Figure 1. An example of a simple trapping process is the coulombic attraction of an electron and an

X^- ion vacancy in a material of the type M^+X^- and the processes of non-radiative charge trapping have been discussed in depth by Henry and Lang (12) and by Pässler (13).

With reference to Figure 1, the absorption of a photon with energy greater than the band gap results in the creation of a free electron and a corresponding free hole. These charges move independently throughout the crystal until they become localized at suitable trapping sites. Each charge may undergo several trapping and de-trapping cycles before being localized at a center in which the binding energy of the trapped charge is greater than about 25kT. Under these circumstances the charges become localized and this gives rise to a non-equilibrium population of trapped charge in metastable energy levels (ie. trapped electrons in energy states above the equilibrium chemical potential (Fermi level) and trapped holes states below the Fermi level). The energy levels in question arise from the presence of lattice disorder within the material, such as foreign ions, lattice vacancies, dislocations, etc. Such lattice disorder is a prerequisite for charge storage in this manner.

Excitons. Localization of the excitons occurs via the process of 'self-trapping' to produce so-called 'Self-Trapped Excitons' (STE). For a description of STE's we refer to Figure 2 in which are sketched three typical configurations for STE's in an M^+X^- crystal. Toyozawa (15) discusses the formation of STE's in which the electron and hole are localized concentrically (STE 1 and STE 2) or eccentrically (STE 3). In types 2 and 3 the hole is trapped on an X_2^- molecule and the strong coulombic repulsion between it and the trapped electron make this type of STE highly unstable.

In halite-structure materials both STE 2 and STE 3 form, with type 2 converting into type 3 via the process depicted in Figure 3. The coulombic repulsion induces motion of the X_2^- molecule along a close-packed $\langle 110 \rangle$ direction. This initiates a displacement sequence which, as we will see later, is of fundamental importance in the formation of stable interstitials and vacancies.

In fluorite-structure compounds the self-trapped exciton configuration is that of type 3, as depicted in Figure 4. Here it should be noted that the X_2^- molecule is aligned along a $\langle 111 \rangle$ direction which is not a close-packed direction in the CaF_2 structure. In SiO_2 eccentric (STE 3) excitons are also formed in which the electron is localized in an oxygen vacancy, forming an E_1' center, and the hole is localized on adjacent oxygens forming an O_2^- molecule, or peroxy radical (see Freund's paper in this publication).

The next stage in the defect formation process involves the transfer of energy from the electronic excitation to the lattice. Although the exact details of the necessary excited states which induce the instability are the subject of some controversy, it is known that the basic cause of the transformation is the coulombic repulsive interaction between the electron and the X_2^- molecule. It appears that there is strong coupling between the electron in an excited state and the hole, also in an excited state. The instability manifests itself by motion of the X_2^- molecule in the $\langle 110 \rangle$ direction (in M^+X^- crystals). The X_2^- molecule can be

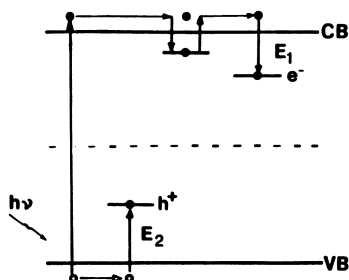


Figure 1. Phenomenological model of electron-hole pair production and charge trapping following absorption of an energetic photon of energy greater than the band gap.

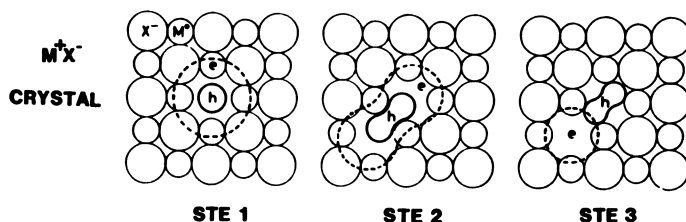


Figure 2. Three typical configurations of Self-Trapped Excitons (STE), named STE 1, STE 2 and STE 3. (Reproduced with kind permission from Ref. 14. Copyright 1986 Gordon and Breach.)

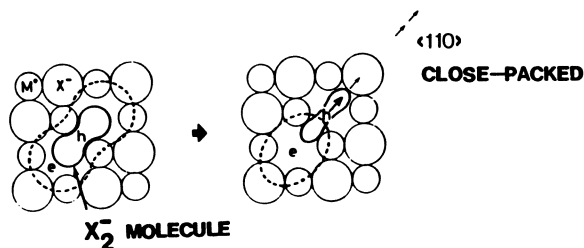


Figure 3. Transformation of STE 2 into STE 3 in M^+X^- crystals (eg. halite). (Reproduced with kind permission from Ref. 14. Copyright 1986 Gordon and Breach.)

separated from the electron by several lattice spacings in a matter of several picoseconds (11,13) and in this way the electronic excitation energy is transferred directly to the lattice.

It is important to note that in the halite-structure materials the displacement sequence is along a close-packed direction enabling momentum transfer to occur such that the interstitial becomes separated from the vacancy by several atomic positions. In the fluorite-structure compounds and in crystalline SiO_2 , however, such a displacement sequence is not possible since the STE is not aligned along a close-packed direction. As a result stable, well-separated interstitials and vacancies are very unlikely in these materials at all but the very lowest temperatures. Transient defect formation only is observed (9,16).

In the discussion so far we have neglected to mention any effects due to lattice disorder. This will surely be of major importance in mineralogical materials. We have noted how, in the alkali halides, stable interstitial atoms ($\underline{\text{H}}$ -centers) and electrons in vacancies ($\underline{\text{F}}$ -centers) may be formed, even in a perfect crystal, whereas in CaF_2 and quartz only transient defects are formed, with interstitial-vacancy recombination occurring rapidly. If lattice disorder (structural imperfections, polycrystallinity, amorphous structure, impurities) is introduced into the system the interstitials and vacancies may be stabilized by these entities forming 'perturbed' $\underline{\text{H}}$ - and $\underline{\text{F}}$ -centers. Such perturbed centers may be formed, for example, if the mobile X_2 molecule becomes trapped by (say) an impurity, thus preventing interstitial/vacancy recombination. Recalling that the exciton is a highly mobile species before it becomes self-trapped, one might even expect that the exciton itself moves through the lattice until it finds a lattice imperfection at which point exciton localization occurs and the defect creation sequence is initiated (17). The net result is that lattice disorder enhances the formation of stable defects following irradiation.

The existence of free interstitial point defects forming the complements to the vacancy centers is generally not observed following irradiation at room temperature. At these temperatures the interstitials cluster together to form interstitial aggregates and dislocation loops. However, lattice disorder can slow down or prevent the aggregation process due to interstitial trapping.

Prompt Luminescence. Before going on to discuss the mechanisms by which the stored energy can be released from the lattice we shall pause here to discuss what happens to the electronic excitation energy if it is not stored in the lattice by any of the mechanisms discussed above. In wide-band-gap insulators such as those discussed here direct band-to-band recombination of electrons with holes is not generally observed and indirect, Shockley-Read recombination via localized states in the band gap is the main cause of electron-hole recombination. The recombination process results in the emission of phonons or photons. Since we are interested in luminescence emission in this paper it is the emission of photons that we shall consider. The emission wavelength can be characteristic of the position (in terms of energy) of the localized state within the band gap, or via the process of energy transfer, it may

be a property of the type of defect which gives rise to the localized state. For example, recombination states arising from the presence of rare-earth impurities often result in line emissions which are characteristic of those ions. The details of the emission can often give information about the exact structure of the site in which the ion is located. (See Wright's paper elsewhere in this publication.) Once again we see that lattice disorder is required for prompt emission from electron-hole recombination.

For excitons, the electron and hole can annihilate each other with emission wavelengths which are a property of the particular excited states of the exciton and the local lattice environment. For example, "intrinsic" luminescence due to exciton annihilation in pure NaCl is at 250nm (low-energy triplet state) and 370nm (high energy singlet state) (18). In CaF₂ the intrinsic emission appears at 280nm (9), while in SiO₂ it is at 440nm (16). With the introduction of impurities the intrinsic luminescence becomes perturbed. For example, in NaCl perturbed triplet-state emissions appear at 440nm and 424nm, depending on the identity of the perturbing impurity (18). Similarly, impurity-perturbed exciton annihilation emissions occur in CaF₂ at approximately 290nm (19).

Thermally Stimulated Energy Release: Thermoluminescence (TL)

Electron-Hole Recombination. A phenomenological representation of an electron-hole recombination process is shown in Figure 5. For illustration we assume that it is the electron that is the thermally-freed carrier although the discussion could just as well proceed on the basis that the hole is thermally liberated.

The process begins when phonon coupling with the lattice enables the trapped electrons to absorb an amount of thermal energy kT . The probability that this energy will surmount the potential energy barrier E is then $p = s \exp[-E/kT]$, where s is a constant related to the lattice vibration frequency and the entropy change associated with the reaction. At a suitably high temperature the trapped electron will be liberated into the conduction band and be delocalized. Recombination with trapped holes can then take place and light may be emitted in a similar fashion to that described in the previous section. As a result we have the thermally stimulated return of the system from its metastable state to its equilibrium state, with the excess energy liberated as light. Not all such recombination processes are radiative, of course, but, as with prompt luminescence, we are interested here only in those processes that lead to luminescence.

There are many examples of this simple process in a wide variety of materials. For illustration we discuss here the TL emission that occurs at approximately 100°C in SiO₂ following the absorption of ionizing radiation at room temperature. The emission is characterized by two, overlapping, broad bands, peaking at 470nm and 380nm (Figure 6). The picture that has emerged from a detailed study of this TL peak is that during irradiation electrons are trapped at Ge impurities and holes are trapped at Al and H centers, according to:

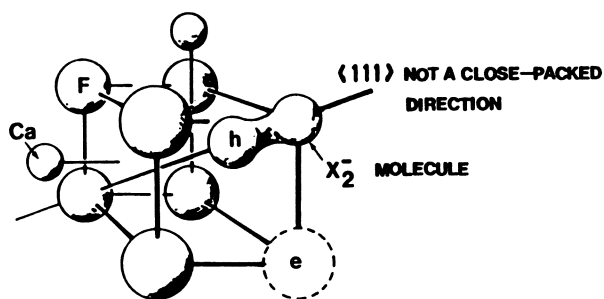


Figure 4. Self-trapped exciton in CaF₂.

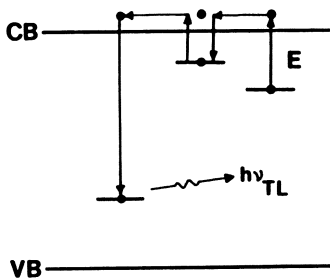


Figure 5. Phenomenological representation of the thermal release of trapped electrons and their recombination with trapped holes to yield TL.

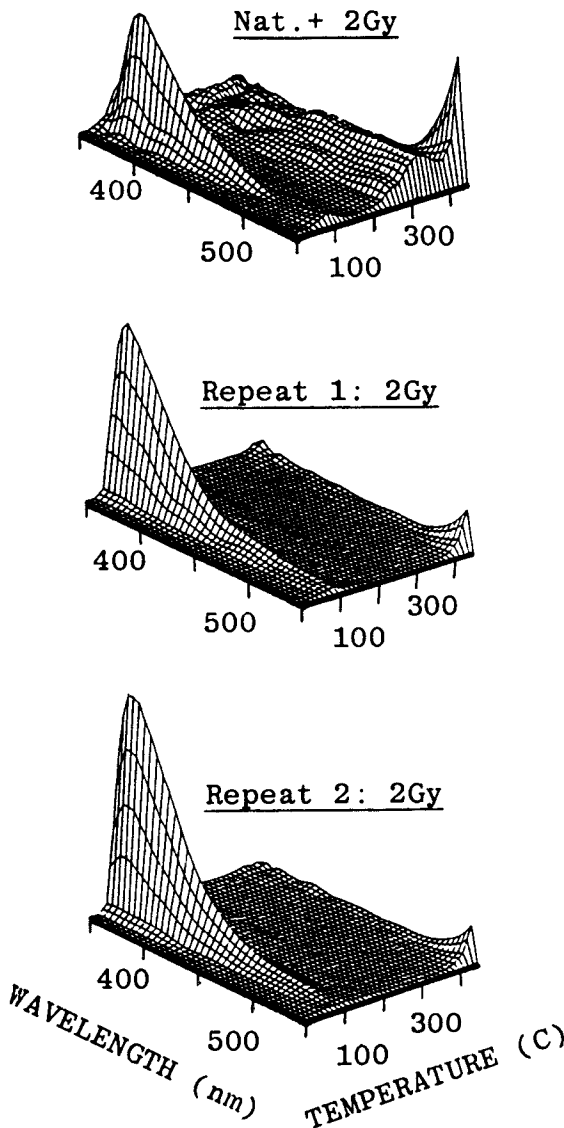
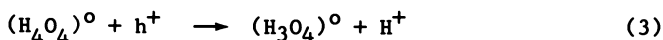
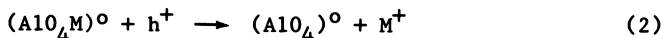
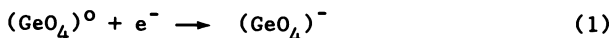
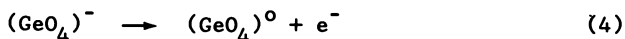


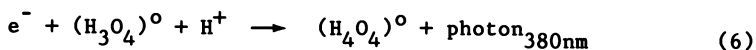
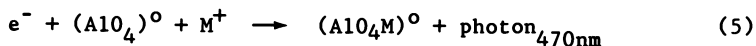
Figure 6. Isometric plot of TL emission versus wavelength versus temperature for a sample of natural quartz. The TL signal is produced via the mechanism described in Equations (1-6). (Reproduced with permission from Ref. 20. Copyright 1988 Pergamon Press.)



where M is an alkali metal, usually Li or Na (21,22). During heating the electron is released thus:

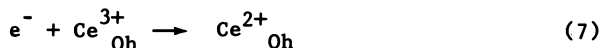


and recombines with the trapped holes to produce TL:

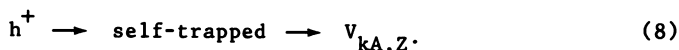


The exact energy states which give rise to the 470nm and 380nm emissions are unknown.

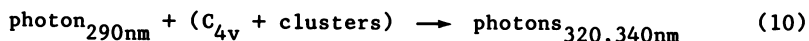
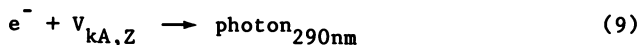
A second example is provided by CaF_2 doped with Ce^{3+} ions. Ce^{3+} enters the CaF_2 lattice substitutionally for the host Ca^{2+} ions. Several site symmetries are possible depending upon the charge compensation. Non-locally compensated Ce^{3+} produces a center of O_h symmetry, whereas C_{4v} symmetry results when F^{-} ions in interstitial positions take up nn positions to the impurities along $\langle 110 \rangle$ directions. In addition many higher-order cluster configurations of these impurity-interstitial pairs exist (23). When irradiated at room temperature the non-locally compensated centers trap electrons to yield Ce^{2+} in O_h symmetry, while the holes become self-trapped producing perturbed V_k centers (24), thus:



and



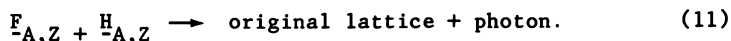
The subscripts A and Z imply a perturbation by monovalent or aliovalent impurities, respectively. Heating the sample stimulates the release of the trapped electrons causing the recombination with the self-trapped holes and emission at 290nm. However, rather than simply producing TL, this emission is strongly reabsorbed by the C_{4v} and cluster centers which have strong absorption bands in this spectral region. This in turn excites the Ce^{3+} impurities into an excited 5d state. Subsequent relaxation to the ${}^2\text{F}_{5/2}$ and ${}^2\text{F}_{7/2}$ ground states yields TL at 320nm and 340nm. Hence in this system we have an excellent example of energy transfer processes occurring during TL production. The reactions may be summarized:



The TL signal that is produced as a result of this reaction is illustrated in Figure 7.

It should be noted that in the above examples significant energy migration can occur between thermal stimulation and recombination since the electron is free to diffuse throughout the sample. Other electron-hole recombination processes occur, however, in which the excited states of the charge carrier are not to be found in the delocalized bands. An example of this, recently noted in the literature, concerns the TL emission from oligoclase feldspar in which the thermal stimulation involves the transition of the electron to a localized, intermediate state - see Figure 8 (25). One consequence of this type of transition is that the defect state is unstable at room temperature, even though the TL signal itself is produced only when the sample is heated to about 280°C (26). This process leads to what is often termed "anomalous fading" (18).

Vacancy-Interstitial Recombination. If stable vacancy and interstitial defects have been created during the irradiation then recombination of these will restore the lattice to its pre-irradiation state, viz:



Here the subscripts A and Z refer to \underline{F} - and \underline{H} -centers perturbed by the presence of monovalent or aliovalent impurity ions, respectively. Unperturbed \underline{F} - and \underline{H} -centers are unlikely in mineralogical materials irradiated at room temperature. This recombination process can take place radiatively, with the emission of a photon. Thus by heating the sample trapped interstitial atoms can be released and recombine with vacancies according to the above description, yielding TL emission. The emission wavelength is characteristic of the nature of the defects taking part in the process, perturbed by the nearby impurities. Thus, the same emission wavelengths as were noted in the section on prompt luminescence can be emitted in this process also, with the exception that the high-energy singlet state emission does not occur. This is a result of the fact that the stable \underline{F} - \underline{H} pair is in a configuration which is higher in energy than the triplet state, but lower than the singlet state (27). Thus triplet-state emission only can be seen in TL processes arising from \underline{F} - \underline{H} recombination.

Often, however, in processes of this nature even the perturbed intrinsic emission does not appear in TL. Instead emission characteristic of an impurity is all that is seen. The interpretation generally placed on this is that the energy is transferred to the impurity. $\text{CaF}_2:\text{Ce}$ provides us with a useful example. In CaF_2 the simple \underline{F} -center is unstable at room temperature and does not form as a product of irradiation. However, when trivalent rare-earth impurity ions are present impurity/vacancy pairs are formed following irradiation. These are of C_{3v} symmetry with the vacancy

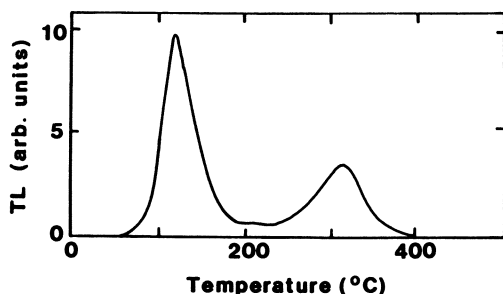


Figure 7. Thermoluminescence from $\text{CaF}_2:\text{Ce}$ following room temperature irradiation. The intense emission at low temperature is caused by electron-hole recombination processes as described in Equations (7-10). The emission at high temperatures is caused by vacancy-interstitial recombination. The spectrum of both emissions is characteristic of Ce^{3+} ions.

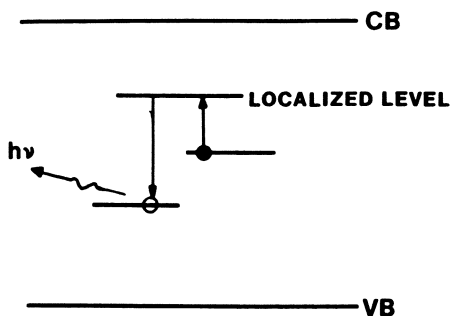


Figure 8. The Localized Transition Model for TL emission from oligoclase feldspar. The TL signal appears near 280°C .

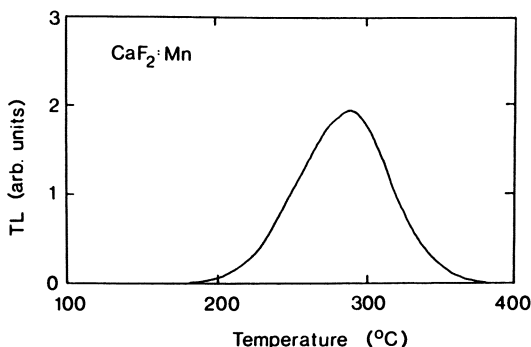


Figure 9. TL emission from CaF_2 containing 3 mol percent Mn. The light is emitted in a broad band peaking at 495nm and is characteristic of Mn^{2+} ions.

being located in a $\langle 111 \rangle$ direction with respect to the impurity and the whole complex having trapped two electrons. The complex can be considered as a divalent impurity with an F-center in a $\langle 111 \rangle$ nn position (28). During heating interstitial-vacancy recombination occurs and this process was recently investigated in Ce-doped CaF_2 (24). In this system, however, it was shown that the perturbed intrinsic emission that results from the recombination was reabsorbed by the Ce C_{4v} centers and clusters of these centers with the consequent emission of the characteristic 320nm and 340nm TL which is associated with Ce^{3+} . The TL emission occurs at about 300°C, as demonstrated in Figure 7.

Somewhat similar mechanisms are believed to occur in Mn-doped CaF_2 . Here the divalent Mn is a poor electron trap but some of our recent (unpublished) examinations of the symmetry of the radiation-induced optical absorption bands in this system lead to the speculation that two Mn^{2+} ions can stabilize an F-center, producing a defect of C_{2v} symmetry. Again, thermally stimulated vacancy-interstitial recombination results in the generation of perturbed intrinsic luminescence but this time this emission is reabsorbed by Mn defects, producing the characteristic Mn^{2+} emission at 495nm (due to a ${}^4\text{T}_{1g}({}^4\text{G})$ -to- ${}^6\text{A}_{1g}({}^6\text{S})$ transition) (29). This yields TL near 300°C (Figure 9). It should be noted that in both the Ce-doped and the Mn-doped samples the TL emission due to vacancy-interstitial recombination is near 300°C, indicating that it is the same trapped species that is becoming mobile in both cases. This is consistent with the view that it is the interstitials that are being released with the vacancy centers forming the recombination sites.

Summary

The discussions in this paper have been intended to highlight the primary mechanisms of both energy storage during irradiation, and the consequent thermally stimulated release of this energy, in materials of mineralogical significance. We have discussed how electronic excitations are the primary mechanisms of energy storage. This occurs via electron-hole pair production and trapping, and via exciton creation, followed by self-trapping, electron-lattice coupling and stable defect formation. These processes are strongly modified by the presence of lattice disorder, particularly in the form of impurities.

The energy may be released by the thermal stimulation of either the trapped electronic charge, leading to electron-hole recombination, or the trapped interstitials, leading to vacancy-interstitial annihilation. In either of these processes photons may be emitted (as TL). Energy migration, owing to the delocalization of the electronic charge and the interstitials, and energy transfer are important processes in the mechanisms of TL production.

The materials which have been chosen in this paper to illustrate various examples of the type of process that can arise all have naturally occurring forms, and are thought to typify the sort of mechanism that one can expect in minerals.

Acknowledgments

The research at Oklahoma State University was sponsored by the National Science Foundation (Grant RII-8610676) and the Naval Surface Warfare Center (Grants N60921-84-M-2714, N60921-85-M-4286 and N60921-85-M-7416).

Literature Cited

1. Hughes, A.E.; Henderson, B. In Point Defects in Solids; Crawford, J. H. Jr.; Slifkin, L. M., Ed.; Plenum: New York, 1972, p 381.
2. Henderson, B. Radiat. Effects, 1982, 64, 35.
3. Crawford, J. H., Jr. J. Nucl. Mater., 1982, 108/109, 644.
4. Fowler, W. B. Semiconductors and Insulators, 1982, 5, 583.
5. Griscom, D. L. Proc. Thirty-Third Frequency Control Conference, 1978, p 98.
6. Itoh, N. In Defects in Insulating Crystals; Tuchkevich, V. M.; Shvarts, K. K., Ed.; Springer-Verlag: Berlin, 1981, p 343.
7. Itoh, N. Radiat. Effects, 1982, 64, 161.
8. Itoh, N. Adv. Phys., 1982, 31, 491.
9. Hayes, W.; Stoneham, A. M. In Crystals with the Fluorite Structure; Hayes, W., Ed.; Clarendon: Oxford, 1974, p 185.
10. Devine, R.A.B. Phys. Rev. Letts., 1989, 62, 340.
11. Itoh, N. Cryst. Latt. Defects and Amorph. Mater., 1985, 12, 103.
12. Henry, C. H.; Lang D. V. Phys. Rev. B, 1975, 5, 989.
13. Pässler, R. Phys. Stat. Solidi B, 1978, 85, 203.
14. Itoh, N.; Tanimura, K. Proc. Third Int. Conf. on Radiat. Effects in Insul., Wilson, I. H.; Webb, R. P., Ed.; Gordon and Breach: London, 1986, p 435.
15. Toyozawa, Y. Physica, 1983, 116B, 7.
16. Tanimura, K.; Tanaka, T.; Itoh, N. Phys. Rev Letts., 1983, 51, 423.
17. Townsend, P.D. Nucl. Instrum. Meth. Phys. Res., 1982, 197, 9.
18. McKeever, S.W.S. Thermoluminescence of Solids, Cambridge University Press, Cambridge, 1985.
19. Beaumont, J.H.; Hayes, W.; Kirk, D.L.; Summers, G.P. Proc. Roy. Soc., 1970, A315, 69.
20. Prescott, J.R.; Akber, R.A.; Robertson, G.B. Nucl. Tracks Radiat. Meas., 1988, 14, 21.
21. McKeever, S.W.S.; Chen, Y.; Halliburton, L.E. Nucl. Tracks, 1985, 10, 489.
22. Yang, X.H.; McKeever, S.W.S. Nucl. Tracks Radiat. Mes., 1988, 14, 75.
23. Catlow, C.R.A.; Chadwick, A.V.; Greaves, G.N.; Moroney, L.M., Cryst. Lat. Def. and Amorph. Mat., 1985, 12, 193.
24. Jassemnejad, B.; McKeever, S.W.S. J. Phys. D: Appl. Phys., 1987, 20, 323.
25. Tyler, S.; McKeever, S.W.S.; Nucl. Tracks Radiat. Meas., 1988, 14, 149.

26. Templer, R.H., Radiat. Protect. Dosim., 1986, 17, 493.
27. Itoh, N.; Stoneham, A.M.; Harker, C.K. J. Phys. C: Sol. State. Phys., 1977, 10, 4197.
28. Staebler, D.L.; Schnatterly, S.E. Phys. Rev. B, 1971, 3, 516.
29. McKeever, S.W.S.; Jassemejad, B.; Landreth, J.F.; Brown, M.D. J. Appl. Phys., 1986, 60, 1124.

RECEIVED February 22, 1989

Chapter 10

Three-Dimensional Thermoluminescence Spectroscopy of Minerals

John R. Prescott¹, Riaz A. Akber¹, and R. K. Gartia²

¹Department of Physics and Mathematical Physics, University of Adelaide, Adelaide 5001, Australia

²Physics Department, Manipur University, Imphal 795003, India

A new application of thermoluminescence (TL) to the study of minerals is described. The intensity of TL light emission as a function of both temperature and wavelength defines a three-dimensional picture which is characteristic of a particular mineral or group of minerals. The apparatus is briefly described together with its application to the study of the physical structure of some alkali feldspars. Examples are given of a K-rich and Na-rich feldspar and a potential method is discussed for identifying the nature of the phases of samples of mixed K/Na composition.

The work described here had its genesis in a project to study thermoluminescence (TL) in a range of feldspars, with the aim of systematising their general characteristics as an aid to TL dating. Some of the results of this study are presented here. For the present work, discussion is confined to the consideration of the information that TL can give about some aspects of physical structure, including microstructure, in the alkali feldspars. Consideration of trapping and luminescence centres will be only incidental to the discussion; and the broader study will be described elsewhere.

The second purpose of the work is to describe the use of three-dimensional (3-D) spectroscopy in which the TL intensity is measured as a function of both temperature and wavelength.

Feldspars

The feldspar minerals are aluminosilicates of alkali and alkali-earth cations and are chemically classified by the mole percentages of three end-members: orthoclase (Or: KAlSi_3O_8) albite (Ab: $\text{NaAlSi}_3\text{O}_8$) anorthite (An: $\text{CaAl}_2\text{Si}_2\text{O}_8$). The three constitute a ternary system with extensive solid solutions along the Or-Ab and Ab-An axes. The nomenclature on the basis of the mole percentages

0097-6156/90/0415-0180\$06.00/0
© 1990 American Chemical Society

of the end-members is shown in Figure 1 which also shows the approximate location of the region of phase stability.

The TL emission spectra of feldspars have been reported in the past by a number of workers (1-6). Recently, measurements of TL emission spectra of feldspars with the help of spectrometers of much increased sensitivity have been reported (7-9). TL spectra presented in this paper are recorded with the help of a new high-sensitivity spectrometer based on Fourier transform spectroscopy.

The 3-D Spectrometer

Apparatus for the study of TL is usually simple in its design and principles (see, e.g., (10)). The sample, prepared either as grains or a slice a fraction of a mm thick, is placed on an electrically heated plate in an inert gas and, as the temperature is raised, the light output is recorded using a photomultiplier.

The graph of TL intensity vs temperature so obtained is known as a "glow-curve". In the present context it is better described as a "2-D glow-curve", the dimensions being intensity and temperature. Understanding of the basic TL phenomena is greatly aided by the information of "3-D glow-curves" i.e., TL emission spectra in which the intensity is displayed as a function of both temperature and wavelength. In this mode, temperature peaks are characteristic of traps and the wavelength peaks carry information about the charge recombination sites (luminescence centres). The advantages of 3-D spectroscopy were reviewed by Levy (11) and further by Jensen and Prescott (12).

The designer of a 3-D spectrometer has to address two challenging problems: the low intensity level, and its variation with temperature and hence with time. It is characteristic of TL measurements that the temperature changes monotonically during observations. Consequently spectral measurements must be made continuously or, in practice, as discrete samples over specified temperature intervals.

The present equipment, based on Fourier-transform spectroscopy, makes use primarily of the so-called "throughput advantage", i.e., the data corresponding to all wavelengths of light are collected simultaneously from an extended source. These characteristics increase the sensitivity for TL emission spectroscopy and have achieved the aim of making it possible to study TL emission phenomena at low radiation levels, comparable with those received by the mineral or phosphor samples during their actual application.

The equipment and its design criteria have been described in detail elsewhere (13). Only its essential features will be described here.

In its basic design, the equipment is similar to a 2-D TL glow-curve system as described previously, but with the addition of a modified Twyman-Green, Michelson type, interferometer between the oven and the photomultiplier. As the sample is heated, the TL signal is recorded while the movable mirror of the interferometer is scanning a given optical path difference in a preset number of steps. The interference pattern corresponding to each one-way scan

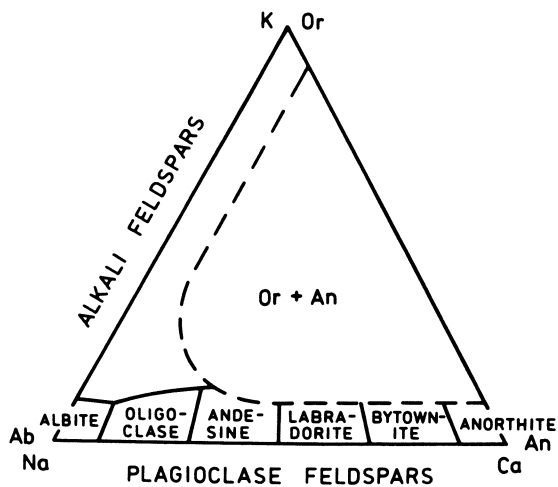


Figure 1. Ternary diagram showing the conventional nomenclature of feldspars.

is called an interferogram. Each interferogram is the Fourier transform of the input spectrum during the corresponding temperature interval and its inverse Fourier transform subsequently yields the spectrum.

Fourier transform spectroscopy is mainly applied to the lower wavenumber or infrared region. Special considerations were required to apply the technique in the visible/UV region. The resolution of the equipment is normally about 20 nm around 500 nm but this offers no serious problem, because in most cases the TL emission is expected to be broad band with full width at half maximum extending up to a few tens of nanometres. The total intensity of the TL light spectrum from the samples varies continuously with temperature, and hence with the mirror displacement, over the sampling time interval. The interferogram is superimposed on this non-constant level. As the Fourier theorem is strictly only valid for constant spectral emission, misleading information (false detail) is produced by the raw interferograms. The interferograms are corrected for this effect. The spectra are further corrected for the spectral response of the equipment in the 350-600 nm range. The calibration is highly stable from day to day but is routinely calibrated under the current operating conditions by interferograms with the 633 nm light from a He-Ne laser. The system has now been upgraded to extend the response to cover 250-740 nm.

The results may be displayed either as an isometric 3-D plot of intensity vs temperature and wavelength or as a contour map. Individual interferograms can also be summed to display a conventional 2-D glow-curve over the full temperature range.

Results

Sixteen samples on the Na-K axis (Figure 1) have been studied. In what follows, only the "natural" TL (NTL) is considered i.e., the TL in the sample "as received" without any prior heating or additional radiation.

High Potassic Feldspars. A high potassic feldspar from Kingston, South Australia, (mole % K:Na:Ca = 81:18:1) represents a typical NTL spectrum for members of this group. Figures 2a and 3a show the 3-D and contour plots respectively. An emission band near 400 nm with FWHM of about 40 nm is prominent in the glow-curve. The NTL peaks occur between 250-350°C followed by another high temperature peak around 500°C.

The Sodic End Members. Figures 2b and 3b show the NTL behaviour of an albite from Amelia, Virginia, U.S.A. which has very low K and Ca content (K:Na:Ca: = 2:98:-). The main emission band is around 560 nm which peaks near 320°C. This broad (in wavelength and temperature) peak is characteristic of low K, low Ca feldspars. There is also a low intensity emission at shorter wavelengths and higher temperatures. The Amelia albite emits two to three times more TL light per mg than the high potassic end-member feldspars and considerably more than those of intermediate composition.

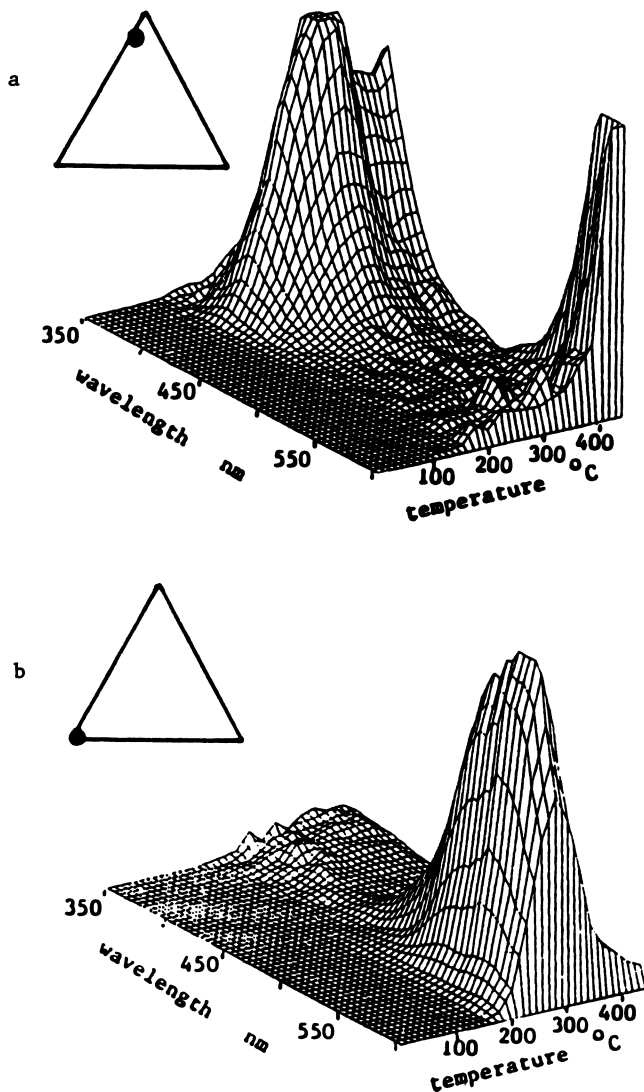


Figure 2. 3-D spectra of alkali feldspars. For each sample, the triangle indicates the mole composition on the ternary diagram.

- (a) Kingston orthoclase
- (b) Amelia albite

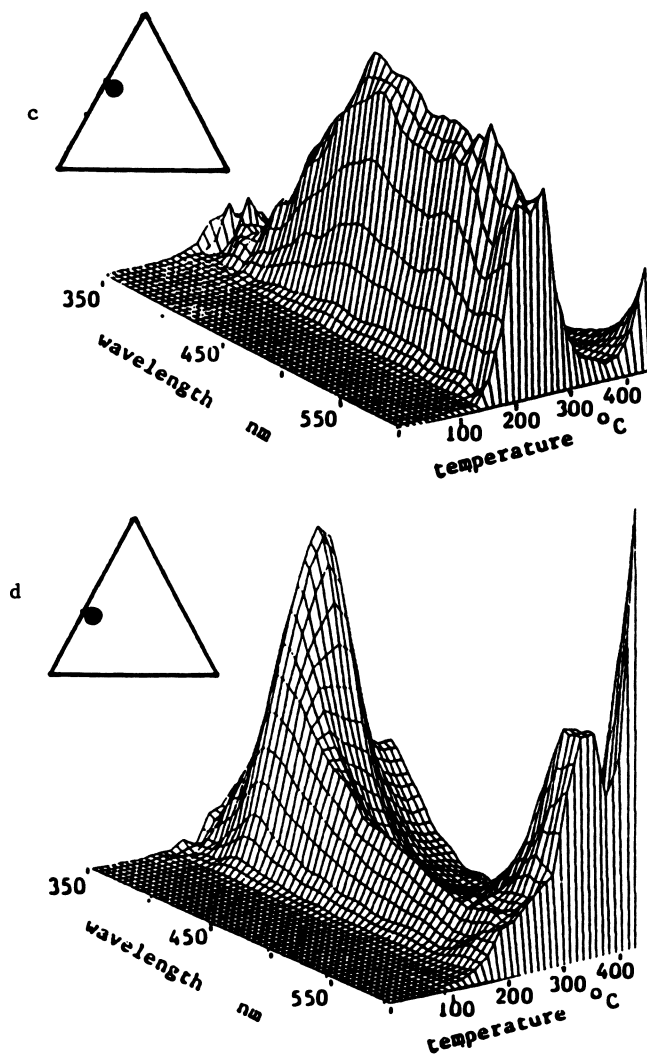


Figure 2. Continued. 3-D spectra of alkali feldspars. For each sample, the triangle indicates the mole composition on the ternary diagram.

- (c) Mount Soma "sanidine"
(d) Wisconsin moonstone

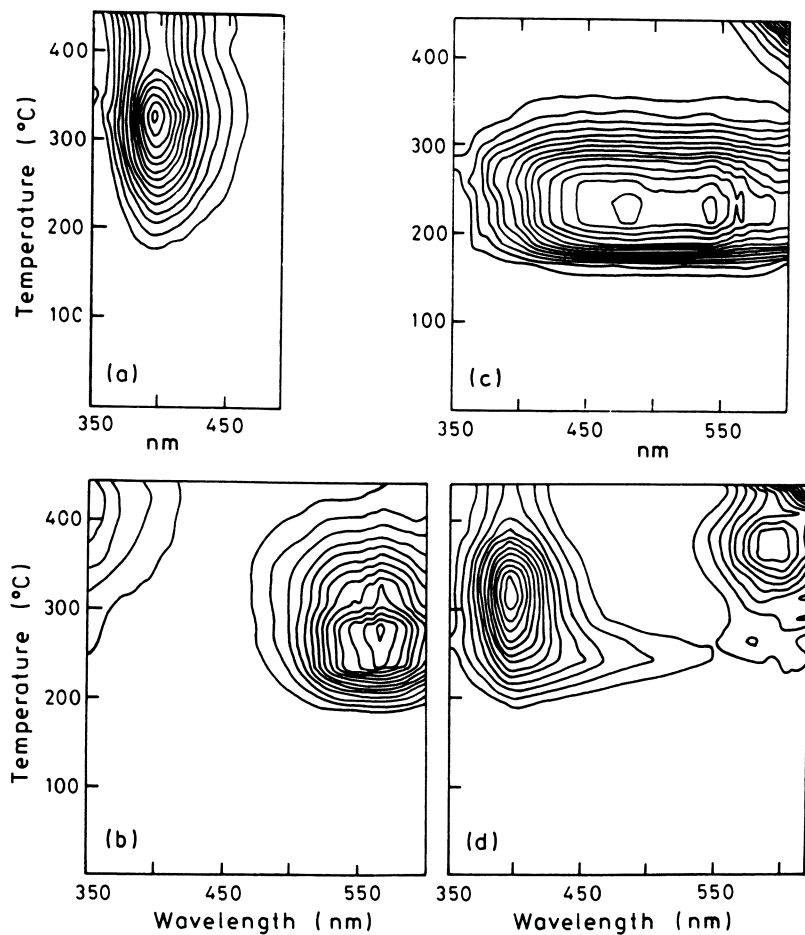


Figure 3. These contour diagrams are for the same samples and occupy the same relative positions as the compounds in Figure 2. (Reprinted with permission from ref. 13. Copyright 1988 Optical Society of America.)

Intermediate Alkali Feldspars. The alkali feldspars with intermediate composition vary in their TL signal when seen in detail. All of them differ significantly as a group from the end members. However, several interesting common features throw light on their overall behaviour. These features suggest a new means for identifying structure, which differs from the traditional optical and X-ray diffraction methods.

The NTL emission spectrum for an intermediate alkali feldspar, a high temperature sanidine from Mount Soma, Italy, (K:Na:Ca = 54:43:3) is shown in Figures 2c and 3c. The spectrum is broad, extending from about 400 to 570 nm, at a temperature of around 250°C, and is likely to be the composite effect of more than one emission band. The 280°C/560 nm peak observed in high sodium feldspars is either absent or appears very little in this or in most other intermediate composition samples. Nor does the 400 nm high-K peak. The samples show TL sensitivity between one to two orders of magnitude less than that of the end members. The broad band extending across the spectrum is present to some degree in all the intermediate samples studied.

TL and Structure. The examples in Figures 2a, b and c typify the three main spectral types in the alkali feldspars. As might be expected, feldspars of intermediate composition show various combinations of these. As an example we consider a moonstone, which is a mixed alkali feldspar. Moonstones derive their name from the diffuse reflection from fine, lamellar, physically separate intergrowths, presumed to be of potassic and sodic end members. Figures 2d and 3d represent the 3-D NTL emission of a moonstone from Wisconsin, USA. The moonstone (K:Na:Ca = 37:58:5) is definitely a physical mixture since it owes its "moonstone" appearance to crystal intergrowths. Comparison of the moonstone NTL spectrum with the other "type" spectra in Figures 2 and 3 reveals that much of the light comes from the high-K component (Figures 2a and 3a). One can also identify a weaker broad band component extending across the spectrum at a temperature around 250°C. This corresponds to a feldspar of intermediate composition such as is shown in Figures 2c and 3c. There is no obvious component corresponding to the Na-rich albite (Figures 2b and 3b) and this suggests that the two intergrowths are orthoclase and intermediate in composition rather than say orthoclase and albite. In addition, in this moonstone there is an emission around 370°C at a wavelength of 590 nm which is not accounted for by the other "type" spectra.

Since the broadband spectrum shown in Figures 2c and 3c is quite distinct from those of the two end members, we interpret it as from a single phase solid solution of intermediate composition. This is consistent with what is known of the properties and provenance of the individual samples, and with its consistent presence in spectra for most feldspars of intermediate composition.

A sample from Slieve Gullion, Ireland (K:Na:Ca = 43:57:-), described as a sanidine, has exactly the same spectral characteristics as the moonstone (Figure 2d) namely, a mixture of high-K and intermediate. This sample does not have a "moonstone" appearance but is nevertheless clearly a similar mixture of phases

but presumably the crystal intergrowths are too small to show optically. On the other hand, US synthetic feldspar standard NBS 99a (K:Na:Ca = 32:57:11) is evidently a mixture of high-K and high-Na feldspars. This was a surprise to our mineralogists but the evidence seems strong. The mixed phase character is also revealed by some feldspar samples which are classified as sanidine and orthoclase on the basis of their cell structure analysis using X-ray diffraction technique. This still requires explanation.

It is interesting to note that the occasional higher TL sensitivity in the intermediate composition region (of which the synthetic sample 99a is an example) corresponds to the degree of mixed end-member TL spectra character shown by such samples.

Discussion

There is an extensive literature on the gross structure and microstructure of feldspars and the methods for determining them. Three of the most recent comprehensive treatments at review level are found in references (14) and (15) and in the classic, "Feldspar Minerals", by J.V. Smith (16), now in its second edition. Optical methods, X-ray diffraction and electron diffraction are all so well-established that it hardly seems necessary to do more than give a brief reminder of their particular characteristics.

Optical methods are rapid and cheap and frequently useful in observations of twinning and sample homogeneity and, to some extent, composition. Electron optical studies have established that, apart from a few end members and some high temperature samples, most feldspars consist of two or more types of domains that differ in orientation or composition, or both, on a scale of 3 to 100 nm. Since this scale is significantly smaller than the wavelength of light, optical methods necessarily average over these structures, and their optical properties are averages of the optical properties of individual members of the composite (17). On the other hand, the very high resolution of electron optical techniques allows the identification of detail on a very much smaller scale, together with ancillary information such as provided by microprobe X-ray emission analysis. X-ray diffraction hardly needs further comment because of its long-established contribution to structural studies at the atomic level.

The thermoluminescence properties of feldspars described here suggest that, properly calibrated, TL emission spectra can make TL a simple but powerful tool for estimating levels of mixed phases in feldspars. It appears that the difference in TL sensitivity and the difference in the spectra are able to give information about the composition of the phases concerned, at least to the extent of determining bulk composition and average structural state. In this respect, the technique has some similarities to the optical methods referred to above. The TL method differs in that it identifies the phases from their spectral characteristics. Further, as an emission rather than a scattering phenomenon, the spatial resolution is better. Optical microscopy reveals structures down to, say, 500 nm; X-ray and electron diffraction extend this to structures roughly an order of magnitude smaller; and electron

microscopy to structures smaller still. The TL technique suggested here extends to somewhere near the bottom of the size range since the optical emission is related to structures on the atomic scale in lattices which do not need to be ordered to the extent necessary to give coherent X-ray or electron scattering.

Acknowledgments

The work was supported by the Australian Research Grants Committee and the Research Grant of the University of Adelaide. RKG expresses his appreciation for support from the University of Adelaide which made possible a visit to the Physical Archaeometry Research Group of that university. Phil Fox provided the analysis for some of the Figures, and John Hutton and Gillian Robertson provided useful comments.

Literature Cited

1. McDougall, D.J. In Thermoluminescence of Geological Materials; McDougall, D.J., Ed.; Academic: London, 1968; 527-544.
2. Geake, J.E.; Walker, G.; Telfer, D.J.; Mills, A.A. Trans. Roy. Soc. London 1977, A285, 403-408.
3. Pasternack, E.S.; Levy, P.W. Geological Abstracts with Programs 1978, 10, 468.
4. Marfunin, A.S. Spectroscopy, Luminescence and Radiation Centres in Minerals; Springer-Verlag: Berlin, 1979.
5. Dalal, M.L.; Kirsh, Y.; Rendell, H.M.; Townsend, P.D. Nucl. Tracks and Radiat. Meas. 1988, 14, 57-62.
6. Kirsh, Y.; Townsend, P.D. Nucl. Tracks and Radiat. Meas. 1988, 14, 43-48.
7. Akber, R.A.; Prescott, J.R. Nuclear Tracks 1985, 10, 575-580.
8. Akber, R.A. Materials and Techniques for Thermoluminescence Dating. Ph.D.Thesis, University of Adelaide, Australia, 1986.
9. Huntley, D.J.; Godfrey-Smith, D.I.; Thewalt, M.L.W.; Berger, G.W. Jour. Luminescence 1988, 39, 123-136.
10. McKeever, S.W.S. Thermoluminescence of Solids; Cambridge University Press, 1985.
11. Levy, P.W. PACT 1979, 3, 466-480.
12. Jensen, H.E.; Prescott, J.R. PACT 1982, 6, 542-548.
13. Prescott, J.R.; Akber, R.A.; Jensen, H.E. Applied Optics 1988, 27, 3496-3502.
14. Ribbe, P.H. Ed. Feldspar Mineralogy; Mineralogical Society of America: Washington, DC, 1983.
15. Brown, W.L., Ed.; Feldspars and Feldspathoids; NATO ASI Series C, 137; Riedel: Dordrecht, 1984.
16. Smith, J.V.; Brown, W.L. Feldspar Minerals, 2nd. edition; Springer-Verlag: New York, 1988.
17. Stewart, D.B.; Ribbe P.H. in Feldspar Mineralogy; Ribbe, P.H. Ed.; Mineralogical Society of America: Washington, DC, 1983, 121-137

RECEIVED March 21, 1989

Chapter 11

Induced Thermoluminescence and Cathodoluminescence Studies of Meteorites

Relevance to Structure and Active Sites in Feldspar

Derek W. G. Sears¹, John M. DeHart¹, Fouad A. Hasan¹,
and Gary E. Lofgren²

¹Cosmochemistry Group, Department of Chemistry and Biochemistry,
University of Arkansas, Fayetteville, AR 72701

²NASA Johnson Space Center, Houston, TX 77058

The thermoluminescence (TL) sensitivity of meteorites is primarily related to the amount of feldspar present, and since feldspar is formed by devitrification during metamorphism and destroyed during shock these processes may be monitored by its measurement. For instance, the ordinary chondrite class shows a 10^3 -fold variation in TL sensitivity as devitrification during metamorphism causes the crystallization of feldspar (the TL phosphor) in the primary igneous glass (which has little or no TL); this is particularly true at the lowest levels of metamorphism. The cathodoluminescence (CL) properties of polished sections of ordinary chondrites also vary systematically with metamorphism and enable petrographic studies of the processes presumably controlling the TL variations to be made. Such studies demonstrate (1) the importance of feldspar in determining the bulk TL properties of meteorites, and (2) that the active sites vary as metamorphism causes compositional, as well as structural, changes in the feldspar. Annealing experiments on meteorites and terrestrial feldspars, and studies of separated components from meteorites, suggest that the high and low temperature forms of feldspar have distinctive TL peak temperatures and widths and thus provide a new means of exploring equilibrium temperatures and cooling rates. Induced TL properties have therefore enabled new insights into low-grade metamorphism and devitrification, shock, brecciation and the postulated Martian origin of certain meteorites and their components.

0097-6156/90/0415-0190\$09.25/0
© 1990 American Chemical Society

Probably the first modern reference to meteorite thermoluminescence is that of Herschel (1), although it is possible that the luminescence observed by Howard after passing an electric charge "from 34 square feet of glass" across the Siena meteorite could, in part, have been TL (2). Herschel reported naked eye observations of the TL produced by dust from the Middlesbrough meteorite as it was sprinkled on a hotplate, and he suggested, correctly, that the luminescent component was feldspar.

During this century there has been considerable interest in the application of thermoluminescence studies to the recent history of meteorites. Natural TL provides a means of exploring radiation history and thermal environment in a manner which is complementary to isotopic methods, and the measurement of natural TL is now routine for the numerous meteorites being returned each year from the Antarctic (3,4). However, induced TL measurements have also proved of considerable interest, because the measurements have implications for the earliest history of meteorites. Essentially, the induced TL properties of meteorites are determined, with a few notable exceptions, by the amount and the nature of the feldspar in them, and feldspar is very sensitive to the major processes experienced by meteorites. In the present paper, we describe our recent work on the induced TL properties of meteorites and briefly discuss how these data relate to early meteorite history. We emphasize the relationship between the TL data and mineral properties. We also present here detailed descriptions of the cathodoluminescence properties of primitive meteorites, as these provide new insights into mineralogical controls on TL properties.

Thermoluminescence Sensitivity Variations in Ordinary Chondrites

The largest class of meteorites are the ordinary chondrites; aggregates of olivine, pyroxene, feldspar, Fe,Ni alloys, FeS and over 100 minor and trace minerals. Structurally, they are noteworthy for containing 50-75 volume % of "chondrules", silicate beads, ~100 micron to a few millimeters or so in diameter. Chondrules consist of olivine or pyroxene grains, with a variety of textures, imbedded in a "mesostasis" of glass or feldspar. The origin of the chondrules has long perplexed meteorite researchers, most modern workers preferring a theory in which pre-existing dust was flash melted and allowed to cool rapidly. The aggregates of dust, metal, sulfide and chondrules are presumed to have formed in the early solar system as part of the process which formed the planets, and there is some evidence that grains of pre-solar origin may also be present in certain meteorites. Once formed, these aggregates accumulated into the parent bodies of the present meteorites, and on these bodies a number of secondary processes occurred, such as metamorphism, shock, brecciation and

aqueous alteration. Fortunately, not all ordinary chondrites suffered all these processes to equal degree, and a fruitful line of enquiry has been to sort the meteorites according to the degree of alteration. This has not only enabled particularly significant individual meteorites to be identified, but is also leading to an improved understanding of the various processes. For metamorphism, Van Schmus and Wood have developed the highly successful petrologic types 1-6 (5). Time has led to a better understanding of some of the geological parameters used in the scheme, and it now appears that the least metamorphosed ordinary chondrites are type 3 and the most heavily metamorphosed are type 6; there are also one or two partially melted individuals sometimes described as type 7.

The level of thermoluminescence that can be induced in an ordinary chondrite (i.e. the "TL sensitivity") shows a 10^5 -fold range, which is related to petrologic type (Figure 1). The type 3 chondrites alone show a 10^3 -fold range, and several of the petrologic parameters that enable types 1-6 to be defined vary with TL sensitivity within the type 3 ordinary chondrites (6), suggesting that metamorphism is responsible for the range in TL sensitivity. On the basis of the TL data, it would seem that the type 3 chondrites, although clumped together by Van Schmus and Wood and others, exhibit a range of metamorphism comparable to, or perhaps greater than, the other types put together. Since the type 3 ordinary chondrites are especially significant, as they best represent the least altered solar system material available in our laboratories, subdivision of type 3 into types 3.0-3.9 has proved worthwhile. The scheme is now widely used and has enabled several new insights into the metamorphic process and the nature of unaltered solid solar system material.

Van Schmus and Wood used the relative abundance of glass and feldspar as an important criterion in establishing the petrologic types (5). In type 3 chondrites, there appears to be no feldspar, but instead there exists a glass of, approximately, feldspathic composition. In type 4 chondrites, this glass becomes translucent, and in type 5 chondrites grains of feldspar <50 microns in size have crystallized in the glass. In type 6 chondrites, the grains have grown to >50 micron. Mineral separations by French researchers have confirmed Herschel's suggestion that the phosphor in ordinary chondrites, at least in the type 5 or 6 (sometimes called the 'equilibrated' ordinary chondrites), is feldspar (7). It was therefore suggested that the range of TL sensitivity observed in the ordinary chondrites reflects the amount of feldspar in the meteorite and that the reason for the relationship between TL sensitivity and metamorphism was that unmetamorphosed meteorites contain glass which crystallizes during metamorphism to produce feldspar (6). This being so, TL sensitivity is capable of determining the relative abundance of feldspar when it is present in the meteorite in trace amounts, far

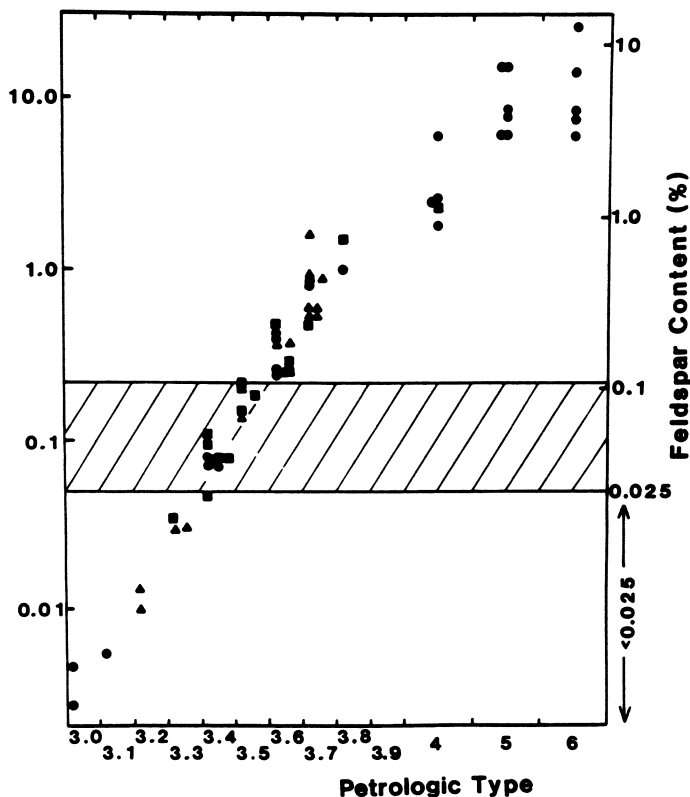


Figure 1. Plot of thermoluminescence sensitivity against petrologic type (5,6), which reflects the degree of metamorphic alteration : 3, least metamorphosed; 6, most metamorphosed. The feldspar scale is calculated on the assumption that the TL sensitivity is directly proportional to feldspar abundance and type 5,6 chondrites typically contain about 8% of this mineral. The cross-hatched region refers to TL sensitivity levels at which the feldspar is thought to be in the low-temperature ordered form (see Figure 13). The symbols refer to the three data sources (6,8,14). (Reprinted by permission from Ref. 31. Copyright 1986 American Geophysical Union.)

below the detection limits of X-ray diffraction and even electron microscopy. The "detection limit" for the feldspar is determined by the presence of other phosphors and is approximately 0.025wt%.

Metamorphism-Related Variations in Thermoluminescence Peak Shape

Early work also revealed a relationship between the shape of the TL peak in ordinary chondrites that was induced by a standard radiation dose and their metamorphic history (8). Thermoluminescence data are obtained in the form of "glow curves", plots of light emitted against temperature. The shape of the induced glow curve is shown in Figure 2. Typically the glow curve consists of a single broad band of luminescence between 100-250°C; the band is a composite of several overlapping individual peaks. The apparent composite peak may be characterized in terms of peak temperature (the temperature of maximum TL emission), and the width of the composite peak (the full-width at half-maximum, FWHM). Within the range 3.2-3.9, peak temperature and peak width vary in a systematic way with petrologic type. (For the types 3.0-3.1, the peak shapes vary widely from sample to sample and the peaks tend to be very broad and hummocky). On a plot of peak temperature versus peak width (Figure 3) the type 3 ordinary chondrites produce two clusters, one consisting essentially of type 3.2-3.5 with peak temperatures and widths of 120-160°C and 80-130°C, respectively, and one consisting of essentially of types 3.5-3.9 with peak temperatures and widths of 160-220°C and 140-180°C, respectively (9). Clearly, there is information of relevance to metamorphic history contained in the shape of the induced TL peak. Laboratory experiments, described below, confirm that this behavior is typical of feldspar and the changes in peak shape and width are controlled by thermal history; the underlying mechanism is associated, in a complex way, with structural changes in the feldspar lattice.

The Characterization and the CL and TL Properties of Feldspars and Feldspathic Materials

In natural systems such as ordinary chondrites, with their bewildering array of minerals and mineral chemistries, reasonable interpretation of the meteorite TL trends need further investigation which is best achieved using a variety of approaches. We have tested the idea that crystallization of the glass was the major process affecting TL sensitivity and that the peak width and temperature changes were related to disordering by three sets of measurements. (1) We examined the cathodoluminescence of a suite of type 3 ordinary chondrites of various petrologic types, and performed complementary analytical studies with the electron microprobe, to characterize in

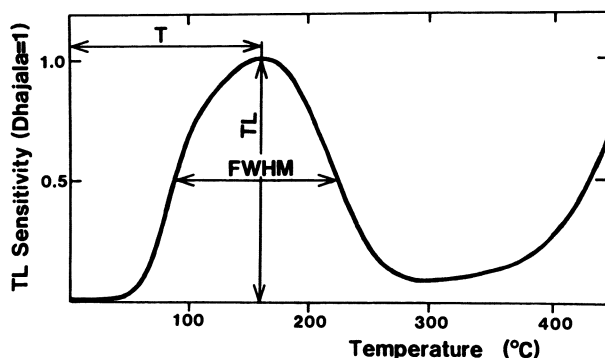


Figure 2. Typical glow curve for an ordinary chondrite meteorite (in this case Dhajala) showing how peak temperature (T), peak width (FWHM) and TL sensitivity (TL) are measured. TL sensitivity is the level of TL emitted at the peak divided by the same quantity for an arbitrarily chosen meteorite, Dhajala (14). (Reprinted by permission from ref. 14. Copyright 1983 American Geophysical Union.)

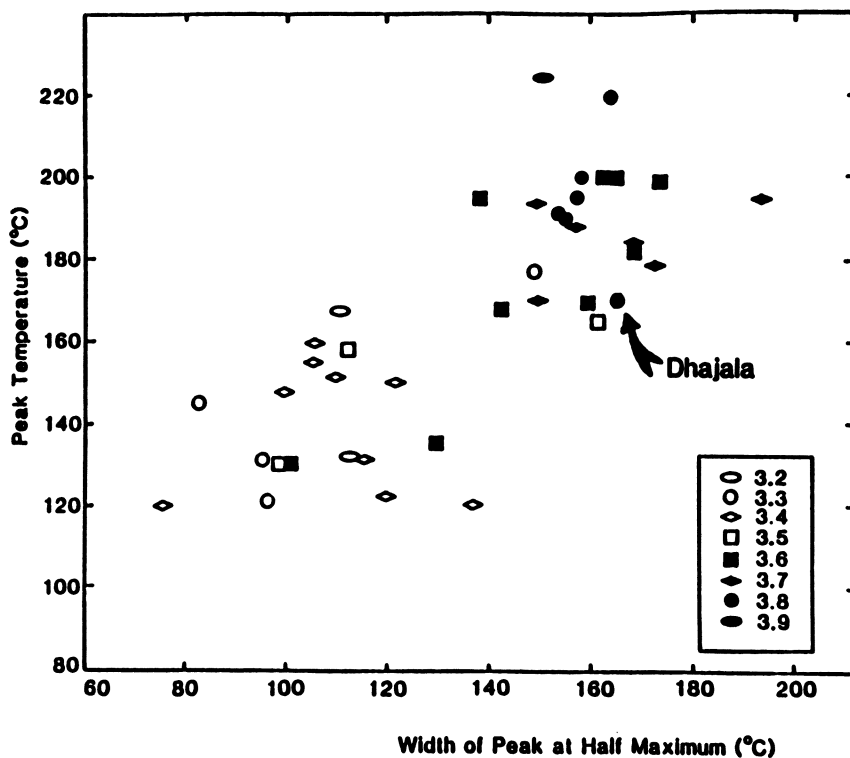


Figure 3. Peak temperature against peak width for type 3.2–3.9 ordinary chondrites. The petrologic types are indicated by the symbols. (Reprinted with permission from ref. 9. Copyright 1985 Pergamon.)

detail the CL and compositional properties of the luminescent material (most of which is feldspathic) and their relationship to metamorphism. (2) We attempted to reproduce the increase in TL sensitivity by treating low type meteorites in a way that would cause crystallization of the glass. Both studies confirmed the original theory for the TL sensitivity-metamorphism relationship, but both studies also revealed new and significant details. (3) We have also performed laboratory annealing experiments on meteorites and terrestrial feldspars and found that we could reproduce the meteorite TL peak temperature and width trends. X-ray diffraction measurements of the annealed terrestrial feldspar showed that the trends are probably related to disordering but that the details are not well understood.

Cathodoluminescence Studies of Type 3 Ordinary Chondrites

Our photomosaics of the cathodoluminescence of a suite of type 3 ordinary chondrites are presented as Figs. 4-7. To obtain these photomosaics, a Nuclide Corporation "Luminoscope" was attached to a standard petrographic microscope and a defocussed electron beam (typically 1 cm x 0.7 cm), operated at 14 ± 1 keV and 7 ± 1 μ A, was directed onto a polished section of the meteorite using hand magnets. Photographs were taken at 50x using a 35mm camera with Kodak VR400 film and exposure times of 1.0-2.5 minutes. The commercial C-40 process was used for development. Each photomosaic consists of 30-40 photographs.

In terms of their CL, as well as many other properties, Semarkona is unique, and Bishunpur and Krymka are unusual and share several of Semarkona's properties (Figure 4). On the basis of these CL properties, Krymka has been reassigned type 3.1 from our previous TL-based assignment of type 3.0. These three low-type ordinary chondrites (type 3.0-3.1) contain a great diversity in: (1) CL color, (2) kinds of components displaying CL, and (3) the textures of the CL-bearing components. Chainpur and Allan Hills A77214, both type 3.4, have relatively few CL-bearing components, but the most noteworthy are the mesostases of the chondrules (Figure 5a,b). The fine-grained smoke-like matrix that produced red CL in Semarkona, and little CL in Bishunpur and Krymka, shows virtually none in the two type 3.4 chondrites. With petrologic types >3.4 the proportion of chondrules showing CL increases, and at even higher types the matrix begins to show blue CL, but the intensity, color and texture of the CL of the matrix suggests that it may simply be chondrule fragments (Figure 6). Ngawi is a spectacular example of a breccia, a rock composed of fragments of previously existing rock, in which there are fragments of type 3.1 material in a host which is a mixture of types, but predominantly type 3.6 (Figure 5c).

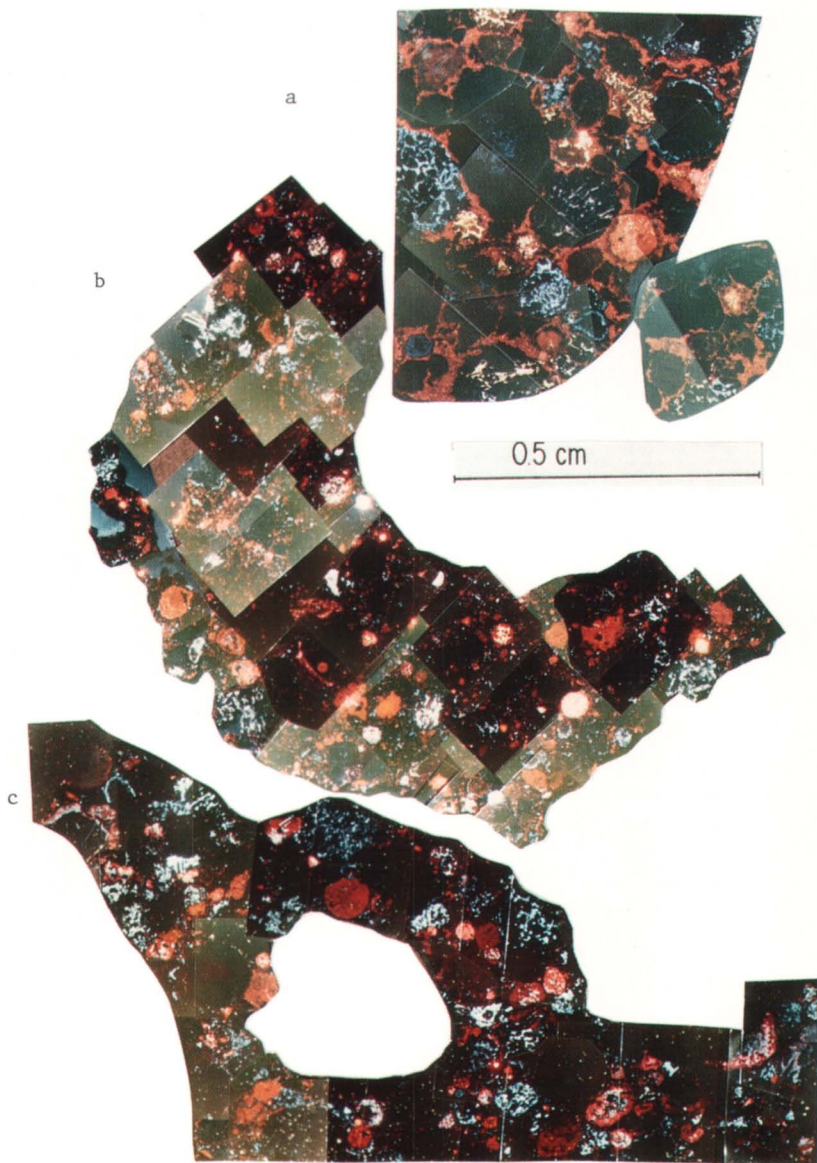


Figure 4. Photomosaics of the cathodoluminescence of three low petrologic type meteorites; (a) Semarkona (type 3.0, top), (b) Bishunpur (type 3.1, middle), and (c) Krymka (type 3.1, bottom). The scale bar shown refers to Semarkona, the scale bar for the others is the same as in Figure 5. In general, red luminescence is produced by Fe-free olivine and pyroxene, and blue and yellow CL is produced by chondrule mesostases of plagioclase composition.

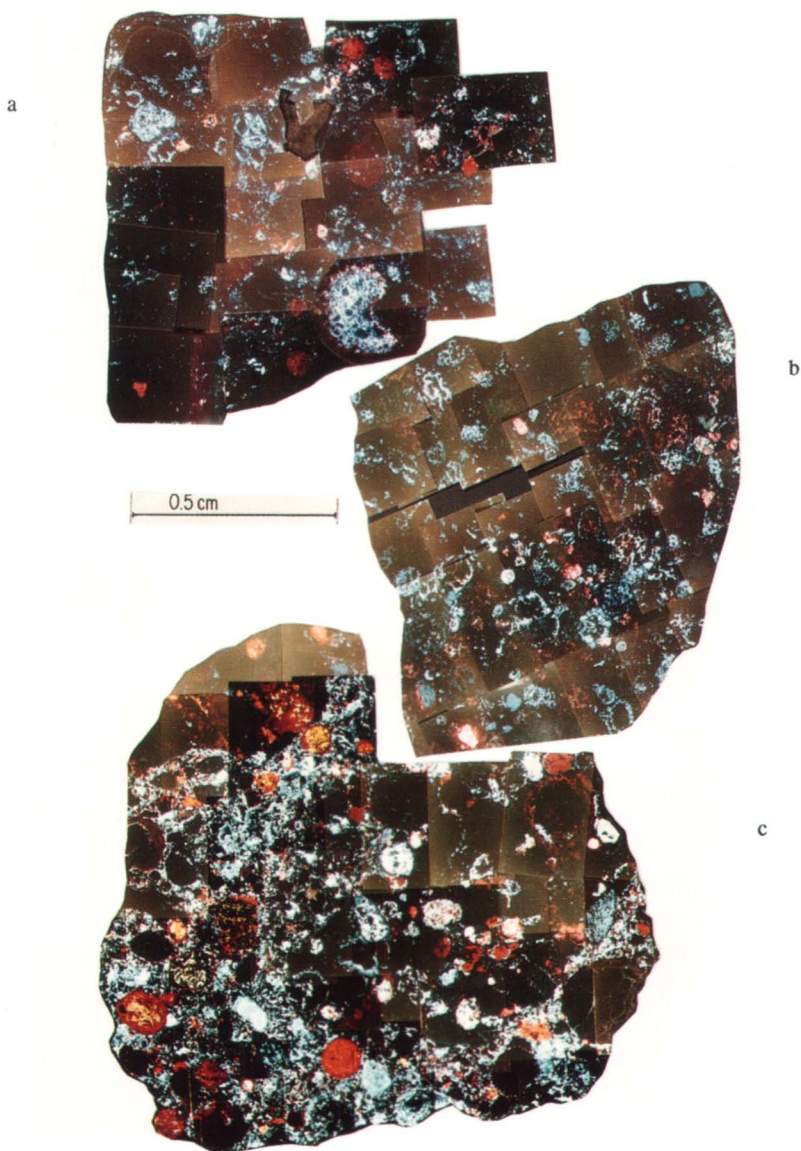


Figure 5. Photomosaics of the cathodoluminescence of three intermediate petrologic type meteorites; (a) Chainpur (type 3.4, top), (b) Allan Hills A77214 (type 3.4, middle), and (c) Ngawi (most predominantly type 3.6 containing clasts of type 3.1, bottom). With increasing petrologic type, the diversity of CL properties within a meteorite decreases, red luminescent material becomes scarce and blue material becomes more abundant.

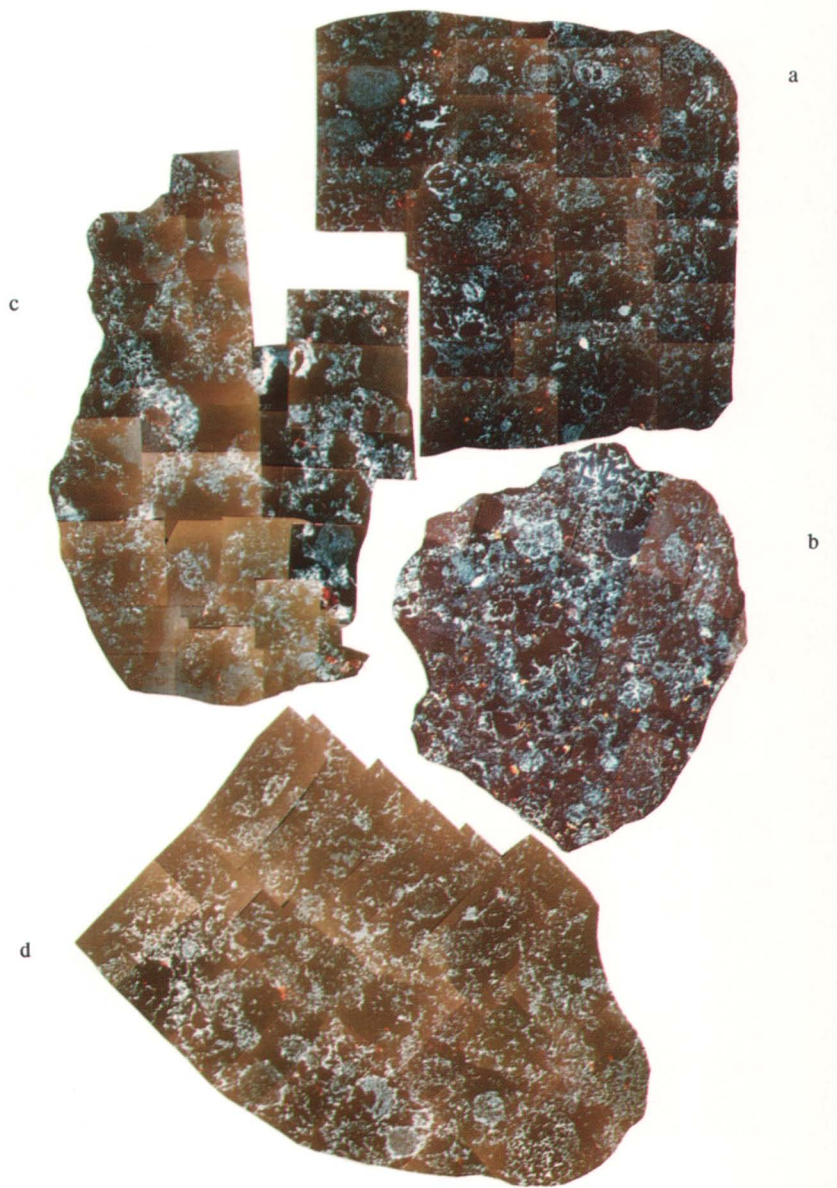


Figure 6. Photomosaics of the cathodoluminescence of four meteorites of types 3.7-5; (a) Hedjaz (type 3.7, top right), (b) Dhajala (type 3.8, center right), (c) Bremervorde (type 4, center left), and (d) Barwell (type 5, bottom). Scale bar, as in Figure 5. These relatively high petrologic type chondrites show a uniform blue feldspar CL, with only an occasional phosphate grain with red CL.

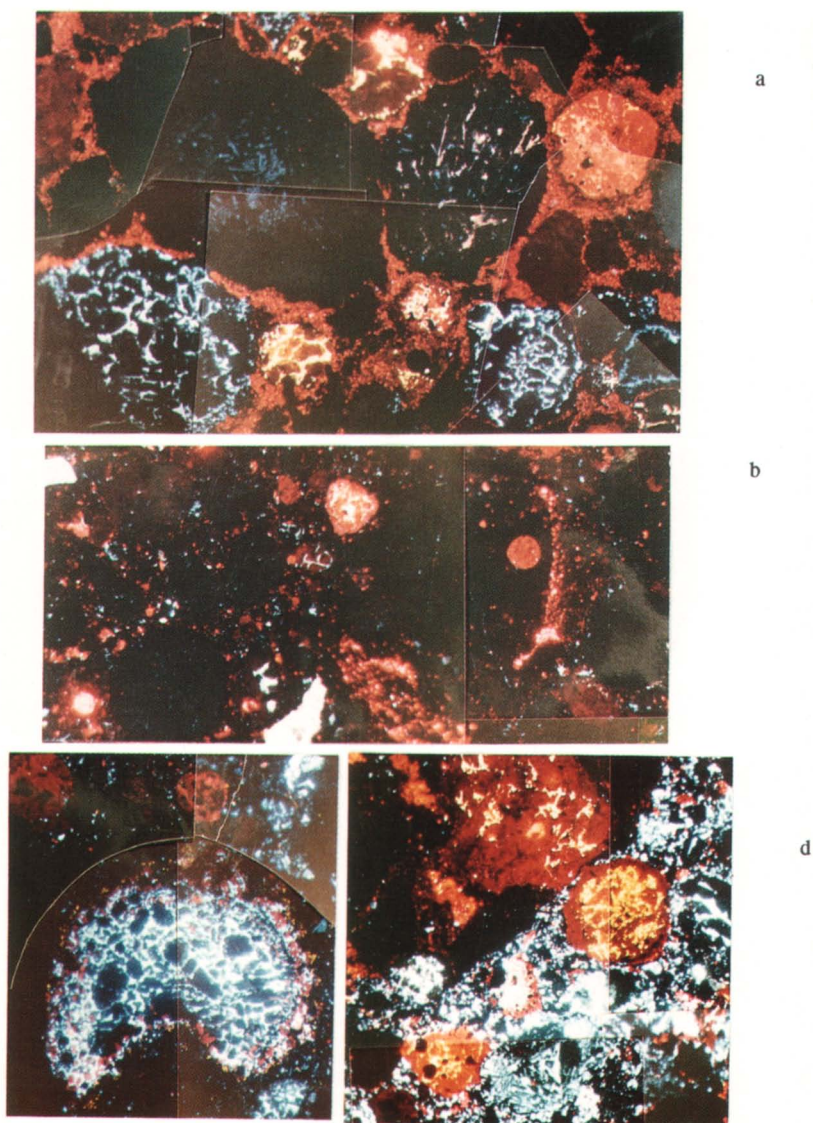


Figure 7. Details from four photomosaics of the cathodoluminescence of type 3 ordinary chondrites. (a) Detail from Semarkona (top, horizontal field of view 5.0 mm). (b) Detail from Bishunpur (middle, horizontal field of view 3.5 mm). (c) Detail from Chainpur (bottom left, horizontal field of view 2.0 mm). (d) Detail from Ngawi showing the boundary between type 3.1 clast material in the top left half of the field, and the host matrix of type 3.6 material (bottom right, horizontal field of view 2.3 mm).

We have analyzed the cathodoluminescent phases in four of these meteorites in detail (10-12), and found that a major source of CL is the chondrule mesostasis and it is those mesostases which most readily crystallize that first display CL as the level of metamorphism experienced by the meteorite increases. Some of the analytical data obtained with the electron microprobe are shown in Figure 8, a plot of CaO against Na₂O. The regression line through the luminescent chondrule mesostases has a slope with a CaO/Na₂O ratio corresponding to the feldspar, plagioclase (a solid solution of albite, NaAlSi₃O₈, and anorthite, CaAl₂Si₂O₈). Chondrules whose mesostases are either not luminescent, or only weakly luminescent, have compositions which are rich in quartz (SiO₂). The other CL-producing phases in Semarkona and the other low types are not yet well studied, but are usually Fe-free olivines and pyroxenes. With these important exceptions, the CL in ordinary chondrites is almost entirely produced by feldspar, whose composition homogenizes with increasing metamorphism. Some of the trace minerals in ordinary chondrites, like calcium phosphates and rare Ca-Al rich minerals, show CL in the higher types, but do not contribute significantly to the bulk TL properties of the meteorites.

A surprise difference between the chondrule mesostases of Semarkona and Krymka was that while the luminescent chondrule mesostases in Krymka luminesce blue, in Semarkona, chondrule mesostases display yellow CL when the mesostasis is calcic in composition and blue CL when they are sodic (Figure 8). Calcic compositions differ from sodic compositions in that they crystallize more readily, and, in terrestrial weathering studies, react more readily with water than sodic feldspars. It is probable that the yellow CL may be signalling aqueous alteration or the presence of a metastable phase easily destroyed by metamorphism.

The detailed CL trends displayed by the type 3 ordinary chondrites are therefore a unique means of determining not only the mineralogical factors affecting TL sensitivity, but they also provide a new means of examining the compositional (by complementary electron microprobe analysis) and structural (i.e. petrographic) changes associated with metamorphism-induced changes in CL properties. In the next few sections we summarize the CL properties of the ordinary chondrites.

Semarkona (3.0) (Figure 4a, detail Figure 7a). The ubiquitous fine-grained, opaque matrix in Semarkona, which appears interstitial to all the major components, produces a distinctive uniform red CL. There appears no perceptible difference in CL between the matrix material that rims chondrules and that which lies between chondrules, although some workers have argued that there is a compositional difference. There are also a small proportion of the chondrules which contain euhedral grains with red CL, and some chondrules appear a uniform dull

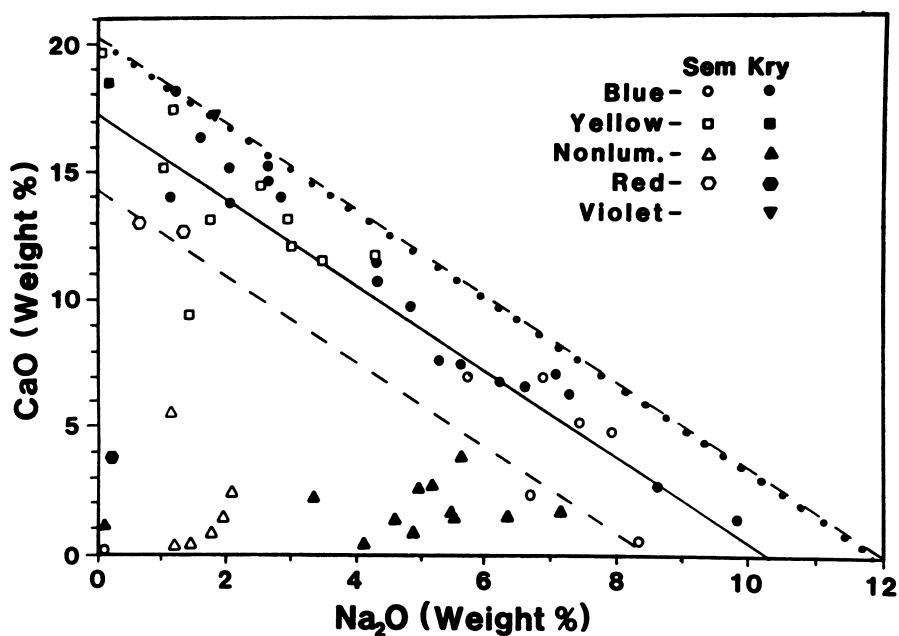


Figure 8. Plot of CaO against Na₂O for the chondrule mesostases in Semarkona and Krymka. The diagonal line is a regression line through the data for mesostases which luminesce and the broken lines refer to 2 σ uncertainties on the intercepts of this line. The dotted line refers to the theoretical line for plagioclase. (Reprinted by permission from Ref. 11. Copyright 1987 Lunar and Planetary Institute.)

red. In the case of the chondrule grains, and probably also the matrix, the red CL is being produced by low-Fe olivine.

The glassy mesostases of the chondrules may show either yellow or blue CL, or be non-luminescent. In many instances, usually larger chondrules, there are large uniform areas of yellow luminescing mesostasis enclosing non-luminescent euhedral grains, while in other instances the yellow material and the enclosed grains have a very fine texture. There are many spectacular instances of yellow mesostasis enclosing euhedral grains with red CL, the proportion of red grains to yellow mesostasis varying considerably from chondrule to chondrule. Some of the blue luminescing chondrule mesostases in Semarkona are bright enough to grade into white on the photomosaics, while several particularly large chondrules have centers which luminesce dull-blue, and there are several irregular-shaped fine-grained objects that luminesce blue. Additionally, some chondrules have strings of fine-grained material on their circumference.

Bishunpur (3.1) (Figure 4b, detail Figure 7b). The interstitial material that most resembles the fine-grained material in Semarkona, has quite different CL properties in Bishunpur; it is largely non-luminescent, but where it appears to show some luminescence, the grains are coarse and irregularly scattered throughout the matrix and display red CL. Although it is difficult to be sure, it seems that the very fine-grained non-luminescent interstitial matrix is the primary dust (termed "Huss matrix" by some workers), while the coarse-grained material is composed of chondrule fragments. The chondrules sometimes contain red euhedral grains, in some cases with blue luminescent mesostases. Chondrule mesostases are either non-luminescent or show blue CL, and often the intensity is so high, relative to the red luminescence, that they quickly grade into overexposed white features. Chondrules with yellow mesostases are rare. A few blue/blue-white chondrules are irregular and fine-grained.

Overall, the CL properties of Bishunpur are very distinct from Semarkona, the luminescence being lower in intensity, less diverse in color and the grains coarser and less well developed.

Krymka (3.1) (Figure 4c). Like Bishunpur, the material analogous to the fine-grained matrix in Semarkona does not luminesce, except for occasional isolated grains. Chondrule mesostases are either non-luminescent or show blue/blue-white CL, but occasional fine-grained objects are also present. The grains within the chondrules are generally non-luminescent, but in a few instances luminesce red, and there is one instance in our section of lathes of red euhedral grains imbedded in a red mesostasis with the composition of Fe-free, calcic pyroxene. A few chondrules contain fine-grained material, surrounding material with red luminescence.

Chainpur (3.4) (Figure 5a, detail Figure 7c). Like Bishunpur and Krymka, Chainpur has much less luminescent material than Semarkona, but there are some noteworthy exceptions to this generalization. The matrix material is virtually all non-luminescent, although there are regions where relatively coarse and irregularly dispersed blue grains occur. However, the chondrule mesostasis is either non-luminescent or shows bright luminescence (grading into overexposed blue/white), and

in this form the appearance can be quite spectacular. A few chondrules contain grains which show red CL, some are very low in intensity, and there are a few isolated grains with red CL which may be chondrule fragments. One large chondrule with a bright blue luminescing mesostasis has a string of fine red grains encircling it (Figure 7c). There is also a large region of chondrule mesostasis which appears purple to the naked eye. There are also many fine-grained irregular shaped objects with blue luminescence, and several isolated grains with blue interiors and red exteriors; presumably the isolated olivine grains described by Steele (13).

Allan Hills A77214 (3.4) (Figure 5b). Chondrule mesostases in Allan Hills A77214 (ALHA 77214) show either blue/blue-white or dull-red to purple CL, and in several cases it is only the mesostasis near the outer perimeter of the chondrule that luminesces. The electron microprobe data show that these regions are also higher in Na than the more central mesostasis regions (12). As in Chainpur, the matrix shows very little cathodoluminescence, only a few areas of coarse grains with blue CL are randomly scattered throughout.

Ngawi (clasts of type 3.1 in a brecciated host of mean type 3.6) (Figure 5c, detail Figure 7d). Ngawi shows a spectacular range of CL colors and textures, consisting primarily of a brecciated "host" of high type 3 material and clasts of low type 3 material. The host does not resemble any particular type 3 ordinary chondrite in its CL properties, but appears to consist of fragments resembling type 3.6 to type 4 material enclosing chondrules with a variety of CL properties, similar to those in Semarkona, Bishunpur and Krymka; yellow mesostases enclosing red euhedral grains, bright to dull red chondrules, non-luminescent chondrules. There are two clasts in our section, both resemble Bishunpur and Krymka in their CL properties; the interface between the type 3.1 clast material and type 3.7 host material is shown in Figure 7d. The clasts both contain spectacular chondrules with a variety of CL textures and colors, and virtually a non-luminescent matrix. One of the clasts contains matrix with occasional dull red grains, similar to that in Bishunpur.

Hedjaz (3.7) and Dhajala (3.8) (Figs. 6a and 6b). In many chondrules, the mesostasis is an intense blue (grading into white), while in approximately half of the chondrules the mesostasis is a dull-blue grading into purple. In both cases the mesostasis often exists as large uniform fields. In Hedjaz and Dhajala, the interchondrule material is also producing blue CL, but the intensity is consistently lower than that of the bulk of the chondrules, so that the chondrules and their interior textures stand out clearly. In Hedjaz, much of the matrix contains occasional grains of very dull red material, reminiscent of the matrix of Bishunpur and Krymka but much less abundant.

Bremervorde (4) and Barwell (5) (Figs. 6c and 6d). Bremervorde is a breccia of type 3.8 and type 4 (14); our section is entirely type 4 material. Chondrule mesostases luminesce brightly, often highlighting chondrule textures. The non-chondrule silicate portions of the meteorites appear to consist of fragmental material similar to the chondrules in its CL colors and intensities; clearly any interstitial

material present is quite different to the matrix in the previous meteorites. Thus the CL of Bremervorde and Barwell is almost entirely blue, due to feldspar, with only occasional isolated grains of phosphate minerals with red CL dispersed throughout the sections.

Increasing levels of metamorphism therefore destroy the red luminescence typical of olivine and pyroxene in types 3.0-3.1 by causing Fe levels to homogenize and Fe-free olivines and pyroxenes to disappear. Similarly, metamorphism causes chondrule glass to devitrify, sometimes also converting the quartz-rich mesostases to feldspar-rich mesostases in the process. The usual CL color for feldspar in ordinary chondrites is blue (probably due to Mn^{2+} activation), but a highly unstable phase (with bulk feldspar composition but of unknown identity) in Semarkona has yellow CL and a weakly luminescing material of feldspar composition in Allan Hills A77214 has dull-red purple CL (possibly Fe^{3+} activated feldspar). The CL data for this metamorphic suite of ordinary chondrites therefore not only provides further insight into the processes accompanying metamorphism, they provide fresh data on active sites in feldspar. These points are discussed at length by DeHart, Lofgren and Sears (Geochim. Cosmochim. Acta, in press).

Laboratory Studies of the Induced Thermoluminescence Properties of Ordinary Chondrites and Feldspar

Our attempts to explore the role of devitrification, in determining the TL sensitivity of ordinary chondrites, are partially summarized by Figure 9, a series of glow curves for the Sharps type 3.4 chondrite. Samples were annealed at 755-855°C with various quantities of water and sodium disilicate, agents which facilitate the formation of feldspar from glass in conventional phase diagram studies (15), in sealed gold vials at a pressure of 1000 atmospheres. In the Sharps case, the TL sensitivity increased by a factor of 3. A subsequent, detailed series of annealings for four type 3 ordinary chondrites produced more spectacular increases in TL sensitivity. The Semarkona meteorite underwent a 40-fold increase in TL sensitivity after annealing at 900°C for 168 h (Figure 10). The data confirm the idea that the increase in the TL sensitivity of ordinary chondrites as a result of increasing metamorphism is caused by the formation of feldspar via the crystallization of primary glass.

We also observed, during the annealing experiments on Semarkona and Allan Hills A77214, that annealing under relatively mild conditions did not cause an increase in TL sensitivity, but rather caused a significant (factor of 10 or so) decrease in TL sensitivity. Either activators were being affected, or the phosphor was being physically destroyed by reaction with the water in the capsules. Simultaneously with the production of these data, Hutchison et al. reported the observation of calcite and hydrated

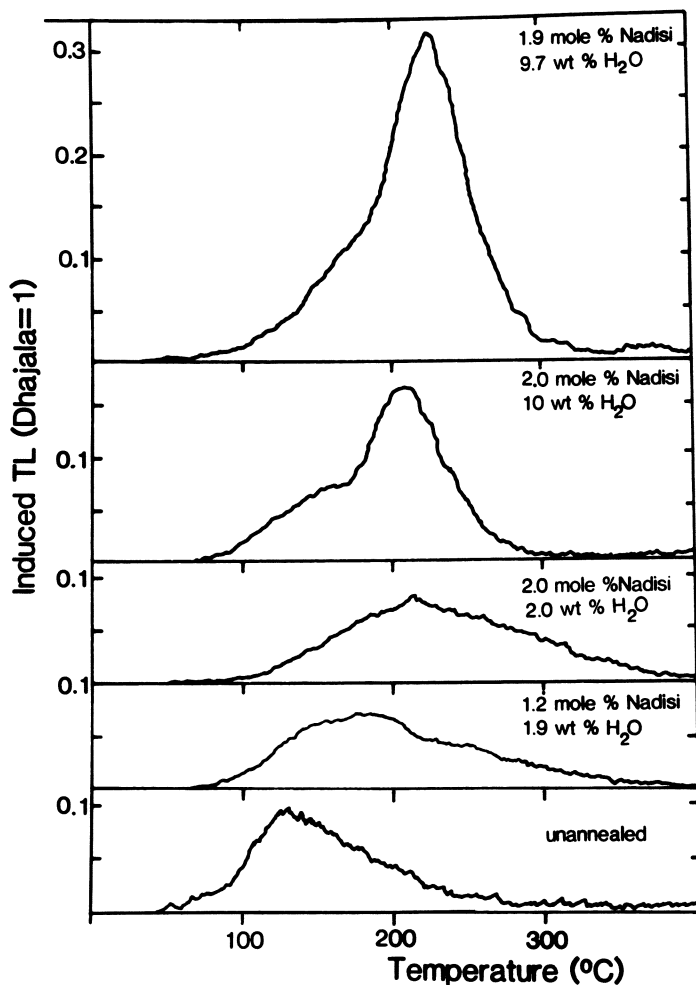


Figure 9. Glow curves for the Sharps meteorite (type 3.4) before and after annealing at 755-855°C and 0.77-1 kbar for 168-174 h in the presence of water and sodium disilicate. (Reprinted by permission from Ref. 31. Copyright 1986 American Geophysical Union.)

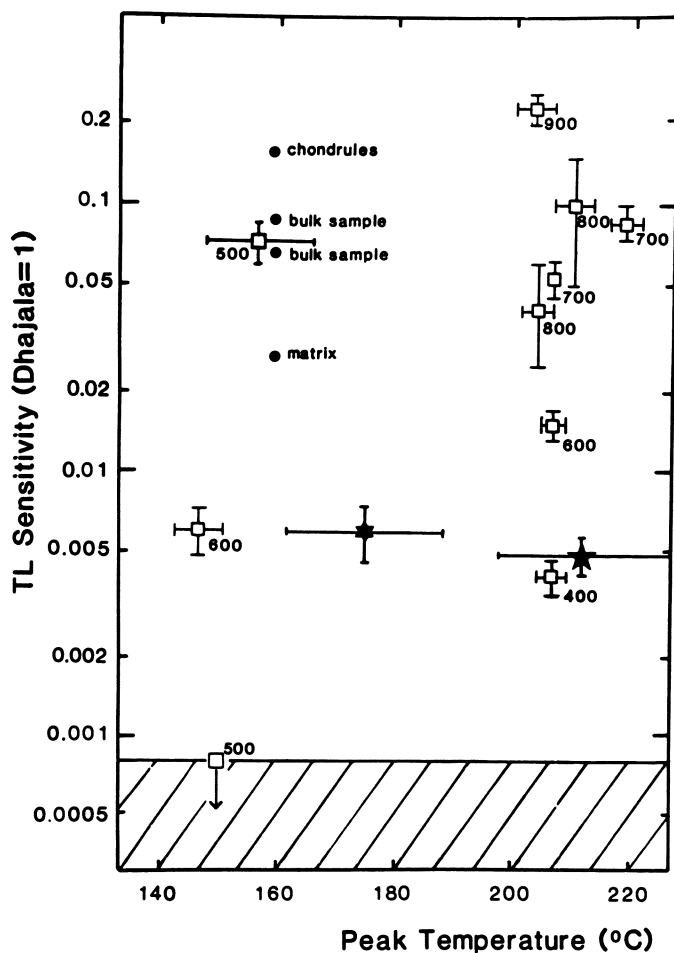


Figure 10. Samples of the Semarkona meteorite annealed at 1 kbar at the temperatures indicated ($^{\circ}\text{C}$) for 168 hours, in the presence of water and sodium disilicate. The stars refer to data for samples of the unannealed material, which is very heterogeneous, and the dots refer to four samples produced by subdividing the sample responsible for the anomalous 500°C data. The cross-hatched field refers to 11 samples whose TL sensitivity was below detection limits. (Reprinted by permission from Ref. 32. Copyright 1988 Pergamon Press.)

silicates in Semarkona and suggested that the meteorite had been aqueously altered (16). They suggested that the water was extraterrestrial because Semarkona releases water with considerable deuterium enrichments upon step-wise heating (17,18). It is, of course, possible that the water was produced from other components in the meteorite during the step-wise heating experiment, but Sears *et al.* have recently found that there is a weak correlation between TL sensitivity and deuterium enrichment for individual chondrules from Semarkona, which might suggest that the TL sensitivity had been lowered and the deuterium increased by passage of heavy water through the meteorite while still on its parent body (19). However, the CL data described above, and a detailed study of the associated compositional properties of chondrules in four of these samples, are best interpreted in terms of chondrule formation mechanisms and subsequent metamorphism, and do not require a substantial role for aqueous processes (DeHart, Lofgren and Sears, *Geochim. Cosmochim. Acta*, in press).

Laboratory annealing treatments also cause the temperature and width of the induced TL peak to increase, and quantitatively the changes are very similar to those observed for the type 3.2-3.9 ordinary chondrites. Figure 11 shows glow curves for a type 3.4 ordinary chondrite before and after annealing at 900°C for 200 h and in Figure 12 laboratory annealing data are compared with the type 3 ordinary chondrite data. Whatever the detailed explanation for peak shape changes, the annealing data confirm the idea that the variations in TL peak shape are related to thermal (i.e. metamorphic) history. The increase in peak temperature and width occurs at temperatures similar to the transition temperature for low-temperature (ordered) feldspar to high-temperature (disordered) feldspar, between 500 and 700°C (20), so the simplest explanation for the changes in peak shape would be that types 3.2-3.5 ordinary chondrites contain feldspar in the low form, while types 3.6-3.9 contain feldspar predominantly in the high form.

Physical separation of the feldspar in types 3.2-3.5 ordinary chondrites is extremely difficult since it is very fine-grained (<1 μm) and mixed with other phases. We have therefore performed similar annealing experiments with terrestrial feldspars, fully cognizant of the differences in formation conditions and trace element chemistry of these feldspars and meteoritic feldspar (21). Several terrestrial feldspars in the low-temperature form (ordered Si-Al chain) have peak temperatures and widths similar to those of type 3.2-3.4 ordinary chondrites. Furthermore, and like the meteorites, they undergo an increase in peak temperature when annealed in the laboratory. The degree of disordering in the terrestrial oligoclase increases slowly as the TL peak temperature increases, and at higher annealing temperature the disordering increases rapidly with small increases in peak temperature (Figure 13). The activation energy for disordering is greater than for the

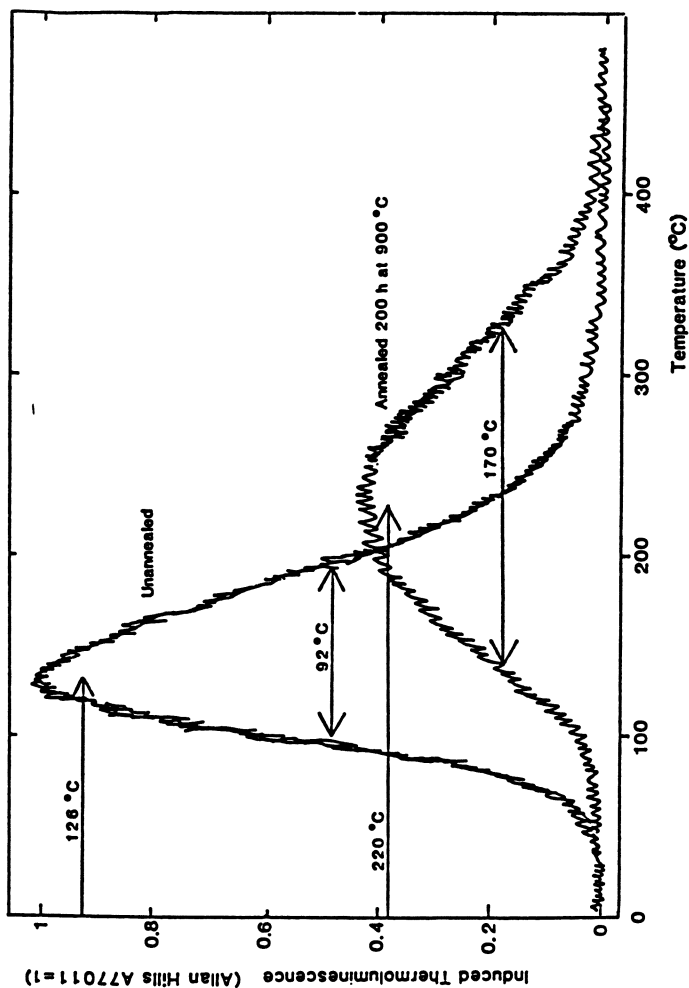


Figure 11. Two glow curves for the type 3.4 ordinary chondrite Allan Hills A77011 (which may actually be a fragment of the same meteorite as Allan Hills A77214) before and after annealing at 900°C for 200 h in a dry nitrogen atmosphere at atmospheric pressure. (Reprinted by permission from Ref. 33. Copyright 1984 MacMillan Journals.)

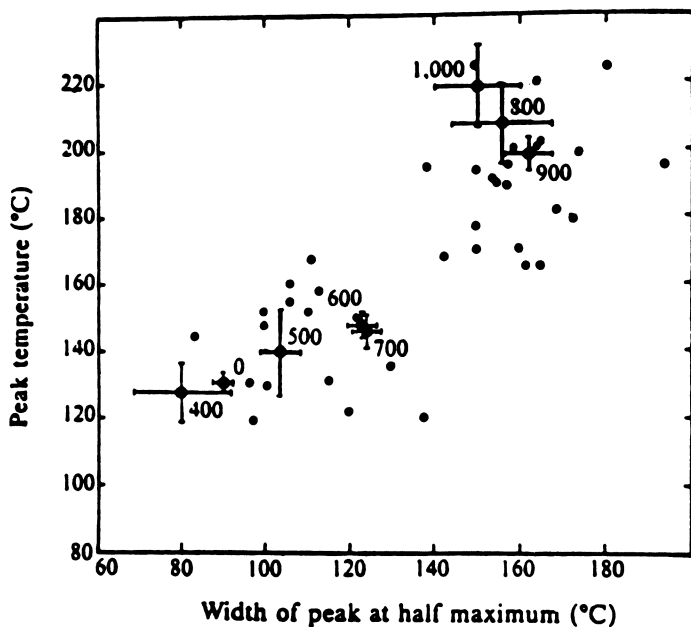


Figure 12. Plot of peak temperature against peak width for samples of Allan Hills A77214 annealed in a dry nitrogen atmosphere at atmospheric pressure, and at the temperatures indicated, for 100 h. Type 3 ordinary chondrites (c.f. Figure 3) are plotted as dots. (Reprinted with permission from Ref. 9. Copyright 1985 Pergamon Press.)

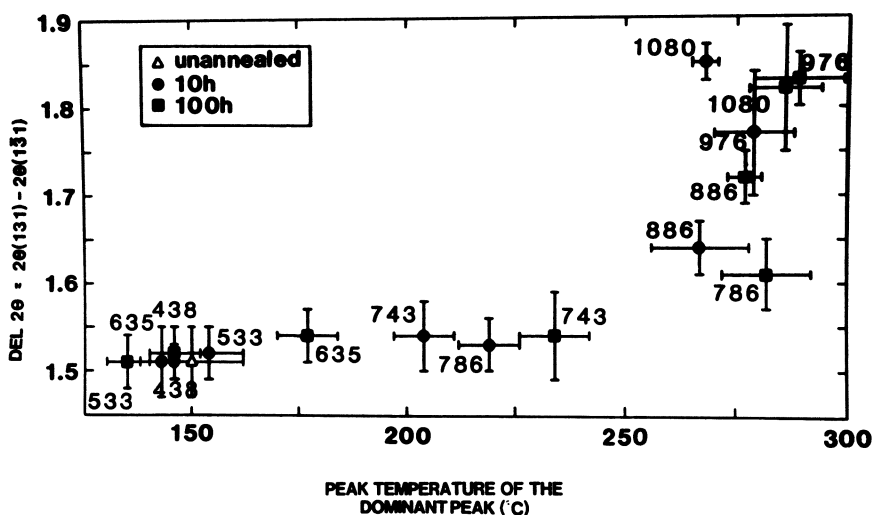


Figure 13. The difference in 2θ angle for the 131 and 131 reflections in the X-ray diffraction patterns for the plagioclase oligoclase ($\sim 1.5^\circ$ for the ordered and $\sim 2.0^\circ$ for the disordered phases) plotted against TL peak temperature for samples annealed at the temperatures ($^\circ\text{C}$) and the times indicated. (Reprinted with permission from Ref. 21. Copyright 1987 Lunar and Planetary Institute.)

change in TL peak shape, 21 kcal/mol compared with 74 kcal/mol (9). Pasternak suggested that the TL changes were caused by changes in lattice defect structure which preceded, but were associated with, disordering (22). We have also synthesized doped-feldspars in the laboratory, to explore the TL and structural relationships (35), and the data similarly suggest that the relationship between peak temperature and disordering is not straight-forward, and that intermediate feldspars, for example, may be involved. A major study of the TL properties of terrestrial and synthetic feldspars is warranted, but it is clear from existing data that annealing not only affects disordering, but it also affects peak temperatures and that the two are somehow related.

Other Studies

We end this review of meteorite TL and CL and their relationship with feldspar properties with a brief description of some applications to several meteorite problems not previously mentioned. The details presented here are minimal, and intended to illustrate that even though our understanding of some of the basics is still incomplete, there is considerable potential for the application of the work to a variety of geological problems.

Shock Studies. Many meteorites suffered a shock event at a time they were located on their parent bodies. This left many petrographic signs of alteration, but estimating the temperatures and pressure involved has proved fairly difficult. Figure 14 shows a histogram of TL sensitivities for meteorites of type 5 and 6 with petrologic shock classifications (i.e. "facies") indicated; facies a is unshocked and facies f is heavily shocked. The heavily shocked individuals have lower TL sensitivities than the others, since shock pressures in excess of 30 GPa cause the feldspar to convert the glass to maskelynite, either by melting or via a solid state transformation. Samples of the unshocked Kernouve meteorite, after annealing at a variety of temperatures for 10 h, showed a decrease in TL sensitivity, especially after annealing at 1100°C (sodic feldspar melts at 1120°C); the data are shown across the top of Figure 14 (23). These data confirm petrologic estimates for the post-shock temperature for facies e-f of around 1100°C.

Induced thermoluminescence measurements on a suite of artificially shocked terrestrial low-feldspar samples were reported by Hartmetz *et al.* (24). There were changes in the induced TL peak shape comparable to those discussed above, suggesting that either disordering, or the changes in defect structure preceding disordering, occurred during the shock process. There has been considerable discussion in the literature as to whether the shock process causes disordering of ordered feldspars, and of its significance

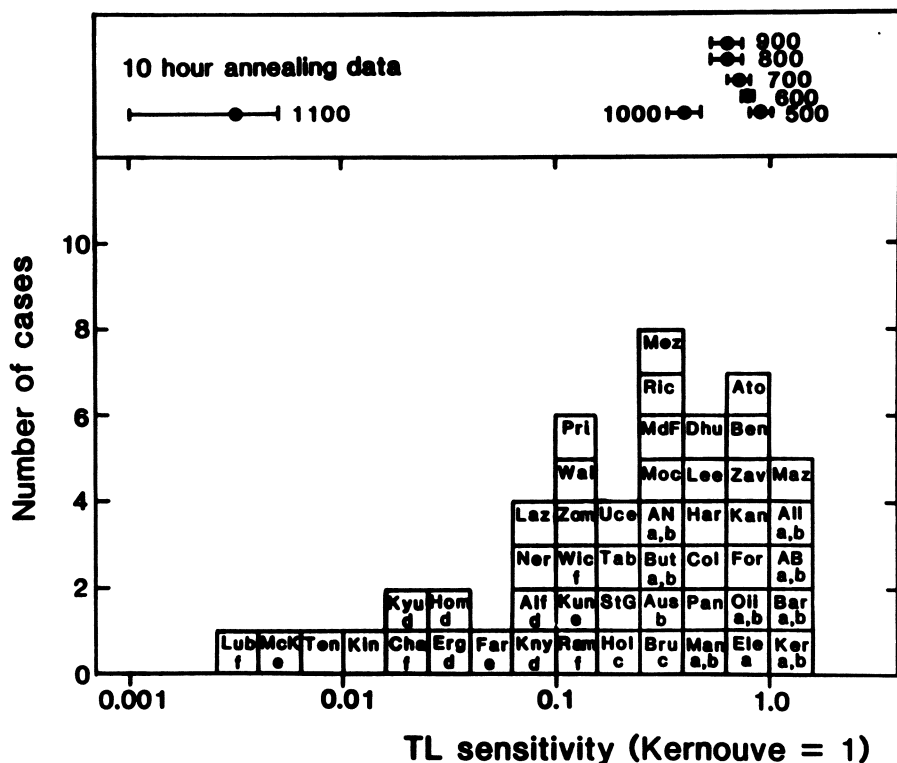


Figure 14. Histogram of TL sensitivity values for type 5,6 ordinary chondrites. The meteorites are identified by the first three letters of their names, and the letter under the name refers to a qualitative ranking according to the intensity of shock experienced; a is unshocked and f is most heavily shocked. The data along the top of the figure refer to observed TL sensitivities for samples of the Kernouve meteorite annealed for 10 h at the temperatures indicated ($^{\circ}\text{C}$). (Reprinted with permission from Ref. 23. Copyright 1984 Pergamon Press.)

for understanding the shock history of feldspar-bearing rocks from terrestrial craters. Efforts to measure disordering directly, using X-ray diffraction and spectroscopic methods, are of marginal success because of the small amounts of feldspar surviving conversion to glass by shock.

Antarctic Meteorites. Numerous meteorites being recovered in Antarctica seem to have fallen 10^5 years ago, maybe more. Several authors have suggested that there are elemental and isotopic differences between meteorites found in the Antarctic and those falling currently, and that the earth may be sampling a different parent object or a different part of the parent object that was supplying meteorites to earth 10^5 years ago (25). It is clear that some of these data reflect terrestrial weathering, but some of the purported differences are difficult to explain this way. Figure 15 shows plots of TL peak temperature against TL peak width for meteorites found in the Antarctic (Figures 15b,d) and those observed to fall in the last 250 years or so (Figures 15a,c). The two largest classes of ordinary chondrites, the H and L chondrites, which are distinguished on the basis of bulk chemistry, are plotted separately because they clearly came from separate objects in space. For the L chondrites (Figures 15c,d), the data are rather sparse and, at best, only suggestive of a difference between non-Antarctic and Antarctic meteorites, but for the H chondrites (Figures 15a,b) there is a marked difference. Since it seems clear that peak temperature and width are controlled by the relative proportions of low and high feldspar, or some other high temperature phase with unique TL properties, the position on this plot is governed by peak metamorphic temperature and post-metamorphic cooling rate. There are apparently metamorphically-related differences between the meteorites currently falling and those that fell to earth 10^5 years ago.

Chondrules. There are systematic differences in the thermoluminescence properties of chondrules physically separated from meteorites. Figure 16 shows plots of TL sensitivity against peak temperature and peak width for chondrules separated from the Dhajala ordinary chondrite (type 3.8). The TL sensitivities of individual chondrules in Dhajala range over about two orders of magnitude and show a factor of two range in their peak temperatures and widths. About 80% of the chondrules have relatively low TL sensitivity and broad peaks at high glow curve temperatures; much like the type 3.5-3.9 chondrites or samples of the Allan Hills A77214 meteorite annealed above 700°C (Figure 12). The feldspar in these chondrules presumably crystallized at temperatures $>700^\circ\text{C}$, or the feldspar in the chondrules formed at lower temperatures and has subsequently been heated to temperatures $>700^\circ\text{C}$. The remaining 20% of the chondrules separated from Dhajala have rela-

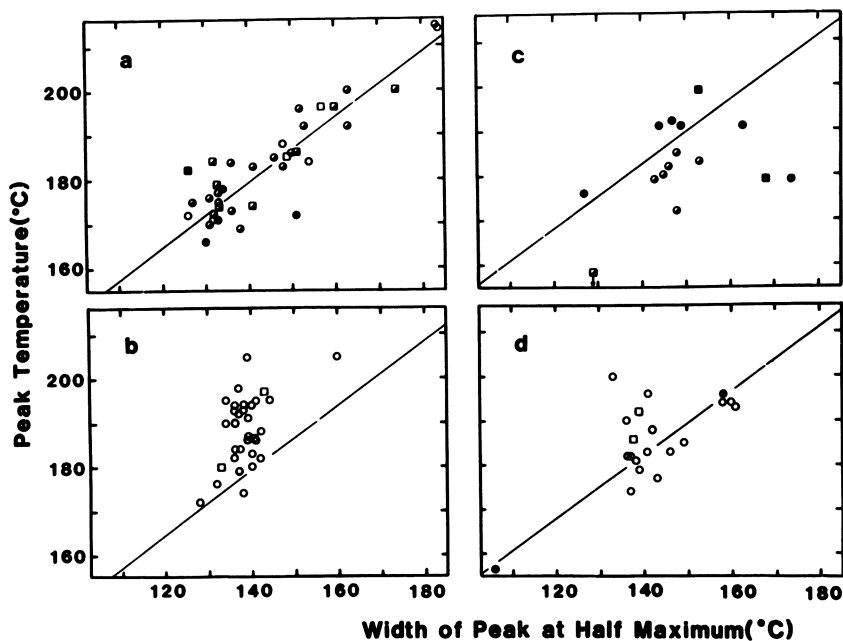


Figure 15. Plots of peak temperature against peak width for meteorites collected in the Antarctic (figures b and d) and for meteorites observed to fall elsewhere in the world (figures a and c). Two classes of ordinary chondrite are plotted separately, H chondrites (figures a and b) and L chondrites (figures c and d). Shock classes are indicated, where known, by the shading of the symbols (shock classes a-c, half filled; shock classes d-f, filled; shock class unknown, open). A few type 4 chondrites are plotted as squares. (Reprinted with permission from Ref. 34. Copyright 1988 Pergamon Press.)

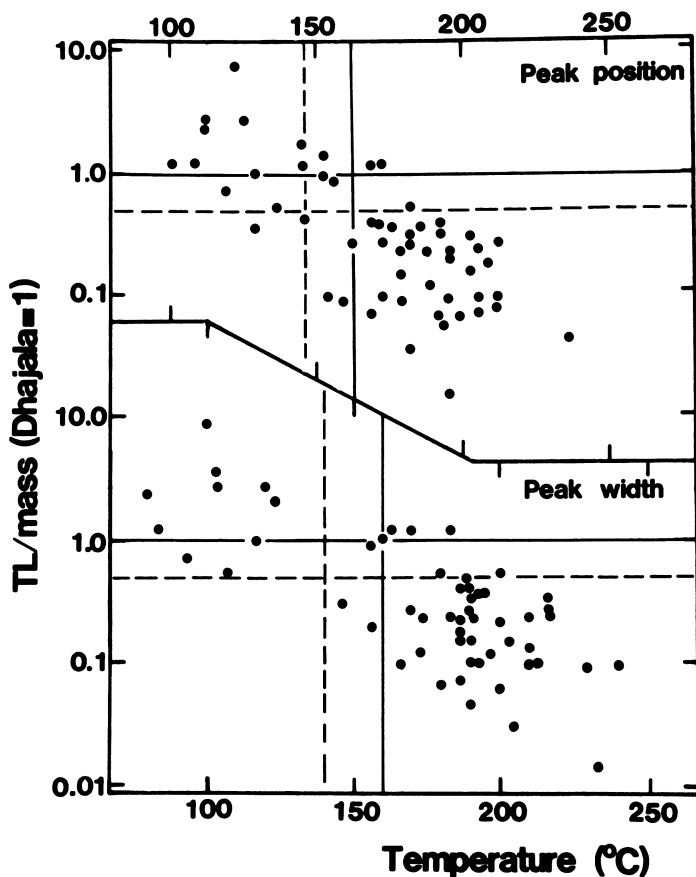


Figure 16. Plot of TL sensitivity against peak temperature and peak width for chondrules separated from the Dhajala meteorite (type 3.8). Because the chondrule masses vary over several orders of magnitude, their TL data have been divided by mass. (Reprinted with permission from Ref. 26. Copyright 1984 Pergamon Press.)

tively high TL sensitivities and they have narrow TL peaks at low glow curve temperatures; much like the type 3.2-3.5 chondrites in Figure 12. It is clear that the crystallization of feldspar has taken place over a variety of temperatures and has occurred to different extents in different chondrules. Some authors have suggested that chondrules in these meteorites suffered metamorphism prior to being incorporated into the meteorite, and these data seem to confirm that idea. However, there are relationships between TL properties and the composition of the mesostases in the Dhajala chondrules which suggested to Sears *et al.* that the facility of crystallization affects TL sensitivity (26). Each chondrule therefore experienced the same metamorphic history, but while the glass in some chondrules crystallized relatively little, and became closed systems at high temperatures, other chondrules continued to crystallize as the post-metamorphic temperature fell into the fields of lower-temperature forms of feldspar. We have recently extended this study to other type 3 ordinary chondrites of various petrologic types and found that the distribution of data over plots analogous to Figure 16 varies with type in the way expected for crystallization of the glass during various metamorphic regimes.

CO Chondrites. The CO chondrites are a class of carbonaceous chondrites, whose bulk composition distinguishes them from ordinary chondrites, but which are mineralogically and petrologically somewhat analogous to the ordinary chondrites. For example, they are petrologic type 3, and have experienced a range of metamorphic intensities; McSween divided them into petrologic subtypes I, II, and III (27). One of the petrologic trends observed by McSween is the crystallization of primary glass to form feldspar. Unlike the ordinary chondrites, the CO chondrites contain numerous inclusions of Ca,Al-rich minerals, among which is plagioclase.

The induced TL curves consist of two peaks, one at peak temperatures corresponding to the low form and one at a peak temperature corresponding to the high form. Annealing causes the low peak to disappear and merge with the high peak. The low peak varies in intensity with McSween's petrologic subtype, and the numerous petrologic data on which they are based, while the high peak is independent of metamorphism experienced (28; Figure 17). It was suggested that the low peak was due to feldspar formed by crystallization in the low field and that the high peak was due to primary feldspar in the Ca,Al-rich inclusions.

Shergottites. The shergottite meteorites are a rare class of meteorites which consist essentially of pyroxene and maskelynite. Their composition, petrography, age and gases trapped within the fabric of the meteorite have led to a widespread idea that these meteorites, and the related nakhlites and Chassigny meteorites, were ejected from Mars,

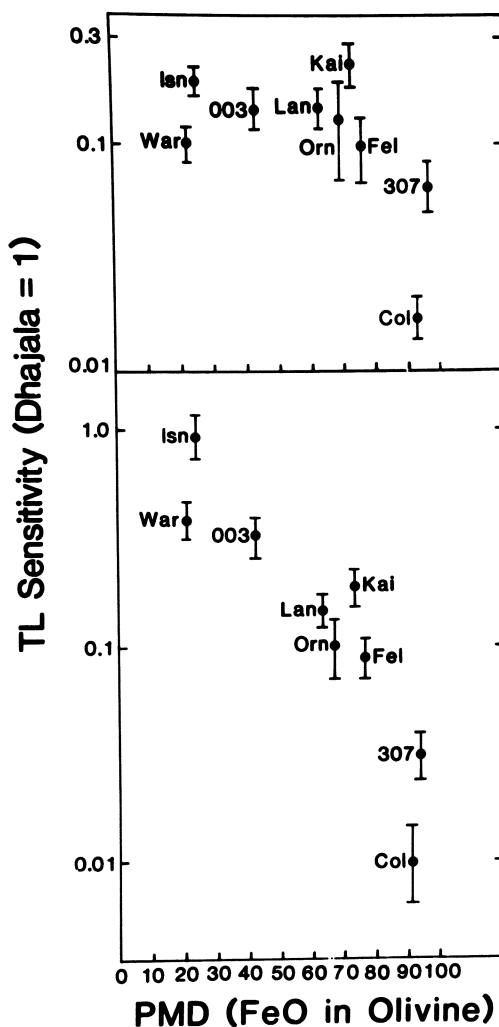


Figure 17. TL sensitivity against silicate heterogeneity (a measure of metamorphic intensity since metamorphism homogenizes silicate compositions) expressed as percent mean deviation from the mean for the CO chondrite class. The 130°C peak is plotted in the lower portion of the diagram and the 250°C peak is plotted in the upper part of the diagram. The meteorites, which are identified by the first three letters or last three numbers of their names, have been assigned to petrologic (metamorphic) types I-III (I low) on the basis of petrologic data by McSween (27) and others as follows: Isna III, Warrenton III, Allan Hills A77003 II, Ornans II, Lance II, Felix II, Allan Hills A77307 I, Kainsaz I, Colony I. (Reprinted with permission from Ref. 28. Copyright 1987 Pergamon Press.)

and it was the force of ejection that converted their feldspar into maskelynite (29). The biggest difficulty in understanding such an origin concerns the feasibility of ejecting large objects from the surface of a planet. Plausible mechanisms have been devised that might explain the ejection of meter-sized objects, but not the 10-100 m objects the shergottites were thought to be at the time of ejection. The estimated ejecta size is based on diffusion calculations for the loss of argon from the meteorites, and such calculations are critically dependent on the assumed value for the temperature following the formation of maskelynite by shock. A value of 400°C is suggested by annealing experiments on shergottites and the associated changes in refractive index, and this leads to calculated ejecta sizes in the 10-100 m range. The arguments have been succinctly summarized by McSween (29).

The shergottites show trends in TL peak temperature, peak width and TL sensitivity which are most readily interpreted in terms of the TL being produced by trace amounts of feldspar in the maskelynite (30). Maskelynite crystallizes very readily, and laboratory heating for an hour at 900°C is sufficient to cause 10-fold increases in TL sensitivity. If, as seems likely, the feldspar in the maskelynite formed during post-shock cooling, then the existence of a high form of feldspar that can be produced in the laboratory by annealing above 600°C, suggests that post-shock heating of the shergottites as they were ejected from Mars was in excess of 600°C. The situation is summarized by Figure 18. The corresponding estimated size for the ejecta is in the meter range, and current theories are well capable of accounting for the ejection of objects this small from Mars.

Summary and Concluding Remarks

In this brief review of the induced TL and CL properties of meteorites we have summarized the factors accounting for TL sensitivity and the main features of the peak shape (peak temperature and peak width). The TL sensitivity of meteorites is governed primarily by the amount of feldspar; in all but a few meteorites, the TL is produced almost exclusively by plagioclase. This has been demonstrated by mineral separation experiments, by petrographic and electron microprobe studies of the cathodoluminescence properties of meteorites, and by annealing experiments with meteorites and terrestrial feldspars. The shape of the TL peak is also governed by thermal history. Most probably, the conversion of the low temperature, ordered form of feldspar to the high temperature, disordered form of feldspar is responsible for the considerable increases in peak temperature and width observed with increasing metamorphism or laboratory annealing. However, the relationship between TL properties and disordering is not simple; the TL changes

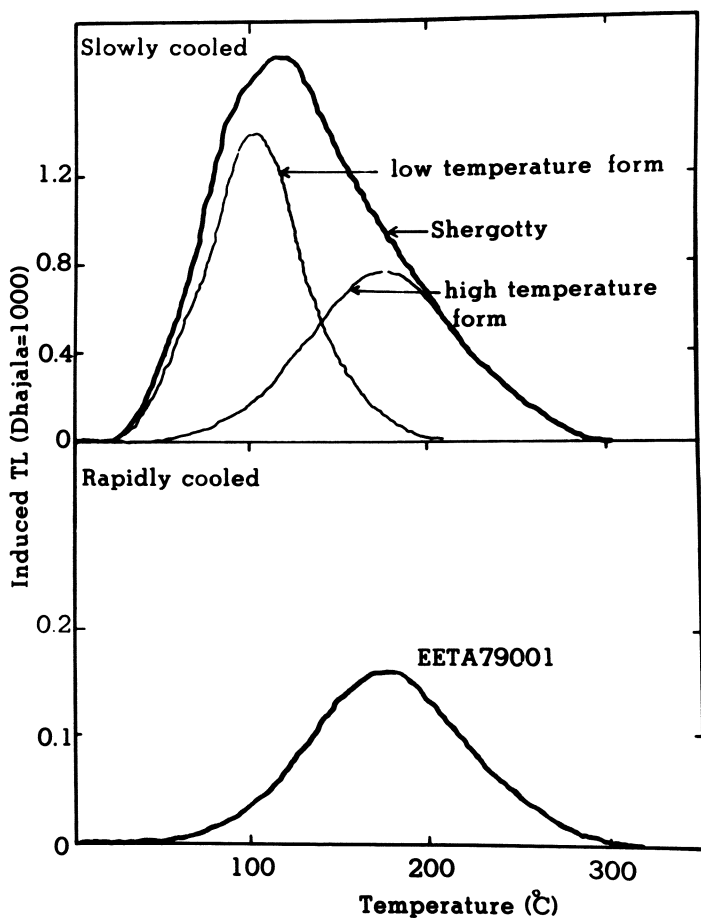


Figure 18. Glow curves for two Shergottite meteorites with an explanation for the differences in glow curve shape based on two components whose relative abundance depends on maximum temperature and cooling rates. (Reprinted with permission from Ref. 30. Copyright 1986 Pergamon Press.)

appear to occur more readily than disordering and may be associated with processes preceding disordering.

Several studies of various kinds of meteorites have shown that induced TL properties provide new insights into these processes, sometimes in a quantitative way. This is despite the uncertainty in the details of the peak shape - disordering relationship, because even an empirical application of laboratory data leads to many useful conclusions. To date, the applications have been mainly to meteoritic problems, but there are many instances in which one can envisage useful application to terrestrial problems. Low grade metamorphism and weathering are examples of processes that might reasonably be addressed using induced TL properties.

Acknowledgments

We are grateful to Walter Manger, Department of Geology, University of Arkansas, for the use of his cathodoluminescence apparatus, two anonymous reviewers, and especially, Ed Scott for constructive reviews, and Raye Stucker and Hazel Sears for help with manuscript preparation. This work is supported by grants from NASA (NAG 9-81 and NGT-50064 to D.W.G. Sears) and the Quintana Petroleum Corporation, Houston (to W. Manger).

Literature Cited

1. Herschel, A.S. Nature 1899, **60**, 29.
2. Howard, E. Phil. Trans. 1802, **92**, 168-212.
3. Hasan, F.A.; Haq, M.; Sears, D.W.G. Proc. 17th Lunar Planet Sci. Conf., Part 2, J. Geophys. Res. 1987, **92**, E703-9.
4. Antarctic Meteorite Newsletter, Johnson Space Center, Houston, TX, 1988
5. Van Schmus, W.R.; Wood, J.A. Geochim. Cosmochim. Acta 1967, **31**, 747-65.
6. Sears, D.W.; Grossman, J.N.; Melcher, C.L.; Ross, L.M.; Mills, A.A. Nature 1980, **287**, 791-95.
7. Lalou, C.; Nordemann, D.; Labyrie J. C.r. hebd. Seanc. Acad. Sci. (Paris) Serie D 1970, **270**, 2104-2401.
8. Sears, D.W.; Grossman, J.N.; Melcher, C.L. Geochim. Cosmochim. Acta 1982, **46**, 2471-81.
9. Guimon, R.K.; Keck, B.D.; Weeks, K.S.; DeHart, J.; Sears, D.W.G. Geochim. Cosmochim. Acta 1985, **49**, 1515-24.
10. DeHart, J.; Sears, D.W.G. Lunar and Planetary Science XVII, 1986, pp 160-61.
11. DeHart, J.M.; Lofgren, G.E.; Sears, D.W.G. Lunar and Planetary Science XVIII, 1987, pp 225-26.
12. DeHart, J.M.; Lofgren, G.E.; Sears, D.W.G. Lunar and Planetary Science XIX, 1988, pp 259-60.

13. Steele, I.M. Geochim. Cosmochim. Acta 1986, 50, 1379-95.
14. Sears, D.W.G.; Weeks, K.S. Proc. 14th Lunar Planet. Sci. Conf., Part 1, J. Geophys. Res. 1983, 88, A773-78.
15. Lofgren, G.E. Bull. Geol. Soc. Amer. 1971, 82, 111-24.
16. Hutchison, R.; Alexander, C.M.O.; Barber, D.J. Geochim. Cosmochim. Acta 1987, 51, 1875-82.
17. McNaughton, N.J.; Barthwicks, S.; Fallick, A.K.; Pillinger, C.T. Nature 1981, 294, 639-641.
18. McNaughton, N.J. Proc. Lunar Planet. Sci. Conf. XIII, J. Geophys. Res. 1982, 87, A297-302.
19. Sears, D.W.G.; Morse, A.D.; Hutchison, R.; Guimon, R.K.; Alexander, C.O.; Wright, I.P.; Pillinger, C.T. Lunar and Planetary Science XIX, 1988, pp 1051-52.
20. Smith, J.V. Feldspar Minerals; Springer-Verlag: New York, 1974.
21. Hartmetz, C.P.; Sears, D.W.G. Lunar and Planetary Science XVIII, 1987, pp 397-98.
22. Pasternak, E.S. Ph.D. Thesis, University of Pennsylvania, Philadelphia, 1978.
23. Sears, D.W.G.; Bakhtiar, N.; Keck, B.D.; Weeks, K.S. Geochim. Cosmochim. Acta 1984b, 48, 2265-72.
24. Hartmetz, C.; Ostertag, R.; Sears, D.W.G. Proc. 17th Lunar Planet. Sci. Conf., Part 1, J. Geophys. Res. 1986, 91, E263-74.
25. Dennison, J.E.; Lingner, D.W.; Lipschutz, M.E. Nature 1986, 319, 390-92.
26. Sears, D.W.G.; Sparks, M.H.; Rubin, A.E. Geochim. Cosmochim. Acta 1984, 48, 1189-1200.
27. McSween, H.Y. Geochim. Cosmochim. Acta 1977, 41, 477-91.
28. Keck, B.D.; Sears, D.W.G. Geochim. Cosmochim. Acta 1987, 51, 3013-22.
29. McSween, H.Y. Geology 1984, 12, 3-6.
30. Hasan, F.A.; Haq, M.; Sears, D.W.G. Geochim. Cosmochim. Acta 1986, 50, 1031-38.
31. Guimon, R.K.; Lofgren, G.E.; Sears, D.W.G. Geophys. Res. Lett. 1986, 13, 969-72.
32. Guimon, R.K.; Lofgren, G.E.; Sears, D.W.G. Geochim. Cosmochim. Acta 1988, 52, 119-27.
33. Guimon, R.K.; Weeks, K.S.; Keck, B.D.; Sears, D.W.G. Nature 1984, 311, 363-65.
34. Haq, M.; Hasan, F.A.; Sears, D.W.G. Geochim. Cosmochim. Acta 1988, 52, 1679-89.
35. Guimon, R.K.; Lofgren, G.E.; and Sears, D.W.G. Lunar and Planetary Science XVIII, pp. 374-75.

RECEIVED February 22, 1989

Chapter 12

Emission of Particles and Photons from the Fracture of Minerals and Inorganic Materials

S. C. Langford and J. T. Dickinson

Physics Department, Washington State University, Pullman, WA 99164-2814

During the mechanical deformation and failure of a material, localized excitations can occur which lead to the emission of photons and various particles. This emission, called fracto-emission, can include the release of electrons, ions, neutral particles, photons, and long wavelength electromagnetic radiation. We review recent results on the characterization of fracto-emission, the determination of emission mechanisms, and the relationships between emission features and particular fracture situations. Of particular interest are the identities of the emitted species (e.g. the ions and neutral atoms and molecules), the particle and photon energies, and the time dependence of emission intensities relative to crack growth. We also relate certain fracto-emission characteristics to fractographic features determined by optical and scanning tunneling microscopy. Geological implications are also discussed.

Fracto-emission (FE) is the emission of particles and photons accompanying deformation and fracture. These emissions typically include electrons (EE), positive ions (PIE), neutral atoms and molecules, including both ground state neutrals (NE) and excited neutrals (NE*), visible photons (phE)—also called triboluminescence in this context, and long wavelength electromagnetic radiation (RE: radio emission). FE can be a sensitive probe of crack growth and the accompanying chemical and electronic processes. In addition, FE may prove useful in the remote detection of fracture events, and have implications in material transport and chemistry in geological and astronomical systems.

Past studies of FE relevant to geologic materials have included work on organic and inorganic crystals (1-12), glassy materials (13), and various minerals (14-15). Several review articles have addressed phE due to fracture, generally under the term triboluminescence (16-18). As the detection of charged and neutral particles requires a vacuum environment, FE measurements are frequently carried out in vacuum. The general features of FE from fracture in vacuum are the following (1):

- (a) In materials displaying plastic deformation, weak phE and other emissions can be observed during deformation.

0097-6156/90/0415-0224\$06.25/0

© 1990 American Chemical Society

- (b) Most emissions reach peak intensity during fracture.
- (c) Emissions often persist with reduced intensity after fracture, implying that the fracture surface is in an excited state which relaxes towards equilibrium.
- (d) Emission intensities often depend on the degree and nature of surface damage and on sample strength. More highly damaged and stronger samples generally yield more intense emissions.

In this chapter, we first briefly describe some of the apparatus used in FE studies. Then we discuss some of the FE observations which have been made during the various stages of deformation, fracture, and relaxation to equilibrium, with emphasis on the processes believed to be responsible for the emissions. Finally, we list some of the potential applications and implications of this work.

Experimental Procedures

Details of the experimental arrangements are presented in References 1-5 and 13. The majority of the experiments reported here were performed in vacuum at pressures ranging from 10^{-7} to 10^{-9} torr. For many studies, the samples are loaded into a carousel sample holder and sequentially rotated into position for testing. Typical sample dimensions are $2 \times 6 \times 12$ mm³. The samples are usually loaded in three point bend. The load force is usually monitored to determine the rate of loading, the force at fracture, and the time of fracture.

Charged particles are often detected with a Channeltron Electron Multiplier (CEM), which produces fast (10 ns) pulses with high detection efficiencies for both electrons and positive ions. Excited neutrals with sufficient internal energy can also ionize upon collision with the CEM and be detected. By varying the CEM bias voltage and the voltages on nearby grids or barriers, the charge of the detected particles can be determined unambiguously. Photons are usually detected with a photomultiplier tube, which also produces fast (30 ns) pulses with reasonable detection efficiencies, especially in the blue and ultraviolet. When used in air, photomultiplier tubes can be readily cooled, greatly reducing background noise levels.

The identifications of atomic and molecular species is undertaken with a variety of mass spectroscopies. Time-of-flight (TOF) mass spectroscopy is of value for very short lived or highly peaked emissions. More sustained emissions are more readily studied with a quadrupole mass spectrometer (QMS), which can be tuned to a single mass peak. The time evolution (on a microsecond time scale) of a particular mass emission can be determined from the observed signals. Under the appropriate conditions, both these tools can be applied to studies of neutral emission (with ionizer) and positive or negative ion emission (without ionizer).

RE is usually detected with a coil antenna, with or without a ferrite core, placed near the sample. This antenna couples to the changing B fields associated with electromagnetic emissions. RE is especially interesting, as it is often associated with electrical discharges within the crack and on the fracture surfaces.

Results and Discussion

Emission During Deformation. Ionic crystals which undergo plastic deformation prior to fracture often yield pHE prior to fracture (9-11). Figure 1 shows typical pHE and EE during and after loading of single crystal MgO in three point bend (2). Little if any EE is observed during loading, but significant pHE does occur and increases in intensity until fracture. Both pHE and EE have been observed during the compression

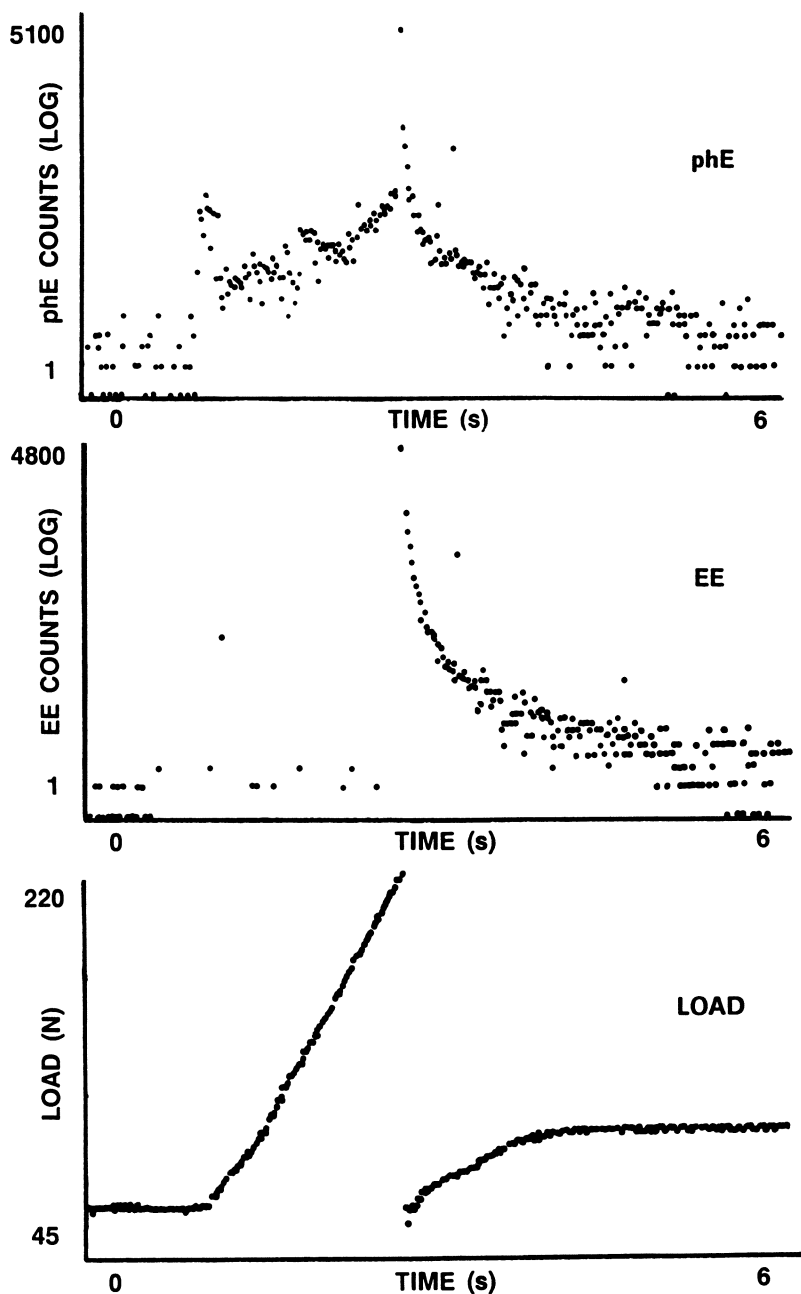


Figure 1. phE, EE, and load measurements taken before, during, and after the fracture of single crystal MgO in three point bend. The three plots are aligned in time. Fracture coincides with the peaks in phE and EE, and the drop in load. (Reproduced with permission from Ref. 2. Copyright 1987 American Institute of Physics.)

of colored and uncolored alkali halide crystals (9,10). Due to the relatively high strength of these materials in compression, large plastic strains are much more easily achieved in compression than in three point bend. In addition to slowly varying emission such as that shown in Figure 1, short pH E pulses of 30-40 ns duration are also observed during compression (9). RE has also been observed (12).

The slowly varying pH E has been attributed to local electronic excitations at vacancy clusters in the bulk material. As dislocations move and multiply in response to the applied stress, vacancies are produced by a jog dragging mechanism. These vacancies may be produced in electronically excited states, or they may be subsequently excited as other dislocations move nearby. Electronic excitations can be facilitated by energy level shifts due to the high stress fields in the vicinity of dislocations. By way of analogy to the molecular case, one can imagine that under stress the energy of bonding (valence) orbitals is likely to rise while the energy of nonbonding (conduction) orbitals is likely to drop. Computational estimates indicate that these energy shifts can be as large as a few eV (8). This is sufficient to promote charge exchange between the localized states in the vacancy clusters and localized dislocation states. Electronic excitations are also facilitated by the tendency of dislocations in ionic crystals to pick up charge in the form of primary defects. A typical recombination event might involve the transfer of an electron from a dislocation-related state to a "self-trapped hole" localized at an oxygen ion adjacent to a vacancy cluster. When recombination occurs, an intermediate excited state (exciton) similar to an excited oxygen ion is formed. This exciton can decay radiatively to produce a photon which escapes through the transparent crystal to the detector. Similar emissions are observed in cathodoluminescence studies of plastically deformed MgO (19).

pH E and EE spikes during compression of alkali halides have been attributed to electrical discharges between patches of the sample surface (9). Although no evidence of microcracking was observed in the alkali halides, we have frequently observed pH E, EE, and NE spikes accompanying loading of semi-brittle materials and composites which we have attributed to microcracking. We also mention that regions of fairly high charge density are formed on fracture surfaces in vacuum as charge carriers are brought to the surface by moving dislocations.

Emission During Fracture. As seen in Figure 1, fracture can be associated with very intense pH E and EE. Figure 2 shows pH E on a much faster time scale during the fracture of MgO in three point bend, along with a timing signal which marks the progress of the crack through the sample (Langford, S. C.; Dickinson, J. T.; Jensen, L. C. to be published). In three point bend, the sample is supported near both ends and loaded in the middle from the opposite side. During loading, one face of the sample experiences tensile stress and the other compressive stress. In this experiment, fine Au wires (30 nm thick) were plated onto the sample so that pH E could be correlated with the progress of fracture. A small voltage applied across the strips allows the observation of a current drop as each strip is broken. Seven strips were plated along the tensile side of the sample, and two on the edges of the sample toward the compressive side. Fracture usually initiates at a corner of the sample on the tensile side, then travels across the tensile side. Thus the strips on the tensile side break first. As the figure indicates, the pH E intensity is rapidly rising during the interval in which these strips break, then drops somewhat. The final drop in current marks the approximate end of crack propagation through the compressive side. A decay in the pH E is observed after the completion of fracture which is approximately first order with a time constant of about 2 μ s.

These measurements indicate that markedly different pH E intensities are associated with different stages of fracture in MgO. Fracture along the tensile side yields especially intense pH E, while the remainder of the fracture event yields less intense pH E. These stages of fracture are evident in photographs of the fracture

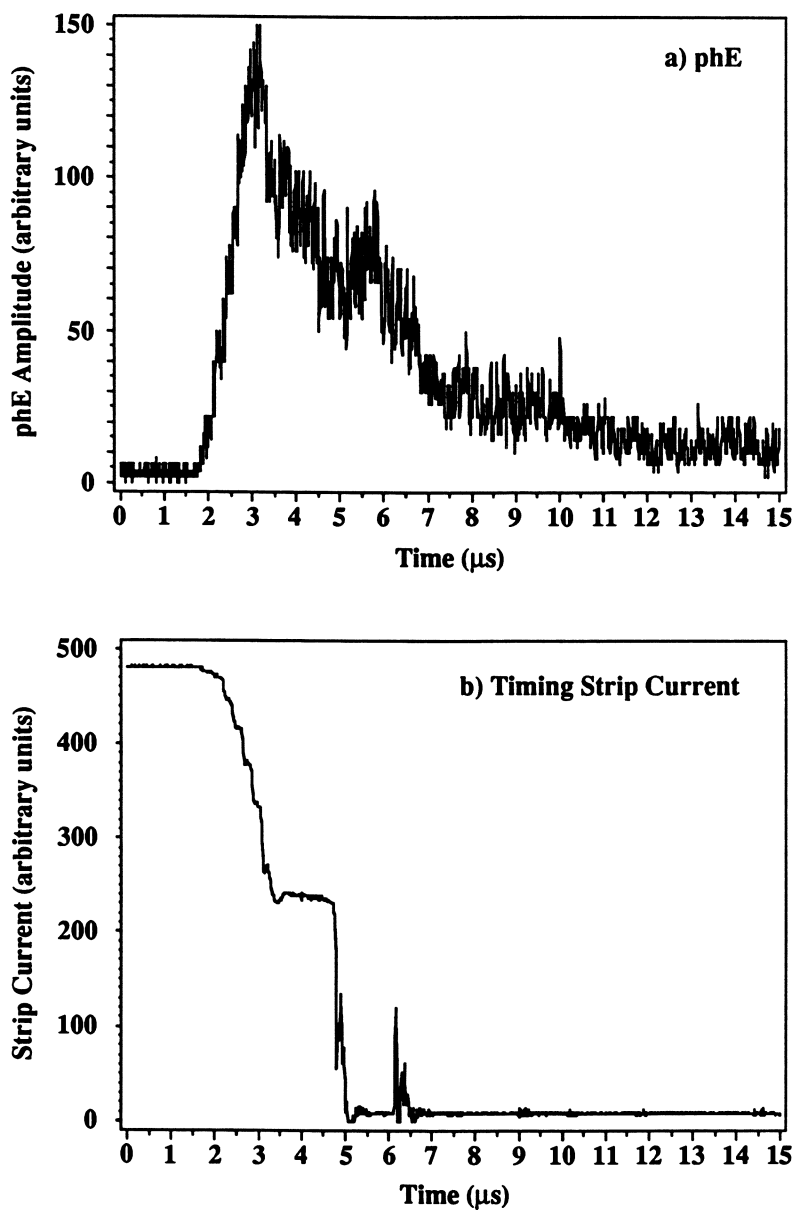


Figure 2. pH E and timing strip current measurements showing variations in pH E intensity during the fracture of single crystal MgO in three point bend. The progress of fracture is marked by drops in the timing strip current.

surface, shown in Figure 3. The surface formed along the tensile side appears dark in this photograph, which was illuminated along the [100] axis of the crystal, because the surface itself is inclined about 16° to the (100) surface. (The geometry of the fracture surface is indicated in Figure 4d). The tensile surface is $\sim(720)$ in orientation. The remainder of the fracture surface is (100) in orientation and appears bright in the photograph. The general features of Figure 3 are typical of fracture in this geometry, appearing in previously published photographs of MgO fracture surfaces (20,21). MgO readily cleaves along {100} planes, which are the lowest energy surfaces of this material. We suspect that the relatively intense emission accompanying fracture along the tensile side of these samples is related to the higher energy required to create the observed non-{100} planes in this region. Except for occasional steps, both tensile and compressive surfaces appear to be microscopically smooth on scales as small as 100 nm when observed with an SEM. The defects or structures responsible for the intense pH E from the tensile side appear to be less than 100 nm in extent.

pH E during fracture results from a variety of processes. Radiative decay of excitons, similar to that expected to occur at *internal* surfaces (vacancy clusters) during deformation, is a likely major source of pH E in MgO *during* fracture. Bulk excitons in MgO generally decay nonradiatively, but exciton related surface luminescence is readily stimulated in MgO powders by UV irradiation (22). There is evidence that excitons bound at corner sites differ significantly from those at edge and (nondefective) surface sites. Such a mechanism would explain the higher emission intensities observed from the more defective surfaces (therefore, more corner sites) on the tensile side of our MgO samples, relative to the surface formed later. In any case, the nature and density of defects and irregularities of the fracture surface are definitely related to the observed emissions.

Recently, we have obtained Scanning Tunneling Microscope (STM) images of surfaces of materials such as MgO by tunneling to very thin Au coated surfaces following the method of Jaklevic et al. (23,24). We have observed good stability and conductivity in films 20-100 Å in thickness, with no evidence of Au clusters. The best resolution to date is ~ 2 Å laterally (in the plane of the surface) and 5-10 Å vertically (normal to the surface).

Three STM scans of a gold-coated MgO fracture surface are shown in Figure 4. The scans shown in Figures 4a and 4b were taken on the tensile side of the fracture surface, while that of Figure 4c was taken on the compressive side of the fracture surface. A variety of smooth and rough regions were found on both compressive and tensile sides of the fracture surface. Figure 4a shows a typical flat region of the tensile side. It is $\sim(720)$ in orientation, and is flat to within ~ 36 Å. A number of similar planes were found over the entire tensile side and were typically of μm dimensions. Interspersed between the smooth regions were patches of rough topography, one of which is shown in Figure 4b. The larger facets are still of $\sim(720)$ orientation, and appear to be joined by regions of a variety of orientations. At our present resolution (5-10 Å), these facets do not appear to be composed of (100) (cleavage plane) steps. Large (100) regions do appear on the compressive side of the sample, as shown in Figure 4c. We have not yet succeeded in imaging the steps necessary to accommodate the $\sim(720)$ inclination of the tensile side, which must therefore be at most several atomic layers high. Further work is needed to determine whether these atomic or nearly atomic steps are responsible for the intense emission from the tensile side, or whether it is due to larger structures, such as those displayed by the rough area in Figure 4b.

Intense EE and PIE have been observed during fracture as well. In recent work, we have succeeded in determining the predominate ionic species created during the fracture of UV grade fused silica. (Langford, S. C.; Dickinson, J. T.; Jensen, L. C. *J. Vac. Sci. Technol. A*, in press.). Both time-of-flight and quadrupole mass spectroscopy indicate the presence of ions of mass 16, 28, 44, and 76, which we

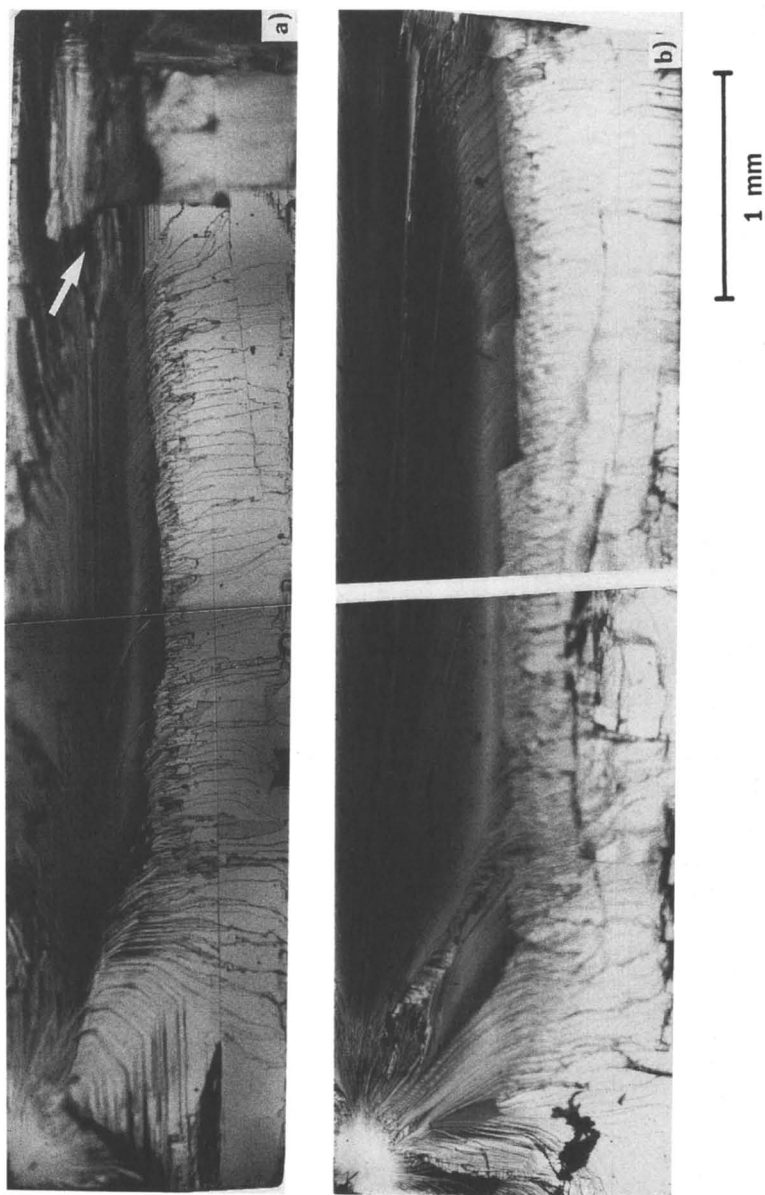


Figure 3. Photographs of fracture surfaces of single crystal MgO fractured in three point bend. The surface of a) yielded EE of typical intensity, while that of b) yielded unusually intense EE. (Reproduced with permission from Ref. 2. Copyright 1987 American Institute of Physics.)

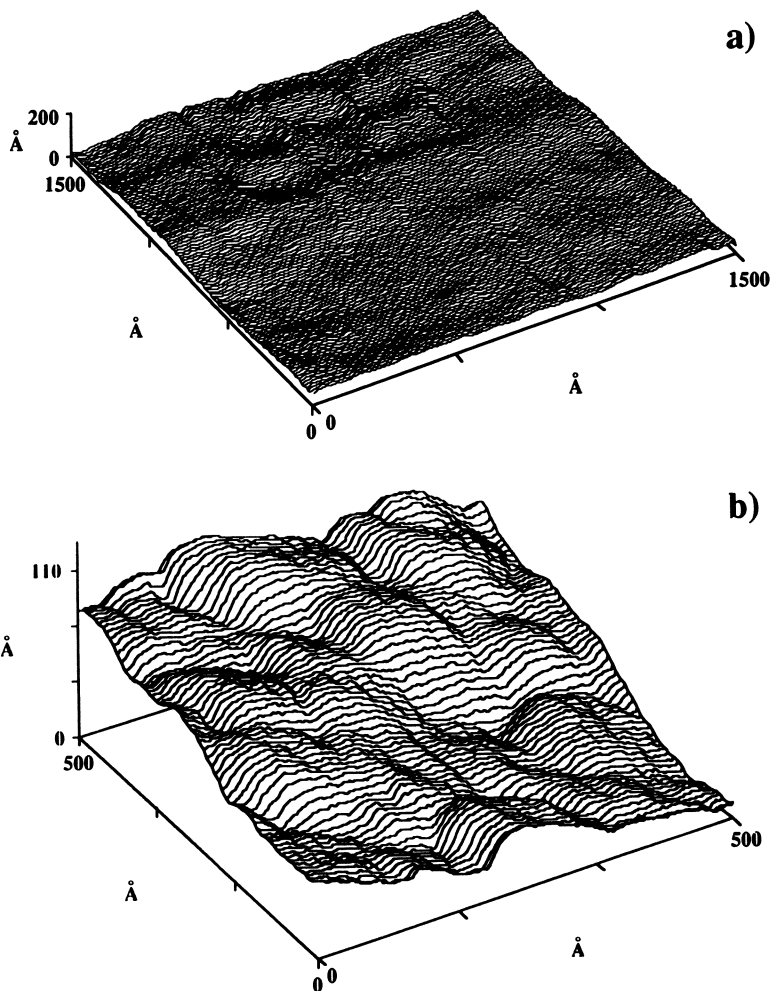


Figure 4. STM scans of an MgO fracture surface produced in three point bend: (a) a typical smooth $\sim(720)$ region on the tensile side of the sample, and (b) a typical rough region on the tensile side of the sample. *Continued on next page.*

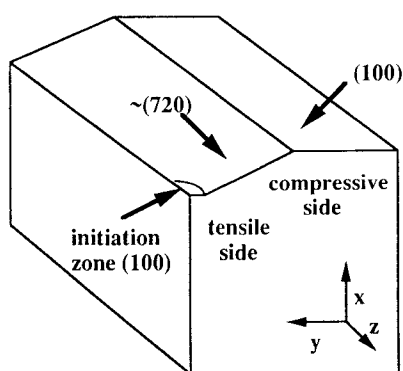
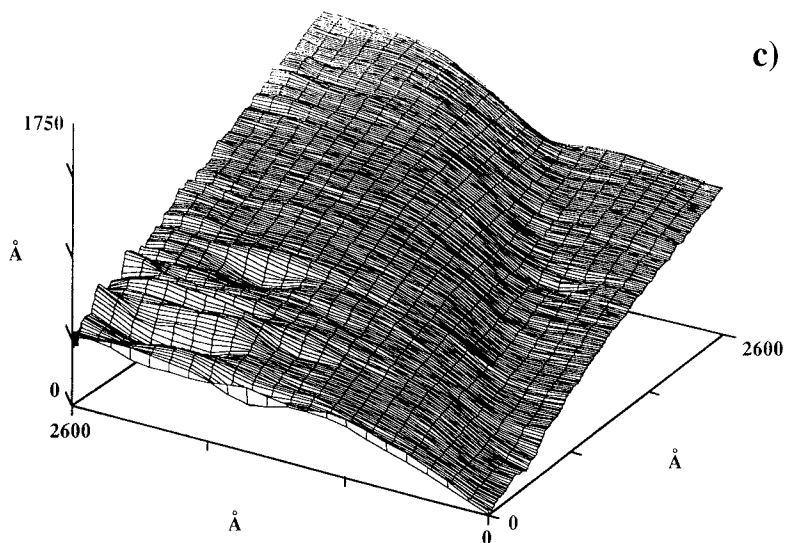


Figure 4. Continued. STM scans of an MgO fracture surface produced in three point bend: (c) a step between two (100) facets in a typical, smooth region on the compressive side of the sample. A schematic representation of the broken crystal is shown in (d). Note the contrasting distance scales in the figures.

identify with O^+ , Si^+ , SiO^+ , and Si_2O^+ , respectively. PIE measurements made with a quadrupole mass spectrometer tuned to mass 44 are shown in Figure 5. The mass resolution of the quadrupole is about ± 2 AMU in this region. The duration of SiO^+ emission correlates well with the duration of intense pH Emission, indicating that emission is confined to the duration of the fracture event. The emission of Si^+ and Si_2O^+ is also confined to the duration of the fracture event. Since four Si-O bonds must be broken to release Si-containing species from an ideal glass network, these observations suggest that either "defective" lattice Si is involved or that multiple bond breaking is a regular feature of fracture in fused silica. Haneman and Lagally argue that fracture in single crystal Si involves three broken bonds per surface atom (25). Since the structure of fused silica is at least locally similar to that of crystalline Si, it is reasonable to expect that multiple bond breaking occurs in fused silica as well. This extra bond breaking may in part account for the high fracture toughness of fused silica relative to that expected on the grounds of ideal surface energy estimates (26). In contrast to the emission of Si-containing species, the emission of O^+ persists long after fracture. We have attributed the post-fracture emission of O^+ to electron stimulated desorption of oxygen from the fracture surfaces, which is discussed further below.

The production of free charge carriers during fracture of single crystal silicon has recently been inferred from transient increases in conductivity during this period (5). pH Emission in the visible portion of the spectrum is not observed from silicon, presumably due to the small band gap of this material. However, EE has been observed (27). This is remarkable considering that the energy required to promote a silicon valence electron to the vacuum level is on the order of 4 eV, well in excess of the band gap energy.

These emissions indicate that fracture is associated with a high degree of electrical and chemical activity. Severe distortion of the lattice in the region of the crack tip is expected to be associated with energy level shifts comparable to those expected in the region of dislocations. Electronic states in this region can also undergo localization due to randomness in the local distortions, in a manner similar to that proposed by Anderson (28). Localized states of gradually increasing energy would be ideal for the production of mobile charge carriers in semiconductors and for the population of nearby, low-lying defect states in insulators (5). Random variations in the surface defect density or their population by charge carriers may result in locally charged surfaces. Even one excess charge in a million surface sites can yield very strong electric fields at the surface. Charged fracture surfaces are naturally expected in piezoelectric materials. It appears that the fracture of other crystalline and even amorphous materials can result in locally charged surfaces as well.

Intense EE in the presence of charged surfaces would result in intense electron bombardment of the newly formed fracture surfaces. Variations of surface charge have been measured directly on the surfaces of various alkali halides (6). Small excesses of positive charge can result in regions of high positive potential, which would be sites of energetic electron bombardment. Energetic (up to 10 keV) x-ray emission has been reported to accompany fracture of mica, presumably due to electron bombardment (29). This bombardment would certainly result in the production of mobile charge carriers, some of which are trapped at surface and near surface defects. These trapped charge carriers would then recombine promptly or after some delay to yield pH Emission, PIE, and other emissions. EE produced by optical stimulation of freshly cleaved NaCl with broad band visible light has been shown to originate only from regions of negative or neutral surface charge, suggesting that the electron escape probability is in part determined by the local surface electric fields (7). Thus positively charged surface regions are poor sources of EE because emitted electrons lack the energy to overcome the surface potential. However, these regions would be expected to be reasonable sources of PIE.

phE and Quadrupole Selected PIE from SiO₂

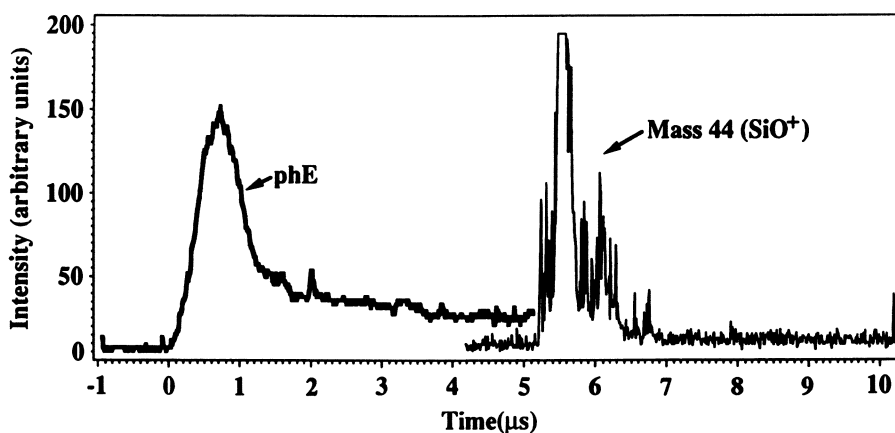


Figure 5. phE (dark line) and PIE measured by a QMS tuned to mass 44 (light line) accompanying the fracture of fused silica rod in three point bend. Time $t = 0$ is chosen to coincide with the onset of phE, which corresponds closely to the onset of fracture. (Reproduced with permission from Langford, S. C.; Dickinson, J. T.; Jensen, L. C. *J. Vac. Sci. Technol. A*, in press. Copyright 1989 American Vacuum Society.)

Electrical discharge is an extreme example of electron bombardment resulting from high charge densities. The local surface charge density is expected to be especially high at surface asperities. Discharges can be stimulated by the release of neutral molecules into the near surface vacuum, where catastrophic ionization can lead to breakdown. Such discharges can yield the intense bursts of phE, EE, and RE which apparently accompany the fracture of many materials. Indeed, the spectra of many triboluminescent materials show strong nitrogen lines, presumably due to the ionization of atmospheric or occluded nitrogen. This phE and the accompanying particle emission can excite other luminescent centers in these materials as well (Sweeting, L. M. this volume).

Significant neutral emission is also observed during and after fracture. When analyzing the time dependence of the observed NE, one must take into account both the time dependence of the emission itself and the time-of-flight of the neutral species (associated with Boltzmann velocity distributions) from the source to the mass spectrometer. We expect NE intensities to be much higher than the PIE intensities of the same molecular species due to the high probability of reneutralization as ions leave the surface. NE will be discussed more fully in the following section.

Emission Following Fracture. The relaxation of the fracture surface to chemical and electrical equilibrium can take considerable time. In ionic crystals, thermodynamic equilibrium can require surface charges and defect densities which would not be fully realizable at room temperature (30-32). As shown in Figure 1, phE and EE from some materials can persist for some seconds following fracture. These emissions result from the recombination of charges trapped at surface defects. At long times, the phE decay of MgO follows a $(1/t)^\beta$ relation, where $\beta \sim 1.2$. This is consistent with the recombination of immobile, trapped charge carriers by tunneling (33, 34). The tunneling probability is an exponential function of the distance between participating centers, resulting in very long decays. An alternative mechanism for generating similar decay curves is the recombination of mobile charge carriers due to thermally stimulated motion of one carrier under conditions of high retrapping probability. In either case, EE generally requires an Auger process (35), where, for example, an electron recombines with an appropriate defect center, resulting in the ejection of second electron from the fracture surface.

Similar mechanisms are responsible for the long EE decays observed in *cleaved* LiF (7); these long, intense EE decays are completely absent in LiF fractured in tension or three-point bend (Mathison, J. P.; Langford, S. C.; Dickinson, J. T. *J. Appl. Phys.*, in press). We have associated the prolonged EE with damaged regions at the point of cleavage blade/sample contact. This reflects the strong sensitivity of FE processes to the nature and density of defects produced during fracture. Very similar results are found in the fracture of pentaerythritol tetranitrate molecular crystals (36) where crushed samples yield intense, long lasting EE, as opposed to failure under three point bend loading which produces no detectable emission. In general, higher energy fracture surfaces, such as those formed when the crack departs from low energy cleavage planes or when extensive crack branching occurs, yield more intense, long lasting emission.

The nature of the participating defects in EE from LiF has been studied by thermally stimulated luminescence (TSL) (8). TSL peaks from LiF samples pulverized in a mortar and pestle are quite similar to the peaks from LiF irradiated with UV light, suggesting that the same defects participate in both emissions. TSL studies of MgO powders suggest that above room temperature the rate controlling process involves electron traps. phE and EE decay from MgO follow very similar kinetics, as seen in Figure 1, suggesting that phE and EE are rate limited by the concentration of the same defect.

Many geologically important minerals and rocks also display long lived phE and EE from fracture. Figure 6 shows phE and EE accompanying the fracture of

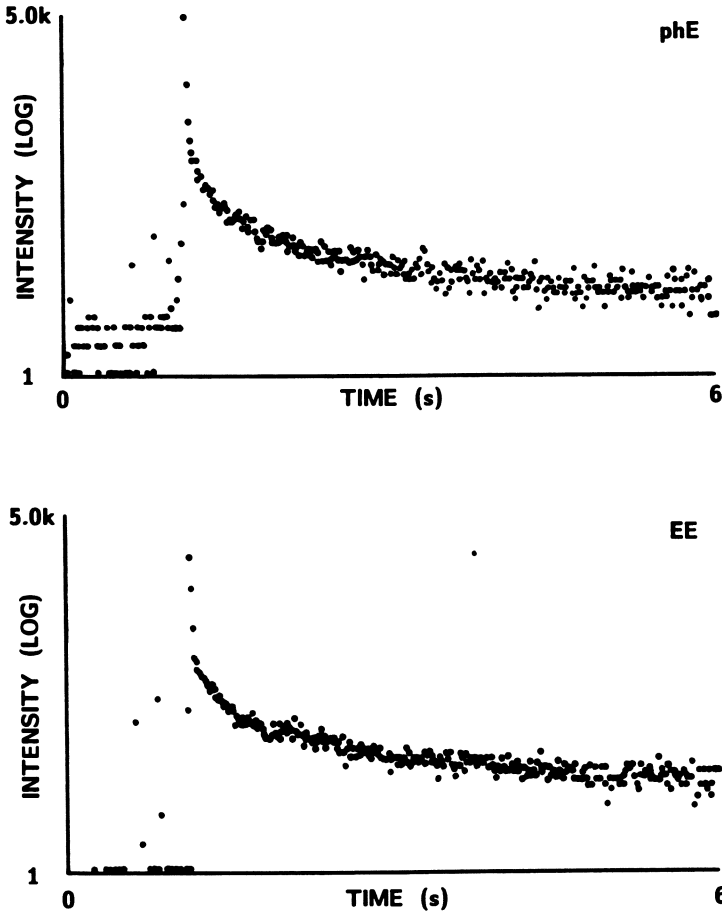


Figure 6. phE and EE accompanying the fracture of granite from Salida, Colorado, USA, in three point bend.

Publication Date: November 29, 1990 | doi: 10.1021/bk-1990-0415.ch012

granite from Salida, Colorado, USA. phE prior to fracture is very weak in this material, but otherwise both emissions are similar in form to that displayed in Figure 1. Substantial emissions were also observed from basalt, indicating that minerals without substantial quartz content can yield significant FE. The piezoelectric nature of quartz is associated with especially intense emissions from many quartz containing materials, but piezoelectricity is by no means a prerequisite for FE.

PIE can persist for some time after fracture as well, as in the case of sodium trisilicate glass. As shown in Figure 7, the PIE and EE from this glass display similar decay kinetics (13). EE intensity reflects in a proportional sense the number of electrons participating in electron bombardment of the fracture surface; thus the strong correlation between EE and PIE suggests that the persistent components of PIE are due to electron stimulated desorption (37). Fast time scale measurements of PIE from fused silica indicate that the persistent PIE from fused silica is due to O^+ , which is known to be emitted from fused silica under energetic electron bombardment. As surface defects play an important role in the surface chemistry of the silicate glasses, emission measurements on glasses containing various types of defects, such as nonbonding oxygen ions, are of interest. Also of interest is the possible emission of alkali ions (which have low ionization potentials) from alkali rich glasses.

NE is observed from the fracture of many ceramic and polymeric materials. Figure 8 displays NE signals accompanying the fracture of MgO with a QMS tuned to masses 16 and 24 (3,4). The emission of mass 16, which is due to atomic oxygen, follows a rather typical pattern—a sharp rise at fracture followed by a prolonged decay. The rise is rate limited by the response time of the electronics. The decay is real in the sense of being due to continued emission from the sample. The speed of the vacuum pumps in this experiment is sufficient at these pressures to remove gas at a much faster rate than indicated by the decay shown. The emission of mass 24, due to neutral atomic Mg, follows a much different pattern—an exponential rise in emission followed by a rather abrupt decay. This emission is autocatalytic; i.e., the emission increases at an accelerating rate until the reactants are depleted. We propose that the Mg emission results from variations in local surface stoichiometry on atomic scales. One possible surface intermediate created at fracture is clusters or patches of Mg atoms which desorb in a collective fashion (the more atoms that desorb, the lower the binding energy of the Mg atoms that remain). Numerical models of such kinetics describe the observed accelerated desorption.

Neutral emission of species other than atomic Mg from MgO is a strong function of impurity content or microstructure (4). Samples with a cloudy appearance due to the presence of brucite ($Mg(OH)_2$) precipitates, displayed especially high NE intensities of O_2 , CO, H_2O , and CH_4 . The cloudy MgO is nominally as pure as the clear with respect to metallic impurities. Single crystals of MgO are often grown in an arc furnace, with water and carbon as minor impurities. Small amounts of brucite can precipitate in portions of the crystal mass. The precipitate/MgO interface can serve as a sink for many species which are then emitted as these interfaces are exposed in fracture. The cloudy MgO is more typical of geologic materials than clear MgO, implying that NE from geologic materials can be quite intense and rich.

This is definitely so in the case of olivine from San Carlos, Arizona, USA. This olivine is believed to be derived from magmatic material. Figure 9 shows the NE detected by a QMS scanning the mass range from 0 to 110 AMU once every 80 ms (14). The time of fracture is indicated by an arrow. A wide variety of emissions are observed and persist for 100's of ms after fracture. Many of these emissions are due to hydrocarbons. We believe that many of these hydrocarbons originate from internal mineral surfaces exposed at fracture. Finally, we mention that the fracture of alkali containing glasses and minerals (e.g., obsidian, feldspar, and rock salt) yield intense alkali atom emission. In the case of alkali halides, we also see emission of

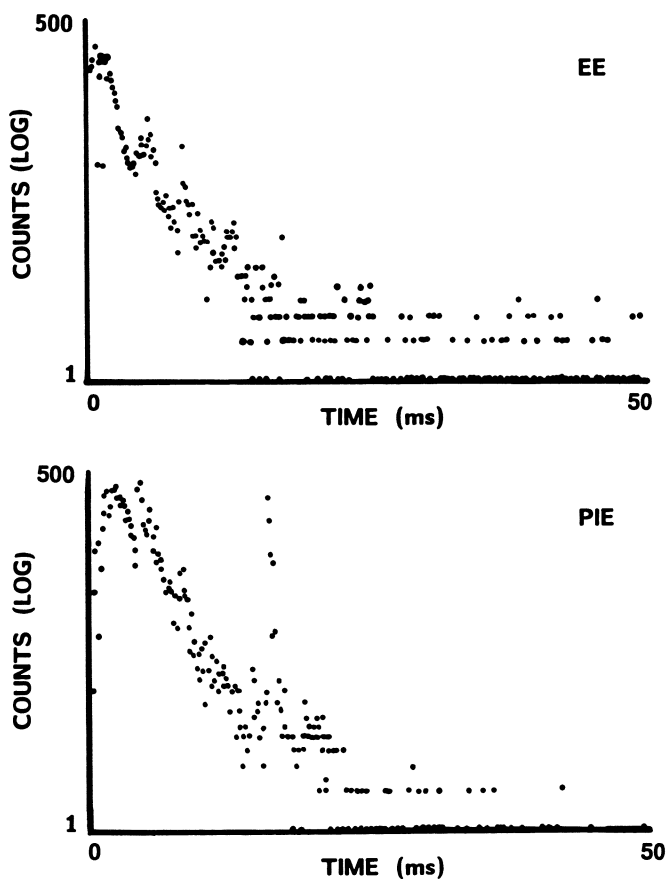


Figure 7. EE and PIE accompanying the fracture of sodium trisilicate glass in three point bend. Fracture occurred at time $t = 0$. Both emissions show evidence of detector saturation at fracture. (Reproduced with permission from Ref. 13. Copyright 1988 American Vacuum Society.)

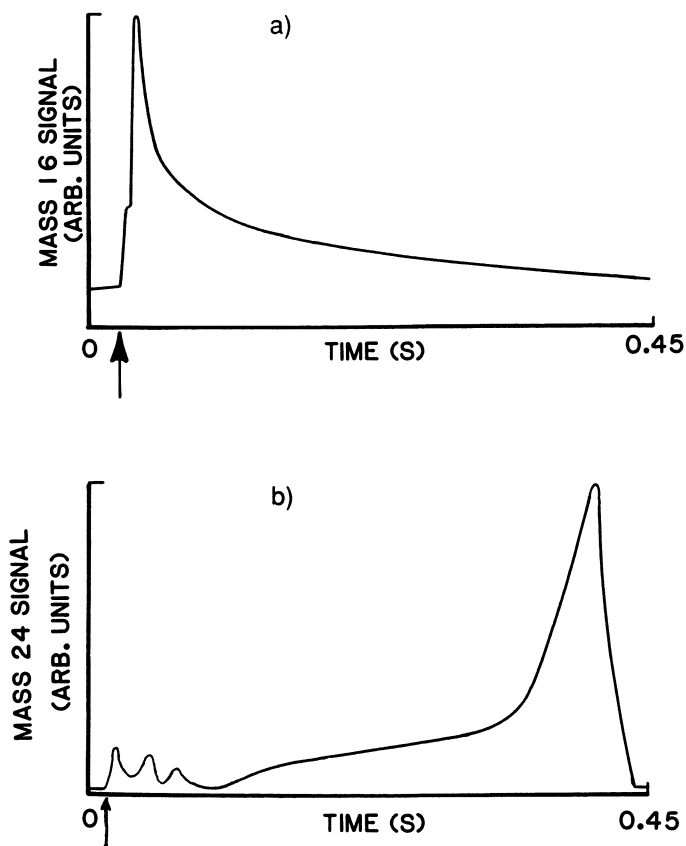


Figure 8. NE measured with a QMS tuned to a) mass 16 and b) mass 24 accompanying the fracture of single crystal MgO in three point bend. The arrows mark the time of fracture. (Reproduced with permission from Ref. 3. Copyright 1986 American Vacuum Society.)

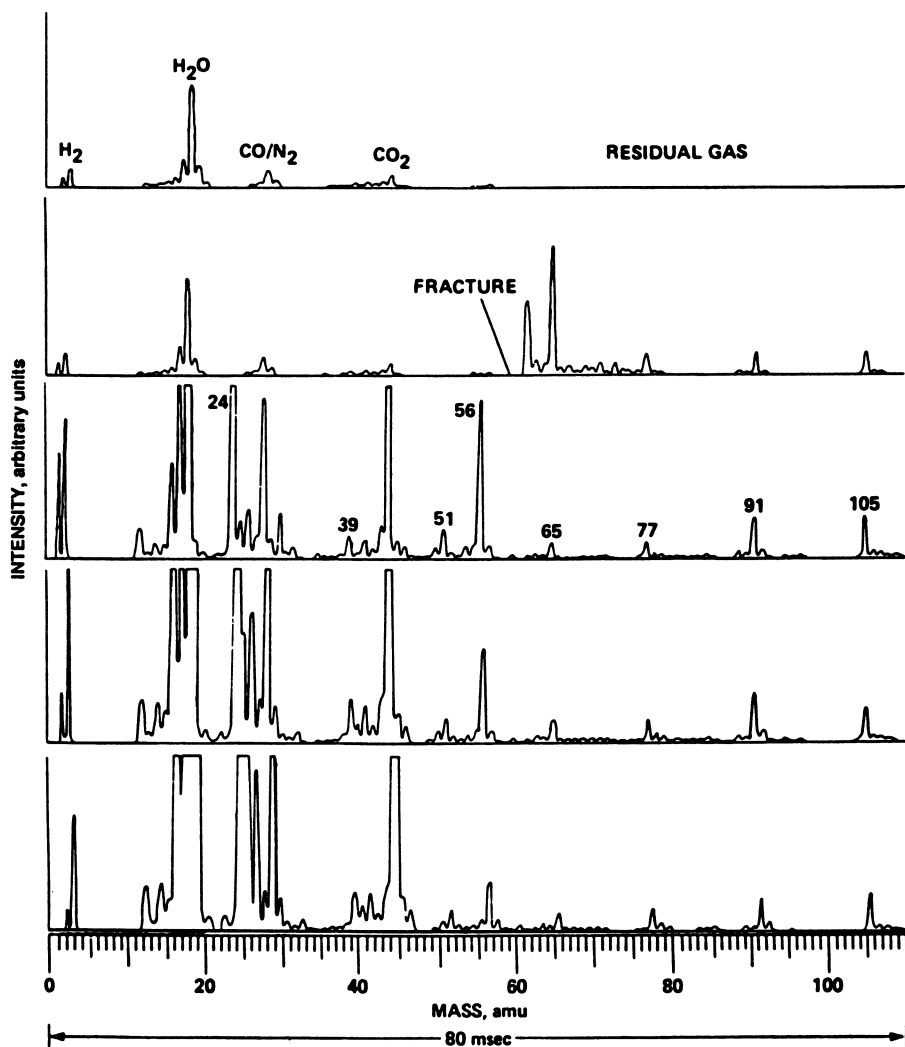


Figure 9. NE measured while scanning a QMS across masses 0 to 110 once every 80 ms during deformation and fracture of olivine from San Carlos, Arizona, USA. Fracture occurred during the second scan, at the time marked by the arrow. NE at some masses saturated the QMS electrometer during the remaining scans. (Reproduced with permission from Ref. 14. Copyright 1986 Kluwer Academic Publishers).

neutral clusters of the form $M(MX)_z$ where $z = 1, 2, 3$. Thus, the instantaneous stoichiometry of the newly created fracture surfaces of such compounds appears to be very unstable for times of a few hundred milliseconds.

Potential Relevance of Fracto-Emission

Most directly, FE studies can be of use in the study of the fracture process in minerals. Since the emission processes are often localized on atomic scales, FE yields information about atomic scale processes, such as bond breaking, which accompany fracture. FE can yield information on microcracking, intergranular failure, and plastic deformation rather directly. FE can also reflect the role of voids and inclusions in the fracture process and the subsequent surface chemistry.

In certain situations, FE could prove useful in the remote detection of fracture. An unusual radio emission observed at several widely spaced receivers six days before the Great Chilean Earthquake of May 22, 1960, has led Warwick, Stoker, and Meyer to speculate that stress induced microfracture along the Chilean fault was the source of this emission (38). More recent observations of RE some hours to tens of minutes before earthquakes have been made by Soviet researchers (39). Nitsan has surveyed a number of minerals for fracture related RE and has concluded that quartz-bearing rocks were sources of rather intense RE (15). Under similar conditions, rocks not containing quartz (basalts, obsidians, limestones) did not yield detectable RE. Therefore, RE is expected to be a strong function of the mineral content (quartz or non-quartz bearing formations). Formation structure (the presence of previously pulverized material, state of stress and strain) is also expected to affect RE intensity. The detection of RE can be affected by the presence of overlying sediments, water, or unfavorable atmospheric conditions. Although the relationship between RE and seismic activity is not clear, this is certainly an area for further study.

Certain transient optical effects occasionally observed to accompany seismic events could well be described as FE processes on geologic scales. The atmospheric luminescence accompanying some earthquakes (earthquake lights) is generally attributed to charge separation and/or gas release accompanying fracture, although the mechanism is far from clear (40). Localized, transient, optical events (transient lunar phenomena) have been reported in lunar observations which appear to be triggered by tidal forces (41) and are believed to be associated with seismic events. Brady and Rowell (42, 43) have recorded the spectra of the pH from compressive fracture of granite and basalt in a number of gaseous atmospheres and found that emission consists of line spectra corresponding to the excitation of atmospheric molecules. Similar results on the pH from rock fracture were observed by Guo Ziqiang et al. (44). We have shown that interfacial failure, which generates intense charge separation, generates pH with very similar spectra (45-47). Although it is not yet clear whether the processes responsible for earthquake lights or transient lunar phenomena are similar to those producing pH on laboratory scales, it is quite possible that in some environments pH or RE from seismic, volcanic, and mining activities is of potential use for detection or prediction purposes.

Researchers interested in predicting volcanic activity, e.g., K. A. McGee, USGS, Vancouver, WA, and M. Sato, USGS, Reston Virginia, have also explored the use of gaseous emissions which occur prior to volcanic eruption (work reviewed in January 7, 1985 issue of *Chemical and Engineering News*, pp 32-33). These emissions, including copious H_2 release and *bursts* of radon, have been attributed to fracture-induced release of gases from deep within the earth, fracture events which precede volcanic eruptions by as much as several days. Anomalies in radon concentrations in groundwater have also been observed days or months prior to significant earthquakes (39).

Atomic and molecular neutral emissions could also be a source of some chemical species released on astronomical and geologic scales. The release of metal

vapor and organic species accompanying fracture could help explain the origin of certain species in interstellar and interplanetary dust clouds (3). Collisions between grains could certainly result in surface induced chemistry, which may be all the more important given the relative inertness of atomic and molecular species in interstellar space. Some authors have speculated that organic material brought to the earth in meteorites or dust particles were important in the evolutionary process (48). The emission of complex organic molecules accompanying the fracture of olivine suggests that terrestrial or extraterrestrial fracture could be responsible for some of this organic material (3,13). The energetics for the production of complex organic molecules tend to be better for reactants absorbed at surfaces than for reactants in the gas phase, and a portion of the mechanical energy released in fracture is also available to drive chemical reactions (49). Thus, fracture related chemistry may also be important in some cosmological and evolutionary processes.

Conclusion

FE from several model materials as well as materials of geologic importance have been studied in laboratory settings. This work has done much to indicate the potential as well as the limitations of FE measurements in the study of various geologic and interplanetary phenomena. However, much remains to be done in elucidating the mechanisms involved in FE production. The rapid production of energetic surfaces, in conjunction with solid/solid bulk chemistry and diffusive processes, provide a unique chemical environment where non-equilibrium is a critical component. The complexity and scale of geologic and astronomical events greatly complicates the interpretation of fracture related observations in these environments. The role of FE in geological and astronomical processes will be a fruitful field for further experimental and theoretical work.

Acknowledgments

This work was supported by the Ceramics and Electronics Materials Division of the National Sciences Foundation DMR 8210406, the Office of Naval Research Contract No. N00014-87-K-0514, and the Washington Technology Center. We also wish to thank Friedemann Freund, NASA-Ames, Phil Rosenberg, Washington State University, as well as Brian Brady and Glynn Cress, Bureau of Mines, for providing mineral samples and helpful discussions.

Literature Cited

1. Dickinson, J. T.; Jensen, L. C. ASM Proceedings for the 13th International Symposium for Testing and Failure Analysis, 1987.
2. Langford, S. C.; Dickinson, J. T.; Jensen, L. C. J. Appl. Phys. 1987, **62**, 1437.
3. Dickinson, J. T.; Jensen, L. C.; McKay, M. R.; Freund, F. J. Vac. Sci. Technol. A 1986, **4**, 1648.
4. Dickinson, J. T.; Jensen, L. C.; McKay, M. R. J. Vac. Sci. Technol. A 1987, **5**, 1162.
5. Langford, S. C.; Doering, D. L.; Dickinson, J. T. Phys. Rev. Lett. 1987, **59**, 2795.
6. Wollbrandt, J.; Bruckner, U.; Linke, E. Phys. Status Solidi A 1983, **77**, 545.
7. Wollbrandt, J.; Bruckner, U.; Linke, E. Phys. Status Solidi A 1983, **78**, 163.
8. Wollbrandt, J.; Bruckner, U.; Linke, E. Radiation Protection Dosimetry 1983, **4**, 194.

9. Poletaev, A. V.; Shmurak, S. Z. *Fiz. Tverd. Tela (Leningrad)* 1984, **26**, 3567 [*Sov. Phys. Solid State* 1984, **26**, 2147].
10. Poletaev, A. V.; Shmurak, S. Z. *Zh. Eksp. Teor. Fiz.* 1984, **87**, 856 [*Sov. Phys. JETP* 1984, **60**, 376].
11. Williams, G. P., Jr.; Turner, T. J. *Solid State Comm.* 1979, **29**, 201.
12. Golovin, Yu. I.; D'yachek, T. P.; Uskov, V. I.; Shibkov, A. A. *Fiz. Tverd. Tela (Leningrad)* 1985, **27**, 555 [*Sov. Phys. Solid State* 1985, **27**, 344].
13. Dickinson, J. T.; Langford, S. C.; Jensen, L. C. *J. Vac. Sci. Technol. A* 1988, **6**, 1084.
14. Freund, F.; Dickinson, J. T.; Becker, C. H.; Freund, M. M.; Chang, S. *Origins Life* 1986, **16**, 291.
15. Nitsan, Uzi *Geophys. Res. Lett.* 1977, **4**, 333.
16. Walton, Alan J. *Advances in Phys.* 1977, **26**, 887.
17. Zink, Jeffrey I. *Accounts Chem. Res.* 1978, **11**, 289.
18. Chandra, B. P. *Nucl. Tracks* 1985, **10**, 225.
19. Gonzalez, R.; Piqueras, J.; Llopis, J. *J. Appl. Phys.* 1983, **53**, 7534.
20. Stokes, R. J.; Johnston, T. L.; Li, C. H. *Philos. Mag. Series 8*, 1959, **4**, 920.
21. Bruneau, A. A.; Pratt, P. L. *Philos. Mag. Series 8*, 1962, **7**, 1871.
22. MacLean, S. G.; Duley, W. W. *J. Phys. Chem. Solids* 1984, **45**, 227.
23. Jaklevic, R. C.; Elie, L. *J. Vac. Sci. Technol. A* 1988, **6**, 448.
24. Jaklevic, R. C.; Elie, L.; Shen, Weidian; Chen, J. T. *Appl. Phys. Lett.* 1988, **52**, 1656.
25. Haneman, D.; Lagally, M. G. *J. Vac. Sci. Technol. B* 1988, **6**, 1451.
26. Wiedehorn, S. M. *J. Am. Ceramic Soc.* 1969, **52**, 99.
27. Dickinson, J. T.; Doering, D. L.; Langford, S. C. In *Atomic and Molecular Processing of Electronic and Ceramic Materials: Preparation, Characterization, and Properties*, Aksay, I. H. et al. Eds.; Materials Research Society: Pittsburgh, 1988, pp 39-46.
28. Anderson, P. W. *Phys. Rev.* 1958, **109**, 1492.
29. Klyuev, V. A.; Lipson, A. G.; Toporov, Yu. P.; Deryagin, B. V.; Lushchikov, V. I.; Strelkov, A. V.; Shabalin, E. P. *Pis'ma Ah. Tekh. Fiz.* 1986, **12**, 1333 [*Sov. Phys. Tech. Phys.* 1986, **12**, 551].
30. Lehovec, Kurt J. *Chem. Phys.* 1953, **21**, 1123.
31. Kliewer, K. L. *Phys. Rev.* 1965, **4A**, 1241.
32. Kliewer, K. L. *Phys. Rev.* 1965, **4A**, 1226.
33. Thomas, D. G.; Hopfield, J. J.; Augustyniak, W. M. *Phys. Rev.* 1965, **140**, 202.
34. Williams, R. T.; Williams, J. W.; Turner, Thomas J.; Lee, K. H. *Phys. Rev. B* 1979, **20**, 1687.
35. Bichevin, V.; Kaambre, H. *Phys. Status Solidi A* 1971, **4**, K325.
36. Miles, M. H.; Dickinson, J. T.; Jensen, L. C. *J. Appl. Phys.* 1985, **57**, 5048.
37. M. L. Knotek, *Phys. Today* 1984, **37**, 24.
38. Warwick, J. W.; Stoker, Carol; Meyer, T. R. *J. Geophys. Res.* 1982, **87**, 2851.
39. Mogi, Kiyoo *Earthquake Prediction*; Academic Press: Tokyo, 1985; pp 133, 140, 208.
40. Derr, J. S. *Bull. Seism. Soc. Am.* 1973, **63**, 2177.
41. Hedervari, P. *Bull. Seism. Soc. Am.* 1981, **71**, 371.
42. Brady, B. T.; Rowell, G. A. *Nature* 1986, **321**, 488.
43. Cress, G. O.; Brady, B. T.; Rowell, G. A. *Geophys. Res. Lett.* 1987, **14**, 331.
44. Guo Ziqiang; Zhou Dazhang; Shi Xingjue; Ma Fusheng; Xie Duan; and Zhou Zhiwen *Acta Geophysical Sinica* 1988, **31**, 37.

45. Donaldson, E. E.; Dickinson, J. T.; Shen, X. A. J. Adhesion 1986, 19, 267.
46. Dickinson, J. T.; Donaldson, E. E. J. Adhesion 1987, 24, 199.
47. Ma Zhenyi; Fan Jiawen; Dickinson, J. T. J. Adhesion 1988, 25, 63.
48. Hodge, P. W. Interplanetary Dust; Gordon and Breach Science Publishers: New York, 1981; pp 219-232.
49. Coyne, Lelia M. Origins Life 1985, 15 161.

RECEIVED March 21, 1989

Chapter 13

What Excites Triboluminescence?

Linda M. Sweeting

Department of Chemistry, Towson State University, Baltimore, MD 21204

We have examined the spectra emitted by triboluminescent materials which are also photoluminescent and attempted to correlate their crystal structures with their triboluminescence (fractoluminescence). The spectra reveal that the primary event is charge separation followed by a discharge (lightning); the UV-vis emission of the discharge is absorbed and excites the photoluminescence of the material. Although a noncentric crystallographic space group resulting in macroscopic piezoelectricity is common in triboluminescent materials, it is neither necessary nor sufficient for triboluminescence to occur: disorder and impurities may also provide a structural basis for triboluminescence.

Triboluminescence, from the Greek word tribein (to rub) is a term used to describe the visible (and UV) emissions of materials when they are stressed to failure. This phenomenon is very common among minerals (see Table I), and is well known to spelunkers who enjoy smashing fluorite deposits to see the light. Earthquake lights (1) (2) are probably triboluminescence on a grand scale.

The term triboluminescence is often used to describe any light emission occurring upon impact with or grinding of a crystalline material, and is certainly more than one phenomenon (3). Light emissions caused by heating during fracture, such as thermoluminescence and blackbody radiation, are common, but neither they nor chemical reactions such as oxidation are strictly considered triboluminescence; they will not be discussed in this paper.

Triboluminescence is sometimes observed during deformation even without fracture. Salts such as zinc sulfide (4) (5) and sodium chloride (6) (7) which have been doped either by photoluminescent ions or by gamma irradiation have been shown to emit light under elastic or plastic deformation. The emission is thought to be produced by the recombination of defects of opposite charge which migrate and recombine during strain of the crystal. Eckhardt has also observed that some piezoelectric crystals will emit light when compressed or stretched without fracture (8). This form of triboluminescence will be referred to as deformation luminescence.

0097-6156/90/0415-0245\$06.00/0
© 1990 American Chemical Society

Table I. Triboluminescent Minerals

a) Fractoluminescent

- lithium fluoride (1)
 sodium nitrate (2)
 sodium sulfate (3)
 potassium nitrate (2)
- magnesium oxide (4)
 magnesium sulfate (3)
 aragonite (CaCO_3) (5)
 calcite (CaCO_3) (Iceland) (6) (7)
 marble (CaCO_3), Yule (8)
 dolomite ($\text{CaMg}(\text{CO}_3)_2$) (9)
 fluorite (CaF_2) (5) (7) (10) (11), doped (12)
 calcium oxide (4)
 basalt, Table Mountain ($\text{Ca}_3(\text{PO}_4)_2$ /etc) (8)
 hydroxyapatite (human bone $\text{Ca}_5(\text{PO}_4)_3\text{OH}$) (13) (14)
 apatite (phosphorite) $\text{Ca}_5(\text{PO}_4)_3\text{F}$ (5)
 gypsum (selenite) ($\text{CaSO}_4 \cdot 2\text{H}_2\text{O}$) (3)
 wallastonite (CaSiO_3) (11)
 celestite (SrSO_4) (3) (5)
 witherite (BaCO_3) (5)
 barium chloride (11)
 barite (BaSO_4) (3) (5)
- cryolite (Na_3AlF_6) (5)
- quartz (SiO_2) (5) (6) (7) (11) (15)
 silica glass (SiO_2) (6), fused quartz (16)
 chalcedony, amorphous (SiO_2) (6)
 clays, on solvation, montomorillonite ($\text{Al}_4(\text{Si}_4\text{O}_{10})(\text{OH})_4$), kaolin
 ($\text{Al}_4(\text{Si}_4\text{O}_{10})(\text{OH})_8$) (17)
 granite, Salida ($\text{SiO}_2/\text{Al}_2\text{O}_3$ /etc. (8) (18)
 mica ($\text{K}_2\text{Si}_2\text{O}_5$?) (5)
 kunzite ($\text{LiAlSi}_2\text{O}_6$ with Mn) (11)
- arsenolite from $\text{HCl}(\text{As}_2\text{O}_3)$ (5) (19)
 claudetite (As_2O_3) (20)
 stibnite (Sb_2S_3) (5)
- rutile (TiO_2) (5)
 manganous sulfate (3)
 iron (21)
 copper (II) sulfate pentahydrate (3)
 willemite (Zn_2SiO_4) (6)
 sphalerite, zincblende (ZnS) (5) (6) (11)

Continued on next page

Table I. Continued

b) Luminescent on Deformation or Showing Black Body Radiation

lithium fluoride (22) (23) (24)
sodium chloride (5) (6) (25), X-irradiated (26) (27)
sodium fluoride (22)
potassium chloride (23) (27)
potassium fluoride (27)

calcite (6) (7)
apatite (6)
gypsum (CaSO₄) with manganese (11)
fluorite (CaF₂) (5) (7) with rare earths (11)
tremolite (a calcium silicate) (11)

quartz (SiO₂) (5) (6) (11) (15) (28)
fused quartz (16)
silica glass (29)
tourmaline (an aluminosilicate with B) (11)
feldspar (an aluminosilicate with K, Na, Ca) (6)

zinc oxide, doped (30)
zinc sulfide, doped (27) (31)

Continued on next page

American Chemical Society
Library

1155 16th St., N.W.

In Spectroscopic Characterization of Minerals and Their Surfaces; Coyne, L., et al.;
ACS Symposium Series; American Chemical Society: Washington, DC, 1990.

Washington, D.C., 20036

Table I. Continued. Footnotes to Table I.

1. Belyaev, L. M.; Martyshev, Yu. N. phys. stat. sol. 1969, 34, 57-62.
2. Chandra, B. P.; Zink, J. I. J. Phys. Chem. Solids, 1981, 42, 529-532.
3. Chandra, B. P.; Zink, J. I. Inorg. Chem. 1980, 19, 3098-3102.
4. Williams, G. P. Jr.; Turner, T. J. Sol. State Commun. 1979, 29, 201-203.
5. Wolff, G.; Gross, G.; Stranski, I. N. Z. Elektrochemie, 1952, 56, 420-428.
6. Wick, F. G. J. Opt. Soc. Amer. 1937, 27, 275-285.
7. Chapman, G. N.; Walton, A. J. PACT (Rixensart, Belgium), 1982, 6, 533-538.
8. Cress, G. O.; Brady, B. T.; Rowell, G. A. Geophys. Res. Lett. 1987, 14, 331-334.
9. Walton, A. J. Adv. Phys. 1977, 26, 887-948.
10. Longchambon, H. C. R. Hebdom. Seances Acad. Sci. Paris, 1923, 176, 691-693.
11. Wick, F. G. J. Opt. Soc. Amer. 1939, 29, 407-412.
12. Chapman, G. N.; Walton, A. J. J. Phys. C Sol. State, 1983, 16, 5543-5551.
13. Krauya, U. E.; Knets, I. V.; Laizan, V. B. Mekh. Polimerov, 1977, 4, 746-749.
14. Dissolution of inorganics from the bone leaves the triboluminescence intact; dissolution of the organic material destroys the triboluminescence. Meir Lahav, personal communication.
15. Chapman, G. N.; Walton, A. J. J. Appl. Phys. 1983, 54, 5961-5965.
16. Kondo, K.; Ahrens, T. J.; Sawaoka, A. J. Appl. Phys. 1983, 54, 4382-4385.
17. Coyne, L. M.; Lahav, N.; Lawless, J. G. Nature, 1981, 292, 819 - 821. Lahav, N.; Coyne, L. M.; Lawless, J. G. Clays Clay Miner. 1982, 30, 73-75.
18. Brady, B. T.; Rowell, G. A. Nature, 1986, 321, 488-492.
19. Trautz, M., Z. Phys. Chem. 1905, 53, 1-63.
20. Stranski, I. N.; Strauss, E.; Wolff, G. Z. Elektrochemie, 1955, 59, 341-350; 1951, 55, 633-636.
21. Ohlman, Y. Physica Scripta, 1979, 20, 620-622.
22. Linke, E. Sitz. Acad. Wissen. 1981, 3N, 105-113.
23. Meyer, K.; Polly, F. phys. stat. sol. 1965, 8, 441-456.
24. Hoffman, K.; Linke, E. Krist. Technik, 1976, 11, 835-845; 1977, 12, 495-503.
25. Frohlich, F.; Seifert, P. Crystal Lattice Defects, 1971, 2, 239-242.
26. Pirog, M.; Sujak, B. Acta Phys. Polon. 1968, 33, 863-873.
27. Alzetta, G.; Chudacek, I.; Scarmozzino, R. phys. stat. sol. 1970, 1, 775-785.
28. Zubov, V. G.; Zakharova, E. K.; Osipova, L. P. Vest. Mosk. Univ. Fiz. 1975, 30, 366-367.
29. Zink, J. I.; Beese, W.; Schindler, J. W.; Smiel, A. J. Appl. Phys. Lett. 1982, 40, 110-112. Smiel, A. T.; Fisher, T. A. Appl. Phys. Lett. 1982, 41, 324-326.
30. Bhushan, S.; Asare, R. P. Czech. J. Phys. 1981, B31, 913-916.
31. Thiessen, P. A.; Meyer, K. Naturwissenschaften, 1970, 57, 423-427. Meyer, K.; Obrikat, D. Z. Phys. Chem. 1969, 240, 309-324.

Materials which emit light on fracture are said to be fractoluminescent and may be classified by their emission spectra. Nonphotoluminescent solids such as quartz, sucrose and tartaric acid have a triboluminescence spectrum indistinguishable from the ${}^3\pi_0 \rightarrow {}^3\pi_0$ emission of dinitrogen characteristic of lightning (Figure 1) (9). It is clear that charge separation is the primary event, followed by electron bombardment of dinitrogen in the air near the charged (presumably new) surface. The emission is accompanied by the expected radio signals, and electron and positive ion release (10), and thus will be called "lightning" throughout this paper. Most of the crystals in this group are noncentric and thus piezoelectric. In fact sucrose has been shown to emit light only for cleavage with a component perpendicular to its pyroelectric axis (9). The observation of lightning provides clear evidence for charge separation and thus good evidence for fracture.

For photoluminescent crystals, the light emitted is very similar to the fluorescence or phosphorescence emission of the solid, with little evidence of the lightning that might indicate charge separation. Figure 2 gives two examples of tribophotoluminescence spectra (Photoluminescence spectra were obtained on a Perkin Elmer LS5B. Triboluminescence spectra were obtained on an EG&G PARC 1421 HQ intensified diode array detector with associated model 1460 OMA III optical multichannel analyzer and model 1229 or 1234 spectrometer.) We have focussed our research on this poorly understood form of triboluminescence.

We propose the following mechanism for tribophotoluminescence, originally proposed by Longchambon (11) and Harvey (12):

1. Breaking a triboluminescent crystal separates charge across the growing crack or between surface patches.
2. Charge can accumulate if the material is piezoelectric or if there are defects in the crystal sufficient to permit significant charge separation.
3. When the voltage is great enough (13), electrons escape from the surface (exoelectron emission) and a discharge occurs through the atmosphere near the new surface. 11.5 eV is needed to excite the dinitrogen bands observed from sucrose and other nonphotoluminescent crystals.
4. Gas molecules (usually dinitrogen) in the gap are excited by electron bombardment.
5. The UV-vis emission of the gas (lightning) excites the molecules of the crystal if they absorb in this region (250 - 450 nm).
6. The molecules of the crystal fluoresce or phosphoresce (tribophotoluminescence).

The excitation of the molecules of the crystal could also occur by electron bombardment, which would produce spectra different from photoluminescence in some cases.

Crystallography

To examine the correlation between crystal structure and triboluminescence we prepared and studied two series of compounds with some brightly triboluminescent members: 9-substituted anthracenes (14) (Series I) and alkylammonium tetrakis(dibenzoylmethanato)europates and other lanthanates (Series II).

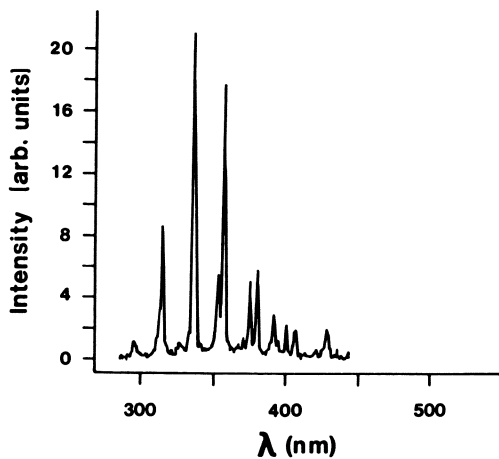


Figure 1. Triboluminescence Spectrum of Sucrose. Spectrum obtained with 5, 10 sec acquisitions and a 25 μm slit using a 142X chevron detector.

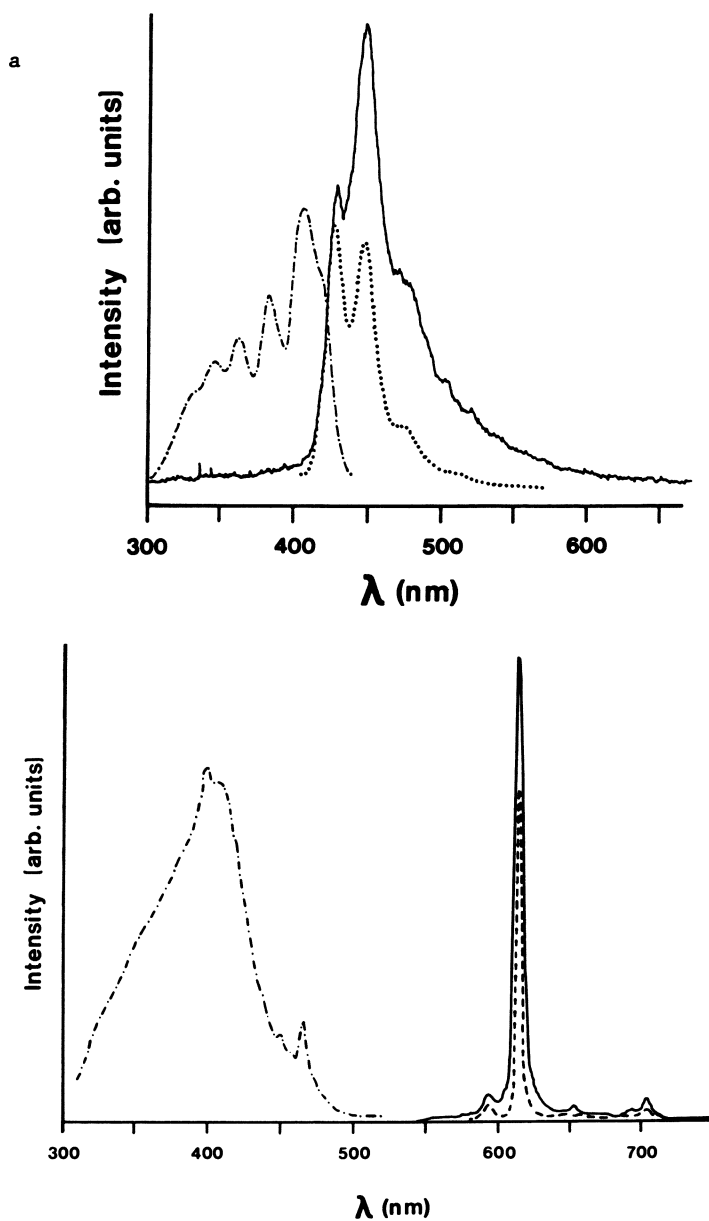
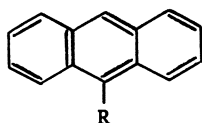


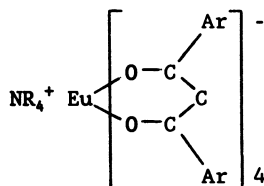
Figure 2. Triboluminescence and Photoluminescence Spectra.
- - - photoluminescence excitation, photoluminescence emission, _____ triboluminescence.

a) 1-(9-Anthryl)ethanol, triboluminescence with 10, 10 sec scans and a 25 μm slit. (Copyright 1988 American Chemical Society.)

b) Triethylammonium tetrakis(dibenzoylemethanato)europate, triboluminescence with 10, 0.5 sec scans and a 25 μm slit.



Series I



Series II

Literature reports of crystal space groups of triboluminescent materials provide evidence for a modest correlation between triboluminescence and noncentric space group (15): of 36 triboluminescent inorganic sulfates (16), 21 are noncentric and 15 are centric; of 19 triboluminescent aromatic organic crystals (17) of known crystal structure, 13 are noncentric and 6 are centric. Many compounds crystallize in more than one space group; thus the literature crystal structures may not be relevant to the triboluminescent materials. We therefore examined samples from the same batch of crystals for triboluminescence activity and crystal structure. The results are shown in Table II, along with some related compounds (6, 12, 13) whose crystal structures were obtained from the literature.

Our results show a poor correlation of triboluminescence with noncentric space group and reveal a possible source of dissymmetry in the crystal that could permit significant charge separation - disorder. We found, for example, that triboluminescent crystals of triethylammonium tetrakis(dibenzoyl)ethanatoeuropate were disordered (phenyl rings and alkylammonium chains); crystals containing dichloromethane were photoluminescent but not triboluminescent and were not disordered (18). Triboluminescence and disorder were also observed in the isomorphous lanthanide salts (King, W.; Rheingold, A. L.; Sweeting, L. M. unpublished study). Disorder is not common in the 9-substituted anthracenes, but is observed for anthryl esters 7 and 9. We conclude that disorder may provide local dissymmetry, deforming the lattice and allowing charge accumulation. Unfortunately crystallography cannot determine how the sites of different conformation are distributed in the crystal. We examined the local environment by testing some of the materials for the generation of a second harmonic on laser irradiation; no correlation with triboluminescence was found.

Some crystals are only triboluminescent when impurities are present; the impurities may deform the lattice to generate dissymmetry and/or may provide a photoluminescent site. We have no reason to believe that the centric triboluminescent crystals (e.g. 4) in Table II are any less pure than the centric nontriboluminescent crystals (e.g. 1). Table II also contains several examples of noncentric crystals which are not triboluminescent (e.g. 5, 13). We are particularly intrigued by the contrast between 4 and 5: the racemic, centric form is triboluminescent but the enantiomerically homogeneous, noncentric form is not.

Spectroscopy

The triboluminescence spectrum can provide information about several steps in the mechanism. Figure 2a shows a typical tribolumi-

Table II. Properties of Potential Triboluminescent Materials

Substituent	Space Group (1)	Tribolumin. Intensity (3)	Photolum. Emission Max. (nm)	SHG (2)
Series I: 9-Substituted Anthracenes				
1. C(CH ₃) ₂ OH	C: P2 ₁ /c (4)	-	437, 57	<.05
2. CH(CH ₃)OH	N: I4 ₁ cd (4)	++++	427, 47	<.05
3. CH ₂ OH	N: Cc (4)	++++	447	0.14
4. CH(CF ₃)OH	C: Pbc _a (4)	++	502	<.05
5. CH(CF ₃)OH(<u>S</u>)	N	-	449	<.05
6. CO ₂ CH ₃	C: P2 ₁ /a (5) C: P2 ₁ /c	-	463	-
7. CO ₂ CHMeEt	CD: P1̄ (6)	+	400, 512	-
8. CO ₂ CHMeEt(<u>S</u>)	N: P1 (6)	+		
9. CO ₂ CHMePr	CD: Pbc _a (6)	+		
10. CO ₂ (<u>E</u> -2-Me cyclohexyl)	C: P1̄ (6)	-		
11. CO ₂ menthyl	N	++++	430	<.05
12. CO ₂ CHEtØ(<u>R</u>)	N: P6 ₃ (7)	+++ (8)		
13. CO ₂ H	N: P1 (5)	-	492	

Continued on next page

Table II. Continued

Series II: Lanthanide Salts				
Tetrakis(dibenzoylmethanato)europate $\{((\text{O}=\text{C})_2\text{CH})_4\text{Eu}\}$				
14. NHEt_3	CD: I2/a (9)	+++++	614	<.05
15. $\text{NHEt}_3\text{CH}_2\text{Cl}_2$	C: I2/a (9)	-	614	
16. NHMe_2Bz	D (10)	++++	611	
Other $\text{NEt}_3 \{((\text{O}=\text{C})_2\text{CH})_4\text{M}\}$ Salts (11)				
17. Samarium	CD: I2/a	+++++	650	
18. Praesodymium	CD: I2/a	++	612	
19. Terbium	CD: I2/a	+		

Footnotes to Table II

1. N = non-centrosymmetric; C = centrosymmetric; D = disordered.
2. Second harmonic generation as a powder, fraction of urea signal; signals <.05 are barely distinguishable from noise. M. C. Etter and G. Frankenbach, unpublished data.
3. Estimated by eye by comparison with sucrose, arbitrarily designated +++; no observed triboluminescence, -.
4. Sweeting, L. M.; Rheingold, A. L. *J. Phys. Chem.* 1988, 92, 5648-5655.
5. Heller E.; Schmidt, G. M. J. *Isr. J. Chem.* 1971, 9, 449-462.
6. Sweeting, L. M. Gingerich, J. M.; Rheingold, A. L. unpublished data.
7. Lahav, M.; Leiserowitz, L.; Roitman L.; Tang, C. P. *J. C. S. Chem. Comm.* 1977, 928-929.
8. Lahav, M. personal communication.
9. Sweeting L. M.; Rheingold, A. L. *J. Am. Chem. Soc.* 1987, 109, 2652-2658.
10. Sweeting, L. M.; Rheingold, A. L. unpublished data.
11. Rheingold, A. L.; King, W. unpublished data.

nescence spectrum, that of 1-(9-anthryl)ethanol, 2. The major difference between the triboluminescence and photoluminescence spectrum is that the relative intensity of the shortest wavelength band in the triboluminescence spectrum is less than it is in the photoluminescence spectrum. We believe this is consistent with the proposed mechanism. Unlike photoluminescence, which is produced by excitation of surface molecules, triboluminescence takes place at cracks distributed throughout the crystal. The light must travel through the crystal and will be absorbed with a spectrum corresponding to the excitation spectrum. An examination of spectra in the literature reveals that this depletion of the shortest wavelength transitions is quite common and may explain the common shift of the tribophotoluminescence to slightly longer wavelength than the photoluminescence.

There are several examples in the literature of triboluminescence spectra which contain both the photoluminescence of the compound and significant contributions from the bands of lightning. Since we had never seen this combination, we decided to reexamine these cases. Saccharin's triboluminescence (19) was reported to be half lightning and half a photoluminescence band centered at 480 nm. Saccharin is only triboluminescent when contaminated and the band at 480 nm is the photoluminescence of *p*-toluenesulfonamide (19) (20). Chlorotriphenylmethane from acetone was reported to have lightning and a band at 540 nm in its triboluminescence (21). We grew crystals from hexane and acetone; neither were triboluminescent. We concluded that chlorotriphenylmethane was also triboluminescent because of impurities, since it turned bright yellow (and gained a photoluminescence maximum at 540 nm) upon exposure to acetone.

To examine the effect of impurities in a systematic way, we chose a well-known triboluminescent solid - wintergreen candy. We prepared mixtures of wintergreen (methyl salicylate) and sucrose of different concentrations (by shaking the solid and liquid thoroughly) and examined their triboluminescence spectra (Figure 3); they consist of both lightning and wintergreen photoluminescence. The spectrum of WintOGreen Lifesavers (22) (Figure 4) corresponds to a concentration of about 0.5%. The spectra in Figure 3 provide evidence that the wintergreen photoluminescence is excited only by the lightning. The excitation of the wintergreen photoluminescence is effected predominantly by light of wavelengths less than 350 nm; the bands of lightning most depleted with increasing wintergreen concentration are those below 350 nm. The ratio of the intensity of the photoluminescence to the intensity of the most intense (0-0) band of lightning (338 nm) is proportional to the square of the concentration, as expected for absorption. (The photoluminescence increases linearly with concentration and the lightning below 350 nm decreases linearly with concentration.) The spectra in Figure 3 allow an estimate to be made of the lightning intensity in a crystal with similar photoluminescence efficiency to wintergreen. For 1% photoluminescent material, the 338 nm/450 nm intensity ratio is about 0.5. In 100% photoluminescent material, the lightning would be 100 times smaller and the photoluminescence 100 times greater, giving an estimated lightning intensity of 0.005% of the photoluminescence - a challenge to detect.

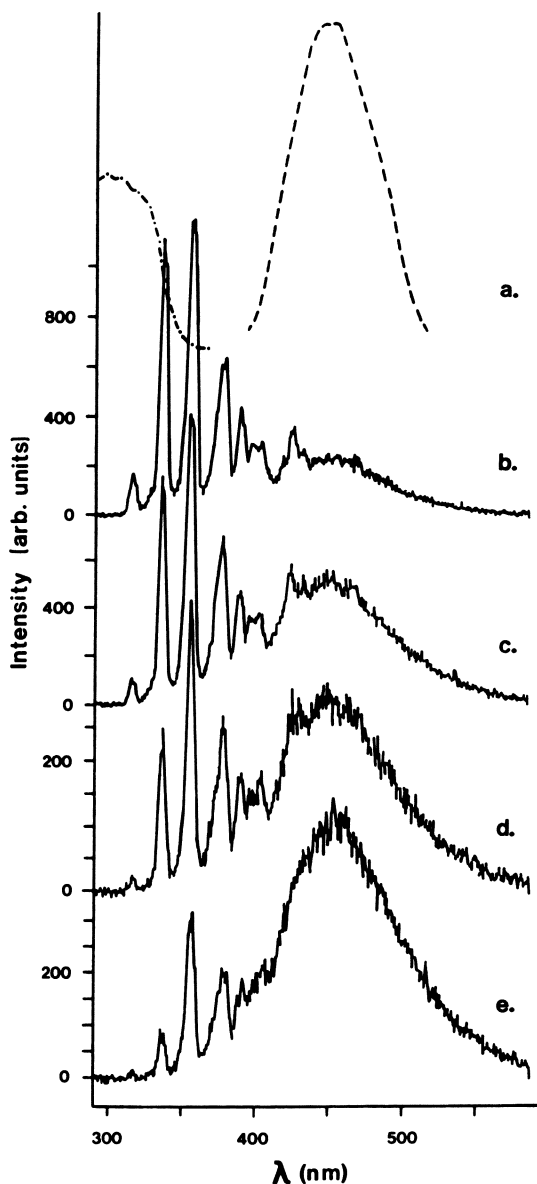


Figure 3. Triboluminescence Spectra of Wintergreen coated on Sucrose. Triboluminescence spectra _____ were obtained with 10, 10 sec scans and a 100 μm slit.

- a) photoluminescence of wintergreen on sucrose; - . . . excitation; - - - emission
 b) 0.10% wintergreen on sucrose
 c) 0.22% wintergreen on sucrose
 d) 0.49% wintergreen on sucrose
 e) 1.04% wintergreen on sucrose

We attempted to detect lightning in uranyl nitrate hexahydrate since its tribophotoluminescence had been reported several times to contain 1% lightning (23). Figure 5 shows the first published triboluminescence spectrum of uranyl nitrate which actually contains the traces of lightning. It is clear from the excitation spectrum why so much lightning remains in the triboluminescence of this solid - the optimum excitation wavelength is about 420 nm, rather than near 338 nm where the lightning emission is most intense. Confirming this interpretation is the observation that the triboluminescence spectrum of uranyl salicylate corresponds to the photoluminescence of the salicylate (excitation maximum 300 nm) (24).

The tribophotoluminescence spectrum of a typical organic compound, 9-anthrylmethanol (3) is shown in Figure 6. The lightning comprises only 0.05% of the anthracene photoluminescence! The absorption by the photoluminescent crystal is once again revealed in the relative intensity of the lightning bands, since the 338 nm band is not the most intense and the bands above 350 nm are not seen. These preliminary results provide encouraging evidence for the proposed mechanism and suggest a multitude of additional experiments to be done.

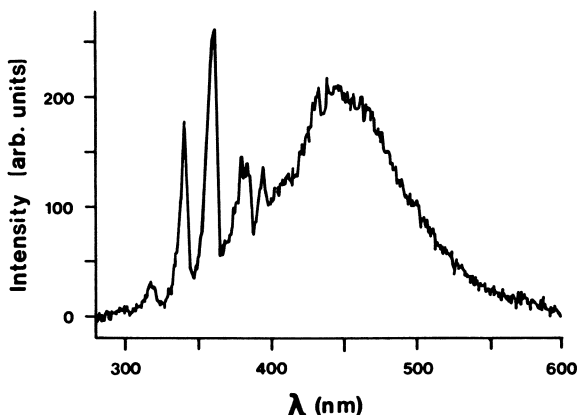


Figure 4. Triboluminescence Spectrum of WintOGreen Lifesavers. Obtained with 4, 30 sec scans and a 100 μm slit.

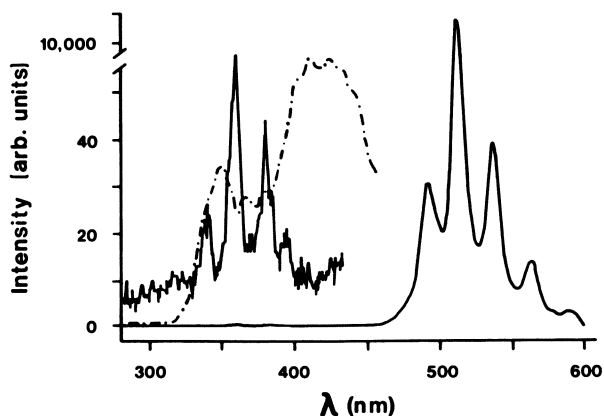


Figure 5. Triboluminescence Spectrum of Uranyl Nitrate Hexahydrate. The photoluminescence excitation spectrum is shown for comparison $-\cdot-\cdot-$; the photoluminescence emission has been discussed previously (25). The triboluminescence spectrum was obtained in a single 180 sec acquisition with a $100\ \mu\text{m}$ slit.

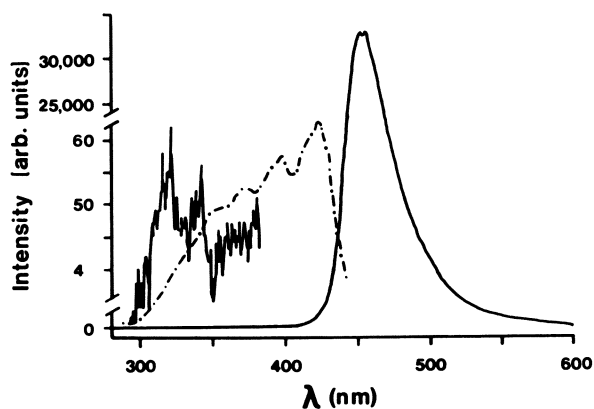


Figure 6. Triboluminescence Spectrum of 9-Anthrylmethanol. The photoluminescence excitation spectrum is shown for comparison $-\cdot-\cdot-$; the photoluminescence emission has been discussed previously (14). The triboluminescence spectrum was obtained in 3, 160 sec acquisitions with a $100\ \mu\text{m}$ slit.

Application to Minerals

The triboluminescence of minerals has been studied visually (see the footnotes to Table I) but only a few minerals have been examined spectroscopically. There are a few clear examples of noncentric crystals, such as quartz, whose emission is lightning, sometimes with black body radiation. Most of the triboluminescent minerals appear to have activity and color which is dependent on impurities, as is the case for kunzite, fluorite, sphalerite and probably the alkali halides. Table I attempts to distinguish between fractoluminescence and deformation luminescence, but the distinctions are not clear cut. A detailed analysis of the structural features of triboluminescent and nontriboluminescent minerals may make it possible to draw conclusions about the nature and concentration of trace impurities that are not obvious from the color or geological site of the crystals. Triboluminescence could be used as an additional method for characterizing minerals in the field, using only the standard rock hammer, with the sensitive human eye as a detector.

Acknowledgments

The following people were essential to this project: Arnold L. Rheingold, professor of chemistry, University of Delaware, who did most of the crystallography; Patrick F. Moy and John Zipper of EG&G PARC, who provided equipment and assistance with the spectroscopy; Reginald F. Pippin III, Janet A. Kling, Joanne M. Gingerich, undergraduates, Towson State University, and Wayne King, undergraduate, University of Delaware, who contributed to the synthesis, spectroscopy and crystallography.

The research was supported by the Towson State University Faculty Research Committee and the Research Corporation.

Literature Cited

1. Tributsch, H.; Langner, P. translator. When the Snakes Awake: Animals and Earthquake Prediction; MIT Press: Cambridge, MA, 1982; pp 143-154.
2. Corliss, W. R. Handbook of Unusual Natural Phenomena; Sourcebook Project: Glen Arm, MD, 1977; pp 415-416.
3. Walton, A. J. Adv. Phys. 1977, 26, 887-948.
4. Jaszczyn-Kopek, P.; Canny, B. J. Lumin. 1983, 28, 319-326.
5. Meyer, K.; Obrikat, D. Z. Phys. Chem. 1969, 240, 309-324.
6. Alzetta, G.; Chudacek, I.; Scarmozzino, R. phys. stat. sol. 1970, 1, 775-785.
7. Hoffman, K; Linke, E. Kristall und Technik, 1977, 12, 495-503.
8. White, K. M.; Dye, R. C.; Eckhardt, C. J. Mol. Cryst. Liq. Cryst. 1986, 134, 265-278.
9. Longchambon, H. Bull. Soc. Francais Miner. 1925, 25, 130-147.
10. Dickinson, J. T.; Brix, L. B.; Jensen, L. C. J. Phys. Chem. 1984, 88, 1698-1701.
11. Longchambon, H. C. R. Hebd. Seances. Acad. Sci. Paris, 1923, 176, 691-693.

12. Harvey, E. N. Science, 1939, 90, 35-36.
13. Gilmore, F. R. J. Quant. Spectrosc. Radiat. Transfer, 1965, 5, 369-390. Allan, M. J. Chem. Educ. 1987, 64, 418-424.
14. Sweeting, L. M.; Rheingold, A. L. J. Phys. Chem. 1988, 92, 5648-5655.
15. Chandra, B. P.; Zink, J. I. J. Lumin. 1981, 23, 363-372. Chandra, B. P.; Elyas, M.; Shrivastava, K. K.; Verma, R. D.; Solid State Commun. 1980, 36, 931-933.
16. Chandra, B. P.; Zink, J. I. Inorg. Chem. 1980, 19, 3098-3102.
17. Wolff, G.; Gross, G.; Stranski, I. N. Z. Elektrochem. 1952, 56, 420-428.
18. Sweeting, L. M.; Rheingold, A. L. J. Am. Chem. Soc., 1987, 109, 2652-2658.
19. Hardy, G. E.; Kaska, W. C.; Chandra, B. P.; Zink, J. I. J. Am. Chem. Soc. 1981, 103, 1074-1079.
20. Pope, W. J. Trans. Chem. Soc. 1985, 67, 985.
21. Chandra, B. P.; Zink, J. I. J. Phys. Chem. 1982, 86, 4138-4141.
22. Angelos, R.; Zink, J. I.; Hardy, G. E. J. Chem. Educ. 1979, 56, 413-414.
23. Longchambon, H. C. R. Hebd. Seances. Acad. Sci. Paris, 1923, 176, 691-693. Chandra, B. P. Indian J. Phys. 1987, 61A, 51-59. The two spectra labelled uranyl nitrate were labelled uranyl acetate in a previous paper (Chandra, B. P. phys. stat. sol. (a) 1981, 64, 395-405.); we believe, as Chandra obviously did, that the results would be similar.
24. Chandra, B. P.; Zink, J. I. J. Lumin. 1981, 23, 363-372.
25. Zink, J. I. Inorg. Chem. 1975, 14, 555-558.

RECEIVED March 21, 1989

Chapter 14

⁵⁷Fe-Bearing Oxide, Silicate, and Aluminosilicate Minerals

Crystal Structure Trends in Mossbauer Spectra

Roger G. Burns and Teresa C. Solberg

Department of Earth, Atmospheric, and Planetary Sciences, Massachusetts
Institute of Technology, Cambridge, MA 02139

Correlations have been sought between Mossbauer spectral parameters and several crystal structure properties of Mg-Al oxide and silicate minerals hosting iron cations as minor constituents. Plots of isomer shift (I.S.) versus various bond length-related parameters, including mean metal-oxygen distance (R) of a coordination site and volume per oxygen in a unit cell (V_{ox}), fail to delimit I.S. ranges for Fe^{3+} ions in tetrahedral, octahedral and five-fold coordination sites. However, I.S. vs polyhedral volume (V_p) of a site cluster in narrow ranges specific to each coordination symmetry. Better correlations exist for ferrous I.S. vs ferric I.S. data when coexisting Fe^{2+} and Fe^{3+} ions occupy similar or identical coordination polyhedra in the same mineral. The upper limit for tetrahedral Fe^{3+} I.S. in silicates is shown to be ≤ 0.25 mm/sec., whereas the lower limit for octahedral Fe^{3+} is ~ 0.29 mm/sec. The correlations point to inconsistencies in Mossbauer spectral parameters and cation site occupancy assignments for clintonite, yoderite and sapphirine. New Mossbauer spectral data obtained for these minerals demonstrate that: clintonites from skarn deposits contain tetrahedral Fe^{3+} and octahedral Fe^{3+} and Fe^{2+} , with relative enrichment of Fe^{3+} in tetrahedral sites; only octahedral Fe^{2+} and Fe^{3+} occur in sapphirines from granulite facies rocks; and five-coordinated Fe^{3+} predominates over octahedral Fe^{3+} ions in yoderites from high grade metamorphic rocks.

Mossbauer spectroscopy has proven to be a useful technique for characterizing the valences, coordination numbers, electronic configurations, and magnetic states of iron cations in rock-forming minerals (1-3). Two diagnostic parameters, isomer shift and quadrupole splitting, usually serve to identify paramagnetic Fe cation species in Mossbauer spectra of silicates measured at ambient temperatures. However, ambiguous crystal chemical assignments have been proposed for iron when it is present as a minor constituent of some minerals, particularly magnesian and aluminosilicate phases containing low concentrations of Fe^{2+} and Fe^{3+} substituting for Mg^{2+} and Al^{3+} ions in octahedral, tetrahedral and five-fold coordination

0097-6156/90/0415-0262\$06.50/0
© 1990 American Chemical Society

environments (4-9). Correlations have been sought, with varying degrees of consistency, between the Mossbauer spectral parameters and a number of crystal structure parameters (5-7) in attempts to demonstrate the presence of tetrahedral or five-coordinated ferric iron in some aluminosilicate minerals. Several of these correlations are examined in this paper and are extended to additional oxides and silicates listed in Table I containing Fe^{2+} and Fe^{3+} ions in a variety of oxygen coordination polyhedra. The limitations of determining iron cation site occupancies in rock-forming minerals from Mossbauer spectral and crystal structure parameters are tested for three Mg-Al-silicates, sapphirine, clintonite and yoderite, in which Fe^{3+} cation assignments are controversial. Since attention is focused on iron-dilute minerals, complications originating from thermal electron-delocalization in the Fe^{2+} - Fe^{3+} minerals magnetite, deerite, ilvaite, cronstedtite, etc. (10,11) and from superparamagnetism in nanocrystalline Fe(III) oxides magnetite, hematite, maghemite, goethite, etc. (12) are not considered here.

Correlations Between Isomer Shift and Quadrupole Splitting Parameters

Distinct regions are clearly defined for Fe^{2+} and Fe^{3+} ions in different coordination environments when the two parameters, isomer shift (I.S.) and quadrupole splitting (Q.S.), derived from room-temperature Mossbauer spectral measurements of a variety of iron-bearing oxide and silicate phases listed in Table II, are plotted against one another as in Figures 1 and 2. Although the Mossbauer parameters summarized in Table II are taken from a variety of sources, the majority of the listed minerals have been measured independently during the course of the present investigation. Errors for the isomer shifts are estimated to be ± 0.03 mm/sec. Ranges of ± 0.1 mm/sec. commonly observed for the quadrupole splitting parameter reflect compositional variations due to atomic substitution in many of the minerals. Figure 1 shows that octahedrally coordinated ferrous iron in the vast majority of rock-forming minerals is clearly distinguished from Fe^{2+} ions in eight-coordination (e.g. garnets, vesuvianite), square planar sites (e.g. gillespite, eudialyte), and tetrahedral coordination (e.g. spinel, staurolite, melilite), although parameters for five-coordinated Fe^{2+} ions (e.g. andalusite, grandidierite, vesuvianite) overlap ranges for octahedral ferrous iron. For ferric iron, however, the separation between ranges of I.S. and Q.S. shown in Figure 2 is less distinct than for ferrous iron when Fe^{3+} ions occur in octahedral, tetrahedral and five-coordination environments. Three problem cases are apparent from the data plotted in Figure 2. They involve sapphirine, clintonite and yoderite. The crystal structures of these minerals each contain Al^{3+} (octahedral ionic radius, $r_{\text{Oct}} = 0.53$ Å) or Mg^{2+} ($r_{\text{Oct}} = 0.72$ Å) ions in two or more environments with different coordination numbers: octahedral, five-fold and/or tetrahedral. Ambiguities exist over site occupancies of Fe^{3+} ions ($r_{\text{Oct}} = 0.65$ Å) deduced from the Mossbauer spectral parameters for each mineral. The I.S. data for Mg-rich sapphirine (SAM) appear to be too low for Fe^{3+} ions in octahedral coordination, leading to suggestions (4,5) that ferric iron substitutes for Al^{3+} in smaller tetrahedral sites instead of octahedral sites having larger metal-oxygen distances. For clintonites (Cl), two doublets assigned to tetrahedral and octahedral Fe^{3+} ions substituting for Al^{3+} in the crystal structure not only lie outside ranges observed for ferric iron in four-fold and six-fold coordinations in other silicate minerals including micas, but also indicate relative enrichments of Fe^{3+} ions in the smaller tetrahedral

Table I. Mineral Formulae and Legend to Figures

Mineral	Ideal Formula	Key to Figures	Structure Reference
andalusite	Al_2SiO_5	AA	<u>18</u> , <u>19</u>
acmite	$\text{NaFe}^{3+}\text{Si}_2\text{O}_6$	AC	<u>20</u>
aenigmatite	$\text{Na}_2\text{Fe}^{2+}_5\text{TiSi}_6\text{O}_{20}$	AE	<u>21</u>
almandine	$\text{Fe}^{2+}_3\text{Al}_2\text{Si}_3\text{O}_{12}$	AL	<u>22</u> , <u>23</u>
annite	$\text{KFe}^{2+}_3\text{Si}_3\text{AlO}_{10}(\text{OH})_2$	AN	<u>24</u>
andradite	$\text{Ca}_3\text{Fe}^{3+}_2\text{Si}_3\text{O}_{12}$	AR	<u>22</u> , <u>23</u>
actinolite	$\text{Ca}_2(\text{Mg}, \text{Fe})_5\text{Si}_8\text{O}_{22}(\text{OH})_2$	AT	<u>25</u>
babingtonite	$\text{Ca}_2\text{Fe}^{2+}\text{Fe}^{3+}\text{Si}_5\text{O}_{14}(\text{OH})$	BA	<u>26</u>
cordierite	$\text{Mg}_2\text{Al}_4\text{Si}_5\text{O}_{18}$	CD	<u>27</u> , <u>28</u>
chloritoid	$\text{Fe}^{2+}_2\text{Al}_4\text{Si}_2\text{O}_{10}(\text{OH})_4$	CH	<u>29</u>
clintonite	$\text{CaMg}_2\text{Al}_4\text{Si}_3\text{O}_{10}(\text{OH})_2$	CL	<u>30</u> , <u>113</u>
corundum	Al_2O_3	CO	<u>31</u>
epidote	$\text{Ca}_2\text{Fe}^{3+}\text{Al}_2\text{Si}_3\text{O}_{12}(\text{OH})$	EP	<u>32</u>
eudialyte	$\text{Na}_4\text{Fe}^{2+}_2\text{ZrSi}_6\text{O}_{17}(\text{OH})_2$	EU	<u>33</u>
ferriannite	$\text{KFe}^{2+}_3\text{Si}_3\text{Fe}^{3+}\text{O}_{10}(\text{OH})_2$	FA	<u>34</u>
ferridiopside	$\text{Ca}(\text{Mg}, \text{Fe}^{3+})(\text{Si}, \text{Al}^{3+}, \text{Fe}^{3+})_2\text{O}_6$	FD	<u>35</u>
ferrifayalite	$\text{Fe}^{2+}\text{Fe}^{3+}_2\text{Si}_2\text{O}_8$	FF	<u>36</u>
grandidierite	$\text{MgAl}_3\text{BSiO}_9$	GD	<u>37</u>
gillespite	$\text{BaFe}^{2+}\text{Si}_4\text{O}_{10}$	GI	<u>38</u> , <u>39</u>
glaucophane	$\text{Na}_2\text{Mg}_3\text{Al}_2\text{Si}_8\text{O}_{22}(\text{OH})_2$	GL	<u>40</u>
grossular	$\text{Ca}_3\text{Al}_2\text{Si}_3\text{O}_{12}$	GR	<u>22</u> , <u>23</u>
hibonite	$\text{Ca}(\text{Al}, \text{Fe}^{3+})_2\text{O}_{19}$	HI	<u>41</u> , <u>42</u>
howieite	$\text{NaFe}^{2+}_{10}\text{Fe}^{3+}_2\text{Si}_{12}\text{O}_{31}(\text{OH})_{13}$	HO	<u>43</u>
ilmenite	$\text{Fe}^{2+}\text{TiO}_3$	IL	<u>44</u> , <u>45</u>
kyanite	Al_2SiO_5	KY	<u>19</u> , <u>46</u>
LiAlO_2 (synth)	LiAlO_2	LA	<u>47</u>
laihunite	$\text{Fe}^{2+}_{0.8}\text{Fe}^{3+}_{0.8}\text{SiO}_4$	LH	<u>48</u>
ludwigite	$(\text{Mg}, \text{Fe}^{2+})_2\text{Fe}^{3+}\text{BO}_5$	LU	<u>49</u>
melilite	$\text{Ca}_2(\text{Mg}, \text{Al})(\text{Si}, \text{Al})\text{O}_7$	ME	<u>50</u>
montmorillonite	$(\text{Na}, \text{Ca}_{1/2})_0.7\text{Al}_4\text{Si}_4\text{O}_{10}(\text{OH})_4$	MO	<u>51</u>
mullite	$\text{Al}_6\text{Si}_2\text{O}_{13}$	ML	<u>52</u>
muscovite	$\text{KAl}_2\text{Si}_3\text{AlO}_{10}(\text{OH})_2$	MU	<u>53</u>
neptunite	$\text{KNa}_2\text{LiFe}^{2+}_2\text{Ti}_2\text{Si}_8\text{O}_{24}$	NE	<u>54</u> , <u>55</u>
olivine	$(\text{Mg}, \text{Fe})_2\text{SiO}_4$	OL	<u>39</u> , <u>56</u>
orthopyroxene	$(\text{Mg}, \text{Fe}^{2+})_2\text{Si}_2\text{O}_6$	OR	<u>57</u>
osumilite	$\text{KMg}_2\text{Al}_3\text{Si}_{12}\text{O}_{30} \cdot \text{H}_2\text{O}$	OS	<u>58</u>
periclase	MgO	PE	<u>59</u> , <u>60</u>
phlogopite	$\text{KMg}_3\text{Si}_3\text{AlO}_{10}(\text{OH})_2$	PH	<u>24</u>
perovskite	CaTiO_3	PV	<u>61</u>
pyrope	$\text{Mg}_3\text{Al}_2\text{Si}_3\text{O}_{12}$	PY	<u>22</u> , <u>23</u>
riebeckite	$\text{Na}_2\text{Fe}^{2+}_3\text{Fe}^{3+}_2\text{Si}_8\text{O}_{22}(\text{OH})_2$	RI	<u>62</u>
Mg sapphirine	$(\text{Mg}, \text{Al})_8(\text{Si}, \text{Al})_6\text{O}_{20}$	SAM	<u>63</u>
Fe sapphirine	$(\text{Mg}, \text{Fe}, \text{Al})_8(\text{Si}, \text{Al})_6\text{O}_{20}$	SAF	<u>64</u>
schorlomite	$\text{Ca}_3(\text{Fe}^{3+}, \text{Ti})_2(\text{Si}, \text{Fe}^{3+})_3\text{O}_{12}$	SC	<u>65</u>
sanidine	KAlSi_3O_8	SD	<u>66</u>
sillimanite	Al_2SiO_5	SI	<u>19</u> , <u>67</u>

Table I. Continued

Mineral	Ideal Formula	Key to Figures	Structure Reference
stilpnomelane	$K(Fe^{2+}, Fe^{3+}Al)_{10}Si_{10}O_{30}(OH)_{12}$	SN	<u>68</u>
spinel	$MgAl_2O_4$	SP	<u>69</u>
staurolite	$Fe^{2+}_2Al_9(Si, Al)_4O_{22}(OH)_2$	ST	<u>39, 70</u>
talc	$Mg_3Si_4O_{10}(OH)_2$	TA	<u>71, 72</u>
taramellite	$Ba_4Fe^{2+}Fe^{3+}_2TiSi_8O_{24}(OH)_4$	TM	<u>73</u>
vesuvianite	$Ca_{19}(Mg, Fe)_4Al_{10}Si_{18}O_{70}(OH, F)_8$	VE	<u>74, 75</u>
voltaite	$K_2Fe^{2+}_5Fe^{3+}_4(SO_4)_{12} \cdot 18H_2O$	VO	<u>76</u>
vivianite	$Fe^{2+}_3(PO_4)_2 \cdot 8H_2O$	VV	<u>77</u>
yoderite	$(Mg, Al)_8Si_4O_{20}$	YO	<u>78</u>

Table II. Crystal Structure and Mossbauer Spectral Parameters for Ferric Iron Coordinated to Oxygen in Oxide and Silicate Minerals

Mineral	Site Symm.	I.S. ^a	Q.S. ^b	R ^c	v_{ox} ^d	v_p ^e	Δ^f	Mossbauer Reference
andalusite	oct	0.35	1.83	1.935	17.12	9.54	32.4	<u>79</u>
(viridine)	5CN	0.22	2.65	1.836	17.12	5.15	3.2	
acmite	oct	0.38	0.30	2.025	17.84	10.87	12.2	<u>80</u>
(aegerine)								
aenigmatite	oct	0.39	1.28	1.976	18.62	10.19	27.1	**
	tet	0.23	0.97	1.649	18.62	2.29	0.8	
annite	oct	0.43	0.99	2.121	21.12	12.53	0	<u>17</u>
	oct	0.39	0.31	2.101	21.12	12.21	0.4	
andradite	oct	0.39	0.55	2.024	18.22	11.05	0	<u>23, 81</u>
actinolite	oct	0.38	0.65	2.101	19.06	12.02	6.7	<u>82</u>
babingtonite	oct	0.38	0.89	2.048	18.56	18.3		<u>83</u>
chloritoid	oct	0.33	0.95	1.935	16.51	8.99	3.8	<u>84, 85</u>
clintonite	oct	0.50	1.10	2.016	18.90	10.88	14.4	<u>6</u>
	tet	0.27	0.68	1.730	18.90	2.63	0.8	
corundum	oct	0.35	0.48	1.913	14.04	9.06	9.0	<u>60, 87</u>
(sapphire)								
epidote	oct	0.36	2.01	2.036	17.78	10.86	24.3	<u>88</u>
ferriannite	oct	0.39	1.01	2.106	21.62		1.3	<u>17</u>
	oct	0.42	0.46	2.107	21.62		1.2	
	tet	0.19	0.39	1.685	21.62		0	
ferridiopside	tet	0.18	1.34	1.629	17.32		0.1	<u>89</u>
ferrifayalite	tet	0.41	0.85	2.077	18.12		10.6	<u>90</u>
grandidierite	5CN	0.33	1.20	2.042	18.17	5.17	2.0	<u>91</u>
glaucophane	oct	0.36	0.48	1.930	18.16	9.44	15.8	<u>92</u>
hibonite	oct	0.42	0.58	1.910	16.78	9.40	1.6	<u>93, 94</u>
	tet	0.18	0.52	1.808	16.78	3.30	0.4	
	5CN	0.22	2.65	1.978	16.78	7.94	74.3	
ilmenite	oct	0.35	0.67	2.081	17.45	12.56	8.4	<u>95</u>
kyanite	oct	0.38	0.99	1.916	14.68	9.16	5.8	<u>96</u>
LiAlO ₂ (syn)	tet	0.16	0.62	1.761	20.96	2.79	0.1	<u>97</u>
lahunite	oct	0.39	0.91	2.077	18.12		10.6	<u>90, 98</u>

Continued on next page

Table II. Continued

Mineral	Site Symm.	I.S. ^a	Q.S. ^b	R ^c	V _{ox} ^d	V _p ^e	Δ ^f	Mossbauer Reference
montmorillonite	oct	0.35	0.56					<u>99</u>
	oct	0.37	0.96					
	tet	0.15	0.11					
mullite	oct	0.40	1.04	1.955	16.76		6.4	<u>100</u>
muscovite	oct	0.37	0.86	1.940	19.54	9.52	0.4	<u>101</u>
orthopyroxene	oct	0.45	0.68	2.106	17.32	11.83		<u>102</u>
	tet	0.18	1.34	1.629	17.32	2.24	0.1	
osumilite	tet	0.25	1.71	1.772		2.59		<u>103</u>
periclae	oct	0.36	0.54	2.106	18.56	12.44	0	<u>60, 104</u>
	tet	0.18	1.33	1.824	18.56	0		
perovskite	oct	0.35	0	1.926	18.61	9.49		**
phlogopite	tet	0.17	0.50	1.649	21.27	2.30	0	17
riebeckite (crocidolite)	oct	0.38	0.43	2.070	18.88		15.7	<u>4, 92</u>
Mg sapphire	oct	0.29	1.23	2.002	16.4	11.63	5.0	<u>5</u>
	oct	0.30	0.76	2.080	16.4	9.47	5.0	
	or tet	0.29	1.23	1.757	16.4	2.75	5.6	
	tet	0.30	0.76	1.758	16.4	2.78	2.0	
Fe sapphire	oct	0.33	0.85	2.022	16.86	10.78	8.3	**
	oct	0.35	1.49	2.087	16.86	12.72	3.3	
schorlomite	oct	0.42	0.62	2.024	18.22	11.0	0	<u>81, 105</u>
	tet	0.18	1.30	1.643	18.22		0	
sanidine	tet	0.21	0.48	1.649	22.47	2.30	0.3	<u>106</u>
sillimanite	oct	0.37	1.11	1.912	16.62	9.18	3.4	<u>107, 108</u>
	tet	0.16	0.53	1.764	16.62	2.79	4.0	
taramellite	oct	0.47	0.44	2.021	22.71		6.5	<u>109, **</u>
vesuvianite	5CN	0.33	0.56	2.107	18.74	6.60	1.8	<u>75, 110</u>
yoderite	oct	0.36	1.00	1.963	16.38	9.82	1.6	<u>8</u>
	or 5CN	0.36	1.00	1.933	16.38	6.07	3.8	

^a Isomer shift relative to Fe metal standard, mm/sec., at 298°K

^b Quadrupole splitting, mm/sec.

^c Mean metal-oxygen distance in coordination site, Å.

^d Volume per oxygen in a unit cell, Å³.

^e Polyhedral volume of a coordination site, Å³.

^f Bond length deviation (16)

** This paper.

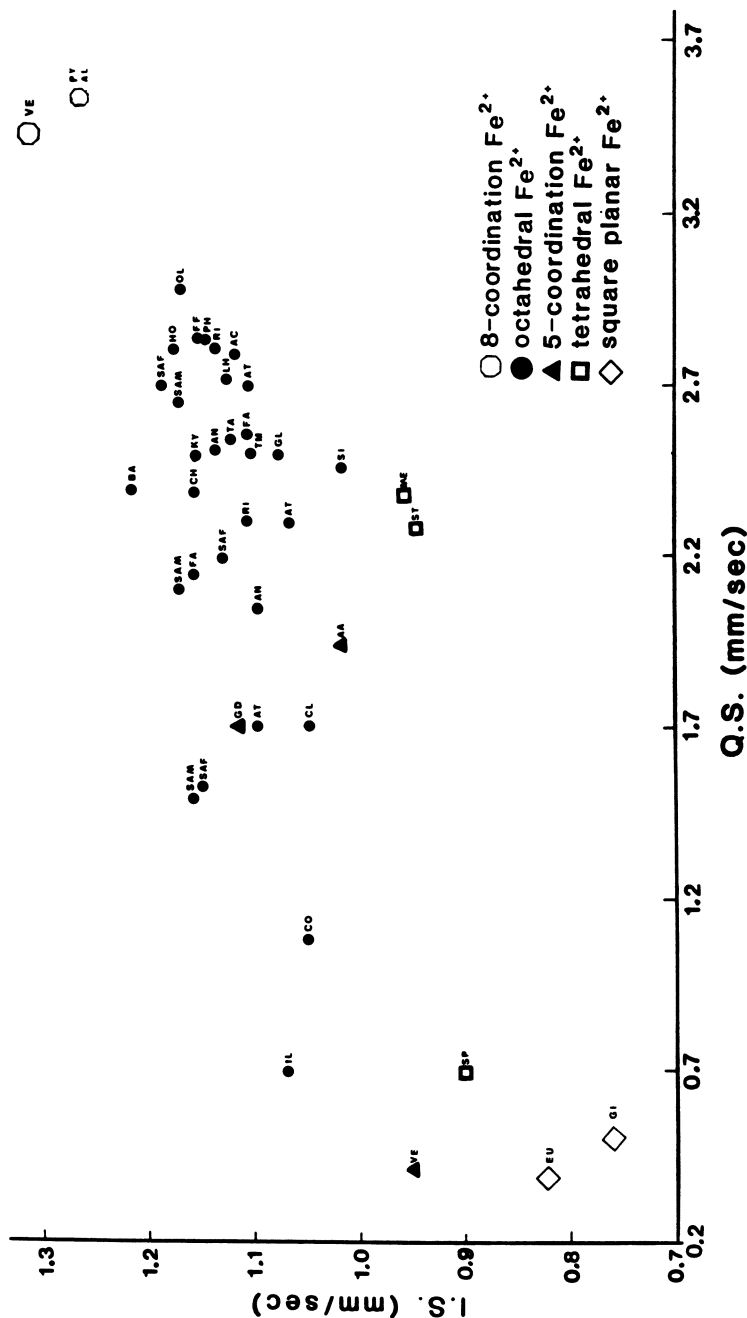


Figure 1. Isomer shift versus quadrupole splitting data for Fe²⁺ ions in a variety of coordination environments in silicate and oxide minerals. Calibration of each 295K Mossbauer spectrum from which the parameters are derived is based on reference zero velocity at the midpoint of the α -Fe spectrum. The legend to mineral symbols is contained in Table I.

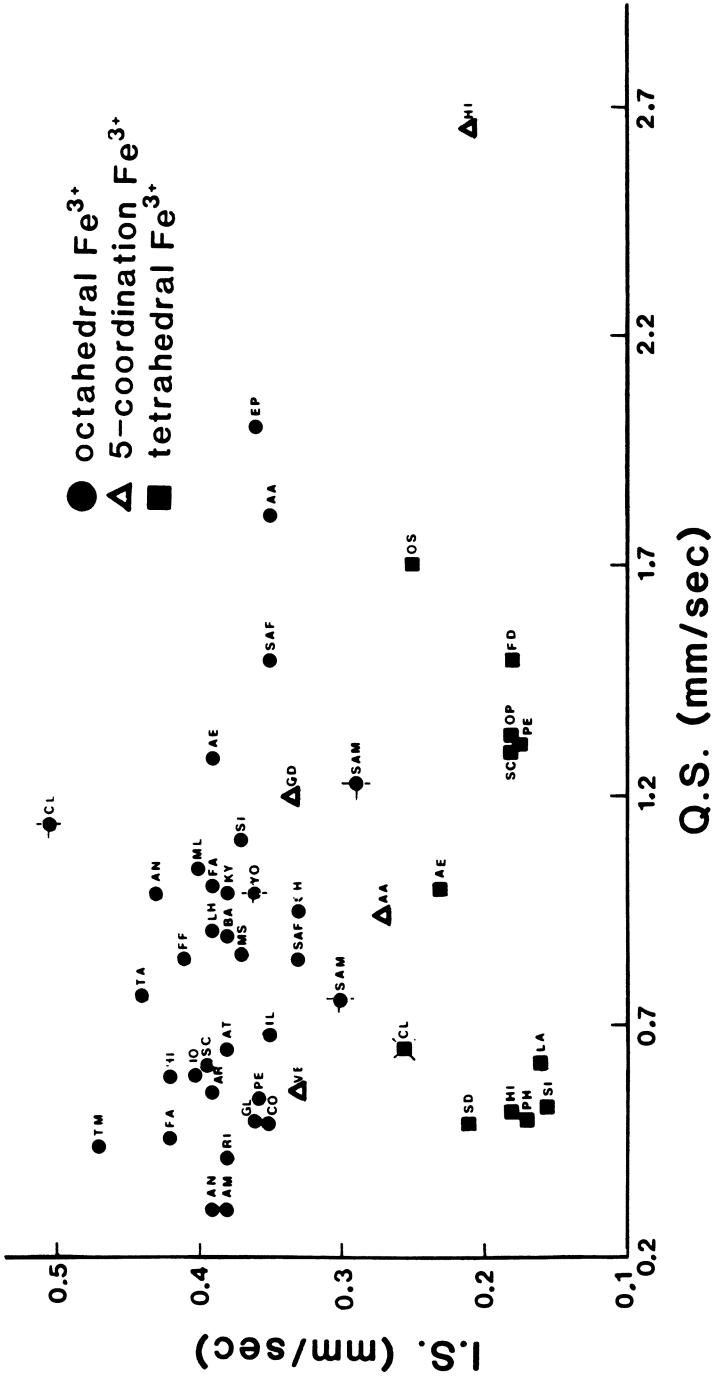


Figure 2. Isomer shift versus quadrupole splitting data for Fe³⁺ ions in several coordination environments in different silicate and oxide minerals. The 295K Mossbauer spectra are calibrated against α -Fe standard.

sites rather than the larger octahedral sites (6,7). Yoderite (YO) has Al and Mg in octahedral and five-fold coordination sites, but it is impossible to determine unambiguously the site occupancy of Fe³⁺ ions in yoderite from its Mossbauer spectral parameters alone (8). In attempts to verify the crystal chemistry of Fe³⁺ ions in these minerals, other correlations have been sought between the two Mossbauer spectral parameters, I.S. or Q.S., and crystal structure parameters based on bond distances and site distortion properties (2,5-9). These correlations are now critically examined.

Correlations Between Isomer Shift and Crystal Structure Parameters

The isomer shift parameter is sensitive to the electron density around the nucleus. Values of I.S. for ⁵⁷Fe are predicted to decrease with increasing s-electron density at the nucleus (7), and to depend on iron oxidation state as well as the type and bond-lengths of ligands coordinated to iron (13). Thus, high oxidation states, increased covalent bond-character and shortened bond distances are each predicted to lower the I.S. of ⁵⁷Fe phases. In oxygen coordination environments, therefore, increased metal-oxygen distances in coordination polyhedra are expected to result in higher I.S. values for Fe cations in such sites. Crystal structure parameters that reflect interatomic distances include: (1) the average metal-oxygen distance in a coordination site, R; (2) the volume per oxygen in a unit cell, V_{ox}; and (3) the polyhedral volume, V_p.

Isomer Shift versus Average Metal-Oxygen. Attempts to establish the presence of tetrahedral Fe³⁺ ions in silicates have sought correlations between I.S. and average bond lengths of (Si,Al)O₄ tetrahedra (2,5-7) but were not extended to other coordination environments. Therefore, data for a wide range of ferric-bearing minerals are shown in Figure 3, in which average metal-oxygen distances, R, for oxygen coordination polyhedra in several mineral structures containing tetrahedral, octahedral and five-coordinated sites are plotted against the I.S. data summarized in Table II. The I.S. data for clintonite, magnesian sapphire and yoderite are each plotted in two separate regions because, as noted earlier, Fe³⁺ site occupancies for these minerals are ambiguous. Figure 3 shows that, although smaller metal-oxygen distances in tetrahedral sites are associated with low Fe³⁺ I.S. values and higher I.S. parameters are found for Fe³⁺ ions in octahedral sites with larger R, the plotted data fail to delimit the upper range for tetrahedral Fe³⁺ ions and the lower range for octahedral Fe³⁺ ions. Nevertheless, there is an indication that ferric iron occurs in octahedral coordination in sapphire and not in tetrahedral sites, but the data for clintonite are less conclusive. For yoderite, although the data for five-coordinated Fe³⁺ ions lie between the ranges for tetrahedral and octahedral ferric iron, the value of the I.S. is also consistent with Fe³⁺ occupancy of the six-coordinated sites in yoderite.

Isomer Shift Versus Volume Per Oxygen. The average metal-oxygen distance parameter plotted in Figure 3 is unsatisfactory in many ways because it obscures differences between oxygen ligand-types (e.g. free O²⁻ and OH⁻ ions, bridging Si-O-Si and non-bridging Si-O⁻, etc.) and between ranges of metal-oxygen distances in distorted coordination polyhedra. Similar criticisms may be leveled at correlations between isomer shift and volume per oxygen, V_{ox}, calculated from unit cell parameters and the number of formula units

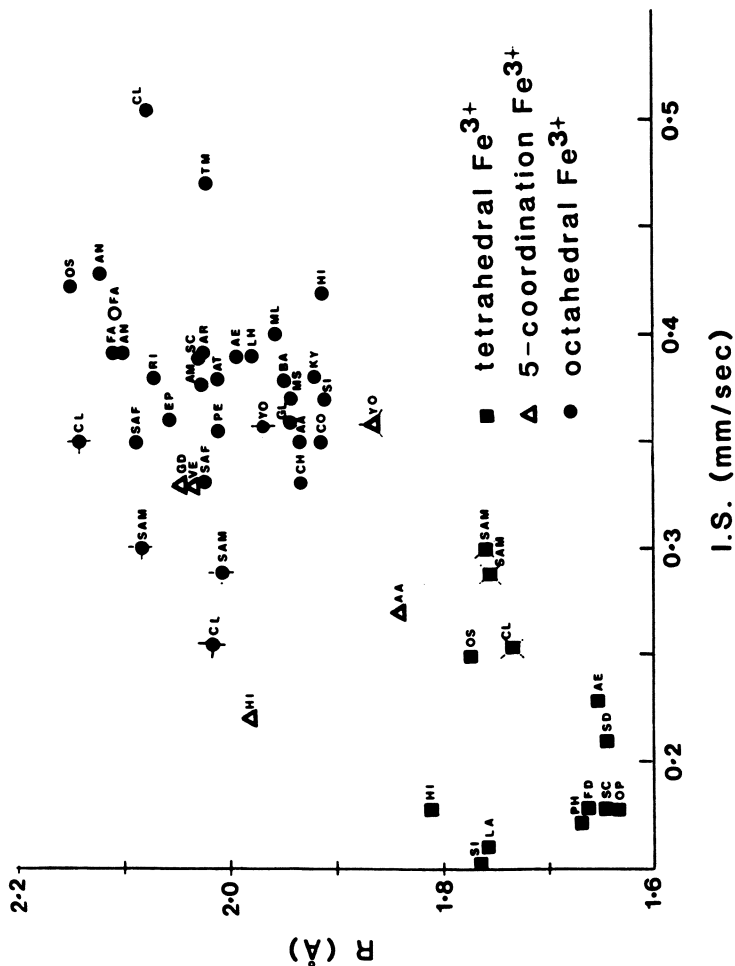


Figure 3. Average metal-oxygen distance plotted against isomer shift for Fe^{3+} ions in different coordination environments in minerals. The data for clintonite (CL), yoderite (YO) and Mg-sapphirine (SAM), which are highlighted by spikes, are each plotted in two regions because dual ferric site occupancies have been suggested for these minerals.

per cell. The V_{ox} versus I.S. data plotted in Figure 4 again show clustering of values for octahedral Fe^{3+} -bearing minerals which are more clearly separated from phases with tetrahedral Fe^{3+} -site occupancies. The small V_{ox} values for Mg-sapphirine and yoderite are indicative of octahedrally coordinated Fe^{3+} , although more dense oxide structures (e.g. corundum, kyanite, garnets) do have somewhat higher octahedral I.S. parameters.

Isomer Shift Versus Polyhedral Volume. A major criticism of the volume per oxygen (V_{ox}) parameter used in Figure 4 is that it fails to distinguish volume elements for the variety of individual coordination polyhedra which exist in all iron-bearing silicate minerals. However, the polyhedral volume parameter, V_p , computed from atomic coordinates of oxygen atoms comprising the nearest-neighbor coordination environment about a cation in a crystal structure (14), might provide a more realistic volume parameter for Fe^{3+} cations in regular and distorted sites. The I.S. versus V_p data plotted in Figure 5 clearly define regions for octahedral, tetrahedral and five-coordinated Fe^{3+} ions. Ranges are plotted for yoderite, clintonite, Mg-sapphirine and other minerals (kyanite, hibonite, annite, etc.) because they each contain two or more 4- 5- or 6-fold coordinated sites that may be occupied by Fe^{3+} ions. Again, however, the site occupancies of Fe^{3+} ions in Mg-sapphirine, yoderite and clintonite are not clearly defined from the trends plotted in Figure 5.

Quadrupole Splitting Versus Crystal Structure Parameters.

Although the isomer shift is generally considered to be a more valuable parameter than quadrupole splitting for determining the valence and coordination of iron, various correlations of Q.S. with crystal structure parameters have been sought to confirm Fe^{3+} site occupancies in silicate minerals (2,6,9). The Q.S. of ^{57}Fe , which originates from the interaction between the nuclear quadrupole moment and the electric field gradient at the nucleus, is influenced principally by the non-spherical distribution of electrons in unfilled orbitals and to a lesser extent by the asymmetry of nearest-neighbor ligands forming the coordination polyhedron and next-nearest neighbor cation interactions. Ferric iron, on account of its spherically symmetrical electronic configuration, $[Ar]3d^5$, usually has lower Q.S. values in oxygen coordination polyhedra than ferrous iron, the sixth 3d electron of which produces asymmetry of electronic charge and a high electric field gradient at the nucleus. The Q.S. of ferric iron in mineral structures, therefore, might be expected to be sensitive to relative distortions of coordination polyhedra from regular (cubic) octahedral or tetrahedral symmetries. Several criteria have been used to describe the distortion of coordination polyhedra from ideal symmetries, including: (1) bond angle variance, σ^2 (15); (2) quadratic elongation, λ (15); and (3) bond length deviation, Δ (16). Although each of these distortion parameters has been correlated with Q.S. parameters (2,5) with limited success, the bond length deviation parameter alone will be examined here.

Quadrupole Splitting versus Bond Length Deviation. The bond length deviation parameter (16), calculated by the equation

$$\Delta = \frac{1}{N} \sum [(R_i - R) / R]^2$$

where R_i and R are individual and mean metal-oxygen distances for octahedral ($N = 6$), tetrahedral ($N = 4$) and five-fold ($N = 5$) coordination sites, respectively, is plotted against the quadrupole

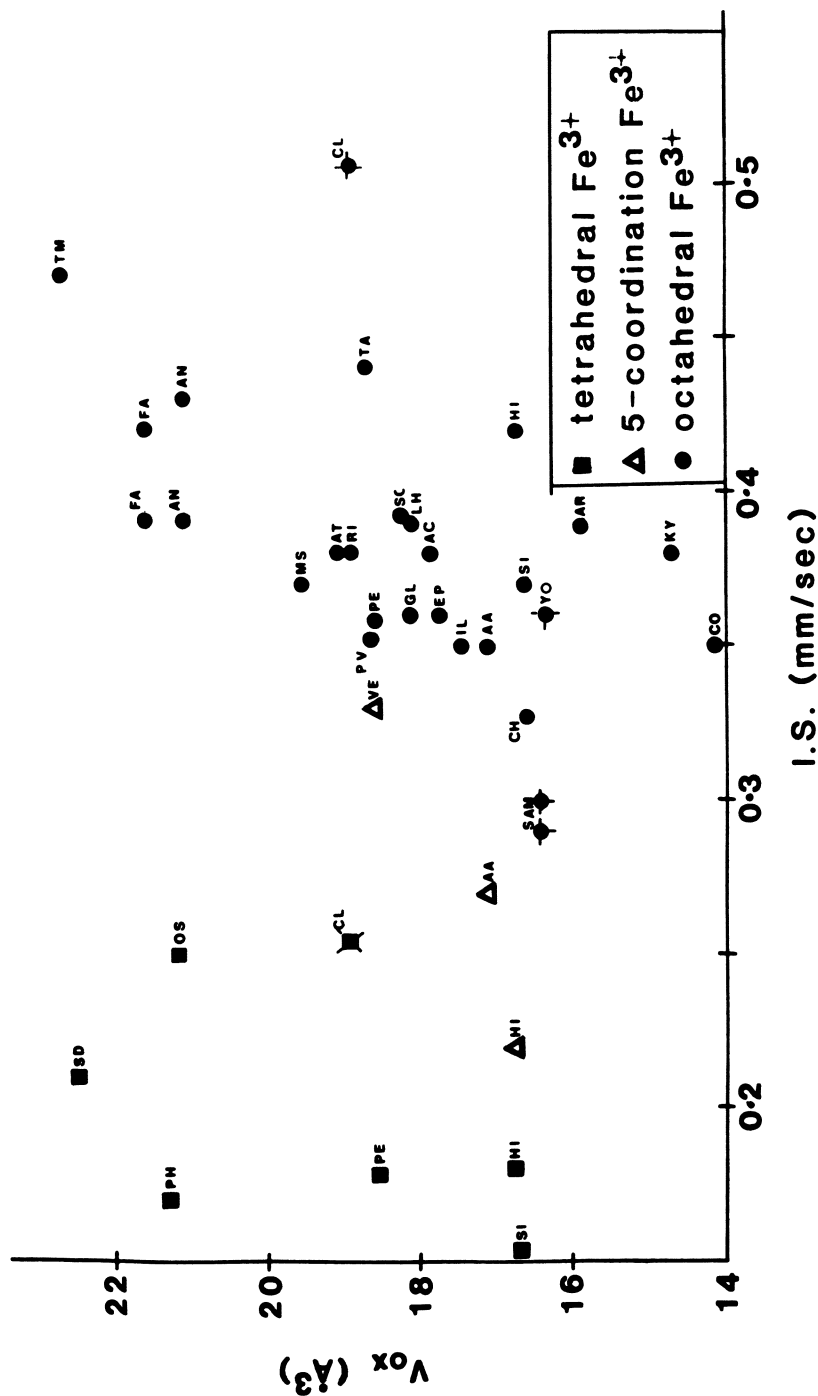


Figure 4. Volume per oxygen plotted against isomer shift of Fe^{3+} ions in the unit cells of different mineral structures.

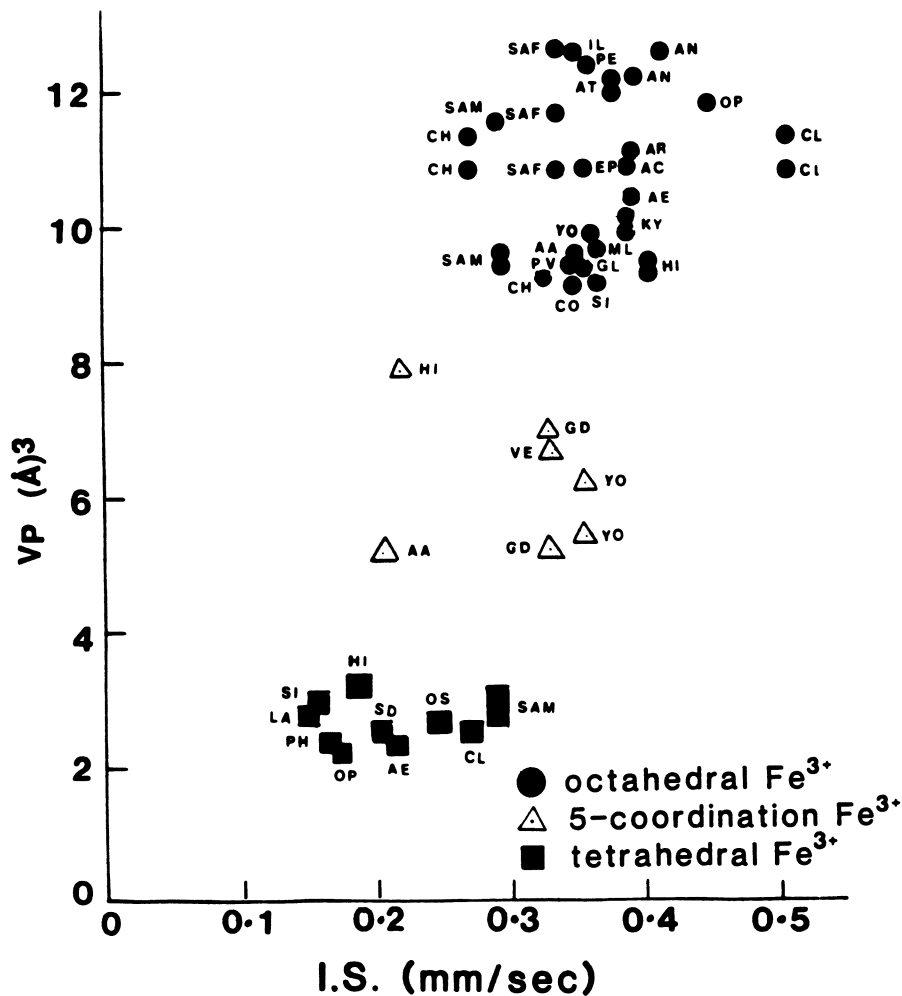


Figure 5. Polyhedral volume plotted against isomer shift for several Fe³⁺-bearing coordination sites in minerals.

splitting parameter for several Fe^{3+} -bearing minerals in Figure 6. The wide ranges of bond length deviation parameters for octahedral and tetrahedral sites in the minerals listed in Table 2 lead to widespread scatter of points in Figure 6. No correlation is evident between Q.S and Δ , in disagreement with earlier suggestions (2,5) based on more limited data-sets. Certainly, no conclusions about the Fe^{3+} site occupancies in sapphirine can be drawn from Figure 6. Note that similar scattering of data occurs in plots of quadrupole splitting against bond-angle variance.

Correlations Between Ferrous and Ferric Isomer Shifts

It becomes apparent from the results plotted in Figures 3-6 that correlations between the various crystal structure parameters and Mossbauer spectral data are not good. Perhaps this is not surprising considering the fact that, while the crystal structure parameters are averages for a specific crystallographic site, they may not represent the configuration of a polyhedron actually occupied by Fe^{3+} ions when the latter are present as minor constituents substituting for major Mg^{2+} , Al^{3+} or Si^{4+} ions in a host mineral. Certainly, the crystal chemistry of Fe^{3+} in the three debatable minerals, sapphirine, clintonite and yoderite, cannot be assigned with confidence from the correlation diagrams shown in Figures 3-6. The one trend that does persist throughout the plotted data, however, is the observation that the Mossbauer spectral parameters of clintonite are consistently out of line when compared to other silicate minerals.

Some of the uncertainties concerning site occupancy assignments of iron cations might be alleviated if comparisons could be made between measurable parameters for different cations in the same coordination site. One such correlation is suggested by the isomer shift parameter for coexisting Fe^{2+} and Fe^{3+} ions in similar coordination environments in a mineral, particularly when the two cations occupy the same crystallographic position in the crystal structure.

Mossbauer spectral parameters for a variety of Fe^{2+} - Fe^{3+} -bearing minerals summarized in Table III are plotted in Figure 7. The data include unpublished results for clintonite, yoderite and two sapphirines, which were each measured and computed under conditions described elsewhere (17). The revised I.S. and Q.S. values obtained for Fe cations in yoderite and Mg-sapphirine resemble published data (4,6,8). However, for clintonite, the I.S. values for the doublets assigned to octahedral Fe^{3+} and Fe^{2+} are significantly higher than earlier results (5), bringing the reduced I.S. value of the second Fe^{3+} doublet (Table III) more in line with other minerals containing tetrahedrally coordinated ferric iron. Recent crystal structure and Mossbauer spectral data for several clintonites support these results (113).

The I.S. data plotted in Figure 7 show a linear trend for octahedrally coordinated Fe cations between ludwigite (borate), vivianite (phosphate) and voltaite (sulfate) to which many Fe^{2+} - Fe^{3+} silicates conform. The new data for clintonites occurring in high-temperature contact metamorphic rocks are consistent with Fe^{3+} ions in both octahedral and tetrahedral coordinations with relative enrichment in the tetrahedral sites [113]. Both octahedral and five-coordinated Fe^{3+} ions appear to exist in yoderites from high grade metamorphic rocks with relative enrichment in the larger of the two five-fold coordinated sites [8]. The I.S. values for other Mg-Al-silicates, notably sapphirine and chloritoid, lie well off the trend suggested by the other minerals containing coexisting Fe^{2+} and Fe^{3+} ions. Nevertheless, the values for sapphirines from high-pressure

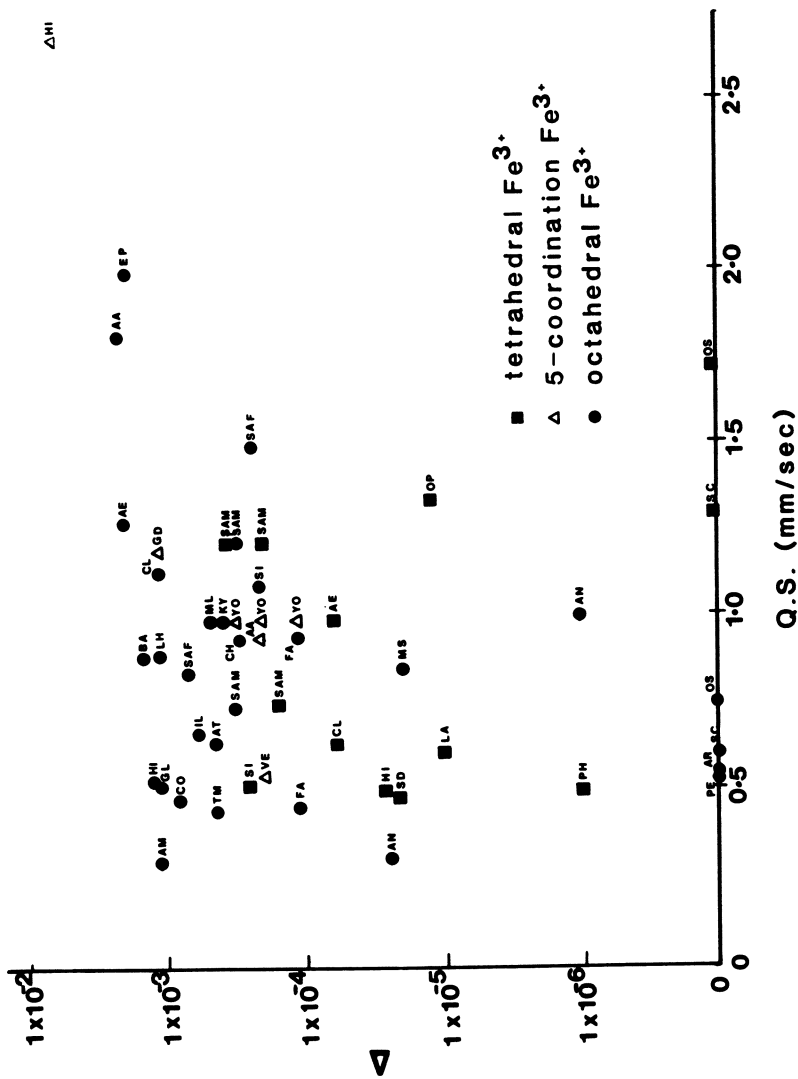


Figure 6. Bond length deviation plotted against quadrupole splitting of Fe³⁺ ions in a variety of distorted coordination sites in minerals.

Table III. Mossbauer Parameters for Minerals with Coexisting Fe²⁺ and Fe³⁺ Ions

Mineral	Fe ²⁺ Site	I.S.	Q.S.	Fe ³⁺ Site	I.S.	Q.S.	Mossbauer Reference
actinolite	oct	1.11	2.71	oct	0.38	0.65	<u>82</u>
	oct	1.07	2.30				
	oct	1.10	1.72				
annite	oct	1.14	2.53	oct	0.39	0.31	<u>17</u>
	oct	1.10	2.06	oct	0.43	0.99	
aenigmatite*	oct	1.13	2.61	oct	0.39	1.28	[1]
	oct	1.13	2.26	tet	0.23	0.97	
	oct	1.13	1.91				
babingtonite	oct	1.22	2.41	oct	0.39	0.90	<u>11, 83</u>
chloritoid	oct	1.16	2.39	oct	0.33	0.95	<u>84</u>
clintonite	oct	1.08	2.48	oct	0.52	1.05	<u>6</u>
	oct	1.04	1.72	tet	0.27	0.62	
clintonite*	oct	1.11	2.25	oct	0.39	2.01	[2], <u>113</u>
				tet	0.21	0.68	
corundum	oct	1.05	1.09	oct	0.35	0.48	<u>60, 87</u>
epidote	oct	1.07	1.66	oct	0.36	1.87	<u>4, 88</u>
ferrifayalite	oct	1.16	2.82	oct	0.41	0.85	<u>90</u>
ilmenite	oct	1.07	0.71	oct	0.35	0.67	<u>95</u>
kyanite	oct	1.16	2.49	oct	0.38	0.99	<u>96</u>
laihunite	oct	1.13	2.75	oct	0.39	0.91	<u>90, 98</u>
ludwigite*	oct	0.99	2.09	oct	0.35	1.25	[3]
periclase	oct	1.05	0	oct	0.36	0.54	<u>60, 104</u>
				tet	0.18	1.33	
perovskite*	oct	1.05	2.15	oct	0.35	0	[4]
riebeckite	oct	1.14	2.83	oct	0.38	0.43	<u>4, 92</u>
	oct	1.11	2.32				
	oct	1.18	2.65	oct	0.29	1.03	[5]
Mg-sapphirine*	oct	1.17	2.13				
	oct	1.16	1.51				
	oct	1.18	2.71	oct	0.33	0.85	[6]
Fe-sapphirine*	oct	1.13	2.19	oct	0.35	1.49	
	oct	1.15	1.57				
	oct	1.16	2.60	oct	0.42	0.60	<u>81, 105</u>
schorlomite	oct	1.02	2.47	oct	0.38	1.11	<u>107, 108</u>
				tet	0.16	0.53	
talc*	oct	1.13	2.57	oct	0.44	0.77	[7]
taramellite*	oct	1.11	2.51	oct	0.47	0.44	[8]
vesuvianite*	5CN	0.95	0.42	5CN	0.33	0.56	<u>75, 110</u>
	oct	1.11	2.77				[9]
vivianite	oct	1.18	2.45	oct	0.38	1.06	<u>11, 111</u>
	oct	1.21	2.98	oct	0.40	0.61	
voltaita	oct	1.27	1.80	oct	0.45	0	<u>112</u>
yoderite	5CN	1.15	2.51	5CN	0.36	1.00	<u>8</u>
yoderite*	oct	1.15	2.50	oct	0.43	0.53	[10]
				5CN	0.33	1.17	

Table III. Continued

* This work:

- [1] aenigmatite, Kola Peninsular, U.S.S.R.,
 $\text{Na}_{3.97}\text{K}_{0.02}\text{Ca}_{0.13}\text{Fe}^{2+}_{8.06}\text{Mg}_{0.70}\text{Mn}_{0.59}\text{Fe}^{3+}_{0.99}\text{Al}_{0.21}\text{Ti}_{2.07}\text{Si}_{11.26}\text{O}_{40}$;
 contains 10.7% ferric iron, ~6% of which is in tetrahedral coordination.
- [2] clintonite (xanthophyllite), Crestmore, California,
 $\text{Ca}_{0.99}\text{Mg}_{2.10}\text{Fe}^{2+}_{0.04}\text{Fe}^{3+}_{0.13}\text{Al}_{2.54}\text{Si}_{1.18}\text{O}_{10}(\text{OH})_2$;
 contains ~76% ferric iron, including ~64% in tetrahedral coordination.
- [3] ludwigite, Willis Quadrangle, New York,
 $(\text{Mg}_{1.90}\text{Fe}^{2+}_{0.10})\text{Fe}^{3+}\text{BO}_5$;
 contains 95% ferric iron in octahedral coordination.
- [4] perovskite #OL-2 from the British Museum (Natural History),
 $\text{Ca}_{0.95}\text{Sr}_{0.01}\text{REE}_{0.05}\text{Ti}_{0.91}\text{Nb}_{0.02}\text{Al}_{0.02}\text{Fe}_{0.05}\text{O}_3$;
 contains 95% ferric iron in octahedral coordination.
- [5] Mg sapphire, Bekily, Madagascar,
 $\text{Mg}_{7.40}\text{Fe}^{2+}_{0.22}\text{Fe}^{3+}_{0.02}\text{Al}_{17.07}\text{Si}_{3.37}\text{O}_{40}$;
 contains ~7.5% ferric iron in octahedral coordination.
- [6] Fe sapphire, Wilson Lake, Labrador,
 $\text{Mg}_{7.04}\text{Fe}^{2+}_{1.34}\text{Mn}_{0.08}\text{Fe}^{3+}_{0.88}\text{Al}_{16.20}\text{Si}_{3.46}\text{O}_{40}$;
 contains ~ 40% ferric iron in octahedral coordination.
- [7] iron talc, Sterling Mine, Antwerp, NY,
 $(\text{Mg}_{1.90}\text{Fe}^{2+}_{0.98}\text{Fe}^{3+}_{0.06}\text{Al}_{0.02})\text{Si}_{4.04}\text{O}_{10}(\text{OH})_2$;
 contains ~6% ferric iron in octahedral coordination.
- [8] taramellite, Rush Creek, Fresno Co., California,
 $\text{Ba}_{7.71}\text{Fe}^{2+}_{1.96}\text{Fe}^{3+}_{0.65}\text{Ti}_{3.91}\text{Mg}_{0.91}\text{Mn}_{0.12}\text{V}_{0.14}\text{Al}_{0.15}\text{Si}_{15.85}\text{O}_{54}$;
 contains ~25% ferric iron in octahedral coordination.
- [9] vesuvianite, Sanford, Maine,
 $\text{Ca}_{10.6}\text{Na}_{0.1}\text{Mg}_{1.1}\text{Fe}_{1.8}\text{Mn}_{0.2}\text{Ti}_{0.2}\text{Al}_{10.2}\text{Si}_{17.8}\text{O}_{69.9}\text{OH}_{4.9}\text{F}_{3.2}$;
 contains 27% Fe^{3+} and 38% Fe^{2+} in the five-coordination sites, in addition to 35% octahedral Fe^{2+}
- [10] yoderite, Mautia Hill, Tanzania,
 $\text{Mg}_{1.98}\text{Fe}^{2+}_{0.02}\text{Fe}^{3+}_{0.45}\text{Al}_{5.56}\text{Si}_{3.91}\text{O}_{17.73}(\text{OH})_{2.27}$;
 contains 94% ferric iron, including ~73% in five-fold coordination.

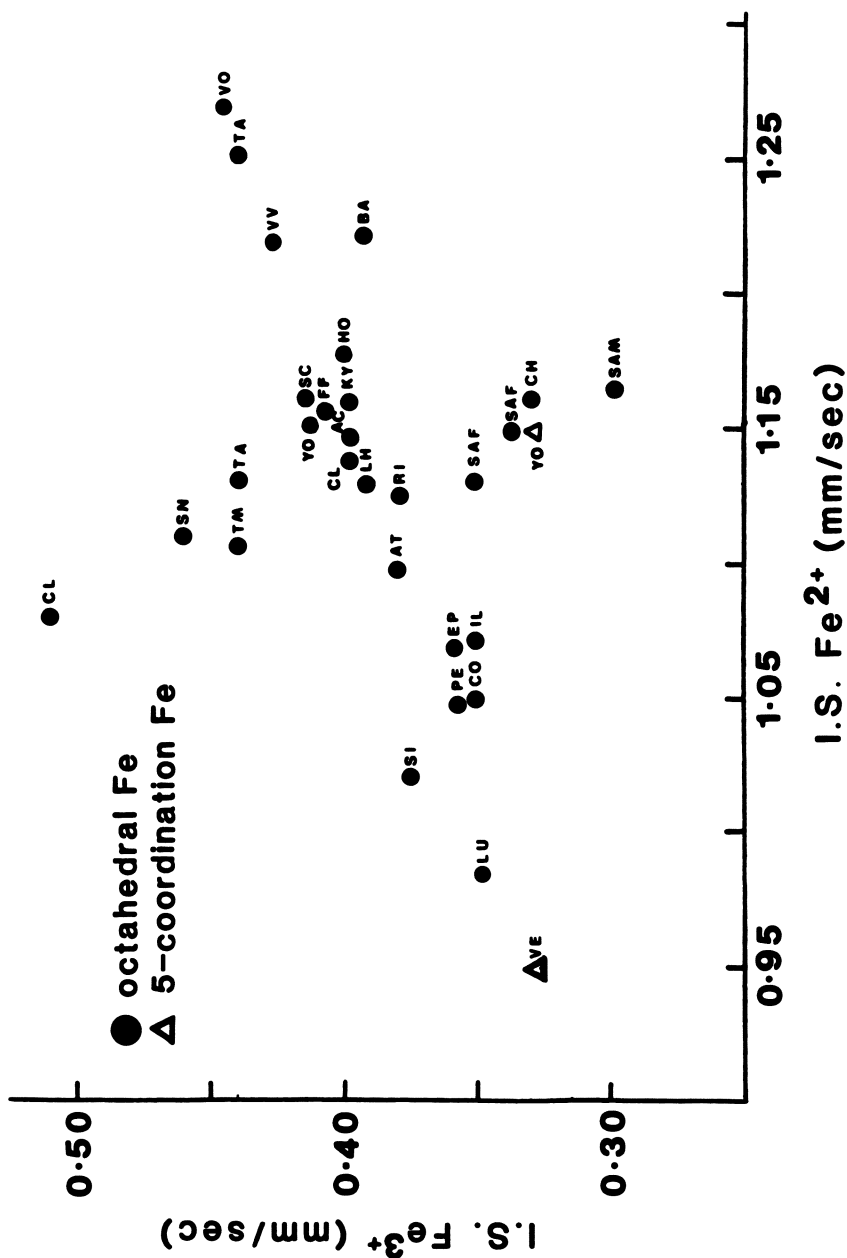


Figure 7. Correlations between ferric and ferrous isomer shifts for minerals containing coexisting Fe²⁺ and Fe³⁺ ions.

metamorphic rocks are more consistent with octahedral Fe³⁺ site occupancies than tetrahedral, since higher coordination environments for iron cation in silicates are predicted and observed at high pressures.

Discussion

The ferric I.S versus crystal structure parameters plotted in Figures 3-5 show that, although definite trends exist for each volume-related property between different coordination numbers, there appear to be no strong correlations within the ranges for a specific coordination environment. However, the situation is improved for the I.S vs R (Figure 3) and I.S. vs V_p (Figure 5) correlations when the tetrahedral Fe³⁺ I.S. value for clintonite is revised to ≤ 0.23 mm/sec. (see Table III and [113]). The upper limit for tetrahedral Fe³⁺ I.S in silicates is now ~0.25 mm/sec., whereas the lower limit for octahedral Fe³⁺ I.S. in oxygen environments is now ~0.29 mm/sec. The boundaries for five-coordinated Fe³⁺, however, are not so well constrained.

The lack of a strong correlation between isomer shifts and Fe-oxygen distances has been attributed to covalency effects beyond the immediate coordination polyhedron surrounding an iron cation (13). The inductive effect of different types and arrays of next-nearest neighbor cations bonded to oxygen atoms at vertices, edges and faces of coordination sites occupied by iron influences the ionic-covalent character of Fe-oxygen bonds. These Fe-O bonds are more ionic if the next-nearest cation has a larger charge, smaller ionic radius, and occupies a lower coordination number site than the adjacent Fe cation, leading to a higher I.S. Thus, oxygens shared with tetrahedral Si⁴⁺ should produce a higher I.S. than those shared with octahedral Al or Mg. The inductive effect factor may contribute to the low I.S. of octahedral Fe³⁺ ions in Mg²⁺-Al³⁺-silicates such as sapphirine and chloritoid, the crystal structures of which contain bands of edge-shared Mg and Al octahedra. In aenigmatite, on the other hand, which has a structure similar to sapphirine, the higher I.S. of octahedral Fe³⁺ ions may be attributed to the presence of larger, less ionic Fe²⁺ and Ti⁴⁺ in adjacent edge-shared octahedra. The situation becomes more complicated, however, when each oxygen belonging to an Fe coordination polyhedron is bound to different populations of next-nearest cations in their own coordination sites as a result of extensive atomic substitution of Fe²⁺, Fe³⁺, Ti⁴⁺, etc., for Mg and Al. Such chemical and bonding variations for different mineral structures and the variability of inductive effects from adjacent cations are probably sufficiently strong to account for large ranges of isomer shifts exhibited within a specific coordination symmetry in silicate minerals.

Acknowledgments

We thank Dr. L. W. Finger for providing the program for computing polyhedral volumes and polyhedral distortion parameters from a set of atomic coordinates in a unit cell (114). Mineral spectroscopic research on terrestrial and planetary minerals is supported by the National Aeronautics and Space Administration (NASA grant number NSG-7604).

Literature Cited

1. Bancroft, G. M. Mossbauer Spectroscopy. An Introduction for Inorganic Chemists and Geochemists; McGraw-Hill: New York, 1973.
2. Coey, J. M. D. In Chemical Applications of Mossbauer Spectroscopy; Long, G. J., Ed; Plenum: New York, 1984, Vol. 1, Chapt. 14, 443-509.
3. Hawthorne, F. C. In Spectroscopic Methods in Mineralogy and Geology; Hawthorne, F. C., Ed.; Rev. Mineral., 1988, **18**, 255-340.
4. Bancroft, G. M.; Burns, R. G.; Stone, A. J. Geochim. Cosmochim. Acta, 1968, **32**, 547-59.
5. Steffen, G.; Seifert, F.; Amthauer, G. Amer. Mineral., 1984, **69**, 339-48.
6. Annersten, H.; Olesch, M. Canad. Mineral., 1978, **16**, 199-203.
7. Tang Kai, A.; Annersten, H.; Ericsson, T. Phys. Chem. Mineral., 1980, **5**, 343-9.
8. Abu-Eid, R. M.; Langer, K.; Seifert, F. Phys. Chem. Mineral., 1978, **3**, 271-89.
9. Heller-Kallai, L.; Rozenson, I. Phys. Chem. Mineral., 1981, **7**, 223-38.
10. Burns, R. G. Ann. Rev. Earth Planet. Sci., 1981, **9**, 345-83.
11. Amthauer, G.; Rossman, G. R. Phys. Chem. Mineral., 1984, **11**, 37-51.
12. Murad, E.; Johnston, J. H. In Mossbauer Spectroscopy Applied to Inorganic Chemistry; Long, G. J., Ed.; Plenum: New York, 1987; Vol. 2, Chapt. 12, 507-12.
13. Menil, F. J. Phys. Chem. Solids, 1985, **46**, 763-89
14. Smyth, J. R.; Bish, D. L. Crystal Structures and Cation Sites of the Rock-Forming Minerals; Allen and Unwin: Boston, 1988.
15. Robinson, K.; Gibbs, G. V.; Ribbe, P. H. Science, 1971, **172**, 567-70.
16. Fleet, M. E. Mineral. Mag., 1976, **40**, 531-33.
17. Dyar, M. D.; Burns, R. G. Amer. Mineral., 1986, **71**, 955-65.
18. Burnham, C. W.; Buerger, M. J. Zeit. Krist., 1961, **115**, 269-90.
19. Winter, J. K.; Ghose, S. Amer. Mineral., 1979, **64**, 573-86.
20. Clark, J. R.; Appleman, D. E.; Papike, J. J. Mineral. Soc. Amer. Spec. Pap., 1969, **2**, 31-50.
21. Cannillo, E.; Mazzi, F.; Fang, J. H.; Robinson, P. D.; Ohya, Y. Amer. Mineral., 1971, **56**, 427-46.
22. Novak, G. A.; Gibbs, G. V. Amer. Mineral., 1971, **56**, 791-825.
23. Amthauer, G.; Annersten, H.; Hafner, S. S. Zeit. Krist., 1976, **143**, 14-55.
24. Hazen, R. M.; Burnham, C. W. Amer. Mineral., 1973, **58**, 889-900.
25. Mitchell, J. T.; Bloss, F. D.; Gibbs, G. V. Zeit. Krist., 1971, **132**, 273-300.
26. Araki, T.; Zoltai, T. Zeit. Krist., 1972, **135**, 355-75.
27. Gibbs, G. V. Amer. Mineral., 1966, **51**, 1068-87.
28. Cohen, J. P.; Ross, K. K.; Gibbs, G. V. Amer. Mineral., 1977, **62**, 67-78.
29. Hanscom, R. H. Acta Cryst., 1975, **B31**, 780-84.
30. Takeuchi, Y. Proc. 13th Nat. Conf. Clays Clay Minerals; Bradley, W. F.; Bailey, S. W., Eds.; Pergamon: Oxford, 1964; Clays Clay Minerals, Mono. 25, pp. 125.
31. Newnham, R. E.; de Haan, Y. M. Zeit. Krist., 1962, **117**, 235-37.

32. Dollase, W. A. Amer. Mineral., 1971, 56, 447-64.
33. Giuseppetti, G.; Mazzi, F.; Tadini, C. Tschermaks Mineral. Petrogr. Mitt., 1971, 16, 105.
34. Donnay, G.; Morimoto, N.; Takeda, H.; Donnay, J. D. H. Acta Cryst., 1964, 17, 1369-73.
35. Peacor, D. Amer. Mineral., 1967, 52, 31-41.
36. Ferrifayalite Research Group. Acta Geol. Sinica, 1976, 2, 161-75.
37. Stephenson, D. A.; Moore, P. B. Acta Cryst., 1968, B24, 1518-22.
38. Pabst, A. Amer. Mineral., 1943, 28, 372-90.
39. Bancroft, G. M.; Burns, R. G.; Maddock, A. G. Geochim. Cosmochim. Acta, 1967, 31, 2219-46.
40. Papike, J. J.; Clark, J. R. Amer. Mineral., 1968, 53, 1156-73.
41. Kato, K.; Saalfeld, H. Neues J. Mineral. Abh., 1968, 109, 192-200.
42. Harder, M.; Muller-Buschbaum, H. Z. Naturforsch., 1977, 32b, 833-4.
43. Wenk, H. R. Amer. Mineral., 1974, 59, 86-97.
44. Raymond, K. N.; Wenk, H. R. Contrib. Mineral. Petrol., 1971, 30, 135-40.
45. Wechsler, B. A.; Prewitt, C. T. Amer. Mineral., 1984, 69, 176-85.
46. Burnham, C. W. Zeit. Krist., 1963, 118, 337-60.
47. Marezio, M. Acta Cryst., 1965, 19, 396-400.
48. Shen, B.; Tamada, O.; Kitamura, M.; Morimoto, N. Amer. Mineral., 1986, 71, 1455-60.
49. Swinnea, J. S.; Steinfink, H. Amer. Mineral., 1983, 68, 827-32.
50. Smith, J. V. Amer. Mineral., 1953, 38, 643-61.
51. Besson, G.; Bookin, A. S.; Dainyak, L. G.; Rautureau, M.; Tsipursky, S. I.; Tchoubar, C.; Drits, V. A. J. Appl. Cryst., 1983, 16, 374-83.
52. Burnham, C. W. Carnegie Inst. Washington Year Book, 1963, 62, 158-65.
53. Richardson, S. M.; Richardson, J. W. Amer. Mineral., 1982, 67, 69-75.
54. Cannillo, E.; Mazzi, F.; Rossi, G. Acta Cryst., 1966, 21, 200.
55. Bancroft, G. M.; Burns, R. G.; Maddock, A. G. Acta Cryst., 1967, 22, 934-5.
56. Birle, J. D.; Gibbs, G. V.; Moore, P. B.; Smith, J. V. Amer. Mineral., 1968, 53, 807-24.
57. Burnham, C. W.; Ohashi, Y.; Hafner, S. S.; Virgo, D. Amer. Mineral., 1971, 56, 850-76.
58. Hesse, K. F.; Seifert, F. Zeit. Krist., 1982, 160, 179-86.
59. Hazen, R. M. Amer. Mineral., 1976, 61, 266-71.
60. Burns, R. G.; Burns, V. M. In Structure and Properties of MgO and Al₂O₃ Ceramics; Kingery, W. D., Ed.; Amer. Ceram. Soc: Columbus, Ohio, 1984; Adv. Ceram., 10, 46-61.
61. Kay, H. F.; Bailey, P. C. Acta Cryst., 1957, 10, 219-26.
62. Hawthorne, F. C. Rev. Mineral., 1981, 9A, 1-102.
63. Higgins, J. B.; Ribbe, P. H. Contrib. Mineral. Petrol., 1979, 68, 357-68.
64. Merlino, S. Zeit. Krist., 1980, 151, 91-100.
65. Weber, H. P., Virgo, D., Huggins, F. E. Carnegie Inst. Washington Year Book, 1975, 74, 575-9.
66. Phillips, M. W.; Ribbe, P. H. Amer. Mineral., 1973, 58, 263-70.

67. Burnham, C. W. Zeit. Krist., 1963, 118, 127-48.
68. Eggleton, R. A. Mineral. Mag., 1972, 38, 693-711.
69. Fischer, P. Zeit. Krist., 1967, 124, 275-302.
70. Smith, J. V. Amer. Mineral., 1968, 53, 1139-55.
71. Perdikatsis, B.; Burzlauff, H. Zeit. Krist., 1981, 158, 177-86.
72. Guggenheim, S.; Eggleton, R. A. Canad. Mineral., 1986, 24, 479-97.
73. Mazzi, F.; Rossi, G. Amer. Mineral., 1980, 65, 123-28.
74. Rucklidge, J. C.; Kocman, S. H.; Whitlow, S. H.; Gabe, E. J. Canad. Mineral., 1975, 13, 15-21.
75. Allen, F. Chemical and Structural Variations in Vesuvianite. Ph.D. Thesis: Harvard, 1985.
76. Mereiter, K. Tschermaks Mineral. Petrogr. Mitt., 1972, 18, 185.
77. Mori, H.; Ito, T. Acta Cryst., 1950, 3, 1-6.
78. Higgins, J. B.; Ribbe, P. H.; Nakajima, Y. Amer. Mineral., 1982, 67, 76-84.
79. Abs-Wurmbach, I.; Langer, K.; Seifert, F.; Tillmanns, E. Zeit. Krist., 1981, 155, 81-113.
80. Dollase, W. A. Amer. Mineral., 1982, 67, 311-27.
81. Schwartz, K. B.; Nolet, D. A.; Burns, R. G. Amer. Mineral., 1980, 65, 142-53.
82. Burns, R. G.; Greaves, C. J. Amer. Mineral., 1971, 56, 2010-33.
83. Amthauer, G. Amer. Mineral., 1980, 65, 157-62.
84. Halenius, U.; Annersten, H.; Langer, K. Phys. Chem. Mineral., 1981, 7, 117-23.
85. Tricker, M. J.; Jefferson, D. A.; Thomas, J. M.; Manning, P. G.; Elliott, C. J. J. Chem. Soc. Faraday Trans. 2, 1978, 74, 174-81.
87. Jonas, K.; Solyman, K.; Zoldi, J. J. Mol. Struct., 1980, 60, 449-52
88. Dollase, W. A. Zeit. Krist., 1973, 138, 41-63.
89. Hafner, S. S.; Huckenholz, H. G. Nature Phys. Sci., 1971, 233, 9-11.
90. Schaefer, M. W. Amer. Mineral., 1985, 70, 729-36.
91. Seifert, F.; Olesch, M. Amer. Mineral., 1977, 62, 547-53.
92. Bancroft, G. M.; Burns, R. G. Mineral. Soc. Amer. Spec. Pap., 1969, 2, 137-48.
93. Glasser, F. P.; Woodhams, F. W. D.; Meads, R. E.; Parker, W. G. J. Solid State Chem., 1972, 5, 255-61.
94. Burns, R. G.; Burns, V. M. J. Geophys. Res., 1984, 89, C313-21.
95. Gibb, T. C.; Greenwood, N. N.; Twist, W. J. Inorg. Nucl. Chem., 1969, 31, 947-54.
96. Parkin, K. M.; Loeffler, B. M.; Burns, R. G. Phys. Chem. Mineral., 1977, 1, 301-11.
97. Waychunas, G. A.; Rossman, G. R. Phys. Chem. Mineral., 1983, 9, 212-5.
98. Kan, X.; Coey, J. M. D. Amer. Mineral., 1985, 70, 576-80.
99. Cardile, C. M.; Johnston, J. H. Clays Clay Mineral., 1986, 34, 307-13.
100. Cameron, Phys. Chem. Mineral., 1977, 1, 265-72.
101. Finch, J.; Gainsford, A. R.; Tennant, W. C. Amer. Mineral., 1982, 67, 59-68.
102. Annersten, H.; Olesch, M.; Seifert, F. Lithos, 1978, 11, 301-11.
103. Goldman, D. S.; Rossman, G. R. Amer. Mineral., 1978, 63, 490-8.

104. Waychunas, G. A. Mossbauer, X-Ray, Optical, and Chemical Study of Cation Arrangement and Defect Association in Fm3m Solid Solutions in the System Periclase-Wustite-Lithium Ferrite; Ph.D. Thesis: U.C.L.A., Los Angeles, 1981.
105. Kunberger, A.; Fehr, Y.; Huckenholz, H. G.; Amthauer, G. Phys. Chem. Mineral., 1988, in press.
106. Annersten, H. Neues Jb. Mineral. Mh., 1976, 337-43.
107. Rossman, G. R.; Grew, E. S.; Dollase, W. A. Amer. Mineral., 1982, **67**, 749-61.
108. Haaleni, U. Neues Jb. Mineral. Mh., 1979, 165-74.
109. Alfors, J. T.; Pabst, A. Amer. Mineral., 1984, **62**, 358-73.
110. Tricker, M. J.; Vaishnava, P. P.; Manning, P. G. J. Inorg. Nucl. Chem., 1981, **43**, 1169-74.
111. McCammon, C. A.; Burns, R. G. Amer. Mineral., 1980, **65**, 361-6.
112. Long, G. J.; Longworth, G.; Day, P.; Beveridge, D. Inorg. Chem., 1980, **19**, 821-9.
113. MacKinney, J.A.; Mora, C.I.; Bailey, S.W. Amer. Mineral., 1988, **73**, 365-75.
114. Hazen, R.M.; Finger, L. W. Comparative Crystal Chemistry; Wiley: New York, 1982; Appendix III, pp. 103-11.

RECEIVED April 18, 1989

Chapter 15

Crystal Chemistry, Electronic Structures, and Spectra of Fe Sites in Clay Minerals

Applications to Photochemistry and Electron Transport

David M. Sherman

U.S. Geological Survey, Denver, CO 80225

The electronic structures of Fe^{3+} and $\text{Fe}^{3+}\text{-Fe}^{2+}$ bearing clays and oxides are described with reference to SCF-X α -SW molecular orbital calculations on FeO_6 , FeO_4 and Fe_2O_{10} clusters. The results are used to interpret the optical spectra of iron bearing clays and iron oxides and provide some insight onto the possible mechanisms of photochemical redox reactions associated with those minerals.

Iron bearing clays and oxide minerals, because of their partially occupied Fe(3d) orbitals, may participate in a number of redox processes in nature. For example, photochemically induced electron transfer between organic molecules and colloidal iron oxides is a significant process in natural waters (1-2). Clays are thought by many to have played a central role in the chemistry which led to the origin of life (3). Because mixed-valent iron bearing clays can both donate and accept electrons, one is tempted to speculate that such clays may have had a role in the early prebiotic pathways for electron transfer and metabolism.

A basic understanding of the electronic structures of iron bearing clays and oxides is needed before one can understand the mechanisms of electron transfer and photochemical reactions associated with these minerals. This chapter will discuss the electronic structures of iron bearing clays and oxides (primarily from cluster molecular orbital calculations) and compare theoretical results with experiment. The discussion will be confined to states associated with simple Fe^{3+} and Fe^{2+} coordination sites in minerals and will not go into electronic states associated with defects.

Crystal Chemistry of Fe-Bearing Clays

Before describing the electronic structures of Fe coordination sites, it is worthwhile to first outline the crystal chemistry of clay minerals and describe the kinds of coordination environments that Fe^{3+} and Fe^{2+} cations may enter.

This chapter not subject to U.S. copyright
Published 1990 American Chemical Society

2:1 Clay Structures. The structure of a 2:1 clay such as nontronite, $(Ca/2,Na)_{.66}Fe_4(Si_{7.34}Al_{.66})O_{20}(OH)_4nH_2O$, is shown in Figure 1. One sheet of $(Fe,Al,Mg)_2O_4(OH)_2$ octahedra is sandwiched between two sheets of $(Si,Al)_2O_4$ tetrahedra. Between these 2:1 layers is an expandable interlayer region which can accommodate H_2O molecules, cations such as Na^+ , K^+ , and Ca^{2+} , organic molecules and even transition metal aquo complexes. Most Fe^{3+} and Fe^{2+} in 2:1 clays occupies the sites in the octahedral sheet. Clays in which the octahedral cation has a charge of +3 are described as being dioctahedral since only 2/3 of the octahedral sites are occupied. As can be seen in Figure 1, there are two kinds of octahedral sites: cis- $MO_4(OH)_2$ and trans- $MO_4(OH)_2$. In the case of the dioctahedral smectite clays such as nontronite and montmorillonite, there is some debate as to whether the cations are ordered within the octahedral sheet. In the disordered structure, 2/3 of both the cis and trans sites are occupied. In the ordered structure, shown in Figure 2, all of the cis sites are occupied and all of the trans sites are vacant. Mossbauer spectra of nontronites, when fit to two quadrupole doublets, suggest that iron is disordered in nontronite (4). As shown in Figure 3, the area ratios of the inner and outer Fe^{3+} doubles are 1/3:2/3 consistent with that expected for iron disordered over the cis and trans sites. The disordered arrangement also accounts for the low Neel temperature (1.3K) of nontronite (5). Electron diffraction measurements of the plane group of the octahedral sheet, however, suggest an ordered structure (6,7). Alternative interpretations of the magnetic behavior of nontronite (8) also suggest an ordered structure. Several investigators have attempted to explain how an ordered arrangement of Fe^{3+} cations can yield two quadrupole doublets by invoking next-nearest neighbor effects (9-12).

A small fraction of iron may enter the tetrahedral sites in 2:1 clays. In nontronite, there is often enough tetrahedral iron (ca. 5 %) to be detectable using Mossbauer spectra. The Mossbauer spectra in Figure 3, for example, shows a weak quadrupole doublet due to tetrahedral Fe^{3+} . Optical spectra of nontronites in the visible region also show an absorption band that is assigned to tetrahedrally coordinated Fe^{3+} . This is discussed in more detail below.

Iron may also occur as an interlayer species. Mossbauer spectra show the presence of an Fe^{2+} aquo complex in the interlayer of montmorillonite (13). The labile nature of this Fe^{2+} is suggested by the large temperature dependence of its recoil-free-fraction. In contrast, Fe^{3+} aquo complexes are unlikely to occur as discrete species in a clay interlayer. Instead, $Fe(OH)_2(H_2O)_4$ complexes will condense to form ferric hydroxy polymers which, in a clay interlayer, might form two-dimensional sheets or three-dimensional pillars. Such pillars in nontronite have been characterized by Gangas et al. (14).

1:1 Clay Structures. The 1:1 structures are the simplest since they contain only a single octahedral sheet and a single tetrahedral layer. The double layers are held together by hydrogen bonding. The most notable iron phyllosilicates with the 1:1 structure are berthierine and cronstedite. Very little iron

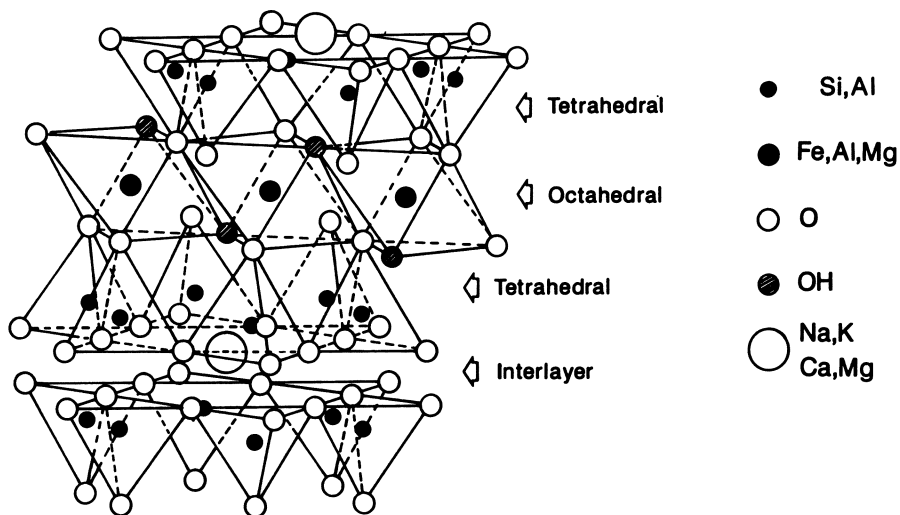


Figure 1. Generalized structure of a 2:1 phyllosilicate (e.g., smectite clay). There are two different octahedral sites corresponding to $\text{cis-MO}_4(\text{OH})_2$ and $\text{trans-MO}_4(\text{OH})_2$. (Modified from Grimm, R.E. "Clay Mineralogy" McGraw-Hill, 1968).

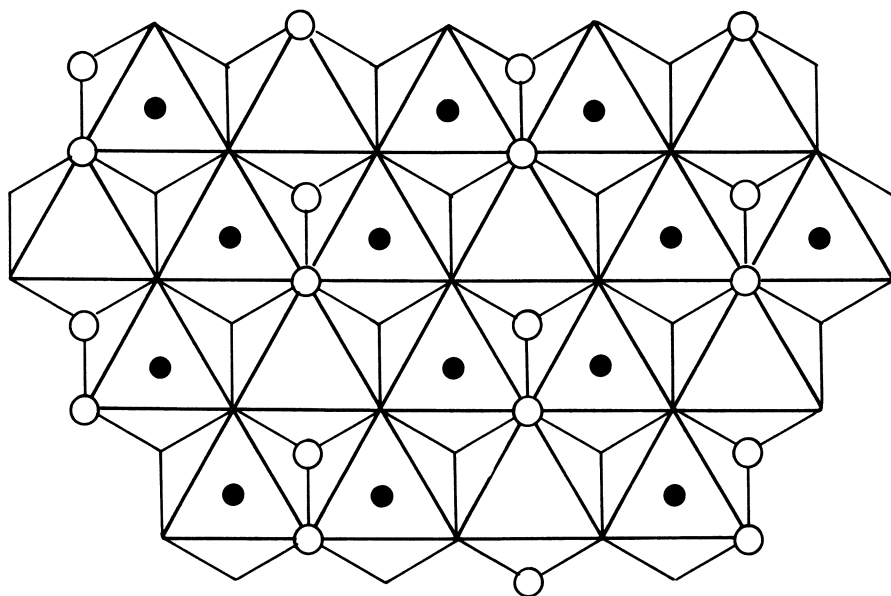


Figure 2. Structure of the octahedral sheet of a dioctahedral clay showing the completely ordered (cis only) configuration. The disordered structure would have $2/3$ of the cis-sites and $2/3$ of the trans sites occupied.

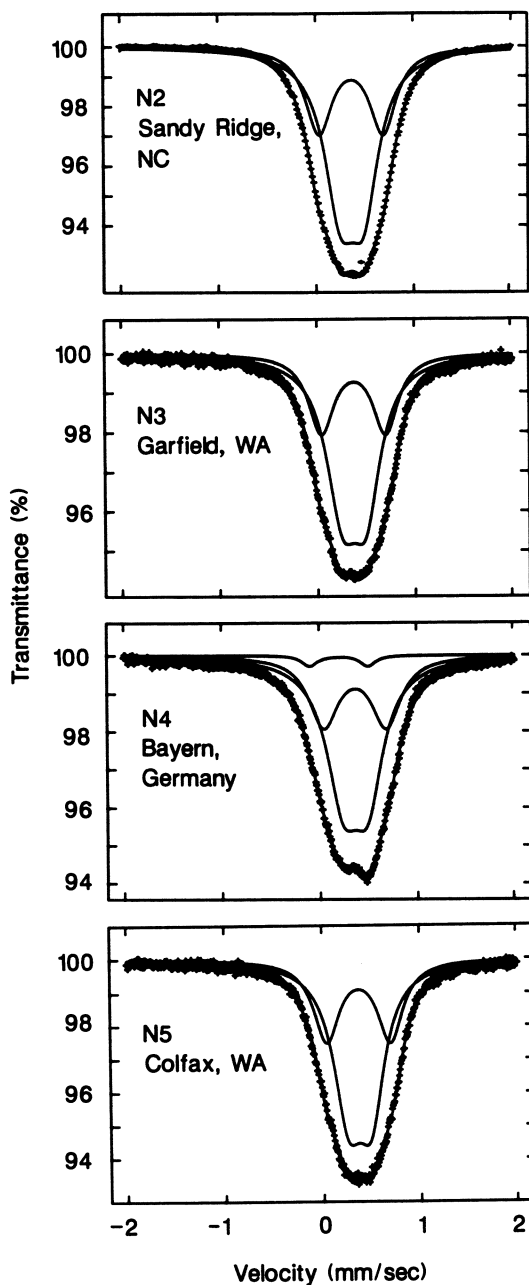


Figure 3. Room temperature Mossbauer spectrum of several nontronites showing two kinds of octahedrally coordinated Fe³⁺ and a small fraction of Fe³⁺ in tetrahedral coordination. (Adapted from (4)).

occurs in the more common phyllosilicates with the 1:1 structure (e.g., kaolinite).

Electronic Structures of Fe Sites in Clays and Oxides

Theoretical Preliminaries. It is worthwhile to first outline some essential concepts before discussing the electronic structures of Fe sites in clays and oxides. The electronic structure of an atom, molecule or solid is obtained by solving the Schrodinger equation

$$\hat{H} \Psi = E \Psi$$

where \hat{H} is the appropriate Hamiltonian operator, Ψ is the wavefunction which describes the system, and E is the total energy of the system when it is in the state Ψ . For anything more complex than a hydrogen atom, of course, the Schrodinger equation is a many-body problem and cannot be solved exactly. We can, however, introduce an important formalism known as the independent electron approximation and express our many-body wavefunction $\Psi(r_1, r_2, \dots, r_n)$ in terms of one-electron orbitals $\psi_1(r_1), \psi_2(r_2), \dots, \psi_n(r_n)$ provided that we obey the Pauli exclusion principle by having $\Psi(r_1, r_2, \dots, r_n)$ take the form of a Slater determinant:

$$\Psi = \begin{vmatrix} \psi_1(r_1) & \psi_1(r_2) & \dots & \psi_1(r_n) \\ \psi_2(r_1) & \psi_2(r_2) & \dots & \psi_2(r_n) \\ \dots & \dots & \dots & \dots \\ \psi_n(r_1) & \psi_n(r_2) & \dots & \psi_n(r_n) \end{vmatrix}$$

If we put this determinantal form of the wavefunction into our original Schrodinger equation, we get a set of N coupled differential equations for the one-electron orbitals:

$$(-\nabla^2 + V_c + V_{ex}) \psi_i(r_i) = \epsilon_i \psi_i(r_i)$$

Here, V_c is the coulomb potential (describing the electron-electron repulsion and electron-nuclear attraction) while V_{ex} is the exchange potential which is purely quantum mechanical in origin. For the case of an atom, our one-electron orbitals are the 1s, 2s, 2p, 3s, 3p, 3d etc. atomic orbitals. For a molecule, our one-electron ψ 's are molecular orbitals which are linear combinations of atomic one-electron orbitals, ϕ_i :

$$\psi_i = c_1 \phi_1 + c_2 \phi_2$$

For a crystal, our one-electron ψ 's take the form of Bloch wave functions:

$$\psi_{\mathbf{k}}(\mathbf{r}) = u_{\mathbf{k}}(\mathbf{r}) \exp(i\mathbf{k}\mathbf{r})$$

where $u_{\mathbf{k}}(\mathbf{r})$ has the translational periodicity T of the crystal lattice $u_{\mathbf{k}}(\mathbf{r}) = u_{\mathbf{k}}(\mathbf{r} + T)$. The one-electron orbital formalism is not only the basis for computational quantum chemistry but also underlies our thinking when attempting to understand chemical phenomena in terms of quantum mechanics. For example, in our one-electron orbital formalism we can think of chemical bonds as resulting from the overlap of one-electron atomic orbitals. However, we must ultimately return to the complicated notion of multi-electronic wavefunctions if we are to correctly understand the electronic states of an atom, molecule or solid.

Because clay minerals and iron oxides are solids, it seems that their electronic structures should be given in terms of Bloch wavefunctions. However, band structure calculations on something as complex as a typical clay would be impractical. More fundamentally, however, is that the electrons of interest in silicates and oxides, namely those in the Fe(3d) orbitals, are quite localized. (This reflects the partial ionic character of the bonding in these minerals.) Bloch wavefunctions are awkward to use when attempting to describe electronic transitions between localized states. A different approach would be to look at the electronic structure of a small cluster of atoms representing some structural unit in the crystal by using molecular orbital theory. This approach has its precedent in ligand field theory and should be useful to the extent that the Fe(3d) electrons are localized. With increasing cluster size, the molecular orbital description will converge to the band structure of the crystal. The molecular orbital view can account for both localized (ionic) electrons and (if the cluster is sufficiently large) delocalized (metallic) electrons. Some applications of molecular orbital theory to the chemistry of clay minerals have been done. For example, Aronowitz et al. (15) modeled the electronic structures of clays using extended Huckel molecular orbital calculations on a cluster approaching the full unit cell. Those calculations were able to predict trends in isomorphic substitution of octahedral Al^{3+} by Fe^{3+} , Mg^{2+} , Fe^{2+} , Na^+ , Ca^{2+} and K^+ . We are primarily interested in the Fe(3d) electrons. The unpaired electrons of iron make the electronic structures of iron bearing clays too complex to treat with simple extended Huckel calculations on large clusters. More sophisticated approximations are possible (in particular the Self-consistent field X α -Scattered Wave method) but these will require us to limit the cluster size. However, the Fe(3d) electrons tend to be almost entirely localized to the Fe atom and its immediate coordination site. Hence we should be able to describe the Fe(3d) electronic states in terms of the molecular orbitals of simple FeO_6 , $\text{FeO}_4(\text{OH})_2$, and FeO_4 clusters. There are situations (Fe^{2+} - Fe^{3+} charge transfer, in particular) in which the Fe(3d) electrons are delocalized over more than one FeO_6 coordination polyhedron. To understand such delocalized states, we will have to use larger clusters. Calculations on $(\text{Fe}_2\text{O}_{10})^{15-}$ dimers have been done and will be described here. As computers become faster, sophisticated calculations on even larger clusters will become practicable.

Accurate molecular orbital calculations on transition metal

oxide clusters cannot be easily done using current Hartree-Fock type *ab initio* methods based on the linear combination of atomic orbital (LCAO) formalism. A very successful approach, however, is the $X\alpha$ -scattered wave method. Here, the complicated exchange potential is simplified by using the $X\alpha$ approximation (16) while the molecular orbitals are obtained using the scattered wave formalism (17).

Electronic Structure of Fe^{3+} in Octahedral Coordination. Figure 4 shows the molecular orbital diagram for a $(FeO_6)^{9-}$ cluster with and Fe-O bond length of 200 pm. The electronic structure of the same cluster with a somewhat longer Fe-O bond length is discussed in detail elsewhere (18). The O(2p) like molecular orbitals are Fe-O bonding while the Fe(3d) like molecular orbitals are Fe-O antibonding. Some of the orbitals are labeled according to their associated irreducible representation of the O_h point group. The orbitals of e_g symmetry are σ -bonding ($3e_g$) or σ -antibonding ($4e_g$). The orbitals with t_{2g} symmetry are π -bonding ($1t_{2g}$) or π -antibonding ($2t_{2g}$). The calculation was done using a spin-unrestricted exchange potential. This gives separate exchange potential for spin-up (α -spin) and spin-down (β -spin) electrons and is essential for describing the electronic structures of open-shell configurations. Note that the spin-unrestricted molecular orbital results correctly show that Fe^{3+} will be in the high spin configuration in its ground state. Low spin Fe^{3+} or Fe^{2+} has not been observed in any silicate or oxide mineral. Presumably, one must attain pressures comparable to those in the lower mantle for the spin pairing transition to occur.

Two kinds of electronic transitions can be described using this simple cluster: d-d or "ligand field" transitions and ligand-to-metal charge transfer (LMCT) transitions. These are also the only electronic transitions of iron(III) clays that can be induced by sunlight on the Earth's surface. As discussed in (18), the one-electron orbitals give only a partial description of the different ligand field states of the Fe^{3+} cation. The ligand to metal charge transfer transitions, however, seem to be well described in terms of the one-electron orbitals of the $(FeO_6)^{9-}$ cluster. The lowest energy LMCT transition, from the O(2p) band to the $2t_{2g}(\beta)$ orbital, is calculated to lie near $38,000\text{ cm}^{-1}$. This energy agrees well with that found in the spectra of iron(III)-bearing clays (4,19,20). Spectra of several clay minerals with dilute concentrations of lattice Fe^{3+} show an $O^{2-} \rightarrow Fe^{3+}$ band and are given in Figure 5.

The energies of the states arising from the different configurations over the Fe(3d) one-electron orbitals ($4e_g$ and $2t_{2g}$) can not be directly calculated from the molecular orbital diagram. This is because a given one-electron orbital configuration corresponds to several multielectronic states. For example, the one-electron orbital transition $4e_g(\alpha) \rightarrow 2t_{2g}(\alpha)$ corresponds to both the ${}^6A_{1g} \rightarrow {}^4T_{1g}$ and ${}^6A_{1g} \rightarrow {}^4T_{2g}$ spectroscopic transitions that are observed in the visible and near infrared spectra of iron(III) clays. We can, however, understand the states arising from the d-orbital electronic configurations using ligand field theory. Ligand field theory expresses the state energies in terms of the

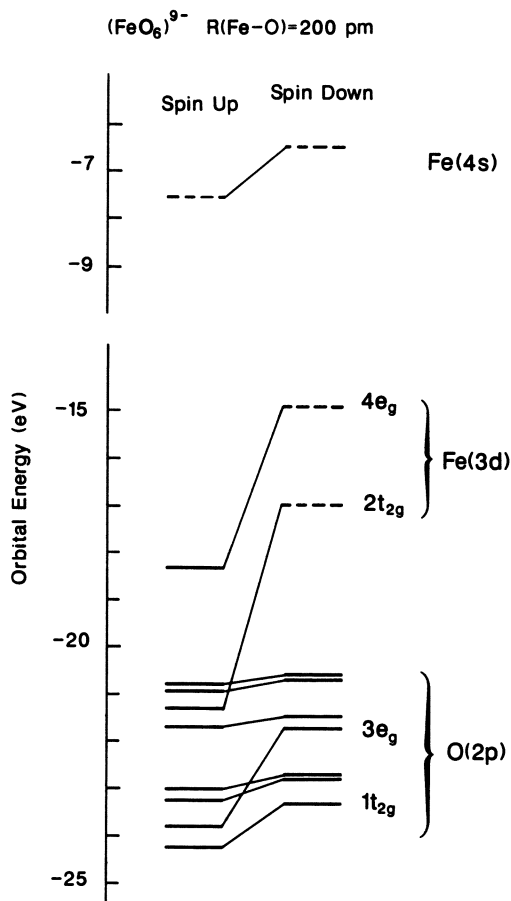


Figure 4. Spin-unrestricted molecular orbital diagram for an $(\text{FeO}_6)^{9-}$ cluster with $R(\text{Fe}-\text{O})=200$ pm. The orbitals indicated by dashed lines are unoccupied. Note that orbital energy differences do not correspond exactly to the energies required for electronic transitions between these orbitals. Since an electronic transition will change the electronic configuration, it will also change the interelectronic potential. To determine electronic transition energies, one must perform a "transition state" calculation (16). The "transition state" approach will account for the orbital energy relaxation about the new electronic configuration. For simplicity, only the most important Fe-O bonding and antibonding orbitals are labelled. The remaining orbitals ($6a_{1g}$, $5t_{1u}$, $6t_{1u}$, $1t_{2u}$, and $1t_{1g}$) are mostly O(2p) non-bonding.

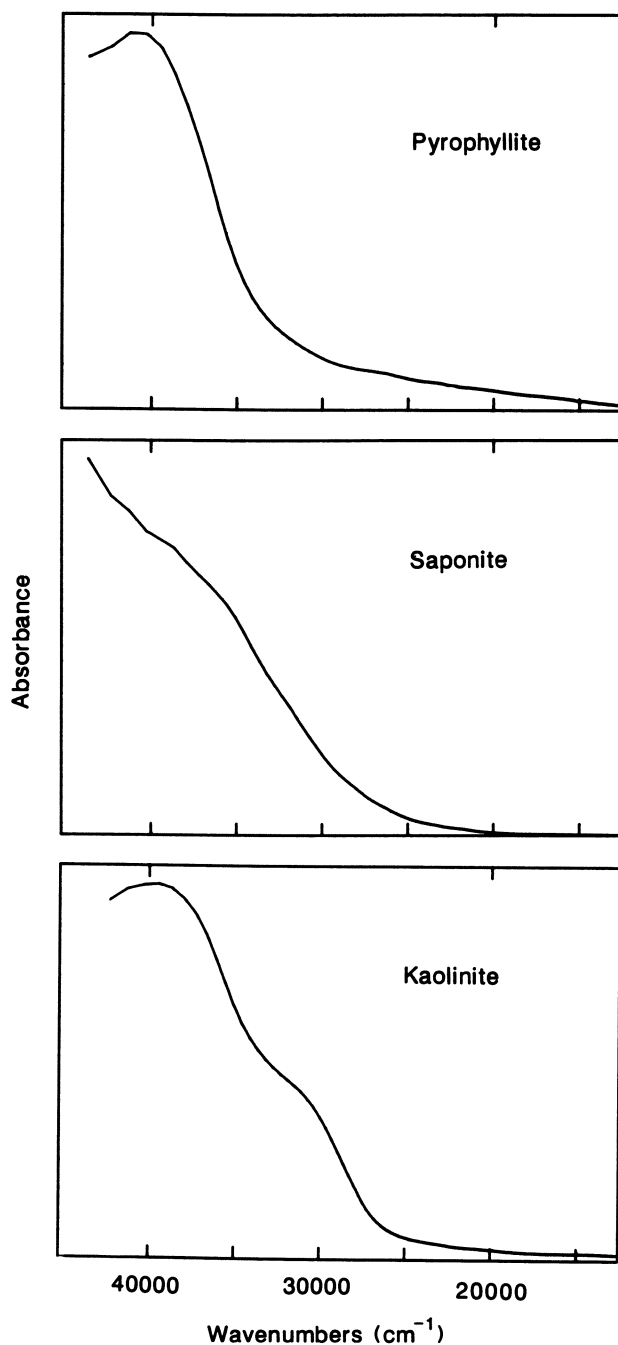


Figure 5. Near ultraviolet to visible region spectra of kaolinite, pyrophyllite, and saponite showing an absorption band near 40,000 cm^{-1} due to O^{2-} - Fe^{3+} charge transfer. (Data from reference 25).

three parameters $10Dq$, B and C . $10Dq$ is a measure of the splitting between the $4e_g$ and $2t_{2g}$ orbitals; B and C are related to the coulomb and exchange integrals. In principle, we can calculate these parameters from the one-electron orbitals. However they are usually determined from optical spectra. The energies of the $Fe(3d)$ states in terms of the ligand field parameters are given in Table 1.

Table 1. Energies for the Fe^{3+} Ligand Field States (21,22)

State	Energy
$(t_{2g})^3 (e_g)^2:$	
${}^6A_{1g}$	0
$(t_{2g})^4 (e_g)^1:$	
${}^4T_{1g}$	$-10Dq + 10B + 6C - 26B^2/10Dq$
${}^4T_{2g}$	$-10Dq + 18B + 6C - 38B^2/10Dq$
$(t_{2g})^3 (e_g)^2:$	
${}^2A_{2g}$	$-10Dq + 12B + 9C$
${}^2T_{1g}$	$-10Dq + 13B + 9C$
$(t_{2g})^3 (e_g)^2:$	
${}^4A_{1g}, {}^4E_g$	$10B + 5C$
${}^4T_{2g}$	$13B + 5C$
4E_g	$17B + 5C$
${}^4T_{1g}$	$19B + 7C$
${}^4A_{2g}$	$22B + 7C$

An example (4) where transitions to some of these states are easily resolved is the spectrum of nontronite (Figure 6). Here, bands near 10700 cm^{-1} , 15600 cm^{-1} , and 22200 cm^{-1} are assigned to transitions from the ${}^6A_{1g}$ state to the ${}^4T_{1g}$, ${}^4T_{2g}$, and ${}^4A_{1g}, {}^4E_g$ states. Values for $10Dq$, B and C are found to be 15050 cm^{-1} , 614 cm^{-1} , and 3268 cm^{-1} . For Fe^{3+} , the free ion value of B is $\sim 1100\text{ cm}^{-1}$. The reduction to 56% of that value in nontronite indicates the fairly covalent nature of the Fe-O bond.

The Fe^{3+} ligand field transitions are spin-forbidden since

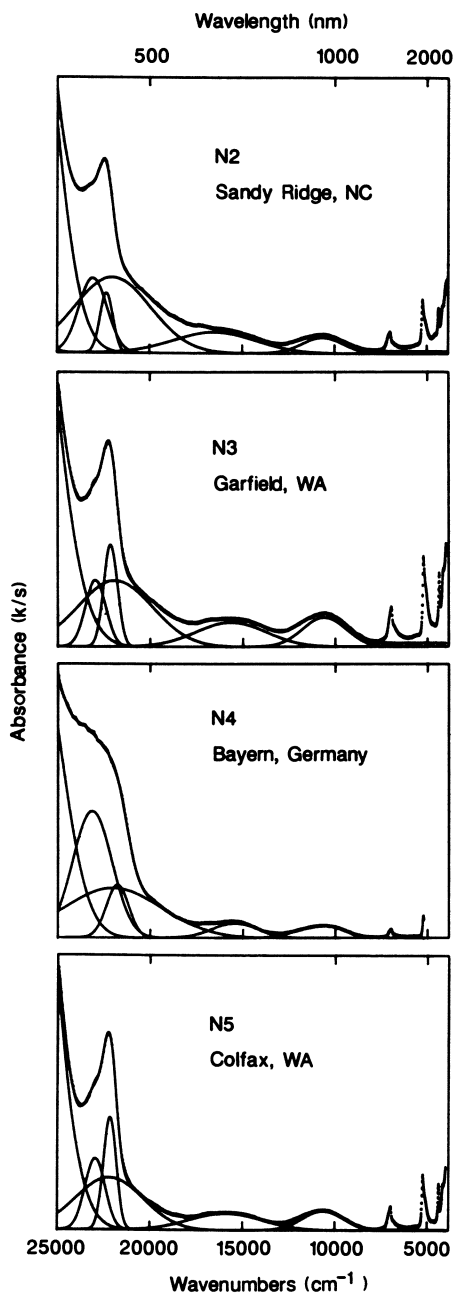


Figure 6. Visible to near-infrared spectra of several nontronites showing the Fe^{3+} ligand field transitions (Adapted from reference 4).

the ground state has spin quantum number $S=5/2$ while the excited states have $S=3/2$ or $1/2$. One would expect the ligand field bands in Fe^{3+} minerals to be very weak. However, the spin-selection rule can be effectively relaxed when next nearest neighbor Fe^{3+} cations are magnetically coupled to each other (23,24). The extent to which the spin selection rule is relaxed depends on the strength of the magnetic coupling between Fe^{3+} cations. A pair of Fe^{3+} cations are coupled antiferromagnetically by superexchange. The superexchange interaction depends on the nature of the bridging ligand L and on the Fe-L-Fe bond angle. There is a great deal of theoretical work that can be done to understand the quantum mechanical nature of superexchange and its dependence on the mode of Fe-Fe bridging. Simple molecular orbital arguments show that superexchange is a direct consequence of the spin-dependency of the chemical bond (18,26). We expect that coupling due to superexchange will increase as the covalency of the Fe-L bond increases. Superexchange coupling via Fe-O-Fe bridging is relatively strong. However, if the bridging oxygen is also bonded to a strong electron-withdrawing center (Lewis acid) such as H^+ or Si^{4+} , then we would expect the superexchange coupling to be weaker. This effect is seen in minerals: strong superexchange due to Fe-O-Fe bridging in iron oxides results in strong intensification of the Fe^{3+} ligand field transitions and gives these minerals their red to orange color. Weaker superexchange via Fe-OH-Fe and Fe-O(Si)-Fe coupling in nontronite results in a weaker intensification of the Fe^{3+} ligand field bands and gives nontronite a green to pale yellow color.

The intensification of the Fe^{3+} ligand field band in the iron oxides is strong enough to give an absorption edge in the visible region spectra of these minerals. This edge is often mistaken for the optically induced band gap transition. Since band gaps in semiconductors are often obtained from optical measurements, one may see erroneously low values for the band gap energies of iron oxides in the literature. For example, band gap energies for the iron oxides as tabulated in (27) range from 1.1 to 2.3 eV. Such values imply that iron oxides would be extremely photoreactive under sunlight (which has a peak intensity on the Earth's surface near 2.1 eV). The actual band gap in iron(III) oxides and silicates corresponds to the $\text{O}^{2-} \rightarrow \text{Fe}^{3+}$ charge transfer transition (i.e., the $\text{O}(2p)$ to $\text{Fe}(3d)$ band gap). The energy for this, as discussed above, is $38,000 \text{ cm}^{-1}$ or 4.7 eV is well into the near-ultraviolet. Note that for iron-dilute silicates (e.g., Fe^{3+} in kaolinite), the $\text{Fe}(3d)$ orbitals would not be able to form an $\text{Fe}(3d)$ band. The $\text{Fe}(3d)$ orbitals would be impurity levels within the $\text{O}(2p)$ - $\text{Al}(3s)$ band gap. The $\text{O}^{2-} \rightarrow \text{Fe}^{3+}$ transition would then be viewed as an extrinsic semiconduction process. Given the energy required for the $\text{O}^{2-} \rightarrow \text{Fe}^{3+}$ transition, it follows that iron oxides and silicates should not be highly photoreactive under sunlight at the Earth's surface. As discussed below, some photochemical reactivity is observed with hematite ($\alpha\text{-Fe}_2\text{O}_3$) at energies beginning near $20,000 \text{ cm}^{-1}$ (e.g., 34-35). Photoelectrochemical reactions induced by visible light are most-likely associated with the tail of the $\text{O}^{2-} \rightarrow \text{Fe}^{3+}$ charge transfer band that extends into the visible region of the spectrum. The quantum efficiency of these reactions

increase rapidly as the photon energy is moved towards the near-ultraviolet.

Electronic Structure of Fe³⁺ in Tetrahedral Coordination. As mentioned earlier, some Fe³⁺ in clays may substitute for Si in the tetrahedral sheet. In the case of nontronite, the fraction of tetrahedrally coordinated iron is only a few percent. Other phyllosilicates (such as cronstedite) can have a considerable fraction of iron in tetrahedral coordination.

The electronic structure of Fe³⁺ in tetrahedral coordination (18) is given by the molecular orbital diagram for an (FeO₄)³⁻ cluster in Figure 7. As before, the Fe(3d) orbital are Fe-O anti-bonding while the O(2p) orbitals are Fe-O bonding and O nonbonding. The lowest energy LMCT transition is calculated to occur at 40,400 cm⁻¹ when the Fe-O bond length is 186.5 pm.

The ligand field transitions of tetrahedrally coordinated Fe³⁺ are Laporte-allowed. Consequently, small amounts of tetrahedrally coordinated Fe³⁺ may have a large effect on the spectra of iron-bearing clays. In the optical spectrum of nontronite (4), the small amount of tetrahedral Fe³⁺ gives an intense absorption band near 23,000 cm⁻¹ that is assigned to the ⁶A₁→⁴A₁,⁴E transition.

Electronic Structure of Fe²⁺ in Octahedral Coordination. Figure 8 gives a molecular orbital diagram for an (FeO₆)¹⁰⁻ cluster with R(Fe-O) = 216 pm. The overall topology of the orbitals is the same as in the analogous Fe³⁺ cluster. The one-electron orbital transition 2t_{2g}(β)→4e_g(β) corresponds to the ⁵T_{2g}→⁵E_g absorption band observed in the optical spectra of Fe²⁺ silicates near 10,000 cm⁻¹. The calculated energy for this transition is 11,600 cm⁻¹ which is in reasonable agreement with experiment. The lowest energy ligand-to-metal charge transfer transition in the Fe²⁺ cluster is calculated to be 6.6 eV or 53200 cm⁻¹. As expected from the decreased electronegativity of Fe²⁺ over Fe³⁺, O²⁻→Fe²⁺ charge transfer is at much higher energy than O²⁻→Fe³⁺ charge transfer.

A potentially significant group of electronic transitions are those of the type Fe(3d)→Fe(4s). Although the Fe(3d) orbitals are strongly localized to the Fe²⁺ atom, the Fe(4s) orbital is greatly delocalized over both the Fe and O atoms. In the solid, the Fe(4s) orbitals will give rise to a wide Fe(4s) conduction band. Transitions to this band may allow Fe²⁺-to-ligand electron transfer processes and are discussed below. The lowest energy Fe(3d) to Fe(4s) transition is from the 2t_{2g}(β) orbital. The energy of that transition is calculated to be 7.27 eV or 58600 cm⁻¹. In the band structure of a mineral, however, the Fe(3d)-Fe(4s) gap will be smaller owing to the large dispersion of the 4s band.

Fe²⁺→Fe³⁺ Charge Transfer. Partial reduction of Fe³⁺ clays results in Fe²⁺ and Fe³⁺ cations occupying edge-sharing FeO₆ coordination polyhedra. Such a condition allows for optically (and perhaps thermally) induced intervalence charge transfer (IVCT) transitions:

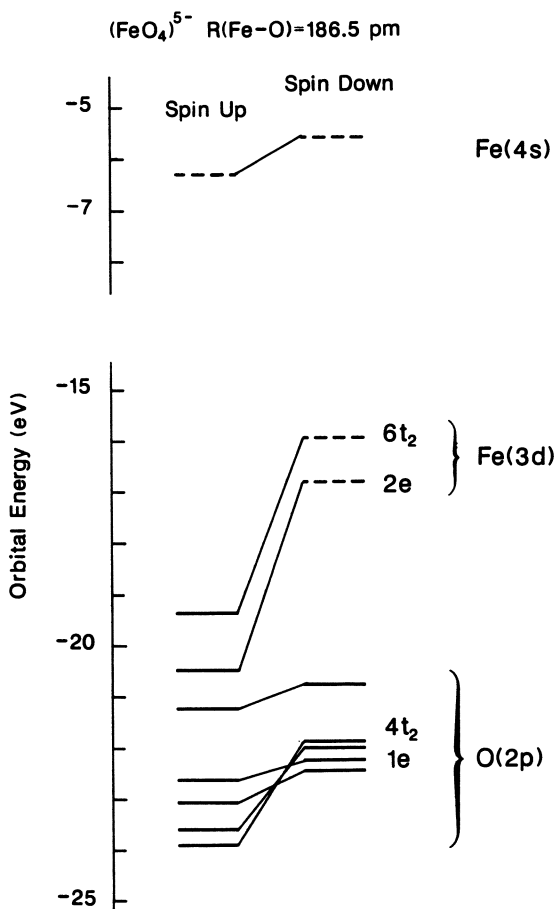


Figure 7. Molecular orbital diagram for an $(\text{FeO}_4)^{5-}$ cluster.

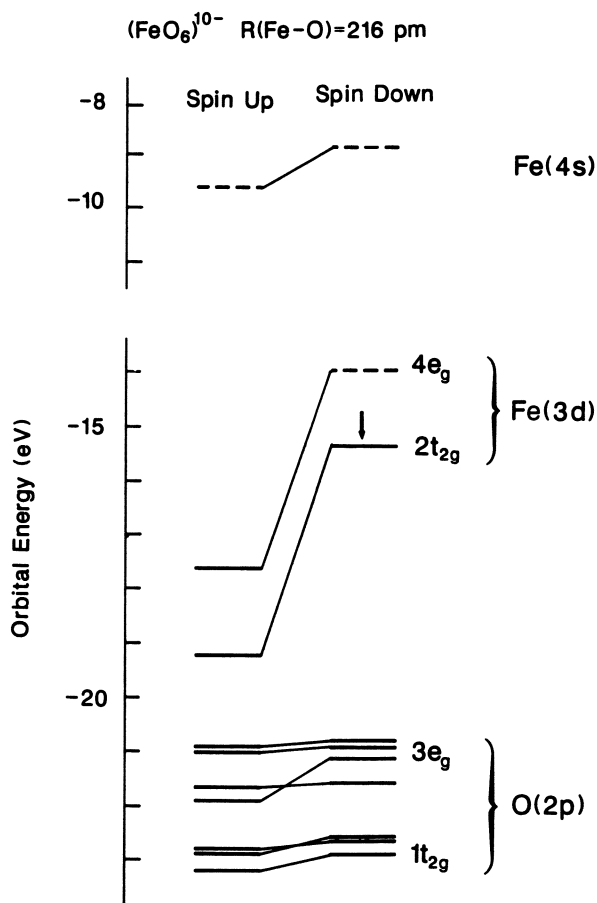
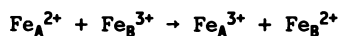
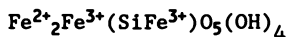


Figure 8. Molecular orbital diagram for the $(\text{FeO}_6)^{10-}$ cluster (Adapted from reference 18).



where A and B refer to two different sites (which may be crystallographically equivalent). Optically induced IVCT gives rise to an absorption band near $14,000 \text{ cm}^{-1}$ in the optical spectra of reduced nontronite (28,29) and glauconite. Spectra of a montmorillonite and glauconite showing a band due to IVCT are given in Figure 9.

Thermally induced IVCT would have implications to the electrochemistry of clay minerals since it would afford a mechanism by which Fe(3d)-electrons could be transferred from the bulk to the (010) surface. Thermally induced IVCT is readily observed in the Mossbauer effect since (in paramagnetic minerals) it results in a quadrupole doublet with an isomer shift midway between that expected for Fe^{2+} and Fe^{3+} . An apparent broad quadrupole doublet in the 298 K Mossbauer spectrum of glauconite has been assigned to thermally induced IVCT (30) but our own fit of glauconite spectra (Figure 10) suggest that the broad doublet is only due to octahedrally coordinated Fe^{2+} . Minerals in which thermally induced IVCT occurs are characteristically black owing to a very intense optical IVCT band (glauconite is green). The only known phyllosilicate in which thermally induced IVCT occurs at room temperature is cronstedite (31). Cronstedite is an iron-rich serpentine (1:1 structure) with formula



The activation energy for electron hopping in cronstedite is 0.25 eV which yields an electrical conductivity (at 298K) of $3 \times 10^{-3} \text{ S/m}$.

Understanding the nature of IVCT (and the orbitals pathways involved) in minerals is of great fundamental interest insofar as it relates to electron transfer and redox mechanisms. The basic theoretical model for ICVT is given in the potential surfaces for an $(\text{Fe}_2\text{O}_{10})^{15-}$ dimer shown in Figure 11. This dimer consists of Fe^{2+} and Fe^{3+} cations occupying octahedral coordination sites sharing a common edge. The dimer has C_{2v} symmetry (Fe sites inequivalent). If we consider the two sites A and B, we can consider two zeroth-order states corresponding to the two possible charge configurations:

$$\psi_1 = \text{Fe}_A^{2+} + \text{Fe}_B^{3+}$$

$$\psi_2 = \text{Fe}_A^{3+} + \text{Fe}_B^{2+}$$

What we are interested in is the energies of these states along a configurational coordinate q . Here, q is a normal mode of A_1 symmetry along which the Fe-O bond length of one site expands while that for the other site contracts. Let us designate the equilibrium Fe^{2+} -O and Fe^{3+} -O bond lengths by R_1 and R_2 , respectively. (In oxides and silicates, R_1 is about 216 pm and R_2 is about 200 pm.) We are interested in the electronic structure of our dimer at several points along our configurational coordinate q : At $q = -\lambda$,

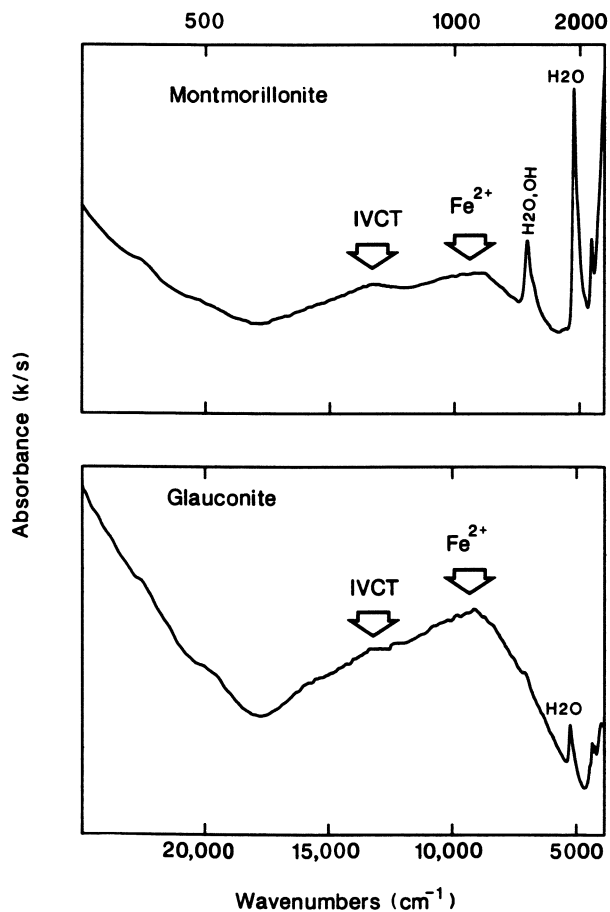


Figure 9. Optical spectra of glauconite and iron-bearing montmorillonite showing the band near 14,000 cm⁻¹ due to Fe²⁺→Fe³⁺ intervalence charge transfer.

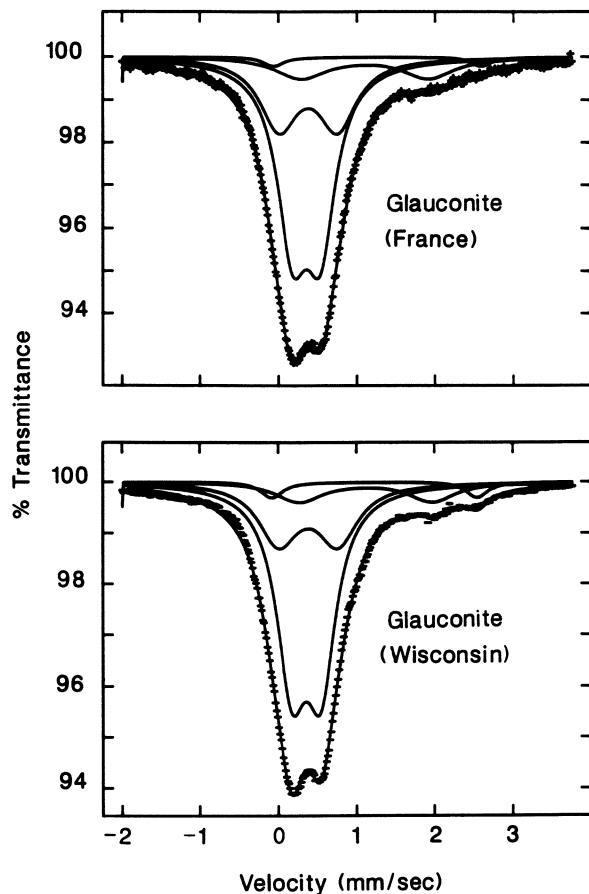


Figure 10: Mossbauer spectra of several glauconites showing fit to two Fe^{2+} and two Fe^{3+} sites. No evidence for thermally induced IVCT is present in the Mossbauer spectra of these samples.

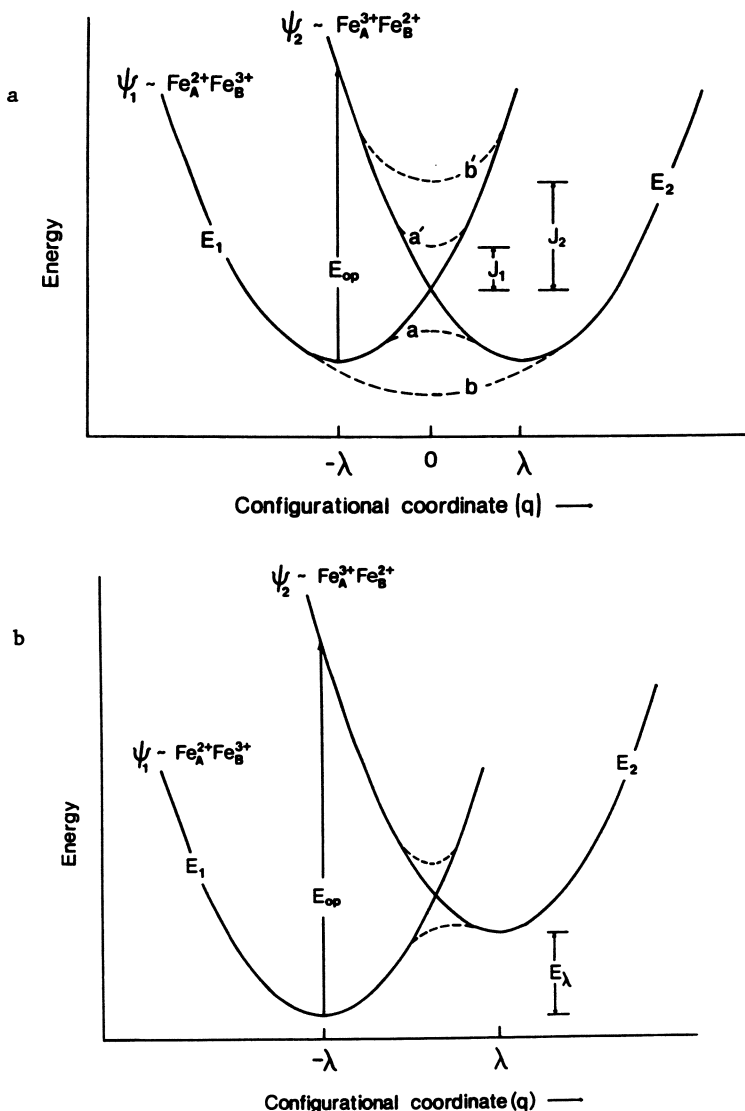


Figure 11: Potential energy surfaces describing charge transfer. The solid curves correspond to the potential for the "ionic" states ψ_1 and ψ_2 . The dashed curves correspond to the potential energy surfaces for the states ψ_+ and ψ_- that result from coupling ψ_1 and ψ_2 . The curves a-a' correspond to the case of weak coupling and give an activation barrier for thermally induced IVCT. The curves b-b' correspond to strong coupling which completely delocalizes the Fe^{2+} ($t_{2g}(\beta)$) electron over the two Fe sites. Two cases need to be considered: (a) symmetrical charge transfer where both Fe sites are energetically equivalent and (b) asymmetrical charge transfer where the potential at site B is greater than that at site A.

we have $R(\text{Fe}_A\text{-O})=R_1$ and $R(\text{Fe}_B\text{-O})=R_2$. At $q=\lambda$, we have $\text{Fe}_A=R_2$ and $\text{Fe}_B=R_1$. At $q=0$, $R(\text{Fe}_A\text{-O})=R(\text{Fe}_B\text{-O})=(R_1+R_2)/2$ pm. At $q=-\lambda$, the lowest energy configuration is $\text{Fe}_A^{2+}\text{Fe}_B^{3+}$. At $q=\lambda$, the lowest energy configuration is $\text{Fe}_A^{3+}\text{Fe}_B^{2+}$. If there is a weak coupling between the Fe atoms at sites A and B, the states ψ_1 and ψ_2 will mix to form the new states

$$\Psi_+ = \alpha \psi_1 + (1 - \alpha^2)^{1/2} \psi_2$$

$$\Psi_- = (1 - \alpha^2)^{1/2} \psi_1 - \alpha \psi_2$$

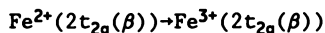
where α is the delocalization coefficient and describes the degree to which the Fe^{2+} ($2t_{2g}(\beta)$) electron is delocalized over the two sites. From simple perturbation theory,

$$\alpha^2 = 1/2 - \Delta E / 2 (\Delta E^2 + 4J^2)^{1/2}$$

Here, ΔE is the energy difference between ψ_1 and ψ_2 ; J is the "resonance integral" which describes the degree of coupling between the states ψ_1 and ψ_2 .

Suppose the Fe-Fe pair is at the point $q = -\lambda$. The optical IVCT transition is then $\Psi_+ \rightarrow \Psi_-$. The energy for this is indicated by E_{op} in Figure 11. Since α is small, this effectively corresponds to an electron transfer from site A to B. The thermally induced IVCT process is for the dimer to stay in the ground Ψ_+ state but to move along the q coordinate from $q = -\lambda$ to $q = \lambda$. If the coupling between the ionic configurations ψ_1 and ψ_2 is weak ($J = J_1$ in Figure 11), there will be an activation barrier.

Molecular orbital calculations can give us some insight on the physical nature of the coupling integral J . Coupling can occur either by direct Fe-Fe bonding or through "superexchange" via the bridging oxygens. A simple molecular orbital approach to the problem is to look at the electronic structure of an $(\text{Fe}_2\text{O}_{10})^{15-}$ cluster. The electronic structure of this cluster has been calculated using the SCF-X α -SW method (32). Fe^{2+} - Fe^{3+} charge transfer is allowed through weak Fe^{2+} - Fe^{3+} d-orbital overlap across the shared polyhedral edge. The J parameter is simply a description of the Fe^{2+} - Fe^{3+} bonding interaction through such d-orbital overlap. A simplified MO diagram for the cluster is shown in Figure 12. Using the transition state formalism, it is found that the optically induced intervalence charge transfer band results from the transition



In the context of the $(\text{Fe}_2\text{O}_{10})^{15-}$ cluster, the $\text{Fe}^{2+}(2t_{2g}(\beta))$ orbitals are Fe^{2+} - Fe^{3+} bonding while the $\text{Fe}^{3+}(2t_{2g}(\beta))$ orbitals are Fe^{2+} - Fe^{3+} antibonding (all of the Fe(3d)-like molecular orbitals are Fe-O antibonding, of course). To determine the kind of activation energies associated with thermally induced IVCT would require that we calculate the total energy of the $(\text{Fe}_2\text{O}_{10})^{15-}$

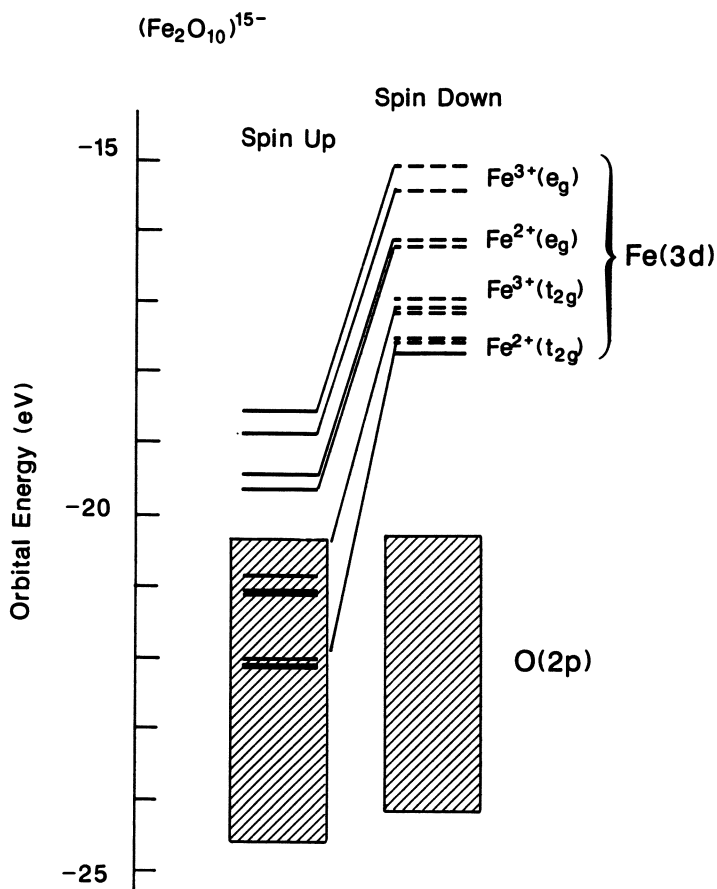
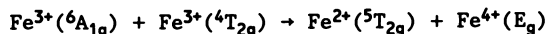


Figure 12. Molecular orbital diagram for an Fe_2O_{10} cluster used to understand the orbitals involved in Fe^{2+} - Fe^{3+} charge transfer. The absorption band observed near $13,000\text{ cm}^{-1}$ in the spectra of mixed-valence silicates is due to the transition from the $\text{Fe}^{2+}(t_{2g}) \rightarrow \text{Fe}^{3+}(t_{2g})$ orbitals. A transition state calculation for that energy in the cluster presented here gives $10,570\text{ cm}^{-1}$ in fair agreement with experiment.

cluster along to q coordinate. Such calculations cannot be accurately done using the SCF- $X\alpha$ -SW method but might be possible using the Discrete Variational $X\alpha$ approach. It appears, however, that most iron phyllosilicates are best described by the situation in Figure 11b where the two Fe sites are energetically different. In addition to the activation barrier, electrons must also overcome the site potential energy difference (E_A) for electron transfer to occur. For this reason, thermally induced IVCT is seldom observed in these minerals. We can consider the Fe(3d) electrons to be trapped at their parent Fe site.

Applications to Photochemistry, Electron transport and Reactivity

The trapped and localized nature of the Fe(3d) electrons in clays and iron oxides would suggest that the Fe(3d) orbitals in lattice iron play no direct role in heterogeneous (i.e., mineral-solution) electron transfer processes. The only iron that may act as an electron acceptor or donor is that iron on the mineral surface. On the other hand, electrons excited from the O(2p) valence band into the Fe(3d) orbitals by ultraviolet radiation would result in (presumably mobile) holes in the O(2p) band. To understand the orbital pathways by which such holes may be transported would require molecular orbital calculations on much larger clusters. In passing it should be mentioned that Marusak et al. (34) obtained an interesting result when measuring the photoconductivity of hematite (α -Fe₂O₃). A peak in the photoconductivity spectrum was found at an energy corresponding to the ${}^4A_{1g} \rightarrow {}^4T_{2g}$ transition near 15,000 cm⁻¹. This transition results in a one-electron orbital configuration $(t_{2g})^4(e_g)^1$ which means that both the $t_{2g}(\beta)$ and $e_g(\alpha)$ Fe(3d) bands are partially occupied. The conductivity implies that electrons in one of these bands must be mobile (probably the one in the $t_{2g}(\beta)$ band) and that electron transport can occur via the charge-transfer transition



Regardless of the electron transfer mechanism, light-induced electron transfer processes on iron(III) clays must involve the O²⁻→Fe³⁺ charge transfer transition in the ultraviolet. On the Earth's surface, the solar spectral irradiance curve (Figure 13) cuts off at a maximum energy of ~33,000 cm⁻¹ (0.3 microns). This limits the kinds of photochemical processes we may expect in the natural environment. The energy of the O²⁻→Fe³⁺ charge transfer transition (38,000 cm⁻¹) is outside the present spectrum of solar radiation incident on the Earth's surface. Nevertheless, the width of the charge transfer absorption band is sufficiently broad (~10,000 cm⁻¹ half-width) to allow some photochemical activity due to sunlight on the Earth's surface (1,2,35,36).

For Fe²⁺ in octahedral coordination, we do not expect photo-oxidation of organic molecules via O²⁻→Fe²⁺ charge transfer. However, the possibility of photoreduction of organics via transitions from the Fe(3d) orbitals to the Fe(4s) orbitals or Fe(4s) conduction band should be considered. The lowest energy Fe(3d)→Fe(4s) transition is calculated to be 58600 cm⁻¹. Although

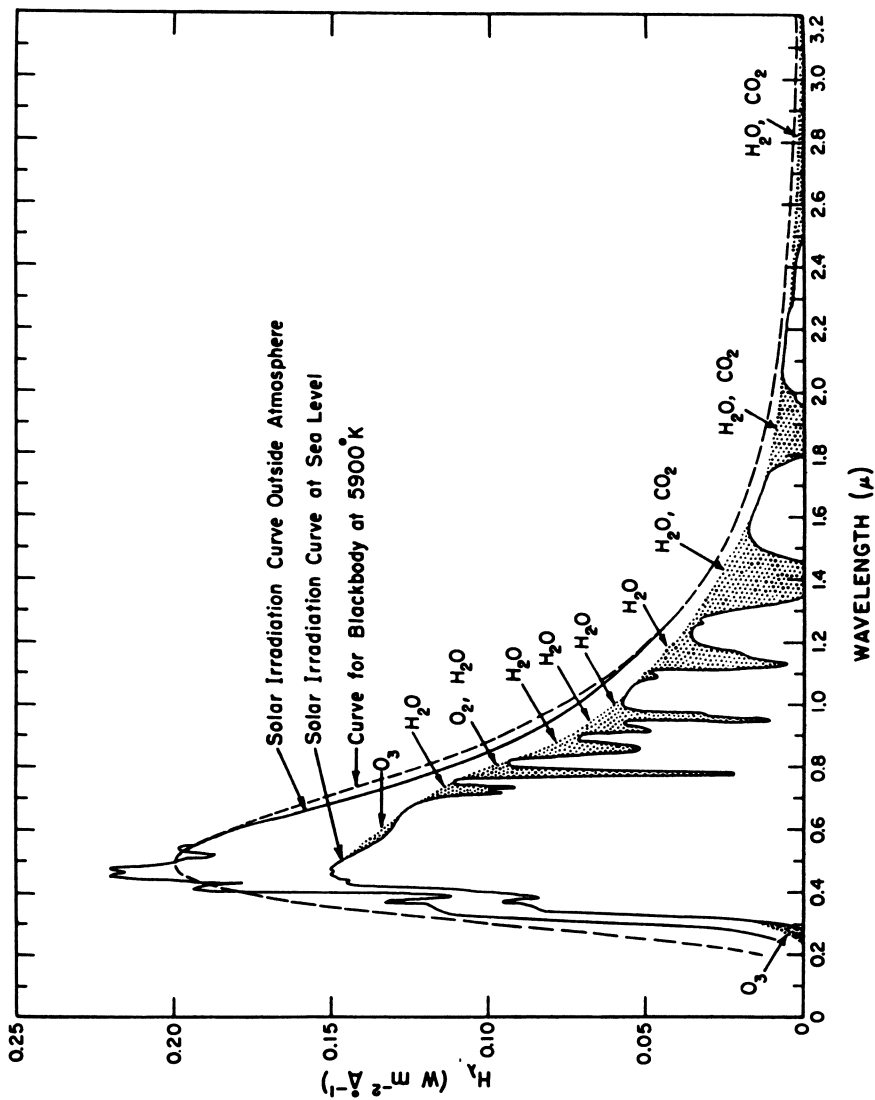
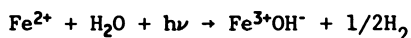
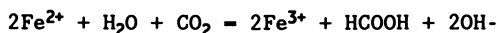


Figure 13. Solar spectral irradiance curve (From reference 33).

this is outside the range of presently available solar energy at the Earth's surface, the tail of the absorption band may allow transitions induced by near-ultraviolet radiation (i.e., below 50000 cm^{-1}). Indeed, as shown by Getoff (37), Fe^{2+} cations can reduce water molecules when irradiated by light at 254 nm (40,000 cm^{-1})



In the precambrian (or on present day Mars), the absence of an ozone layer allowed solar UV radiation with energies as high as $\sim 40,000 \text{ cm}^{-1}$ (0.25 microns). Photoreduction transitions via the $\text{Fe}(3d)$ to $\text{Fe}(4s)$ transition may have been very significant. The photochemical oxidation of Fe^{2+} , and the precipitation of FeOOH , may be the origin of the extensive precambrian banded iron formations (38-40). Moreover, the photooxidation of Fe^{2+} may have reduced CO_2 to organic molecules (37,41):



It would be a worthwhile experiment to investigate the photoredox properties of those Fe^{2+} bearing clays (e.g., glauconite and ferrosaponite) that were abundant in the precambrian.

Areas for Future Investigation

The theoretical results described here give only a zeroth-order description of the electronic structures of iron bearing clay minerals. These results correlate well, however, with the experimentally determined optical spectra and photochemical reactivities of these minerals. Still, we would like to go beyond the simple approach presented here and perform molecular orbital calculations (using the $X\alpha$ -Scattered wave or Discrete Variational method) which address the electronic structures of much larger clusters. Clusters which accommodate several unit cells of the crystal would be of great interest since the results would be a very close approximation to the full band structure of the crystal. The results of such calculations may allow us to address several major problems:

1. What are the long-range superexchange pathways which give rise to the magnetic structures of iron bearing phyllosilicates?
2. What prevents thermally activated electron hopping in mixed valent clays? What is the nature of the d-band structure?
3. When electrons are excited from the $\text{O}(2p)$ band to the $\text{Fe}(3d)$ band, what kind of orbital pathways may allow holes in the $\text{O}(2p)$ band to migrate to the surface or interlayer region and facilitate electron transfer processes?
4. Assuming large clusters may approximate the band structure of the crystal, what energy is required to excite electrons into the $\text{Fe}(4s)$ conduction band in Fe^{2+} bearing clays? Can such electrons reduce organic molecules adsorbed in the surface or trapped in the interlayer?

Literature Cited

1. Waite, T.D., in, "Geochemical Processes at Mineral Surfaces; ACS Symposium Series 323, Davis, J.A.; Hayes, K.F., Eds". American Chemical Society: Washington DC, 1986, Chap. 20.
2. Stone, A.T., in, "Geochemical Processes at Mineral Surfaces, ACS Symposium Series 323, Davis, J.A.; Hayes, K.F., Eds."; American Chemical Society: Washington DC, 1986, Chap. 21.
3. Cairns-Smith, A.G.; Hartmann H. (eds.) "Clay Minerals and the Origin of Life"; Cambridge University Press: Cambridge, 1986.
4. Sherman, D.M.; Vergo, N. American Mineral. 1988, 73, 1346-1354.
5. Bonnin, D. These d'Etat, Universit e de Paris. 1981, 82 pp.
6. Besson, G.; Bookin, A.S.; Dainyak, L.G.; Rautureau, M.; Tsi-pursky, S.I.; Tchoubar, C.; Drits, B.A. J. Appl. Crystall. 1983, 16, 374-383.
7. Mering, J; Oberlin, A. Clays Clay Mineral., 1967, 27, 3-25.
8. Townsend, M.G.; Longworth, G.; Ross, C.A.M.; Provencher, R. Phys. Chem. Mineral. 1987, 15, 64-70.
9. Johnston, J.H.; Cardile, C.M. Clays Clay Mineral. 1985, 33, 21-30.
10. Daynyak, L.G.; Drits, V.A. Clays and Clay Mineral. 1987, 35, 363-372.
11. Cardile, C.M.; Johnston, J.H. Clays Clay Mineral. 1985 33, 295-300.
12. Goodman, B.A. Clays Clay Mineral. 1978, 26, 176-177.
13. Diamant, A.; Pasternak, M.; Banin, A. Clays Clay Mineral. 1982, 30, 63-66.
14. Gangas, N.H.J.; van Wouterghem, J.; Morup, S.; Koch, C.J.W. J. Phys. C. 1985 18, L1011-L1015.
15. Aronowitz S.; Coyne L.; Lawless, J.; Rishpon, J. Inorg. Chem., 1982, 21, 3589-93.
16. Slater, J.C. The Self-consistent Field for Molecules and Solids, Volume 4: Quantum Theory of Molecules and Solids; McGraw-Hill: New York, 1974.
17. Johnson, K.H. Adv. Quantum Chem. 1973, 7, 143-185.
18. Sherman, D.M. Phys. Chem. Mineral. 1985, 12, 161-175.
19. Chen C.J.; Shaked D.; Banin A. Clay Mineral., 1979, 14, 93-102.
20. Karickhoff, S.W.; Bailey, G.W. Clays Clay Mineral., 1973, 21, 59-70.
21. Lever, A.B.P. "Inorganic Electronic Spectroscopy"; Elsevier: Amsterdam, 1968; Chapter 7.
22. Griffith, W.S. "The theory of transition metal ions"; Cambridge University Press: Cambridge, 1961.
23. Krebs, J.J.; Maisch, W.G. Phys. Rev. B 1971, 4, 757-769.
24. Lohr, L.L. Coordination Chem. Rev., 1972, 8, 241-259.
25. Clark, R.N.; King, T.; Klejwa, M.; Swayze, G.; Vergo, N. J. Geophys. Res. (submitted).
26. Sherman, D.M. Phys. Chem. Mineral., 1985, 12, 311-314.
27. Strehlow, W.H.; Cook, E.L. J. Phys. Chem. Ref. Data 1973, 2, 163.

28. Anderson, W.L.; Stucki, J.W. Dev. Sedimentology 1979, 27, 75-84.
29. Lear, P.R.; Stucki, J.W. Clays Clay Mineral. 1987, 35, 373-378.
30. McConchie, D.M.; Ward, J.B.; McCann, V.H.; Lewis, D.W. Clays Clay Mineral., 1979, 27, 339-48.
31. Coey, J.M.D.; Mourkarika, A.; McDonagh, C.M. Solid State Commun., 1982, 41, 797.
32. Sherman, D.M. Phys. Chem. Mineral. 1987, 14, 364-367.
33. Valley, S.L. (Ed.), "Handbook of geophysics and space environments"; Air Force Cambridge Research Laboratories, 1965, 649 p.
34. Marusak, L.A.; Messier, R.; White, W.B. J. Phys. Chem. Solids, 1980, 41, 981-984.
35. Dare-Edwards, M.P.; Goodenough, J.B.; Hamnett, A.; Trellick, P.R., J. Chem. Soc., Faraday Trans., 1983, 79, 2027-2041.
36. Faust, B.C.; Hoffmann, M.R., Environ. Sci. Technol., 1986, 20, 943-948.
37. Getoff, N., Z. Naturforsch. Teil B., 1962, 17, 87; 1963, 18, 169.
38. Cairns-Smith, A.G., Nature (London), 1978, 276, 807.
39. Braterman, P.S., Cairns-Smith, A.G.; Sloper, R.W., Nature (London), 1983, 303, 163.
40. Braterman, P.S., Cairns-Smith, A.G.; Sloper, R.W.; Truscott, T.G.; Craw, M., J. Chem. Soc. Dalton Trans., 1984, 1441-1445.
41. Bauer, M.E. Chem. Geol., 1978, 22, 189-206.

RECEIVED May 18, 1989

Chapter 16

Dissociation and Recombination of Positive Holes in Minerals

Friedemann Freund^{1,2,4}, François Batllo^{3,5}, and Minoru M. Freund^{3,6}

¹SETI Institute, Mountain View, CA 94043

²Physics Department, San Jose State University, San Jose, CA 95192

³NASA-Ames Research Center, Moffett Field, CA 94035

Positive holes are electronic defects in the O^{2-} sublattice of oxides and silicates, e.g. O^- in an O^{2-} matrix. Positive holes frequently form as a result of radiation damage. Examples are $Al^{3+}\cdots O^-$ -Si and $Fe^{3+}\cdots O^-$ -Si centers in quartz. However, they may also form without attendant ionizing radiation. One possibility is the redox conversion of OH^- or Si-OH pairs into molecular H_2 plus peroxy. Such OH^- or Si-OH pairs derive from traces of dissolved "water". Peroxy anions, O_2^{2-} , or peroxy entities, $X/OO/Y$ ($X, Y=Si, Al, Fe^{3+}\dots$) are equivalent to self-trapped positive hole pairs. They thermally dissociate into two O^- states some of which are highly delocalized forming mobile charges carriers. Such mobile O^- states repel each other and diffuse to the surface. At the surface they cause a positive surface charge and form oxidizing centers with peroxide/superoxide functionality: $O^- + O^- = O_2^{2-}$ or $O_2^{2-} + O^- = O^{2-} + O_2^-$. Charge Distribution Analysis or CDA is a new technique which measures the dielectric polarization in an inhomogeneous electric field. By CDA we can determine O^- generation as a function of temperature, O^- mobility as a function of time and surface charge carrier density. CDA data on obsidian, a volcanic glass, are presented and corroborated by impedance measurements.

Radiation Centers

Many radiation-induced redox reactions involve the removal of an electron from O^{2-} which then becomes O^- . Such O^- states represent defect electrons or positive holes in an O^{2-} sublattice. Having an unpaired spin they are paramagnetic. Electron paramagnetic resonance (EPR) spectroscopy is the

⁴Current address: NASA-Ames Research Center, Mail Stop 239-4, Moffett Field, CA 94035

⁵Current address: Université de Bourgogne, Faculté des Sciences Mirande, F-21004 Dijon, France

⁶Current address: Eidgenössische Technische Hochschule, HPF E-6, ETH-Hönggerberg, CH-8093 Zürich, Switzerland

0097-6156/90/0415-0310\$06.00/0

© 1990 American Chemical Society

most widely used tool to study O^- states in natural and synthetic systems (1,2).

O^- states have a tendency to delocalize over a relatively large volume of the surrounding structure. When local charge imbalances occur, such as upon substitution of Al^{3+} for Si^{4+} in quartz, an O^- can be trapped near the Al site to compensate for the local charge deficit (1,3). At low temperatures the structure locally deforms expressed by an increase of the $Al...O^-$ bond distance. The deformation provides an energy well in which the O^- becomes localized (4). At higher temperatures, $>200K$, the O^- delocalizes over the four oxygens adjacent to the Al site. This delocalization is equivalent to a fast exchange, $O^- + O^{2-} = O^{2-} + O^-$. It causes a broad absorption in the visible range of the spectrum, giving quartz crystals which contain $Al^{3+}...O^-$ -Si centers their characteristic smoky appearance (5,6).

If Fe^{3+} substitutes for Si and traps an O^- , the delocalization appears to be less pronounced. This leads to a narrower distribution of the absorption energies and to the violet color of amethyst (7). The equilibrium $Fe^{3+}...O^-$ -Si = $Fe^{4+}...O^{2-}$ -Si, lies largely on the right hand side, attesting to the strong oxidation power of O^- within the framework of the quartz structure (8). In other cases homovalent cations, such as Ti^{4+} substituting for Si^{4+} in quartz, trap an electron and convert to Ti^{3+} (1). The reason is that d^0 cations such as Ti^{4+} and V^{5+} tend to have large cross sections for electron capture, probably because they stabilize in slightly distorted lattice sites by adding the extra d electron. Which valency is stable depends sensitively upon local lattice environments which are often not well known. For instance in x-ray irradiated dolomite an enhancement of the Fe^{3+} concentration was observed (9) suggesting lattice sites where trivalent cations are stabilized, probably by their proximity to point defects requiring charge compensation. This is particularly noticeable when multiple oxidation states exist in the same crystal reflecting different trapping mechanisms for electrons and/or positive holes (10).

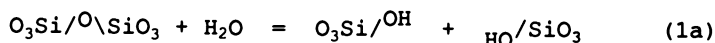
Complicated internal redox reactions occur when atomic H is involved as a reducing agent. In quartz where the reduction of Ti^{4+} has been attributed to reactions with atomic H (11): $Ti^{4+} + H + O^{2-} = Ti^{3+} + OH^-$, atomic H is stable only at low temperature (1). In brazilianites H may be responsible for the reduction of Fe^{3+} to Fe^{2+} plus OH^- (12). Because H easily combines to H_2 it becomes unreactive or escapes. The irreversibility of the redox reaction in brazilianites may be due to loss of H_2 .

Peroxy as Dormant O^- Centers

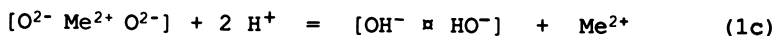
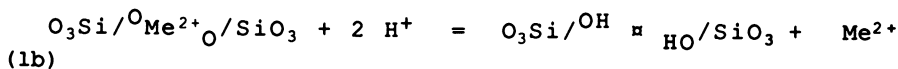
First a few words on the terminology. When O^- states form dimers their signal disappears from the EPR spectrum because of spin pairing. In a predominantly ionic host matrix

O⁻ dimers may appropriately be called peroxy anions, O₂²⁻. In a silicate matrix they appear to occur as peroxy links or, more generally, peroxy entities, X^{/OO\}Y where X, Y = Si⁴⁺, Al³⁺, Fe³⁺... Chemically a peroxy entity represents an extra oxygen: it may be called an interstitial oxygen atom though this does not correctly convey the covalent binding in the O-O bond.

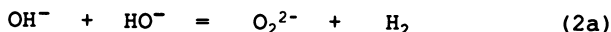
The question arises: How can an extra oxygen be introduced into a solid matrix? A possible source is dissolved "water" by way of OH⁻ or silanol groups, Si-OH. The basic hydrolysis reaction is:



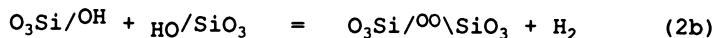
Eq. (1a) describes a solid solution formation with H₂O. A cation of valency n may be replaced by n H⁺, keeping the number of oxygen anions constant. For instance, if n = 2, we have in the case of a silicate or oxide respectively:



where \square symbolizes the cation vacancy. It has been reported that OH⁻ pairs adjacent to Mg²⁺ vacancies in MgO are not stable. They undergo an *in situ* redox reaction to peroxy plus molecular H₂ (15):



Similarly Si-OH pairs in silica and Si-OH pairs in olivine, (Mg,Fe)₂SiO₄, appear to be prone to the same reaction (12-14):



This reaction is unusual. It deserves its own name. It has been called a charge transfer (CT) conversion (15).

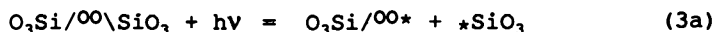
On the basis of an EPR study, using γ - and x-ray activation, peroxy bonds in high purity fused silica have been implicated (16,17). Because the O-O distance is very short, <1.5 Å, the "extra" oxygen does not take much space. In other words, because the peroxy entity is small, it does not cause large structural distortions and peroxy links can be substituted for the O₃Si-O-SiO₃ bridge without increasing the average Si...Si distance (18). The validity of the CT concept, though not yet rigorously proven, is supported by the correlation between the Si-OH and peroxy concentrations in glasses prepared from hydrous gels (19).

The point to retain is that, according to eqs. (2a/b), peroxy may derive from traces of dissolved "water" (13). Since traces of "water" are ubiquitous in oxide and silicate

materials, both natural and synthetic, this may have far-reaching consequences for material properties.

Peroxy Detection

Peroxy anions or entities cannot be detected by any currently known technique unless the O-O bond is activated. One method is ionizing radiation. In the case of high purity fused silica irradiating with γ - and x-rays led to peroxy radicals (*) and dangling bonds at the three-fold coordinated silicon which were fully characterized using EPR (16,17):



Peroxy entities may also dissociate thermally. In fact, O^- centers have been detected in CaO after rapid quenching from $T < 550^\circ\text{C}$ without application of ionizing radiation (20). Dissociation occurs at the covalent O-O bond which is isoelectronic with the F-F bond in the F_2 molecule. The O-O bond is weak because of the repulsive interaction between the two oxygen nuclei at $< 1.5 \text{ \AA}$ distance. Dissociation leads to two O^- radicals:



The message of eqs. (3b/c) is: If peroxy entities exist in insulating materials, they are in fact dormant charge carriers. In the following we shall refer to O^- to mean any kind of thermally generated O^- or $\text{O}_3\text{Si}-\text{O}^\bullet$ radical state irrespective of its detailed environment in the host matrix.

The electrostatic interaction is apparently insufficient to bind both O^- to the cation vacancy: While one O^- remains with the vacancy, though locally delocalized (22), the other becomes unbound (32). An unbound O^- is a mobile charge carrier moving through the host matrix by a succession of electron jumps from O^{2-} to O^{2-} . Because the O^- states are positively charged with respect to O^{2-} they have been called "positive holes" (22). O^- states repel each other in the bulk and tend to diffuse towards the surface causing the surface to become positively charged.

Being paramagnetic O^- can be detected by EPR at low temperatures (20,22). At the same time O^- states are potent oxidation agents: they interact with transition metal cations in low oxidation states causing their oxidation, e.g. $\text{Fe}^{2+} + \text{O}^- = \text{Fe}^{3+} + \text{O}^{2-}$. Thus, one way to follow the peroxy dissociation is to study the concomitant changes in the oxidation states of transition metal impurities by EPR (23). At the surface the chemical expression of O^- states is one of peroxide and/or superoxide functionality. A superoxide may be viewed as an O^- trimer or as O^- trapped by a surface peroxy:

$O_2^{2-} + O^- = O^{2-} + O_2^-$. This reaction may be of interest for understanding the oxidizing nature of Martian soil (24,25) with peroxy photodissociation generating O^- states.

The paramagnetism of O^- can also be measured by means of a Faraday balance (26). This technique has the advantage of being applicable to in situ measurements at high temperatures and is sensitive enough to detect O^- in synthetic MgO (26). We are currently pursuing this work with a Faraday balance and hope shortly to be able to report on new data.

Mobile O^- states must also manifest themselves in electric conductivity and impedance measurements. The experimental difficulties encountered in such types of measurements are threefold. First, O^- states which diffuse to the surface generate a positive surface charge which wraps around the whole sample. When metal electrodes are put in contact with the surface and a potential is applied, the surface current will short-circuit the charge. Second, O^- states may chemically react with the the sample/electrode interface leading to polarization at the contact. Third, O^- states may react with each other at the surface or interface forming peroxy which decompose: $O^- + O^- = O_2^{2-} \Rightarrow O^{2-} + 1/2 O_2$. This irreversibly removes O^- charge carriers from the system.

Charge Distribution Analysis

We have developed a new technique, *Charge Distribution Analysis* or CDA. It holds promise of being widely applicable to the study of peroxy and O^- in insulators. It draws on three diagnostic properties of O^- states: (i) as long as they are dimerized (= peroxy) they are electrically inactive, (ii) upon dissociation at least some O^- become mobile charge carriers, (iii) O^- which diffuse to the surface cause a positive surface charge.

CDA consists of measuring the dielectric polarization P . If a dielectric material with the dielectric constant ϵ is placed in an external electric field of strength E_{ext} , it becomes polarized. In homogeneous fields its polarization is:

$$P = \frac{\epsilon_0(\epsilon-1)}{4\pi} E_{ext} \quad [4]$$

ϵ_0 = permittivity of vacuum. P has at least four contributions

$$P = P_0 + P_1 + P_2 + P_3 \quad [5]$$

P_0 denotes the contribution from the ideal dielectric arising from the deformation of electron clouds and the displacements of nuclei. P_1 denotes contributions from local dipoles which can rotate but not diffuse. P_2 denotes contributions from charges which diffuse over macroscopic distances. P_3 denotes contributions from surface charges.

CDA makes use of the fact that a force \mathbf{F} acts on any dielectric material when placed in an inhomogeneous electric field. \mathbf{F} increases with temperature T , if local dipoles and/or mobile charge carriers are thermally activated. \mathbf{P}_0 , \mathbf{P}_1 and \mathbf{P}_2 cause an attraction towards denser electric field, irrespective of the sign of the field. By contrast \mathbf{P}_3 causes the sample to be either attracted to or repelled from the region of higher electric field depending upon the signs of the surface charge and of \mathbf{E}_{ext} . We use a cylindrical capacitor arrangement as depicted in Fig. 1a. The top electrode is the bias electrode and the vertical axis is taken as the z -direction. The force \mathbf{F}_z^\pm is given as:

$$\mathbf{F}_z^\pm = - \int_V (\mathbf{P} \cdot \nabla) \mathbf{E}_{\text{ext}} dV \quad [6]$$

The integral is to be taken over the volume V including the sample but not the sources of the field. We separate contributions from $(\mathbf{P}_0 + \mathbf{P}_1 + \mathbf{P}_2)$ and \mathbf{P}_3 by means of linear combinations $\mathbf{F}^+ + \mathbf{F}^-$ and $\mathbf{F}^+ - \mathbf{F}^-$, where $\mathbf{F}^+ = \mathbf{F}(\mathbf{E}_{\text{ext}})$ and $\mathbf{F}^- = \mathbf{F}(-\mathbf{E}_{\text{ext}})$, and define:

$$\mathbf{F}_\Sigma \equiv \frac{1}{2} (\mathbf{F}^+ + \mathbf{F}^-) = - \int [(\mathbf{P}_0 + \mathbf{P}_1 + \mathbf{P}_2) \nabla] \mathbf{E}_{\text{ext}} dV \quad [7a]$$

$$\mathbf{F}_\Delta \equiv \frac{1}{2} (\mathbf{F}^+ - \mathbf{F}^-) = - \int (\mathbf{P}_3 \nabla) \mathbf{E}_{\text{ext}} dV \quad [7b]$$

In the absence of a \mathbf{P}_3 contribution we have:

$$\mathbf{F}_z^\pm = - \frac{\epsilon_0(\epsilon-1)}{4\pi} \int_V \nabla \cdot \mathbf{E}_{\text{ext}}^2 dV \quad [8]$$

Since \mathbf{E}_{ext} is proportional to the potential difference U between the electrodes, $\mathbf{F}_z^\pm \propto U^2$. Plotting $\sqrt{|\mathbf{F}|}$ versus U , we expect straight lines with slopes proportional to $(\epsilon-1)^{1/2}$.

Experimental

For the CDA experiments described below a PERKIN-ELMER TGS-1 system was used with a cylindrical furnace on alumina ceramic, 6 mm i.d., with bifilar Pt windings as sketched in Fig. 1b. The sample, 4x4 mm and 1.5-3 mm thick, was suspended from a fused silica hang-down wire and rested on a fused silica loop below the rim of the furnace. A Ni electrode 3 x 5 mm was introduced sidewise above the furnace, parallel to the sample surface at a distance of <0.5 mm. The temperature (T) was calibrated by means of the Curie points of ferromagnetic alloys. During the runs the balance was

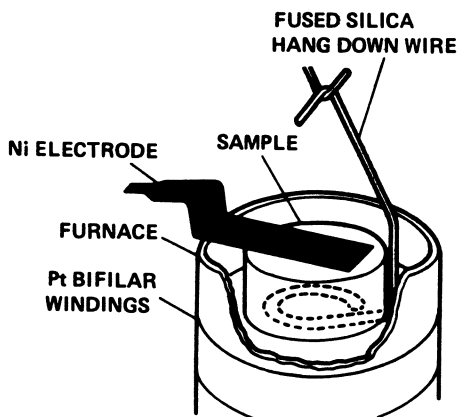
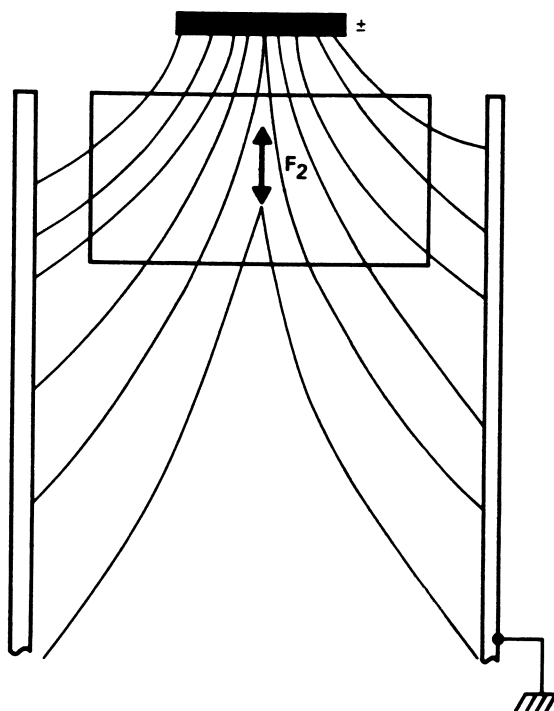


Figure 1. Top: Schematic cross section through the cylindrical inhomogeneous capacitor; bottom: Sample-electrode-furnace assembly used in the present experiments.

purged with high purity N_2 gas at 40 ml/min. The heating and cooling rates were varied between very fast and $0.5^\circ\text{C}/\text{min}$.

Impedance measurements (50 Hz to 10 KHz) were carried out using a GENERAL RADIO Impedance Bridge. A fused silica sample holder was inserted into a screened 50 mm i.d. fused silica tube purged with high purity N_2 gas at 10 ml/min. The samples were ≈ 30 mm diameter and 1.0 - 3.4 mm thick. At variance to common practice we used non-contacting electrodes (20x20 mm Au foil, 0.1 mm thick) separated from the sample by 25x25 mm fused silica microscope cover slides, 0.1 mm thick.

CDA was tested with KBr single crystals and alkali silicate soft glass, a microscope slide. The KBr crystals behaved as expected for a dielectric containing local dipoles which reorient in an externally applied field. The soft glass showed a monotonous $(\epsilon-1)$ vs. T behavior with a decreasing positive surface charge.

The first natural material which we studied by CDA was obsidian. Obsidians are alkali-rich, high-silica natural glasses associated with explosive volcanism and chemically identical to the tuff and pumice ejected during large volcanic eruptions. Originating in magma chambers pressurized under several Kbar P_{H_2O} , many obsidians are relatively "water"-poor ($<0.3\% H_2O^+$) but are believed to have erupted with 3-4.5% water. If Si-OH pairs convert to peroxy plus H_2 as suggested by eq. [2b], obsidian could have also lost H_2 but retained peroxy. Their black appearance suggests the presence of defects which absorb over a wide energy range in the visible, similar to "smoky quartz" where the color center is known to be due to O^- (5,6). We chose a low-Fe obsidian from Glass Butte, OR. All results presented refer to samples which were previously heated to at least 700°C and cooled several times.

CDA Results

Fig. 2 shows how a CDA experiment may typically be performed. The obsidian was heated in steps (at $80^\circ\text{C}/\text{min}$) and allowed to thermally equilibrate for 4-6 min. A bias of -75 V was then applied. The force F_z , expressed as apparent weight loss Δm , was measured at a function of time (solid lines). The bias was removed and the return to the baseline was monitored (dashed lines) before T was raised to the next value. In an ideal dielectric (P_0 only) the response Δm will be proportional to $(\epsilon-1)$.

Below 440°C the spontaneous response is moderate but does not reach a stable value immediately, indicating some additional contributions to P . Between $440-520^\circ\text{C}$ Δm increases multifold. In the upward "creeping" interval the return to the baseline is slow, indicating residual polarization. Above 550°C the Δm response is fast again.

$F\Sigma$ gives the sum of $P_0 + P_1 + P_2$ contributions (eq. [7a]).

Fig. 3 plots $F\Sigma$ values measured at ± 75 V. Four ΔT regions

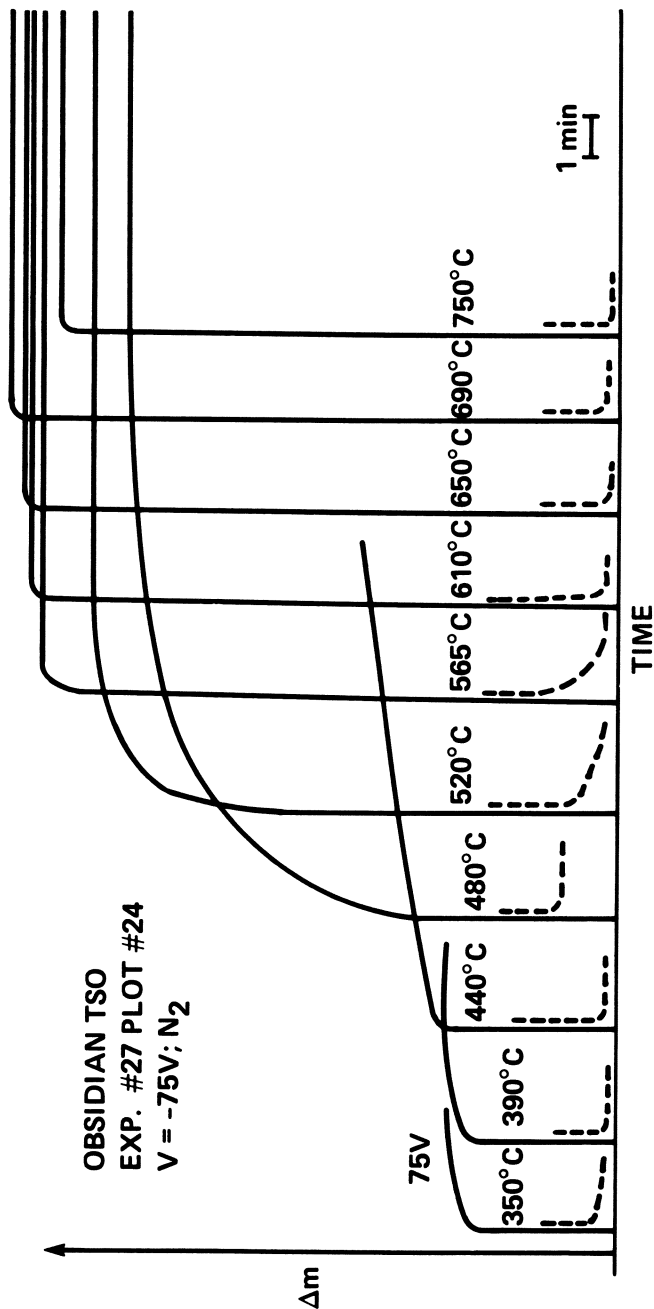


Figure 2: Series of CDA measurements with obsidian alternating between 0 V and -75 V. Note multifold increase in the polarization above 440°C.

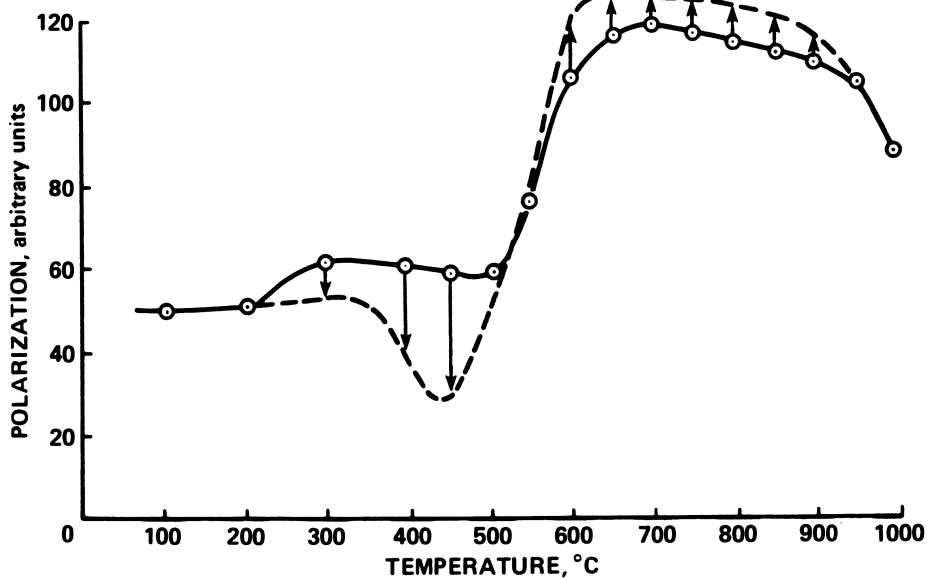


Figure 3: Polarization (F_{Σ}) of obsidian measured at ± 75 V as a function of temperature.

can be identified: (i) up to $\approx 200^\circ\text{C}$ $F\Sigma$ is constant and low, (ii) between $200\text{--}500^\circ\text{C}$ $F\Sigma$ is higher but decreases with time (downward arrows), (iii) between $500\text{--}600^\circ\text{C}$ $F\Sigma$ increases at least fourfold and remains high up to $\approx 900^\circ\text{C}$ with a tendency to further increase with time (upward arrows), (iv) $F\Sigma$ decreases above 900°C . The dashed curve represents $F\Sigma$ values measured after 15 min. The dotted curve depicts the corresponding $F\Sigma(T)$ dependence of soft glass: $F\Sigma$ decreases monotonously over the whole ΔT interval.

Another way of performing CDA experiments is to increase the \pm bias from 0 V in increments of 2, 4, 10 or 20 V at constant T. In Fig. 4a/b we plot $|F_z|^{1/2}$ versus +U and $|F_z|^{1/2}$ versus -U for selected T's. For $P_0 + P_1 + P_2$ contributions such plots would give straight lines, identical for + and - bias, passing through the origin and with slopes proportional to $(\epsilon-1)^{1/2}$.

The observation depict a different behavior: the $|F_z^\pm|^{1/2}$ vs. U plots become straight parabolic lines only at high \pm bias voltages, diverging for +U and -U with slopes changing as a function of T. At low + bias a strong repulsion is seen at all T's up to $\approx 440^\circ\text{C}$. Conversely, at - bias, enhanced attraction is noted. Both attest to a contribution from P_3 corresponding to a positive surface charge.

With reference to Fig. 4a we may define the + bias at which F_z becomes zero as the equipotential point, V_{eq} , the physical meaning being that the repulsion due to P_3 balances the sum of $P_0 + P_1 + P_2$ contributions.

In Fig. 5 we plot V_{eq} vs. T using a more complete set of data than in Fig. 4a. Below 250°C the V_{eq} values sensibly react to the cooling rate, yielding higher and lower V_{eq} values for fast and slow cooling, respectively. Between $250\text{--}400^\circ\text{C}$, at low fields, V_{eq} cannot be accurately determined since F_z^\pm is nearly field-independent. Obviously the obsidian surface carries a positive charge below $\approx 250^\circ\text{C}$ but the charge density strongly depends upon the cooling rate: rapid cooling increases the surface charge, while slow cooling decreases it. This behavior indicates that the surface charge carriers are metastable. Around 350°C the surface appears negatively charged or carry a weakly bound, "soft" positive charge which is easily polarized by low fields. Above 450°C V_{eq} rises to high positive values, indicating that the surface charge is "hard" and stable. V_{eq} peaks around 630°C . Above 900°C V_{eq} decreases. By contrast the soft glass has a positive surface over the whole ΔT interval with V_{eq} decreasing monotonously.

Fig. 6 shows how one can measure conductivity s and capacitance C of an obsidian which is expected to develop surface charges. It is unwise to directly apply the metal electrodes onto the sample because this would only lead to shortcircuiting. Instead, as shown by the detail, we insert two fused silica microscope cover glasses (0.1 mm thick).

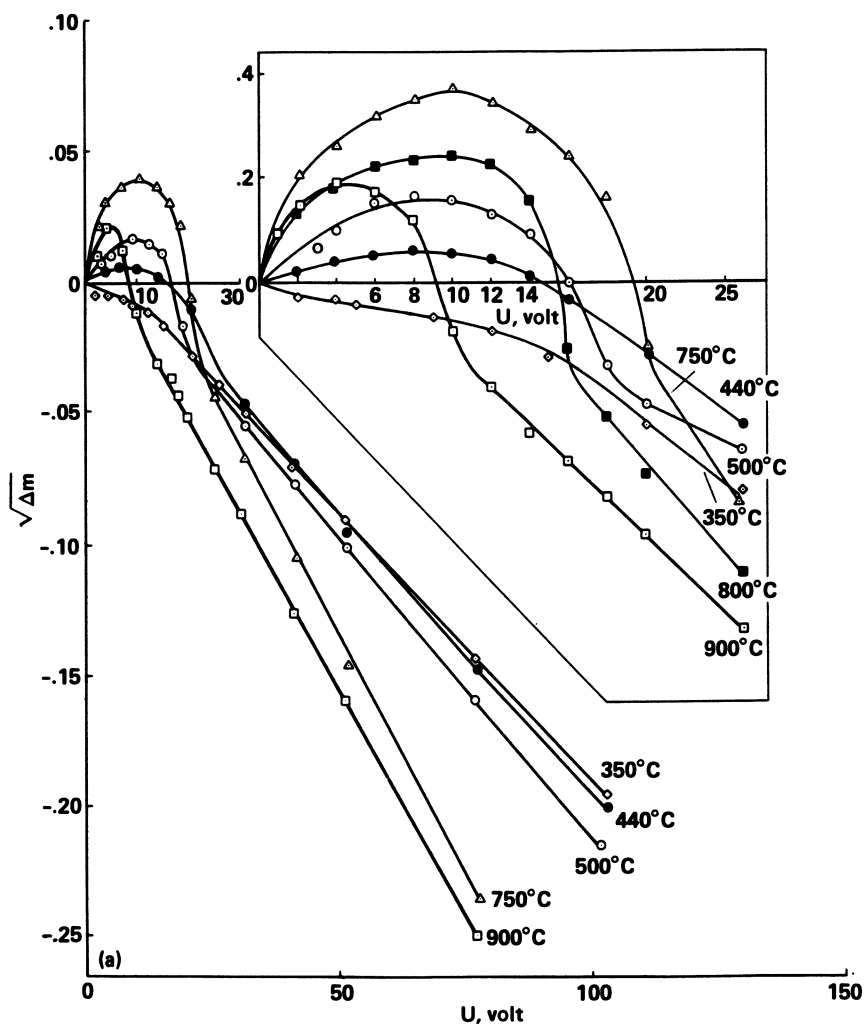


Figure 4a. Change of the force plotted as $(\Delta m)^{1/2}$ versus the electric field U at selected temperatures under positive bias. *Continued on next page.*

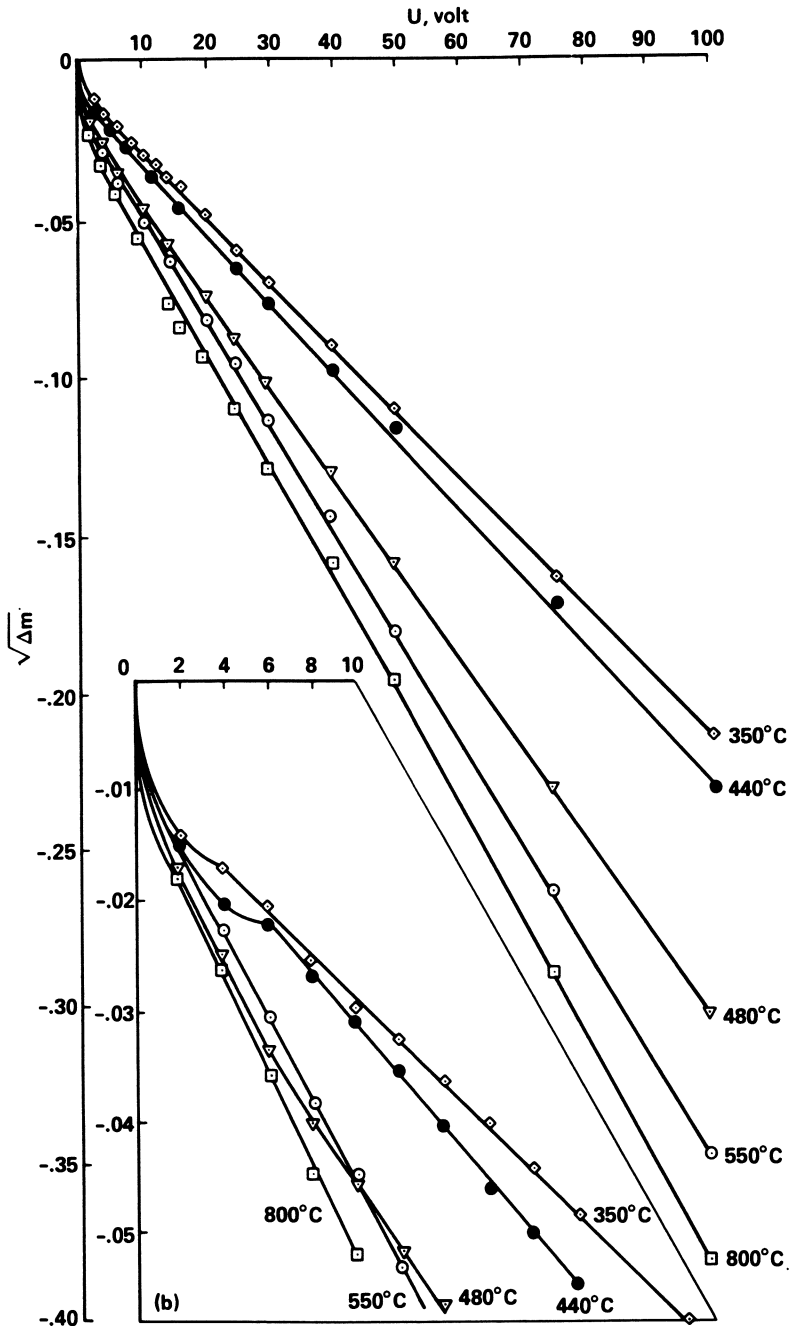


Figure 4b. Change of the force plotted as $(\Delta m)^{1/2}$ versus the electric field U at selected temperatures under negative bias.

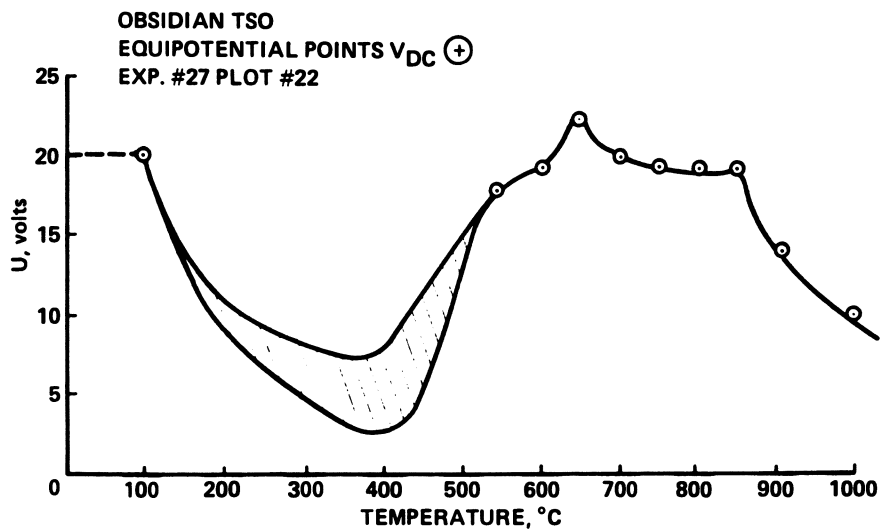


Figure 5: Equipotential points as a function of temperature demonstrating the build-up of a positive surface charge above 450°C.

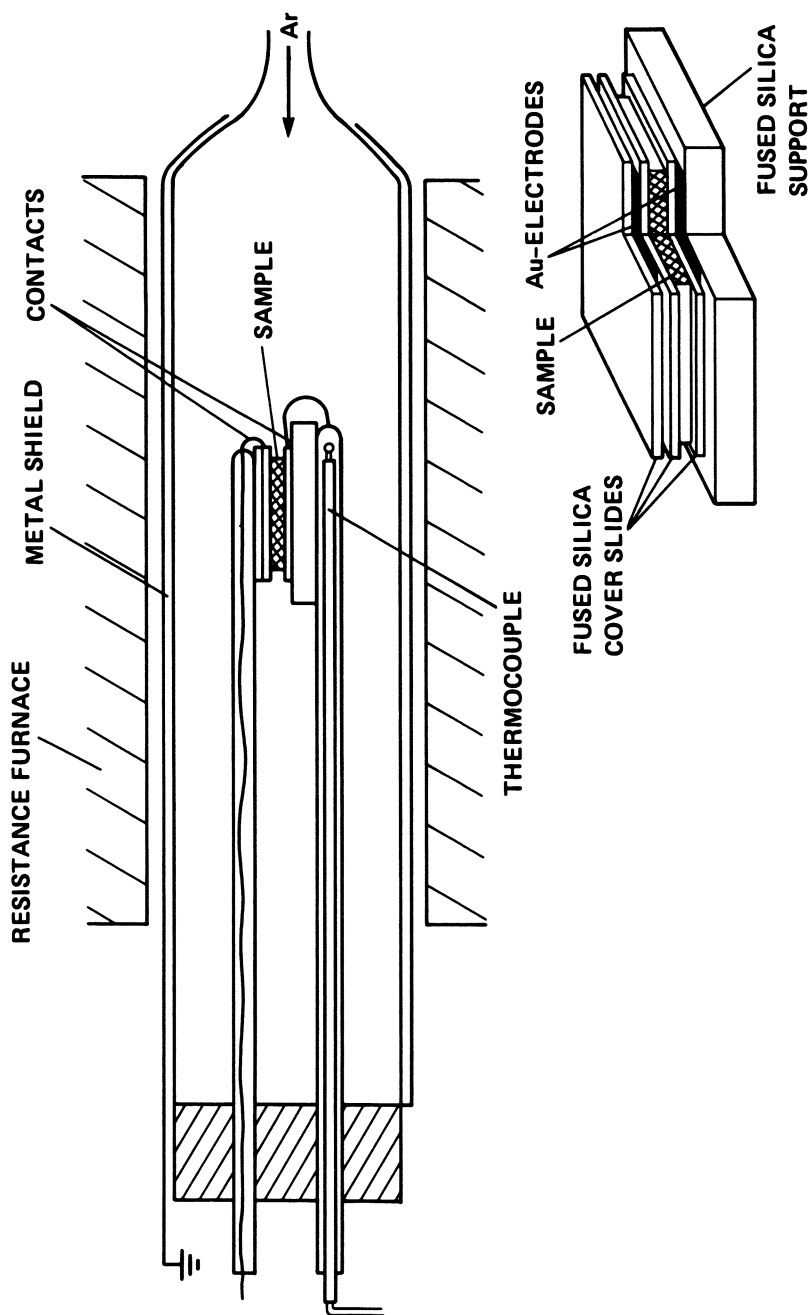


Figure 6: Sample arrangement for impedance measurements. Note the fused silica cover slides (0.1 mm) inserted between the electrodes and the sample

Fig. 7a/b shows how σ and C vary as a function of T , measured at 200 Hz with non-conducting electrodes. Between 100-200°C we observe a σ maximum which shifts as a function the thickness of the sample. For the sake of brevity we only consider the region $>400^\circ\text{C}$. The dashed line delineates the cationic conductivity. It is superimposed by a σ maximum near 600°C (solid line). The C maximum which occurs at the same temperature indicates the presence of highly polarizable but unstable charge carriers. The V_{eq} peak near 630°C (**Fig. 5**) probably corresponds to the σ peak near 600°C, the apparent displacement of the maximum being due to the different heating modes and furnaces used.

Discussion

There are two observations which are obviously linked: (i) the reversible appearance/disappearance of mobile charge carriers around 450°C and (ii) the appearance/disappearance of a positive surface.

Surface charges are not by themselves surprising. Ionic solids have been predicted long ago to develop surface/subsurface charge layers arising from differences between the free energies of formation of anion and cation vacancies (27). The magnitude and sign of the charges have been calculated for pure and doped alkali halides from thermodynamic equilibrium data (28). In ceramic systems the presence of charged grain boundaries has been demonstrated by preferred grain boundary segregation of heterovalent impurities (29,30). Alkaline silicate glasses usually carry a positive surface charge due to segregation of alkaline cations and/or to surface leaching (31,32).

In obsidian the increase of $F\Sigma$ above 450°C and the appearance of the positive surface charge between 450-630°C do not suggest a thermo-dynamically determined surface charge layer nor Na^+ segregation. If Na^+ segregation were the cause, the obsidian behaviour should resemble that of soft glass, e.g. $F\Delta$ should decrease monotonously with increasing T .

While an $F\Sigma$ increase (**Fig. 3**) may also be caused by dipoles which become mobile and reorient in the externally applied electric field, the CDA response to dipoles must be invariant towards the change of polarity. The remarkable divergence between the $|F_z^\pm|^{1/2}$ vs. U plots and their different slopes (**Fig. 4a/b**) suggest that the $F\Sigma$ increase above 450°C is due to charge carriers which satisfy the following four criteria:

- (i) they are highly mobile,
- (ii) they produce strong positive surface charges,
- (iii) they are generated above 450°C,
- (iv) they disappear upon cooling but can be quenched by rapid cooling.

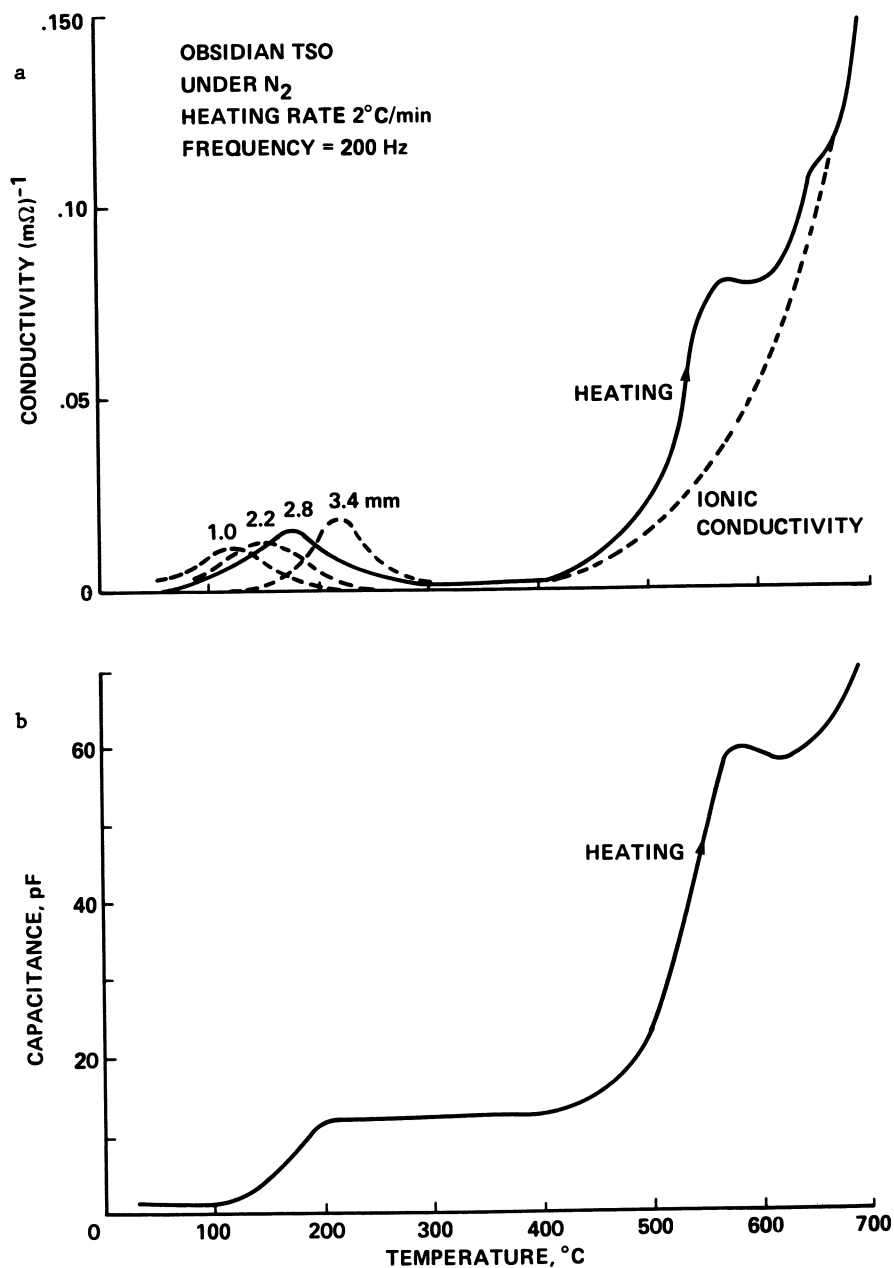


Figure 7: (a) Conductivity σ and (b) capacitance C (2.8 mm thick sample only) as a function temperature indicating the presence of mobile charge carriers, presumably O^- generated by peroxy dissociation.

The high mobility suggests that the charge carriers are electronic in nature. Their positive sign identifies them as positive holes. Positive holes in obsidian can only be $O^{\cdot-}$ states in the O^{2-} matrix.

We have observed similar F_{Δ} and F_{Σ} effects in MgO, natural olivine from the upper mantle and sanidine from the lower continental crust (33-35). While there are distinct differences, the overall observation repeats itself: Highly mobile charge carriers of positive sign are generated within a narrow ΔT range. They increase the dielectric polarization and set up a positive surface charge. The observations jointly point at $O^{\cdot-}$ states which are thermally generated from "dormant" precursors. No such charges are produced in KBr nor in the soft glass.

Ionizing radiation is generally believed to be a necessary ingredient to form $O^{\cdot-}$: $O^{2-} + h\nu = O^{\cdot-} + e^{-}$. However, since the samples under study are wide band gap insulators, heating will certainly not suffice to ionize O^{2-} to $O^{\cdot-}$. Therefore we are compelled to invoke precursors which are capable of thermally generating $O^{\cdot-}$ states. Peroxy entities which dissociate according to eqs. [3b/c] are the most likely candidates.

Hence, our first conclusion is: The obsidian must contain peroxy linkages or similar $O^{\cdot-}$ precursor entities.

This immediately leads to the question: when and where did the obsidian acquire peroxy entities? The parent magma was certainly not so highly oxidized as to dissolve oxygen according to the scheme: $O^{2-} + 1/2 O_2 = O_2^{\cdot-}$ or $X/OX + 1/2 O_2 = X/OO\backslash X$. Magmas tend to be always reduced, ranging from strongly reduced like basalts (36) to weakly reduced like the obsidian where the Fe^{3+}/Fe^{2+} ratio is reportedly of the order of 0.5 (37).

In accordance with the Charge Transfer (CT) reaction mechanism outlined by eqs. [2a/b] peroxy was probably introduced into the obsidian via the dissolution of "water", e.g. via Si-OH pairs which converted to $Si/OO\backslash Si$ plus H_2 . Since the glass structure which is relatively open some or most of the H_2 molecules thus generated may have diffused out over geological time, leaving the peroxy entities behind.

Peroxy entities may indeed represent an ubiquitous type of defects in oxides and silicates, both natural and synthetic. The reason is that traces of dissolved "water" are everywhere. In optical waveguide fibers made of low-OH fused silica a dramatic increase of Si-OH and attendant loss of transmittance have been reported upon exposure to H_2 probably by way of the reaction $Si/OO\backslash Si + H_2 = 2 Si-OH$ (15,35).

As expected $O^{\cdot-}$ charge carriers also affect the conductivity (see Fig. 7a/b). Since this study has shown that $O^{\cdot-}$ preferentially diffuse to the surface, the surface conductivity must increase. This effect may be of considerable interest in technical applications of insulating materials: the inadvertent presence of peroxy may lead to electric shortcircuiting via surface currents carried by $O^{\cdot-}$.

Lastly, a note on the chemical surface properties of O^- . So far we have carried out only a few preliminary CDA experiments adding 5 vol.-% H_2 to the N_2 . The observed decrease of the polarization and, hence, of the charge carrier density at the surface suggests that H_2 consumes O^- , probably by way of oxidation: $H_2 + 2 O^- = H_2O + O^{2-}$. Further work will be required to study these reactions in more detail.

Acknowledgments

The work was supported in part by the SETI Institute/NASA Ames Research Center Cooperative Agreement NCC 2-446. We thank Sherwood Chang and Theodore Wydeven for stimulating discussions and Rodney C. LeRoy for technical assistance.

Literature Cited

1. Weil, J. A. Phys. Chem. Minerals 1984, **10**, 149-165.
2. Vassilikou-Dova, A.B.; Lehmann, G. Fortschr. Min. 1987, **65**, 173-202.
3. Nuttal, R.H.D.; Weil, J.A. Canad. J. Phys. 1981, **59**, 1696-1708.
4. Bossoli, R.B.; Halliburton, L.E. Phys. Stat. Sol. 1986, **136**, 709-714.
5. Nassau, K.; Prescott B.E. Phys. Stat. Sol. (a) 1975, **29**, 659-663.
6. Schirmer, O.F. Solid State Comm. 1976, **18**, 25-33.
7. Cohen, A.J. Amer. Mineral. 1985, **70**, 1180-1185.
8. Adekeye, J.I.D.; Cohen, A.J. Appl. Geochem. 1986, **1**, 153-160.
9. Prissok, F.; Lehmann, G. Phys. Chem. Minerals 1986, **13**, 331-336.
10. Stoneham, A.M.; Sangster, M.J. Phil. Mag. 1981, **B43**, 609-619.
11. Okada, M.; Rinneberg, H.; Weil, J.A.; Wright, P. Chem. Phys. Lett. 1971, **11**, 275-276.
12. Requard, A.; Lehmann, G. Phys. Status Solidi (b) 1985, **127**, 695-701.
13. Freund, F. J. Phys. Chem. Solids 1985, **71**, 195-202.
14. Freund, F.; Oberheuser, G. J. Geophys. Res. 1986, **91**, 745-761.
15. Freund, F.; Wengeler, H. J. Phys. Chem. Solids 1982, **43**, 129-145.
16. Friebele, E.J.; Griscom, D.L.; Stapelbroek, M.; Weeks, R.A. Phys. Rev. Lett. 1979, **42**, 1346-1349.
17. Griscom, D.L.; Friebele, E.J. Phys. Rev. B 1981, **24**, 4896-4898.
18. Edwards, A.E.; Fowler, W.B. Phys. Rev. B 1982, **26**, 6649-6660.
19. Wolf, A.A.; Friebele, J.E.; Tran, D.C. J. Non-Cryst. Solids 1985, **71**, 345-350.
20. Tomlinson, A.C.; Henderson, B. J. Phys. Chem. Solids 1969, **30**, 1793-1799.
21. King, B.V.; Freund, F. Phys. Rev. B 1984, **29**, 5814-5824.
22. Henderson, B.; Wertz, J.E. Defects in Alkaline Oxides. Taylor & Francis, London, 1977.
23. Kathrein, H.; Freund, F.; Nagy, J. J. Phys. Chem. Solids 1984, **45**, 1155-1163.
24. Hunten, D.M. Rev. Geophys. Space Phys. 1974, **12**, 529-536.
25. Ballou, E.V.; Wood, P.C.; Wydeven, T.; Lehwalt, M.E.; Mack, R.E. Nature 1978, **271**, 644-645.
26. Freund, F.; Knobel, R.M.; Kathrein, H.; Wengeler, H. Nucl. Instrum. Meth. Phys. Res. 1984, **B1**, 223-234.

27. Lehovec, K. J. Chem. Phys. 1953, 21, 213-228.
28. Kliewer, K.L.; Koehler, J.S. Phys. Rev. A 1965, 140, 1226-1240.
29. Kingery, W.D. J. Amer. Ceram. Soc. 1974, 57, 1-8.
30. Colbourn, E.A.; Mackrodt, W.C.; Tasker, P.W. J. Mater. Sci. 1983, 18, 1917-1924.
31. Dunken, H.H. Treatise Mat. Sci. Technol. 1982, 22, 1-74.
32. Lee, C.T.; Clark, D.E. Appl. Surf. Sci. 1985, 20, 397-412.
33. Freund, F.; Batllo, F.; Freund M.M. Phys. Rev. Letters
34. LeRoy, R.C.; Batllo, F.; Wydeven, T.; Freund, F. Eos Trans. Amer. Geophys. Union 1988, 69, 1436 (Abstract).
35. Lerski, S.; Batllo, F.; Wydeven, T.; Freund, F. Eos Trans. Amer. Geophys. Union 1988, 69, 1468 (Abstract).
36. Sato, M. Geophys. Res. Lett. 1978, 5, 447-449.
37. Hildreth, W. J. Geophys. Res. 1981, B11, 10153-10192.
38. Shelby, J.E. J. Appl. Phys. 1979, 50, 2589-2593.

RECEIVED July 17, 1989

Chapter 17

Variable Oxidation States of Iron in the Crystal Structure of Smectite Clay Minerals

Joseph W. Stucki and Paul R. Lear¹

University of Illinois, Urbana, IL 61801

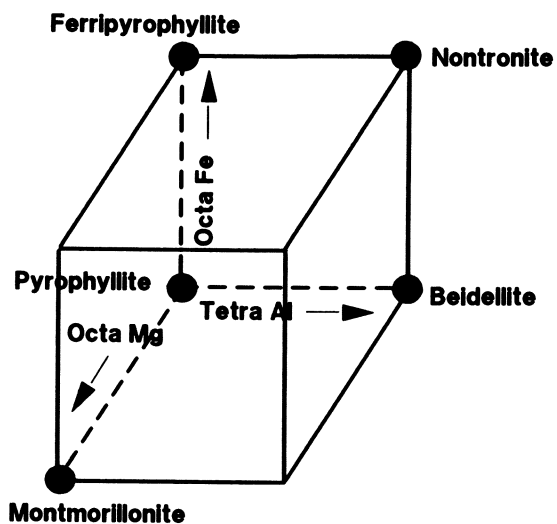
The oxidation state of iron in smectite clay minerals may vary between Fe^{3+} and Fe^{2+} , either through natural or laboratory processes, with accompanying changes in chemical and physical properties. Properties affected include color, surface charge, surface area, swellability in water, and magnetic exchange interactions. Methods are described for varying and measuring the oxidation state; and techniques for drying, characterizing, and manipulating air-sensitive clays are reviewed. Processes associated with the reduction and reoxidation of iron in the clay crystal structure likely involve dehydroxylation-rehydration reactions, as well as possible self-reduction of the mineral through intracrystalline electron transfer.

Smectite clay minerals play a dominant role in determining the chemical and physical properties of many soils and sediments. As a group, smectites are formally defined as phyllosilicates with layer charge between 0.2 and 0.6 per half unit-cell (1), but are best known for their high swellability, surface area, and cation exchange capacity. They vary widely in composition with respect to metal cations (e.g., Si^{4+} , Al^{3+} , Mg^{2+} , Fe^{3+} , Fe^{2+} , and Li^+) in their crystal structures as illustrated in Figure 1; but virtually all contain some amount of structural Fe. Studies have shown that Fe is perhaps the most significant of all constituent ions because the *in situ* variation of its oxidation state invokes profound changes in a number of fundamental clay mineral properties. The purpose of this Chapter is to review the phenomena associated with variable oxidation states of Fe in dioctahedral smectites, and to describe methods for their preparation, handling, and characterization.

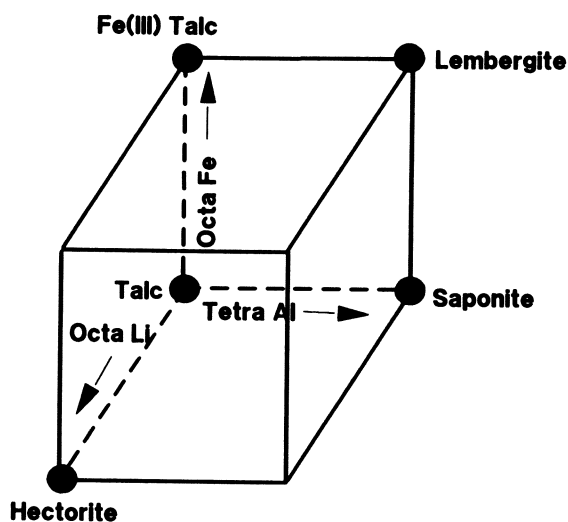
¹Current address: EPL Bioanalytical Services, Box 1708, Decatur, IL 62525

0097-6156/90/0415-0330\$08.25/0

© 1990 American Chemical Society



A



B

Figure 1. Composition and classification of known end members of dioctahedral (A) and trioctahedral (B) smectites.

Among the Fe-bearing smectites, nontronite is the most studied, and with a few exceptions will be the focus of the work described herein. Evidence suggests, however, that many of the principles and phenomena that apply to nontronite also apply to other dioctahedral smectites because the effects of oxidation state are generally independent of total Fe content. Exceptions are those cases where the clustering of Fe is fundamental to the effect (e.g., magnetic exchange and electron transfer between Fe centers), in which cases the effect will vary with total Fe content insofar as the Fe distribution is homogeneous throughout the crystal layers.

The precise location of Fe in the crystal structure of nontronite is a subject of much current interest. As much as 1-15% of Fe³⁺ may exist in the tetrahedral sheets (2-7) with the remainder in the octahedral sheets, but the precise quantitative distribution among tetrahedral, *cis*-octahedral, and *trans*-octahedral sites is unknown.

Fundamental to characterizing the relationships between Fe oxidation state and clay properties are appropriate methods for preparing and maintaining clays in a reduced or partially reduced state, and a knowledge of the chemical reactions and changes in crystal chemistry associated with the reduction process. Significant progress has been made in some of these areas, but much still remains to be learned. The following discussion will, therefore, focus first on methods, then review the important results linking oxidation state to crystal chemistry, physical properties, and behavior of reduced clays.

Methods of Preparation and Characterization

One of the more troubling aspects of working with reduced clays is the problem of preparing samples without causing reoxidation. Several options present themselves for the initial reduction, but depending on the intended purpose or use of the sample, subsequent steps may become rather complicated or require specialized equipment and procedures in order to preserve the desired oxidation state. Procedures which are routine under natural oxidation states frequently become so awkward under inert atmosphere conditions that most researchers have simply avoided the problem by focussing only on those measurements which require minimal or no handling of the reduced sample. Many chemical and spectroscopic methods for characterizing and analyzing clay samples, however, can be optimized only if certain preparation steps have been completed, such as drying (self-supporting films, powders, thin films on a grid or support), exchanging the counterion, or attaining a specific ionic strength or ionic concentration. Indeed, some measurements are impossible unless the sample has been treated in one or more of these ways. And the measurement itself usually requires careful control of the atmosphere or environment surrounding the sample.

Reducing Agents. Smectites may be reduced in one of several different ways (Table I), either in aqueous suspension or in the dry state, but the most effective methods require intimate contact between the clay surfaces and the reducing agent. The diffusion of reactants and products, such as the diffusion of H₂O out of or H⁺ into the clay lattice (Equations 2 and 3, p.350), appears to be an important aspect

Table I. Methods used to reduce structural Fe in smectites

Reducing Agent	Smectite	References*
CBD [‡]	nontronite, montmorillonite	17, 30-32, 41, 45-46
Sodium dithionite (Na ₂ S ₂ O ₄)	nontronite, montmorillonite	16, 19
Hydrazine (N ₂ H ₄)	nontronite, montmorillonite	16-18, 30
Sodium sulfide (Na ₂ S)	nontronite, montmorillonite	48
Sodium hydro- sulfide (NaHS)	soil clays, montmorillonite	49
Benzidine	hectorite, montmorillonite	50-51
Hydrogen gas at high temper- ature (> 300 °C)	nontronite	52-53
Electron irra- diation	vermiculite, talc	54
Microorganisms	nontronite, montmorillonite	12-13, 15

*Numbers correspond to those in the Literature Cited.

[‡]Na₂S₂O₄ added to a suspension in 1 N citrate-bicarbonate.

of reduction and reoxidation. Hence, suspensions commonly are more reducible than are dry powders or films.

Sodium dithionite ($\text{Na}_2\text{S}_2\text{O}_4$) is by far the most commonly used reducing agent, even though it is unstable in H_2O and reagent grade quality is difficult to obtain. The chemistry of this compound is very complex, and includes both redox and disproportionation reactions that render it unstable in aqueous solution (8). This is probably why "solutions" of dithionite are rather ineffective reducing agents for smectite compared to adding the solid powder of the compound directly to the clay suspension. Odors commonly associated with S are easily detected in reducing suspensions. Another consequence of adding dithionite to aqueous solutions is a definite decrease in pH ($\text{pH} < 2$), which obviously has a potential negative impact on the clay crystal structure. Such consequences can be mitigated, however, by including a pH buffer, such as NaHCO_3 , in the solution in which the clay is suspended. Studies in the authors' laboratory (9) utilize a more dilute variation of the citrate-bicarbonate method described by Mehra and Jackson (10) which maintains the suspension between about pH 7 and 8. The effects of buffered vs. unbuffered dithionite treatments on clay properties were reviewed by Stucki (11), and clearly show that the lower pH liberates large quantities of structural cations, suggesting considerable mineral dissolution.

The extent of reduction can be controlled by varying the relative amounts of dithionite and clay in the suspension (9), but reaction time, temperature, O_2 content, and open- vs. closed-system are also very important variables. Open systems may be established using a septum-capped reaction vessel, such as one described by Stucki *et al.* (9), and bubbling N_2 gas through the suspension during reduction. Using such a system, Komadel *et al.* (Komadel, P.; Lear, P.; Stucki, J. W. *Clays Clay Miner.*, in press) achieved virtually complete reduction of the structural Fe in nontronite without destroying the clay structure. The open system removes gaseous reaction products which otherwise build up inside the vessel and thus create a thermodynamic inhibition to the continued reduction of Fe. Temperature clearly affects the rate of reduction, but also shifts the thermodynamic equilibrium more to the right.

Microbial reduction of Fe in smectites apparently has been reported only recently. The senior author and co-workers demonstrated that certain microorganisms are capable of reducing structural Fe in smectites (12-13). While the absolute level of reduction was only on the order of about 0.3 mmole/g, the effect per colony forming unit (CFU) was significant, suggesting that in a continuous reactor the levels of reduction may increase dramatically. The reduction of Fe oxides by microorganisms has been known for many years (14), but the authors are aware of only one other report of biological reduction of Fe in smectites (15). This method of Fe reduction may be impractical for some detailed studies of the effects of oxidation state on clay properties, but in field applications where cost and environmental impact are of concern, such possibilities for Fe reduction hold great potential. This method also provides a means for probing the effects of mineralogy on Fe nutrition of plants, and studying the mineral-microorganism-root dynamics in the rhizosphere.

Hydrazine and other reducing agents have been used on a more limited basis. Among the non-dithionite reducing agents, hydrazine in either the anhydrous (16-18) or hydrate (19) form has been employed most often. The most distinguishing characteristic of Fe reduction by the vapors of this compound is its relatively low reducing ability -- on the order of about 0.3 mmole/g -- in spite of its very high reduction potential. This effect may be the result of interaction with the edge rather than planar surfaces of the clay mineral, or it may simply be a diffusion phenomenon. The principal attraction to and advantage of hydrazine as a reducing agent is that its vapors penetrate dry clay powders or films, thus enabling reduction in the dry state. In the dry state, however, surfaces of individual clay layers are less available than in the suspension state, and thus reduction of octahedral Fe, which is imbedded within each individual clay layer, is more difficult than if the clay were mixed intimately with the reducing agent. However, attempts to increase the level of reduction by bringing the dry clay film directly in contact with the liquid phase of either anhydrous hydrazine (Stucki, J. W., University of Illinois, unpublished data) or hydrazine hydrate (19) have generally failed; so, perhaps the actual explanation is the former, i.e., due to the specific nature of the surface interactions between clay and reducing agent.

Other reducing agents which have been reported (see Table I) include Na_2S , NaHS, Benzidine, H_2 gas at high temperature (>300 °C), and electron irradiation. None of these methods has gained common usage, and all are primarily of only academic interest.

Removal of Excess Reducing Agent and Salts. One of the most important of all procedures in working with reduced clays is the ability to establish any desired ionic strength and cation saturation in the sample. Stucki *et al.* (9) described a special reaction vessel and washing apparatus which allows the sample to be washed with degassed solutions through a cyclic centrifugation-decantation-resuspension process. The reaction vessel is illustrated in Figure 2, and consists of a 50-ml polycarbonate centrifuge tube capped with a custom-made aluminum cap. The cap is threaded to match the tube, is sufficiently deep to accommodate a double septum (made of polyacrylamide and teflon) and PVC washer, and has a 10-mm diameter access hole in the top. The septum and washer seal to the rim of the vessel via a rubber gasket when the cap is tightened. The vessel contents are accessed without removing the cap by using six-inch, 22-gauge septum penetration needles (made on special order by Popper and Sons, New Hyde Park, NY 11040).

An apparatus was designed (Figure 3) which enables either N_2 gas, vacuum, or one of two different degassed solutions to access the reduced suspension without opening the reaction vessel. Solutions are degassed by boiling the solution in a condenser flask, while at the same time passing N_2 gas through the solution and across the top of the condenser. By selecting the appropriate solute concentrations in the solutions and washing a sufficient number of times, any desired solute concentration and counterion can be achieved. One caveat is that, in order for the clay to separate from the suspension under a force of $40,000 \times g$, the solute concentration must be maintained above about $5 \times 10^{-3} \text{ M Na}^+$. This also prevents hydrolysis of

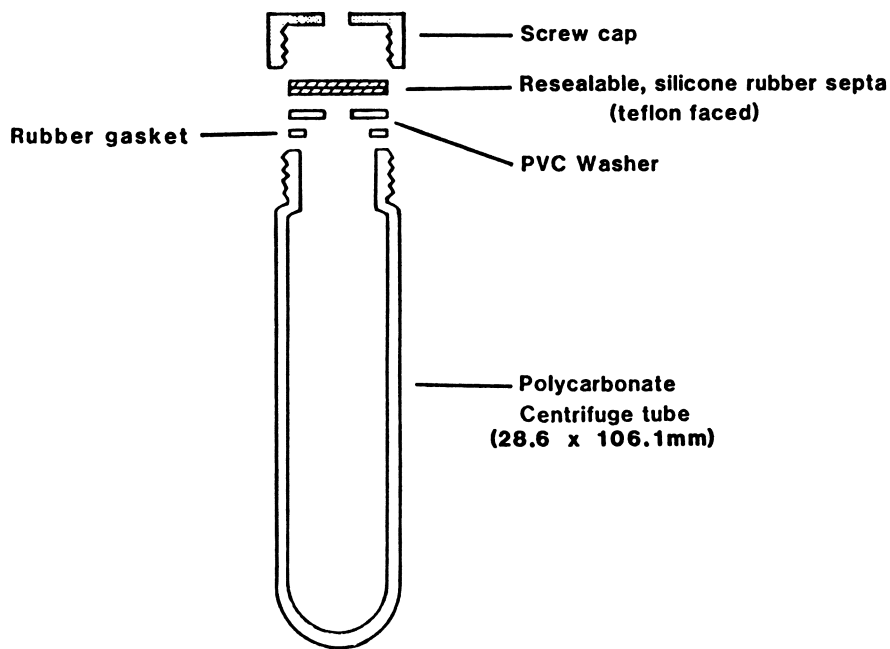


Figure 2. Schematic representation of inert-atmosphere reaction vessel. (Reproduced with permission from Ref. 9. Copyright 1984 The Clay Minerals Society.)

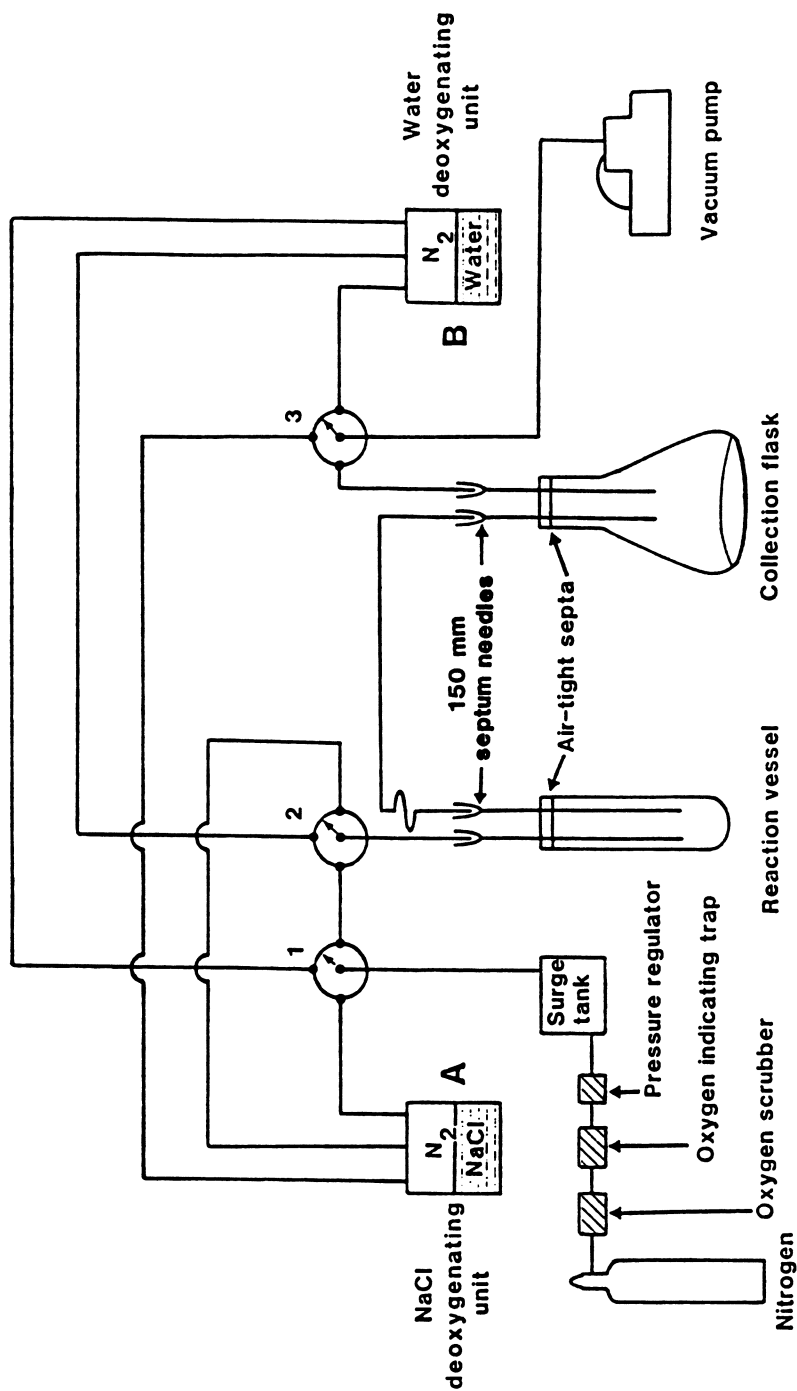


Figure 3. Schematic representation of apparatus for washing reduced clay suspensions. (Reproduced with permission from Ref. 9. Copyright 1984 The Clay Minerals Society.)

Na⁺ ions on the clay surfaces. For more details about the procedure, the reader should refer to the original publication (9).

An alternative method for reducing excess salts was described by Chen *et al.* (20), wherein the sample was placed in a dialysis tube then dialyzed against a degassed, dilute salt solution. This method and apparatus are effective when large amounts of reduced sample are required.

Sample dialysis or washing as described above is effective for removing excess salts and for quenching the reduction reaction when the reducing agent is a salt, such as Na₂S₂O₄. When microorganisms are the reducing agent, the removal of reducing agent is less straight-forward, but may be accomplished by heating the sample to about 60 °C then washing as described above. Heating to this temperature destroys the microorganisms and may denature the constituent proteins sufficiently to render them largely removable through the supernatant. Alternatively, one could try a density gradient separation.

Drying. The most straight-forward method of drying reduced samples is freeze-drying. This can be accomplished by purging the freeze-drier with N₂ gas before attaching the samples. Freezing of the samples may be achieved by either placing the closed reaction vessel in a conventional freezer or by immersing the vessel in a pool of liquid N₂. For many applications this technique is sufficient, but caution is advised that once thus dried a sample will still reoxidize if unprotected from the atmosphere. Long-term storage of reduced samples, even after drying, is not recommended.

Preparation of self-supporting and thin films, in which the clay particles are oriented normal to the c* axis, is one of the more useful drying methods. A simple apparatus in which such films can be prepared is illustrated in Figure 4. The sample suspension is transferred through the ball valve and placed onto the drying surface, which may be either a porous plate, porous filter overlying the porous plate, or a non-porous window resting on the porous plate. The porous plate normally would be used for X-ray diffraction analysis, whereas the filter paper is an excellent method for obtaining a self-supporting film. A dried clay film will easily lift off the filter paper if the pore-size of the paper is < 0.025 μm. In each of these cases the sample is filtered, i.e., solution is extruded through the porous support and expelled through the bottom outlet tube by applying gas pressure at the top. To evaporate a film onto a window or non-porous plate, the clamping bolts are usually loosened slightly to allow the purge gas to flow through the system and thereby maintain a dry atmosphere into which the clay solution can evaporate. One obvious advantage of drying onto a non-porous window, as compared to a self-supporting film, is that very small amounts of clay per unit area are attainable. This is particularly important in studying spectroscopic features which have very high absorptivities, such as the Si-O bands in the infrared and the O-Fe³⁺ electron charge transfer in the ultra-violet region of the spectrum. If necessary, the whole drying apparatus can be placed in a glove box, either before or after drying, in order to transfer the sample to other chambers or sample holders. Because of their consolidated nature, samples dried in this manner usually reoxidize slowly (over

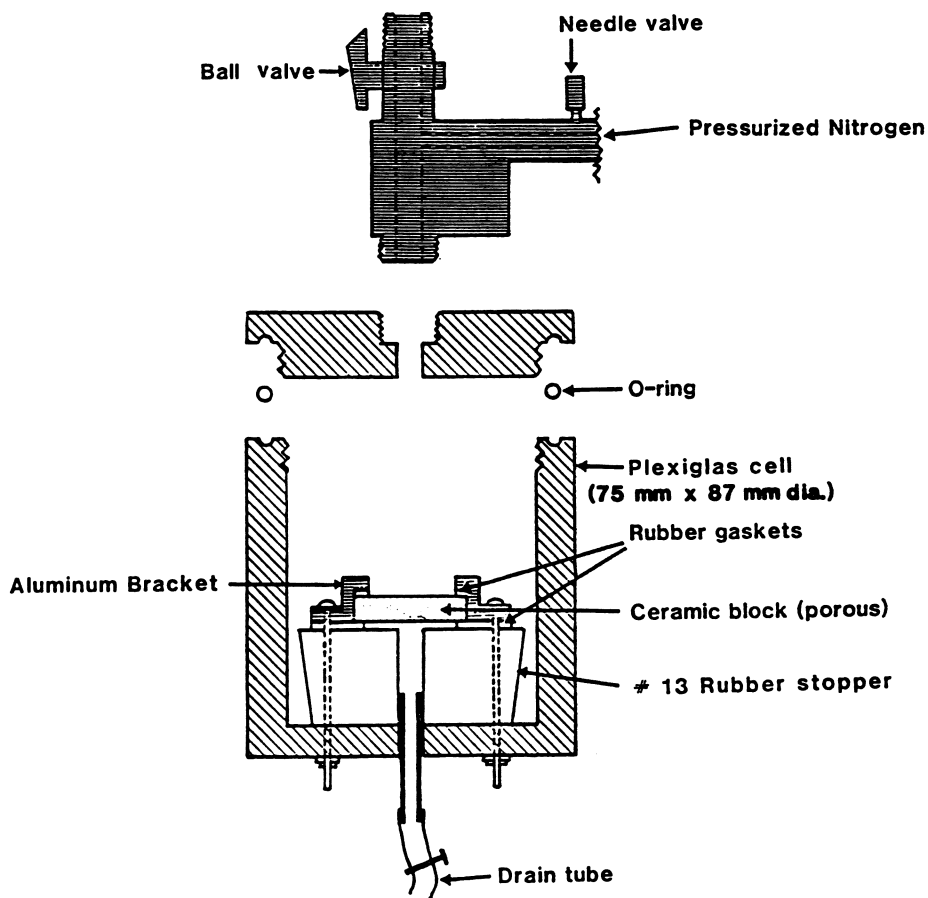


Figure 4. Schematic representation of apparatus for preparing oriented films of reduced clays. (Reproduced with permission from Ref. 9. Copyright 1984 The Clay Minerals Society.)

several hours or days). One therefore has greater flexibility in handling such dried specimens as compared to freeze-dried or wet samples.

A well-known fact is that the interparticle arrangements of dried clay samples depend on the method of drying, so the reader is cautioned to identify the intended purpose of the sample before choosing a drying method. No studies have been reported where reduced clays were dried with solvent-exchange methods (such as by critical-point drying), but one of the authors (Stucki, J. W. University of Illinois, unpublished data) recently began a study of the effect of Fe oxidation state on the inter-particle arrangements of smectites in suspension in which reduced samples were prepared successfully for high resolution electron microscopy by successively exchanging the water solvent with methanol, propylene oxide, and Spurr or LR-White epoxy resins for subsequent thin-sectioning, following the techniques of Tessier (21). By degassing the solvents as described in Section 2.2, the reduced state may be largely preserved.

Differentiating Fe²⁺ and Fe³⁺. A number of methods are available for the quantitative determination of Fe²⁺ and Fe³⁺ in minerals (22-24). Some of these methods are quite tedious and difficult to carry out, or require expensive or specialized chemicals and equipment. Those which utilize the tris(1,10-phenanthroline)iron(II) complex (phen) or related phen derivatives, however, provide a wide array of advantages and few disadvantages (23). The phen method described by Komadel and Stucki (24), which is a revision of the method of Stucki (25), is the method of choice in the authors' laboratory. This method recognizes and utilizes the fact that two complexes are formed when phen is added to a system containing both Fe²⁺ and Fe³⁺: tris(1,10-phenanthroline)iron(II), which is red (absorbance maximum at about 510 nm); and tetrakis(1,10-phenanthroline)- μ -oxodiiron(III), which is colorless but reduces photochemically to the former in the presence of blue to ultra-violet light (26-27). Analyte solutions are kept in darkness or under dim red light from the time of sample digestion through spectroscopic measurement of the initial Fe²⁺ complex, then the analyte is exposed to Hg vapor light for 90 min and reanalyzed spectroscopically. The 90-min exposure photochemically reduces all of the tetrakis(1,10-phenanthroline)- μ -oxodiiron(III) complex to tris(1,10-phenanthroline)iron(II), which then gives the total Fe present in the sample. The amount of Fe³⁺ is calculated by difference or ratio. Hence, the method yields both Fe²⁺ and total Fe (and Fe³⁺ by difference) quantitatively in the same analyte solution.

Mössbauer spectroscopy may be used for semi-quantitative or qualitative determination of Fe²⁺/Fe³⁺ ratios. Table II shows that a rather good correlation exists between Mössbauer and chemical analysis for Fe²⁺/Fe³⁺ ratios in clay mineral samples, but these measurements must be obtained at lower temperatures (< 150 K) in order to maximize the recoil-free fractions of both valence states in the sample.

Effects of Oxidation State on Smectite Properties

Changes in the oxidation state of Fe in the octahedral sheets of clay minerals have a pronounced effect on the physical and chemical

Table II. Comparison of $\text{Fe}^{2+}:\text{Fe}^{3+}$ ratios in reduced ferruginous smectite (sample SWa-1 from the Source Clay Minerals Repository of The Clay Minerals Society) determined by Mössbauer spectroscopy at various temperatures and by chemical analysis using the method of Stucki (25) (taken from Table 9 of Reference 34)

Sample	Temperature (K)	$\text{Fe}^{2+}:\text{Fe}^{3+}$ Ratio	
		Mössbauer	Chemical Analysis
SWa-1 Reduced 1	120	34	
	150	33	
	200	33	
	250	25	
	296	24	35
SWa-1 Reduced 2	89	13	
	120	13	
	150	13	
	200	10	
	250	10	
	296	8	13

properties of the clay. The presence of octahedral Fe^{2+} decreases the swelling pressure and surface area (28-29; Lear, P. R., Stucki, J. W. *Clays Clay Miner.*, in press); increases layer charge, cation exchange capacity, and the number of occluded counterions (30-32; Lear, P. R., Stucki, J. W. *Clays Clay Miner.*, in press); converts the color from yellow to green, blue, light-blue, and ultimately light-gray (33; Komadel, P., Lear, P. R., Stucki, J. W. *Clays Clay Miner.*, in press); transforms the magnetic ordering from frustrated antiferromagnetic to well-behaved ferromagnetic (33-34); and causes a number of other modifications in clay crystal chemistry (Table III).

Surface Area and Interlayer Forces. Studies clearly show that octahedral Fe^{2+} causes smectite layers to collapse, and thus become less expandable with less available surface area. Wu *et al.* (Wu, J., Low, P. F., Roth, C. B. *Clays Clay Miner.*, in press) reported coexistent expanded (> 4.0 nm) and partially collapsed (1.6-1.9 nm) layers in reduced nontronite gels in equilibrium with various applied swelling pressures. These X-ray spectra (Figure 5) provide tangible evidence that Fe^{2+} alters swelling by modifying the relative numbers of collapsed vs. expanded layers. The unanswered question is whether some fully collapsed layers also exist, which can be addressed directly only by applying X-ray scattering theory to very pure spectra of wet clay gels (35; Pons, C. H., The University of Orleans, France, Personal Communication, 1988). But surface area measurements (Lear, P. R., Stucki, J. W. *Clays Clay Miner.*, in press) give clear, although indirect, evidence that some layers must be totally collapsed (Figures 6 and 7). The same study presented an hypothetical model system to estimate the possible fractions of collapsed, partially collapsed, and fully expanded layers required to account for the observed surface areas and water contents that occur with changes in oxidation state. The results show that even in the least reduced system, up to 20% of the layers may be collapsed. Layer collapse, therefore, accounts for the loss of swellability and surface area, as well as the increase in cation occlusion in the clay particles. The mechanism by which Fe^{2+} brings about layer collapse, however, has yet to be established.

The current hypothesis is that layer collapse depends uniquely on the crystal chemistry of Fe^{2+} in the octahedral sheet of the clay or on changes in crystal chemistry that accompany the process of Fe reduction. This hypothesis excludes the possibility that layer collapse occurs in response to an increased electrostatic charge on the clay layer due to the substitution of a divalent for a trivalent ion. Such exclusion is justified on the basis of observations by Mulla (36) that the surface area of smectites depends only on octahedral Fe^{2+} , tetrahedral Al, and interlayer K contents. Noticeably absent from this dependence is Mg^{2+} , which has the same valence and about the same size as Fe^{2+} , but has no apparent influence on surface area.

Optical Spectra. The optical properties of smectites have been studied by various workers (32,37-40), and involve several different types of electronic transitions. One important type of transition is the intervalence charge transfer (IT), which is observed in the optical spectra of minerals containing both Fe^{2+} and Fe^{3+} in their

Table III. Effects of structural Fe on smectite properties

Property	Change in Property Due to*			References [‡]
	Fe ³⁺		Fe ²⁺	
	Octa	Tetra	Octa	
	Di octahedral			
Layer Charge/ Cation Exchange Capacity	0	+	+	31, 55-58
Swelling in Water	-	?	-	28-29, 59
Crystallographic b-dimension	+	+	+	4, 56-58, 60-65
Surface Area	?	?	-	29, 36
Color	yellow brown	?	blue, green blue-grey	4, 33, 49, 66-68 19, 48
Chemical and Thermal Stability	-	-	-	17, 19, 31, 46, 48, 53-55, 57-58, 61, 69-76
	Tri octahedral			
Surface Charge/ Cation Exchange Capacity	0	+	+	56
Crystallographic b-dimension	+	+	+	56, 58, 60, 62, 63, 65, 77-76
Color	yellow brown	?	green blue	56, 67-68, 75, 80-81
Chemical and Thermal Stability	-	?	+	54, 58, 82-83

*Symbols signify positive (+), negative (-), unknown (?), and no (0) correlation between the property and Fe²⁺.

[‡]Numbers correspond to those in Literature Cited.

SOURCE: Adapted from ref. 11.

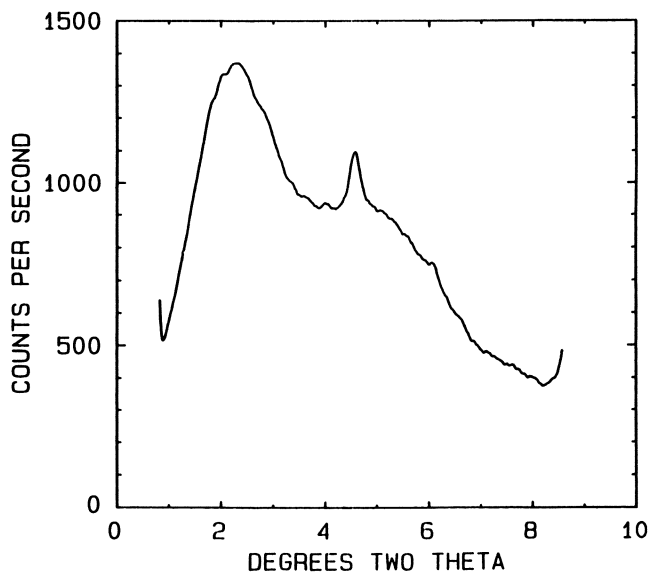


Figure 5. X-ray diffractogram of reduced Na-nontronite (sample API H-33a from Wards Natural Science Establishment, Rochester, New York) when $\text{Fe}^{2+}/\text{Fe}^{3+} = 0.64$ and $\Pi = 5$ atm. (Reproduced with permission from Wu, J.; Low, P. F.; Roth, C. B. *Clays Clay Miner.* in press. Copyright 1989 The Clay Minerals Society).

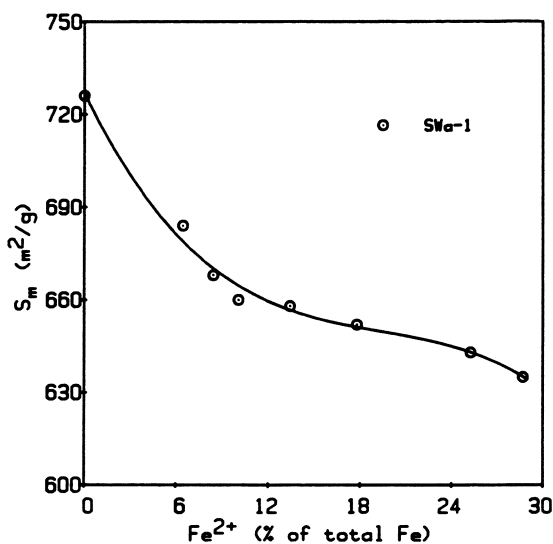


Figure 6. Observed relationship between specific surface area (S_m) and Fe^{2+} content of a chemically reduced series of ferruginous smectite (sample SWa-1 from the Source Clay Minerals Repository of The Clay Minerals Society). (Reproduced with permission from Lear, P. R.; Stucki, J. W., *Clays Clay Miner.* in press. Copyright 1989 The Clay Minerals Society).

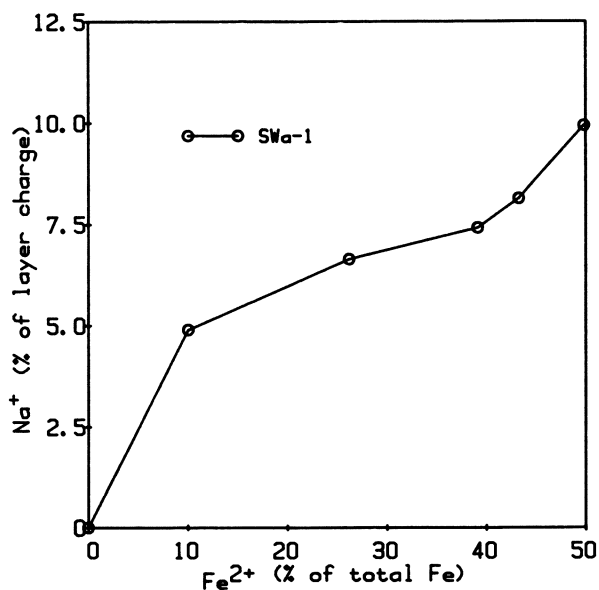


Figure 7. Relationship between non-exchangeable Na⁺, expressed as % of layer charge, and Fe²⁺ content of ferruginous smectite (sample SWa-1 from the Source Clay Minerals Repository of The Clay Minerals Society). (Reproduced with permission from Lear, P. R.; Stucki, J. W., *Clays Clay Miner.* in press. Copyright 1989 The Clay Minerals Society).

crystal structures (37). Such IT transitions occur via vibronic coupling of the two states ($\text{Fe}^{2+}\text{Fe}^{3+}$) and ($\text{Fe}^{3+}\text{Fe}^{2+}$). Vibronic coupling may be described simply as the overlap between the vibrational potential energy wells of the two mixed-valent Fe states, as illustrated by the vibrational potential energy diagram presented in Figure 8 for electron transfer in one of the normal modes of a symmetric system. The particular normal mode of the potential energy wells shown is intended to represent the symmetric breathing mode associated with the Fe-O bond at a given Fe center. The electron transfer between Fe centers occurs via the vibrationally excited state (B^*) rather than through an electronically excited state. The ground state energy for the ($\text{Fe}^{2+}\text{Fe}^{3+}$) state is the same as for ($\text{Fe}^{3+}\text{Fe}^{2+}$). The energy required for the optical excitation transition ($E_{\text{op}} = E_B^* - E_A$) depends on the equilibrium displacement of the two potential energy curves. This displacement is referred to as the vibronic coupling parameter, λ . The point of intersection, E_B , on the potential energy curves defines the classical energy of activation for thermal electron transfer.

The IT transition in reduced SWa-1 nontronite is observed as a broad band centered near 730 nm ($13,700 \text{ cm}^{-1}$), which increases in intensity as the Fe^{2+} content approaches 40% of the total Fe (Figure 9). Lear and Stucki (33) used computer simulations to relate this behavior to the number of $\text{Fe}^{2+}\text{-O-Fe}^{3+}$ linkages present in the structure as a function of the Fe^{2+} content. At very high levels of reduction, the intensity of the IT transition decreases and finally almost disappears due to the formation of $\text{Fe}^{2+}\text{-O-Fe}^{2+}$ linkages at the expense of the $\text{Fe}^{2+}\text{-O-Fe}^{3+}$ linkages, which produce the IT transition (Figure 10).

This ability to shuttle electrons between Fe centers may lead to the use of reduced Fe-rich smectites in reactions requiring electron donors and receptors, such as oxidative catalysis or electrochemical transformations.

Magnetic Ordering and Mössbauer Spectra. In phyllosilicates, magnetic ordering occurs because of the presence of paramagnetic ions in the crystal structure, mainly high spin Fe^{3+} and Fe^{2+} which have atomic magnetic moments. The type of exchange coupling of magnetic moments between cations on adjacent sites determines whether the moments are aligned parallel (ferromagnetic) or antiparallel (antiferromagnetic). In oxides and clays, the $\text{Fe}^{2+}\text{-O-Fe}^{2+}$ exchange interactions are ferromagnetic and $\text{Fe}^{3+}\text{-O-Fe}^{3+}$ exchange interactions are antiferromagnetic. For mixed valence $\text{Fe}^{2+}\text{-O-Fe}^{3+}$ pairs, the magnetic coupling is ferromagnetic and may be due to double exchange (Figure 11).

Magnetization measurements on a series of nontronites, which contain almost exclusively $\text{Fe}^{3+}\text{-O-Fe}^{3+}$ interactions, indicate that antiferromagnetic exchange coupling occurs between Fe^{3+} centers and that the Curie-Weiss temperature, which approximates the temperature at which long-range magnetic ordering occurs, ranges from 80 to 20 K (Lear, P. R.; Stucki, J. W., unpublished data). However, long-range magnetic order is absent from these nontronite samples because of magnetic frustration, which probably occurs because of the presence of Fe^{3+} in both *cis* and *trans* octahedral sites.

For a series of reduced SWa-1 nontronite samples, the introduc-

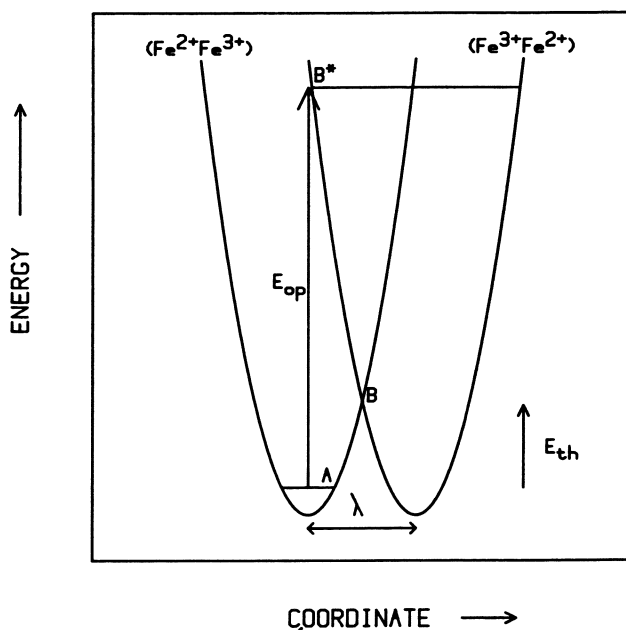


Figure 8. Vibrational potential energy vs. configurational coordinate for electron transfer via vibronic coupling between two symmetric states of a single oscillator. A, initial state; B*, vibrationally excited state; B, thermally excited state; λ , vibronic coupling parameter; E_{op} , optical transition energy; E_{th} , thermal transition energy. (Reproduced with permission from Ref. 33. Copyright 1987 The Clay Minerals Society).

American Chemical Society
Library

1155 16th St., N.W.

In Spectroscopic Characterization of Minerals and Their Surfaces; Coyne, L., et al.; ACS Symposium Series 400; American Chemical Society: Washington, DC, 1990.

Washington, DC, 20036

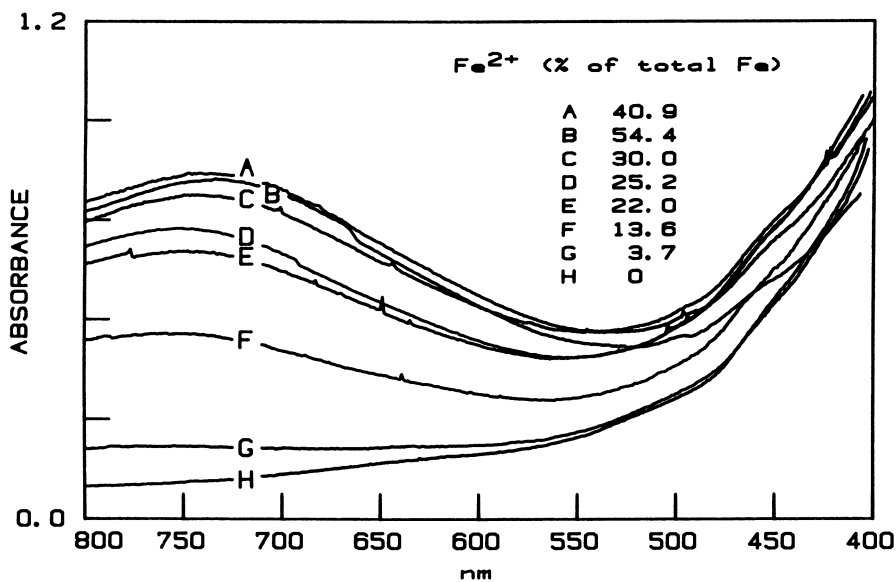


Figure 9. Visible absorption spectra of suspensions of reduced and unaltered ferruginous smectite (sample SWa-1 from the Source Clay Minerals Repository of The Clay Minerals Society) (2.2 mg clay/mL). Inset reports Fe²⁺ content as % of total Fe. (Reproduced with permission from Ref. 33. Copyright 1987 The Clay Minerals Society).

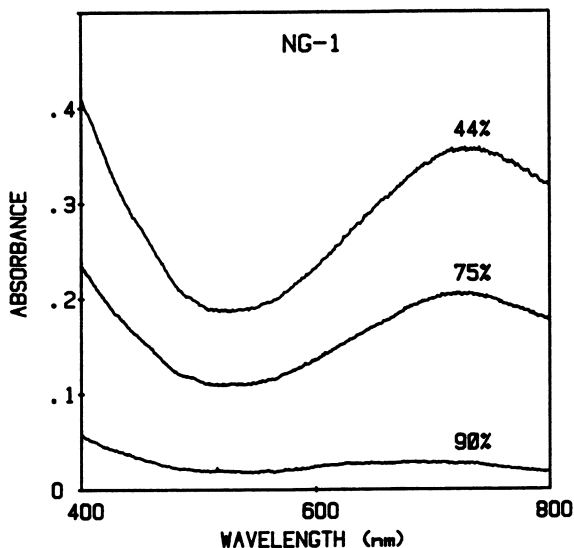


Figure 10. Visible absorption spectra of highly reduced Hohen Hagen nontronite (sample NG-1 from the Source Clay Minerals Repository of The Clay Minerals Society) suspensions (2.2 mg clay/mL). Numbers aside curves indicate Fe^{2+} content as % of total Fe. (Reproduced with permission from Komadel, P.; Lear, P. R.; Stucki, J. W. *Clays Clay Miner.* in press. Copyright 1989 The Clay Minerals Society).

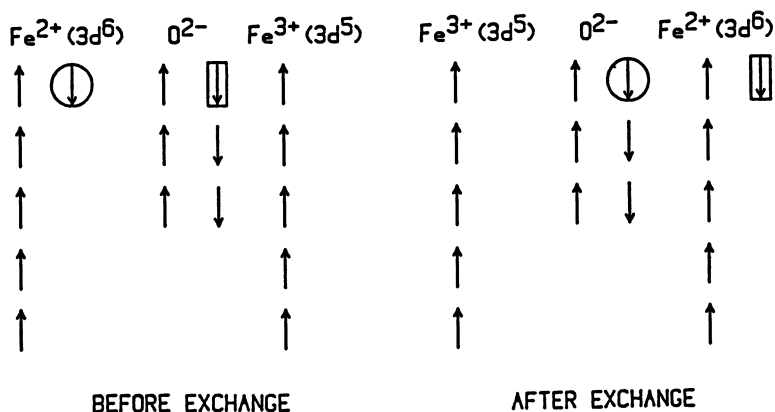


Figure 11. Proposed mechanism to account for ferromagnetic coupling in mixed-valent nontronite. Exchanged electrons are indicated by enclosure in either a circle or rectangle. (Reproduced with permission from Ref. 33. Copyright 1987 The Clay Minerals Society).

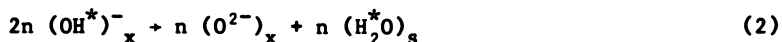
tion of Fe^{2+} changes the bulk magnetic ordering from antiferromagnetic to ferromagnetic as more $\text{Fe}^{2+}\text{-O-Fe}^{3+}$ and $\text{Fe}^{2+}\text{-O-Fe}^{2+}$ interactions are formed (Figure 12). Interestingly, in the slightly reduced samples (C and D, Figure 12), which are dominated by $\text{Fe}^{3+}\text{-O-Fe}^{3+}$ interactions with only small domains of $\text{Fe}^{2+}\text{-O-Fe}^{3+}$, the ferromagnetic component is sufficiently prominent to produce a positive ordering temperature. The moderately reduced samples (E and F, Figure 12) are dominated by $\text{Fe}^{2+}\text{-O-Fe}^{3+}$ moieties and show what appears to be long-range ferromagnetic ordering. At higher levels of reduction (G and H, Figure 12), an additional ferromagnetic component may be present due to the formation of $\text{Fe}^{2+}\text{-O-Fe}^{2+}$ interactions.

The Mössbauer spectra of reduced nontronite samples show the presence of both Fe^{2+} and Fe^{3+} and may give semi-quantitative results as stated above. As the extent of reduction increases, the area associated with Fe^{2+} increases at the expense of that associated with Fe^{3+} (Figures 13 and 14). Using two Fe^{3+} doublets to fit the spectra of unaltered SWa-1, Lear (34) postulated that the reduction of Fe^{3+} to Fe^{2+} occurs predominately at one of the two Fe^{3+} sites. Interpretations of Mössbauer spectra is always speculative, however, because results from the computer-fitting used to analyze the data may represent only one of many possible solutions, and unavoidably reflect operator bias.

Reversibility of the Redox Process. The extent of reversibility upon reoxidation of the chemical and physical changes which occur during reduction depends on the reducing agent used and how it was employed. The reversibility of the reduction reaction has mostly been studied using Mössbauer or IR spectroscopy. Roth and Tullock (41), Russell *et al.* (19), and Lear (34) suggested that the reduction process was largely reversible. Rozenon and Heller-Kallai (16) stated that the reduction process was only reversible for Al-OH-Fe groups, but not for Fe-OH-Fe groups, though their samples were reoxidized with H_2O_2 .

Redox Mechanisms

Accurate characterization of the mechanism for Fe reduction is fundamental to understanding the relationships between oxidation state and physical-chemical properties. Lear and Stucki (30) proposed that the reduction process for Fe in smectites obeys the following general reactions:



where x and s denote clay and solution phases, respectively; m and n are stoichiometry coefficients which depend on the clay; and * identifies protons initially part of the clay mineral structure. Equation 1 represents the transfer of an electron from the reducing agent to structural Fe^{3+} , and Equations 2 and 3 represent the condensation of structural OH^- to form a water molecule, which then diffuses into solution. The structural oxide is reprotonated by H^+ from solution.

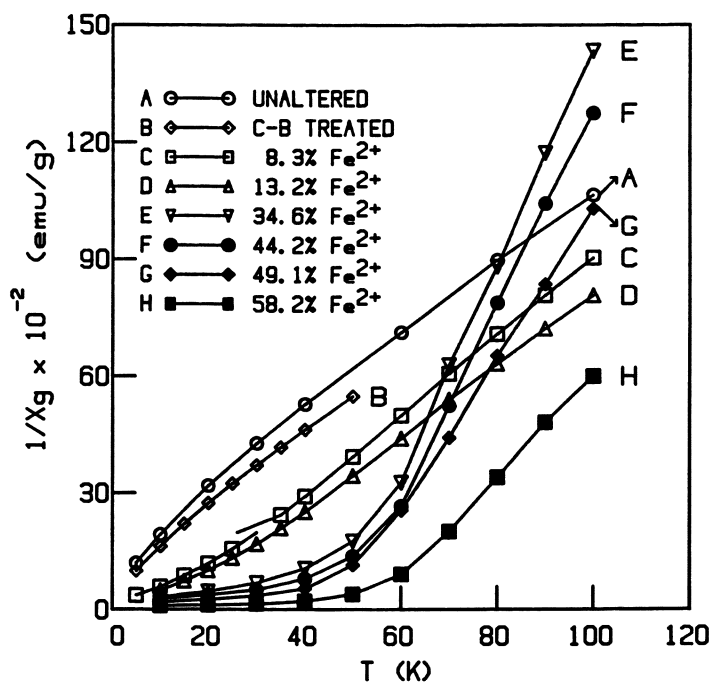


Figure 12. Inverse magnetic susceptibility ($1/\chi$) vs. temperature (T) at 0.1 Tesla of reduced and unaltered powders of ferruginous smectite (sample SWa-1 from the Source Clay Minerals Repository of The Clay Minerals Society). Insert reports Fe^{2+} contents as % of total Fe. (Reproduced with permission from Ref. 33. Copyright 1987 The Clay Minerals Society).

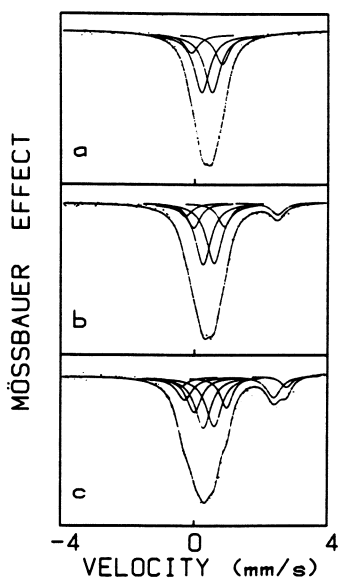


Figure 13. Mössbauer spectra of (a) unaltered, (b) slightly reduced ($\text{Fe}^{2+} = 13\%$ of total Fe), and (c) moderately reduced ($\text{Fe}^{2+} = 34\%$ of total Fe) ferruginous smectite (sample SWa-1 from the Source Clay Minerals Repository of The Clay Minerals Society) at 120 K. (Adapted from Ref. 34.)

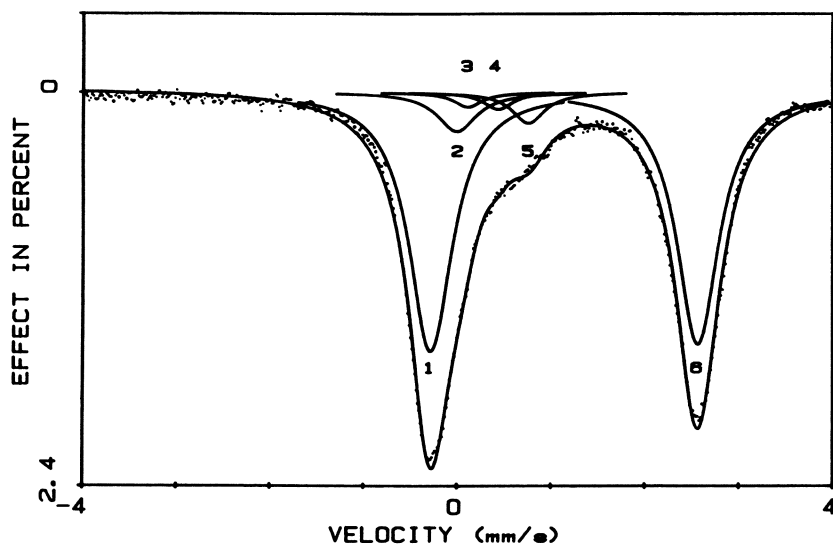


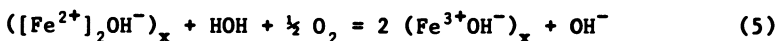
Figure 14. Mössbauer spectra of highly reduced ($\text{Fe}^{2+} = 86\%$ of total Fe) Hohen Hagen nontronite (sample NG-1 from the Source Clay Minerals Repository of The Clay Minerals Society) at 120 K. (Reproduced with permission from Komadel, P.; Lear, P. R.; Stucki, J. W. *Clays Clay Miner.* in press. Copyright 1989 The Clay Minerals Society).

The accompanying change in layer charge should, then, be calculable from the general relation

$$v = v_0 + k(1 - n/m) \Delta Fe^{2+} \quad (4)$$

where ΔFe^{2+} is the difference between the observed and initial Fe^{2+} concentrations in the clay; v and v_0 are the observed and initial values for layer charge; and k is a constant which converts the units of change in oxidation state to units of v . If v is expressed in meq/g, and if ΔFe^{2+} is in mmole/g and represents a one-electron change in oxidation state, for example, then $k = 1$ meq/mmole.

Reoxidation occurs essentially by rehydration, viz.,



where the defect site (which was occupied by OH^- prior to reduction) is first hydrated with HOH but rapidly loses the extra H^+ (42).

If the only reaction occurring during reduction were the electron transfer to structural Fe^{3+} , one would find a linear 1:1 relationship between Fe^{2+} content and layer charge (curve A, Figure 15). Studies by Stucki and Roth (30) and Stucki *et al.* (31) show, however, that the layer charge increases much more slowly than predicted by Equation 1 (curve C, Figure 15), and follows the best-fit polynomials reported in Table IV.

The dehydroxylation process represented by Equations 2 and 3, with the accompanying loss of negative charge, compensates a fraction of the increased negative charge due to Equation 1. Assuming that Equations 2 and 3 are an accurate description of the role of H^+ in the reduction mechanism, Lear and Stucki (32) concluded from tritium exchange experiments that $n = 0.32$ m for nontronite SWa-1, from which the predicted layer charge is then given by the reduced form of Equation 4, viz.,

$$v = v_0 + 0.68 k \Delta Fe^{2+}. \quad (6)$$

This equation is plotted as curve B in Figure 15. While Equation 6 brings the predicted line closer to the observed curve, a significant difference in form and magnitude still exists between the predicted and observed layer charge for sample SWa-1 (Table IV).

At least two possible explanations exist for this discrepancy. The first possibility is that Equations 2 and 3 are incorrect and the mobility of H^+ during reduction and reoxidation is due to some other process. In other words, the movement of H^+ into and out of the clay structure may not represent a dehydroxylation-rehydration process. While no other process has been conceived which is consistent with all of the observations, no direct evidence exists to explicitly validate the movement of hydroxyl oxygen into and out of the clay structure.

An alternative explanation is that the proposed reactions are valid but provide an incomplete picture of the reduction process. The actual mechanism may contain additional reactions or species to those given by Equations 1-3. Notably, reaction components which reduce structural Fe without increasing layer charge must be incorporated. The following reaction is proposed as a possible replace-

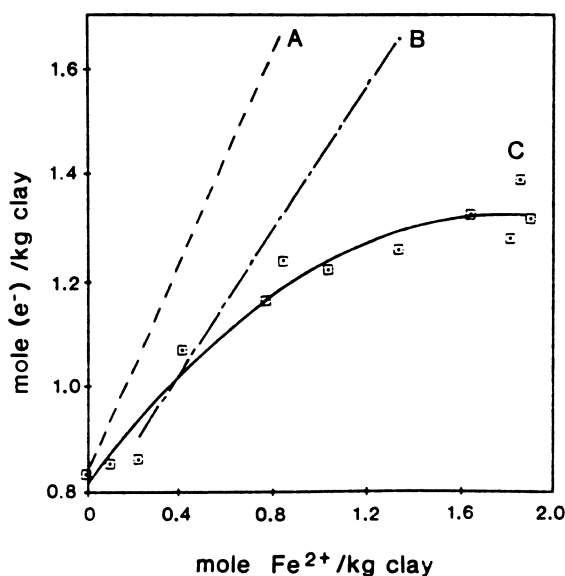


Figure 15. Layer charge of ferruginous smectite (sample SWa-1 from the Source Clay Minerals Repository of The Clay Minerals Society). (A) Predicted by Equation 1; (B) Predicted by Equation 6; (C) observed. (Reproduced with permission from Ref. 32. Copyright 1985 The Clay Minerals Society).

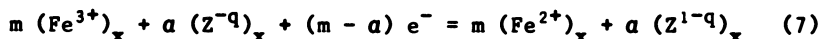
Table IV. Coefficients for the best-fit polynomials describing the observed functional relationships between layer charge and Fe^{2+} content of smectites (31,42). Polynomial form:

$$v = c_0 + c_1 [\text{Fe}^{2+}] + c_2 [\text{Fe}^{2+}]^2$$

Smectite [‡]	c_0	c_1	c_2
UPM	0.830	1.648	-1.979
CZM	0.493	0.802	-0.903
NZM	0.797	0.544	-0.403
GAN	1.042	0.703	-0.242
SWa-1	0.813	0.580	-0.165

[‡]Same samples as used by Stucki *et al.* (29) and Lear and Stucki (32). UPM=Upton (API 25) montmorillonite; CZM=Czechoslovakia #650 montmorillonite; NZM=New Zealand montmorillonite; GAN=Garfield (API H-33a) nontronite; SWa-1=ferruginous smectite (Source Clay Minerals Repository, The Clay Minerals Society).

ment of Equation 1:



where $(\text{Z}^{-q})_{\text{x}}$ represents an electron donor source somewhere within the clay crystal which gives up an electron to form $(\text{Z}^{1-q})_{\text{x}} + (e^{-})_{\text{x}}$, and a and $m - a$ are the corresponding stoichiometry coefficients. The electron, in turn, finds a pathway to a structural Fe site and brings about reduction. The net result of this aspect of the reaction is an increase in Fe^{2+} content with no increase in layer charge because, in effect, self-reduction of the clay has occurred. For nontronite SWa-1, the value of a may therefore be given as a function of ΔFe^{2+} by

$$a = (0.68 - c_1/k) - (c_2/k) \Delta\text{Fe}^{2+} \quad (8)$$

where c_1 and c_2 are obtained from Table IV. The corresponding relationship with v would become

$$v = v_0 + k (0.68 - a) \Delta\text{Fe}^{2+} \quad (9)$$

Notice that the polynomials in Table IV predict that the layer charge increases initially, but eventually will decrease as the Fe^{2+} content becomes sufficiently large. This exact phenomenon was observed by Stucki *et al.* (31) in Garfield nontronite. Hence, at high levels of reduction, electrons must begin to flow in the opposite direction, i.e., the clay becomes an electron donor rather than an acceptor, while continuing to increase the level of Fe^{2+} in the octahedral sheet.

One can only speculate as to the exact identity of the Z^{-q} or Z^{1-q} species, but the presence or formation of $(\text{O}^{-})_{\text{x}} + (e^{-})_{\text{x}}$ centers in the clay structure should be investigated. Ideas advanced by Coyne (43) and Freund and Batllo (44) regarding (O^{-}) and (O_2^{2-}) centers in clay minerals could, therefore, play an important part in the development of a complete understanding of the Fe reduction mechanisms in smectites.

Literature Cited

1. Bailey, S. W. *Clays Clay Miner.* 1980, **28**, p 73-8.
2. Osthau, B. B. *In Clays and Clay Minerals*; Swineford, A.; Plummer, N., Eds.; *Proc. 2nd Natl. Conf.*, Columbia, Missouri, 1953. *Natl. Acad. Sci. Natl. Res. Council. Publ.*, 327, Washington, D.C., 1954; p 404-17.
3. Goodman, B. A.; Russell, J. D.; Fraser, A. R.; Woodhams, F. W. *D. Clays Clay Miner.* 1976, **24**, 53-9.
4. Eggleton, R. A. *Clay Miner.* 1977, **12**, 181-94.
5. Besson, G.; de la Calle, C.; Rautureau, M.; Tchoubar, C.; Tsipurski, S. I.; Dritz, V. A. *Proc. Int. Clay Conf., Bologna and Pavia, 1981, 1982*, p 29-40.
6. Besson, G.; Booking, A. S.; Dainyak, L. G.; Rautureau, M.; Tsipurski, S. I.; Tchoubar, C.; Dritz, V. A. *J. Appl. Cryst.* 1983, **16**, p 374-83.
7. Cardile, C. M. *Clays Clay Miner.* 1989, **37**, 185-8.
8. Burlamacchi, L.; Guarini, G.; Tiezzi, E. *Trans. Faraday Soc.* 1969, **65**, 496-502.

9. Stucki, J. W.; Golden, D. C.; Roth, C. B. Clays Clay Miner. 1984, 32, 191-7.
10. Mehra, O. P.; Jackson, M. L. In Clays and Clay Minerals; Swineford, A., Ed.; Proc. 7th Natl. Conf., Washington, D.C., 1958. Pergamon Press: New York, 1960; p 317-27.
11. Stucki, J. W. In Iron in Soils and Clay Minerals; Stucki, J. W.; Goodman, B. A.; Schwertmann, U., Eds.; D. Reidel, Dordrecht, 1988; p 625-75.
12. Stucki, J. W.; Komadel, P.; Wilkinson, H. T. Soil Sci. Soc. Am. J. 1987, 51, 1663-5.
13. Stucki, J. W.; Komadel, P.; Wilkinson, H. T. In Proc. Sixth Meeting; European Clay Groups. 1987; p 322-4.
14. Fischer, W. R. In Iron in Soils and Clay Minerals. D. Reidel: Dordrecht, 1988; p. 715-48.
15. Wu, J.; Roth, C. B.; Low, P. F. Soil Sci. Soc. Am. J. 1988, 52, 295-6.
16. Rozenson, I.; Heller-Kallai, L. Clays Clay Miner. 1976, 24, 271-82.
17. Stucki, J. W.; Roth, C. B. Clays Clay Miner. 1976, 24, 293-6.
18. Stucki, J. W.; Roth, C. B.; Baitinger, W. E. Clays Clay Miner. 1976, 24, 289-92.
19. Russell, J. D.; Goodman, B. A.; Fraser, A. R. Clays Clay Miner. 1979, 27, 63-71.
20. Chen, S. Z.; Low, P. F.; Roth, C. B. Soil Sci. Soc. Am. J. 1987, 51, 82-6.
21. Tessier, D. Ph.D. Thesis, University of Paris, France, 1984.
22. Loveland, P. J. In Iron in Soils and Clay Minerals. Stucki, J. W.; Goodman, B. A.; Schwertmann, U., Eds.; D. Reidel: Dordrecht, 1988; p 99-140.
23. Clemency, C. V.; Hagner, A. F. Anal. Chem. 1961, 33, 888-92.
24. Komadel, P.; Stucki, J. W. Clays Clay Miner. 1988, 36, 379-81.
25. Stucki, J. W. Soil Sci. Soc. Am. J. 1981, 45, 638-41.
26. Wehry, E. L.; Ward, R. A. Inorg. Chem. 1971, 10, 2660-4.
27. David, P. G.; Richardson, J. G.; Wehry, E. L. J. Inorg. Nucl. Chem. 1972, 34, 1333-46.
28. Foster, M. D. Am. Mineral. 1953, 38, 994-1006.
29. Stucki, J. W.; Low, P. F.; Roth, C. B.; Golden, D. C. Clays Clay Miner. 1984, 32, 357-62.
30. Stucki, J. W.; Roth, C. B. Soil Sci. Soc. Am. J. 1977, 41, 808-14.
31. Stucki, J. W.; Golden, D. C.; Roth, C. B. Clays Clay Miner. 1984, 32, 350-6.
32. Lear, P. R.; Stucki, J. W. Clays Clay Miner. 1985, 33, 539-45.
33. Lear, P. R.; Stucki, J. W. Clays Clay Miner. 1987, 35, 373-8.
34. Lear, P. R. Ph.D. Thesis, University of Illinois, Urbana, IL, 1987.
35. Ben Rhaïem, H.; Pons, C. H. Clay Miner. 1984, 19, p 257-60.
36. Mulla, D. J. Ph.D. Thesis, Purdue University, 1983.
37. Hush, N. S. In Progress in Inorganic Chemistry; Cotton, F. A., Ed.; Interscience: New York, 1967; Part I, p 357-98.
38. Karickhoff, S. W.; Bailey, G. W. Clays Clay Miner. 1973, 21, 59-70.
39. Sherman, D. M.; Vergo, N. Am. Mineral. 1988, 73, 1346-54.

40. Sherman, D. M. Chapter 15, This Volume.
41. Roth, C. B.; Tullock, R. J. In Proc. Int. Clay Conf., Madrid, 1972; Serratos, J. M., Ed.; Div. Ciencias C.S.I.C.: Madrid, 1973; p 107-14.
42. Lear, P. R. M.S. Thesis, University of Illinois, Urbana, IL, 1984.
43. Coyne, L. Origins of Life 1985, 15, p 161-207.
44. Freund, F.; Batllo, F. Chapter 16, This Volume.
45. Anderson, W. L.; Stucki, J. W. Proc. Int. Clay Conf., Oxford, 1978, 1979, p 75-83.
46. Ericsson, T.; Linares, J.; Lotse, E. Clay Miner. 1984, 19, 85-91.
47. Chen, Y.; Shaked, D.; Banin, A. Clay Miner. 1979, 14, 93-102.
48. Rozenson, I.; Heller-Kallai, L. Clays Clay Miner. 1976, 24, 283-8.
49. Kawasaki, H. Nippon Dojo Hiriyogaku Zasshi 1974, 45, 318-20.
50. Tennakoon, D. T. B.; Thomas, J. M.; Tricker, M. J. J. Chem. Soc. (Dalton Trans.). 1974, 1974, 2207-11.
51. McBride, M. B. Clays Clay Miner. 1979, 27, 224-30.
52. Addison, W. E.; Sharp, J. H. Clays Clay Miner. 1963, 11, 95-104.
53. Malathi, N.; Puri, S. P.; Saraswat, I. P. J. Phys. Soc. Jap. 1971, 31, 117-22.
54. Drago, V.; Saitovitch, E. B.; Danon, J. Inorg. Nucl. Chem. 1977, 39, 973-9.
55. Aronowitz, S.; Coyne, L.; Lawless, J.; Rishpon, J. Inorg Chem. 1982, 21, 2589-93.
56. Bischoff, J. L. Clays Clay Miner. 1972, 20, p 217-23.
57. Brigatti, M. F. Clay Miner. 1983, 18, p 177-86.
58. Brindley, G. W.; MacEwan, D. M. C. In Ceramics: A Symposium. The British Ceramic Society, London. 1953, p 15-99.
59. Egashira, K.; Ohtsubo, M. Geoderma. 1983, 29, 119-27.
60. Despraires, A. Clay Miner. 1983, 18, 165-75.
61. Heller-Kallai, L.; Rozenson, I. Clays Clay Miner. 1980, 28, 355-68.
62. Radoslovich, E. W. Am. Mineral. 1962, 47, 617-36.
63. Ross, C. S.; Hendricks, S. B. U.S. Geol. Surv. 1945, Profess. Paper 205b, 23-79.
64. Russell, J. D.; Clark, D. R. Clay Miner. 1978, 13, 133-8.
65. Smillie, G. W.; Curtin, D. Clays Clay Miner. 1981, 29, 277-84.
66. Bart, J. C.; Burriesci, N.; Cariati, F.; Micera, G.; Gessa, C. Clays Clay Miner. 1980, 28, p 233-6.
67. Bosio, N. J.; Hurst, V. J.; Smith, R. L. Clays Clay Miner. 1975, 23, p 400-3.
68. Craw, D. Lithos. 1981, 14, 49-57.
69. Bahranowski, K.; Dubiel, S.; Stoch, L. Mineral. Pol. 1981, 12, p 3-14.
70. Heller, L.; Farmer, V. C.; Mackenzie, R. C.; Mitchell, B. D.; Taylor, H. F. W. Clay Miner. Bull. 1962, 5, 56-72.
71. Lindquist, B.; Jansson, S. Am. Mineral. 1962, 47, 1356-62.
72. MacKenzie, K. J. D.; Rogers, D. E. Thermochim. Acta. 1977, 18, 177-96.
73. McBride, M. B.; Mortland, M. M. Soil Sci. Soc. Am. Proc. 1974, 38, 438-15.

74. Novák, I.; and Cícel, B. Clays Clay Miner. 1978, 26, 341-4.
75. Poppi, L.; Brigatti, M. F. Miner. Petrogr. Acta. 1976, 21, 43-52.
76. Sudo, T.; Nakamura, T. Am. Mineral. 1952, 37, 618-21.
77. Banks, H. H. Smithson. Contrib. Earth Science 1972, 9 p 39-42.
78. Kohyama, N.; Shimoda, S.; Sudo, T. Clays Clay Miner. 1973, 21, 229-37.
79. Suquet, H.; Malard, C.; Copin, E.; Pezerat, H. Clay Miner. 1981, 16, 53-67.
80. Craw, D. Clay Miner. 1984, 19, 509-20.
81. Harder, H. Clays Clay Miner. 1978, 26, 65-72.
82. Borggaard, O. K.; Lindgreen, H. B.; Mørup, S. Clays Clay Miner. 1982, 30, p 353-63.
83. Farmer, V. C.; Russell, J. D.; McHardy, W. J.; Newman, A. C. D.; Ahlrichs, J. L.; Rimsaite, J. Y. H. Mineral. Mag. 1971, 38, 121-37.

RECEIVED September 21, 1989

Chapter 18

Surface Activities of Clays

Jose J. Fripiat

Department of Chemistry and Laboratory for Surface Studies,
University of Wisconsin—Milwaukee, Milwaukee, WI 53201

Clays, and especially swelling clays, are made from anisotropic microcrystals displaying large specific surface areas. However, because these microcrystals have a strong tendency to aggregate into tactoids, only a fraction of the surface area is available for surface reactions.

Therefore, not only the nature of the surface active sites, as related to the structure, but their availability, as related to the particular texture are discussed as well. The relationship between these two aspects of clay surface reactivity is more heavily emphasized here than is the specific chemistry of reactions occurring on the surface of clays.

The hydration water in the interlamellar space is acidic and, therefore, able to work as an acid catalyst. The nature of the acid sites is discussed with respect to the origin of the lattice charge (tetrahedral or octahedral). The mechanism of cross-linking smectites with oligomeric inorganic cations shed light on the reactivity of the basal planes as well.

In addition to acid catalyzed reactions, this paper deals with charge and/or energy transfer reactions between adsorbed species and the lattice, or between co-adsorbed species. Reduction of lattice iron(III), as well as luminescence quenching of $\text{Ru}(\text{bpy})_3^{2+}$, photoaquation of $\text{Cr}(\text{bpy})_3^{3+}$ and photooxidation of water, are examples chosen for illustrating this aspect of the reactivity of clays.

Among the minerals found in the earth's crust, those belonging to the phyllosilicate family, namely the clays, are especially interesting from the point of view of their surface activity. Being finely divided, their specific surface area is large. Their

0097-6156/90/0415-0360\$06.00/0
© 1990 American Chemical Society

lattices contain a large number of defects generating surface active sites of various kinds. The microcrystals are anisotropic and their morphologies are quite diverse, being thin extended sheets, lathes or fibers.

This review paper will deal exclusively with clay minerals (1). Other minerals occurring in nature, such as aluminum or iron oxides which are very often associated intimately with clays, also display large surface areas. They will be ignored here, in spite of the fact that their surface activity can not be neglected. In addition, the review will cover the domain familiar to the author.

The lattices of clay minerals have a common feature: they contain continuous planes made from oxygen atoms linked to cations (silicon or aluminum) in tetrahedral coordination and to cations (such as magnesium, aluminum, lithium, or iron) in octahedral coordination. Because of isomorphic substitutions, for instance Si^{4+} by Al^{3+} in tetrahedral coordination, the overall charge of these lattices is negative. At the edges of the sheets dangling bonds may generate a positive charge, according to the pH of the surrounding medium. Because the overall charge is negative, the electro-neutrality is obtained by the adsorption of cations, such as Na^+ , K^+ , Ca^{2+} , etc. which are, in most cases, exchangeable. It is commonly accepted that isomorphic substitutions in the tetrahedral layer give rise to negative charges localized near the substitutions, whereas isomorphic substitutions within the octahedral layer yield negative charges smeared out on the surface of individual sheets. These intuitive ideas have recently received support from theoretical calculations by Bleam and Hoffman.(2) Note that the negative charges arising from isomorphic substitutions are permanent charges, independent of the pH.

In summary, there are two kinds of charges, namely those which are pH independent and those which are pH dependent. The latter may be either positive or negative, depending on the value of the isoelectric point (3). The former are negative and either localized or delocalized.

One more source of complexity comes from the fact that the lattice generally contains cations with several degrees of oxidation. Iron is the most common example. Therefore, charge transfer may occur between adsorbed species and some lattice sites. Vacancies in the lattice may play a similar role.

It must be recognized that the description of the average chemical formulae by the chemical analysis of clay minerals is not a simple matter. Sheets of the same clay from the same deposit are likely to be heterogeneous with respect to composition and distribution of lattice elements. The charge distribution, as a consequence, is heterogeneous as well.

The colloidal chemistry of very diluted clay suspensions is usually described by the double layer theory (3). In more concentrated suspensions or thick pastes, where the average distance between sheets is shorter, the Van der Waals forces have to be considered. The combination of all these effects influences the distribution of the individual sheets and, thus, the viscosity of the slurry. From the viewpoint of this review, these spatial distributions of the individual sheets affect the availability of the surface area with the important consequence that the surface area is no longer an extensive property of the material. Disordered

materials of this nature can, eventually, be described in terms of fractals. The fundamentals of the fractal theory and of its applications to disordered solids are developed in (4). Reviewing this interesting aspect here would be outside the scope of this review.

The Tactoid Concept

It has been taught in the past that smectites, and especially Na^+ or Li^+ smectites, could be dispersed completely into individual elementary sheets in very dilute suspensions and in media of very low ionic strength. Under these restricted conditions this complete dispersion may occur, but in most cases, and, for instance, in a suspension containing more than 0.01% w/w solid in water, it seems highly probable that some aggregation "face to face" occurs, forming tactoids (5). The aggregation process does not produce perfect stacks, but irregularly shaped particles as represented in Figure 1, from (6).

If such an image is magnified, the sheets represented in close contact are, in fact, separated by a few monolayers of water corresponding to what we shall call an irreducible distance d . If the sheets are ideally parallel when at this distance, X ray diffraction will yield a reflection with basal spacing $(d + D)$ where D is the sheet thickness. In the tactoid shown in Figure 1, the fraction of the surface area of the layers at distance d is 50% of the total area. Let us call this fraction a ; in Figure 1, $a = 0.5$. The $(1-a)$ fraction of the surface area encloses columns of voids, eventually filled with water, with heights larger than d . Therefore, reflections at larger spacings can be detected by small angle X-ray scattering (SAXS), if sufficient ordering is achieved.

In addition, a tactoid containing n sheets in such a disordered state is separated from an adjacent tactoid containing n' sheets by inter-tactoid pores. If two adjacent tactoids are tilted with respect to one another, very complicated architecture may exist within the suspension. The description of such architectures should be performed in terms of correlation functions relating the spaces occupied by solids or by voids. Such an analysis is difficult for anisotropic objects.

Any information on these architectures would be, however, worthwhile because the availability of the surface is ruled to a large extent by the size of the tactoids, and by their mutual arrangements.

Water Associated with the External Contour of Tactoids. The existence of tactoids can be evidenced by studying the longitudinal relaxation time of the nuclear magnetic resonance of ^1H or ^2H in aqueous slurries (7-8). In simple terms, the relaxation rate, e.g. the inverse of the relaxation time, is the sum of three terms

$$T_1^{-1} = x_a T_{1a}^{-1} + x_b T_{1b}^{-1} + x_i T_{1i}^{-1} \quad (1)$$

T_{1a}^{-1} , T_{1b}^{-1} and T_{1i}^{-1} are the proton (or deuteron) relaxation rates of the intertactoid water (a), of the water at the external surface of the tactoid (b), and of the few layers (≤ 3) of water within the interlamellar space (i), respectively. The molar fractions

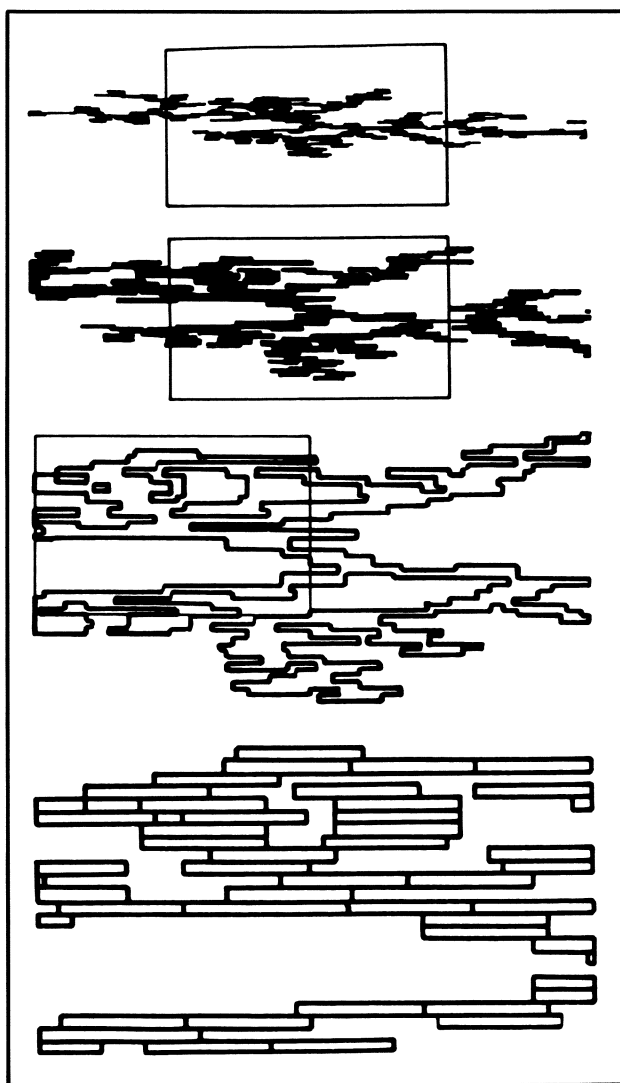


Figure 1. Computer simulation of the formation of clay tactoid by a process of aggregation of 10^3 particles. Ratio length to thickness: 9/1. In the three topmost diagrams each rectangle endorses a portion of the tactoid shown enlarged below. df is represented by the thickness of the line enclosing the "sheets" in contact. Adapted from ref. 6. *N.B.* With respect to the next section, the molar fraction x_i consists of the water in the interlamellar space and in the *closed* spaces within the tactoid. The molar fraction x_b is in a 10 \AA thick layer on the external contour of the tactoid.

associated with these populations are x_a , x_b and x_i , respectively. By combining NMR and heat of immersion measurements it was found the thickness of "phase" b is about 10 Å and constant, irrespective of the material.

Equation (1) is valid if, and only if, there is a fast exchange between these three populations of water. In fact, fast exchange occurs between populations a and b , but not between these two populations and the water (i) occluded within the interlamellar space. It was shown experimentally that T_{1i} is much shorter ($<10^{-2}$ s) than T_{1a} and T_{1b} ($>10^{-1}$ s), and that it is technically possible to remove it from the observed T_{1i} and to drop $x_i T_{1i}$ from Equation (1). This does not mean that $x_i = 0$, but it means that the interlayer water does not participate in the fast exchange as stated above. In that case, $x_a + x_b$ is made equal to one, and relation (1) can be reduced to the two first terms. In addition, T_{1b} can be calculated (2). Therefore, it is possible to carry out relaxation time measurements in such a way as to obtain x_b , the volume fraction of the solvent bound to the contour surface of the tactoid. Indeed, in that case T_{1i} appears as a linear function of the content in solid (Figure 2) because $x_i \ll x_a \approx 1$. If the interlayer water were taking part in the exchange (that is, if $T_{1i} \approx T_{1b}$) the slope ($x_b + x_i$) of the linear relationship would be larger than that observed. On the other hand, if x_i was changing with the solid content, then T_{1i} would not be linear with respect to the concentration in solid.

Thus, a linear relationship means that in suspensions of smectites with clay/water (w/w) concentrations ranging from 0.1 to 10%, the external surface of a tactoid and the number of water layers on this surface are constant in first approximation. Increasing the concentration in solids in this range increases the number of tactoids, whereas their average size remains constant. With kaolinite and non swelling materials, the external surface area obtained from x_b was in good agreement with the BET (N_2) surface area.

The size of the tactoids is a function of the nature of the charge balancing cation, of the ionic strength within the suspension, and of the microcrystalline morphology.

Beyond some critical concentration in solid, aggregation of tactoids occurs undoubtedly. The critical concentration depends, obviously, on many factors, but at the present time we are not aware of any experimental studies on this matter, nor on the factors controlling the critical concentration. This further aggregation process yields larger objects with complicated texture and porous structure. Upon drying thick pastes, some kind of cards house structure has been reported (3). However, irregular stacks composed of tactoids with face to face aggregation have been commonly observed (2).

Availability of Internal Surfaces to Dye Molecules. Absorption of cationic dyes by dilute suspension is an interesting tool for obtaining information on the availability of the clay surface. Dyes such as methylene blue, safranin, etc. undergo protonation and molecular association within the interlamellar space. Both these chemical driving forces may overcome the cohesion forces between clay sheets. Table 1 shows the results of the analysis of the

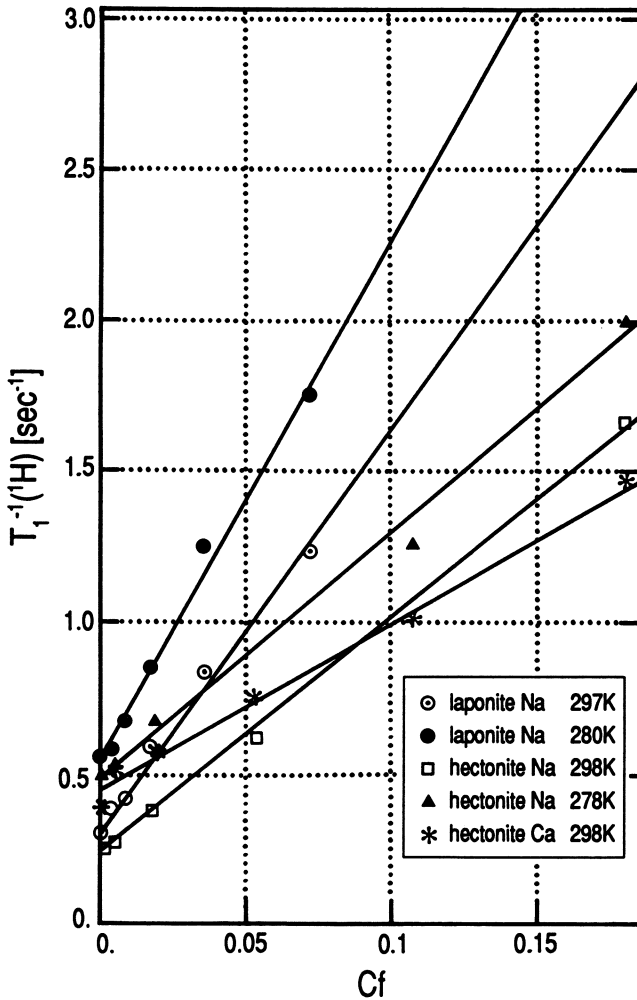


Figure 2. Variation of the proton relaxation rate T_1^{-1} vs. the solid content (C_f) in water for various smectites. The contour (external) surface area of hectorite is ca $80 \text{ m}^2/\text{g}$, the average number of sheets within a tactoid being about 10. (Reprinted with permission from ref 7. Copyright 1982 Academic.)

adsorption of safranine by a Na^+ , Ni^{2+} and Fe^{3+} montmorillonite, originally completely saturated by these cations (10). These results were obtained through chemical and spectroscopic analyses and, therefore, their accuracy is within $\pm 15\%$. It is clear that the availability of the exchange sites for safranine is reduced upon exchanging Na^+ by Ni^{2+} or Fe^{3+} .

TABLE I

Surface composition of safranine exchanged montmorillonite. S^+ = safranine, SH^{2+} = protonated safranine, S = total safranine content, expressed in $10^{-3}\text{M}/100\text{ g clay}$. Metal cation remaining after exchange: M, ($10^{-3}\text{ eq}/100\text{ g clay}$)

	S	S^+	SH^{2+}	M
Na^+ -safranine-Mt	43.5	24.4	19.1	33
Ni^{2+} -safranine-Mt	19.3	9.6	9.6	60
Fe^{3+} -safranine-Mt	25	5	20	72.5

N.B.: The computed total charge is $\sim 100\text{ meq}/100\text{ g clay} \pm 15\%$.

SOURCE: Adapted from ref. 9.

In addition, with respect to the frequency of the main absorption band of safranine in water (495 nm, $5 \times 10^{-3}\text{ M}$), the spectrum observed for the Na clay suspension, 0.1% solid/water, is blue shifted (468 nm), whereas it is red shifted (510 nm) for the Ni and Fe clays suspensions. X ray data suggested that bimolecular layers of safranine are formed within the interlayer space of the Na clay. The blue shift was suggested to result from dimerization of S^+ because of lower acidity due to higher clay dilution. Upon drying clay films, the Na-safranine clay spectrum is red shifted (at 504 nm, whereas the Fe and Ni-safranine clay spectra are further red shifted (at $\sim 540\text{ nm}$) suggesting higher protonation.

Another dye of interest is methylene blue (MB) whose use for measuring surface area and CEC was already suggested by Hang and Brindley (11). More recently, the adsorption of MB was extensively studied by Schoonheydt's group in Leuven, Belgium (12). Cationic monomer MB^+ , dimer $(\text{MB}^+)_2$, trimer $(\text{MB}^+)_3$ and protonated monomer MBH^{2+} have been distinguished by their spectral features in the UV-V range. Sites on the external surface are always available for adsorption, whereas sites on the interlamellar surface are available, if the clay contains three layers of water between the platelets within the tactoid. This is the case for Na and Ca hectorite and laponite, whereas their Cs and K homologues offer less sites in the interlamellar space. The distinction is made possible because the absorption band of MB is red shifted on the external surface, whereas it is blue shifted when MB is adsorbed on internal surfaces. Dimers are observed at all loadings, whereas trimers are formed on external surfaces only. This is an additional evidence of the restricted spacing existing between adjacent sheets in tactoids.

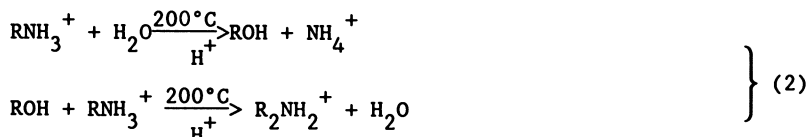
Related to the studies on dye absorption are also the investigations with fluorescent probes, such as [3-(1-pyrenyl) propyl]trimethyl ammonium or PN⁺ (13). Even at very low loading, beside the typical fluorescence of the monomeric form, a broad band resulting from ground state complexes and very efficient excimer formation is observed in the adsorbed state in clays containing less than 0.06% Fe₂O₃. The fact that excited-state complexes are observed even at low loadings suggests a random distribution of the adsorbed molecules. The replacement of Na⁺ by Ca²⁺ before the adsorption of dye decreases the excimer fluorescence intensity, because the low mobility of PN⁺ prevents the formation of excimers in more compact tactoids.

At the present symposium Schoonheydt *et al.* (14) have presented quantitative data on the surface areas available to different dyes, which show the same trend as those obtained via NMR measurements (Equation 1). The reader will find more information in their paper.

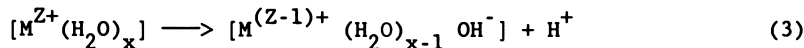
Surface Acidity

Swelling Clays. The first layers of water within the interlayer space are very acidic. The general belief is that the water molecules in the hydration shell of exchangeable cations are submitted to a strong polarizing field due to the small radius of curvature of the cation, as compared with the quasi infinite radius of curvature of the "anionic" sheet (15).

Many surface acid catalyzed reactions have been described (16-17). A typical one is the transalkylation reaction of alklammonium which can be schematically described as follows (18),



In the absence of interlayer water this reaction was undetectable. The source of protons can be visualized by the hydrolysis reaction,



the proton being delocalized on the network of water within the interlayer space. Upon mild dehydration conditions reaction (3) is reversible.

Upon more severe conditions, such as deamination or dehydration of H₃O⁺ on exchange sites, what is the fate of the protons left behind? When the negative charge of the lattice arises from Si⁴⁺ by Al³⁺ substitution in the tetrahedral layer, opening of Si-O-Al bridges resulting in a structure such as that known in acid zeolites,



has been evidenced either by acid leaching of beidellite or thermal decomposition of NH_4^+ -beidellite (19) (see Figure 3). A precursor state for the proton transfer may be evidenced by the C_{3v} symmetry of the exchangeable NH_4^+ in beidellite as opposed to its T_d symmetry in clays with octahedral substitution. Lowering the symmetry from T_d to C_{3v} makes the A_1 stretching band active in IR (20). It might be suggested that in montmorillonite, where the negative charge arises from isomorphous substitution within the octahedral layer and where reaction (4) is not observed, the proton left upon deamination would nest in the octahedral layer. An argument in favor of this hypothesis is that the loss of constitutional water starts and is completed at a lower temperature in NH_4^+ -montmorillonite than in K^+ -montmorillonite, whereas in NH_4^+ and K^+ beidellite the TGA traces are quasidentical for both exchanged forms (20). This suggests, indeed, that the extra protons in the octahedral layer help to nucleate water from constitutional hydroxyls. Under mild dehydration though, there is no direct evidence of proton migration towards octahedral cavities.

Pillared Clays. Another consequence of the origin of the negative charge in smectites is in the difference between the cross-linking mechanism in clay pillared with Al oligomer, the Keggin-like cation Al_{13} . Thermally activated pillared beidellite seems to be cross-linked by inverting Al tetrahedra towards the interlayer (21), as suggested by high resolution solid state NMR, whereas under the same conditions pillared montmorillonite shows no evidence for this reaction. However, inverting silicon tetrahedra was suggested to occur in octahedrally substituted materials with high F for OH⁻ replacement (fluorhectorite). The single ^{29}Si resonance in the starting material is split into a doublet after pillaring and thermal activation (22), Figure 4. By contrast this was not observed in hectorite (21). The larger degree of OH⁻ by F⁻ substitution within the octahedral layer, as well as Al substitution in the tetrahedral layer, could thus play a role in the reactivity of the tetrahedral layer towards the pillaring agent. In the particular case of Al-pillared clays the protons nesting in the octahedral cavities in thermally activated pillared montmorillonite are brought back by NH_3 into the interlayer of pillared montmorillonite, as reported by Vaughan, quoted by Tennakoon *et al.* (23). In unpillared clays, such an experiment cannot be carried out because of the collapse of the interlayer gallery upon heat treatment.

Charge or Energy Transfer From Interlayer to the Lattice

Evidences for electron transfer from surface to bulk. According to the nature of the clay, variable amounts of Fe^{3+} are present in the lattice. Glauconite, which is an iron rich member of the dioctahedral smectite family, reacts at pH 7 with sodium

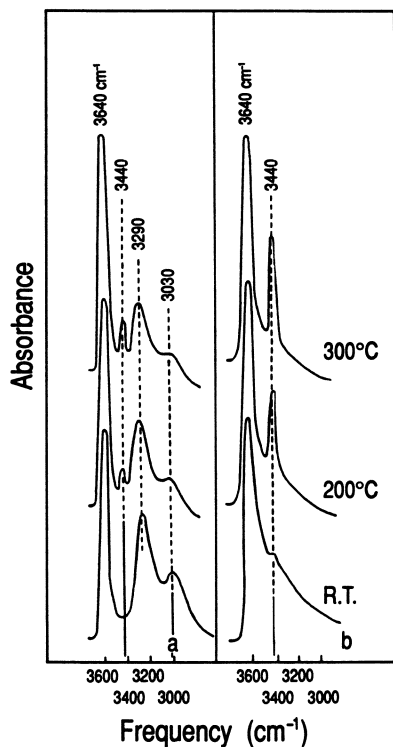


Figure 3. Formation of surface Si-OH-Al acidic groups upon heating NH₄⁺ beidellite (a) and leaching Na beidellite with an acid solution, followed by calcination at the indicated temperature (b). (Reprinted with permission from ref. 19. Copyright 1987 Clay Minerals Society.)

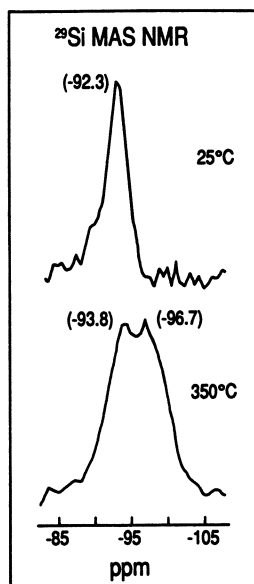


Figure 4. ²⁹Si magic angle spinning high resolution NMR spectra (79.41 MHz) for uncalcined (25 °C) and calcined (350 °C) Al₁₃ pillared fluorohectorite. (Reprinted from ref. 22. Copyright 1985 American Chemical Society.)

hydrosulfite with only slight alteration of the crystallinity, even after a pronounced increase of the $\text{Fe}^{2+}/\text{Fe}^{3+}$ ratio (24). The increase of this ratio by a factor of 4 also increases the loss of constitutional H_2O measured between 250°C and 430°C by a factor of 2, approximately. Octahedral iron in nontronite can be reduced by hydrazine and dithionite as well (25-26). Therefore, electron transfer from interlayer to lattice constituents occurs quite easily. Another evidence is the immediate formation of TTF^+ observed in exposing Fe bearing smectites to TTF (tetrathiafulvalene) (27).

After exchanging between 50 and 100% of the CEC with TTF the d_{001} spacing (~17Å) can be fitted either by a double layer of molecules parallel to the surface or a single layer of molecules perpendicular to the surface. DC conductivity of a TTF^+ loaded film is weak, suggesting that no macroscopic conduction pathway exists in the network of intercalated TTF.

In the examples quoted above the electron transfer is driven by chemical potential gradient. Is electron transfer responsible for the quenching mechanism of intercalated fluorescent probes?

Quenching mechanism. Steady state measurements of the luminescence quantum yield of $\text{Ru}(\text{bpy})_3^{2+}$ intercalated in clay films brings about more detailed information with respect to the possible role of electron transfer in luminescence quenching. The quantum yield is dependent upon the amount of co-adsorbed water and is strongly depleted by transition metal impurities, such as Fe^{3+} or Cr^{3+} in the lattice (28).

In iron bearing clays the time law of the luminescence decay of $\text{Ru}(\text{bpy})_3^{2+}$ is multiexponential (29). In the long time limit ($>1 \mu\text{s}$) the decay approaches an exponential law, but at shorter time ($\leq 300 \text{ ns}$), a more complex decay has been observed. The decay mechanism has been explained by a simple localized model based on the assumption that on each particle the quenching process can be described as occurring in an ensemble of small independent subsystems. Each subsystem is composed of an excited probe system (with a very reduced mobility) and of the nearest lattice sites of the solid which may be occupied by the quencher ions. For the sake of simplicity, it has been assumed that the adsorbed probe molecules occupy the sites of a superlattice which matches the lattice containing randomly distributed quenchers (Fe^{3+} , for instance) (Figure 5). The theory applicable to this model predicts single-exponential decay at long times and multiexponential decays at short times. The extrapolated intercept of the long time exponential decay at time zero should be proportional to the average number of quenchers per subsystem (see ref. 29 for detail). In fact, this intercept varies as the third root of the concentration in iron over a range of iron content between 500 to 250 10^3 ppm ! An exponent lower than one (as that expected from the theory) seriously questions that quenching occurs through a one-one electron transfer between excited $\text{Ru}(\text{bpy})_3^{2+}$ and the lattice iron.

That deactivation of an excited coordination compound occurs through mechanisms other than electron transfer is confirmed, if, for instance, the variations of quantum yield with water content within the interlamellar space of the low iron hectorite partially exchanged with $\text{Ru}(\text{bpy})_3^{2+}$ and $\text{Cr}(\text{bpy})_3^{3+}$ are compared (30) (see

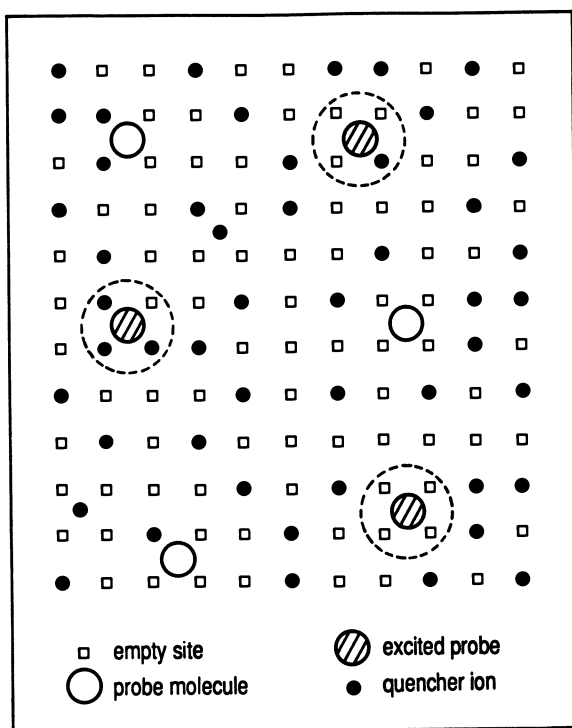
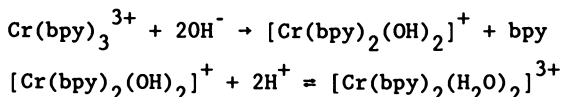


Figure 5. Sketch of the model suggested for the multi-exponential decay observed for the $\text{Ru}(\text{bpy})_3^{2+}$ luminescence probe molecule decay in the interlamellar space. To a square lattice for quencher ions is superimposed a $(1/2, 1/2)$ translated square lattice for the probe molecules. (Reprinted with permission from ref. 29. Copyright 1984 Royal Society of Chemistry.)

Figure 6). The luminescence quantum yield (ϕ) in solution for excited $[\text{Ru}(\text{bpy})_3^{2+}]$ is 4%. The same quantum yield is observed for adsorbed $\text{Ru}(\text{bpy})_3^{2+}$ in dehydrated hectorite. The luminescence quantum yield of $[\text{Cr}(\text{bpy})_3^{3+}]$ is 0.1% in solution and also in hydrated (~16% H_2O w/w) hectorite. Upon hydrating the hectorite film loaded with the Ru complex, ϕ increases slightly, whereas dehydrating the film loaded with the Cr complex increases ϕ by a factor of 100. In order to understand these opposite behaviors, the chemical reactivity of $\text{Cr}(\text{bpy})_3^{3+}$ and of $\text{Ru}(\text{bpy})_3^{2+}$ with respect to water must be recalled.

In solution, at room temperature $\text{Ru}(\text{bpy})_3^{2+}$ does not undergo a photo-induced ligand substitution over a wide pH range, whereas at 95°C complete labilization occurs in a few hours. In acidic solution $\text{Cr}(\text{bpy})_3^{3+}$ is photo-inert. At room temperature at neutral or alkaline pH, a bidentate complex is formed rapidly



and the *trans* isomer is obtained.

In the interlamellar space XRD and IR dichroism (28) suggest that $\text{Cr}(\text{bpy})_3^{3+}$ orients two of its three ligands parallel to the silicate layer, i.e. an orientation which favors the formation of the *cis* isomer upon aquation, whereas in adsorbed $\text{Ru}(\text{bpy})_3^{2+}$ the three ligands are tilted at a high angle with respect to the *ab* plane. In the adsorbed state and in contrast with solution, photoaquation of $\text{Cr}(\text{bpy})_3^{3+}$ occurs rapidly and the *cis* isomer is obtained, rather than the *trans* isomer obtained on alkaline solution. In addition, the removed bpy molecule is protonated and the reaction is partially reversible in the dark. This result is surprising at first sight because of the acidity of the interlamellar water, but it must not be forgotten that a higher proton concentration in the pool of adsorbed water implies that the environment in the cation hydration shell is more hydroxide-like (Equation 3). By contrast the adsorbed $\text{Ru}(\text{bpy})_3^{2+}$ is not photoaquated as evidenced by absorption and emission spectra. Keeping these experimental observations in mind, the two opposite variations of ϕ with the water contents of clays containing either $\text{Ru}(\text{bpy})_3^{2+}$ or $\text{Cu}(\text{bpy})_3^{3+}$ can be readily explained.

In the absence of a specific quencher (clays with low iron content) and considering photoaquation as a possible reaction,

$$\phi = \frac{k_r}{k_r + k_{nr} + k_q(\text{H}_2\text{O})}$$

where k_r and k_{nr} are the radiative and non-radiative monomolecular process rate constants, respectively, and where k_q is the bimolecular rate constant for the photoaquation reaction.

The non-radiative process consists of the thermal excitation of the ligands by the photonic energy. k_{nr} decreases when the motional freedom of the ligands decreases. Thus, the large increase of ϕ observed for $\text{Cr}(\text{bpy})_3^{3+}$ as dehydration proceeds would indicate that $k_q(\text{H}_2\text{O})$ decreases because the water content decreases, and that k_{nr} decreases also because of the immobility of the ligands "sticking"

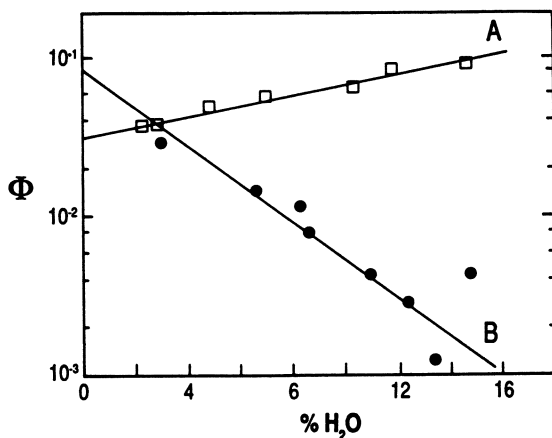
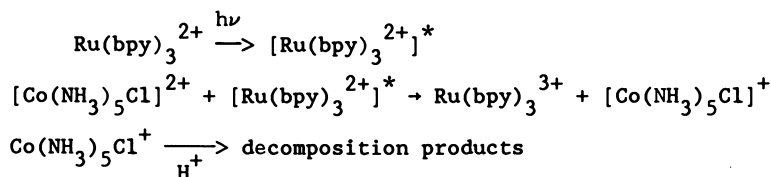


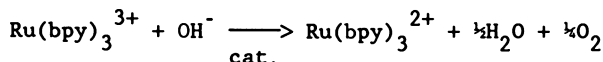
Figure 6. Luminescence quantum yield (ϕ) of $\text{Ru}(\text{bpy})_3^{2+}$ (A) and of $\text{Co}(\text{bpy})_3^{3+}$ (B) as a function of the hydration level of hectorite (% $\text{H}_2\text{O}/\text{clay}$, w/w). (Reprinted with permission from ref. 29. Copyright 1984 Royal Society of Chemistry.)

to the layers more efficiently at low water contents. The slight increase of ϕ observed for $\text{Ru}(\text{bpy})_3^{2+}$ as hydration increases may be a consequence of the orientation of the ligand which permits water molecules to be squeezed within interligand pockets reducing the ligand mobility. Water in this situation seems also to contribute to the radiationless quenching since, when adsorbed H_2O is substituted by D_2O , $\phi(\text{D}_2\text{O})/\phi(\text{H}_2\text{O}) = 1.7$, because of the diminished spacing between the vibronic levels of D_2O relative to H_2O .

Electron Transfer Between Co-adsorbed Species. So far, the most notable examples for photo-induced electron transfer on clay surfaces occur between co-adsorbed species as illustrated by the sacrificial oxidation of water. In water the system is the following (31):



The fast decomposition of the sacrificial electron acceptor prevents back electron transfer. The formation of molecular oxygen results from



The catalyst was a colloidal suspension of RuO_2 (diameter $\sim 150\text{\AA}$).

The same reaction has been studied in clay slurry (32). The colloidal system $[\text{Ru}(\text{bpy})_3^{2+}]$ exchanged hectorite/ RuO_2 in an aqueous suspension of $[\text{Co}(\text{NH}_3)_5\text{Cl}]^{2+}$ in large excess with respect to the clay CEC, did not photolyze water when illuminated with radiation whose wavelength was larger than 400 nm. $[\text{Co}(\text{NH}_3)_5\text{Cl}]^{2+}$ has access to the interlamellar space, but the catalyst (RuO_2) has no access because of its size (Figure 7a). Note that there is no spectroscopic evidence for desorption of $[\text{Ru}(\text{bpy})_3^{2+}]$ into the solution.

If hectorite was pretreated at a temperature high enough to collapse the tactoid, and subsequently exchanged with a mixture of $[\text{Ru}(\text{bpy})_3^{2+}]$, $[\text{Co}(\text{NH}_3)_5\text{Cl}]^{2+}$ and RuO_2 , then photooxidation is observed in the colloidal suspension because the catalyst is in contact with the reagents, all components being on the external surface (Figure 7b).

On the opposite, photooxidation should occur with a cationic catalyst having access to the interlamellar space.

This has been shown to be correct by using *cis*- $[\text{Ru}(\text{bpy})_2(\text{H}_2\text{O})_2]^{2+}$ as catalyst; then all the components for the reaction are within the interlamellar space and photooxidation proceeds at a rate comparable with that observed in solution (Figure 7c). These observations outline the importance of the textural arrangement of the clay sheets with respect to the availability of the surface sites, in line with what has been previously discussed in the paragraph dealing with the concept of tactoids.

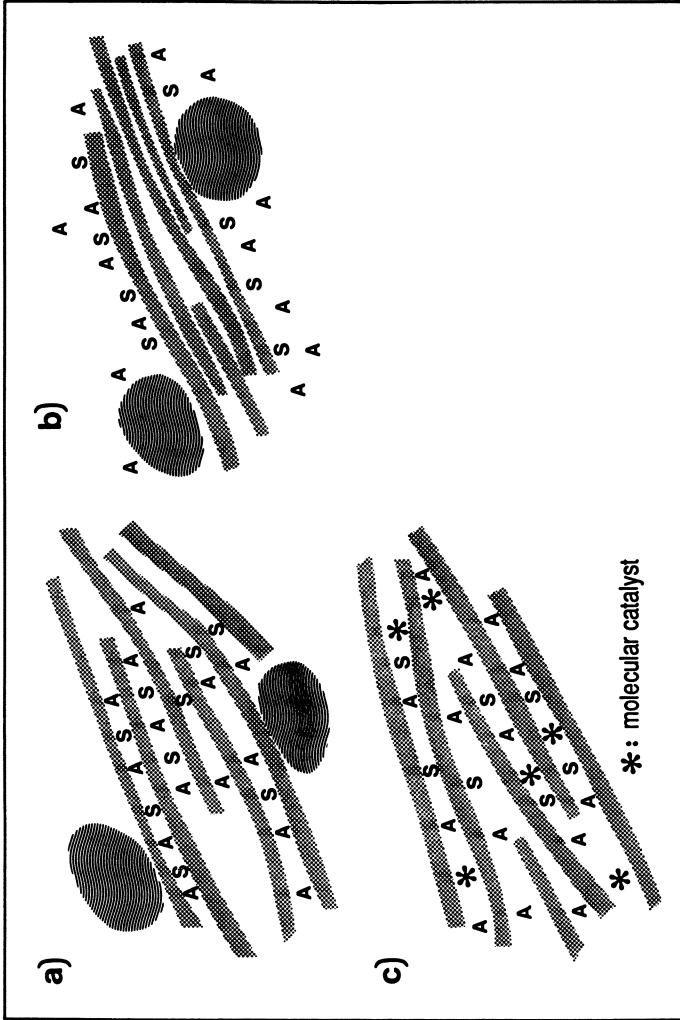


Figure 7. Models suggested for explaining the observation of the photooxidation of water by a sensitizer S, $(\text{Ru}(\text{bpy})_3^{2+})$, which in the excited state S transfer an electron to a sacrificial acceptor A, $[\text{Co}(\text{NH}_3)_6\text{Cl}]$, in the presence of a colloidal catalyst (RuO_2) or a molecular catalyst $(\text{cisRu}(\text{bpy})_2(\text{H}_2\text{O})_2^{2+})$. See text for the significance of a, b, and c. (Reprinted with permission from ref. 32. Copyright 1983.)

Conclusions

Hydrated clay surfaces are acidic. When isomorphous substitution occurs in the tetrahedral layer, acid leaching or NH_4^+ thermal decomposition may generate acidic surface OH. For clays whose negative charges are produced by isomorphous substitutions in the octahedral layer, mild dehydration removes the source of acidity, because of the reversibility of reaction (3). Deamination of the ammonium exchanged clay with octahedral substitution drives protons into the octahedral layer, as evidenced by the lowered temperature at structural dehydroxylation.

Acid catalyzed reactions occur on the surface of clays as long as water molecules are present within the interlamellar space. Charge transfer reactions between adsorbed reagents and structural iron are clearly established, but photo-triggered electron transfer has not been proved unless the donor and acceptor moieties are co-adsorbed. Irrespective of the nature of the reaction, the strong tendency of clay anisotropic particles to agglomerate into tactoids, as well as the intricate spatial distribution of tactoids, reduces the availability of surface sites. Upon pillaring a noticeable fraction of the surface sites remains available for reaction processes operating at high temperature.

Literature Cited

1. Grim, R. E. Clay Mineralogy, 2nd Edt., McGraw: New York, 1968.
2. Bleam, W. F.; Hoffman, R. Inorgan. Chem., 1988, **27**, 3180.
3. Van Olphen, H. An Introduction to Clay Colloid Chemistry, 2nd Ed., John Wiley and Sons, Inc., 1977.
4. Avnir, D., Ed. The Fractal Approach to Heterogeneous Chemistry: Surface, Colloids, Polymers, J. Wiley Publisher, 1989.
5. Banin, A.; Lahav, N. Israel J. Chem., 1968, **6**, 235.
6. Van Damme, H.; Levitz, P.; Fripiat, J. J.; Alcover, J. F.; Gatineau, L.; Bergaya, F. In Physics of Finely Divided Matter; Boccara N.; Daoud, D., Ed.; Springer: Berlin, 1985; p. 24.
7. Fripiat, J. J.; Cases, J.; Francois, M.; Letellier, M. J. Coll. and Interface Sci., 1982, **89**, 378.
8. Fripiat, J. J.; Letellier, M.; Levitz, P. Phil. Trans. Royal Soc., 1984, **A311**, 287.
9. Tessier, D.; Pedro, G. In International Clay Conference, 1981; Developments in Sedimentology No. 35, Van Olphen, H.; Veniale, F. Eds.; Elsevier: Amsterdam, 1982; p. 165.
10. Van Damme, H.; Crespin, M.; Cruz, M. I.; Fripiat, J. J. Clays and Clay Min., 1977, **25**, 19.
11. Hang P.T.; Brindley, G.W. Ididem, 1970, **18**, 203.
12. Cenens J.; Schoonheydt, R. A. Ibidem, 1988, **36**, 214.
13. Viane, K.; Caigui, J.; Schoonheydt, R. A.; DeSchryver, F. C., Langmuir, 1987, **3**, 107.
14. Schoonheydt R. A.; Cenens, J. This Symposium.....
15. Mortland, M. M.; Fripiat, J. J.; Chaussidon, J.; Ytterhoeven, J. B. J. Phys. Chem., 1963, **67**, 248.
16. Thomas, J. M. In Intercalation Chemistry; Wittingham, M. S.; Jacobson, A. J., Eds.; Academic Press: New York, 1982; p. 56.

17. Balantine, J. A. In Chemical Reaction in Organic and Inorganic Constrained Systems; Setton, R., Ed.; NATO, ASI Series C 165: Reidel, Dordrecht, 1986; p. 197.
18. Durand, B.; Pelet, R.; Fripiat, J. J. Clays and Clay Min., 1972, 20, 21.
19. Schutz, A.; Stone, W. E. E.; Poncelet, G.; Fripiat, J. J. Ibidem, 1987, 35, 251.
20. Chourabi, B.; Fripiat, J. J. Ibidem, 1981, 29, 260.
21. Plee, D., Borg, F.; Gatineau, L.; Fripiat, J. J.; J. Amer. Chem. Soc., 1985, 107, 2362.
22. Pinnavaia, T. J.; Landau, S. D.; Tzou, Mingh-Shin; Johnson, I. D.; Lipsicas, M. J. Amer. Chem. Soc., 1985, 107, 2362.
23. Tennakoon, D. T. B.; Jones, W.; Thomas, J. M.; J. Chem. Soc. Faraday Trans I, 1986, 82, 3081.
24. Cloos, P.; Fripiat, J. J.; Vielvoye, L. Soil Sci., 1961, 91, 55.
25. Russel, J. D.; Goodman, B. A.; Fraser, A. R. Clays and Clay Min., 1979, 27, 63.
26. Stucki, J. W.; Roth, C. B.; J. Soil Science Society of America, 1977, 41, 808, and references therein.
27. Van Damme, H.; Obrecht, F.; Letellier, M. Nouveau J. de Chimie, 1984, 8, 681.
28. Krenske, D.; Abdo, S.; Van Damme, H.; Cruz, M.; Fripiat, J. J. J. Phys. Chem., 1980, 8, 681.
29. Habti A.; Keravis, D.; Levitz, P.; Van Damme, H. J. Chem. Soc., Faraday Trans. 2, 1984, 80, 2447.
30. Van Damme, H.; Nys, H.; Fripiat, J. J. J. Molec. Cat., 1984, 27, 123, and references therein.
31. Lehn, J. M.; Sauvage, J. P.; Ziessel, R. Nouveau J. de Chimie, 1979, 3, 423.
32. Nys, H.; Van Damme, H.; Bergaya, F.; Habti, A.; Fripiat, J. J. J. Molec. Catalys., 1983, 21, 223, and references therein.

RECEIVED July 13, 1989

Chapter 19

Probing the Surface of Clays in Aqueous Suspension by Fluorescence Spectroscopy of Proflavine

Jos Cenens¹, Robert A. Schoonheydt², and Frans C. De Schryver³

¹Chemical Research Centre, Shell Louvain-La-Neuve, Avenue Jean Monnet
1, B-1348 Ottignies Louvain-La-Neuve, Belgium

²Laboratorium voor Oppervlaktechemie, K.U.Leuven, K. Mercierlaan,
92, B-3030 Leuven, Belgium

³Department of Chemistry, K.U.Leuven, Celestijnenlaan,
200F, B-3030 Leuven, Belgium

Aqueous suspensions of barasym SSM-100, hectorite and laponite, exchanged with Na⁺, K⁺, Cs⁺ and Ca²⁺ were investigated by fluorescence spectroscopy of adsorbed proflavine. Monomers, dimers and protonated species are found on the surface. The relative concentration of these species depends on the type of clay, the exchangeable cation and the loading. On the basis of the evolution of the emission intensities with loading three categories of clays are described. The first category comprises Na⁺-, Ca²⁺- and K⁺-hectorite, barasym at pH = 9 and Ca²⁺-laponite. For these clays the fluorescence intensity decreases with loading, following Perrin's law. Effective surface areas in aqueous suspension are estimated for the first time with Na⁺-hectorite as a reference. The second category is composed of Na⁺- and K⁺-laponite and barasym at pH = 7. A minimum in the fluorescence intensity is found at a characteristic loading. This is due to non-homogeneous distribution of proflavine molecules and/or a change in the state of aggregation of the clay. Cs⁺-laponite and Cs⁺-hectorite comprise the third category. Here preferential adsorption of proflavine occurs in the interlamellar space of the aggregates with formation of monolayers of monomers and quenching of the fluorescence with increasing loading does not occur to an appreciable extent.

0097-6156/90/0415-0378\$06.00/0

© 1990 American Chemical Society

Proflavine or 3,6-diaminoacridine (PFH^+) is a cationic dye, the structure of which is shown in Figure 1. In dilute aqueous solution its visible absorption band at 445 nm (22400 cm^{-1}) and the shoulder around 425 nm (23530 cm^{-1}) are respectively the 0-0 and 0-1 vibronic components of a $\pi-\pi^*$ transition. The corresponding fluorescence band is almost structureless at room temperature with a maximum at 506 nm (19760 cm^{-1}). Upon protonation a second proton is attached to one of the N's in position 3 or 6 (PFH_2^{2+}). This leads to a red shift of both the absorption and the fluorescence bands to 455 nm (22000 cm^{-1}) and 545 nm (18350 cm^{-1}) respectively. When the concentration is increased, the 425 nm band increases, due to overlap with a band at 428 nm (23360 cm^{-1}). It is the dimer ($(\text{PFH}^+)_2$) absorption, which has no fluorescence (1-3).

When the dye is ion-exchanged on clays, it is concentrated in a relatively small volume around the clay particles. The size of the volume depends on the swelling characteristics of the clay and thus on such factors as (1) the size and the charge density of the clay particles; (2) the type of exchangeable cation and (3) the ability of the dye to penetrate in the interlamellar space of the aggregates.

This concentration effect shows up in the absorption and emission spectra of the adsorbed dyes, because it affects the relative amounts of monomers and dimers. This has been shown by a study of the absorption spectra of adsorbed methylene blue and proflavine(4,5). For Na^+ - and Ca^{2+} -hectorite and barasym the absorption spectra can be quantitatively interpreted in terms of the following equilibrium on the surface



with $n = 2$ or 3 (6). This is not possible for laponites and K^+ - and Cs^+ -exchanged hectorites. This inability has been ascribed to the fact that the surface is not freely available to both monomers and aggregates, presumably because of aggregation of the elementary clay platelets (6,7).

These data indicate that a study of the relative intensities of the absorption bands gives qualitative insight into the aggregation of clay particles in aqueous suspensions. In principle, similar information can be obtained from the fluorescence spectra of proflavine, because PFH^+ fluoresces intensively and $(\text{PFH}^+)_2$ does not fluoresce in aqueous solution.

In a preliminary account we have discussed the fluorescence spectra of proflavine on clays in aqueous suspension (5,7). The positions of both the absorption and fluorescence bands of the different forms of proflavine on clays and in aqueous solution are shown in Figure 2. The extinction coefficients are given in Table

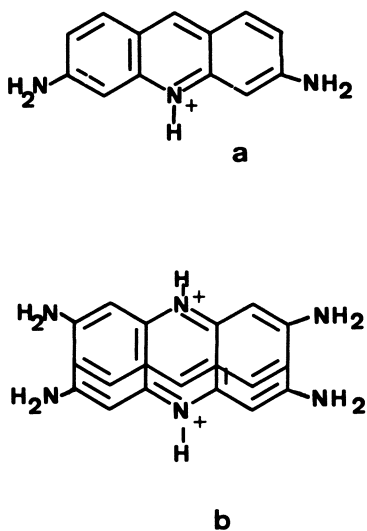


Figure 1: Proflavine monomer (a) and dimer (b)

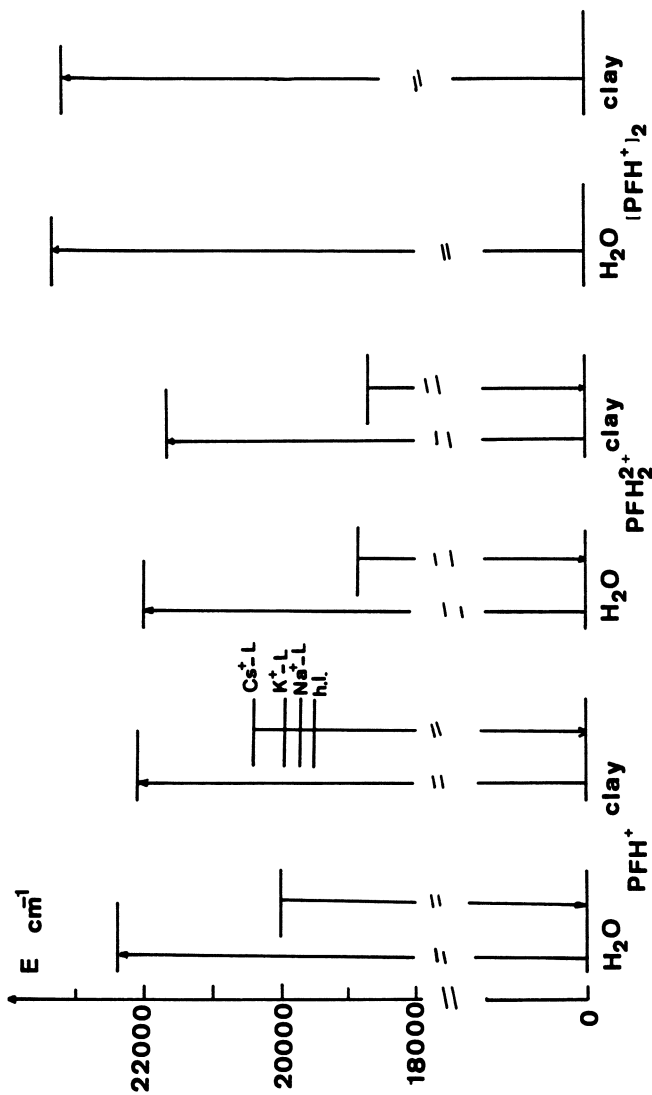


Figure 2: Schematic representation of the positions of the absorption and fluorescence bands of PFH⁺, PFH₂⁺ and (PFH⁺)₂ in aqueous solution and on clays. h.l. = high loadings.

I. The small changes in band positions reflect the slightly different environment offered by the clay suspensions with respect to aqueous solutions.

This paper is concerned with a quantitative study of the fluorescence intensity of proflavine on several clays. The intensity of the fluorescence changes with loading in a characteristic way, which depends on the type of clay and the type of exchangeable cation. An attempt is presented to calculate effective surface areas in aqueous suspension.

Experimental

Hectorite (H), barasym SSM-100 (BS) from the Source Clays Repository of the Clay Minerals Society and laponite B (L) from Laporte Industries were used. The clays were exchanged with 1 M NaCl solutions three times, the < 2 mm fraction was separated by centrifugation and stored in 1 M NaCl at 277°K.

The preparation of the < 0.3 μm fraction, the ion exchange with the monomer of proflavine, PFH^+ , and the spectroscopy have been described in detail (5).

All manipulations were done in the dark. The total dye concentration in the suspensions was 2.5×10^{-6} M. At pH = 7 and in the absence of clay the ratio of the monomer to the protonated monomer, $[\text{PFH}^+]/[\text{PFH}_2^{2+}]$, was larger than 3×10^6 and the solution contained 0.2% - 1.3% dimers, $(\text{PFH}^+)_2$, the exact number depending on the dimerization constant used in the calculation. Loadings in the range 0 - 30% of the $^{22}\text{Na}^+$ exchange capacity (CEC) were realized by adjusting the amount of clay in the suspension. Adsorption was quantitative. The CEC values were 0.464, 0.526 and 0.568 meq/g for respectively BS, H and L. Buffered suspensions (pH = 9) were prepared by adding 10 cm^3 of a solution, containing 1 mmol/dm^3 NaOH/ NaHCO_3 and 10 $\mu\text{mole}/\text{dm}^3$ proflavine to 30 cm^3 of clay suspension. When the exchanges were done without pH control, we call them exchanges in neutral conditions.

Samples of hectorite and laponite saturated with K^+ , Cs^+ and Ca^{2+} were prepared by exchanging desalted Na-clay with the desired Cl^- salt and dialyzing until no Cl^- was detected with the AgNO_3 test.

In all cases the absorbance of the suspensions at 445 nm was smaller than 0.2. This small absorbance value minimizes reabsorption of the emitted light. Oxygen was not removed from the suspensions, since no measurable effect on the fluorescence intensity was found.

Excitation spectra were recorded in the range 350 - 500 nm with the emission wavelength preset at fixed positions in the range 500 - 600 nm with a SPEX Fluorolog model 1691 spectrofluorimeter.

Results

Spectroscopy. The absorption and fluorescence spectra of proflavine on H and BS are published (5) and the positions of the band maxima are summarized in figure 2. Typical excitation spectra are shown in figure 3. For H and L the maximum is at 456 nm with shoulders at 430 nm and in the range 400-410 nm. These are respectively the 0-0, 0-1 and 0-2 vibronic bands of PFH^+ . The positions are independent of the emission wavelength in the range 500 - 580 nm and the loading. For neutral BS suspensions, the excitation spectra have a maximum at 460 nm and there is a weak band at 365 nm, which is due PFH_2^{2+} . The 460 nm band is then a mixture of the 0-0 vibronic components of PFH^+ and PFH_2^{2+} . The latter disappears at pH = 9.

Fluorescence spectra of proflavine on laponite are compared with the spectrum of a 2.5×10^{-6} M solution in figure 4. These spectra are typical for PFH^+ . In general, the emission maximum shifts to the red and the intensity decreases with increasing loading. Both phenomena are due to dimerization. The extent of the red shift depends on the type of exchangeable cation, as shown in figure 2. For Cs^+ it is from 490 nm at 0.2% loading to 512 nm at 8.2%; for K^+ from 502 to 512 nm and for Na^+ and Ca^{2+} from 508 to 514 nm. Similar red shifts were observed for hectorites. For BS the emission maximum is at 535 nm at the smallest loadings at neutral pH. This is due to PFH_2^{2+} (5). At higher loadings or at pH = 9 for all loadings the emission maximum is at 502 nm, typical for PFH^+ .

Quantum Yields. The quantum yield is the ratio of the fluorescence intensity to the amount of light absorbed. The ratios of the quantum yield of a 2.5×10^{-6} M solution, containing only PFH^+ , and the quantum yields of proflavine on the clays, ϕ_0/ϕ with $\phi_0 = 0.34$ (1), are shown in figures 5-8 as a function of the loading, expressed in % of the CEC. An increase of ϕ_0/ϕ means a decrease of the fluorescence intensity for adsorbed PFH^+ , as illustrated in the spectra of figure 4. It is due to increasing amounts of dimers on the surface (5). On the basis of these plots the clay suspensions can be divided in three categories.

The samples, characterized by an initially fast increase of ϕ_0/ϕ with loading and a leveling off at higher loadings are Na^+ -, Ca^{2+} - and K^+ -H, Ca^{2+} -L and BS at pH = 9 (Figures 5, 6 and 7), comprise a first category.

The second category is made up of Na^+ -L, K^+ -L and neutral BS suspensions. The curves ϕ_0/ϕ versus loading have a maximum, which is characteristic for the type of counter-ion. Thus, for these samples the fluorescence intensities of adsorbed proflavine decrease with loading to attain a minimum value at a characteristic loading and

TABLE I. Band maxima (λ) and extinction coefficients (ϵ) of proflavine

species	aqueous solution		on clays	
	λ (nm)	ϵ ($\text{dm}^3 \text{mole}^{-1} \text{cm}^{-1}$)	λ (nm)	ϵ ($\text{dm}^3 \text{mole}^{-1} \text{cm}^{-1}$)
PFH ⁺	445	40000(1)	453	64000
PFH ₂ ²⁺	490	sh	490	sh
	455	20000(2)	462	26400
	360	15000(2)	360	15440
(PF) ₂	428	38000(1)	430	64000

(1), ref. 1. (2) ref. 15. sh = shoulder.

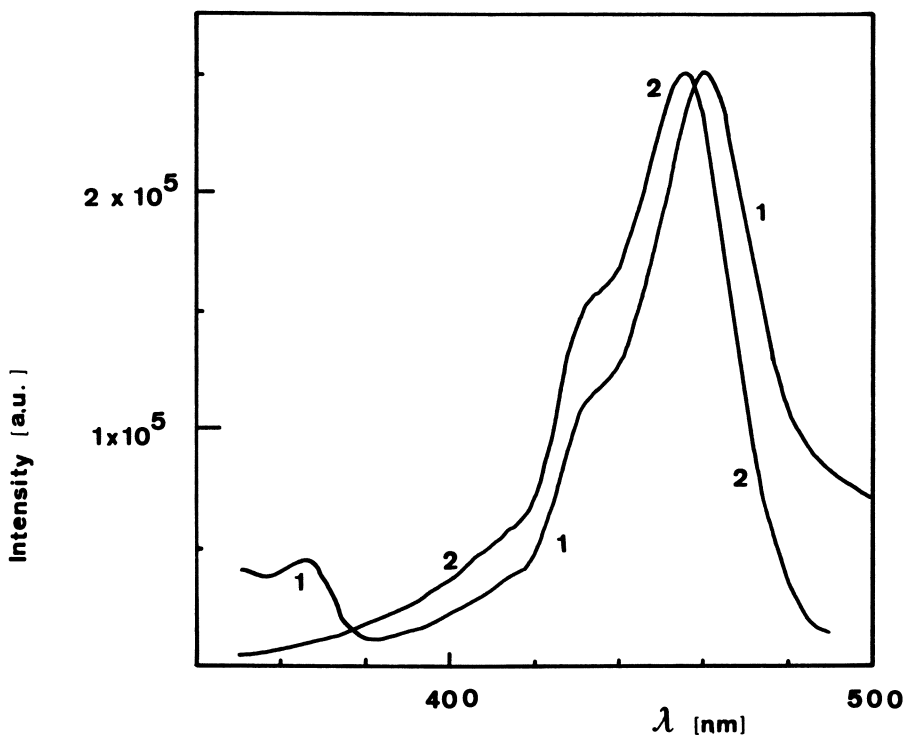


Figure 3: Excitation spectra of proflavine on Na⁺-BS (1) and on Ca²⁺-L (2) in neutral conditions. The fluorescence wavelength was respectively 580 nm and 500 nm.

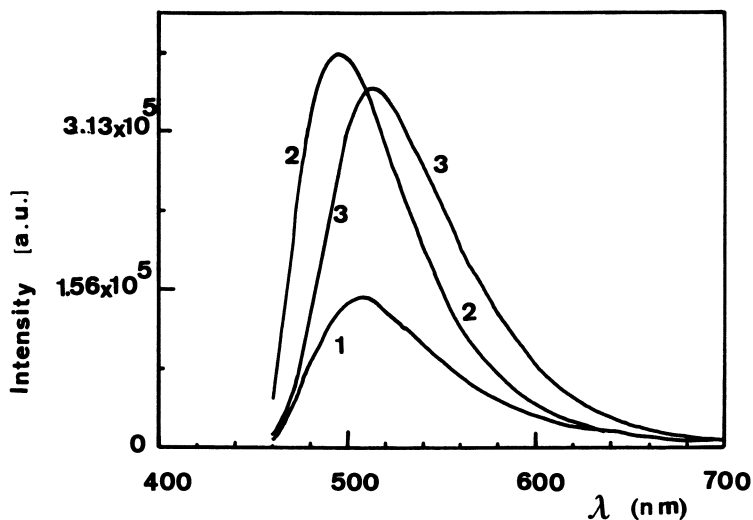


Figure 4: Fluorescence spectra of proflavine on $\text{Na}^+\text{-L}$ in aqueous suspension at loadings of 0.3% (1) and 0.03% (2) of the ^{22}Na -exchange capacity. (3), fluorescence spectrum of a 2.5×10^{-6} molar solution of proflavine at $\text{pH} = 4$. The excitation wavelength is 458 nm.

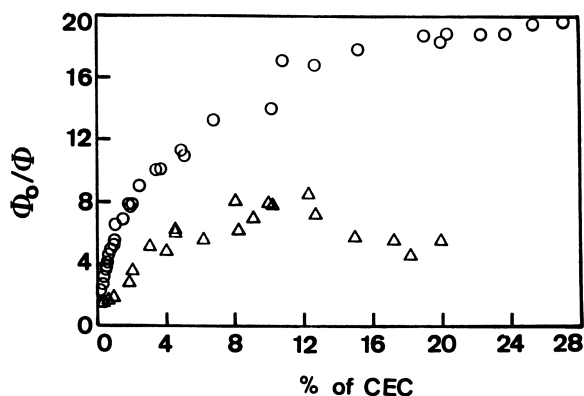


Figure 5: Ratio of the emission quantum yields of proflavine, Φ_0/Φ , as a function of the loading for $\text{Na}^+\text{-H}$ (O) and $\text{Na}^+\text{-BS}$ (Δ) in neutral conditions.

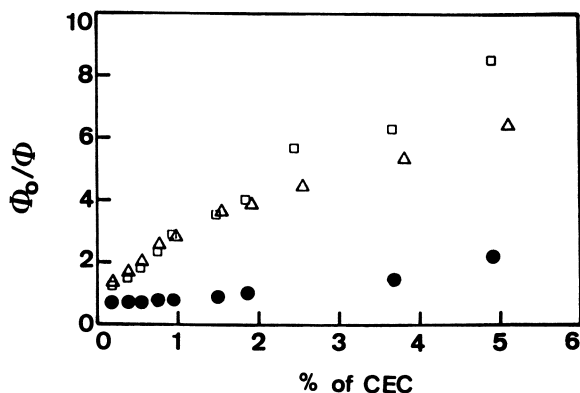


Figure 6: Ratio of the quantum yields, Φ_0/Φ , of proflavine as a function of the loading for Cs⁺-H (●) and K⁺-H (□), both at pH = 9, and Ca²⁺-H (△) in neutral conditions.

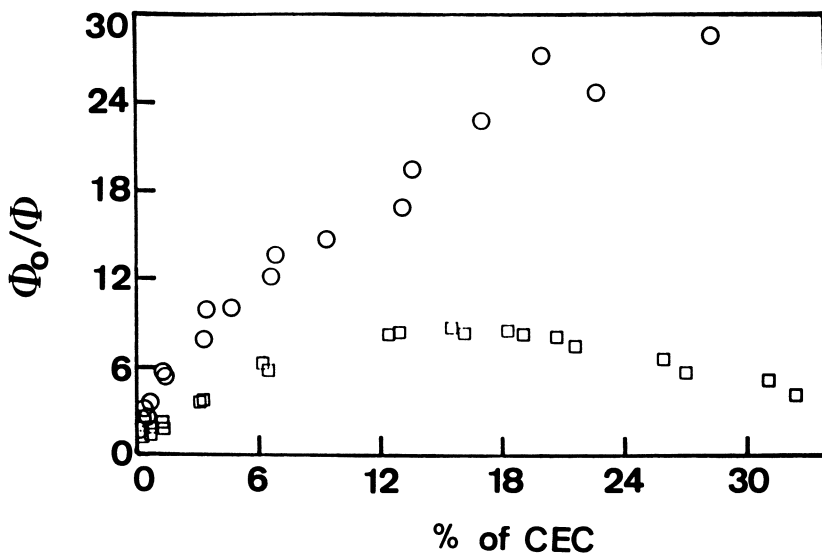


Figure 7: Ratio of the quantum yields, Φ_0/Φ , of proflavine as a function of the loading for Ca²⁺-L (○) and Na⁺-L (□) in neutral condition.

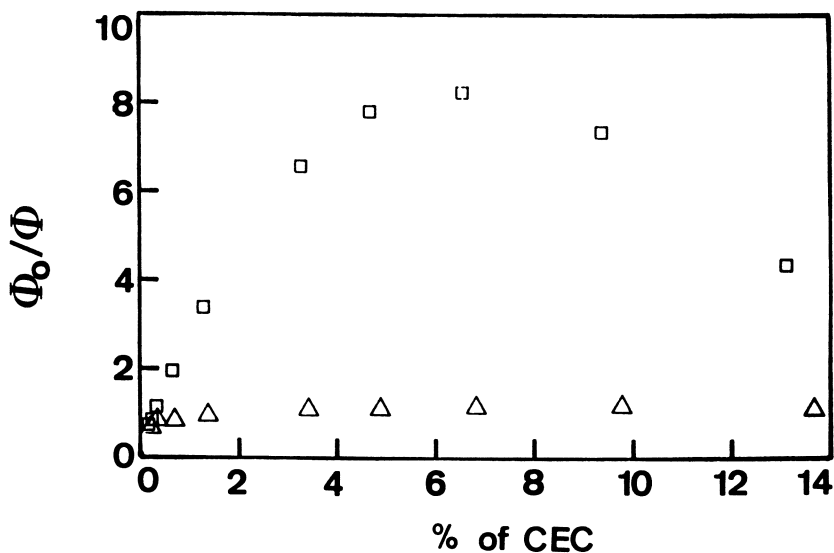


Figure 8: Ratio of the quantum yields, Φ_0/Φ , of proflavine as a function of the loading for Cs⁺-L (Δ) and K⁺-L (\square) at pH = 9.

increase again at higher loadings. These loadings and the corresponding values of Φ_0/Φ are given in Table II.

To check whether this increase of the fluorescence intensities at higher loadings was due to proflavine in solution, the suspensions were centrifuged or dialyzed in H₂O. The supernatant and the dialysate were investigated spectroscopically at 445 nm. No proflavine could be detected.

The third category is made up of Cs⁺-L and Cs⁺-H. In the former case the quantum yield remains almost constant over the range of loadings investigated (figure 8). For Cs⁺-H the quantum yield is constant up to 2% of the CEC and starts to decrease slowly at higher loadings (figure 6).

Discussion

The characteristic evolution of the quantum yields with loading, shown in figures 5-8, are clear fingerprints of the type of exchangeable cation and the type of clay in aqueous suspension. The following conditions must be

Table II. Maximum values of ϕ_0/ϕ and corresponding loadings

clay	loading % of the CEC	ϕ_0/ϕ
Na ⁺ -L	15	8.5
K ⁺ -L	7	8.3
Na ⁺ -BS	12	8.8

fulfilled: (1) The clay must be Fe-free to avoid quenching of the fluorescence by either structural Fe³⁺, ion-exchanged Fe³⁺ or Fe³⁺ impurities. (2) The loading with proflavine must be small on one hand to keep the clay suspensions stable, on the other hand, to avoid excess of dimers and therefore too low fluorescence intensities.

Spectroscopy. The important parameters, which determine the characteristic evolution of the fluorescence intensities with loading are (1) the particle size of the clays (hectorite vs. laponite); (2) the exchangeable cation (Na⁺, Ca²⁺, K⁺ vs. Cs⁺) and (3) for BS the pH. The latter is due to the extensive protonation of proflavine on the surface even in neutral suspension (Figure 3 and reference 5).

In this way fluorescence spectroscopy of adsorbed dyes is a useful tool to characterize clays in aqueous suspension. From figures 5-8 it is noted that (1) laponites behave differently from hectorites, except Ca²⁺-L; (2) PFH⁺ is the dominant species on Cs⁺-H and Cs⁺-L, because the fluorescence intensity is almost independent of the loading and thus no quenching due to dimers occurs; (3) the difference between neutral BS suspensions and BS suspensions at pH = 9 is the presence of PFH₂²⁺ in the former case.

A comparison with the absorption spectra of methylene blue on these clays gives interesting similarities, but also differences (4). Thus, protonation of methylene blue is found in neutral BS suspensions. The laponites are clearly distinguishable from hectorites, because of trimerization of methylene blue on laponites, which does not occur on hectorites. Finally, Cs⁺-

saturated clays are special in that methylene blue is preferentially adsorbed as a monomer (4). Differences are (1) that in the fluorescence of proflavine $\text{Ca}^{2+}\text{-L}$ behaves like the hectorites; (2) that $\text{K}^+\text{-H}$ and $\text{K}^+\text{-L}$ take a clear intermediate position between $\text{Na}^+\text{-}$ and $\text{Ca}^{2+}\text{-H}$ or -L when studied by the absorption spectra of methylene blue. This is not so clear in the case of the fluorescence of proflavine.

Quantum Yields. In aqueous solution the quantum yield for PFH^+ fluorescence is 0.34 (1). When the concentration is increased the quantum yield decreases. This decrease is ascribed to the quenching of the fluorescence of PFH^+ by dimers or higher aggregates (1,8). On clays monomers and dimers have been found and the dimer concentration on the surface increases with loading (5,6). Fluorescence quenching by these dimers is expected and also observed. The characteristic behavior of the quantum yield with loading, shown in figures 5 - 8, indicates that this quenching process is modulated by the clay.

The samples of the first category are characterized by a monotonous decrease of the quantum yield with loading. This means that at all loadings the quenching of the emission of the monomers by the dimers is possible. Either the clay particles occur as elemental clay platelets or they occur as aggregates with the interlamellar space freely available to both monomers and dimers. This is the case of $\text{Na}^+\text{-H}$, $\text{Ca}^{2+}\text{-H}$, $\text{K}^+\text{-H}$ and $\text{Ca}^{2+}\text{-L}$. For BS the quenching reaction occurs on the external surface of the aggregates only, because this clay is mica-like (9). When the data are presented in a semi-logarithmic plot against the surface concentration (figures 9 and 10), straight lines can be drawn. This is indicative for Perrin-type of quenching (appendix 1). For BS at pH = 9 one straight line is obtained; for the other samples of category 1 straight lines are obtained with slopes, characteristic for the exchangeable cation, above a characteristic loading. Below that loading a second straight line can be drawn through the data points with a higher slope, except for $\text{Ca}^{2+}\text{-L}$ and $\text{Cs}^+\text{-H}$.

For category 2 samples a minimum in the quantum yield of adsorbed proflavine at characteristic loadings occurs (Table II). Below the characteristic loadings of Table II they behave as the samples of the first category i.e. there is a gradual build-up of dimers, which quenches the monomer emission. Above the characteristic loadings of Table II this quenching is less efficient. This can be qualitatively explained by a combination of two factors. (1) The adsorption of proflavine occurs initially on external surfaces of aggregates of clay particles. This is followed by preferential interlamellar adsorption above the characteristic loading. The fluorescence of these interlamellar PFH^+ molecules is not quenched by $(\text{PFH}^+)_2$ on the external surface and the

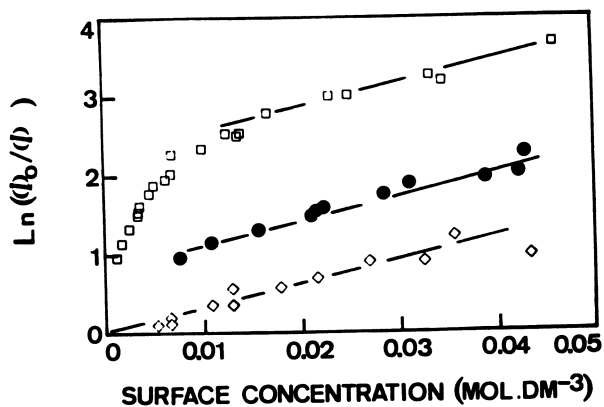


Figure 9: Perrin plots for $\text{Na}^+\text{-H}$ (\square) and $\text{Na}^+\text{-BS}$ (\diamond). The surface areas for the calculation of the surface concentration are respectively 775 and $110\text{ m}^2/\text{g}$. The black dots are the points of $\text{Na}^+\text{-H}$ at small loadings recalculated with a surface area of $125\text{ m}^2/\text{g}$.

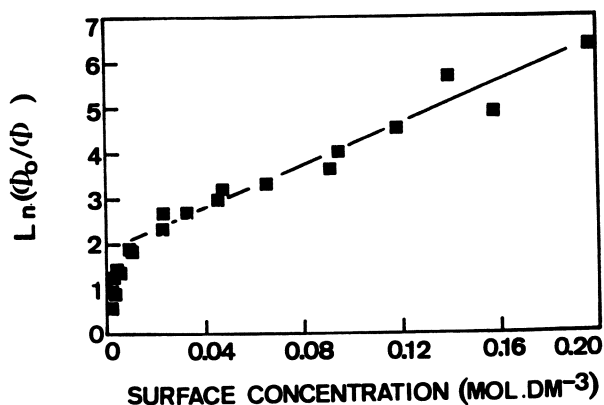


Figure 10: Perrin plot of $\text{Ca}^{2+}\text{-L}$. The surface concentration is calculated with a surface area of $819\text{ m}^2/\text{g}$.

quantum yield increases with loading. (2) Due to adsorption of proflavine the clay particles change their aggregation state at the characteristic loadings of Table II. PFH^+ becomes intercalated and unavailable for quenching.

Additional evidence that one or both of the mechanisms are operative comes from the data obtained on Cs^+ -saturated clays. Now, the individual clay platelets in the aggregates are separated by at most a monolayer of water (10). The proflavine molecules adsorb preferentially in that interlamellar space to replace the water and to form a monolayer of proflavine molecules. No dimers are formed, except for a small amount on the external surface of the aggregates, and the quantum yield is almost independent of the loading.

Surface Areas in Aqueous Suspension. Following Perrin's law, the slopes of the straight lines in figures 9 and 10 are proportional to the quenching volume (appendix 1). On the other hand, the spectra of figures 2-4 show that the spectroscopic properties of the adsorbed molecules are, on the average, independent of the type of clay and of the type of sites. Equal quenching volumes or equal slopes are then expected. Differences in slopes must then be ascribed to the fact that the surface concentrations were calculated with the wrong surface areas (775, 819 and 133 m^2/g for respectively H, L and BS). They can be adapted to give equal slopes by calculation of an effective surface area, keeping the thickness of the adsorbed layer constant at 1 nm. This can be done with the assumption that for $\text{Na}^+\text{-H}$ the surface concentration, calculated with the surface area of 775 m^2/g is exact (figure 9). The slopes of the straight lines for the other clays can be made equal to that of $\text{Na}^+\text{-H}$ by adapting the surface concentrations or the surface areas (appendix 2).

The effective surface areas, so obtained, are shown in Table III. For BS at $\text{pH} = 9$ 110 m^2/g is obtained, a value which is very close to the $\text{N}_2\text{-BET}$ surface area. It follows that the BS particles in aqueous suspension are, in our conditions, the particles of the powder: there is no swelling or disaggregation. $\text{Ca}^{2+}\text{-H}$ and $\text{Ca}^{2+}\text{-L}$ have almost the same surface area as $\text{Na}^+\text{-H}$ they are fully swollen so as to have their total surface area available to monomers and dimers of proflavine. $\text{K}^+\text{-H}$ and $\text{Cs}^+\text{-H}$ have smaller effective surface areas and thus are clearly aggregated in aqueous suspension.

For $\text{Na}^+\text{-H}$, $\text{Ca}^{2+}\text{-H}$ and $\text{K}^+\text{-H}$, which have a second straight line in figures 9 and 10 at the lowest loadings, effective surface areas for this low loading regime can be calculated in the same way: by recalculating the surface concentration so as to make the slopes of the straight lines equal to that of $\text{Na}^+\text{-H}$ at higher loadings. This is shown in figure 9 for $\text{Na}^+\text{-H}$. The effective

Table III. Calculated surface areas (m^2/g) of category 1 clays in aqueous suspension

clay	external surface	total surface
$\text{Na}^+\text{-H}$	125	775
$\text{Ca}^{2+}\text{-H}$	165	725
$\text{Cs}^+\text{-H}$	-	580
$\text{K}^+\text{-H}$	135	485
$\text{Ca}^{2+}\text{-L}$	-	840
$\text{Na}^+\text{-BS}$	110	110

surface areas are 125, 165 and 135 m²/g. It looks as if, at these small loadings, proflavine probes only the external surface of aggregates of clay particles and does not penetrate into the interlamellar space.

The picture of these clays in aqueous suspension, which emerges from these data, is that they occur as aggregates of individual clay platelets. At the smallest loadings (< 1% of the CEC) proflavine adsorbs preferentially on the external surface of the aggregate. At higher loadings interlamellar adsorption occurs both in the form of PFH⁺ and of (PFH⁺)₂ on the total surface in the case of Na⁺ and Ca²⁺; on part of the surface in the case of K⁺-H.

The data points of Cs⁺-H above a loading of 2% of the CEC can also be fitted with the Perrin equation. The resulting effective surface area (Table III) is similar to that of K⁺-H. As there are only four data points, the value of the effective surface area is subject to some uncertainty. But, qualitatively, as for K⁺-H, proflavine probes only part of the surface due to aggregation.

Conclusions

The fluorescence spectroscopy of proflavine is a technique to study the surface of clays in aqueous suspensions. The clays must be essentially Fe-free. The information, which one can obtain is similar to that obtained from absorption spectroscopy. The evolution of the fluorescence intensity with loading is characteristic of the type of clay and the type of exchangeable cation. Three categories of samples can be distinguished. The first category comprises Na⁺- Ca²⁺- and K⁺-H, Ca²⁺-L and BS (pH=9). The monotonous decrease of the quantum yield with loading follows Perrin's law. From this effective surface areas of these clays in aqueous suspensions can be calculated. This is the first time that it has been possible. The second category of samples comprises Na⁺-L, K⁺-L and BS in neutral suspension: the quantum yield goes through a minimum with loading. This can be attributed to a non-homogeneous distribution of the molecules over the surface or to a change in clay aggregation with loading. The Cs⁺-clays are special in that they preferentially adsorb PFH⁺ in the interlamellar space.

Appendix 1.

For the quenching of the fluorescence of PFH⁺ by (PFH⁺)₂ on the surface of clays Perrin's equation (11) is

$$\ln (\phi_0/\phi_m) = V N_a [(PFH^+)_2]$$

Here, the dimer concentration is the surface concentration of dimers, calculated from the dimer

absorption band at 430 nm (5,6) with the following procedure. N_a is Avogadro's number.

Assume a random distribution of the adsorbed proflavine molecules over the surface. The surface areas are 775, 819 and 133 m^2/g for H, L and BS respectively. The number for BS is obtained from Van Olphen and Fripiat (12). The two other numbers are calculated for average particle sizes of 300 nm and 30 nm for H and L respectively. The former is the size fraction of H used for our experiments, the latter is taken from Van Olphen and Fripiat (12). The surface volume is taken as the surface area times 1 nm, the thickness of the adsorbed layer in which the proflavine molecules reside. The same thickness has been taken by Nakamura and Thomas (13) and DellaGuardia and Thomas (14) for tris(2,2'-bipyridine)ruthenium(II) on laponite and montmorillonite. One could also take the thickness of the double layer, if it were possible to calculate. This only changes the numbers in the abscissae in figures 9 and 10.

V is the quenching volume. It is the volume around the excited molecule in which the quencher quenches the emission with unit efficiency. Quencher molecules outside that volume don't quench the emission.

Physically, Perrin's equation is valid for static quenching: excited molecules and quenchers don't move in and out the quenching volume within the lifetime of the excited state.

Appendix 2

The surface volume is, expressed in dm^3 , the surface area in dm^2 times the thickness of the Stern layer. We assume it to be 1 nm or 10^{-8} dm. In every clay suspension that we have investigated the proflavine concentration was $2.5 \cdot 10^{-6}$ M. The surface concentration is then $2.5 \cdot 10^{-6}$ M/surface volume or 250/ surface area (dm^2).

Acknowledgment

The authors thank the Fund for Joint Basic Research (Belgium) for financial support of this work. R.A.S. acknowledges the National Fund for Scientific Research (Belgium) for his position as Research Director. J.C. acknowledges a Ph.D. grant from the Instituut voor Wetenschappelijk Onderzoek in Nijverheid en Landbouw. The authors thank Laporte Industries Ltd for the gift of Laponite.

Literature cited

1. Haugen, G.R.; Melhuish, W.H. Trans. Faraday Soc. 1964, 60, 386 - 394.

2. Zanker, V.; Miethke, E. Z. Naturforschung A 1957, 12, 385-395.
3. Bailey, M.L. In Heterocyclic Compounds - Acridines; Acheson, R.M., Ed.; J. Wiley & Sons: New York; 1973; Chapter 10.
4. Cenens, J.; Schoonheydt, R.A. Clays and Clay Min. 1988, 36, 214 - 224.
5. Cenens, J.; Vliers, D.P.; Schoonheydt, R.A.; De Schryver, F.C. in Proc. Int. Clay Conf. Denver 1985; Schultz, L.G., Van Olphen, H. and Mumpton, F.A., eds., The Clay Minerals Society, Bloomington, Indiana, 1987; pp 352 - 358.
6. Cenens, J.; Schoonheydt, R.A. Int. Clay Conf. Strasbourg 1989, submitted.
7. Cenens, J Ph.D. Thesis, Katholieke Universiteit Leuven, Leuven, 1987.
8. Lopez Arbeloa, F.; Ruiz Ojeda, P.; Lopez Arbeloa, I. J. Photochem. & Photobiol. A: Chem. 1988, 45, 313-323.
9. Wright, A.C.; Granquist W.T.; Kennedy, J.V. J. Catalysis 1972, 25, 65-80.
- 10 Newman, A.C.D. In Chemistry of Clays and Clay Minerals; Newman, A.C.D., Ed.; The Mineralogical Society: London, 1987; p. 237.
11. Turro, N.J. Modern Molecular Photochemistry; Benjamin/Cummings: Menlo Park, 1978; 628pp.
12. Van Olphen, H.; Fripiat, J.J. Data handbook for clay minerals and other non-metallic minerals; Pergamon Press: New York, 1979; 346pp.
13. Nakamura, T.; Thomas, J.K. Langmuir 1985, 1, 568-573.
14. DellaGuardia, R.A.; Thomas, J.K. J. Phys. Chem. 1983, 87, 990-998.
15. Schoonheydt, R.A.; Cenens, J.; De Schryver, F.C. J. Chem. Soc., Faraday Trans. I 1986, 82, 281-289.

RECEIVED August 7, 1989

Chapter 20

Multinuclear Magnetic Resonance Studies of Structure and Dynamics at the Interface of Clay Materials

Jean Grandjean^{1,2} and Pierre Laszlo^{1,2}

¹Laboratoire de Chimie Fine aux Interfaces, Université de Liège, Sart Tilman par 4000 Liège, Belgium

²Laboratoire de Chimie Fine, Biomimétique et aux Interfaces, Ecole Polytechnique, F-91128 Palaiseau, France

Nmr studies of layer aluminosilicates are reviewed, with emphasis on the information uniquely provided by quadrupolar nuclei. Deuterium monitors local ordering and microdynamics for heavy water molecules. Lithium-7 and sodium-23 show residual quadrupolar splittings that are diagnostic of the precise state of the hydrated alkali metal cations. The example of tactoids formed by suspensions in aqueous solution of Ecce Gum BP clay is detailed: increase in their number with a greater amount of suspended clay; orientation under application of a very high magnetic field; preferred modes of reorientation for those water molecules pinched in-between condensed counterions and the charged clay platelets, in relation with Lewis and Brønsted acidities for the clay.

Our interest in layer silicates stems from the use we have made of clay minerals and of modified clays to catalyze important organic reactions (1-4). One example will suffice to illustrate the considerable improvements in reaction rates that are feasible. The cyclohexadienone-phenol sigmatropic rearrangement, on a given substrate whose details are unimportant here, can be catalyzed by sulfuric acid in n-hexane solution: the half-life is about 5 h at a temperature of about 80°C. By resorting to the acidic K10 montmorillonite, with a surface acidity placing it between concentrated nitric acid and oleums of sulfuric acid, the half-life remains about the same -- but at room temperature! If now one exchanges the interlayer cations of the clay partly with ferric ions, the half-life becomes 5 min at room temperature. And if the doping with ferric ions is combined with careful drying of the clay, in order to boost both its Brønsted and its Lewis acidities, then the half-life becomes 5 s, still at room temperature. This amounts to an acceleration by five or six orders of magnitude by comparison to the reaction catalyzed by sulfuric acid under homogeneous conditions.

We present in this chapter some of the results that have been obtained, by us and by others, on the structure and on the

0097-6156/90/0415-0396\$06.00/0
© 1990 American Chemical Society

dynamics at clay interfaces, by nuclear magnetic resonance (nmr) methods. Our rationale for using high-resolution liquid-phase nmr is three-fold : (i) the method, while not cheap, is inexpensive with respect to other techniques for studying surfaces, such as EELS, LEEDS, Auger, ESCA, etc.; it is general, and need not be restricted to crystallographically well-defined surfaces of clean metal and metal oxide surfaces; (ii) the method has the asset of being local, i.e. it provides information only about the nuclei examined and about their immediate chemical environment; (iii) we have had extensive experience in the use of nmr methodologies in this laboratory, accumulating about 50 years of nmr practice during the course of both our careers.

To summarize briefly the use of nmr methods for the structural and dynamic problems at hand, a first class of applications is the direct observation of the nuclei present in the solid support (^{29}Si , ^{27}Al , ^{17}O , in the first place). Alternatively, one may examine nuclei of ionic species (^{23}Na , ^{35}Cl , ^{39}K , etc.) or of neutrals (^1H , ^{13}C , etc.) interacting with the clay surface. In this second mode, one reaps information about restriction in ionic or molecular mobility, translational and reorientational, due to the proximity of the aluminosilicate solid surface.

Phyllosilicate clays are built from tetrahedral sheets made of SiO_4 silicate units and of octahedral sheets resulting from the condensation of octahedra -- such as the aluminate AlO_6 octahedron -- centered on a divalent or on a trivalent cation. Layers can be constituted of one tetrahedral sheet associated with one octahedral sheet (1:1). Or they can be made of one octahedral sheet sandwiched in-between two tetrahedral sheets (2:1). There are other combinations, associating up to four sheets.

The 2:1 phyllosilicates whose planar sheets bear negative charge extensively delocalized are perhaps the most interesting, from their catalytic activity. Depending upon occupation of the octahedral sites, full or only to the extent of 2/3, they are known as tri- or di-octahedral phyllosilicates. The presence of superficial negative charge is due to isomorphous substitution. The clay structure is locally irregular. A divalent cation may substitute for aluminum (III) in the octahedral layer. Or a trivalent cation replaces silicon (IV) in the tetrahedral layer. Accordingly, the valences of the oxygens are no longer saturated -- and some of the surface oxygens end up bearing formal negative charges (see in Fripiat's chapter the distinction between pH-dependent and independent charges). In order for electroneutrality to be maintained, positive ions, Na^+ for instance, flock to the interface (5). Depending upon water content, the interstitial cations swim in more or less water. Starting with a totally dehydrated and collapsed smectite clay, letting in water increases the basal spacing d_{001} determined by X-ray diffraction by discrete amounts as one inserts one monomolecular water layer, two, three, etc. (5,6). Furthermore, one may exchange the interlamellar cations with other inorganic or even organic cations. Depending upon their size these guest ions will affect the interlamellar space. Conversely, if one wants to hold open the interlamellar spacing at a given value, one may resort to pillaring the clay (7); pillared clays are covered in another chapter, that by Tom Pinnavaia.

Quadrupolar nuclei to probe local ordering : principles and selected applications (8)

Quadrupolar nuclei, such as ^{17}O and ^{27}Al ($I = 5/2$ for both), are potential probes for local order whenever their environment is anisotropic on a time average. The most widely used nucleus for this purpose, though, is deuterium. It has been applied to the local and to the overall ordering within model membranes and within biological membranes (9). Because the analogy of phyllosilicate clays and membranes is not so far-fetched -- an organophilic clay, having quaternary ammonium ions with at least one long hydrophobic chain as the interlamellar cations, has a hydrophobic interior and an outer surface with polar head groups, just like a bilayer membrane -- we shall review quickly some of the vital pieces of information provided by deuterium quadrupolar residual splittings on the microdynamics of membranes. They will serve as guidelines for the type of information that can be obtained in like manner with phyllosilicate 2:1 clays.

With a spin quantum number $I = 1$ the deuterium nucleus has the $2I + 1 = 3$ spin states $+1$, 0 , and -1 . The two transitions $(+1, 0)$ and $(0, -1)$ are allowed, but they are also degenerate. Two conditions are necessary to remove the degeneracy : the presence of an electrostatic field gradient (efg) at the nucleus, and anisotropic reorientation. The residual splitting observed $\delta\nu$ depends both on the magnitude of the deuterium quadrupolar coupling constant, and on the time-averaged anisotropic reorientation of the main axes of the quadrupolar tensor with respect to the applied directing magnetic field B_0 .

Take the example of a carbon-deuterium C-D bond. The residual splitting $\delta\nu$ is given by $\delta\nu = 0.75 \times S_{\text{C-D}}$, where the order parameter $S_{\text{C-D}}$ has the form $(3 \cos^2\alpha - 1)$, where α is the angle between the C-D vector and B_0 . For example, consider a molecule of phospholipid within a membrane that has been labeled with deuterium in various positions. The different C-D vectors reorient, in a time-dependent manner, because of the various motions : torsional around the phospholipid axis; or the slower lateral diffusion of the phospholipid, within the bilayer; or by the sliding of the two halves of the bilayer with respect to one another. One finds experimentally for liposomes, for example that the $S_{\text{C-D}}$ order parameter decreases as a function of the distance from the membrane surface : the head group is anchored rigidly at the water interface, and the chain gains mobility as it is looked at further away from this fixed point. Such local mobility and segmental motion in phospholipid chains have been monitored as the chain is made locally rigid by unsaturation, as peptides, proteins, or steroids are added, etc. (9-11).

Another source of microdynamic information comes from the deuterium relaxation rates. The quadrupolar coupling constant (e^2qQ/h) expresses the magnitude of the coupling between the electric quadrupole moment Q of the nucleus and the efg q at the nucleus (e is the electronic charge, and h is Planck's constant). It provides a relaxation mechanism for the quadrupolar nucleus of its Fourier component at the Larmor (resonance) frequency for this nucleus is non-negligible. It has such a Fourier component because tumbling of the molecule the quadrupolar nucleus is part of, in a

fluid, modulates (e^2qQ/h) with a characteristic time τ_R , the reorientational correlation time. Any nmr relaxation mechanism depends on the square of the interaction strength that provides such a relaxation pathway. Accordingly, the deuterium relaxation rates, which are determined predominantly by quadrupolar relaxation, are proportional to $(e^2qQ/h)^2 \times \tau_R$, under extreme narrowing conditions. Since deuterium quadrupolar coupling constants (e^2qQ/h) are of the order of 200 kHz, this internal clock will be able to measure correlation times τ of the order of $(e^2qQ/h)^2$, i.e. 5 μ s. Outside the extreme narrowing conditions, i.e. when molecular tumbling is not very fast (τ_R values greater than 10 ps, to give an order-of-magnitude), the longitudinal and transverse relaxation rates differ. The former is measured along the direction of B_0 , the latter is measured perpendicular to it. Their expressions involves spectral densities $J(\omega)$. By looking at these detailed expressions (which all the standard books on nmr carry), it is apparent that the accessible correlation times τ_R are shorter than about 10 ns. Accordingly, the longitudinal relaxation rate remains unaffected by the slower motion of the order director, perpendicular to the surface of the membrane (11). Conversely, the transverse relaxation rate is affected both by the fast segmental motion of the phospholipid chain and by the much slower lateral diffusion of the phospholipid molecules (12).

Deuterium nmr describes in equally clear-cut and elegant a manner the static (order parameter) and the microdynamic (correlation time τ_R) properties of hydrocarbon chains in aggregated surfactants (13). The example of octanoate, in various phases, resembles the membrane behavior of phospholipids: a decrease of the S_{C-D} order parameter is found for deuterium relaxation rates, they conform to a model combining fast local reorientation and a much slower overall motion (14). Long-chain polymers also form oriented mesophases (for instance, polybenzylglutamate, a rigid-rod-like macromolecule, orders itself into a nematic mesophase under the application of B_0), and deuterium nmr again provides a wealth of information (15-16). Interesting studies have been made on thermotropic polymers, correlating their mechanical response to such molecular properties obtained by deuterium nmr. Polyester fibers are an example (17). In this last instance, nmr had the unique virtue of finding an equilibrium between two phases (17).

Not only can molecules constituting the oriented phase be thus studied. Solutes present in this mesophase will also be oriented through operation of anisotropic intermolecular forces. An example is that of deuterium-labeled D gramicidin. When dissolved in a nematic mesophase, it displays a series of deuterium doublets. Their residual splittings $\delta\nu$ are almost temperature-independent. This points to a rigid structure for the peptide, an helix that reorients about the director of the liquid crystalline phase (18).

Information derived from nmr of quadrupolar hydrated cations.

Usually, there is fast exchange of the looked-at cations between several sites, typically the bulk solvent (water, most often) and the anionic head-group of the surfactant, or of a charged solid surface (for a 2:1 phyllosilicate). If the quadrupo-

lar interaction is not made vanishingly small by the mobility of the cation at its point of attachment (which can occur either by mass action site binding, or by ionic condensation for mutual screening of adjoining charges), one observes a residual quadrupolar splitting. It is proportional to the mole fraction of attached cations.

Thus the ^{23}Na residual splittings have given information about interaction of various sodium salts with a zwitterionic surfactant. They allow conclusions to be made on the predominant localization of the sodium ions : with NaSCN , they penetrate in-between the polar groups of the surfactant; they don't with Na_2CO_3 (19). The residual splitting also depends on the hexagonal or lamellar type of the mesophase (19).

Likewise, ^7Li ($I = 3/2$, as for the ^{23}Na nucleus) nmr monitors interaction of lithium cations with model membranes. Competition with divalent cations shows up as a reduction in the lithium residual splitting (20).

Sometimes, the residual splitting is too small to be measured : because the aggregates are too small. In such a case, other nmr observables, the chemical shifts or relaxation rates, can still provide useful information. The observed values are weighted averages of the values characteristic of each site, free or bound, under fast chemical exchange. Such means have been applied to ^{23}Na nmr studies of the aggregation of an ionic surfactant (21). Analysis of the data is no longer unambiguous : due to superimposition of several absorptions the lineshape becomes complex. Even for the simple case of sodium laurate, for which the observed ^{23}Na resonance was not a simple lorentzian absorption, two different analyses have been published (22).

Relaxation rates can provide uniquely useful information about the dynamics of the reorientation for a quadrupolar ion, for instance a cation interacting with the charged surface of a layer clay . The transverse relaxation rate can be at a maximum in three types of situations :

- (i) the counterion is affixed to an entity undergoing slow reorientation; under such conditions, the extreme narrowing limit is not fulfilled (23));
- (ii) the counterion diffuses between regions of the sample differing in their efg's (24);
- (iii) the cation exchanges rapidly between two sites in differing environments, such as the isotropic liquid and a surface (a particular case of (ii), (23)).

In this last case, the ratio of enhancements of the longitudinal and transverse relaxation rates, relative to those of the "free" solvate cation in solution, gives access to the value of the reorientational correlation time of the cation interacting with the surface.

Let us summarize here this part of the study, since it is published elsewhere (25). First, it is important to ascertain the fast exchange of the sodium counterions between the bulk solution and the vicinity of the platelets. This is done by checking the effect of temperature on relaxation rates. For instance, for a sample of the Ecce Gum BP bentonite (44.2 mg/mL water) the sodium-23

longitudinal relaxation rate varies from 133 s^{-1} at 274 K to 19 s^{-1} at 308 K.

The next crucial observation is the non-identity of the longitudinal and transverse relaxation rates. It joints unambiguously to case (iii) above. The appropriate expression for the ratio of the enhancements ΔR_1 of the longitudinal ($i=1$) and transverse ($i=2$) relaxation rates is a function of the spectral densities $J(\omega)$ at frequencies zero, Larmor, and twice the Larmor frequency ($\omega = 0, \omega_0, 2\omega_0$), as follows :

$$\frac{\Delta R_1}{\Delta R_2} = \frac{\frac{0.4 \tau_c}{1 + \omega^2 \tau_c^2} + \frac{1.6 \tau_c}{1 + 4 \omega^2 \tau_c^2}}{0.6 \tau_c + \frac{\tau_c}{1 + \omega^2 \tau_c^2} + \frac{0.4 \tau_c}{1 + 4 \omega^2 \tau_c^2}}$$

We find experimentally a ratio $\Delta R_1 / \Delta R_2 = 0.2$ for three samples differing in clay content, at 301 K.

We have used this procedure to determine as 8.2 ns the correlation time for sodium cations hovering in the vicinity of the charged surface of a montmorillonite (Ecca Gum BP, English China Clay). Such a value (25) is not unprecedented. Similar values have been reported for sodium ions near a silica surface (26).

Tactoids formed by phyllosilicate gels. Orientation under application of a strong magnetic field.

We suspend a gel of montmorillonite in light or in heavy water. The clay is again Ecca Gum BP (English China Clay, St. Austell, Cornwall), a di-octahedral 2:1 phyllosilicate, with isomorphous substitution confined to the octahedral layer. We see a doublet for the deuterium resonance of D_2O . Observation of such a residual splitting $\delta\nu$ implies (a sufficient but not a necessary condition), the existence of a local order of the clay platelets, which in turn orders about the water molecules. Only the water molecules closest to the clay interface will be affected. They are in chemical exchange with the interlayer (gallery positions) and with the bulk water molecules. The alignment of the clay platelets with respect to the applied magnetic field B_0 was confirmed experimentally, in the following manner : for the highest clay content (0.05 g.mL^{-1}), we observed a gradual increase of the residual splitting $\delta\nu$ with the residence time in the superconducting magnet ($B_0 = 7.0463 \text{ Tesla}$) till it reached a constant value, after about 0.5 h . This observation is analogous to previous reports for nematic mesophases (27).

Furthermore, we find linear relations between the observed residual splitting and the amount C of suspended clay :

$$\delta\nu = -7.5 \pm 2.0 + (2,620 \pm 90) \times C$$

We interpret this finding in the simplest way, as an increase in the number of tactoids (but not in their size) as more and more

clay material is available for their formation (28; and Fripiat's chapter in this volume).

The analysis of the data is straightforward, and parallels that given for D_2O molecules oriented in other nematic mesophase. The residual splitting D is given by

$$D = (3e^2qQ/h) \langle (3 \cos^2 \alpha - 1) A \rangle \quad (4I)(2I-1),$$

where α is the angle made by the local director with B_0 . We assume slow modulation so that the angle α remains constant; by slow is meant slower than the residual quadrupolar anisotropy (of the order of $10^5 s^{-1}$).

The residual anisotropy A describes the orientation assumed by heavy water molecules. It is expressed as a function of the Saupe order tensor and of the Euler angles describing the orientation of the D_2O water molecule with respect to the local director (29) :

$$A(2H) = \frac{1}{2} (3\cos^2\beta - 1 + \eta\sin^2\beta)S_{33} - \frac{1}{6} (3\sin^2\beta + \eta(\cos^2\beta + 1))(S_{11} - S_{22})$$

S_{ii} = principal axes of the Saupe ordering tensor

$\beta \stackrel{ii}{=} 1/2$ (DOD angle)

η = asymmetry parameter of the efg tensor

Because water molecules exchange (relatively fast) between the surface of the clay platelets and the bulk sites, the observed residual splitting $\delta\nu$ is simply proportional to the mole fraction of water at the periphery of the tactoids, and to the quadrupolar coupling constant (e^2qQ/h). From knowledge of the characteristics of the clay (specific surface), one can estimate the mole fraction of water present at the interface for the various clay contents C (28). Thus, the linear experimental dependence (such as was quoted above) yields a deuterium quadrupolar coupling constant of 176 ± 20 kHz. This result, because it is within the narrow range for deuterium quadrupolar coupling constant observed by a variety of methods (30,31), provides a handsome check on the self-consistency of our treatment. In so doing, we postulate a two-site exchange. This is an over-simplification (see detailed description in Fripiat's chapter): the straight line does not go through the origin. However, it is also a good approximation : forcing the regression to go through the origin changes the slope by a mere 6%!

Polarization of water molecules and surface acidity, in relation to the nature of interlamellar cations.

Examining suspensions of homoionic montmorillonites, we find a residual quadrupolar splitting dependent upon the nature of the interlamellar cations,

<u>cation</u>	<u>$\delta\nu(^2\text{H})$</u>	<u>$\delta\nu(^{17}\text{O})$</u>	<u>$\delta\nu$ ratio: $^{17}\text{O}/^2\text{H}$</u>
Li	7.9	0	0
Na	14.5	76	5.1
K	26.2	130	5.0

clay content C = 0.0238 g.mL; T = 320 K

Similar observations were made for a sodium clay, with increasing amounts of the divalent calcium or magnesium ions (32). In the presence of calcium ions, one can even witness a change in the sign of the deuterium quadrupolar residual splitting. A similar observation was reported recently with heavy water molecules present in and oriented by an uniaxial mesophase (33).

Since the residual quadrupolar splitting $\delta\nu$ for deuterium changes sign, this implies in turn a sign change for the residual anisotropy A, which in turn indicates a change in the mode of preferred reorientation for water molecules. The water molecules concerned are those that are squeezed in-between the charged silicate surface and the positively-charged counterions. The present measurements make for direct observation of fully hydrated condensed counterions.

A bit of explanation is required here for those readers unfamiliar with the condensation concept, a key notion to describe polyelectrolytes. Consider as here a polyanion. If the charges are brought closer to one another, on the average, below a critical distance their mutual repulsion is such that -- in order to continue to obey first principles electrostatics such as the Poisson equation -- they screen themselves with an atmosphere of counterions. This atmospheric condensation, which can coexist with ionic binding at the individual sites, boosts the local concentration of counterions in the space surrounding the polyelectrolyte by as much as three orders of magnitude. The nmr measurements analyzed here focus on these water hydration molecules coordinated to condensed sodium counterions, next to the surface of the tactoids (see Fripiat's chapter).

Such water molecules at the clay interface have an option between two preferred modes of reorientation : by rotation around the O-D axis, i.e. around the hydrogen bond anchoring them to the clay surface; or by reorientation around the O-M axis, where M denotes the metallic cation coordinated onto the water oxygen through one of the two lone pairs.

The switch in sign of the deuterium residual splitting shows that, as there is more divalent ions, the preferred mode of reorientation goes from the O-D axis to the O-M axis : as the electrostatic bond to the metallic cation is made stronger, water molecules tend to reorient predominantly about it -- a not unexpected conclusion.

With lithium counterions, as compared with sodium cations, a similar explanation holds. The water-lithium interaction is stronger than the water-sodium interaction. Hence, there is a somewhat greater tendency for lithium-coordinated water molecules to reorient around the O-M axis -- hence the observed smaller value

of $\delta\nu$ for lithium than for sodium (or for sodium compared with potassium), in the above Table.

Restricted mobility within the interlamellar space

For the self-same clay samples, we have measured longitudinal relaxation rates for deuterium nuclei in heavy water. The relaxation rate is enhanced in proportion to the amount of suspended clay, according to:

$$R_1(\text{obs}) - R_1(\text{pure D}_2\text{O}) = 0.01 + (20.7 \pm 1.2) \times C.$$

The chemical exchange involved between the coexisting sites is fast, as can be ascertained by the dependence of these relaxation rates upon temperature. With a two-site model, the last term (20.7 C) can be identified with the product of the mole fraction p_B of bound water at the interface by the relaxation rate characteristic of this water affixed at the clay interface. The readers will recall that the water molecules reorient according to a combination of two motions: a fast motion of water molecules around the local director (that describes the local orientation within the sample), a slow motion of this local director with respect to the applied directing magnetic field B_0 (29,34). The former has a correlation time of about 10 ps, the latter has a correlation time greater by three orders of magnitude, with a value greater than 10 ns (34). At the Larmor frequency of our measurements (46.1 MHz), the spectral densities are such that longitudinal relaxation remains unaffected by the slow motion (34).

Deuterium nuclei in water molecules have negligible asymmetry parameters and residual anisotropies. After correcting for the paramagnetic impurities present, that affect relaxation rates somewhat (35), one obtains from the experimental data a value of the longitudinal relaxation rate for the water deuterons in the bound state of 650 s^{-1} . This value incorporates the quadrupolar coupling constant (above determined) and the correlation time for bound waters. Using the standard expression for quadrupolar relaxation (29,35) yields a value for $\tau_c = 1.6 \text{ ns}$.

Such a value appears to be intermediate between the two types of motion mentioned above. The explanation is that the above values apply to fully dispersed systems. We are monitoring here the "fast" reorientation of a local director for clay platelets that have stacked-up into tactoids and that therefore are much slower in reorienting.

Another descriptor of the mobility of water molecules in contact with the clay layers is the water self-diffusion coefficient. A fine recent review summarizes the theoretical and practical aspects of measurement by spin-echo nmr methods of this parameter (36). The plot of the decrease in the water self-diffusion coefficient as a function of C, the amount of suspended clay, for the same samples, is again a straight line going through the origin. By resorting once more to a similar analysis in terms of a two-state model (bound and "free" water), one comes up (25) with a self-diffusion coefficient, for those water molecules pinched in-between counterions and the clay surface, of $1.6 \cdot 10^{-15} \text{ m}^2 \cdot \text{s}^{-1}$,

in order of magnitude agreement with a result from inelastic neutron scattering (37).

Summary, by way of conclusion

Nmr methods have unrivalled potential to explore interfaces, as this account has striven to show. We have been able to determine the mobility of hydrated sodium cations at the interface of the Eccla Gum BP montmorillonite, as 8.2 ns. We have been able to measure the translational mobility of water molecules at the interface, their diffusion coefficient is $1.6 \cdot 10^{15} \text{ m}^2 \cdot \text{s}^{-1}$. We have been able to determine also the rotational mobility of these water adsorbate molecules, it is associated to a reorientational correlation time of 1.6 ns. Furthermore, we could show the switch in preferred reorientation with the nature of the interlayer counterions, these water molecules at the interface tumbling about either the hydrogen bond to the anionic surface or around the electrostatic bond to the metallic cation they bear on their back. And we have been able to achieve the orientation of the Eccla Gum BP tactoids in the strong magnetic field of the nmr spectrometer.

Acknowledgments

The authors thank Ministère de l'Education Nationale, Brussels for a grant (2.4516.82) in support of their NMR studies. Jean Grandjean gratefully acknowledges support from Fonds National de la Recherche Scientifique, Brussels to perform self-diffusion experiments at the University of Uppsala, Sweden. These measurements were only made possible thanks to the hospitality and the expertise of Professor Peter Stilbs, now at Stockholm, and Dr. R. Rymdem, in Uppsala.

Literature Cited

1. Preparative Chemistry Using Supported Reagents, Laszlo, P., Ed.; Academic Press : San Diego, CA, 1987.
2. Chemical Reactions in Organic and Inorganic Constrained Systems, Setton, R., ed.; D. Reidel Publ. : Dordrecht, Holland, 1986.
3. Laszlo, P., Science 1987, 235, 1473.
4. Laszlo, P., Accounts Chem. Res. 1986, 19, 121.
5. Theng, B.K.G., The Chemistry of Clay-Organic Reactions, J. Wiley and Sons : New York, 1974; chapter 1.
6. Fukushima, Y., Clays Clay Minerals 1984, 32, 320.
7. Pinnavaia T.J., Science 1983, 220, 365.
8. Laszlo, P., ed., NMR of Newly Accessible Nuclei, Academic Press, New York, 2 vols, 1983 and 1984.
9. Seelig, J.; MacDonald, P.M., Acc. Chem. Res. 1987, 20, 221; Watts, A., J. Bioenerg. Biomembranes 1987, 19, 625.
10. Salmon A.; Dodd, S.W.; Williams, G.D.; Beach, J.M.; Brown, M.F., J. Am. Chem. Soc. 1987, 109, 2600.
11. Jarell, J.C.; Smith, I.C.P.; Jovall, P.A., Mantsch, H.H.; Siminovitch, D.J., J. Chem. Phys. 1988, 88, 1260.
12. Bloom, M.; Sternin, E., Biochemistry 1987, 26, 2101.

13. Soderman, O. in Nuclear Magnetic Resonance, Webb, G.A., Ed.; Specialist Periodical Report, 14; Royal Society of Chemistry: London, 1985, p. 350.
14. Soderman, O.; Henriksson, U., J.C.S. Faraday Trans I 1987, 83, 1515.
15. Samulski, E.T., Polymer 1985, 26, 177.
16. Spiess, H.W., Adv. Polymer Sci. 1985, 66, 23.
17. Muller, K.; Schleicher, A.; Ohmes, E.; Ferrani, A.; Kotche, G., Macromolecules 1987, 20, 2761.
18. Davis, J.H., Biochemistry 1988, 27, 428.
19. Rendall, K.; Tiddy, G.T.D.; Trevethan, M.A., J. Colloid Interface Sci. 1984, 98, 565.
20. Fossel, E.T.; Sarasua, M.M.; Koehler, K.A., J. Magn. Resonance 1985, 64, 536.
21. Kilpatrick, P.K.; Miller, W.G., J. Phys. Chem. 1984, 88, 1645.
22. Lerner, L.; Torchia, D.A., J. Am. Chem. Soc. 1986, 108, 4264.
23. Lindman, B.; Forsén, S. NMR Basic Principles and Progress, vol. 12; Diehl, P.; Fluck, E.; Kosfeld, R., Eds; Springer-Verlag: Heidelberg, 1976, p. 274.
24. Berendsen, H.J.; Edzes, H.J., Ann. N.Y. Acad. Sci. 1973, 204, 459.
25. Grandjean, J.; Laszlo, P.; J. Magn. Resonance, in press.
26. Jung, H.M.; Fuerstenau, D.W., Langmuir 1987, 3, 1114.
27. Bastiaan, E.W., Mac Lean, C.; Van Zyl, P.C.M.; Bothner-By, A.A., Ann. Rep. NMR Spectry, G.A. Webb, Ed.; Academic Press, London, 1987, 19, 35.
28. Fripiat J.; Cases, J.; François, M.; Letellier, M., J. Colloid Interface Sci. 1982, 89, 378.
29. Halle, B.; Wennerström, J., J. Chem. Phys. 1981, 75, 1928.
30. Fripiat, J.J.; Letellier, M., J. Magn. Resonance 1984, 57, 279.
31. Cruz M.I.; Letellier, M.; Fripiat, J.J., J. Chem. Phys., 1978, 69, 2018.
32. Grandjean, J.; Laszlo, P., Clays Clay Minerals, in press.
33. Guo, W.; Wong, T.C., Langmuir 1987, 3, 537.
34. Piculles, L., J.C.S. Faraday Trans I. 1986, 112, 556.
35. Woessner, D.E., J. Magn. Resonance 1980, 39, 297.
36. Stilbs, P., Progr. NMR Spectrosc. 1987, 19, 1.
37. Breen, C.; Adams, J.M.; Riskel, C., Clays Clay Minerals 1985, 33, 245.

RECEIVED September 21, 1989

Chapter 21

Near-Infrared Correlation Spectroscopy

Quantifying Iron and Surface Water in a Series of Variably Cation-Exchanged Montmorillonite Clays

Lelia M. Coyne^{1,6}, J. L. Bishop¹, T. Scattergood², A. Banin³, G. Carle⁴, and J. Orenberg⁵

¹San Jose State University, San Jose, CA 95192

²State University of New York at Stony Brook, Stony Brook, NY 11794

³Hebrew University, Rehovot 76100, Israel

⁴NASA-Ames Research Center, Moffett Field, CA 94035

⁵San Francisco State University, San Francisco, CA 94132

Minerals are multisite catalysts for a variety of natural reactions. Clay minerals contain most of the generic types active sites of all minerals. Determining reaction mechanisms on natural catalysts is difficult because they frequently are not monomineralic and contain multiple active centers. Near Infrared Reflectance Analysis (NIRA) is a promising method for studying determinants of chemical reactions on mineral surfaces. Using NIRA, the quantitative relationship between absorbance and both iron and hydration was examined in a series of variably Ca/Fe-exchanged montmorillonite clays prepared from crude SWy and Otay montmorillonites (naturally occurring in the Na/Ca form). We have found linear relationships in the 600-1100 nm wavelength region between spectral absorbance and total iron (as Fe₂O₃) over a range of 1-7% (0 - 100% of the cation exchange capacity for both parents) and in the 600-1100 nm and 1100-2500 nm wavelength regions between spectral absorbance and water content resulting from variation of relative humidity over a range of 4-100%. The correlation with iron is relatively insensitive to the location (surface *vs.* structural) of the iron. The correlation with moisture is keenly sensitive to the environment of adsorbed water. We also have determined that, on increasing water content, absorbance is increased over most of the 600-1100 nm (iron) wavelength range in Na- or Ca-clays whereas it is decreased in Fe-clays. By contrast, absorbance is

⁶Current address: Mail Stop 239-4, NASA-Ames Research Center, Moffett Field, CA 94035

0097-6156/90/0415-0407\$06.75/0

© 1990 American Chemical Society

increased with increasing water for all clays in the 1100-2500 nm (hydroxyl) region. The sign reversal of the correlation with water in the region of iron absorption in the Fe-clay can be attributed to hydroxylation of the surface iron with consequent decrease of iron absorption.

Clay minerals have long been recognized as multisite catalysts for a variety of organic reactions (1-7). Among the demonstrated determinants of catalytic activity are structural cation substitutions and their charge compensating exchangeable cations, the number and condition of the structural hydroxyls and the degree of hydration of the surface. Some examples of these determinants are: a) structural ferric iron in the mechanism of montmorillonite-induced hydrazine oxidation (8); b) exchangeable iron in the oxidation of carboxylic acids (the labeled release experiment used as one of the Viking biology experiments to test the surface of Mars for life) (9); c) residual structural hydroxyls in the polymerization of styrene on calcined clay aluminosilicates (10, p. 181); d) dissociable water in the dehydration of alcohols (11). Trapped separated charge pairs stored as O⁻-centers have been shown in other mineral systems (12) and postulated in clay systems (13-14) to influence surface reactivity.

The activity of clay minerals, proven in the reactivity of terrestrial (15-16), and postulated in Martian (9) soils, is disproportionate to their quantity, relative to other minerals. This is the result of several factors: small particle size, high specific surface area, Bronsted and Lewis acidity, redox and other potentially catalytically active sites common to clay minerals, and a limited capacity for size exclusion (which is influenced by the number and valence of exchangeable cations (6)).

Although the surface reactivity of clays has been studied, there are several reasons why the true determinants of reactivity have not yet been cleanly characterized. These are:

- a) Clay minerals represent a broad class of non-stoichiometric compounds, thus they occur with a wide range of compositions.
- b) Experimentally it is demanding to select or prepare natural materials which differ in the concentration or condition of only one type of site. Therefore, attributing the dependence of a reaction to a given site is difficult, because any change in the reaction rate induced by alteration of this site may be enhanced or diminished by adventitious alteration of another.
- c) A putative site, in itself, may be less important than covarying factors. For example, activity may appear to be correlated with increasing cationic substitution

in the crystal structure, but instead may actually be associated with acidity of the waters of hydration of the exchangeable cations.

- d) Recent studies have shown interaction between several clay sites previously considered to be independent, i.e. interlayer hydration, the oxidation state of structural iron, and the O-center population (17).
- e) The optimal concentration of a structural entity serving in more than one role may result from a compromise between amounts maximizing its different effects. For instance, the acidity of the surface of clays is a strong function of the degree of dryness, as Bronsted acidity is thought to result from the dissociation of water of hydration of exchangeable cations (18-20). Thus, the activity of the surface in an acid catalyzed reaction, such as styrene polymerization (10), should be increased by increasing dryness. On the other hand, the mobility of reactants toward the surface and products away from it will be influenced by the presence of a transporting solvent, such as water. Therefore, the optimal water concentration may lie somewhere between those maximizing acidity and mobility. In fact, the formation of peptide bonds on clay surfaces is efficiently promoted only in a wet/dry cycling reaction protocol (21), a common condition in geological settings and, likely, of great reactive significance.
- f) Exclusive responsibility of a single site for a given reaction may not be the case. More than one site may be involved, as most reactions proceed through several steps, not all of which may be facilitated by the same site. For instance, montmorillonite is a multifunctional catalyst in the cyclization of 3' AMP to 2', 3'-cyclic AMP, where it serves as a selective adsorbent for products and reactants, and as a catalyst for two reactions within the overall transformation (22).

For all of the above reasons, studies of relationships between mineral sites and mineral reactivity would be simplified, and the confidence in the findings increased, if statistically testable methods were to be used to identify key variables and to test hypotheses. Near infrared reflectance analysis (NIRA) is such a method. It was developed by Karl Norris in the 1960's to quantitate the concentration of key constituents in multicomponent mixtures such as wheat (23).

In NIRA, after measurement of the absorption spectra, (determined from reflectance data) independently determined values of quantities of interest are entered into a computer as constituent data. A linear regression of constituent amount as a function of wavelength is performed throughout the spectrum. Analytical wavelengths suitable for quantifying the constituent of interest are selected using correlation coefficients, standard errors

and the sensitivity of the absorbance changes with change in constituent (24).

The structural and spectral complexity of clay minerals is sufficient to consider a single mineral as a multicomponent mixture in itself. Detectable by near infrared spectroscopy are adsorbed water and structural hydroxyls (25), exchangeable and structural transition metal cations (26 and this work), adsorbed species including atmospheric gases (27), organic materials (2), accessory minerals (28) and, possibly, trapped hole centers ($O^{\cdot-}$ -centers). Thus it is of interest to adapt NIRA to studies of mineral surface activity. We have done this by examination of a small set of highly homologous clays in which laboratory control of only one variable at a time could be accurately achieved and independently confirmed.

In the current study, we tested the applicability of near infrared spectroscopy coupled with correlation analysis to quantitation of the dependence of montmorillonite spectra on two of the structural features known to be of importance in clay surface chemistry - hydration and exchangeable iron. These clays were developed as Mars Soil Analog Materials (MarSAMs) in that they satisfy the constraints of the mineralogical composition of Mars as determined from consideration of the Martian reflectance signature, the elemental analysis and simulations of Martian surface chemistry determined by Viking, and the presumed geological history of Mars.

Experimental

Clays. The variably exchanged Ca/Fe montmorillonite clays used for the iron dependence aspect of this study were prepared and analyzed using methods described in Banin *et al.* (29). The total iron contents of the clays prepared from two parent materials having different amounts of structural iron are summarized in **Table I**. For the adsorbed water studies, crude SWy and its 100% Ca and Fe forms prepared in 1987 by the same method were used.

Table I. IRON CONTENT OF MARSAM '85 SAMPLE SET

MATERIAL	%Fe ₂ O ₃
CRUDE SWY	3.61
~ 0 % Fe (1985)	3.87
~ 20 % Fe (1985)	4.11
~ 50 % Fe (1985)	5.21
~ 80 % Fe (1985)	5.96
~ 100 % Fe (1985)	6.08
~ 100 % Fe (1982)	6.87
CRUDE OTAY	1.11
~ 100 % FE OTAY (1985)	3.54

Pellet Preparation. Clay samples of 1.06 grams each (an amount just adequate to fill a stainless steel planchette with the crude material after pressing) were placed in the die of a pellet press obtained from English China Clays International and covered with an inverted 2.54 cm o.d by 2 mm deep type 304 stainless steel planchette. They were pressed for 30 seconds against a glass optical flat using a pressure of 1.2 kgm/cm² at the piston head in order to form a compact, but soft, pellet. As the densities of the various clays were different, some of the materials overfilled the planchettes. These samples were struck off with a stainless steel blade, re-weighed and the pellet re-pressed upright against the flat to smooth the surface. The filled planchette was centered on a spring-loaded platform in the sample holder and covered with a thin quartz cover plate sealed into a screwcap cover. The re-pressed samples appeared smooth after placement in the sample holder, but some surface roughness may have resulted from the striking-off procedure.

Humidity Equilibration. The clays were humidified at 25°C in desiccators using a series of eutectic salts. Each dessicator was controlled at a different relative humidity using one of the saturated salt solutions listed in **Table II**. The samples were weighed repeatedly until equilibrium (constant weight) was reached. After the spectra were obtained, the samples were broken into three aliquots, reweighed and dried for ~24 hours at 105°C to obtain the dry weights of the clay, from which the water contents were calculated. The water contents, as percent dry weight of the clay, are also shown in **Table II**.

Table II. Eutectic Salts and Desiccants Used in Relative Humidity Study

Salt/Desiccant		%RH	T(°C)	Ref.	% Water Content		
					crude	CA	Fe
CaCl ₂	(solid)	6.5	--	(30)	2.7	4.3	1.4
CH ₃ COOK	(satd. sol.)	20.	20.	(31)	5.1	10.0	7.7
		22.5	25.	(32)			
Ca(NO ₃) ₂	(satd. sol.)	51.	24.5	(31)	10.6	17.6	12.7
NH ₄ Cl	(satd. sol.)	79.	25.	(32)	14.3	18.2	14.8
CuSO ₄	(satd. sol.)	98.	20.	(32)	26.9	---	26.9

Reflectance Spectroscopy. Spectra were taken from 600 - 2500 nm using a Mark II 6250 Diffuse Reflectance Spectrometer obtained from Pacific Scientific. This

spectrometer is a single beam instrument with $0/45^\circ$ illumination/detection. All of the spectra were referenced to a ceramic standard, which exhibits $82 \pm 2\%$ reflectance in the 600-2500 nm range.

Measurements of spectra using different sizes of planchettes showed that planchettes of $1\frac{1}{4}$ " (3.18 cm) diameter gave spectra equivalent to those of 1" (2.54 cm) planchettes. Increased noise and spectral distortion occurred using $\frac{3}{4}$ " (1.91 cm) planchettes due to interception of the incident light beam by the edge of the planchette. Since no differences were found in spectra using sample thicknesses from 2 to 5 mm, only 2 mm thick samples were used. The iris of the spectrometer was set at $1/4$ full opening to minimize the undesirable spectral contributions from noise and from the Wood's anomaly of the grating which appears at 1510-1520 nm for the NIR grating (blazed at 2000 nm) and at ~ 770 nm for the mid-NIR grating (blazed at 900 nm). In order to minimize spectral variations resulting from sample placement, several reflectance curves were measured for each sample as a function of sample rotation. Fifty replicate scans were made in each of six horizontal rotations and averaged, giving a final spectrum for each clay composed of 300 scans \times the number of replicate samples.

Samples used for the iron determination were scanned in the wavelength region of 600-1100 nm using the first order of the mid-NIR grating. Samples used for the moisture determination were scanned in wavelength region of 1100-2500 nm in the first order of the NIR grating and from 680-1235 nm using the second order of the same grating. Second order spectra show slight anomalies attributable to incomplete rejection of first order light.

Data Analysis. A 10 point curve smoothing using 10 nm segments was performed on the data in preparation for derivatization. The smoothing makes no apparent change in the appearance of the original spectra in the 1100-2500 nm wavelength region, and only suppresses minor noise in the 680-1235 or 600-1100 nm regions. However, noise in unsmoothed spectra might result in more significant errors in the correlation coefficients calculated from derivative spectra. The reproducibility of crude SWy clay spectra taken in the two wavelength regions is shown in **Figures 1 & 2**. First derivatives (called D1) of those spectra taken using both orders of the NIR grating (giving 1100-2500 nm and 680-1235 nm regions) were calculated using 10 nm segments with gaps of 10 nm between segments. Second derivatives (called D2) of spectra using this grating were calculated using 20 nm segments and no gap between segments. First derivatives of spectra taken using the mid-NIR grating (600-1100 nm) were calculated like those of first derivatives using the NIR grating, but second derivatives were calculated using 20 nm segments and 10 nm gaps between them. Baseline offsets are removed by the first derivative, and constant slopes in the

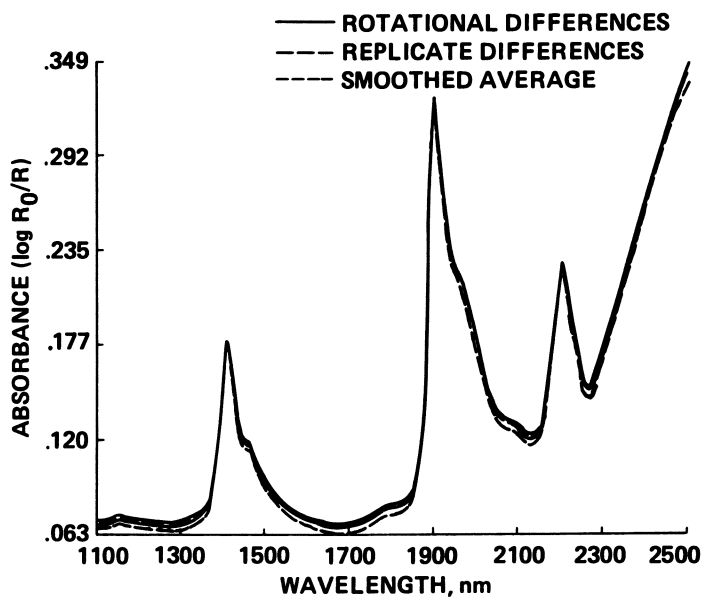


Figure 1. Reproducibility of absorbance spectra (1100-2500 nm) of iron-containing montmorillonites as a function of sample rotation. Shown are spectra of two replicate samples demonstrating maximal divergence from each other, spectra of one of the replicates taken in two positions showing maximal divergence from each other, and the smoothed average of three replicates in the six positions described in the text, i.e., an average of 18x50 spectra.

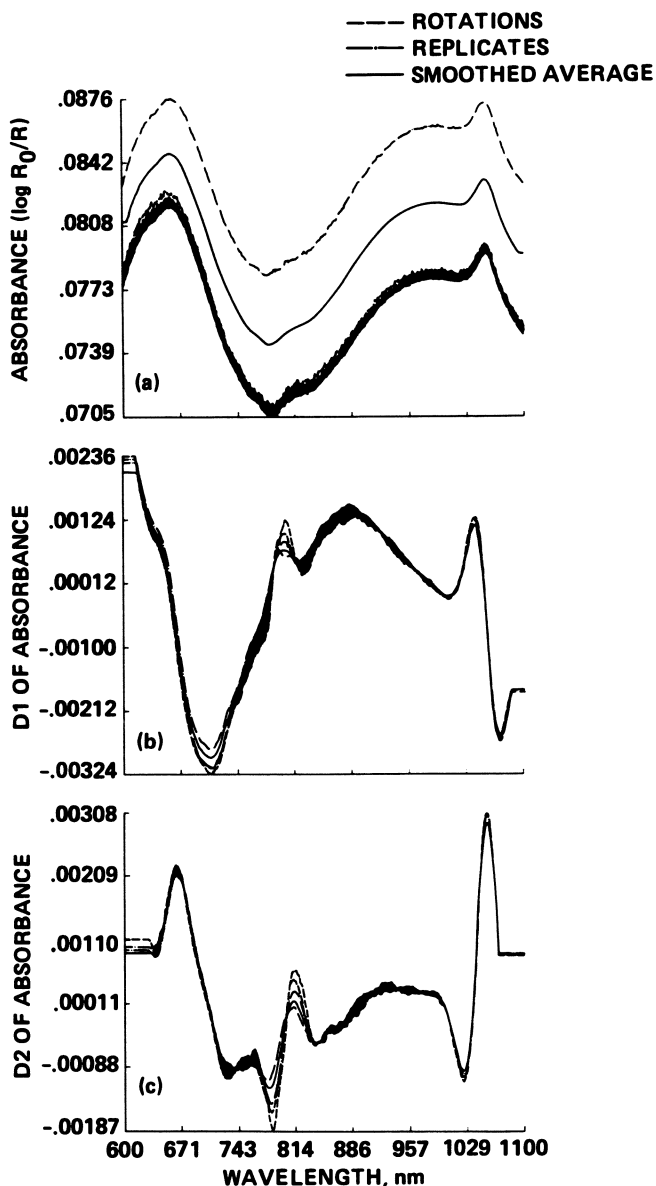


Figure 2. Reproducibility of absorbance spectra (600-1100 nm) of iron-containing montmorillonites as a function of sample rotation. As in Figure 1, but the smoothed average is of two replicates, not three replicates in the six positions, i.e., an average of 12x50 spectra. b) first derivative transform. c) 2nd derivative transform.

baseline are removed by the second derivative. Positions of peaks, shoulders and valleys are estimated most easily by examination of the primary absorbance data ($\log R_0/R$) but quantitation of absorbing constituents is improved by using second derivative data.

The Pacific Scientific (PSCO) simple regression analysis, based on Draper and Smith (33) was applied to the absorbance data itself and to the 1st and 2nd derivative data using as constituent data total iron determined by XRF, and water by gravimetric measurement. Regressions reported here were performed at the wavelength selected by the computer as giving the best correlation and also at a number of additional wavelengths associated with prominent spectral features.

Results

Dependence of the Spectra on Iron Content in a Region Dominated by Iron Absorption. Spectra of the five homologous iron exchanged clays prepared from SWy montomorillonite in 1985 are shown in **Figure 3a**. Those of crude SWy and Otay clays and of the 100% Fe forms of SWy prepared in 1982 and Otay are shown in **Figure 3b**.

Plots of the correlation coefficients obtained from the absorbance and its first and second derivatives (D1 and D2) are shown superimposed on the absorbance spectrum of the 100% Fe SWy in **Figure 4a**. Correlation coefficients for the full set, superimposed on the absorbance spectrum for 100% Fe Otay sample, are shown in **Figure 4b**. The quality of the correlation is significantly improved using 1st derivative data and improved still further using 2nd derivative data. This can be seen from **Table III** where a summary of the correlation coefficients obtained from absorbance and first and second derivatives of absorbance at several prominent wavelengths, including the computer optimum, are displayed.

Table III. CORRELATION COEFFICIENTS FOR IRON ABSORPTION OF THE HOMOLOGOUS SET AT SEVERAL WAVELENGTHS CALCULATED FROM PRIMARY ABSORBANCE DATA AND FROM 1ST AND 2ND DERIVATIVE TRANSFORMS

DATA TYPE	WAVELENGTH			
	600nm	970nm	(1051nm)	COMPUTER OPT.
ABSORBANCE	.987 ±.19	.967 ±.30	.962 ±.32	.987 (600 NM)
D1	-.991 ±.15	.989 ±.17	-.930	.997 (900 NM)
D2	-.996 ±.10	-.985 ±.20	-.492 ±1.03	1.000 (1000 NM)

Lines of best fit for D2 of calculated **vs.** measured iron content computed from regression analysis at the

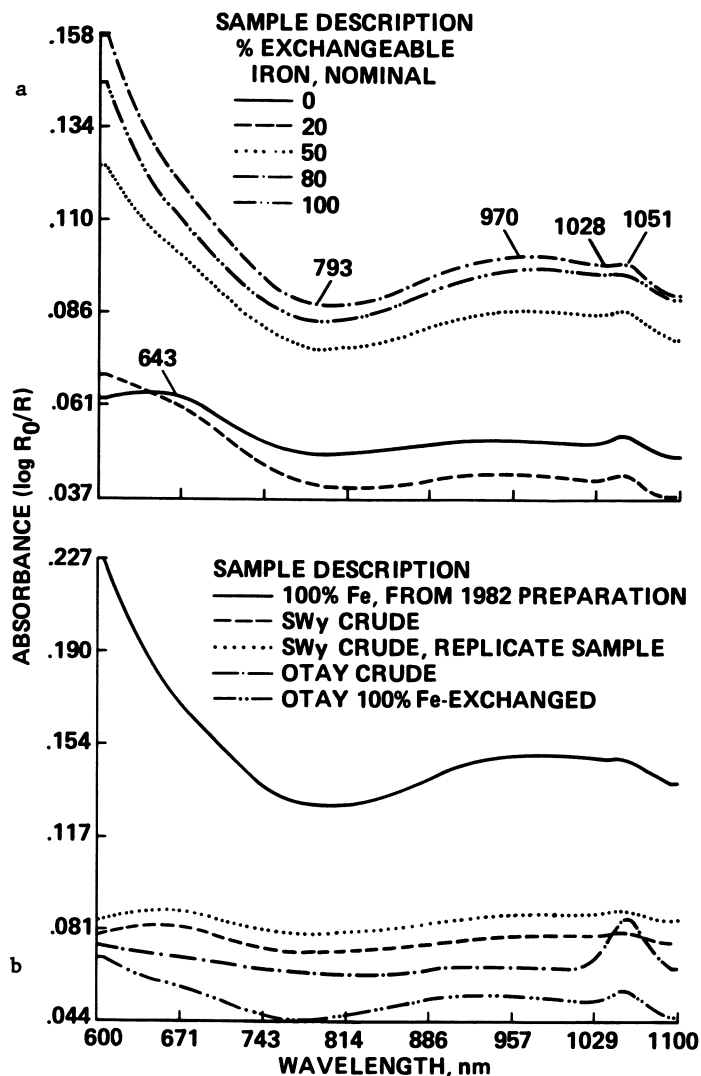


Figure 3. Absorbance spectra of the 1985 set of MarSAMs. a) absorbance spectra of five variably Ca/Fe-exchanged materials prepared from SW_y montmorillonite of nominal iron substitutions of 0, 20, 50, 80 and 100 % of the exchange capacity. b) absorbance spectra of two replicate samples of the crude parent SW_y, a 100% exchanged form of SW_y prepared in 1982, the crude parent Otay, and a 100% Fe-exchanged form of Otay.

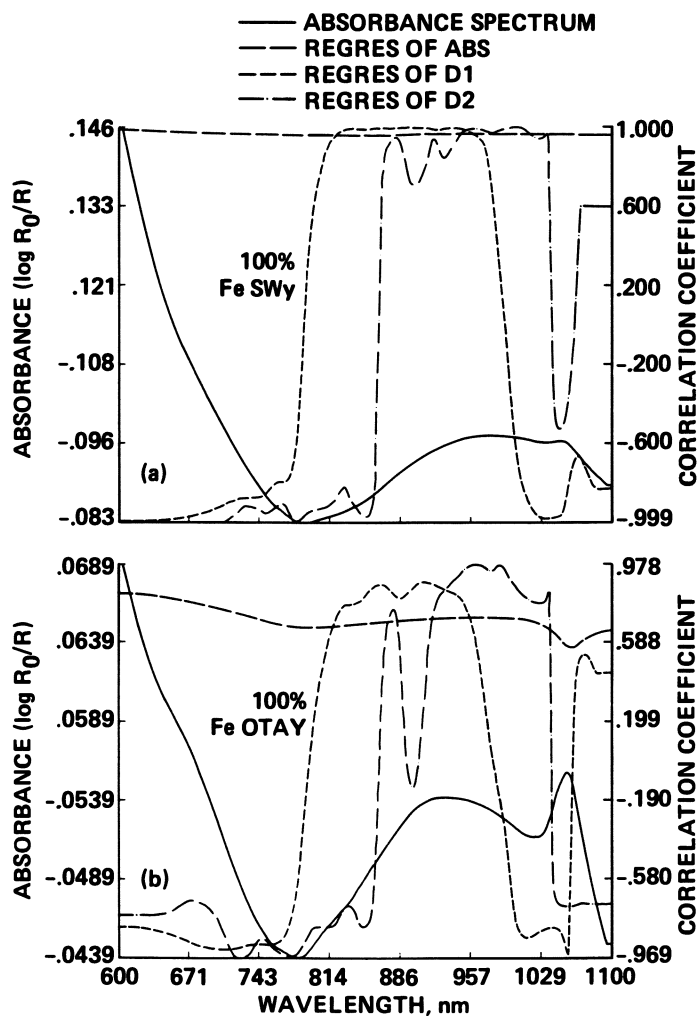


Figure 4. Correlation coefficients of total iron content as a function of wavelength calculated from absorbance and its first and second derivatives. a) data for the homologous sample set. b) the full sample set. The correlation coefficients are superposed on the spectrum of the 100 % Fe SWy in a and on the 100% Fe Otay in b for comparison.

broad peak are shown in **Figure 5 a & b**, for homologous and full sets respectively.

Dependence of the Spectra on Water Content in Regions of Water and Structural Hydroxyl Absorption. 1100-2500 nm spectra of the crude SWy montmorillonite as a function of increasing water content are shown in **Figure 6a**. Similar families of curves were obtained for the Ca- and Fe-exchanged forms. Spectra of the crude, 100% Ca- and 100% Fe- forms equilibrated at ~4% relative humidity are compared in **Figure 6b**. Using D2 of absorbance data at several wavelengths attributable to water or structural hydroxyl absorption, calculated lines of best fit for absorbance **vs.** analytically measured water contents are shown in **Figures 7 a-f**. Similar data for the Ca- and Fe- clays and for the composite set of crude, Ca- and Fe-forms are tabulated in **Table IV**.

Dependence of Spectra on Water Content in a Region Dominated by Iron Absorption. Regression analyses were performed on D2 of the absorbance **vs.** measured water content at the wavelength determined to be optimal for the correlation with iron (as above). The results of these analyses on the crude SWy clay and its 100% Fe- and Ca-forms are shown in **Figures 8 a-c**.

Discussion

Dependence of the Spectra on Fe Content in a Region Dominated by Iron Absorption. Discernable increases in absorbance (reflectance decreases) are produced by increasing iron content in two wavelength regions - the absorption tail diminishing throughout the uv-visible portion of the spectrum (sampled at the short wavelength limit of the spectra) and the broad peak at ~970nm. These features are attributable to a series of d-d transitions of ferric and ferrous iron (34).

From the absolute value of the correlation coefficient, which was > 0.95 over most of the wavelength range for the homologous set, it is clear that the spectral absorbance is linear with increasing iron content over the full range of iron concentrations examined. As was shown in **Table III**, quantitation is improved at 'appropriately' selected analytical wavelengths using derivative transforms of the data. This improvement is demonstrated by increases in the correlation coefficient and by decreases in the standard deviation of the average of the residuals of the measured values from the computed calibration curve. With regard to the word 'appropriate', it should be noted that the apparent correlation of the peak at 1051 nm in the homologous set disappears when second derivative data are used and is non-existent for the the full set. The apparent correlation in the primary absorbance data for the homologous set is an artifact of the underlying broad 970 nm peak. The overall

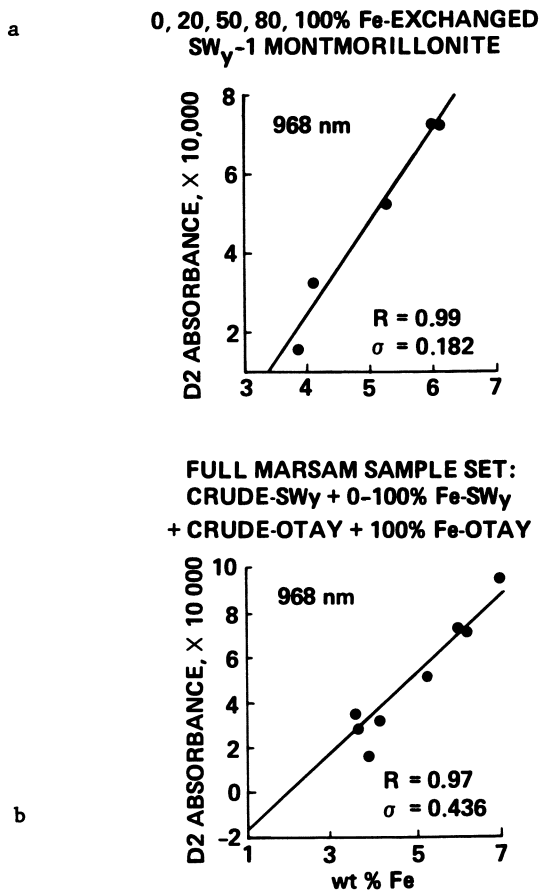


Figure 5. Regression lines relating absorbance to measured iron at the 970 peak using 2nd derivative data. a) homologous series, b) full sample set.

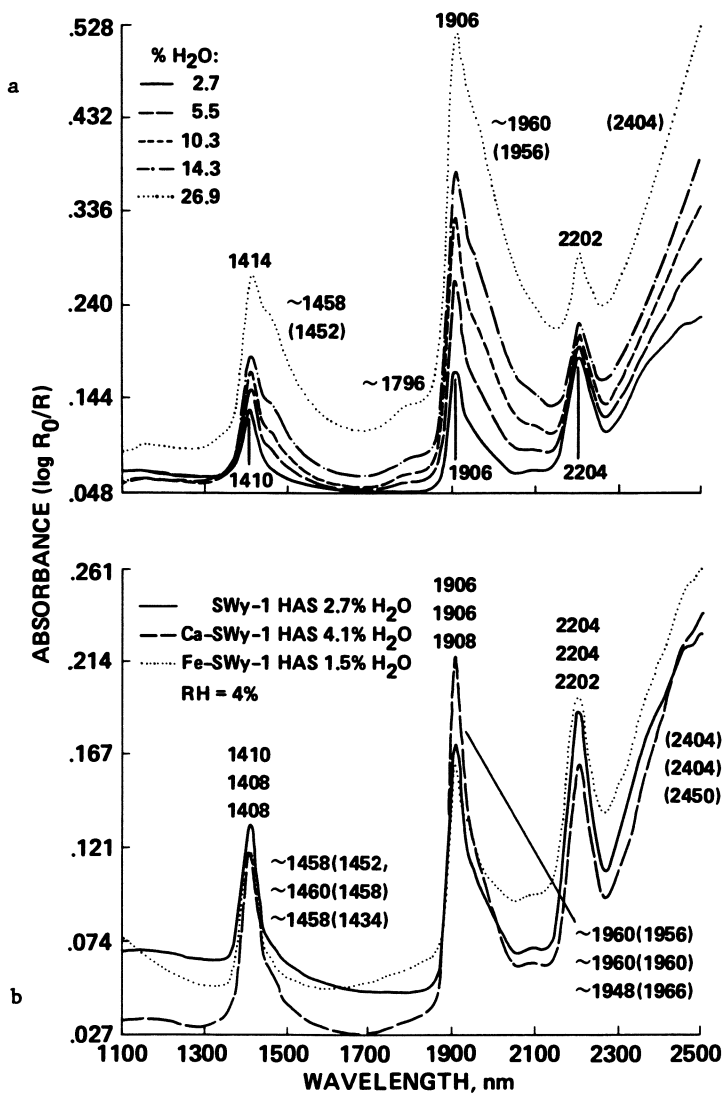


Figure 6. Absorbance spectra for selected clays in the region of water and structural hydroxyl absorption (1100-2500 nm). a) absorbance of SWy montmorillonite as a function of relative humidity. b) SWy, 100% Ca and Fe forms at a R.H. of 4%. Numbers in parentheses represent computer selected wavelengths giving maximal correlation coefficients in the region of interest.

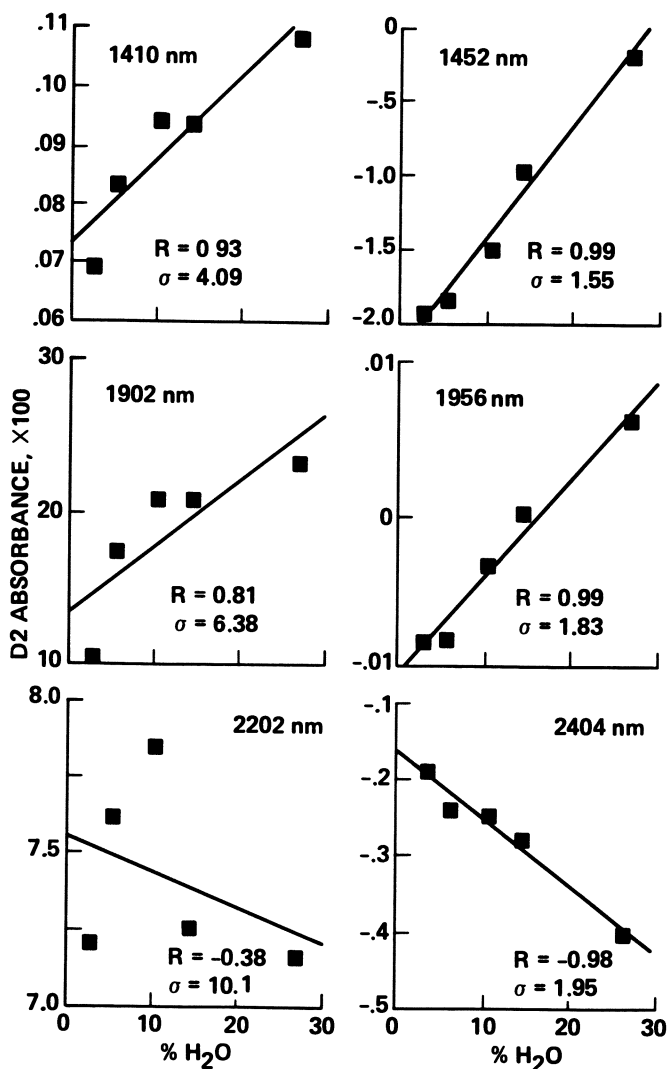


Figure 7. Regression lines relating D2 of absorbance of crude SWY to measured water content at several key wavelengths characteristic of water or structural hydroxyl groups.

Table IV
CORRELATION OF ABSORBANCE WITH WATER CONTENTS FOR
VARIABLY EXCHANGED SWy CLAYS IN REGIONS OF STRUCTURAL
HYDROXYL AND ADSORBED WATER

CLAY	SPECTRAL FEATURE	FROM 2nd DERIVATIVE DATA		
		WAVELENGTH, nm	R	STD ERROR
CRUDE-SWy Ca-SWy Fe-SWy COMPOSITE SET	$\nu_w + 2\partial_w$ SHOULDER (STRONGLY SELF- INTERACTING WATER)	(1452) (1458) (1434) (1460)	0.990 0.987 0.978 0.971	1.55 1.34 2.29 2.00
CRUDE-SWy Ca-SWy Fe-SWy COMPOSITE SET	$\nu_w + \partial_w$ PEAK (WEAKLY SELF- INTERACTING WATER)	1902 1902 1902 1902	0.812 0.961 0.721 0.703	6.38 2.29 7.53 6.00
CRUDE-SWy Ca-SWy Fe-SWy COMPOSITE SET	$\nu_w + \partial_w$ SHOULDER (STRONGLY SELF- INTERACTING WATER)	(1956) (1960) (1966) (1960)	0.986 0.992 0.961 0.876	1.83 1.05 3.02 4.06
CRUDE-SWy Ca-SWy Fe-SWy COMPOSITE SET	RIISING FUNDAMENTALS STRUCTURAL OH AND ADSORBED WATER	(2404) (2404) (2450) (2448)	-0.984 -0.991 -0.990 -0.946	1.95 1.10 1.53 2.74
CRUDE-SWy Ca-SWy Fe-SWy COMPOSITE SET	COMPUTER CALCULATED OPTIMUM OVER ENTIRE SPECTRUM	(1572) (1244) (1652) (1476)	-0.999 -0.999 -0.999 0.983	0.358 0.286 0.72 1.56

() = COMPUTER CALCULATED OPTIMA WITHIN THE REGION OF THE INDICATED SPECTRAL FEATURE. SPECTRAL FEATURE IDENTIFICATIONS ACCORDING TO CARIATI (1983).

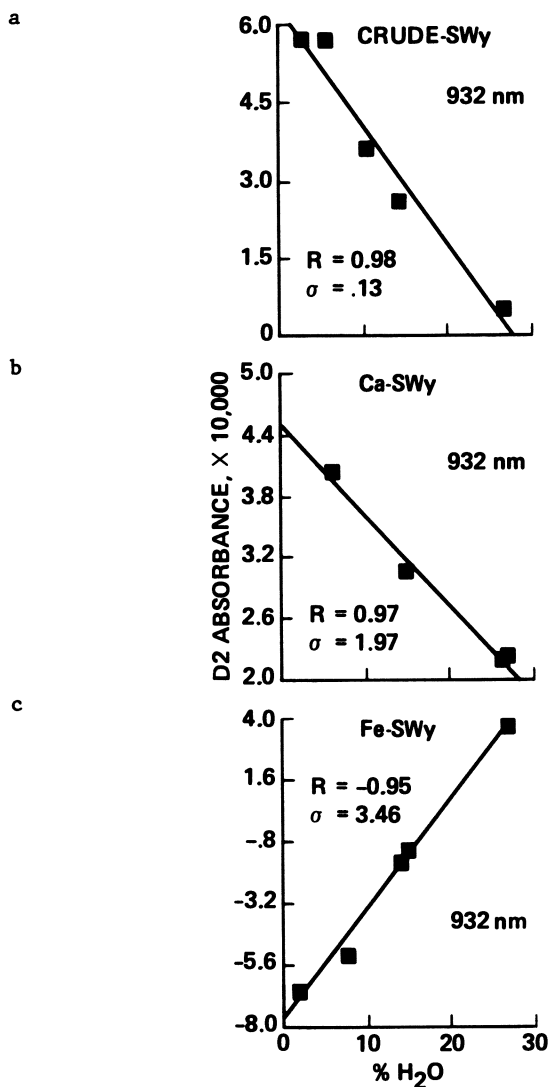


Figure 8. Regression lines relating D2 of absorbance to measured water content in a wavelength region dominated by Fe absorption. a) crude SWy. b) 100% Ca SWy. c) 100% Fe Swy.

non-specificity of the correlation with wavelength is not surprising, considering the broadness of the iron-dependent features.

It should be recognized that iron in clays occurs in both ferrous and ferric oxidation states and in multiple forms, as exchangeable cations on the surface, and also in octahedral and, possibly, tetrahedral environments in the structure. Fe (II or III) ions may be isolated or clustered in any of these locations. Although more wavelength specific, when 2nd derivative data are examined, it is clear that the correlation remains robust for the full set (the full set contains, in addition to the homologous set, crude and 100% Fe-forms of a clay of low structural iron, two crude SWy samples and a sample of 100% Fe-SWy prepared earlier), as shown in **Figure 4**. That the correlation is not seriously deteriorated when the crude parents, as well as 100% Fe Otay clay, are added to the homologous sample set of SWy clays indicates that, in the wavelength region considered, structural and surface iron are not readily distinguished. This insensitivity is not too surprising considering that iron, both in the structure and on the surface, is coordinated to oxygen or hydroxyl groups and is expected, for most part, to be in octahedral sites and in the Fe(III) state. That the spectra of the 1985 and 1982 forms of the Wyoming clay are only slightly different from each other is taken to mean that the preparation method yields similar materials and that there were not significant changes in the spectra over time.

The individual spectra of SWy and Otay clays are similar except that the ~970 nm peak in the Otay forms is considerably less intense and the small peak at ~1051 nm is more intense in the Otay than in the SWy materials. Otay clay contains about 1/3 of the structural iron content of the Wyoming form, explaining the diminished 970 nm peak in Otay. It is also known that Otay clay absorbs more water than does SWy and that the crude form absorbs more water than the iron-exchanged form (Banin, unpublished data). The 1051 nm peak, which, as mentioned above, shows no correlation with iron, may be attributable to water itself, characteristic of the edge sites on which the additional water is thought to be adsorbed, or to some other distinguishing attribute. Since the 1051 nm peak occurs weakly in the spectrum of the SWy clay, too, its intensity, but probably not its presence, may prove to distinguish various types of montmorillonites. Whether shifts in the positions of the two peaks will be revealed when a broader selection of clays and other materials containing trace iron are considered is of interest. Since the Fe(III)/Fe(II) ratio has not been determined for these clays, attribution of the 970 nm peak to either Fe(II) or Fe(III) can not be ascertained. Stucki, *et al.* (35) have shown that it is possible to reduce a substantial fraction of the ferric iron in clays, so determination of the oxidation state should be possible.

Dependence of the Spectra on Water Content in the Region of Water and Structural Hydroxyl Absorption. To interpret the linearity of the absorbance with water content, it is necessary to consider the assignments of the numerous overlapping bands in the region from 1100 - 2500 nm. In the vicinity of 1400 nm a peak with trailing shoulder is observed. By heating and deuteration studies, the peak at 1409 nm (seen here between 1408 and 1414 nm, depending on the exchangeable ion and moisture content) has been assigned by Cariati *et al.* (25) to be an overtone of the structural hydroxyl stretching vibration in the clay itself, with some contribution from an unspecified transition of adsorbed water. The shoulder, seen here at 1458 nm, has been assigned to the combination of the OH stretch and a bending overtone of weakly self-hydrogen bonded water. Sposito, *et al.* (36), have assigned the peak (unspecified by Cariati) to weakly, and shoulder to strongly (as did Cariati), self-hydrogen bonded water. Sposito, however did not consider a structural component of the 1410 nm band. The data of **Figure 7 a,b** show a poor, but real correlation between water and the intensity of the 1410 nm peak and an excellent one with the 1458 nm adsorbed water shoulder in the crude SWy clay. The correlation at 1410 nm may be due to the weakly self-interacting water, or, in part, to overlap with the 1458 nm shoulder produced by strongly self-interacting water.

Sposito, *et al.* like Cariati, *et al.* (25) have assigned the peak, seen in **Figure 6** at 1906 - 1908 nm, to a combination OH stretch and bend of weakly self-hydrogen bonded water. All assign the shoulder, seen here at 1960 nm, to strongly self-hydrogen-bonded water. The adsorption isotherm studies of Banin *et al.* (29) have shown that for the SWy clay, monolayer adsorption sites are saturated at ~10% water content, which occurs at roughly 20% relative humidity in our preparation. The data in **Figure 7c** show a distinct tendency toward saturation at 10% water content, suggesting that the weakly self-interacting (monolayer) water may not be well-correlated with water adsorption over a broad range of relative humidities. The correlations shown by our data in **Figure 7a-d** are better at the 1452 and 1956 nm shoulders than at the 1410 and 1906 nm peaks, suggesting that over the full humidity range the correlation is better with strongly self-interacting water. Clearly there is no correlation with water in the 2200 nm region, **Figure 7e**, associated with absorption of structural hydroxyls and free of close lying water bands. Good correlation is again obtained in the region of the rising water and structural hydroxyl fundamentals, **Figure 7f**.

In summary, the correlations in the three water absorption regions are excellent over the entire range of relative humidities and associated water contents. The locations of the best correlations of moisture content with the reflectance are in similar regions, but found at

somewhat different wavelengths depending on the ionic form of the clay. They are keenly sensitive to the adsorption environment, which is, in turn, dependent on the degree of surface hydration.

Dependence of Spectra on Water Content in a Region Dominated by Iron Absorption. A correlation with water content was also sought in the 680-1235 nm wavelength region (scanned using the 2nd order of the NIR grating). Some wavelength shifts and differences of the peak shapes were noted between spectra measured with this grating and those shown in **Figures 3 a,b** scanned using the more suitable (as explained earlier) grating covering the 600-1100 nm region, but the spectra were comparable. Several weak overtone or combination bands of water have been reported in this region (36), although no clearly identifiable water peaks are seen here.

The spectral effects of varying the water content of the clay were striking, in spite of the absence of water peaks. Plots of D2 absorbance *vs.* H₂O at the iron absorbance peak are shown in **Figure 8** for the crude, 100% Ca- and 100% Fe-exchanged clays. The relationships are linear throughout the moisture range studied, but of opposite sign for the crude and Ca-clays compared with the Fe-clay. The sign reversal is not simply due to differences in the wavelength of the absorption maximum for the Na- and Ca- forms of the clay as compared to the Fe-form, as the wavelengths were the same. Rather, the entire family of spectral curves for the former two clays increased in absorbance with increasing water content as expected, whereas the family of spectral curves for the iron clay decreased. Unpublished data of Huguenin revealed the same trend. He attributed it to hydroxylation of surface iron (Fe²⁺ and Fe³⁺), the result of which is strongly diminished extinction coefficients for iron absorption accompanied by slight red shifts of the peaks. Our results suggest a wavelength range in which changes in atmospheric water content will produce opposite effects on alkali and alkaline earth metal-containing, in contrast to iron-containing, minerals.

When the composite set containing crude, Ca- and Fe-clays is considered as well, rather than those of the individual members separately, the correlation of spectral absorbance with water contents seen for the individual clays is only slightly deteriorated in the hydroxyl region (1100-2500 nm), but is totally lost in the iron region (600-1100 nm). The loss in the 600-1100 nm (iron) region is attributable to the sign change discussed above. The deterioration in the 1100-2500 nm (hydroxyl) region can not be attributed to shifts in the positions of the peaks and shoulders (cf. **Figure 6**), nor yet to the differences in adsorption isotherms of the clays (29), as the plots of D2 absorbance were made *vs.* water content and not R.H. However, comparison of ratios of peak heights to a

baseline envelope, drawn by connecting the bottoms of the peaks for the crude, Ca- and Fe-forms of SWy, show a distinct diminution in the peak heights for the iron clays relative to the others. This diminution, comparable to anomalies in the water dependence of the absorbance by iron clays in the 600-1100 nm region (**Figure 8 a-c**), indicate less absorbance by iron relative to the other clays in the hydroxyl as well as iron regions.

If as postulated, iron-substituted materials are surface hydroxylated, there may be multiple environments for adsorbed water, extending the region of water absorption, thus diminishing the contrast of absorption features for iron clays. This observation of a difference between the behaviors of iron from the sodium and calcium clays is under further investigation, as it may be a feature of importance to remote sensing of hydrated mineral surfaces and to remote estimation of mineral-bound water. In addition, it is of potential importance to catalytic activity, because surface acidity is known to be strongly influenced by the degree of hydration of surfaces, and is thought to be associated with iron sites.

General Conclusions. Linear relationships over broad ranges of constituent variation are found between spectral absorbance of variably cation-exchanged montmorillonites and amounts of two constituents, hydration and total iron, which affect their surface chemistry. Quantitation is, in all cases, improved by using derivative transforms of the primary absorbance data. These correlations are insensitive to the location of iron (structural, or surface) in the clay but appear to be keenly sensitive to the molecular environment of the hydroxyl group of the water (weakly, *vs.* strongly self-interacting). Increasing water content produces increasing absorbance (decreasing reflectance) for all clays in the 1100-2500 nm region, and decreasing absorbance for the iron clay in parts of the 680-1235 nm region. It is concluded that NIRA represents a promising method for separating the influences of these and other constituents on reflectance properties and surface reactivity of clays. Establishing quantitative relationships between particular structural features and chemical reactivity, independent of covarying factors, is necessary for accurate determination of the chemical mechanisms on mineral surfaces and for remote sensing of planetary surface mineral composition and hydration.

Acknowledgements

This work was supported by the National Aeronautics and Space Administration jointly through the Exobiology Program of the Life Sciences and the Planetary Geology Program of the Solar System Exploration Divisions.

Literature Cited

1. Theng, B. K. G. The Chemistry of Clay Organic Reactions; John Wiley & Sons: New York, Toronto, 1974; Chapter 7.
2. Solomon, D. H.; Hawthorne, D.G. Chemistry of Pigments and Fillers; John Wiley & Sons: New York, Toronto, 1983.
3. Fripiat, J. J.; Cruz-Cumplido, M. I. Ann. Rev. Earth Planetary Science 1974, **2**, 239-256.
4. Tennakoon, D. T. B.; Thomas, J. M.; Tricker, M. J.; Williams, J. O. J. Chem. Soc., Dalton Trans. 1974 **20**, 2207-11.
5. Tennakoon, D. T. B.; Thomas, J. M.; Tricker, M. J. J. Chem. Soc., Dalton Trans. 1974 **20**, 2211-2215.
6. Pinnavaia, T. Science 1983 **220**, 365-371.
7. Laszlo, P. Science 1987 **235**, 1473-1476.
8. Russell, J. D.; Goodman, B. A.; Fraser, A. R. Clay Minerals 1979 **27**, 63-71.
9. Banin, A.; Rishpon, J. J. Mol. Evol. 1979 **14**, 133-152.
10. Solomon D. H.; Hawthorne, D. G. op. cit. Chapter 5, 181-184.
11. Solomon D. H.; Hawthorne, D. G. ibid 195-196.
12. Che, M.; Tench, A. J. Advances in Catalysis 1982 **31**, 77-133.
13. Coyne, L.; Sweeney, M.; Hovatter, W. Journal of Luminescence 1983 **28**, 395-409.
14. Coyne, L. Origins of Life 1985 **15**, 161-206.
15. Greenland, D. J. ; Hayes, M. H. B. The Chemistry of Soil Constituents; John Wiley & Sons: New York, 1978; p 8.
16. Sposito, G. The Surface Chemistry of Soils; Oxford University Press: New York, 1984.
17. Coyne, L.; Costanzo, P.; Theng, B. K. G. in press, Clay Minerals.
18. Mortland, M. M. Trans. 9th Cong. Int. Soil. Sci. Soc. Adelaide; Angus and Robertson: Sydney, 1968; I 691-699.
19. Mortland, M. M.; Raman, K. V. Clays Clay Miner. 1968 **16**, 393.
20. Touillaux, P.; Salvador, C.; Vandermeersche, C.; Fripiat, J. J. Isr. J. Chem 1968 **6**, 337.
21. Lahav, N.; White, D; Chang, S. Science 1978 **201**, 67-69.
22. Ferris, J. P.; Huang, C.- H.; Hagan, W. J. Origins of Life 1988 **18**, 121-123.
23. Norris, K.; Hart, J. R. In Humidity and Moisture, P. N. Win, ed.; Van Nostrand: Princeton, N. J., 1965; p
24. Hirschfeld T.; Stark, E. In Near Infrared Reflectance Analysis of Foodstuffs, Chapter on Analysis of Foods and Beverages; Academic Press: New York, 1984; 505-550.
25. Cariati, F.; Erre, L.; Micera, G.; Piu, P.; Gessa, C. Clays and Clay Minerals 1981 **29**, 157-159.

26. In Infrared and Raman Spectroscopy of Lunar and Terrestrial Minerals Karr, C., Jr., ed.; Academic Press: New York, San Francisco, London, 1975.
27. Mc Cord, T. B.; Clark, R. N.; Singer, R. B. J. Geophysical Research 1982 **87**, 3021-3032.
28. Hunt, G. R.; Ashley, R. P. Economic Geology 1979 **74**, 1613-1629.
29. Banin, A.; Carle, G.; Chang, S.; Coyne, L.; Orenberg, J.; Scattergood, T. Origins of Life 1988 **18**, 239-265.
30. Bower, J. G. Bur. Standard J. Research 1934 **12**, 241.
31. In C.R.C. Handbook of Chemistry and Physics, 69th Edition; Weast, R. C., ed.; C.R.C. Press, Inc: Florida, 1988.
32. In Lange's Handbook of Chemistry 12th Ed. Dean, J. A., ed.; Mc Graw Hill Book, Co.: New York, 1979.
33. Draper, N. R.; Smith, H. Applied Regression Analysis; John Wiley and Sons: New York, London, Sydney, 1966.
34. Sherman, D. M.; Waite, T. D. American Mineralogist 1985 **70**, 1262-1269.
35. Stucki, J. W.; Komadel, P.; Wilkenson, H. T. Soil Science Soc. Am. J. 1987 **51**, 1663-1665.
36. Hunt, G. R.; Salisbury, J. W. Modern Geology 1970 **1**, 284-300.
37. Sposito, G.; Prost, R.; Gaultier, J.-P. Clays and Clay Minerals 1983 **31**, 9-16.

RECEIVED September 21, 1989

Chapter 22

Raman and FT-IR Spectra of the Kaolinite-Hydrazine Intercalate

Clifford T. Johnston

Department of Soil Science, University of Florida,
Gainesville, FL 32611-0150

In-situ Raman and FT-IR spectra of the kaolinite-hydrazine (KH) intercalation complex are presented. The inner-surface hydroxyl stretching bands of kaolinite are strongly influenced by the presence of hydrazine in the interlamellar region. A strong reduction in the intensities of these bands indicates the formation of hydrogen bonds between the nitrogen atom of hydrazine and inner-surface hydroxyl groups of kaolinite. The -N-H moiety of hydrazine, however, did not participate in the formation of hydrogen bonds, as reflected by the observed increase in the $\nu(\text{N-H})$ bands upon intercalation. Raman spectra of the KH complex below 1200 cm^{-1} showed clearly that the N-N stretching band decreased in frequency, whereas the -NH_2 rocking band decreased in intensity. These observations indicate that the conformation of hydrazine may be different in the interlamellar region from that in solution. Furthermore, the linewidths of several of the adsorbate bands were considerably narrower than their solution values, indicating that the intercalated species may be highly ordered. Upon evacuation of the kaolinite-hydrazine complex, a new band at 3628 cm^{-1} was observed to increase in intensity at the expense of the inner-hydroxyl stretching band. The new band is assigned to a perturbed inner-hydroxyl stretching band which results from hydrazine keying into the kaolinite lattice. The use of perturbed structural hydroxyl bands to probe interlamellar reactions is discussed.

Much effort has been devoted to characterizing the interaction of organic molecules with mineral surfaces. Adsorption of organic amines by clay minerals is one such system which has attracted considerable interest. In addition to concern about the subsurface fate and transport of amine-containing organic pollutants, there is fundamental interest in the ability of organic amines to influence the surface chemistry of layer silicates. Boyd et al. (1,2) have demonstrated recently that the presence of quaternary ammonium cations, such as the hexadecyltrimethyl-

0097-6156/90/0415-0432\$06.75/0
© 1990 American Chemical Society

ammonium cation, on the exchange complex of smectites substantially increases their organophilic sorptive capacities. These modified clays have been shown to be effective sorbents for the removal of toxic nonpolar organic solutes (3) such as trichlorethylene and benzene. Organic amines have also been shown to interact strongly with 1:1 layer silicates. In the case of kaolinite, for example, spontaneous emission of light occurs when organic amines, such as hydrazine, are intercalated into the clay (4,5). These diverse observations result from a similar surface interaction; specifically, that between the $-N(H)_x$ group of the adsorbate and the surface of the clay mineral. The focus of this paper is to examine the interaction between hydrazine and the kaolinite surface as a model system in order to study the interaction of the amine functional group with representative clay surfaces.

Intercalation of small, polar molecules into the interlayer region of kaolinite continues to provide a useful approach for studying adsorbate-surface interactions, and for probing the chemical and physical properties of clay mineral surfaces (6-12). The interlamellar region of kaolinite provides a "protected" 2-dimensional environment for studying the interfacial behavior of adsorbed species free from solvent effects. Upon intercalation, the guest molecule is removed from solution and the interaction between the adsorbate and the internal surface of kaolinite can be examined in detail with little interference from the bulk solution (8). Although the number of chemical compounds which can be directly intercalated into kaolinite is small (13), the information gained about the interaction(s) between the adsorbate and the kaolinite surface relates to a much broader class of clay mineral-adsorbate complexes. The internal siloxane surface of kaolinite, for example, is isostructural to the highly reactive siloxane surfaces of montmorillonite and vermiculite, which are among the most abundant and reactive surfaces found in soils and sediments.

The interlamellar region of kaolinite consists of two molecular sheets: the siloxane surface, consisting of a hexagonal network of siloxane ditrigonal cavities, and an opposing sheet of aluminum hydroxyl groups. The exposed aluminum hydroxyl groups in the interlamellar region can be used as stationary reporter groups to detect changes which occur in this region (14). As the local environment near the hydroxyl groups is altered (e.g., as a result of intercalation), the vibrational bands associated with the inner-surface (ISu) hydroxyl groups are perturbed. This, in turn, can provide diagnostic information about surface conditions. Previous IR and Raman studies have shown that the ISu hydroxyl stretching bands, in particular, are sensitive to changes in the interlamellar region of kaolinite. Vibrational spectra of kaolinite intercalates (8,12,15-20) have several features in common in the hydroxyl stretching region. First, the intensities of the ISu $\nu(O-H)$ bands at 3652, 3668, 3688, and 3695 cm^{-1} are strongly reduced upon intercalation. Second, at the expense of these ISu bands, a "new" set of hydrogen-bonded ISu bands appears in the $\nu(O-H)$ region. This set of bands is shifted to lower frequencies, and increase in intensity as the extent of intercalation increases. The red-shift in frequency results from the formation of hydrogen bonds between the intercalated species and the ISu groups. Finally, the inner-hydroxyl $\nu(O-H)$ band at 3620 cm^{-1} is not affected by the intercalation reaction, due to its recessed location within the kaolinite lattice (16,21).

Changes in the vibrational modes of the adsorbent, however, reflect only those changes which occur to the substrate; they do not provide direct insight into the structure and bonding of the adsorbed species. In order to examine the influence of the surface on the intercalated species, the vibrational modes of the adsorbate must be obtained. In a previous dispersive-IR absorption study of the kaolinite-hydrazine intercalate, Ledoux and White (17) observed that the ISu hydroxyl groups of

kaolinite were strongly perturbed upon intercalation by hydrazine. They observed also that the $\nu(\text{N-H})$ bands of kaolinite were shifted to higher frequencies, which they attributed to depolymerization of the liquid. Their data were restricted, however, to spectral observations in the $\nu(\text{O-H})$ and $\nu(\text{N-H})$ regions (2500 to 4000 cm^{-1}); vibrational data below 2500 cm^{-1} for the kaolinite-hydrazine intercalate have not been reported previously in the literature. With the exception of the $\nu(\text{N-H})$ bands, all of the observed IR and Raman bands occur below 1650 cm^{-1} (22,23). A major disadvantage of IR absorption techniques for surface studies is the opacity of the adsorbent in the low-frequency region below 1200 cm^{-1} (24-26). The strong IR-active absorption bands of the adsorbent block out a significant portion of the incident radiation in this region. Raman methods, however, are particularly well-suited for studying adsorbate vibrational modes in this region, because the Raman-active modes of the clay mineral are very weak (8,27). Thus a secondary, though important, subgoal of this paper is to demonstrate the complementary relationship between Raman and FT-IR spectroscopy in their application to vibrational studies of adsorbed species.

Experimental

The sample studied was KGa-1 kaolinite collected from Washington County Georgia, obtained from the Source Clays Repository of The Clay Minerals Society. A complete description of the physical properties of this clay sample has been given by van Olphen and Fripiat (28). In addition, Raman and IR spectra of this clay have been reported recently (8,27). A dilute aqueous suspension of the kaolinite sample containing less than 2.0 μm equivalent spherical diameter (e.s.d.) particles was prepared by suspending 0.1 grams of oven-dry kaolinite in 100 ml of distilled-deionized water. The clay suspension was dispersed by adjusting its pH to 9.2 by addition of small aliquots of 0.01 M NaOH. The kaolinite suspension was size-fractionated immediately by centrifugation, and the fraction having an e.s.d. of < 2.0 μm was collected. The suspension was then flocculated by adjusting the pH to 6.0 using a few drops of 0.01 M HCl. A small aliquot of the size-fractionated clay suspension was dried on a $25\text{mm} \times 2\text{mm}$ ZnSe disk. The disk then was mounted in a controlled-environment 10-cm pathlength gas cell in the sample compartment of an FT-IR spectrometer. The controlled-environment gas cell was connected to a vacuum/gas manifold, with pressure values within the cell being measured using a combination of Penning and Pirani gauges. The sample compartment, transfer optics, and interferometer of the FT-IR spectrometer were evacuated to 0.05 torr in order to eliminate interferences from atmospheric CO_2 and H_2O vapor.

Infrared spectra were obtained on a Bomem DA3.10 Fourier-transform infrared spectrometer. A Globar[®] ceramic source, Ge-coated KBr beamsplitter, and mercury-cadmium-telluride (MCT) detector with a measured D^* value of 3.13×10^9 $\text{cmHz}^{0.5}$ and a low-frequency cutoff of 400 cm^{-1} (25 microns) were used in this investigation. The optical resolution ranged between 1.0 and 0.5 wavenumbers. A comparison of several spectra obtained using resolution values of 2.0 , 1.0 and 0.5 cm^{-1} showed that the spectra were not instrument-limited for nominal resolution values of 0.5 and 1.0 wavenumbers; the 2.0 wavenumber spectrum was, however, instrument-limited. The Bomem DA3.10 spectrometer was controlled through a general-purpose-interface-bus (GPIB) interface to a DEC Vaxstation-210 computer.

Raman spectra were collected on a Spex 1403 $3/4$ m double monochromator

interfaced to a Nicolet 1180E computer controlled through an Apple Macintosh Plus computer. The 488 nm line of an argon ion laser (Spectra Physics 171) was used at an incident-power output of 100 mW measured at the sample. For the Raman measurements, a small amount of kaolinite was placed in a glass capillary tube, followed by the addition of hydrazine. The capillary tube was then sealed and allowed to stand for 48 hours. Raman spectra were obtained using a 90-degree back-scattering collection geometry. The spectral slit width ranged from 2 cm^{-1} to 1 cm^{-1} . X-Ray diffraction patterns were obtained using a Nicolet computer-controlled X-Ray diffraction system with a stepping-motor accuracy of $0.0025^\circ 2\theta$. Samples were scanned at $2^\circ 2\theta/\text{min.}$, using $\text{CuK}\alpha$ radiation. The X-ray diffractometer did not have a controlled environment cell. Therefore, samples were taken from a controlled-environment desiccator and placed on the "open" XRD stage quickly. The X-ray diffraction patterns were obtained within 15 minutes of removal from the vacuum desiccator.

Results and Discussion

Raman spectra of hydrazine (a) and of the kaolinite-hydrazine (KH) intercalate (b) suspended in liquid hydrazine are shown in Fig. 1. In contrast to the strong IR-active absorption bands characteristic of clay minerals below 1200 cm^{-1} , the corresponding Raman bands of kaolinite are relatively weak. Nonetheless, both the kaolinite and the hydrazine bands can clearly be resolved (Fig. 1b). Hydrazine bands occur at 903, 1111, 1680, 3200, 3280, and 3340 cm^{-1} , whereas the kaolinite bands are found at 140 (not shown), 336, 400, 436, 467, 514, 636, 739, 794, and 3620 cm^{-1} . Observation of lower-frequency adsorbate modes below 1200 cm^{-1} are often obfuscated in IR absorption spectra because of the strong lattice- framework vibrational modes. As the Raman spectrum of the KH complex shown in Fig. 1a indicate, the lower-frequency modes of hydrazine below 1200 cm^{-1} can readily be resolved. The positions of the hydrazine bands in the KH spectrum (Fig. 1b) are similar to those of liquid hydrazine (Fig. 1a) and agree well with published vibrational data for hydrazine (22,23,29-31). The observed band positions for the KH complex, for hydrazine, and for kaolinite are listed in Table 1.

Survey IR spectra of KGa-1 kaolinite (a) and of the KH complex (b) deposited on a ZnSe window at 1 atm of pressure are shown in Fig. 2 in the 700 to 4200 cm^{-1} region. The decreased intensities of the ISu hydroxyl $\nu(\text{O-H})$ bands at 3652 , 3668 and 3695 cm^{-1} in comparison to those of non-intercalated kaolinite indicate that intercalation of hydrazine into the interlamellar region has taken place. The interlayer hydrogen bonds between the ISu hydroxyl groups and the siloxane surface (Fig. 3) are replaced by a "new" set of hydrogen bonds between the lone pair of electrons of hydrazine and the ISu hydroxyl groups of kaolinite. These "new" bonds are somewhat stronger than those of the unperturbed interlayer hydrogen bonds; consequently, the ISu $\nu(\text{O-H})$ bands are shifted to lower frequencies (17). The frequencies of the strong hydrazine bands at 1630 , 3200 and 3330 cm^{-1} in the IR spectrum of the KH complex (Fig. 2b) are similar to those of liquid hydrazine (23). This indicates that most of the hydrazine present in this sample is physically adsorbed on the external surfaces of kaolinite, or condensed in micropores.

The dominant spectral component in the Raman spectrum of the KH intercalate (Fig. 1b) is hydrazine. By comparison, the IR bands of kaolinite are much more prominent than those in the Raman spectrum. Consequently, the strong IR-active

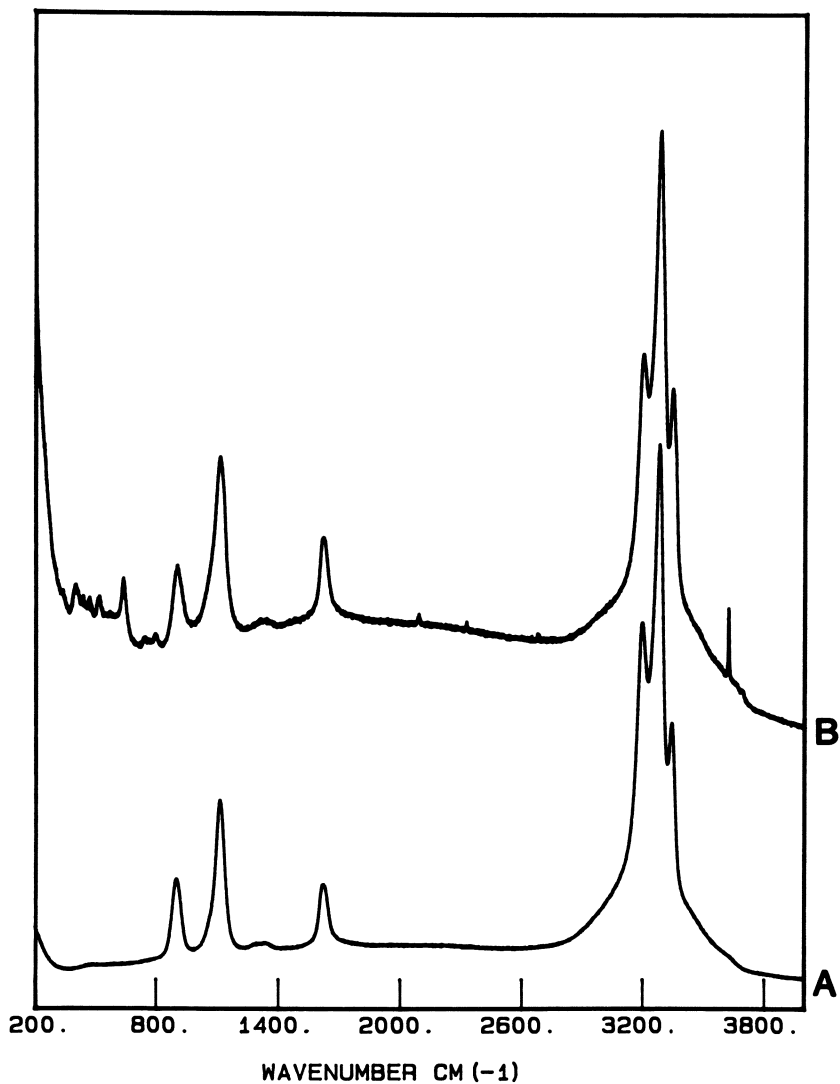


Figure 1. Raman spectra of liquid hydrazine (A), and of the kaolinite-hydrazine complex suspended in liquid hydrazine (B) in the 200 to 4000 cm^{-1} region.

Table 1.
Observed Vibrational Bands for the Kaolinite Hydrazine Complex

Kaolinite-Hydrazine Intercalate			Hydrazine		Kaolinite	
Raman	FTIR(1 atm)	FTIR (evac)	Raman	IR(liquid)	Raman	IR
				130	130	
140	n/a	n/a		201	141	
				244	190	
				271	268	
336	n/a	n/a			338	
					352	
					366	
400	n/a	n/a			397	405
436	n/a	n/a			431	440
467	n/a	n/a			461	470
514	n/a	n/a			512	
					555	
636					637	638
				700	692	
739		750			750	754
794		796			790	792
					799	
	871					
903			903			
903		914			915	918
948		945			940	941
	1014				1018	
1033						
	1044		1042		1040	
1095			1112			1101
1131		1127				1120
1273	1265	1286	1283			
1313	1339		1335	1324		
		1628	1608			
3185						
3200	3196	3225	3195	3189		
3283			3280			
3302						
3310						
3344	3336	3361	3346	3310		
3362						
3620	3620	3628			3621	3620
	3656				3652	
	3673				3668	
					3688	
3692	3694			3696	3695	

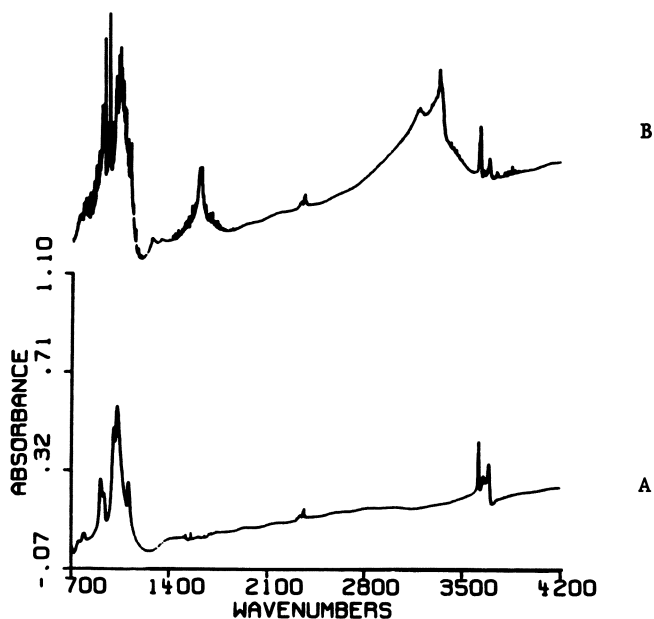


Figure 2. FT-IR spectra of kaolinite (A), and of the kaolinite-hydrazine (B) complex, deposited on a ZnSe window in the 700 to 4200 cm^{-1} region.

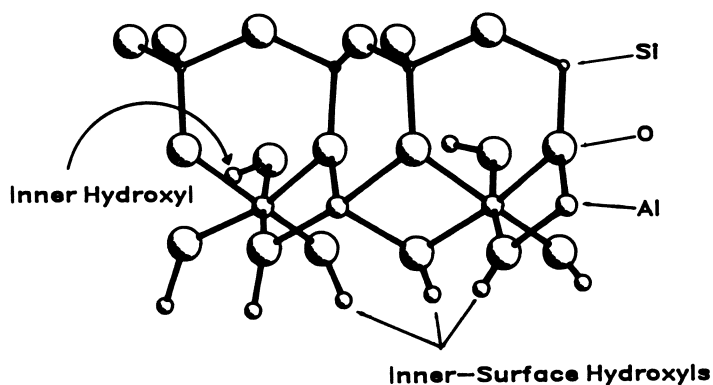


Figure 3. [100] Projection of the kaolinite structure showing the position of the inner and inner-surface-hydroxyl groups of kaolinite.

$\nu(\text{Si-O})$ and $\nu(\text{Al-O})$ bands of kaolinite in the 950 to 1150 cm^{-1} region (Fig. 2a) interfere with the observation of the ν_6 , ν_{12} , and ν_{11} hydrazine bands in this region (Table 2). Unambiguous observation of the IR-active hydrazine bands below 1150 cm^{-1} is obscured by the strong kaolinite bands; these bands, however, are clearly resolved in the Raman spectrum of the KH complex.

$\nu(\text{O-H})$ region. Raman and IR spectra of the KH complex (Figs. 4a,4c) and of non-intercalated kaolinite (Figs. 4b,4d) in the 3600 to 3725 cm^{-1} region at 1 atm of pressure are shown in Fig. 4. The positions and relative intensities of the hydroxyl stretching bands in the Raman spectrum are similar to those observed in the IR spectrum of kaolinite (27,32,33). Five bands are found in the Raman spectrum, whereas only four are observed in the IR spectrum. Four of the bands at 3620, 3652, 3668, and 3695 cm^{-1} are observed in both the Raman and IR spectra; however, the 3688 cm^{-1} band is restricted to the Raman spectrum and does not appear to be IR-active. The 3620 cm^{-1} band has been assigned to the inner-hydroxyl group (Fig. 3), and the 3652, 3668, 3688, and 3695 cm^{-1} bands correspond to the $\nu(\text{O-H})$ modes of the ISu hydroxyl groups (16,27,33). Upon intercalation, the intensities of the ISu $\nu(\text{O-H})$ bands are strongly reduced resulting from the formation of hydrogen bonds with hydrazine. The Raman bands of kaolinite at 3652, 3668, 3688, and 3695 cm^{-1} are not found in the Raman spectrum of the intercalated complex, the only significant feature is the unperturbed inner-hydroxyl band at 3620 cm^{-1} . The 3652 and 3695 cm^{-1} bands in the IR spectrum of the KH complex, however, still retain significant intensity even after intercalation. It is not known, at present, why the residual intensities of the ISu $\nu(\text{O-H})$ bands of the KH complex are greater in the IR spectrum (Fig. 4a) than their Raman counterparts (Fig. 4c). In contrast to the reactive behavior of the inner surface $\nu(\text{O-H})$ bands, the inner $\nu(\text{O-H})$ band at 3620 cm^{-1} is not influenced by the presence of hydrazine. This is because of the recessed location of this hydroxyl group in the kaolinite structure (Fig. 3).

IR spectra in the 2800 to 4000 cm^{-1} region of kaolinite, of the kaolinite-hydrazine intercalate at 1 atm of pressure (Fig. 5b), and of the KH complex evacuated to 10^{-7} atm (Fig. 5c) are shown in Fig. 5. In addition to the $\nu(\text{O-H})$ bands of kaolinite, the strong bands at 3196 and 3336 cm^{-1} (Fig. 5b) correspond to the two IR-active $\nu(\text{N-H})$ bands of physically adsorbed hydrazine (Table 2). In comparison to the IR spectrum on kaolinite (Fig. 5a), there is a considerable loss in intensity of the ISu $\nu(\text{O-H})$ bands for the intercalation complex (Figs. 5b,c). This indicates clearly that hydrogen bonding occurs between these hydroxyl groups and the intercalated hydrazine species. This bonding interaction results in the position of the ISu $\nu(\text{O-H})$ bands being shifted to lower frequencies. The positions of these red-shifted $\nu(\text{O-H})$ bands, however, were not clearly resolved in the present study. There is a broad, poorly resolved band underlying the strong 3196 and 3336 cm^{-1} $\nu(\text{N-H})$ bands which is still present in the spectrum of the evacuated KH complex. This may account for the perturbed ISu hydroxyl groups. However, the large amount of hydrazine physically adsorbed by the kaolinite sample interferes with clear identification of the red-shifted ISu hydroxyl stretching bands. In a previous IR study of the KH complex, Ledoux and White (17) assigned a large band at 2970 cm^{-1} to NH_2 groups strongly hydrogen-bonded with the hydroxylic surface of kaolinite. Although similar results were obtained in the $\nu(\text{O-H})$ region, the band at 2970 cm^{-1} was not observed in the present study (Figs. 1,2). The appearance of a

Table 2. Vibrational Band Assignments for Hydrazine

Symmetry Description / PED ^b	Mode	IR		Raman ^a		Theory ^b		
		N ₂ H ₄ /Ar ^b	N ₂ H ₄ /N ₂ ^b	Solid ^a	Liquid ^a	Vapor ^c	Liquid	Predicted
A								
s-a-HNH str(96)	v ₁	3390	3387			3325	3277	3410
s-s-HNH str(96)	v ₂	----	----	3200	3189		3189	3317
s-sci(100)	v ₃		1595	1603	1806	1493	1628	1639
s-HNH twi(91)	v ₄	1299	1314	1304	1283	----	1295	1290
NN-str(78) + s-wag(17)	v ₅	1086	1091	1126	1098	1098	1111	1087
s-wag(79) + NN str(20)	v ₆	810	----	884	871	780	882	841
torsion(100)	v ₇	388	----	627	---	377		
B								
a-a-HNH str(86)	v ₈	3398	3396	3310	3332	3350	3336	3415
a-s-HNH str(89)	v ₉	3313	3301	3310	3310	3297		3309
a-sci(99)	v ₁₀	----	1595?	1655	1608	1608	1628	1624
a-HNH twi (94)	v ₁₁	1262	1267	1350	1324	1275	1295	1258
a-wag(95)	v ₁₂	953	983	1066	1042	937	1000	3415

a Reference [22]

b Reference [30]

c Reference [29]

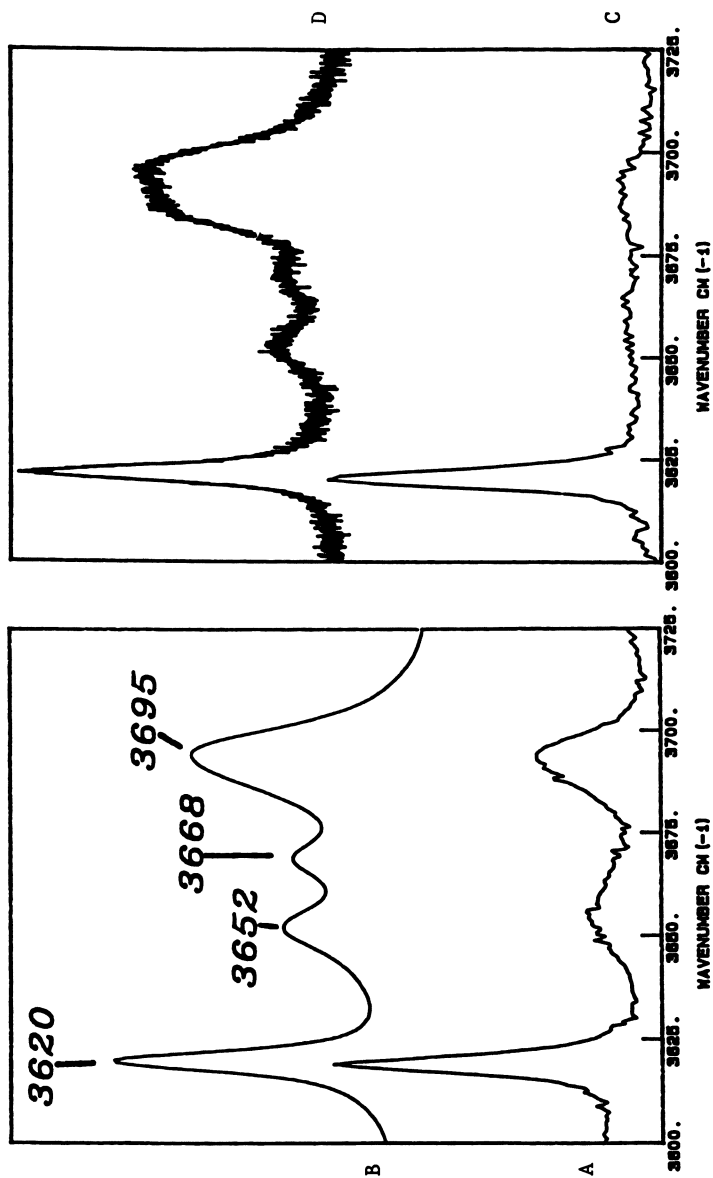


Figure 4. FT-IR (A,B) and Raman (C,D) spectra of non-intercalated kaolinite (top spectra), and of kaolinite-hydrazine intercalates in the 3600 to 3725 cm^{-1} region (bottom spectra). Spectra were obtained at 298 K and 1 atm. pressure.

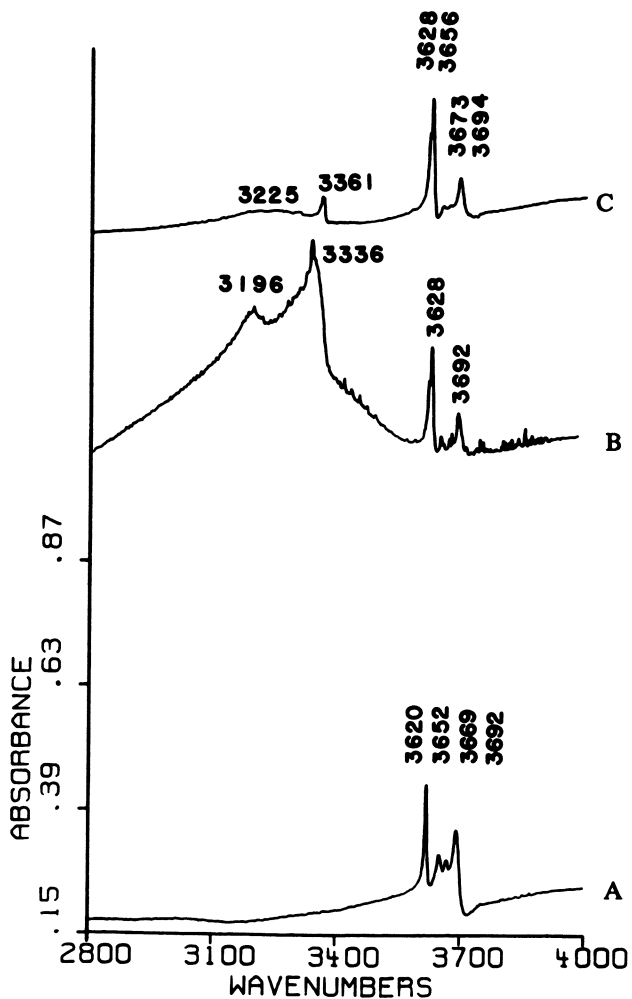


Figure 5. Controlled-environment FT-IR spectra of kaolinite (A), of the kaolinite-hydrazine complex at 1 atm (B) and of the kaolinite-hydrazine complex at 10^{-5} atm in the 2800 to 4000 cm^{-1} region (C).

poorly resolved and perturbed ISu $\nu(\text{O-H})$ band is in contrast to the appearance of well-defined perturbed ISu $\nu(\text{O-H})$ bands for other kaolinite intercalates. For example, the red-shifted $\nu(\text{O-H})$ bands of the kaolinite-dimethyl sulfoxide complex are present as well-resolved bands at 3502 and 3538 cm^{-1} .

Influence of Pressure on the $\nu(\text{O-H})$ Region. Upon evacuation of the KH complex, the position of the inner-hydroxyl $\nu(\text{O-H})$ band at 3620 cm^{-1} increased in frequency to 3628 cm^{-1} (Fig. 5c). Therefore, in order to examine more fully the influence of pressure on the $\nu(\text{O-H})$ bands of the KH complex, IR spectra were collected as a function of pressure (Fig. 6). At 1 atm of pressure, the IR spectrum of the KH complex is similar to the Raman result; intensities of the ISu $\nu(\text{O-H})$ bands are decreased in comparison to those of kaolinite, and the inner-hydroxyl band at 3620 cm^{-1} is not perturbed. Upon decreasing the pressure, however, a "new" band at 3628 cm^{-1} grows in intensity at the expense of the 3620 cm^{-1} band. The 3628 cm^{-1} band was not observed in the earlier IR studies of the KH complex (17), which were conducted at 1 atm pressure.

Bands similar to the 3628 cm^{-1} feature have been reported at 3626, 3625, and 3632 cm^{-1} for the kaolinite-formamide (KF), kaolinite-dimethylformamide (KDMF), and kaolinite-N-methylacetamide intercalates, respectively (20,34). Although the authors (20,34) assigned these bands to red-shifted ISu $\nu(\text{O-H})$ bands, the similarity to our IR spectra for the KH complex suggests that they may correspond to perturbed inner-hydroxyl groups. In the present study, there is little doubt regarding assignment of the 3628 cm^{-1} band to the perturbed inner-hydroxyl group of kaolinite, because of the strong transfer of intensity between the 3620 and 3628 cm^{-1} bands (Fig. 6). The 3628 cm^{-1} band was not detected in the Raman spectrum of the KH complex (Fig. 4c), which is consistent with the IR results obtained at 1 atm (Fig. 4a).

In previous IR studies of kaolinite (16,21,35) the inner-hydroxyl stretching band has been shown to be highly resistant to isotopic exchange with deuterium and to dehydroxylation at elevated temperatures because of its recessed location in the kaolinite structure (Fig. 3). In contrast to the inert behavior of the inner-hydroxyl, the ISu hydroxyl groups are highly accessible in the interlamellar region and can readily participate in hydrogen-bonding interactions. The observed blue-shift of the inner-hydroxyl stretching band is surprising, and suggests that the $-\text{NH}_2$ group of hydrazine interacts with the inner-hydroxyl group of kaolinite. The position and orientation of this hydroxyl group are illustrated qualitatively in the (100) projection of kaolinite (Fig. 3). The atomic coordinates for the kaolinite structure were obtained from Suitch and Young (36). An improved set of atomic coordinates has been obtained recently using X-ray and neutron powder diffraction methods (Bish, D. L. and Von Dreele, R. B., *Clays and Clay Min.*, In press). The low-pressure IR data of the KH complex (Fig. 6) suggest that the $-\text{NH}_2$ moiety of hydrazine, keyed into the siloxane surface of kaolinite, resulting in a slight electrostatic repulsion between the $-\text{NH}_2$ and $-\text{OH}$ groups. This hypothesis is not unreasonable considering the molecular dimensions of the siloxane ditrigonal cavity and of hydrazine. A space-filled (001) projection of the siloxane ditrigonal cavity of kaolinite illustrating the relative proportion of the cavity to hydrazine is shown in Fig. 7.

The 3628 cm^{-1} band occurs upon evacuation of the KH complex and appears as a discrete band. Furthermore, the position of the band remains fixed at 3628 cm^{-1} as

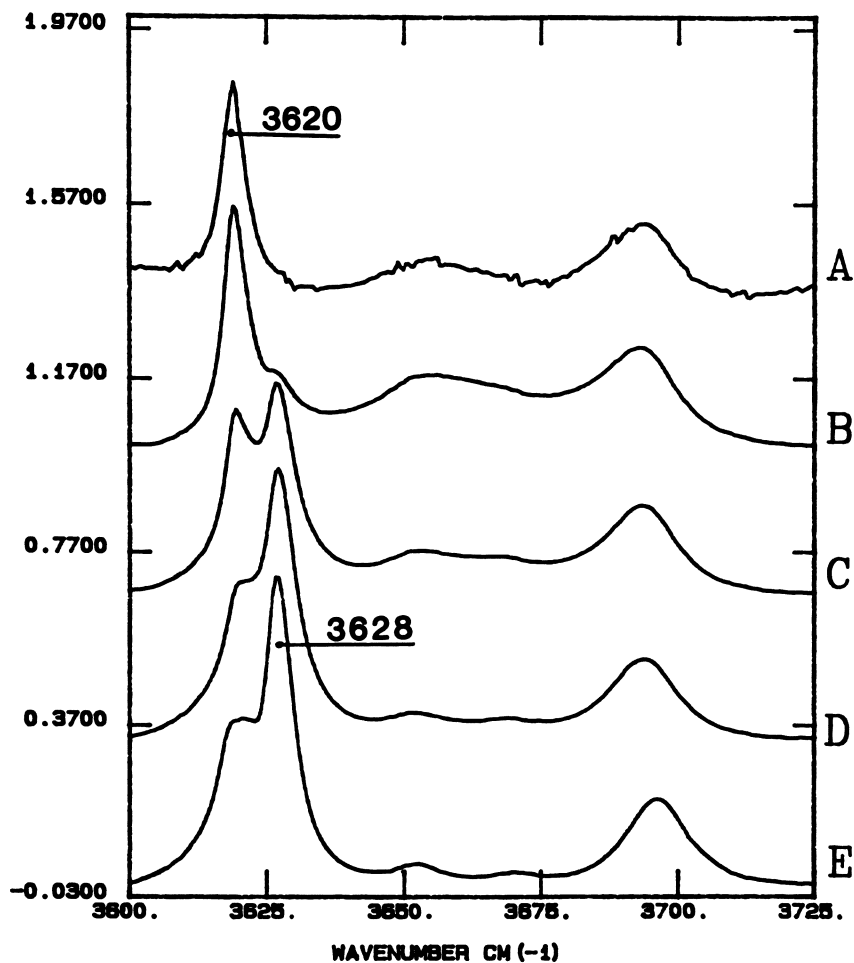


Figure 6. Controlled-environment FT-IR spectra of the KH complex in the 3600 to 3725 cm⁻¹ region as a function of pressure. The pressure of Spectrum A was obtained at 1 atm, whereas spectrum E corresponds to a pressure of 10⁻⁷ atm.

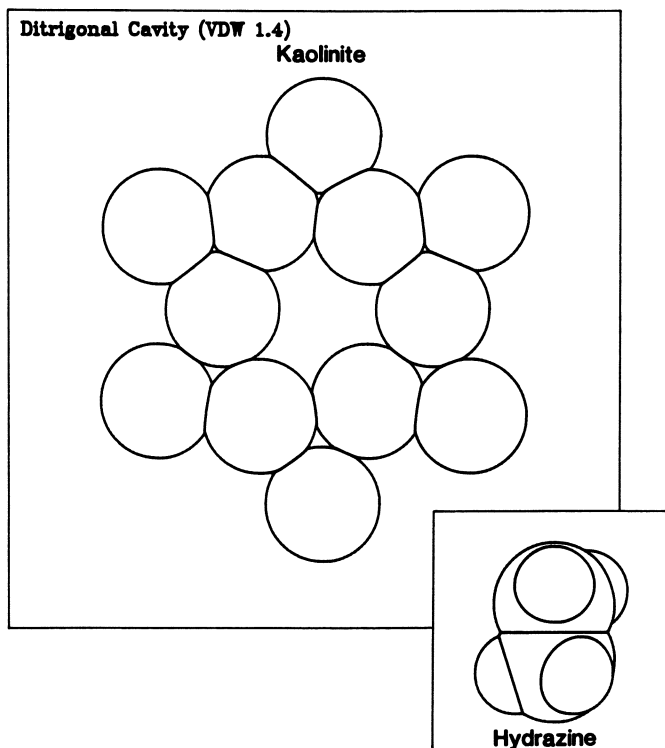


Figure 7. Space-filled [001] projection of the siloxane ditrigonal cavity of kaolinite. Space-filled structure of hydrazine is also shown, drawn to the same scale.

a function of pressure. The presence of two discrete inner-hydroxyl bands indicates that two different conformations of the KH complex exist, and that the conformation responsible for the 3628 cm^{-1} band is favored at lower pressures. The influence of pressure on stability of the KH complex was investigated by determining the weight loss of the complex as a function of pressure. As the gravimetric data shown in Fig. 8 indicate, the KH complex remains intercalated throughout the pressure region examined in this study. The three sets of data points shown in Fig. 8 correspond to three different initial loadings of hydrazine on the sample. Although the loadings were significantly different, all three sets of data converge upon a common value of approximately 0.5 molecules of hydrazine per unit cell of kaolinite after a vacuum of $\approx 10^{-4}$ atm has been achieved.

Oriented x-ray diffraction (XRD) patterns of the KH complex were obtained as a function of pressure (Fig. 9) in order to examine in detail the proposed structural changes. As the data shown in Fig. 9 illustrate, the d_{001} reflection at $8.5^\circ 2\theta$ increased to $9.2^\circ 2\theta$ upon evacuation. This corresponds to a decrease in the basal spacing of the KH complex from 1.04 nm at 1 atm (Fig. 9a) to 0.96 nm at 10^{-7} atm (Fig. 9d), a decrease of 0.08 nm. The d_{001} spacing for non-intercalated kaolinite is 0.715 nm; thus, available space for the guest hydrazine species decreased from 0.32 nm to 0.24 nm upon evacuation. This observed decrease provides structural evidence that a pressure-induced conformational change occurs. The progression of the d_{001} reflections shows a continuous change from 8.5 to $9.2^\circ 2\theta$, which suggests that a gradual collapse of the KH intercalate takes place. The vibrational data, however, indicate that two discrete conformations are present. One possibility which could account for this apparent ambiguity is that not only are two discrete conformations present, but that they are randomly interstratified. The intermediate 8.8 and $9.0^\circ 2\theta$ values would then represent weighted averages of the 8.5 and $9.2^\circ 2\theta$ components.

v(N-H) Region. The IR and XRD data indicate clearly that phases are present at 0.96 nm and 1.04 nm d-spacings, consistent with the appearance of two discrete bands in the IR spectrum and with the observed pressure dependence of the d_{001} values. In order to account for the partial collapse of the KH complex, we propose that, at high surface coverages of hydrazine in the interlamellar region (greater than 1 hydrazine molecule per unit cell), the guest hydrazine species serve as interlamellar molecular props. The d-spacing for this complex is 1.04 nm. The gravimetric weight-loss data suggest that the surface coverage of hydrazine is reduced to ≈ 0.5 hydrazine molecules per unit cell upon evacuation below 10^{-4} atm (Fig 8). The XRD data indicate that, at this surface loading, the hydrazine molecules are permitted to key into the ditrigonal holes and the d-spacing of the KH intercalate consequently is reduced to 0.96 nm (Fig. 9). Similar arguments have been presented by Costanzo and Giese (6,9,12,38) to explain the lower-than-expected d_{001} spacings for several kaolinite-water intercalates.

Upon evacuation of the KH complex to 10^{-7} atm, the bulk v(N-H) bands at 3196 and 3336 cm^{-1} are strongly reduced in intensity and shifted up in frequency to 3225 and 3361 cm^{-1} , respectively. The close agreement between the band positions of the v(N-H) bands of the KH complex (Fig. 5b) and those of liquid hydrazine (23) indicate that much of the hydrazine present on the sample at 1 atm. pressure (Figs. 2b, 5b) is physically adsorbed on the external surfaces of kaolinite. The weight-loss data of the KH complex indicate that a significant portion of the hydrazine is

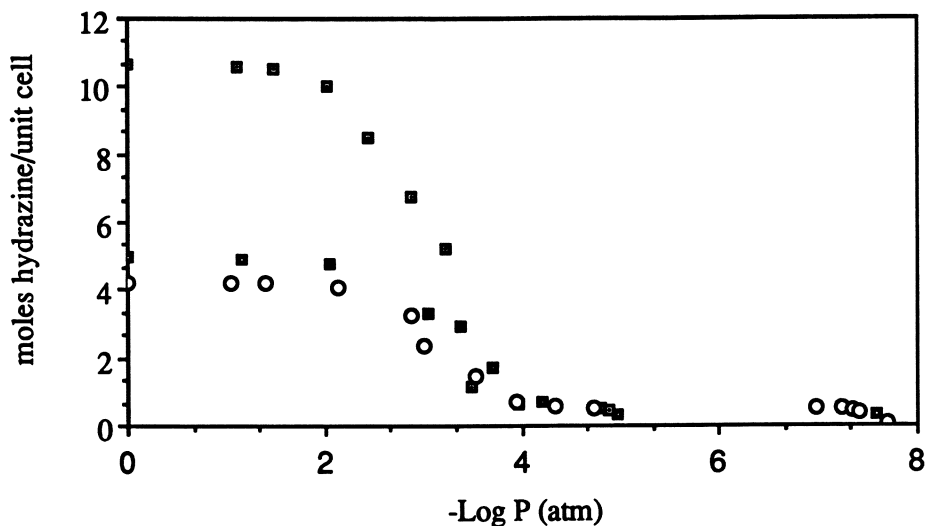


Figure 8. Gravimetric weight loss data for the kaolinite-hydrazine complex as a function of pressure.

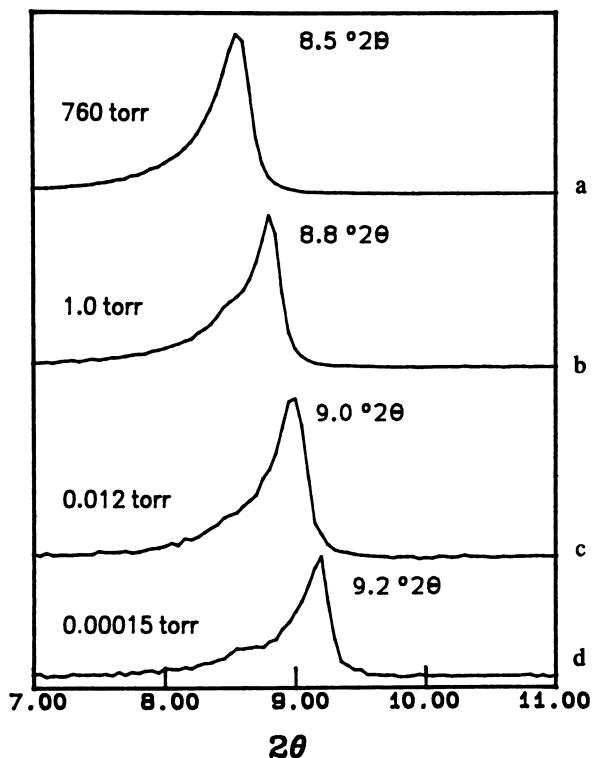


Figure 9. Controlled-environment X-ray diffraction patterns of a kaolinite-hydrazine intercalate in the 7 to 11 °2θ region, obtained as a function of pressure at 298 K.

removed upon evacuation to 10^{-2} torr. In addition, the XRD data obtained under high vacuum provide structural evidence that the KH complex remains intact, even under a high vacuum. Thus, the spectral changes in the KH complex observed upon evacuation (Figs. 5b \rightarrow 5c) can be evaluated in terms of the gravimetric and XRD data. The significant loss in intensity of the 3196 and 3336 cm^{-1} bands corresponds to the loss of physically adsorbed hydrazine from the external surfaces of kaolinite.

The remaining hydrazine (Fig. 6c) corresponds to the intercalated species, and is characterized by $\nu(\text{N-H})$ bands at 3225 and 3361 cm^{-1} . These $\nu(\text{N-H})$ bands, which correspond to the ν_1 and ν_9 modes of hydrazine, are shifted up in frequency from their solution values by $\approx 30 \text{ cm}^{-1}$ (Table 2). For comparison, the position of these $\nu(\text{N-H})$ bands in matrix-isolated hydrazine is 3313, and 3398, respectively (Table 2) (30,38). Thus, the $\nu(\text{N-H})$ frequencies of intercalated hydrazine are intermediate between the solution-like values (where hydrogen bonding and dipolar interactions occur), and the matrix isolated values (where hydrogen bonding between hydrazine molecules has been eliminated). These data show that relatively weak hydrogen bonds are formed between the NH_2 groups of hydrazine and the siloxane surface of kaolinite. The linewidth of the intercalated $\nu(\text{N-H})$ band at 3361 cm^{-1} (Fig. 5c) is considerably narrower than the corresponding $\nu(\text{N-H})$ band in solution at 3336 cm^{-1} . This reduced linewidth indicates that the local environment around the intercalated species is fairly well-ordered in the interlamellar region.

There are three Raman-active $\nu(\text{N-H})$ modes (Fig. 10) in comparison to two IR-active bands (Figs. 2,3, and 6; and Table 2) (22,23,29). In a Raman study of the hydrogen bonding of hydrazine in solution, Durig et al. (22) observed that the intensity of one of the $\nu(\text{N-H})$ bands, which occurs at 3189 cm^{-1} , depended strongly on the temperature. The ratios of the intensities of the 3260 to the 3189 cm^{-1} band plotted against temperature (22) are shown in Fig. 11. Durig et al. proposed that the intensity of the 3189 cm^{-1} band is due, in part, to a hydrogen-bonded dimer. The intensity of this band is also due, in part, to absorption by the monomer. From the data presented in Fig. 11, they calculated a ΔH° value of -1450 cal/mole for the hydrogen-bond enthalpy.

Raman spectra of the KH complex in the $\nu(\text{N-H})$ region are shown in Fig. 10a-c. The top spectrum (Fig 10c) shows the difference between the spectrum of the KH intercalate (Fig 10b) and that of liquid hydrazine (Fig 10a). The negative band at 3185 cm^{-1} (Fig. 10c) reflects the relative loss in intensity of the 3185 cm^{-1} component in comparison to the the other $\nu(\text{N-H})$ bands at 3283 and 3344 cm^{-1} . According to the temperature dependence of the $\nu(\text{N-H})$ bands (22), the lower intensity of the 3185 cm^{-1} band indicates that less hydrogen bonding between hydrazine molecules occurs in the interlamellar region of the kaolinite than in solution, similar to the effect of increasing the temperature of liquid hydrazine. This postulate is supported further by the observed increase in frequency of the remaining two $\nu(\text{N-H})$ Raman bands at 3283 and 3344 cm^{-1} . The $\nu(\text{N-H})$ bands in the difference spectrum (Fig. 10c) are clearly blue-shifted from their solution counterparts to frequencies of 3301, 3310, and 3361 cm^{-1} , respectively. The small splitting the $\nu(\text{N-H})$ bands may indicate that two slightly different conformations of the $-\text{NH}_2$ groups may be present. The 3283 cm^{-1} band is not IR-active; however, the observed increase in frequency from 3344 to 3362 cm^{-1} in the Raman spectrum of the KH complex is in close agreement with the IR data (Fig. 5). The decrease in the relative intensity of the 3185 cm^{-1} , band and the increase in frequency of the 3283 and 3344 cm^{-1} bands, provide conclusive evidence that the $-\text{NH}_2$ groups of

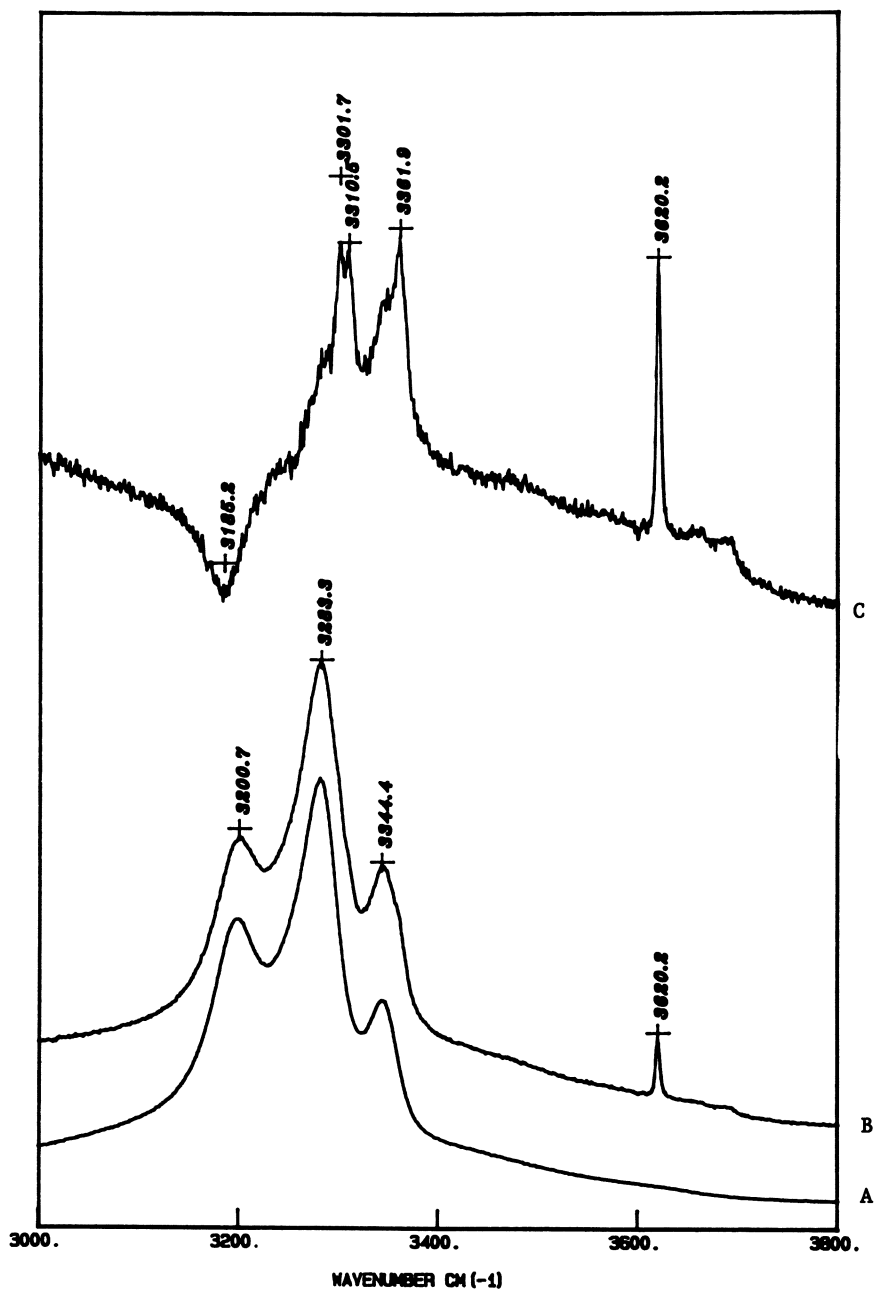


Figure 10. Raman spectra of liquid hydrazine (A), of the kaolinite-hydrazine complex at 1 atm. of pressure suspended in liquid hydrazine (B), and the difference spectrum of [B - A] in the 3000 to 3800 cm^{-1} region (C).

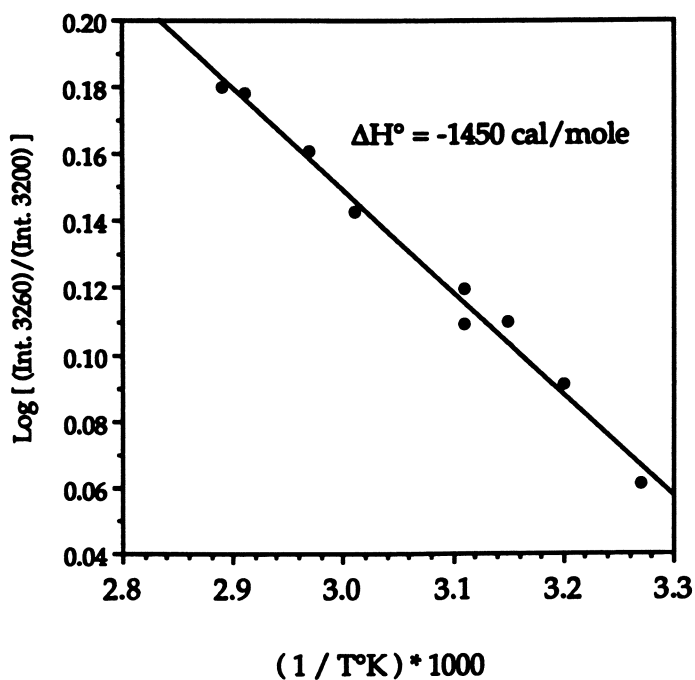


Figure 11. Intensity ratio of the 3260 to 3200 bands as a function of temperature for liquid hydrazine. Data are from ref. 22.

hydrazine do not participate in the formation of strong hydrogen bonds with the siloxane surface of kaolinite. These data show that less hydrogen bonding occurs between hydrazine molecules in the interlamellar region of the clay than in solution, and that the local environment around the hydrazine species is well-ordered.

$\nu(\text{N-N})$ Region. Low-frequency Raman spectra of hydrazine, of the KH complex, and the difference spectrum of (KH - hydrazine), are shown in Figs. 12a-c. The frequencies and relative intensities of the bands in the hydrazine spectrum (Fig. 12a) are in good agreement with published Raman data (23). The difference spectrum (Fig. 12c) was obtained by subtracting the hydrazine spectrum from that of the KH complex. The bands in the difference spectrum (Fig. 12c) shown at 399, 436, 467, 512, 636, 738, and 794 cm^{-1} are kaolinite modes, whereas the bands at 958, 1089, 1328, and 1621 have been assigned to hydrazine. The intensity of the hydrazine ν_6 band (NH_2 rock) at 903 cm^{-1} is decreased relative to that of the ν_5 band at 1111 cm^{-1} (N-N stretch). Although components of the 1111 and 1620 cm^{-1} bands of hydrazine can be seen in the difference spectrum, the Raman intensity in the 900 cm^{-1} region is negligible. In addition, the position of the ν_5 band at 1111 is shifted down in frequency from its solution value of 1111 cm^{-1} to 1089 cm^{-1} (Fig. 12). These observations suggest that the local environment in the interlamellar region of the clay is different from that of the bulk solution. The decreased intensity of the ν_6 band, and the red-shift of the ν_5 mode, may be indicative of a conformational change of the hydrazine molecule in the interlamellar region. The positions of the lower-frequency kaolinite bands in the KH spectrum (Figs. 12b,c) are close to those reported for kaolinite. This indicates that hydrazine does not strongly perturb the structural framework modes of the clay lattice.

Conclusions.

The vibrational data suggest that the predominant interaction between hydrazine and the interlamellar surface of kaolinite is through hydrogen bonding between the ISu hydroxyl groups of kaolinite and the lone pair of electrons on the nitrogen atom of hydrazine. The strength of these hydrogen bonds could not be determined, because the position of the red-shifted ISu $\nu(\text{O-H})$ band(s) is not clearly resolved. The strongly reduced intensities of the ISu $\nu(\text{O-H})$ bands indicate, however, that most of the ISu hydroxyl groups of kaolinite participate in this interaction. In the $\nu(\text{O-H})$ region, the Raman and IR spectra of the KH complex were very similar. The interaction of the $-\text{NH}_2$ group with the siloxane surface is determined to be relatively weak on the basis of the $\nu(\text{N-H})$ modes; the distinct loss in intensity of the 3189 cm^{-1} band and the blue-shift of the 3301, 3310, and 3362 cm^{-1} bands indicate that weaker hydrogen bonds involving the $-\text{NH}_2$ group occurred in the interlamellar region than in solution. The narrower linewidths of the $\nu(\text{N-H})$ bands of intercalated hydrazine in comparison to their solution bandwidths indicate that the molecular environment around the hydrazine species in the interlamellar region is well-ordered.

In contrast to the close agreement found for the high-frequency region, the Raman and IR data of the KH complex are quite different for the lower-frequency region below 1200 cm^{-1} . Although IR methods, in general, are characterized by an intrinsically higher sensitivity than that obtained using conventional Raman techniques, the strong lattice modes of kaolinite interfered with the observation of the hydrazine modes in this region. This restriction did not apply to the Raman data,

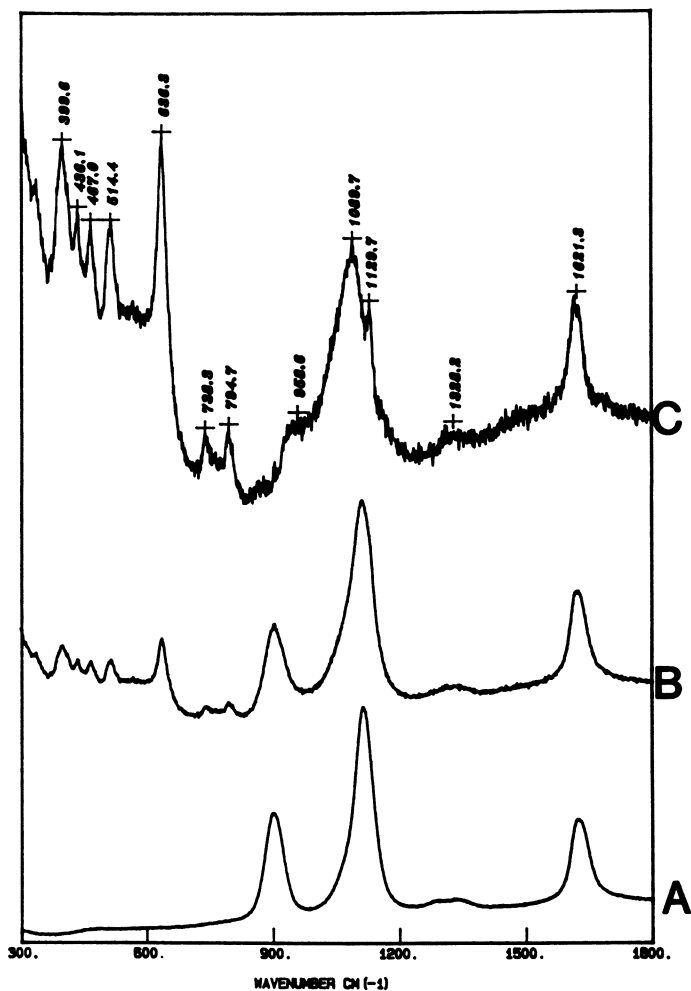


Figure 12. Raman spectra of liquid hydrazine (A), of the kaolinite-hydrazine complex at 1 atm. of pressure suspended in liquid hydrazine (B), and the difference spectrum of [B - A] in the 300 to 1800 cm⁻¹ region (C).

however, because the kaolinite modes are much weaker in the Raman spectrum. Thus, the lower-frequency hydrazine modes are clearly resolved from the weaker kaolinite modes. The mechanism responsible for the decreased intensity of the -NH_2 rocking mode at 903 cm^{-1} and for the red-shift of the $\nu(\text{N-N})$ stretching band of the intercalated hydrazine species is not currently known. These observations suggest that a conformational change for the intercalated hydrazine molecule may occur in the interlayer region.

The pressure-induced growth of the 3628 cm^{-1} band at the expense of the 3620 cm^{-1} band, and the related pressure-dependence of the XRD and gravimetric data, indicate that the inner-hydroxyl group of kaolinite is perturbed by the interlamellar hydrazine species. At higher pressures, the interlamellar hydrazine molecules function as molecular props. Upon evacuation of the complex, the surface density of hydrazine is reduced to ≈ 0.5 hydrazine molecules per unit cell of kaolinite. The lower surface density of hydrazine permits the partial collapse of the KH lattice, which results in a d_{001} spacing of 0.96 nm . The decrease in d_{001} spacing and the concomitant growth of the 3628 cm^{-1} band indicate that the -NH_2 group of hydrazine is brought into closer contact with the inner-hydroxyl group through the siloxane ditrigonal cavity. We propose that the blue-shift of the inner $\nu(\text{O-H})$ band results from increased electrostatic repulsion between the inner-hydroxyl group of kaolinite and the -NH group of hydrazine. This hypothesis is also consistent with the observed blue-shift of the $\nu(\text{N-H})$ bands of the intercalated hydrazine species relative to their frequencies in solution.

Acknowledgments

This work was supported, in part, by the Environmental Sciences Branch of the United States Air Force. The author would like to thank Drs. Rene Prost, David Bish, Zeina Hinedi, Willis Person and Lelia Coyne for helpful contributions to the manuscript.

References

1. Boyd, S.A.; Shaobai, S.; Lee, J.F.; Mortland, M.M. Clays and Clay Min. 1988, 36, 125.
2. Boyd, S.A.; Mortland, M.M.; Chiou, C.T. Soil Sci. Soc. of Amer. J. 1988, 52, 652.
3. Mortland, M.M.; Shaobai, S.; Boyd, S.A. Clays and Clay Min. 1986, 34, 581.
4. Coyne, L.M.; Sweeney, M.; Hovatter, W. J. Luminescence 1983, 28, 395.
5. Coyne, L.M.; Pollock, G.; Kloeping, R. Clays and Clay Min. 1984, 32, 58.
6. Costanzo, P.M.; Giese, R.F.; Lipsicas, M.; Straley, C. Nature 1982, 296, 549.
7. Thompson, J.G. Clays and Clay Min. 1985, 33, 173.
8. Johnston, C.T.; Sposito, G.; Bocian, D.F. J. Phys. Chem. 1984, 88, 5959.
9. Costanzo, P.M.; Giese, R.F. Clays and Clay Min. 1986, 34, 105.
10. Thompson, J.G.; Cuff, C. Clays and Clay Min. 1985, 33, 490.

11. Lipsicas, M.; Straley, C.; Costanzo, P.M.; Giese, R.F. J. Colloid Interface Sci. 1985, 107, 221.
12. Costanzo, P.M.; Giese, R.F.; Lipsicas, M. Clays and Clay Min. 1984, 32, 419.
13. Raussell-Colom, J.A. and Serratos, J.M. In Reactions of clays with organic substances. In: Chemistry of clays and clay minerals, edited by Newman, A.C.D. New York, NY: John Wiley and Sons, 1987, p. 371.
14. Johnston, C.T.; Stone, D.A.; Applewhite, L.A. Vibrational spectroscopic study of the kaolinite-hydrazine intercalation complex. The Third Conference on the Environmental Chemistry of Hydrazine Fuels, Panama City, FL 15-17 Sept. 1987 1987, ESL-TR-87-74, 118.
15. Cruz, M.I.; Laycock, A.; White, J.L. Intl. Clay Conf. Proc., Tokyo 1969, 775.
16. Ledoux, R.L.; White, J.L. Science 1964, 145, 47.
17. Ledoux, R.L.; White, J.L. J. Colloid Interface Sci. 1966, 21, 127.
18. Olejnik, S.; Aylmore, L.A.G.; Posner, A.M.; Quirk, J.P. J. Phys. Chem. 1968, 72, 241.
19. Olejnik, S.; Posner, A.M.; Quirk, J.P. Spectrochim. Acta, Part A 1971, 27A, 2005.
20. Olejnik, S.; Posner, A.M.; Quirk, J.P. Clays and Clay Min. 1971, 19, 83.
21. Rouxhet, P.G.; Samudacheata, N.; Jacobs, H.; Anton, O. Clay Min. 1977, 12, 171.
22. Durig, J.R.; Bush, S.F.; Mercer, E.E. J. Chem. Phys. 1966, 44, 4238.
23. Durig, J.R.; Griffin, M.G.; Macnamee, R.W. J. Raman Spectrosc. 1975, 3, 133.
24. Morrow, B.A. J. Phys. Chem. 1977, 81, 2683.
25. Knozinger, H.; Jeziorowski, H. J. Phys. Chem. 1978, 82, 2002.
26. Yates, J.T.; Madey, T.E. (Eds.) In. Vibrational spectroscopy of molecules on surfaces. New York: Plenum Press, 1987, p. 468.
27. Johnston, C.T.; Sposito, G.; Birge, R.R. Clays and Clay Min. 1985, 33, 483.
28. Van Olphen, H. and Fripiat, J.J. Data handbook for clay materials and other non-metallic minerals, Oxford: Pergamon Press, 1979. Ed. 256 pp. 1-346.
29. Giguere, P.A.; Liu, I.D. J. Chem. Phys. 1952, 20, 136.
30. Tipton, T.; Stone, D.A.; KuBulat, K.; Person, W.B. J. Chem. Phys. 1988, (In Press)
31. Sathyanarayana, D.N.; Nicholls, D. Spectrochimica Acta Part A. 1978, 34A, 263.
32. Wiewiora, A.; Wieckowski, T.; Sokolowska, A. Archiwum Mineralogiczne 1979, 35, 5.
33. Michaelian, K.H. Can. J. Chem. 1986, 64, 285.
34. Olejnik, S.; Posner, A.M.; Quirk, J.P. J. Colloid Interface Sci. 1971, 37, 536.
35. Wada, K. Clay Min. 1967, 7, 51.
36. Suitch, P.R.; Young, R.A. Clays and Clay Min. 1983, 31, 357.
37. Costanzo, P.M.; Giese, R.F. Clays and Clay Min. 1985, 33, 415.
38. Catalano, E.; Sanborn, R.H.; Frazer, J.W. J. Chem. Phys. 1963, 38, 2265.

RECEIVED May 18, 1989

Chapter 23

Reactive Cr-O Sites

Catalytic Properties of Chromia-Pillared Montmorillonite and Preliminary Study Results

Ahmad Moini¹, Thomas D. Brewer¹, Ming-Shin Tzou¹, Steven D. Landau¹,
Boon-Keng Teo², and Thomas J. Pinnavaia¹

¹Department of Chemistry and Center for Fundamental Materials Research,
Michigan State University, East Lansing, MI 48824

²Department of Chemistry, University of Illinois, Chicago, IL 60680

The catalytic and structural properties of two chromia-pillared montmorillonites were compared in an effort to establish structure-reactivity relationships in these materials. The basal spacings of pillared products, prepared by reaction of Na⁺-montmorillonite with base-hydrolyzed Cr(III) solutions, depended in part on the temperature used for the hydrolysis reaction. Catalytic studies on the derivatives with basal spacings of 23.5 and 13.7 Å showed the intercalate with the larger gallery height to be considerably more reactive for the dehydrogenation of cyclohexane to benzene. Preliminary EXAFS results for the 23.5 Å intercalate showed local structural similarities between the chromia pillars and bulk Cr₂O₃. The relationship to chromium oxide was substantiated by the similar catalytic activities obtained for the 23.5 Å chromia-pillared clay and Cr₂O₃ supported on alumina.

Among all layered silicate clays, the smectite family of 2:1 layer lattice structures are preeminent in their ability to adsorb organic molecules and to catalyze their chemical transformations. All metal oxides in the soil environment may exhibit some degree of surface reactivity. However, the adsorptivity and reactivity of typical smectites are facilitated by their relatively high internal surface areas (~ 700 m²/g) and external surface areas (10-50 m²/g).

Solomon and Hawthorne (1) have provided a schematic summary of the functional group reactivity of smectites. More recently, it was pointed out that the types of sites will depend on the state of hydration of the clay as

0097-6156/90/0415-0455\$06.00/0

© 1990 American Chemical Society

shown in Figure 1 (Zielke, R. C.; Pinnavaia, T. J.; Mortland, M. M. In Reactions and Movement of Organic Chemicals in Soils; Sawhney, B. L., Ed.; Soil Sci. Soc. Am.: Madison, in press.) At low hydration levels, the galleries are collapsed and inaccessible for catalysis, and the strength of the Lewis base sites at the edges become more important. At high hydration states, the galleries are swollen and accessible, and the external surfaces are more completely hydrated. This accessibility of internal surfaces, as well as the surface functionality of the clay, is strongly influenced by hydration.

The state of the smectite clay under idealized conditions of dehydration is represented at the bottom of Figure 1. The gallery exchange ions (M^{n+}) are coordinated to the oxygen atoms defining the di-trigonal cavities of a Kagome (2) network. Since the galleries are collapsed, no interlamellar adsorption or ion exchange is possible unless the organic guest itself is highly polar and capable of swelling the interlayers. Thus, the surface functional groups of primary importance under the conditions of low hydration are Lewis acid sites and hydroxyl groups located at external edge positions.

At higher degrees of hydration, however, the gallery ions may become aquated and provide a source of Bronsted acidity due to hydrolysis of exchange ions (3). Regardless of the state of hydration of the surface, smectite clays are capable of shuttling electrons between structural redox centers and organic molecules adsorbed on the external or intracrystalline surfaces. For instance, Mossbauer studies have demonstrated that iron centers in clays can be reversibly interconverted between +2 and +3 oxidation states by reaction with simple oxidizing and reducing agents (4).

The above model of functional group reactivity applies to most smectite clays containing simple alkali metal and alkaline earth cations. However, there exist in nature smectite derivatives in which the gallery cations are extensively hydrolyzed polymeric species such as hydroxycations of aluminum and iron. These so-called "hydroxy-interlayered" (5-8) clays have been recognized as possible catalysts for the transformation of organic molecules in the soil environment. Several hydroxy-interlayered smectites have been synthesized under conditions approximating those in nature. The products are typically chloritic insofar as the basal spacings are similar to the 14 Å observed for chlorite. Thus, the galleries are almost completely occupied ("stuffed") by the hydroxy cations.

More recently, polyoxocations have been used to prepare pillared forms of interlayered clays that are related to the hydroxy-interlayered analogs found in

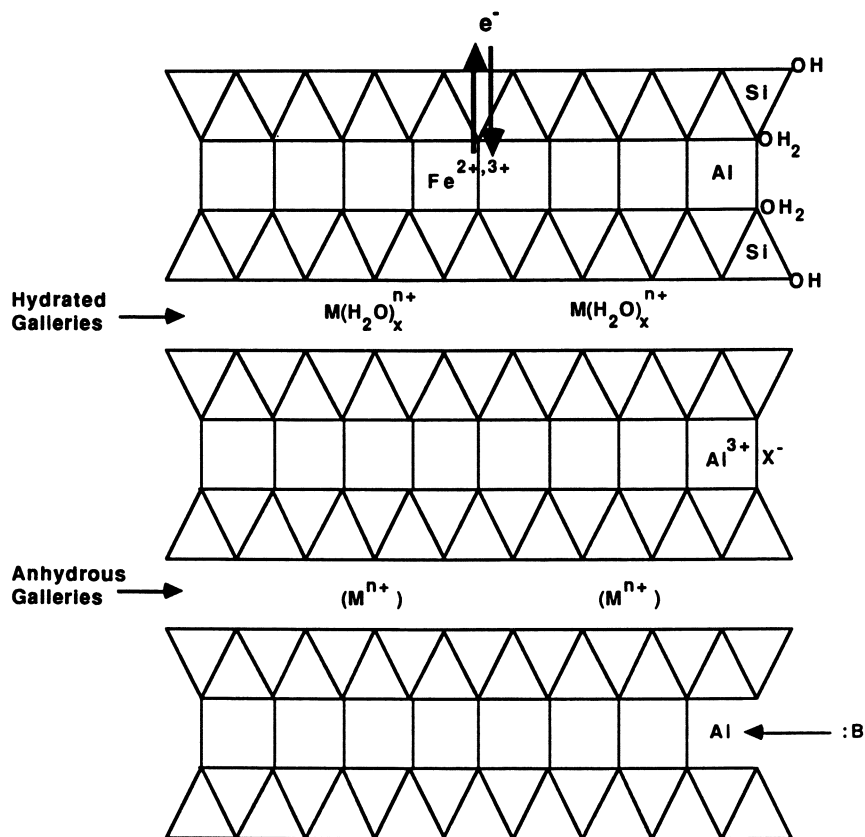
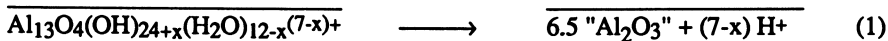


Figure 1. Schematic illustration of the surface functional groups on dehydrated and hydrated states of smectite clay.

nature. The thermal dehydration and dehydroxylation of these hydroxy-interlayered derivatives converts them to metal oxide pillared forms which are stable to high temperatures. These materials exhibit novel properties as catalysts for a wide range of chemical conversions (9-11), many of which are related to processes occurring in the soil environment.

Although hydroxy-interlayered clays found in nature are generally chlorite-like, some forms may resemble the hydroxy-interlayered precursors to metal oxide pillared clays. Figure 2 illustrates the structure of a typical chlorite in which the galleries are occupied by brucite-like sheets of edge-shared $Mg(OH)_6$ and $Al(OH)_6$ octahedra. In contrast, pillared hydroxy-interlayered clays contain more robust polyoxocations such as the $Al_{13}O_4(OH)_{24+x}(H_2O)_{12-x}^{(7-x)+}$ (12) which has the isomeric Keggin structure as shown in Figure 3. Since the latter hydroxy cations are laterally spaced in the gallery of the host clay, their thermal dehydroxylation to metal oxide aggregates, as illustrated in Equation 1, results in acidic galleries which have two-dimensional microporous structures for the adsorption and catalytic conversions of guest molecules.



Metal oxide pillared clays are relatively complex materials and their structural characterization has been a challenging experimental problem. Recent magic angle spinning NMR studies of alumina-pillared clays (13-15) suggest that the Keggin ion-like structure is retained at temperatures below 350°C. Grafting of the pillar to the host layers may or may not occur depending on the constitution of the 2:1 layered silicate structure. Chemical studies of the surface organometallic chemistry of pillared clays suggest that the reactivity of the surface hydroxyl groups of the pillars toward metal cluster carbonyl compounds is similar to the reactivity found on the surfaces of bulk alumina (16).

In an effort to more fully elucidate the structure and reactivity of metal oxide pillared clays, we have been investigating the structure-reactivity properties of chromia-pillared derivatives (17). In the following sections, we provide an example of the structure-catalytic reactivity properties of chromia-pillared montmorillonites. Also, we report our initial efforts to structurally characterize the intercalated chromia aggregates by Extended X-ray Absorption Fine Structure (EXAFS) Spectroscopy. Unlike previously reported metal oxide pillared clays, chromia-pillared clay exhibits strong K-edge absorption and fine structure suitable for determination of metal-oxygen bond distances in the pillars.

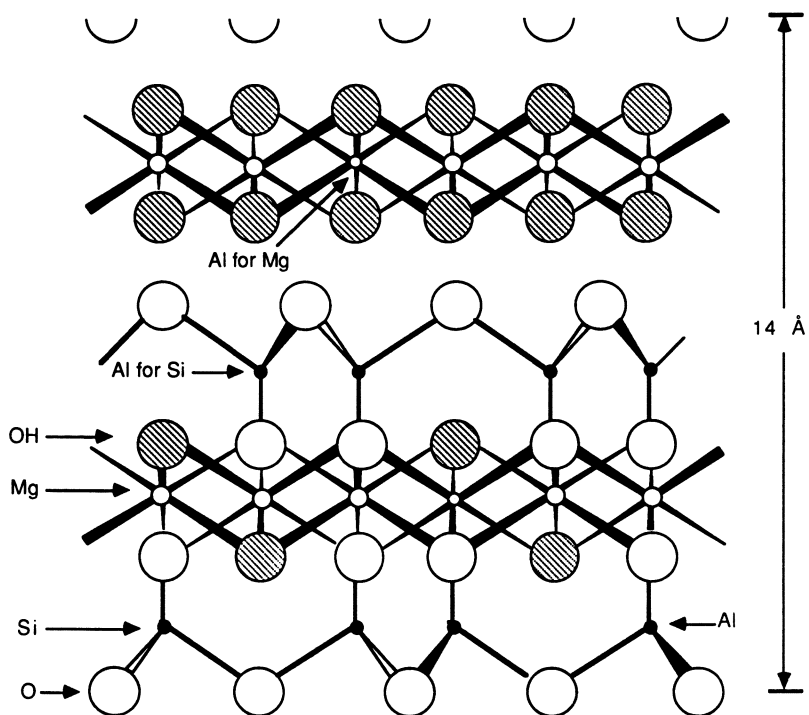


Figure 2. Structure of a typical chlorite-like hydroxy-interlayered clay in which the galleries of a 2:1 smectite structure are filled, or nearly so, with brucite-like sheets of mainly edge-shared $\text{Mg}(\text{OH})$ octahedra. Aluminum occasionally substitutes for magnesium in the brucite sheet to provide the charge balance necessary for electrical neutrality.

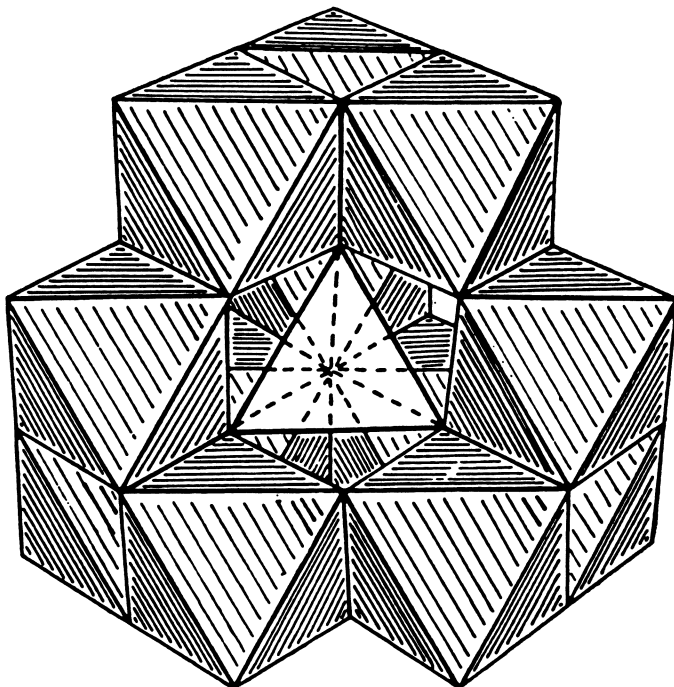


Figure 3. Structure of a typical polyoxocation, namely $\text{Al}_{13}\text{O}_4(\text{OH})_{24+x}(\text{H}_2\text{O})_{12-x}^{(7-x)+}$, used to form a pillared hydroxy-interlayered clay. Twelve aluminum ions occupy positions in octahedral interstices and one aluminum occupies a tetrahedral position in the center to form the Keggin structure. When $x = 0$, the terminal vertices of the octahedra are occupied by water, whereas the shared vertices are occupied by OH groups. The vertices of the central tetrahedron are occupied by oxygen atoms. The dotted lines in the center of the figure define the tetrahedral site and the three octahedra which are partially blocked from view.

Structure-Reactivity Relationships for Chromia Pillared Clays

The properties of hydroxychromium interlayered clays as precursors to chromia-pillared clays depend critically on the nature of the hydroxychromium oligomers which initially occupy the galleries of the host clay. In general, pillaring solutions are prepared by basic hydrolysis of chromium (III) solutions at temperatures above 60°C. The base/metal ratios (n) of these solutions are varied between 1.0 and 2.0. The reaction of Na⁺-montmorillonite with these pillaring agents ($n = 1.0-2.0$) results in the formation of hydroxychromium derivatives with basal spacings in the range 20-28 Å under air-dried conditions. Conversely, the basic hydrolysis of chromium solutions at 25°C results in the formation of smaller oligomers which react with Na⁺-montmorillonite to form derivatives with basal spacings in the range 14-18 Å.

Table I compares the chemical and physical properties of two hydroxychromium montmorillonites prepared by reaction of a Na⁺-exchanged Wyoming montmorillonite (unit cell formula $\text{Na}_{0.6}[\text{Al}_{3.23}\text{Fe}_{0.42}\text{Mg}_{0.47}](\text{Si}_{7.88}\text{Al}_{0.13})\text{O}_{20}(\text{OH})_4$) with chromium pillaring solutions prepared by hydrolysis at 95°C and 25°C and n value of 2.0 (17). The intercalate obtained from the chromium reagent hydrolyzed at 95°C contains 3.53 Cr per $\text{O}_{20}(\text{OH})_4$ unit cell. Henceforth, this material will be referred to as Cr_{3.53}-montmorillonite. In comparison, the chromium solution prepared at 25°C affords a hydroxychromium interlayer product containing 1.88 Cr per $\text{O}_{20}(\text{OH})_4$ unit cell, henceforth abbreviated Cr_{1.88}-montmorillonite. Both materials undergo a reduction in basal spacing upon dehydration and dehydroxylation at temperatures up to 500°C under a nitrogen atmosphere. Upon dehydration at 350°C, the basal spacing of the Cr_{3.53}-montmorillonite (23.5 Å) is substantially larger than the spacing observed for the Cr_{1.88} derivative (14.2 Å). The dehydrated Na⁺-montmorillonite has a basal spacing of 9.7 Å which corresponds to the van der Waals thickness of a montmorillonite layer. The free gallery heights for the Cr_{3.53} and Cr_{1.88}-montmorillonites are therefore 13.8 and 4.5 Å, respectively, after degassing at 350°C.

The large difference in gallery heights for Cr_{3.53} and Cr_{1.88}-montmorillonites leads to dramatic differences in catalytic reactivity (17). Figure 4 illustrates the conversion of cyclohexane to benzene over both materials at 550°C as a function of reaction time. Both catalysts were pre-reduced under H₂ in a continuous flow reactor at 500°C, followed by reaction with cyclohexane (weight hourly space velocity = 3, contact time = 6 sec, He carrier gas.) The clay remains intact at these reaction temperatures as evidenced from the thermal data (17).

Table I. Hydroxychromium Montmorillonites

Sample	Basal Spacings, Å			Surface Area ^c m ² /g
	25°	350°	500°	
Cr _{3.53} -Mont. ^a	27.6	23.5	21.0	353
Cr _{1.88} -Mont. ^b	16.8	14.2	13.7	280

^a This sample, which contained 3.53 Cr per O₂₀(OH)₄ unit cell, was prepared by reaction of Na⁺-montmorillonite with a Cr³⁺ solution hydrolyzed at 95°C and n = 2.0.

^b The pillaring solution used to prepare this derivative was hydrolyzed at 25°C and n = 2.0.

^c Outgassing of samples was carried out at 350°C in the absence of oxygen. The surface areas were determined by nitrogen BET adsorption.

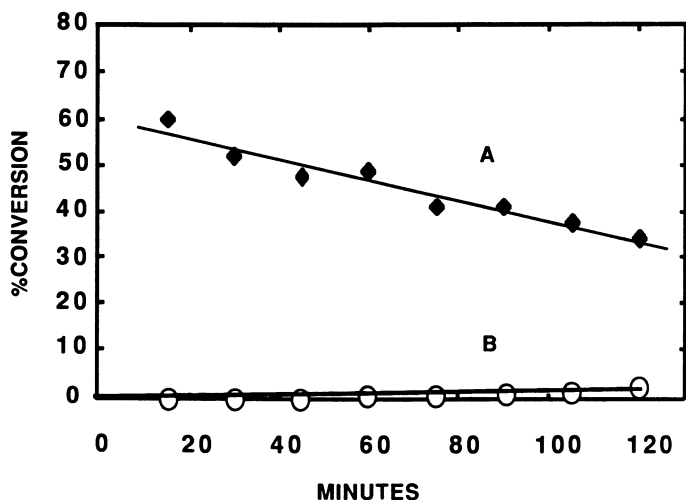


Figure 4. Conversion of cyclohexane to benzene over chromia pillared montmorillonites at 550°C: (A) Cr_{3.53}-montmorillonite, (B) Cr_{1.88}-montmorillonite. The cyclohexane contact time was 6.0 s and the weight hourly space velocity was in the range 1.0-3.0. Each sample was heated under a flow of hydrogen at 550°C prior to use of the catalyst.

Little or no reactivity is observed for $\text{Cr}_{1.88}$ -montmorillonite, but the $\text{Cr}_{3.53}$ derivative with a large gallery height is much more reactive. Also, it should be noted that, as expected, pure Na^+ -montmorillonite showed no catalytic activity. The decrease in reactivity with increasing reaction time for $\text{Cr}_{3.53}$ -montmorillonite most likely arises from the formation of coke and the concomitant occlusion of gallery pores.

The high dehydrogenation activity observed for $\text{Cr}_{3.53}$ -montmorillonite almost certainly arises from the facile accessibility of the chromium oxide aggregates supported in the clay gallery. Substantial contribution to the observed activity due to active sites at the external surfaces of the mineral is precluded by the virtual absence of activity for the $\text{Cr}_{1.88}$ derivative. Thus, $\text{Cr}_{3.53}$ -montmorillonite behaves catalytically much like bulk chromium oxide supported on alumina (17).

Evidence that difference in reactivity for $\text{Cr}_{3.53}$ and $\text{Cr}_{1.88}$ -montmorillonite is due largely to differences in gallery accessibility is provided by the adsorption data in Figure 5. The $\text{Cr}_{3.53}$ derivative, which retains a basal spacing near 21 Å after reaction, is capable of rapidly adsorbing cyclohexane. However, the $\text{Cr}_{1.88}$ derivative with a basal spacing near 13.7 Å adsorbs very little cyclohexane.

EXAFS Studies of Chromia Pillars

The similarities in catalytic reactivity between $\text{Cr}_{3.53}$ -montmorillonite and chromia supported on alumina suggest that the structure of the intercalated chromia particles may resemble the structure of the bulk oxide. In order to obtain structural information for the chromia aggregates in pillared clays, we have initiated structural studies of these materials. Extended X-ray Absorption Fine Structure (EXAFS) spectroscopy is being recognized as an effective tool for determining the local structure of a variety of materials. The basic principles and utility of this technique have been discussed elsewhere (18).

X-ray absorption studies of $\text{Cr}_{3.53}$ -montmorillonite were carried out at the Cornell High Energy Synchrotron Source (CHESS), Cornell University. The measurements were performed at room temperature on the C-2 EXAFS beam line. The sample studied was the 23.5 Å heated chromia-pillared montmorillonite, and the measurements were made at the chromium K absorption edge. The raw data, collected as a function of photon energy (E), was reduced to photoelectron wavevector (k) space, and the background was removed (18,19). This was followed by removal of the high-frequency noise and the truncation of the data at 4.0 and 12.0 Å⁻¹. The resulting EXAFS modulation is shown in Figure 6. The Fourier transform of these data,

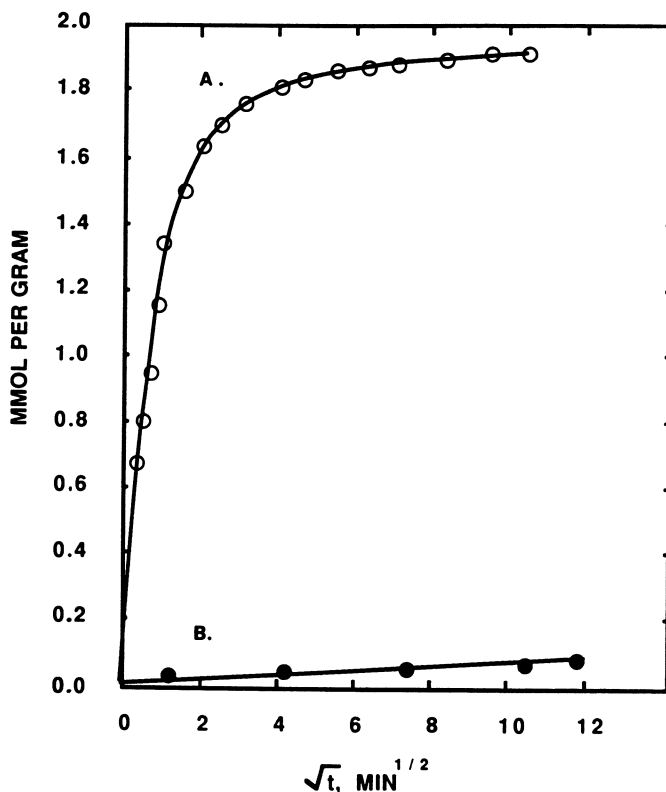


Figure 5. Uptake of cyclohexane at 25°C and $p/p_0 = 0.95$ by chromia pillared montmorillonites: (A) $\text{Cr}_{3.53}$ -montmorillonite, (B) $\text{Cr}_{1.88}$ -montmorillonite. The uptake curves were determined for both materials after use as a catalyst for the conversion of cyclohexane to benzene at 550°C.

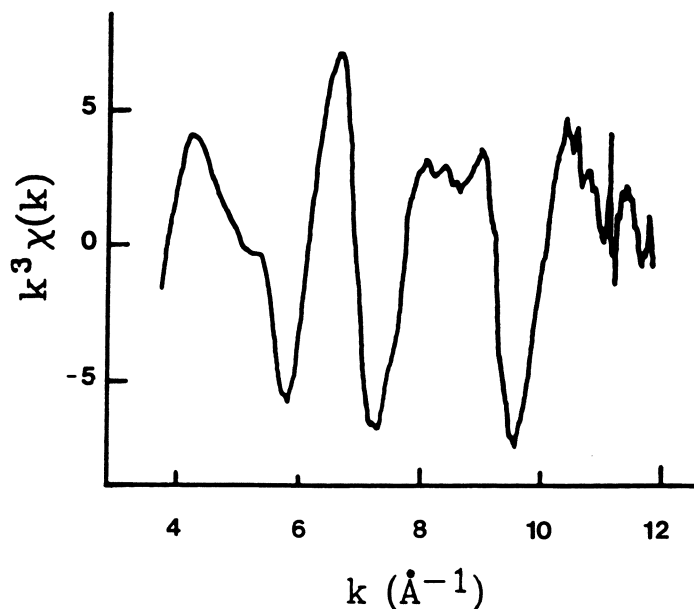


Figure 6. Cr-edge EXAFS spectrum for $\text{Cr}_{3.53}$ -montmorillonite.

shown in Figure 7, gave rise to two major peaks at 1.6 and 2.6 Å before the phase shift correction. No other significant peaks were observed at longer bond distances.

These maxima in the Fourier transform data, which correspond to the different chromium coordination shells, were isolated using a filter window function. The inverse transform of each peak was generated and fitted using a non-linear least squares program. The amplitude and phase functions were obtained from the theoretical curves reported by Teo and Lee (20). The parameters which were refined included a scale factor, the Debye-Waller factor, the interatomic distance, and the threshold energy difference. This process led to refined distances of 1.97(2) and 2.73(2) Å which were attributed to Cr-O and Cr-Cr distances, respectively. Our inability to resolve second nearest neighbor Cr-Cr distances may be a consequence of the limited domain size of the pillars.

Both of the corrected values agree with the range of Cr-O and Cr-Cr distances observed for the oxides (21,22). Crystallographic studies on $\alpha\text{-Cr}_2\text{O}_3$ have revealed the existence of two Cr-O bond lengths (1.97 and 2.02 Å) and two Cr-Cr distances (2.65 and 2.89 Å). It is plausible that the same type of variations in bond distances occurs in the chromia pillars. These variations, however, are too small to be resolved from our EXAFS results.

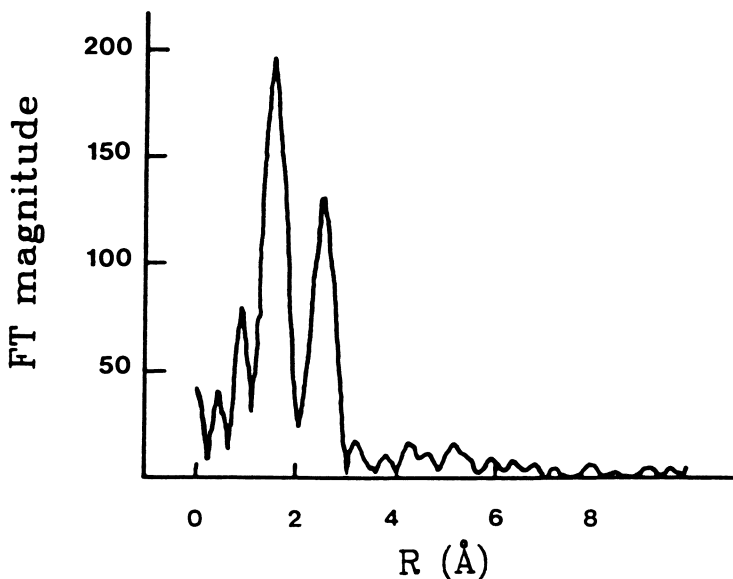


Figure 7. Fourier transform of the background-subtracted EXAFS spectrum for $\text{Cr}_{3.53}$ -montmorillonite.

The relatively small size of the pillars and the relatively low long-range ordering of intercalated clays exclude many surface and crystallographic techniques as suitable means of characterization. The present study is the first attempt to obtain interatomic distances in these systems from EXAFS data. Our results clearly show the utility of this method for local structural analysis of these clay materials. The interatomic distances obtained for chromia-pillared montmorillonite suggest similarities between the structure of the pillars and the structure of Cr_2O_3 (22). This result is in agreement with our catalytic data for the chromia pillared clay which shows reactivity comparable to systems containing the bulk oxide, such as Cr_2O_3 supported on alumina.

Future EXAFS studies of the local structure of reactive sites in pillared clay derivatives and related hydroxy-interlayered clay minerals should help elucidate the reactivity of these materials as catalysts for synthetic organic chemical conversions, as well as for reactions occurring in the natural soil environment.

Acknowledgments

This research was supported by the National Science Foundation (DMR-85-14154) and by the Michigan State University Center for Fundamental Materials Research.

Literature Cited

1. Solomon, D. H.; Hawthorne, D. G. Chemistry of Pigments and Fillers; John Wiley and Sons: New York, 1983.
2. Zallen, R. The Physics of Amorphous Solids; Wiley: New York, 1983, p. 170.
3. Mortland, M. M.; Raman, K. V. Clays Clay Miner., 1968, 16, 393.
4. Goodman, B. A. In Advanced Chemical Methods for Soil and Clay Minerals Research; Stucki, J. W.; Banwart, W. L., Eds.; Reidel: Dordrecht, 1980, p 1.
5. Barnhisel, R. I. In Minerals in Soil Environments; Dixon, J. B.; Weed, S. B., Eds.; Soil Sci. Soc. Am.: Madison, 1977, p 331.
6. Brindley, G. W.; Sempels, R. E. Clay Miner. 1977, 12, 229.
7. Hsu, P. H. In Minerals in Soil Environments; Dixon, J. B.; Weed, S. B., Eds.; Soil Sci. Soc. Am.: Madison, 1977, p 99.
8. Brindley, G. W.; Yamanaka, S. Amer. Mineral., 1979, 64, 830.
9. Shabtai, J. Chem. L'Indust., 1979, 61, 734.
10. Vaughan, D. E. W.; Lussier, R. J. Preprints, 5th International Conference on Zeolites, 1980, p 94.
11. Pinnavaia, T. J. Science, 1983, 220, 365.
12. Johansson, G. Acta Chem. Scand., 1960, 14, 771.
13. Plee, D.; Borg, F.; Gatineau, L.; Fripiat, J. J. J. Am. Chem. Soc., 1985, 107, 2362.
14. Tennakoon, P. T. B.; Jones, W.; Thomas, J. M. J. Chem. Soc., Farad. Trans., 1986, 82, 3081.
15. Pinnavaia, T. J.; Landau, S. D.; Tzou, M.-S.; Johnson, I. D.; Lipsicas, M. J. Am. Chem. Soc., 1985, 107, 7222.
16. Giannelis, E. P.; Rightor, E. G.; Pinnavaia, T. J. J. Am. Chem. Soc., 1988, 110, 3880.
17. Tzou, M.-S.; Pinnavaia, T. J. Catal. Today, 1988, 2, 243.
18. Teo, B.-K. In EXAFS Spectroscopy: Techniques and Applications; Teo, B.-K.; Joy, P. C., Eds.; Plenum: New York, 1981, p 13.
19. Teo, B.-K.; Antonio, M. R.; Averill, B. A. J. Am. Chem. Soc. 1983, 105, 3751.
20. Teo, B.-K.; Lee, P. A. J. Am. Chem. Soc. 1979, 101, 2815.
21. Wells, A. F. Structural Inorganic Chemistry, 5th ed.; Clarendon: Oxford, 1984.
22. Newnham, R. E.; de Haan, Y. M. Z. Krist. 1962, 117, 235.

RECEIVED April 25, 1989

Author Index

- Akber, Riaz A., 180
Banin, A., 407
Batlo, François, 310
Bishop, J. L., 407
Blake, David F., ix
Brewer, Thomas D., 455
Burns, Roger G., 262
Carle, G., 407
Cenens, Jos, 378
Coyne, Lelia M., 1,407
De Schryver, Frans C., 378
DeHart, John M., 190
Dickinson, J. T., 224
Freund, Friedemann, 310
Freund, Minoru M., 310
Fripiat, Jose J., 360
Gaffey, Susan J., 94
Gartia, R. K., 180
Grandjean, Jean, 396
Guthrie, George D., Jr., 75
Hasan, Fouad A., 190
Johnston, Clifford T., 432
Krishnan, Kannan M., 54
Landau, Steven D., 455
Langford, S. C., 224
Laszlo, Pierre, 396
Lear, Paul R., 330
Lofgren, Gary E., 190
Mackinnon, Ian D. R., 32
McKeever, Stephen W. S., 1,166
Moini, Ahmad, 455
Orenberg, J., 407
Pinnavaia, Thomas J., 455
Prescott, John R., 180
Scattergood, T., 407
Schoonheydt, Robert A., 378
Sears, Derek W. G., 190
Sherman, David M., 284
Solberg, Teresa C., 262
Steele, Ian M., 150
Stucki, Joseph W., 330
Sweeting, Linda M., 245
Teo, Boon-Keng, 455
Tzou, Ming-Shin, 455
Veblen, David R., 75
White, William B., 118
Wright, J. C., 135

Affiliation Index

- Ecole Polytechnique, 432
Hebrew University, 407
Johns Hopkins University, 75
K.U.Leuven, 378
Lawrence Berkeley Laboratory, 54
Manipur University, 180
Massachusetts Institute of Technology, 262
NASA Johnson Space Center, 190
NASA-Ames Research Center, ix,310,407
Oklahoma State University, 1,166
Pennsylvania State University, 118
Rensselaer Polytechnic Institute, 94
San Francisco State University, 407
San Jose State University, 1,407
State University of New York
at Stony Brook, 407
Towson State University, 245
United States Geological Survey, 284
Université de Liège, 396
University of Adelaide, 180
University of Arkansas, 190
University of Chicago, 150
University of Florida, 432
University of Illinois, 330, 455
University of Queensland, 32
University of Wisconsin—Madison, 135
University of Wisconsin—Milwaukee, 360
Washington State University, 224

Subject Index

A

- Alkaline earth oxides, laser-excited rare earth luminescence, 143–144
- Allan Hills A77214, cathodoluminescent properties, 198f,204
- Analysis optimization of thin-film analysis criteria for measurement of instrument performance, 47
- factors limiting element detection, 47
- improvements in statistics, 47
- Analytical electron microscope advantages and disadvantages, 32–33
- analytical procedure, 38–39
- applications, 32–33
- commercial types, 38
- development, 33
- rastered beam mode, 38–39
- static beam mode, 38
- X-ray generation volume for thin film, 33,34f,35
- Anhydrous carbonate minerals, VNIR spectral properties, 96,97f,98
- Anorthite, alterations, 158
- Antarctic meteorites, thermoluminescent properties, 214,215f
- 9-Anthryl-methanol, triboluminescent spectrum, 257,258f
- Apparent layer thickness, determination by high-resolution TEM images, 88,90f,91
- Atomic site, determination using channeling and related effects, 65–71
- Atom location by channeling-enhanced microanalysis applications, 48
- comparison to X-ray diffraction, 49r
- description, 48
- examples, 48–49
- monitoring, 50

B

- Barwell, cathodoluminescent properties, 199f,204–205
- Biotite, TEM input structure, 81
- Biotite–chlorite intergrowths, high-resolution TEM image, 85,87f
- Bishunpur, cathodoluminescent properties, 197f,200f,203
- Bremervorde, cathodoluminescent properties, 199f,204–205
- Bulk elemental analysis, schematic representation of secondary X-ray production, 33,34f

C

- Candoluminescence and radical recombination luminescence
- flame-excited and radial recombination excited emission spectra, 129,130f
- minerals, 127–131
- qualitative observations, 127,128f
- recombination energies for active species, 127,128f
- schematic representation of experimental setup, 127,128f,129
- temperature dependence of intensity of emission spectra, 129,131f
- Carbonate skeletons
- characterization by VNIR, 95–112
- chemical and mineralogical composition, 94
- Catalysis of H₂–D₂ exchange on Al₂O₃ and MgO
- activation by heating under vacuum, 20
- dual-vacancy site, 21–22
- mechanism, 21–22
- V₁ centers, 20–21
- Catalysis of H₂–D₂ exchange on silica catalytic site, 16
- ionizing radiation, 15–16
- mechanism, 16–19
- reaction site, 19
- stoichiometric reaction application, 16
- uniqueness of reaction, 15
- Catalytic activity
- acid–base influences, 13–14
- effect of ionizing radiation, 15–16
- geometric influences, 11–13
- oxidizing–reducing entities, 14
- structural determinants, 11–14
- Catalytic site, identification, 16
- Cathodoluminescence
- corundum phase, 162
- definition, 150
- dependence on mineral type, 153
- diamonds, 162
- diopside, 162
- enstatite, 153–154,155f,156
- fassaite, 162
- feldspar, 156–158
- forsterite, 158–159,160f,161
- glasses, 162
- grossular garnet, 162
- hibonite, 161–162
- instrumental techniques, 151–152
- limitations, 150–151
- mellilite, 162
- oldhamite, 161
- other minerals, 161–162

- Cathodoluminescence—*Continued*
 relation between Mg and Al, 157–158
 spinel phase, 162
 types of meteorites observed, 151
- Cathodoluminescence of meteorites
 Allan Hills A77214, 198f,204
 Barwell, 199f,204–205
 Bishunpur, 197f,200f,203
 Bremervorde, 199f,204–205
 Chainpur, 198f,203–204
 Dhajala, 199f,204
 Hedjaz, 199f,204
 Krymka, 197f,203
 Ngawi, 198f,200f,204
 Semarkona, 197f,200f,201,203
 type 3 ordinary chondrites, 196–205
- Cation-exchanged montmorillonites, near-IR spectroscopy, 410–427
- Cation site distribution by thin-film analysis, description, 48,49r,50
- C6 diamond residues
 fine structure of C–K edges, 59,61f
 low-loss plasmon spectrum, 59,60f
 microdiffraction patterns, 59
- Chainpur, cathodoluminescent properties, 198f,203–204
- Characterization of lithosphere, identification of mineral types, 1
- Charge-compensating exchangeable cations, geometric effects on catalytic activity, 12–13
- Charge distribution analysis
 apparatus, 315,316f,317
 appearance–disappearance of positive surface 325–327
 capacitance vs. temperature, 325,326f
 change of force vs. electric field, 320,321–322f
 conductivity vs. temperature, 325,326f
 description, 314–315
 equipotential points vs. temperature, 320,323f
 experimental procedure, 315,316f,317
 force determination, 315
 formation of peroxy entities, 327–328
 measurement examples, 317,318f
 polarization determination, 314
 polarization vs. temperature, 317,319f,320
 reversible appearance–disappearance of mobile charge carriers, 325–327
 sample arrangement for impedance measurements, 320,324f
- Charge transfer conversion reaction, 312
 validity, 312
- Chlorite
 high-resolution TEM images, 82,84f,85
 TEM input structure, 81
- Chloritelike hydroxy-interlayered clay, structure, 458,459f
- Chondrites
 cathodoluminescence of type 3 materials, 196–205
 comparison of chondrule mesostases, 201,202f
 description, 191
 effect of annealing on sensitivity, 205,208,210f
 effect of metamorphism on sensitivity, 205,207f
 establishment of petrologic types, 191
 glow curve, 194–195,205–209
 laboratory studies of induced thermoluminescent properties, 205–212
 origin, 191–192
 photomosaics of type 3 materials, 196,197–200f,201
 photomosaics of type 3.7–5 materials, 196,199f
 thermoluminescent peak temperature vs. width, 194,195f
 thermoluminescent sensitivity vs. petrologic type, 192,193f,194
- Chondrules, thermoluminescent properties, 214,216f,217
- Chromia-pillared montmorillonites
 chemical and physical properties, 461,462r
 conversion of cyclohexane to benzene, 461,462f,463
 Cr-edge extended X-ray absorption fine structure spectrum, 463,465f
 determination of interatomic distances, 463,464–466f
 Fourier-transform data, 466f
 structure–reactivity relationships, 461,462r,f,463,464f
 uptake of cyclohexane, 463,464f
- Chromite spinels, electron energy-loss spectra, 66,70f
- Clay(s)
 large surface areas, 360–361
 surface activities, 360–375
 surface probing via fluorescence spectroscopy of proflavine, 379–394
 use as mineral catalysts, 9–10
- Clay mineral(s)
 activity vs. quantity, 408
 charge-transfer complexities, 361
 common feature, 361
 description, 6,78
 effect of charge-compensating exchangeable cations on swelling properties, 12
 energy storage, 6–7
 examples of energy storage in nature, 7
 factors influencing reactivity determinants, 408–409
 features influencing surface chemistry, 7

- Clay mineral(s)—*Continued*
 high-resolution TEM simulation and imaging, 80–81
 importance, 6
 problems with electron microscopic study, 78
 structures, 78,79f,80
 types of charges, 361
 use as multisite catalysts, 408
 use of double-layer theory to describe colloidal chemistry, 361–362
- Clay mineral interfaces, high-resolution liquid-phase NMR spectroscopy, 396–405
- 1:1 clay structures, description, 285,288
- 2:1 clay structures
 generalized structure, 285,286f
 Mossbauer spectrum, 285,287f
 octahedral sheet, 285,286f
- CO chondrites, thermoluminescent properties, 217,218f
- Computer image simulation, TEM, 77–78
- Condensation concept for polyelectrolytes, description, 403
- Corundum, cathodoluminescence, 162
- Covalently bonding centers, effect on catalytic activity, 14
- Coyne model, mineral energetics, 8
- Crystal chemistry of Fe-bearing clays
 1:1 clay structures, 285,288
 2:1 clay structures, 285,286–287f
- Crystalline materials, dependence on orientation of incident beam, 65–66
- Crystallography, correlation between crystal structure and triboluminescence, 249,252,253–254r
- Crystal structure and luminescence of insulator phosphors
 broad-band emitters, 124,125–126f,127
 emission spectrum for Cr³⁺-activated spinel, 122,123f,124
 emission spectrum for Mn²⁺, 124,125f
 Fe³⁺ luminescence, 127
 Mn²⁺ emission wavenumber vs. interatomic distance, 124,126f
 narrow-band emitters, 122,123f,124
 Tanabe–Sugano diagram for configuration, 122,123f
 Tanabe–Sugano diagram for d⁵ configuration, 124,125f
- Cyclohexane
 conversion to benzene over chromia-pillared montmorillonites, 461,462f,463
 uptake by chromia-pillared montmorillonites, 463,464f
- D
- Deformation, during emission, 225,226f,227
- Deformation luminescence, description, 245
- Deuterium NMR spectroscopy, static and microdynamic properties of hydrocarbon chains, 399
- Deuterium nucleus
 residual splitting, 398
 spin states, 398
- Deuterium nucleus in heavy water, longitudinal relaxation rates, 404
- Deuterium relaxation rates, source of microdynamic information, 398–399
- Dhajala, cathodoluminescent properties, 199f,204
- Diagenetic reactions, importance of water and organic compounds, 94
- Diamonds, cathodoluminescence, 162
- Diopside, cathodoluminescence, 162
- Dolomite
 crystal structure in [1210] orientation, 66,67f
 dependence of X-ray emissions on incident beam orientation, 66,68–69f
- E
- Electrical discharge, example of electron bombardment, 235
- Electron(s)
 emission during deformation, 225,226f,227
 emission during fracture, 227,229–230,233,235
 emission following fracture, 235,236f,237,238f
- Electron energy-loss spectroscopy
 atomic site and species determination, 65–71
 edge formation, 55,57
 edge shapes, 57–58
 electron scattering, 57
 experimental procedure, 71–72
 fine structure analysis, 58–63
 fundamentals, 55–58
 interpretation of energy loss near edge structures, 58
 interpretation of extended energy loss fine structure, 58
 ionization edge threshold, 58
 microanalysis, 62,64–65
 regions of spectrum, 55
 representative spectrum, 55,56f
- Electron-hole pairs
 nonradiative charge trapping processes, 168
 phenomenological model of production and trapping, 167–168,169f
- Electron-hole recombination process
 description, 171
 examples, 171,173f,174
 localized transition model, 175,176f

- Electron-hole recombination process—Continued**
 mechanism, 171,174
 phenomenological representation, 171,172f
 spectra of sample after room-temperature irradiation, 175,176f
- Electronic energy structure of minerals, discussion, 3–8**
- Electronic excitation, defect creation, 167**
- Electronic structures of Fe sites in clays and oxides**
 Bloch wave functions, 288–289
 energies for Fe^{3+} ligand field states, 290,293t,295–296
 $\text{Fe}^{2+} \rightarrow \text{Fe}^{3+}$ charge transfer, 296,299–305
 Fe^{2+} in octahedral coordination, 296,298f
 Fe^{3+} in octahedral coordination, 290–296
 Fe^{3+} in tetrahedral coordination, 296,297f
 molecular orbital diagram for charge transfer, 303,304f,305
- Mossbauer spectra showing fit to sites, 299,301f**
 near-UV to visible region spectra, 290,292f
 optical spectra showing charge transfer, 299,300f
 potential energy surfaces describing charge transfer, 299,302f,303
- Schrödinger equation, 288**
- Slater determinant, 288**
- spin-unrestricted molecular orbital diagram, 290,291f**
 theoretical preliminaries, 288–290
 visible-to-near-IR spectra, 293,294f
- Electron-induced X-ray emission in crystalline materials, orientation dependence, 48**
- Element loss during thin-film analysis determination, 45**
 effect of temperature, 45,46f
- Elemental precision of thin-film analysis**
 k factor, 41–42
 test via element loss under analytical conditions, 44–45
 test via stoichiometry and structural formula, 44
- Emission following fracture**
 example for granite, 235,236f,237
 example for MgO , 237,239f
 example for olivine, 237,240f,241
 example for sodium trisilicate glass, 237,238f
 mechanism, 235
- Energy-analyzing devices**
 principle of operation, 71
 samples, 72
 spectrum formation, 71–72
- Energy relaxation**
 classes of energy transfer, 138–139
- Energy relaxation—Continued**
 factors influencing rate of energy loss to lattice, 138
 mechanisms, 138
- Energy storage following irradiation of minerals**
 electron-hole pairs, 167–168,169f
 electronic excitation, 167
 excitons, 168,169f,170
 prompt luminescence, 170–171
- Energy transfer from interlayer to lattice in clays**
 electron transfer between coadsorbed species, 373,374–375f
 evidences for electron transfer from surface to bulk, 368,370
 quenching mechanism, 370–371,372f,373
- Energy-transfer processes of phosphor grain excitation mechanism, 122**
 schematic representation, 120,121f,122
- Enstatite cathodoluminescence**
 cause of colors, 154
 discrepancies in correlation of visible color, 156
 quantitative measurement of intensity, 154,155f,156
 spectra, 154,155f,156
 visual description, 153–154
- Experimental protocols for thin-film analyses for mineral characterization**
 analysis optimization, 47
 cation-site distribution, 48,49t,50
 elemental precision, 41–46
 qualitative analysis, 39–40
 quantitative analysis, 40
 spatial resolution, 40–41
- F**
- Faraday balance technique, advantages, 314**
- Fassaite, cathodoluminescence, 162**
- Fast electron–thin foil interaction, microanalytical characterizations at high spatial resolutions, 54–72**
- Fe-bearing clays**
 crystal chemistry, 284–288
 electronic structures of Fe sites, 288–305
 role in redox processes in nature, 284
- Fe-bearing oxides, role in redox processes in nature, 284**
- Fe-bearing smectite clay minerals**
 coefficients for best-fit polynomials for layer charge vs. Fe^{2+} content, 353,354t
 differentiating Fe^{2+} and Fe^{3+} , 340,341t
 drying, 338,339f,340
 effect of oxidation state on properties, 340,342–352

Fe-bearing smectite clay minerals—

Continued

- effect of structural Fe on properties, 342,343*r*
- Fe²⁺–Fe³⁺ ratio determination by
 - Mossbauer spectroscopy, 340,341*r*
 - inverse magnetic susceptibility vs. temperature, 346,350,351*f*
- layer charge, 353,354*f*
- mechanism of ferromagnetic coupling, 346,349*f*
- methods of preparation and characterization, 332–341
- Mossbauer spectra, 350,352*f*
- nonexchangeable Na⁺ vs. Fe²⁺ content, 342,345*f*
- optical spectra, 342,346–349
- redox mechanisms, 350,353,354*f,t*,355
- reducing agents, 332,333*r*,334–335
- removal of excess reducing agent and salt, 335,336–337*f*,338
- reversibility of redox process, 350
- specific surface area vs. Fe²⁺ content, 342,341*f*
- surface area and interlayer forces, 342,344–345*f*
- vibrational potential energy vs. configurational coordinate for electron transfer, 346,347*f*
- visible absorption spectra, 346,348–349*f*
- X-ray diffractogram, 342,344*f*
- Feldspar
 - characterization, 194,196
 - classifications, 180
 - contour diagrams, 183,186*f*
 - description, 180
 - effect of annealing on sensitivity, 208,211*f*,212
 - laboratory studies of induced thermoluminescent properties, 205–212
 - methods for structure determination, 188–189
 - role in establishment of petrologic types of chondrites, 192,194
 - ternary diagram of conventional nomenclature, 180–181,182*f*
 - thermoluminescent spectra, 181
 - three-dimensional spectra, 183,184–185*f*
- Feldspar cathodoluminescence
 - occurrence in meteorites, 156
 - spectra of lunar samples, 156–157
- Feldspathic materials, characterization, 194,196
- Fe sites, electronic structures in clays and oxides, 288–305
- Fe sites in clay minerals
 - applications to electron transport, 305,307
 - applications to photochemistry, 305,306*f*,307

- Fe sites in clay minerals—*Continued*
 - applications to reactivity, 305,307
 - areas for future investigation, 307
- Fine-structure analysis by electron energy-loss spectroscopy
 - C₆ diamond residues, 58–59*f*,60–61*f*
 - determination of oxidation states of fourth-period transition metals in minerals, 59,62,63*f*
- Fluorescence intensity of proflavine on clays
 - calculated surface areas of clays, 391,392*r*,393
 - determination of surface volume, 394
 - excitation spectra, 383,384*f*
 - experimental materials and procedures, 382
 - extinction coefficients and band maxima, 379,382,384*r*
 - maximum values of quantum yields vs. loadings, 383,387,388*r*
 - parameters determining evolution, 388–389
- Perrin equation, 393–394
- Perrin plots, 389,390*f*,391
- quantum yields, 383,385–387*f*
- spectra on clay vs. in aqueous solution, 383,385*f*
- Fluorites
 - laser-excited rare earth luminescence, 144–146
 - nature of defect equilibria, 144
 - relative site importance, 146
 - superionic conductivity, 144
- Force, determination, 315
- Formation-induced catalytic entity, H₂–D₂ exchange on Al₂O₃ and MgO, 20–22
- Forsterite cathodoluminescence
 - intensity vs. growth, 159,161
 - range of Cr peak position, 159,160*f*
 - recognition of compositional and growth factors, 161
 - spectral emission bands, 159,160*f*
 - visual color, 158–159
- Fourier-transform IR spectroscopy of kaolinite–hydrazine intercalate
 - controlled-environment spectra, 439,442*f*,443
 - effect of pressure on $\nu(\text{O–H})$ region, 434
 - experimental materials and procedures, 434
 - $\nu(\text{N–N})$ region, 446–451
 - position of kaolinite hydroxyl groups, 435,438*f*
 - projection of siloxane ditrigonal cavity of kaolinite, 443,445*f*
 - spectra, 435,438*f*,439,441*f*
 - vibrational bands, 435,437*t*,439,440*r*
- Fourth-period transition metals in minerals
 - L_{2,3} edges for Mn²⁺ and Mn⁴⁺, 62,63*f*
 - oxidation-state determination, 59,62,63*f*
- Fractoemission
 - applications, 224

Fractoemission—Continued

- association of fracture with high degree of electrical and chemical activity, 233
 - definition, 224
 - effect of visible photon intensities vs. fracture stages, 227,229
 - electrical discharge, 235
 - emission during deformation, 225,226f,227
 - emission during fracture, 227–235
 - emission following fracture, 235–241
 - experimental procedures, 225
 - general features from fracture in vacuum, 224–225
 - measurements of surface-charge variations, 233
 - photographs of fracture surfaces, 227,229,230f
 - potential relevance, 241–242
 - production of free-charge carriers, 233
 - scanning tunneling microscopic scans, 229,231–232f
 - types of emissions, 224
 - visible photons and positive ions measured by quadrupole mass spectrometer, 229,233,234f
- Fractoluminescent materials**
- definition, 249
 - spectra, 249,250f
- Fracture, emission, 227–235**

G

- Geometric influences, catalytic activity, 11
- Granite, emission after fracture, 235,236f,237
- Grossular garnet, cathodoluminescence, 162
- Ground-state neutrals
 - emission during deformation, 227
 - emission during fracture, 235
 - emission following fracture, 237,239–230f,241

H

- H₂–D₂ exchange
 - on Al₂O₃ and MgO, catalysis, 20–22
 - on silica, catalysis, 15–20
- H₂O
 - VNIR spectral properties, 98,101f
 - wavelengths and band assignments, 98,100f
 - wavelengths of fundamental modes, 98,99f
- Hedjaz, cathodoluminescent properties, 199f,204
- Heterogeneous promotion of chemical reactions, classes, 10
- Hibonite, cathodoluminescence, 161–162
- High-purity Ge detectors, advantages, 37

High-resolution imaging methods, TEM, 76–77

- High-resolution liquid-phase NMR spectroscopy of clay mineral interfaces
 - advantages, 397
 - experimental procedures, 397
 - nonidentity of longitudinal and transverse relaxation rates, 401
 - orientation of tactoids, 401–402
 - polarization of water molecules and surface acidity, 402–404
 - quadrupolar hydrated cations, 399–401
 - relaxation rates, 400–401
 - residual splittings, 399–400
 - restricted mobility within interlamellar space, 404–405
 - use of quadrupolar nuclei to probe local ordering, 398–399

High-resolution transmission electron

- microscopic images
 - apparent layer thickness determination, 88,90f,91
 - biotite–chlorite intergrowth, 85,87f
 - chlorite, 82,84f,85
 - correspondence between image and structure, 90f,91
 - illite–smectite, 85,88,89f
 - kaolinite, 82,83f
 - micas, 85,86–87f
 - serpentine, 82,83f

High-resolution transmission electron microscopic simulation and imaging of clay minerals

- formation of sheet silicates, 80
 - microscope parameters, 80–81
 - model input structures, 80
- Hydrazine**
- reducing agent for Fe-bearing smectite clay minerals, 335
 - vibrational bands, 439,440f
- Hydrazine–kaolinite intercalate, See Kaolinite–hydrazine intercalate**

I

- Illite, TEM input structure, 81
- Illite–smectite, high-resolution TEM image, 85,88,89f
- Inert-atmosphere reaction vessel, schematic representation, 335,336f
- Instrumental techniques for cathodoluminescence
 - consideration of optical path of instrument, 152
 - use of scanning electron microscope, 152
 - visual observation in luminescope, 151–152
- Insulator phosphors
 - crystal structure and luminescence, 122–127
 - description, 119

Interferogram, definition, 181,183
 Ionizing radiation, effect on catalytic activity, 15–16
 Iron cations in rock-forming minerals, Mossbauer spectroscopy, 262–279

K

Kaolinite
 composition of interlamellar region, 433
 high-resolution TEM images, 82,83f
 TEM input structure, 81
Kaolinite-hydrazine intercalate
 applications, 433
 effect of surface, 433–452
 gravimetric weight loss vs. pressure, 443,446,447f
 vibrational spectra, 433
 X-ray diffraction patterns, 446,447f
KCl, laser-excited rare earth luminescence, 146
k factors for minerals
 definition, 41
 determination, 41
 experimental plots, 42,43f,44
 plots vs. collection time and temperatures, 45,46f
Krymka, cathodoluminescent properties, 197f,203

L

Laser-excited rare-earth luminescence
 alkaline earth oxide study, 143–144
 applications, 135–136
 capabilities, 140,143
 excitation spectra, 140,141–142f
 experimental procedure, 140
 fluorite study, 144–146
 KCl study, 146
 perovskite materials study, 146
 probe ion in minerals, 139–140,141f
 probe ion spectra, 136,137f,138–139
Layer silicates, role in catalysis of organic reactions, 396
Lewis acid sites, effect on catalytic activity, 13–14
Lightning, definition, 249
Lipids, VNIR spectral properties, 102,103f
Lithosphere, characterization, 1
Long-wavelength electromagnetic radiation
 emission during deformation, 227
 emission during fracture, 235
Low-resolution imaging methods, TEM, 76–77
Luminescence of minerals
 activators, 119–120
 candoluminescence and radical recombination luminescence, 127–131

Luminescence of minerals—Continued
 crystal structure and luminescence of insulator phosphors, 122–127
 energy-transfer processes, 120,121f,122
 insulator phosphors, 119
 material categories, 119
 molecular phosphors, 119
 planetary surface, 129,132–133
 semiconductors phosphors, 119
 Ti⁴⁺ luminescent spectrum, 120,121f
Lunar luminescent phenomena
 contradictions, 132
 energetic particles emitted during solar flares, 132
 red emission events, 132–133

M

Melilite, cathodoluminescence, 162
Metal oxide pillared clay, structural characterization, 458
Meteorites, types, 151
Meteorite thermoluminescence, See Thermoluminescence of meteorites
Meteoritic minerals showing cathodoluminescence
 enstatite, 153–154,155f,156
 feldspar, 156–158
 forsterite, 158–159,160f,161
 list, 153
 other minerals, 161–162
Meteoritic plagioclase
 cathodoluminescence, 157
 relation between Mg and Al, 157–158
Methylene blue, use in surface-area measurement, 366
MgO, emission after fracture, 237,239f
Micas, high-resolution TEM image, 85,86–87f
Microanalysis by electron energy-loss spectroscopy
 calculation of partial ionization cross sections, 64–65
 determination of absolute concentration of atoms, 62,64
 error, 65
 light element quantification, 62
 minimum detectable mass, 65
 minimum detectable mass function, 65
Microcrystalline materials, dependence on orientation of incident beam, 65–66
Microorganisms, reducing agent for Fe-bearing smectite clay minerals, 334
Mineral(s)
 application of triboluminescence, 259
 capacity for long-term electronic energy storage, 5–6
 energetics, 4
 energy-storage capacity, 6–7

Mineral(s)—Continued

- energy-storage mechanisms, 167–172
- environmental history, 3–4
- excited-state structure, 5
- exciton creation, 5
- form, impurities, and imperfections, 3
- prevalence of point defects, 6
- promotion of surface reactions, 6
- relaxation, 5
- thermoluminescent processes, 171–177
- Mineral catalysis, applications and mechanisms, 9
- Mineral characteristics
 - probe ions in minerals, 139–140,141f
 - study by laser-excited rare earth luminescence, 135–146
- Mineral characterization
 - electron energy-loss spectroscopy, 54–72
 - thin-film elemental analyses, 35–50
- Mineral luminescence, *See* Luminescence of minerals
- Mineral-mediated chemistry
 - natural routes to organic synthesis, 4–8
 - role of active sites, 8–22
- Mineral-mediated reaction, photoassistance—photocatalysis, 4
- Mineral-sensitized photochemistry, comparison to organic photochemistry, 5
- Mineral surface chemistry, effect of interrelationships between site types, 14–15
- Molecular phosphors, description, 119
- Moonstones, thermoluminescent emission, 184–186f,187–188
- Mossbauer spectroscopy of iron cations in minerals
 - correlations, 279
 - crystal structure and spectral parameters, 263,266–267t
 - ferrous vs. ferric isomer shifts, 274,276–277t,278f,279
 - isomer shift vs. average metal–oxygen bond lengths, 269,270f
 - isomer shift vs. crystal structure parameters, 269–273
 - isomer shift vs. polyhedral volume, 271,273f
 - isomer shift vs. quadrupole splitting, 263,267–268f,269
 - isomer shift vs. volume per oxygen, 269,271,272f
 - mineral formulas, 263,264–265t
 - quadrupole splitting vs. bond length deviation, 271,274,275f
 - quadrupole splitting vs. crystal structure parameters, 271,274,275f
- Muscovite, TEM input structure, 81

N

- Near-IR reflectance analysis, experimental procedure, 409–410
- Near-IR spectroscopy of cation-exchanged montmorillonites
 - absorbance vs. analytically measured water content, 418,420f,422f
 - absorbance vs. measured water content, 418,421f,423f
 - correlation coefficients of total iron content vs. wavelength, 415t,417f
 - data analysis, 412,413–414f,415
 - dependence of spectra on iron content, 415–419,424
 - dependence of spectra on water content, 418,420–423
 - humidity equilibration, 411–412
 - iron content of clays, 410t
 - pellet preparation, 411
 - reflectance spectroscopy, 411–412
 - regression lines relating absorbance to measure iron, 415,418,419f
 - spec.ra, 415,416f
 - spectra in region of water, 418,420f,425–427
- Ngawi, cathodoluminescent properties, 198f,200f,204
- NMR spectroscopy, quadrupolar hydrated cations, 399–401
- Nonbiogenic carbonates, VNIR spectroscopy, 95–112

O

- Octahedral sheet
 - definition, 79
 - T–O layer, 79
 - T–O–T layer, 79–80
- OH⁻, VNIR spectral properties, 98,101f
- Oldhamite, cathodoluminescence, 161
- Olivine
 - cathodoluminescence, 158–159
 - emission after fracture, 237,240f,241
- Organic compounds, VNIR spectral properties, 98,99–100t,102,103f
- Organic compounds in carbonate skeletons
 - detection limits, 106
 - occurrence, 102
 - sources, 104
 - VNIR spectral properties, 104,105f,106
- Organic molecule–mineral surface interaction, characterization efforts, 432–433

- Organic photochemistry, comparison to mineral-sensitized photochemistry, 5**
- Organic pigments, VNIR spectral properties, 102,103f**
- Organic surface reactivity, effect of mineral energetic factors, 6–7**
- Orientation of tactoids**
determination of residual anisotropy, 402
determination of residual splitting, 402
formation, 401
residual splitting vs. amount of suspended clay, 401
- O⁻ states**
charge distribution analysis, 315–328
delocalization, 311
detection by electron paramagnetic resonance, 313
difficulties in electrical conductivity and impedance measurements, 314
formation, 310
oxidation agents, 313
paramagnetism, 314
positive holes, 313
redox reactions with atomic H, 311
terminology, 311–312
- Oxidizing–reducing entities, effect on catalytic activity, 14**
- P**
- Partial ionization cross sections, calculation methods, 64–65**
- Perovskite materials, laser-excited rare earth luminescence, 146**
- Peroxy anions, definition, 311–312**
- Peroxy entity**
charge distribution analysis, 315–328
definition, 312
detection, 313–314
dormant O⁻ centers, 311–313
formation, 312
thermal dissociation, 313
- Petrologic types of chondrites, establishment, 192,194**
- Photoluminescent materials, spectra, 249,251f**
- Phyllosilicate clays**
formation, 397
structure, 397
- Pillared clays, surface acidity, 368,369f**
- Planetary surfaces, luminescent features, 129,132–133**
- Point defects in minerals**
formation, 139
measurement, 139–140,141f
- Polarization, determination, 314**
- Polyelectrolytes, condensation concept, 403**
- Polyoxocations**
structure, 458,460f
thermal dehydroxylation to metal oxide aggregates, 458
- Polysaccharides, VNIR spectral properties, 102,103f**
- Positive holes, definition, 313**
- Positive ions**
emission during fracture, 229,233,234f,235
emission following fracture, 237,238f
- Primitive meteorites, description, 151**
- Probe ions in minerals**
excitation spectrum of CaO, 140,141–142f,143
measurement of point defects in minerals, 139–140,141f
use of site-selective laser spectroscopy, 140,141–142f,143
- Probe ion spectra for laser-excited rare earth luminescence**
crystal field splittings, 136,137f,138
energy relaxation, 138–139
- Proflavine**
factors influencing concentration effect, 379
fluorescence, 379
fluorescence intensity on clays, 382–394
positions of absorption and fluorescence bands in aqueous solution and on clays, 379,381f,382
structure, 379,380f
surface equilibrium, 379
- Proteins, VNIR spectral properties, 102,103f**
- Protonic acid sites, effect on catalytic activity, 13**
- Q**
- Quadrupolar hydrated cations, NMR spectroscopy, 399–401**
- Quadrupolar nuclei, use in probing local ordering of clay mineral interfaces, 398–399**
- Qualitative analysis by thin films, experimental protocol, 39–40**
- Quantitative analysis by thin films, experimental protocol, 40**
- R**
- Radiation-induced catalytic entity, H₂–D₂ exchange on silica, 15–20**
- Raman spectroscopy of kaolinite–hydrazine intercalate**
experimental materials, 434
experimental procedures, 434–435

Raman spectroscopy of kaolinite-hydrazine—*Continued*

intensity ratio vs. temperature, 448,450f

 $\nu(\text{N-N})$ region, 446–451,452f

spectra, 435,436f,439,441f

vibrational bands, 435,437t,439,440t

Residual anisotropy, determination, 402**Residual quadrupolar splitting, dependence**

on nature of interlamellar cations, 402–403

Residual splitting, determination, 402**S****Safranine-exchanged montmorillonite, surface**

composition, 364,366t

Self-trapped excitons

configuration, 168,169f

configuration in CaF_2 , 168,172f

defect formation process, 168,170

effects due to lattice disorder, 170

production, 168

transformation of concentric to eccentric

configurations, 168,169f

Semarkona, cathodoluminescent properties,

197f,200f,201,203

Semiconductor phosphors, description, 119**Serpentine**

high-resolution TEM images, 82,83f

TEM input structure, 81

Shergottites, thermoluminescent properties,

217,219,220f

Si(Li) detectors

Be windows, 36

description, 35–36

detection efficiency, 36–37

protection by thin films, 36

Site types, effect of interrelationships on

mineral surface chemistry, 14–15

Skeletal carbonates

description, 95

efficacy of grinding and bleaching in

removal of water and organics, 107,109

relationship between water and organics,

109,110f

VNIR spectroscopy, 95–112

Smectite(s)

factors influencing adsorptivity and

reactivity, 455

functional group reactivity, 455

TEM input structure, 81

Smectite clay

gallery exchange ions, 456

model of functional group reactivity, 456

schematic representation of surface

functional groups, 456,457f

Smectite clay minerals

composition and classification, 330,331f

definition, 330

Smectite clay minerals—Continued

role in chemical and physical property

determination, 330

variable oxidation states of iron in

crystal structure, 330–355

See also Fe-bearing smectite clay minerals**Sodium dithionite, reducing agent for**

Fe-bearing smectite clay minerals, 334

Sodium trisilicate glass, emission after

fracture, 237,238f

Spatial resolution by thin films,

experimental protocol, 40–41

Species determination using channeling and

related effects, 65–71

Spectroscopic studies of mineral structure,

considerations, 3–4

Spectroscopy

comparison between triboluminescence

and photoluminescence spectra,

251–252,255–258

determination of chemical and electronic

structure, 3

determination of reaction mechanisms and

transient intermediates, 3

Spinel, cathodoluminescence, 162**Structural determinants of catalytic activity**

covalently bonding centers, 14

examples, 11

geometric features, 11–13

Lewis acid sites, 13–14

oxidizing–reducing entities, 14

protonic acid sites, 13

Structure of clay minerals

structural family, 78–79

structural subunits of sheet silicates, 79t,80

Sucrose, triboluminescence spectrum, 249,250f**Superionic conductor, definition, 145****Superoxide, description, 313–314****Surface acidity**

pillared clays, 368,369f

swelling clays, 367–368,369f

Surface activities of clays

activity, 367–368,369f

charge or energy transfer from interlayer

to lattice, 368,370–375

tactoid concept, 362–367

Swelling, influencing factors, 12–13**Swelling clays, surface acidity, 367–368,369f****T****Tactoid concept**

availability of internal surfaces to dye

molecules, 364,366t,367

computer simulation of clay tactoid

formation, 362,363f

proton relaxation rate vs. solid content

in water for smectites, 364,365f

- Tactoid concept—Continued**
relaxation rate, 362
water associated with external contour, 362
- Tactoids formed by phyllosilicate gels,**
orientation under application of strong magnetic field, 401–402
- Thermally stimulated luminescence,**
determination of nature of participating defects in electrons, 235
- Thermoluminescence of meteorites**
advantages, 191
Antarctic meteorites, 214,215f
chondrules, 214,216f,217
CO chondrites, 217,218f
first observation, 191
laboratory studies of induced properties of chondrites and feldspar, 205–212
metamorphism-related variations in peak shapes, 194,195f
properties of feldspar, 194,196
sensitivity variations in chondrites, 192,193f,194
shergottites, 217,219,220f
shock studies, 212,213f,214
- Thermoluminescence of minerals**
electron-hole recombination, 171–176
localized transition model, 175,176f
vacancy–interstitial recombination, 175,176f,177
- Thin-film analysis**
advantage over conventional X-ray analysis, 33
schematic representation of secondary X-ray production, 33,34f
X-ray generation volume, 33,34f,35
- Thin-film elemental analyses for mineral characterization**
effect of take-off angle, 37–38
experimental protocols, 39–50
geometry and design, 37–38
high-purity Ge detectors, 37
instrumentation, 35–39
microscopes, 38–39
Si(Li) detectors, 35–37
- Three-dimensional thermoluminescent spectroscopy of minerals**
apparatus, 181
application of Fourier-transform spectroscopy, 183
design criteria, 181,183
disadvantages, 181
glow curve, 181
high potassic feldspar, 183,184–186f
intermediate alkali feldspars, 187
moonstones, 184–186f,187–188
sodic end members, 183
structure identification, 187–188
throughput advantage, 181
- Transmission electron microscope**
advantages and disadvantages, 75
attachments, 33
computer-image simulation, 77–78
high-resolution imaging methods, 76–77
imaging principles, 76–77
influencing factors, 75
introduction of clay minerals, 78,79x,80
low-resolution imaging methods, 76
- Transmission electron microscopy (TEM),**
high-resolution simulation and imaging of clay minerals, 80–81
- Triboluminescence**
application to minerals, 259
definition, 245
deformation luminescence, 245
effect of impurities, 255,256–257f
fractoluminescence, 249,250f
minerals, 245,246–248t
photoluminescence, 249,251f
spectrum of 9-anthryl-methanol, 257,258f
spectrum of sucrose, 249,250f
spectrum of uranyl nitrate hexahydrate, 257,258f
spectrum of wintergreen coated on sucrose, 255,256f
spectrum of WintOGreen Lifesavers, 255,257f
- Triboluminescent materials, properties,**
252,253–254t
- Tribophotoluminescence**
crystallography, 249,252,253–254t
mechanism, 249
spectroscopy, 252,255–258
structures of compounds, 249,252
- U**
- Uranyl nitrate hexahydrate,**
triboluminescence spectrum, 257,258f
- V**
- Vacancy–interstitial recombination**
emission from CaF₃ containing Mn, 176f,177
impurity emission, 175,177
preirradiation state of lattice, 175
- Valence-deficient oxygen species, effect**
on catalytic activity, 14
- V_i center**
description, 20
role in H₂–D₂ exchange, 20–21
- Visible and near-IR spectroscopy (VNIR)**
advantages, 96
background, 96–103
spectral properties of anhydrous carbonate minerals, 96,97f,98

Visible and near-IR spectroscopy (VNIR)—*Continued*

spectral properties of H₂O and OH⁻,
98,99–100,101f
spectral properties of organic compounds,
98–100,102,103f

Visible and near-IR spectroscopy of nonbiogenic carbonates

experimental materials, 95
experimental procedures, 95–96

Visible and near-IR spectroscopy of skeletal carbonates

effect of diagenetic processes on water
and organic compounds, 109,111

experimental materials, 95
experimental procedures, 95–96

organic matrices, 104,105f,106
relationship between water and

organic carbonates, 109
unanswered issues, 111–112

water, 106–107,108f

Visible photons

emission during deformation, 225,226f,227

emission during fracture, 227–228,233–235

emission following fracture, 235,236f,237

W

Washing apparatus for reduced clay
suspensions, schematic representation,
335,337f,338

Water in skeletal carbonates

bound H₂O and OH⁻, 106–107,108f
liquid H₂O in fluid inclusions, 106

Water molecules at clay interface, modes
of reorientation, 403–404

Water self-diffusion coefficient,
measurement, 404–405

Weathering, definition, 4

Wintergreen, triboluminescent spectra,
255,256f

WintOGreen Lifesavers, triboluminescent
spectra, 255,257f

Z**Zeolites**

geometric influences, 12–13

use as mineral catalysts, 9–10